

Mechanisms and Machine Science 62

Katia Lucchesi Cavalca
Hans Ingo Weber *Editors*

Proceedings of the 10th International Conference on Rotor Dynamics – IFToMM

Vol. 3

 Springer

Mechanisms and Machine Science

Volume 62

Series editor

Marco Ceccarelli

LARM: Laboratory of Robotics and Mechatronics

DICeM: University of Cassino and South Latium

Via Di Biasio 43, 03043 Cassino (Fr), Italy

e-mail: ceccarelli@unicas.it

Editorial Board Members

Alfonso Hernandez

Mechanical Engineering, University of the Basque Country, Bilbao, Vizcaya, Spain

Tian Huang

Department of Mechatronical Engineering, Tianjin University, Tianjin, China

Steven A. Velinsky

Mechanical and Aerospace Engineering, University of California Davis, Davis, California, USA

Yukio Takeda

Mechanical Engineering, Tokyo Institute of Technology, Tokyo, Japan

Burkhard Corves

Institute of Mechanism Theory, Machine D, RWTH Aachen University, Aachen, Nordrhein-Westfalen, Germany

This book series establishes a well defined forum for monographs, edited Books, and proceedings on mechanical engineering with particular emphasis on MMS (Mechanism and Machine Science). The final goal is the publication of research that shows the development of mechanical engineering and particularly MMS in all technical aspects, even in very recent assessments. Published works share an approach by which technical details and formulation are discussed, and discuss modern formalisms with the aim to circulate research and technical achievements for use in professional, research, academic, and teaching activities. This technical approach is an essential characteristic of the series. By discussing technical details and formulations in terms of modern formalisms, the possibility is created not only to show technical developments but also to explain achievements for technical teaching and research activity today and for the future. The book series is intended to collect technical views on developments of the broad field of MMS in a unique frame that can be seen in its totality as an Encyclopaedia of MMS but with the additional purpose of archiving and teaching MMS achievements. Therefore the book series will be of use not only for researchers and teachers in Mechanical Engineering but also for professionals and students for their formation and future work. Indexed in SCOPUS, Ei Compendex, EBSCO Discovery Service, OCLC, ProQuest Summon, Google Scholar and SpringerLink.

More information about this series at <http://www.springer.com/series/8779>

Katia Lucchesi Cavalca · Hans Ingo Weber
Editors

Proceedings of the 10th
International Conference
on Rotor Dynamics –
IFTToMM

Vol. 3

Editors

Katia Lucchesi Cavalca
Faculty of Mechanical Engineering
University of Campinas
Campinas, São Paulo
Brazil

Hans Ingo Weber
Mechanical Engineering Department
Pontifical Catholic University of Rio
de Janeiro
Rio de Janeiro, Rio de Janeiro
Brazil

ISSN 2211-0984 ISSN 2211-0992 (electronic)
Mechanisms and Machine Science
ISBN 978-3-319-99269-3 ISBN 978-3-319-99270-9 (eBook)
<https://doi.org/10.1007/978-3-319-99270-9>

Library of Congress Control Number: 2018951101

© Springer Nature Switzerland AG 2019

This work is subject to copyright. All rights are reserved by the Publisher, whether the whole or part of the material is concerned, specifically the rights of translation, reprinting, reuse of illustrations, recitation, broadcasting, reproduction on microfilms or in any other physical way, and transmission or information storage and retrieval, electronic adaptation, computer software, or by similar or dissimilar methodology now known or hereafter developed.

The use of general descriptive names, registered names, trademarks, service marks, etc. in this publication does not imply, even in the absence of a specific statement, that such names are exempt from the relevant protective laws and regulations and therefore free for general use.

The publisher, the authors and the editors are safe to assume that the advice and information in this book are believed to be true and accurate at the date of publication. Neither the publisher nor the authors or the editors give a warranty, express or implied, with respect to the material contained herein or for any errors or omissions that may have been made. The publisher remains neutral with regard to jurisdictional claims in published maps and institutional affiliations.

This Springer imprint is published by the registered company Springer Nature Switzerland AG
The registered company address is: Gewerbestrasse 11, 6330 Cham, Switzerland

Preface

Rotordynamics is an area of engineering which congregates a very well-defined community between science and technology. Huge part of power generation uses rotating machines, and engineering had an incredible development since the first steam energy devices. The International Federation for the Promotion of Mechanism and Machine Science (IFTToMM) opened to this community the possibility to present the advances in this area in a quadrennial conference: This resulted in 1982 in the first IFTToMM International Conference on Rotordynamic Problems in Power Plants. The importance of periodically exchanging new ideas and comparing experimental test rigs and field measurements cannot be underestimated. The evolution that took place can easily be followed comparing the papers published in the proceedings since that time. It was obvious to broaden the spectrum and the name became since 1986 IFTToMM International Conference on Rotordynamics. This conference turned out to be a reward for each of the countries and their cities (Tokyo 1986, Lyon 1990, Chicago 1994, Darmstadt 1998, Sydney 2002, Vienna 2006, Seoul 2010, Milano, 2014) for the efforts developing their own research groups on this subject.

Formal academic graduate programs started in Brazil in the late 60s. Only in the 70s, the binomial higher education and research, including hands-on activities in laboratories, started to change the teaching in engineering. UNICAMP, a young university at that time, was a pioneer in graduating engineers able to conceive, design, and construct their ideas. The first crisis of oil prices led to the development of a group handling rotating machines, building flywheels for energy storage, investigating hybrid power systems, and looking for other alternative solutions. In the beginning of the 80s, there was small group of people working in rotordynamics. And there were some recent huge power plants like Ilha Solteira, Jupiá, Itaipú: They needed engineers which could explain the phenomena appearing in a Francis and Kaplan turbines. UNICAMP was eager to put their graduate students to work on open problems in this area. The year was 1982 and the first meeting in Rome was also a good opportunity to start international academic cooperation with several European countries and young researchers on this area as well as engineers had their own cooperation with companies dealing with rotating machines. Several

young scientists then went to Europe to complete their PhD. One highlight in the 2000's was the Alfa II Project, led by Prof. Bachschmidt from Politecnico di Milano on Vibration, Control and Diagnostics (VICONDIA) that put together the Politecnico de Catalunia, DTU, PUC-Rio, UFRJ, University of Uberlândia, ISPJAE from La Habana (Cuba) and University of Concepcion (Chile). But there were several other cooperation programs between Brazilian research groups and, usually, European institutions.

This resulted in a well-developed research area in Brazil. In 1986, the biennial DINAME meeting was started, as a result of a cooperation with Germany, supported by the Alexander von Humboldt Foundation and Volkswagen Foundation investigating the dynamics of a hydraulic Francis turbine. This meeting keeps its tradition and is open to all dynamic problems in mechanical systems. The groups working with rotating machines spread out through the country, and you will find expertise in several applications like turbines, compressors, turbochargers, centrifuges, helicopter blades, dental drills, oil drill strings.

The Brazilian Committee responsible for organizing the present IFToMM Conference felt comfortable to propose Rio de Janeiro in 2018 as the next venue. And this proposal was approved by the IFToMM Rotordynamic Committee at the Milano Conference. The Brazilian Committee is honored to execute this mission. The committee is composed by specialists from several universities throughout the country that shared the burden to organize an important international event. The interaction with industry is the scope of the industry technical committee. The result of the initiative is the selection of 153 papers under 175 submissions, being therefore the second largest IFToMM Rotordynamic conference besides being the first one in Latin America.

The present four volumes printed by Springer Nature with approximately 153 papers reproduce the state of the art of the research throughout the world. These papers were carefully reviewed by two independent reviewers, and its quality as a publication was attested. Volume 1 will focus on bearings and seals, Volume 2 on condition monitoring, fault diagnostics, prognostics as well as dynamic analysis and stability, Volume 3 on active components and vibration control; blades, bladed systems, and impellers; modal testing and identification; nonlinear phenomena in rotordynamics; torsional vibration and geared system dynamics, and Volume 4 on some innovative applications from aero-engines; automotive rotating systems; balancing; electromechanical interactions in rotordynamics; fluid–structure interactions; hydro power plant; parametric and self-excitation; rotordynamics of micro-, nano- and cryogenic machines; turbochargers; uncertainties, reliability, and life predictions of rotating machinery; wind turbines and generators.

As chairwoman and as chairman of the conference, we did not spare efforts in trying to do the best for a successful conference. As we proposed to organize the meeting in 2014, Rio de Janeiro was putting all the effort in the Olympic Games. It was perfectly organized, and everybody was proud of it. It was a climax for the city. In these last two years, there were radical changes some for good like the fight against corruption, some for bad due to the failure in politics and losing control of several important aspects in the everyday life. But Rio is the “marvelous city”

where nature made its best to combine ocean and mountains, and we hope all of the participants will have the opportunity to enjoy it.

Both chairs of the Conference express their gratitude to the TC of Rotordynamics for the thrust and the opportunity given, to the efficient work of the reviewers, to all authors and their students giving reason for the existence of the Conference, to the unbearable support from our colleagues of the local committees. We also appraise the support of the rector of UNICAMP, of its Faculty of Mechanical Engineering and to FUNCAMP foundation for the unconditional support and help with the logistics. We also express our satisfaction for the sponsoring of BorgWarner, MTS Brazil, Siemens, and the funding agencies CNPq—National Council for Scientific and Technological Development and CAPES—Brazilian Federal Agency for Support and Evaluation of Graduate Education.

Katia Cavalca
Hans I. Weber

Acknowledgements

To Prof. Hans Weber, who introduced me to research and guided me through the rotordynamic area, for the partnership and thrust by the challenge to organize this meeting, with respect and admiration.

To Prof. Nicolò Bachschmid, my dear doctor degree advisor in the Polytechnic of Milan.

To the colleagues Gregory B. Daniel, Helio F. de Castro, Ricardo U. Mendes, Tiago H. Machado, and Eduardo P. Okabe, for their confidence and friendship, besides the hard work done in finalizing the articles for publishing.

To my dear students to play a so important role and meaning in my professional and personal life.

To my beloved family, my husband Franco and my daughter Bianca, for the unconditional support, affection, and the everyday inspiring presence in my life.

Katia

To Kurt Magnus and the colleagues at the Institute of TU München where I acquired between 1968 and 1971 the fertile soil to let my own initiative in research grow. To some special friends from that time Peter C. Müller, H. H. Müller Slany, Gerhard Schweitzer.

To friends which were relevant in finding my way to rotordynamics, Robert Gasch, Rainer Nordmann, Michel Lalanne

To my students, the main reward of advising research is the success of the students, our family broad sense. To Francisco Paulo Lepore, my first PhD student and reason of success in the 70s of the group at UNICAMP (we called it GEPROM). To Ilmar Santos, dear student, friend, and colleague. To Katia Cavalca and her incredible capacity of aggregate and leading their students.

To Djenane Pamplona who shares profession and family, for the constant support.

Hans

Contents

Active Components and Vibration Control

Application of Genetic Algorithm for Synthesis of H_∞ Controllers for Active Magnetic Bearing Systems	3
Alican Sahinkaya and Jerzy T. Sawicki	
An Active Elastic Support/Dry Friction Damper: New Modeling and Analysis for Vibration Control of Rotor Systems	19
Siji Wang, Mingfu Liao, Mingbo Song, and Yingge Xu	
Identification of Crack and Internal Damping Parameters Using Full Spectrum Responses from a Jeffcott Rotor Incorporated with an Active Magnetic Bearing	34
Nilakshi Sarmah and Rajiv Tiwari	
Active Control of Rotor Supported by Faulting Journal Bearing	49
Matheus Freire Wu, Tiago Henrique Machado, and Katia Lucchesi Cavalca	
Control of Flexible Rotor Vibration with Flexibly Mounted Active Magnetic Bearings	65
Chris Lusty, Nicola Y. Bailey, and Patrick S. Keogh	
Reduction of Rotor Vibration Amplitude Using PID Tuning Methods	74
Leonardo Biagiotti Saint Martin, Diogo Stuani Alves, Ricardo Ugliara Mendes, and Katia Lucchesi Cavalca	
Experimental Validation of Angular Viscoelastic Dynamic Neutralizers Designed for Flexural Vibration Control in Rotating Machines	89
Danielle Raphaela Voltolini, Samuel Kluthcovsky, Eduardo Márcio de Oliveira Lopes, and Carlos Alberto Bavastri	

Active Control of Rotating Machinery Under Rotor-Stator Contact Conditions	107
Patrick S. Keogh, Chris Lusty, Nicola Y. Bailey, and Fawaz Saket	
Blades, Bladed Systems and Impellers	
Applying Compressed Sensing to Blade Tip Timing Data: A Parametric Analysis	121
Raphael P. Spada and Rodrigo Nicoletti	
Nonlinear Transverse and In-Plane Vibrations of a Thin Rotating Disk	135
Xiang-lin Wu, Ying-hou Jiao, Zhao-bo Chen, and Wen-sheng Ma	
Stiffening Effect and Dry-Friction Damping of Bladed Wheel Model with “Tie-Boss” Couplings - Numerical and Experimental Investigation	148
Luděk Pešek, Ladislav Půst, Petr Šulc, Pavel Šnábl, and Vitězslav Bula	
Parametric Study of the Effects of Varying the Airfoil Section, the Chord and Pitch Distributions Along the Propeller Blade	163
Kamal A. R. Ismail and Célia V. A. G. Rosolen	
Stability Analysis of a Cracked Blade Coupled with a Rigid Rotor	178
Bruno R. F. Rende, Izabela B. da Silva, Tobias S. Morais, Aldemir Ap. Cavalini Jr., and Valder Steffen Jr.	
Effects of Twist Angle on Rubbing Induced Vibration Responses of Blade	193
Hui Ma, Tong Yang, Shiyu Liu, Qi Sun, and Bangchun Wen	
Blade Modal Analysis by Means of Continuous Optical Fiber Sensors	205
Paolo Pennacchi, Gabriele Cazzulani, Martina Chieppi, and Andrea Colombo	
Modal Testing and Identification	
Identification of Coupling Parameters in Flexibly Coupled Jeffcott Rotor Systems with Angular Misalignment and Integrated Through Active Magnetic Bearing	221
R. Siva Srinivas, R. Tiwari, and Ch. Kannababu	
Model-Based Identification of Rotor-Bearing System Parameters Employing Adaptive Filtering	236
Eduardo Moraes Coraça and Milton Dias Junior	

Problems of Rotordynamic Modeling for Built-Up Gas Turbine Rotors with Central Tie Rod Shaft 250
 Konstantin Shaposhnikov and Chuang Gao

A Preliminary Experiment to Excite and Identify Modal Frequencies of a Rotor in the Rotating Frame of Reference 265
 Sudhakar Gantasala and Jan-Olov Aidanpää

Auto Resonance Based Identification of Rotating Systems 278
 Netanel Ariel, Eyal Setter, Adi Minikes, Solomon Davis, and Izhak Bucher

Modal Testing of a Full-Scale Rotating Woven Composite Fan Using Piezoelectric Excitation 291
 Antoine Mabilia, Claude Gibert, Fabrice Thouverez, Edouard De Jaeghere, Lionel Sanchez, and Laura Giovannoni

Kriging-Based Surrogate Modeling for Rotordynamics Prediction in Rotor-Bearing System 306
 Mateus P. F. Barbosa and William M. Alves

Nonlinear Phenomena in Rotordynamics

A Rotordynamics Model for Rotary Drillstring with Nonlinear Interactions in a 3D Well 325
 Khac-Long Nguyen, Quang-Thinh Tran, Marie-Ange Andrianoely, Lionel Manin, Stéphane Menand, and Régis Dufour

Dynamic Behavior of a Rotor-AMB System Due to Strong Base Motions 340
 C. Jarroux, J. Mahfoud, R. Dufour, F. Legrand, B. Defoy, and T. Alban

Computational Analysis of Nonlinear Dynamics of a Multi-disk Rotor-Bearing-Brush Seal System 350
 Yuan Wei, Zhaobo Chen, Yinghou Jiao, and Shulin Liu

Numerical Analysis of the Dead-Band Clearance Effect on the Vibrations of a Vertical Rotor 363
 Lassad Amami, Mihai Arghir, and Pascal Jolly

A Case Study of the Contact Force and Stress in the Backup Bearing of a Generator: Experimental Study and Numerical Simulation of Dropdown 374
 Neda Neisi, Behnam Ghalamchi, Janne E. Heikkinen, Teemu Sillanpää, Toni Hartikainen, and Jussi Sopanen

Rubbing Effect Analysis in a Continuous Rotor Model 387
 Marcus Varanis, Arthur Mereles, Anderson Silva, José Manoel Balthazar, and Ângelo Marcelo Tusset

A Modified Model Reduction Technique for the Dynamic Analysis of Rotor-Stator Rub	400
K. Prabith and I. R. Praveen Krishna	
Analysis of Variable Mass Rotordynamic Systems with Semi-analytic Time-Integration	412
Helmut J. Holl	
Nonlinear Analyses in Rotordynamic Engineering	426
Joachim Schmied and Andreas Fuchs	
Torsional Vibrations and Geared Systems Dynamics	
Multibody Dynamics Simulation of a Mechanism for Generating Continuously Variable Motion	445
Krishna Prakash Bhusal, Behnam Ghalamchi, Charles Nutakor, Jussi Sopanen, and Tommi Nummelin	
Analysis of a Drill-String Experimental Set-Up with Dry Friction-Induced Torsional Vibration	456
Bruno C. Cayres, Cesar A. Fonseca, Guilherme Sampaio, and Hans I. Weber	
Modeling and Simulation of the Drivetrain of a Metal Lathe	470
Eduardo Paiva Okabe and Daniel Iwao Suyama	
Comparison of Lubricant Force Models for Rattle Analysis on Gear Transmissions	482
A. Fernandez-del-Rincon, A. Diez-Ibarbia, M. Iglesias, P. Garcia, A. De-Juan, and F. Viadero	
Hysteretic (Non-reversible) Bit-Rock Interaction Model for Torsional Vibration Analysis of a Drillstring	491
F. F. Real, A. Batou, T. G. Ritto, C. Desceliers, and R. R. Aguiar	
Modeling and Simulation of Decoupler Pulley Effects on FEAD Torsional Vibration	505
L. F. Berto, A. C. Michelotti, P. P. Pastorelli, and A. L. F. Ferreira	
Detection of Gear Tooth Crack in a Wind Turbine Planetary Gearbox	520
Rachna Joshi and Ashish K. Darpe	
Experimental Investigations on Torsional Vibrations of a Rotor During a Rotor-Stator Rub	534
Md. Asjad Mokhtar, Ashish K. Darpe, and K. Gupta	

Active Components and Vibration Control



Application of Genetic Algorithm for Synthesis of H_∞ Controllers for Active Magnetic Bearing Systems

Alican Sahinkaya and Jerzy T. Sawicki^(✉)

Center for Rotating Machinery Dynamics and Control (RoMaDyC),
Washkewicz College of Engineering, Cleveland State University,
Cleveland, OH 44115, USA

{a. sahinakaya, j. sawicki}@csuohio.edu

Abstract. This paper discusses designing of weights for both mixed-sensitivity and signal-based H_∞ controller synthesis for active magnetic bearing (AMB) systems using genetic algorithm (GA) optimization. In mixed-sensitivity problem formulation, the weights represent desired upper bounds to closed loop transfer functions and in signal-based problem formulation, the weights represent desired system response under sinusoidal exogenous inputs. In order to cast weight design process as an optimization problem, appropriate cost functions are chosen to guarantee that desired performance objectives are satisfied with a stable controller. First, the validity of the method is demonstrated in simulation by comparing performances achieved using weights designed through the optimization to the weights selected as performance objectives. Then, the weight design via GA for H_∞ controller synthesis is tested experimentally on a small AMB test rig in a disturbance rejection scheme. The designed H_∞ controllers are implemented on the AMB system and tested up to the maximum design speed of 6000 rpm, where the rotor safely passed the first critical speed. Achieved performances are compared to a benchmark PID controller. Results demonstrate validity of using GA for weights design and show the superiority of H_∞ controllers over PID controller for disturbance rejection in AMB systems.

Keywords: Active magnetic bearing systems · Robust control
Genetic algorithm · H_∞ control

1 Introduction

Active magnetic bearings (AMBs) are devices that provide contact-free support by levitating the rotor inside an air gap using electromagnets with feedback controllers. Adequate controllers are a must for reliable and safe operation of AMB systems. However the design of such controllers is a difficult task due to inherent unstable nature of AMBs, speed dependence of the rotor model, and non-collocated sensor-actuator pairs. For these reasons, the research has focused on model-based robust control techniques to address the challenges associated with AMB system control.

Robust control methods are quite often studied in literature related to AMB systems due to their superior performance over traditional PID control. Sawicki et al. [1]

experimentally demonstrates advantages of μ -synthesis, which combines H_∞ controller synthesis and μ -analysis, over traditional PID controller in the context of adjusting machining spindle tool tip compliance. The H_∞ control theory addresses the controller design problem in its general configuration, where certain performance objectives need to be satisfied in the presence of modeling uncertainties. That is why H_∞ control results in highly robust controllers and the theory is applicable to complex MIMO plants, such as AMB systems. There are three main approaches to design H_∞ controllers; open loop shaping procedure introduced by Glover and McFarlane [2], closed loop shaping procedure called mixed-sensitivity H_∞ control [3], and signal-based H_∞ control [4]. In all three approaches, the control problem is expressed as a mathematical optimization problem, where the uncertainties of the model and performance objectives are defined using the so-called weighting filters, or simply weights.

There are many examples of successful implementation of H_∞ controllers on AMB systems in literature, designed using one of the three above-mentioned approaches. Fujita et al. [5] was one of the first presented studies that successfully designed and implemented open loop shaping and mixed-sensitivity H_∞ controllers to an AMB system where the dynamics due to gyroscopic effects was accounted for via uncertainties. Sivrioglu and Nonami [6] considered gain-scheduled mixed-sensitivity H_∞ controllers to cover the variations of plant dynamics due to gyroscopic effects. Noshadi et al. [7] compared mixed-sensitivity H_∞ control, H_2 control, and lead-lag type control by conducting experiments on an AMB test rig in a disturbance rejection control scheme. The results show superior performance of the H_∞ controller.

The challenge in H_∞ controller design is selecting the weights to achieve desired robustness and performance. In the H_∞ control problem formulation, the weights are first designed based on control objectives. Lundström et al. [8] gives insight on how to choose the weights for different H_∞ control problem formulations. However the weights used in control problem formulation usually needs to be iteratively tuned until satisfactory performance margins are obtained. In order to ease the process of H_∞ controller design, Christiansson and Lennartson [9] proposed to cast the tuning of weights as an optimization problem, where a mixed-sensitivity H_∞ control problem for a simple SISO plant and a more complicated MIMO plant are studied, and the validity of the proposed weight tuning process, using genetic algorithm (GA), is shown.

Application of GA to tune weighting filters for H_∞ control problem is reported to AMB systems in literature. Jastrzebski et al. [10] successfully implements a gain-scheduled signal-based H_∞ controller to an AMB system where the weighting filters are selected through GA and achieved performance is evaluated using experimentally obtained sensitivity function and step responses of non-rotating system.

In this current work, weight design for H_∞ control problem via GA optimization for an AMB system that has its first critical speed within the operating range is experimentally investigated. Model of the AMB system is derived in Sect. 2. Design of a benchmark PID controller, mixed-sensitivity H_∞ controller, and signal-based H_∞ controller are explained in Sect. 3, along with the application of GA in the weight design process. Section 4 presents the results of the experimental comparison between the three controllers.

2 Experimental AMB System Model

The experimental setup for this study is a small AMB test rig manufactured by Revolve Magnetic Bearings, subsidiary of SKF, pictured in Fig. 1. The test rig consists of two identical radial AMBs, which are referred to as non-drive end (NDE) and drive end (DE) bearing, to levitate the rotor, and one thrust AMB to control the axial position of the rotor. The system, due to its horizontal configuration, does not exhibit significant axial forces and the controller design focuses only on radial AMBs. Rotor radial and axial motions are decoupled and the thrust AMB is controlled with a simple PID controller. The radial magnetic forces are applied to the rotor in two perpendicular axes, which have an angle of 45 degrees with vertical axis. To provide resting place for the shaft and to prevent damage to AMBs in the event of a failure, radial AMBs are equipped with rolling element touchdown bearings which have a clearance of around $190\ \mu\text{m}$ with the shaft. A flexible coupling component is used to attach the rotor to a brush type DC motor to drive the system.

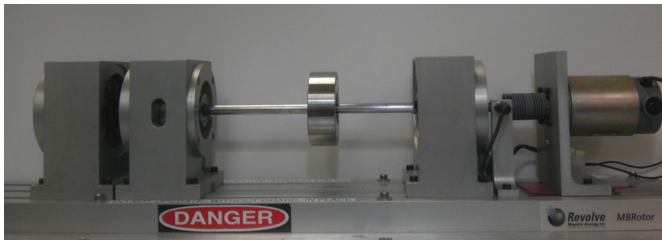


Fig. 1. Small AMB test rig photo

The rotor configuration in this study consists of a solid shaft, two identical radial AMB rotors, one thrust AMB rotor, one disk, and one coupling element. The solid shaft has a diameter of 9.525 mm, a length of 457.2 mm, and is made of stainless steel. The AMB rotors and disk are attached to the shaft via tapered sleeves. Inertial parameters of the AMB rotors, balance disk, and coupling element are shown in Table 1. The model of the rotor assembly is derived by discretizing the shaft into 37 elements and adding the disk, AMB rotors, and coupling element as lumped masses at the nodes corresponding to their respective center of masses, as shown in Fig. 2, which also shows the position of radial magnetic forces (at nodes 6 and 31), and radial position of sensing (nodes 4 and 33).

Since modally reduced state-space representation of rotor models are more convenient for control-oriented applications, the undamped rotor model is first obtained through finite element method (FEM) using Timoshenko beam theory in nodal domain. Then, the resulting nodal model is transformed to modal domain, where modal truncation is applied to retain the two rigid modes and the first four flexible modes (at 91 Hz, 250 Hz, 510 Hz, and 735 Hz). The reason for keeping the first four flexible modes in the model is due to the fact that they are within the bandwidth of the actuators. Free-free rotor model used further in the paper is kept undamped.

Table 1. Inertial parameters of rotor components

Rotor components	Mass [kg]	Moments of inertias	
		Trans. [kg m ²]	Polar [kg m ²]
Balance disk	0.6532	$0.2341 \cdot 10^{-3}$	$0.4302 \cdot 10^{-3}$
Thrust AMB	0.3402	$0.0995 \cdot 10^{-3}$	$0.0995 \cdot 10^{-3}$
Radial AMB	0.2585	$0.0594 \cdot 10^{-3}$	$0.0413 \cdot 10^{-3}$
Coupling	0.0200	$0.2000 \cdot 10^{-5}$	$0.0300 \cdot 10^{-5}$

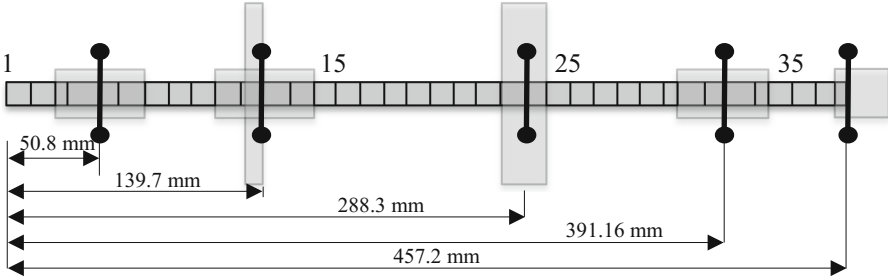


Fig. 2. FE model of the rotor assembly

The AMBs are electromagnetic actuators with built-in sensing capabilities. The sensors used in the AMBs of the system have a bandwidth much higher than operating frequency range; hence their dynamics are ignored in this study. The AMB model is separated into two parts to capture its dynamics: AMB force model and AMB electronics model. AMB force model converts the applied current to coils and the position of the rotor into applied force to the rotor and is determined via linearization of the magnetic force equation at an operating point [11]. The operating point for this study is defined as the center of the bearing with a bias current of 1 A. The resulting position and current stiffness values for the AMB are 0.064 N/ μ m and 25.33 N/A respectively. The AMB electronics model defines the dynamics AMB coils introduce due to their inductive nature and loading to amplifiers. Instead of creating a separate model for the AMB electronics, the model is embedded in to the amplifier model, which is experimentally identified, to ease the modeling process.

The amplifiers used to supply current to the AMB coils are pulse-width modulation (PWM) type and are identified experimentally. In the identification experiment, the AMB coils were attached as load and digital hardware, namely AD/DA converters, is used to obtain the data. That is why the identified amplifier model not only includes the amplifier model, but also the AMB electronics model and time delays due to AD/DA conversions. The identified bandwidth of the amplifiers is 2500 Hz with amplifier slew rate around 900 Hz.

State-space representation of the open loop system is formed by utilizing the free-free rotor model, AMB force model, and the amplifier model. Figure 3 shows the block diagram of the AMB system with open loop model shown in solid lines. The resulting

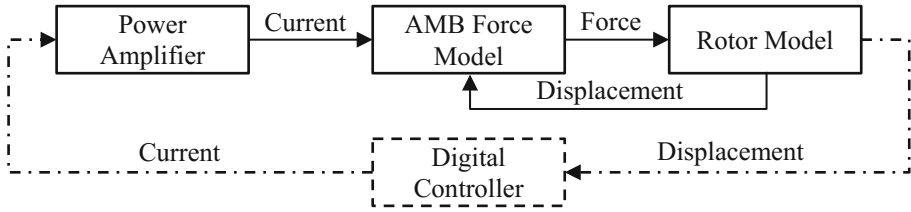


Fig. 3. AMB system model where open loop system model is shown with solid lines

open loop system model is a 4 input 4 output model with 32 states, in which 24 states corresponds to the free-free rotor model and 8 states corresponds to the amplifier model.

Due to the inherent unstable nature of AMBs, direct open loop system identification could not be performed to validate the accuracy of the obtained model. That is why driving point measurements from closed loop system are taken at the 1st node, where a PID controller was used to levitate the rotor, to identify closed loop frequency response function (FRF). Figure 4 presents comparison of identified closed loop FRF and simulated closed loop FRF, which demonstrates relatively good agreement.

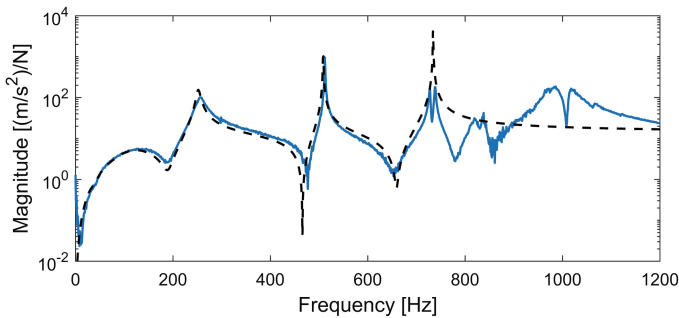


Fig. 4. Impact hammer test; experiment (blue) and model (black) (Color figure online)

3 Controller Design for AMB System

The control objective for the studied AMB system is chosen to keep the orbits within a circle of radius 36 μm without saturating the AMB actuators up to maximum rotational design speed of 6000 rpm in the presence of unbalance force. Moreover, vibration amplitudes at the AMB sensor locations should be lower than 7 μm when the rotor is not rotating. This is a standard objective for AMB systems and is often referred to as disturbance rejection control problem.

In this section, first, benchmark PID controller design is explained, then H_∞ control problem formulation for mixed-sensitivity and signal-based approaches are discussed, and lastly the selection of weights for the H_∞ controller design using GA is explained.

3.1 Decentralized PID Controller Design

Designing a decentralized PID controller for an AMB system is not a trivial task since the dynamics of the system is dependent on the rotational speed of the rotor due to gyroscopic effects. On top of that, a simple PID controller is usually not sufficient to stabilize all the flexible modes of the rotor which are within the bandwidth of the actuators, for this system the 3rd and 4th flexible modes.

For this reason, as a first step in the design process, PID gains are chosen to satisfy the performance objectives within the operating region by calculating required PID gains to achieve desired stiffness at the bearings. A low pass filter is cascaded with the PID controller for noise attenuation as well as to decrease the gain of the controller at high frequencies. For this purpose a low pass frequency of 1500 Hz is used.

With only PID gains, the 3rd and 4th flexible modes of the rotor are lightly damped, which is not desired for stable operation. In order to stabilize the 3rd flexible mode, a lead-lag filter is used, where a zero is placed lower than the 3rd flexible mode frequency and a pole is placed at a higher frequency resulting in increased damping due to phase lead. For the 4th flexible mode, a notch filter is placed below the resonant frequency and similarly the resulting phase lead increases the damping and the gain is also attenuated. The design of both the lead-lag filter and the notch filter take into account the rotational speed dependency of the 3rd and 4th flexible mode frequencies, due to gyroscopic effects. Figure 5 presents the frequency response of the designed PID controller with the filters, which is implemented in all 4 radial axes.

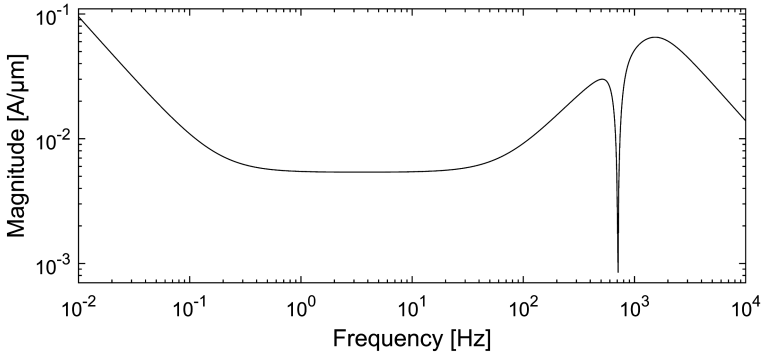


Fig. 5. PID controller for single axis

3.2 H_∞ Controller Design

Design of H_∞ controllers involve the use of standard control configuration, which is shown in Fig. 6, where \mathbf{P} is the generalized plant and \mathbf{K} is the controller to be designed. The exogenous inputs are stacked in the vector \mathbf{w} and the performance outputs are stacked in the vector \mathbf{z} , which are assumed to be normalized via weights, in other words their 2-norm is unity. The generalized plant \mathbf{P} includes the plant model and weights for the exogenous inputs and performance outputs which defines the performance and robustness objectives. The exogenous inputs and performance outputs can be chosen to

shape closed loop transfer functions, in which case the method is called mixed-sensitivity H_∞ control, or they can represent magnitude and frequency content of selected input and output signals of the system, in which case the method is called signal-based H_∞ control.

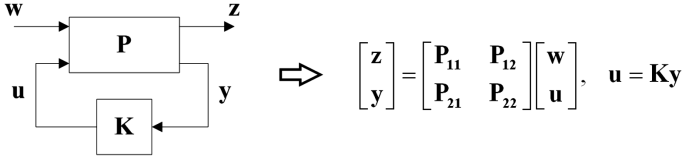


Fig. 6. Standard control configuration and mapping between inputs and outputs

In both mixed-sensitivity and signal-based approaches, the controller \mathbf{K} is designed such that the closed loop system is internally stable and the maximum singular value of the closed loop system, also referred to as H_∞ norm, is minimized.

The closed loop transfer function from exogenous input \mathbf{w} , to performance output \mathbf{z} , can be obtained from the mapping between inputs and outputs and the so called lower Linear Fractional Transformation (LFT), or $F_l(\mathbf{P}, \mathbf{K})$. The relation between the regulated performance output and the exogenous input can be written as

$$\mathbf{z} = F_l(\mathbf{P}, \mathbf{K})\mathbf{w} \quad (1)$$

where the lower LFT is defined as

$$F_l(\mathbf{P}, \mathbf{K}) = \mathbf{P}_{11} + \mathbf{P}_{12}\mathbf{K}(\mathbf{I} - \mathbf{P}_{22}\mathbf{K})^{-1}\mathbf{P}_{21} \quad (2)$$

Then the H_∞ control problem is formulated as

$$\min_{\mathbf{K}} \|F_l(\mathbf{P}, \mathbf{K})\|_\infty \quad (3)$$

Once the problem is formulated, it is solved using a method called γ -iteration [4], where γ refers to the H_∞ norm of the lower LFT. The synthesized controller has the same number of states as the generalized plant \mathbf{P} . Following subsections explain the problem formulation for both mixed-sensitivity and signal-based H_∞ control.

Mixed-Sensitivity H_∞ Control Problem Formulation. In the mixed-sensitivity H_∞ control, exogenous inputs and performance outputs are chosen such that the resulting lower LFT represents closed loop transfer functions to be shaped, in this paper the sensitivity \mathbf{S} and control sensitivity \mathbf{KS} functions. The weights used in this paper are chosen to be diagonal weights due to their ease in interpretation and design compared to non-diagonal weights. Figure 7 illustrates the block diagram of the problem formulation with the resulting lower LFT, where \mathbf{G} is the open loop system model and \mathbf{W}_1 and \mathbf{W}_2 are the weights.

The performance of the synthesized controller is measured by the H_∞ norm of the achieved closed loop transfer function. The smaller the norm is, the more performant

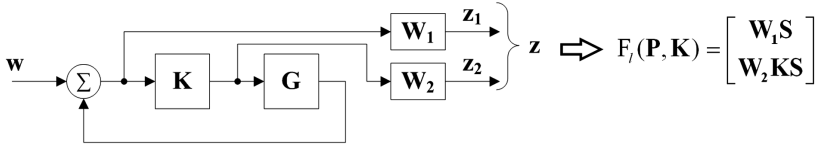


Fig. 7. Mixed-sensitivity H_∞ control problem formulation

and more robust the controller is due to implications of lower maximum singular value of \mathbf{S} and \mathbf{KS} transfer functions. That is why the aim in mixed-sensitivity H_∞ control is to achieve H_∞ norm less than unity, which would mean the inverses of weights are truly an upper bound to their respective closed loop transfer functions.

In the AMB system considered, the disturbance input that represents mainly the unbalance force, is a relatively low frequency signal, therefore it can be rejected by making the maximum singular value of the sensitivity function small over the low frequency region. Also ISO standard for active magnetic bearing systems defines acceptable peak sensitivities for safe and reliable operation, which is maximum of 9.5 dB for newly commissioned AMB systems [12]. These two objectives on \mathbf{S} are enforced by the weight \mathbf{W}_1 . The second objective, which is limiting the control current magnitude, is achieved by putting an upper bound on \mathbf{KS} via weighting filter \mathbf{W}_2 , which is also used to present additive uncertainty for robustness.

Weight selection in mixed-sensitivity H_∞ control is a two-step process; first, structure of the weights are chosen and second, parameters of the weights are chosen, with the constraint that the weights need to be proper and stable. Literature examines the use of different structures for weights and it was shown in [9] that simple structures give satisfactory results. For this reason, first order weights are used to describe the performance objectives. Since the studied AMB system is relatively symmetric, same weights are used for the diagonal elements of \mathbf{S} and \mathbf{KS} . Desired upper bounds on \mathbf{S} and \mathbf{KS} for the control objective stated at the beginning of the section are shown in Fig. 10. However due to controller synthesis procedure being an optimization, usually the weights chosen as desired upper bounds need to be tuned to achieve desired results. In this study GA is used for selecting weights.

Advantages of mixed-sensitivity H_∞ control are rather intuitive in the sense that a simple examination of the relation between inputs and outputs of the closed loop system yields sufficient understanding why upper bounds are desired for certain closed loop transfer functions. On the other hand, the disadvantage of the approach is that defining performance and robustness in frequency domain is a challenging task.

Signal-Based H_∞ Control Problem Formulation. The signal-based approach in H_∞ control is suitable for control problems where multiple control objectives need to be taken into account simultaneously. In this approach the exogenous inputs are chosen such that they represent external signals affecting the system and performance outputs are chosen to represent the output signals to be regulated under sinusoidal excitation through the exogenous inputs. This formulation can be extended to include uncertainties within the system model by simply adding additional input-output signals in a manner representing the uncertainty type.

For the AMB system studied, the exogenous inputs are chosen to be noises in the sensor readings and disturbance forces at AMB actuator positions due to unbalance force at disk location. Performance outputs are chosen to be vibration levels at AMB sensor positions and control current magnitudes. Since it is not possible to construct an exact linear model of an AMB system, as well as to include the change of dynamics of the rotor due to gyroscopic effects, some uncertainties are defined as shown in Table 2. Adding structured uncertainties makes the problem a robust performance problem, where tools such as μ -synthesis can be applied. However in this paper, instead of using μ -synthesis procedure, where the procedure does not guarantee convergence and might result in higher order controllers, μ -analysis is employed in selecting the weights for controller synthesis procedure using γ -iteration. Block diagram of the problem formulation with the uncertain open loop plant \bar{G} is shown in Fig. 8.

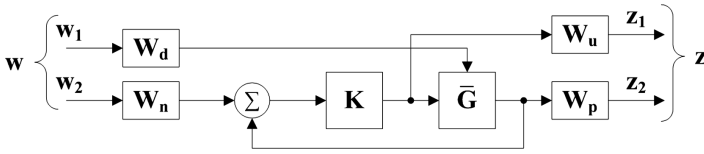


Fig. 8. Signal-based H_∞ control problem formulation

Table 2. Uncertainties in the open loop system model

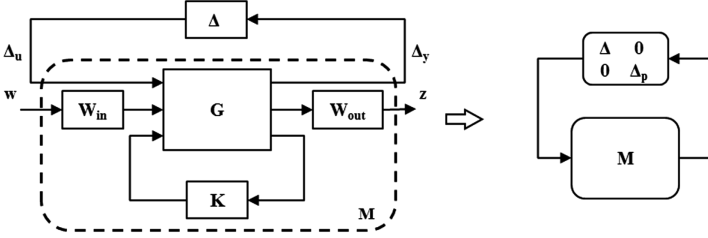
Parameter	Nominal value	Uncertainty	Type
1 st flexible mode	91 Hz	$\pm 2\%$	Complex
2 nd flexible mode	250 Hz	$\pm 2\%$	Complex
3 rd flexible mode	514 Hz	$\pm 2\%$	Complex
4 th flexible mode	735 Hz	$\pm 2\%$	Complex
Current stiffness	25.33 N/A	$\pm 10\%$	Real
Position stiffness	0.064 N/ μm	$\pm 30\%$	Real
Rotational speed	3000 rpm	$\pm 100\%$	Real

The weights in Fig. 8, which are diagonal, describe the expected magnitudes and frequency content of the signals. Table 3 presents the diagonal elements of the weights corresponding to the performance objective stated in the beginning of this section.

In signal-based approach, if structured uncertainties are present in the system model, closed loop performance is evaluated using structured singular value, μ [13]. To perform μ -analysis for robust performance (RP), first the defined uncertain model is separated into nominal model G and perturbation block Δ which represents the defined structured uncertainties. After pulling out the uncertainties, a fictitious full complex Δ_p matrix, where $\bar{\sigma}(\Delta_p) \leq 1$, is added to the system to connect the performance output vector z to exogenous input vector w , as shown in Fig. 9.

Table 3. Parameters describing the weights for signal-based H_∞ control problem formulation

Weights	Low frequency	High frequency	Cross over frequency	Roll-off frequency
\mathbf{W}_d	10 N	8 N	1 Hz	110 Hz
\mathbf{W}_n	0.6 μm	0.6 μm	-	-
\mathbf{W}_p^{-1}	7 μm	36 μm	1 Hz	110 Hz
\mathbf{W}_u^{-1}	1 A	1 A	-	720 Hz

**Fig. 9.** Robust performance analysis

Finally the robust performance of the closed loop system is evaluated by calculating the structured singular value of the transfer function \mathbf{M} . Mathematically, structured singular value is defined as

$$\mu(\mathbf{M}) \triangleq \frac{1}{\min\{k_m | \det(\mathbf{I} - k_m \mathbf{M} \Delta) = 0 \text{ for structured } \Delta, \bar{\sigma}(\Delta) \leq 1\}} \quad (4)$$

A value of μ greater than unity for a system means the system does not guarantee RP, and the desired performances needs to be relaxed and defined uncertainties needs to be reduced by a factor of $1/\mu$ to guarantee RP.

Method called DK-iteration, or μ -synthesis, is commonly employed that adopts the μ -analysis with H_∞ controller synthesis. However μ -synthesis tends to result in high order controllers, which can be computationally expensive to implement, in addition to the fact that the DK-iteration does not guarantee convergence. More comprehensive discussion on application of μ -synthesis to AMB systems can be found in [1, 14]. Alternatively, the weights in the H_∞ control problem formulation can be selected differently to achieve desired μ -value using γ -iteration. In this paper GA is used with the μ -value as part of the cost function to synthesize signal-based H_∞ controller.

The advantage of signal-based H_∞ control is several time domain objectives can be taken into account simultaneously by simply adding additional input and output channels to the system with corresponding weights. Assuming each weight is a dynamic filter, number of states of the generalized plant increases with each additional input and output, which increases the number of states of the controller. Due to computational cost of implementing high order controllers, this is not desired.

Weight Selection via GA. In this paper, weight selection for H_∞ controller synthesis is cast as an optimization problem and solved using GA.

GA is a method for solving optimization problems using the idea behind genetic evolution in real life, in the sense that it treats parameters of the optimization problem as genes and only the fittest genes, measured using a metric, and their offspring are transferred to the next generation [15]. The value of GA is its ability to search the whole variable space, which is important to avoid local minima. The GA is applied to both mixed-sensitivity and signal-based H_∞ control problems.

In order to formulate the weight selection process to be solved by GA, a simple procedure is followed, which can be summarized as;

- Parametrize weights while maintaining desired weight structure.
- Initialize n different sets of parameters that define n different H_∞ control problems.
- Design H_∞ controllers for each set using γ -iteration.
- Evaluate performance of each controller using H_∞ norm for mixed-sensitivity approach or μ -value for signal-based approach, where the weights used for performance evaluation are fixed and defined by the objective.
- Penalize sets resulting in unstable controllers by adding a large enough constant to their performance indicator.
- Sort the sets in terms of their achieved performance index. Carry the elite sets to the next generation and generate new sets as a combination of the best ones from the previous set to complete the number of sets in the new generation to n .

The procedure is iterated until desired performance index is reached. In this study, n is chosen to be 10 to reduce computation time. Initial set of parameters is generated by randomly selecting values from a real number set that has values from zero to twice the corresponding parameter in the weights that describe the objective.

4 Results and Discussion

Comparison of the H_∞ controller synthesis using the weights that define the objective and weights selected through the GA optimization are first carried out in simulation.

For mixed-sensitivity H_∞ controller, achieved closed loop transfer functions are compared to the desired upper bounds, which is shown in Fig. 10. It can be seen that the optimization was able to find weights that satisfies the requirements, which can also be inferred from the achieved cost function value of 0.98. However if the weights describing the objective is used in the controller synthesis, the resulting controller does not keep the sensitivity function below the desired level in low frequency region.

For the signal-based H_∞ controller, achieved μ -value at each frequency is computed using a high density frequency grid, giving specific attention to frequency regions where μ -value is close to unity, as shown in Fig. 11. Since maximum μ -value is 0.99, the controller should be able to satisfy RP as long as the system is within the defined set of uncertain plants and the exogenous input weights accurately represent reality. Without the GA optimization for weight selection, achieved μ -value was 5.4.

Simulation results show the designed controllers achieve the control objective. In order to experimentally confirm the results, the designed continuous time controllers are discretized using zero-order hold on the inputs with a sampling frequency of

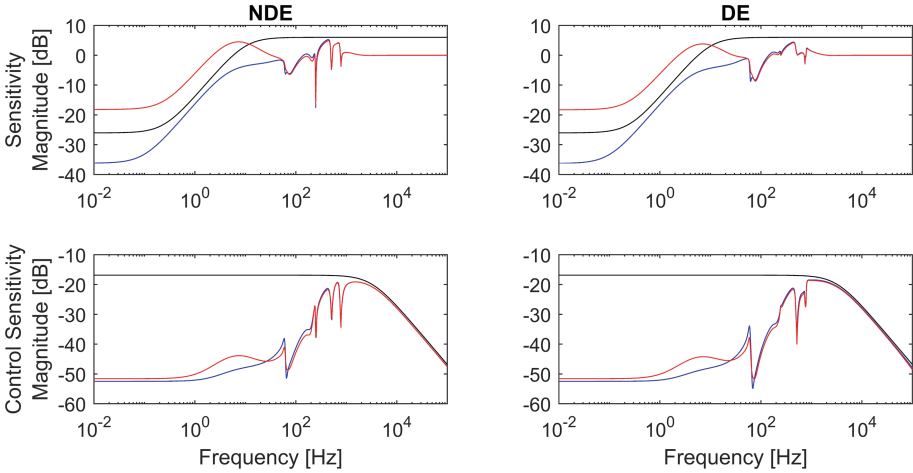


Fig. 10. Comparison of achieved closed loop transfer functions using weights designed by GA (blue) and weights selected as desired upper bounds (red), and desired upper bounds (black) (Color figure online)

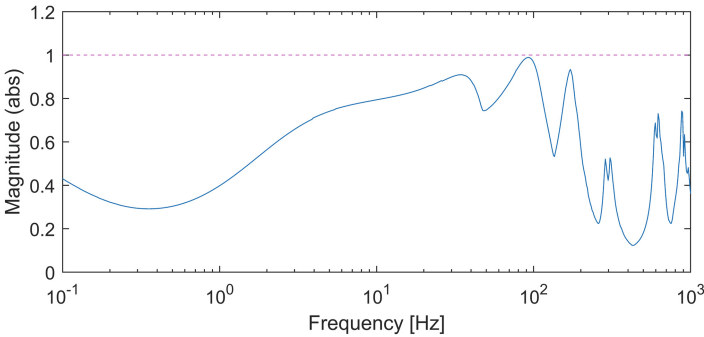


Fig. 11. Achieved μ -value plot of the closed loop system with signal-based H_∞ controller

20 kHz and implemented using dSpace hardware. After implementing the controllers, a series of tests were performed to evaluate the achieved performances.

The first test is to observe the levitation performance of each controller. When the system is not powered, the rotor rests on the touchdown bearings which have a radial clearance of around 190 μm . At 1 s, the system is energized, which is analogous to giving a step input, to move the rotor to the center of the bearing. Position of the rotor at AMB sensor locations are collected, which has 45 degree angle w.r.t vertical Y axis. The vertical position of the rotor is calculated by utilizing a rotation matrix and the measurement data. Results of the test in vertical axis are shown in Fig. 12.

It is clear from Fig. 12 that H_∞ controllers have a smaller rise time which can also be interpreted as faster response to disturbances. However for signal-based approach, this is achieved with an overshoot of around 16 percent. Initial levitation test shows the

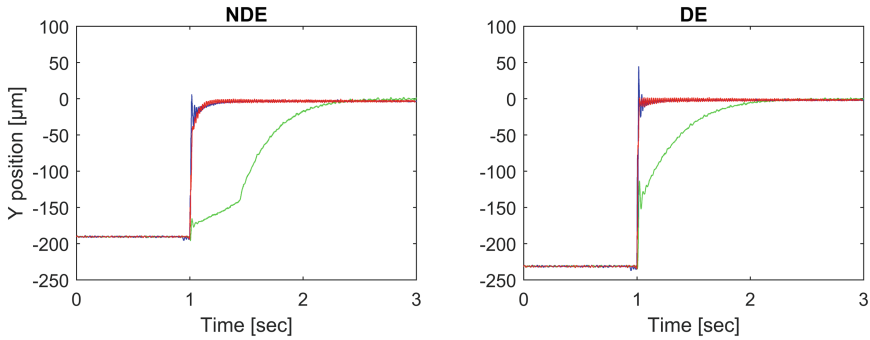


Fig. 12. Initial levitation of the rotor: PID controller (green), mixed-sensitivity H_∞ controller (red), and signal-based H_∞ controller (blue) (Color figure online)

stability of the system when the rotor is not rotating. Since dynamics of the rotor changes with the speed due to gyroscopic effects, a run-up test was performed to check the stability of the system in the design speed range. The system is run from 0 rpm to maximum design speed of 6000 rpm in 60 s with constant acceleration. Peak-to-peak (p-p) displacement of rotor geometric center during the test is shown in Fig. 13. Speed controller for the motor gave poor performance until 1000 rpm, which is one of the reasons behind the erratic behavior seen at the start of the run-up tests.

It can be seen from Fig. 13 that all three controllers were stable in the operating range. However the first critical speed of the system changes depending on which controller is implemented. This is due to PID and H_∞ controllers resulting in different effective stiffness. For an AMB system, effective stiffness provided by a controller is calculated using the frequency response of the controller and AMB force model constants, which is found to be around 1×10^5 N/m for the PID controller and around 2×10^5 N/m for the H_∞ controllers.

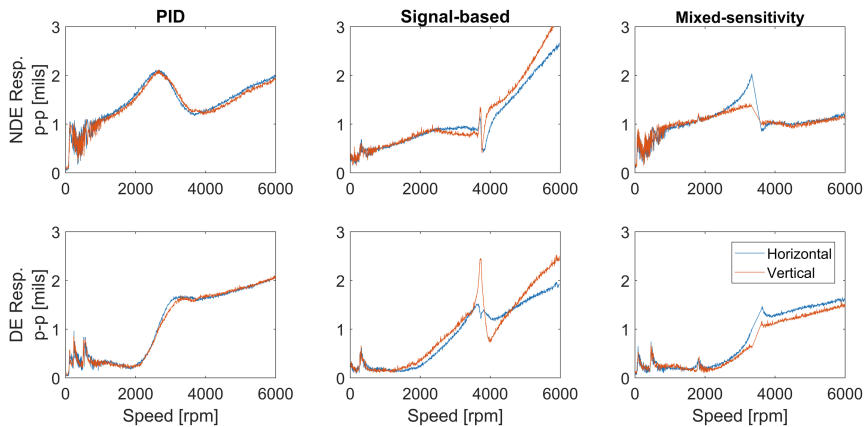


Fig. 13. Run-up test results in vertical (red) and horizontal (blue) directions (Color figure online)

Since the stability objective is met with all three controllers, the next step in performance evaluation process is to see if the objective is met. For this purpose, the rotor is run at 3000 rpm, 4000 rpm, 5000 rpm, and 6000 rpm and the orbits at AMB sensor locations are examined at steady state. Figure 14 shows the achieved orbits with each controller.

It can be seen from the orbit plots that both mixed-sensitivity H_∞ controller and PID controller satisfy the performance objectives, where the former shows superior performance. On the other hand, signal-based H_∞ controller performs better than PID controller up to 5000 rpm, at which point performance of signal-based H_∞ controller degrades compared to others and it does not satisfy the performance objectives at 6000 rpm. Possible reasons for this behavior is underestimating the parametric uncertainties and/or underestimating disturbance force magnitudes at higher speeds in signal-based H_∞ control problem formulation. The μ -value achieved for the signal based controller, after the optimization process for weight selection, was 0.99. This means that if any of the specifications, either the uncertainty amounts or performance criteria, were to be increased by a factor of $1/0.99$, which corresponds to around 1% increase in any of the defined robustness or performance specifications, the system would not guarantee to satisfy performance objectives.

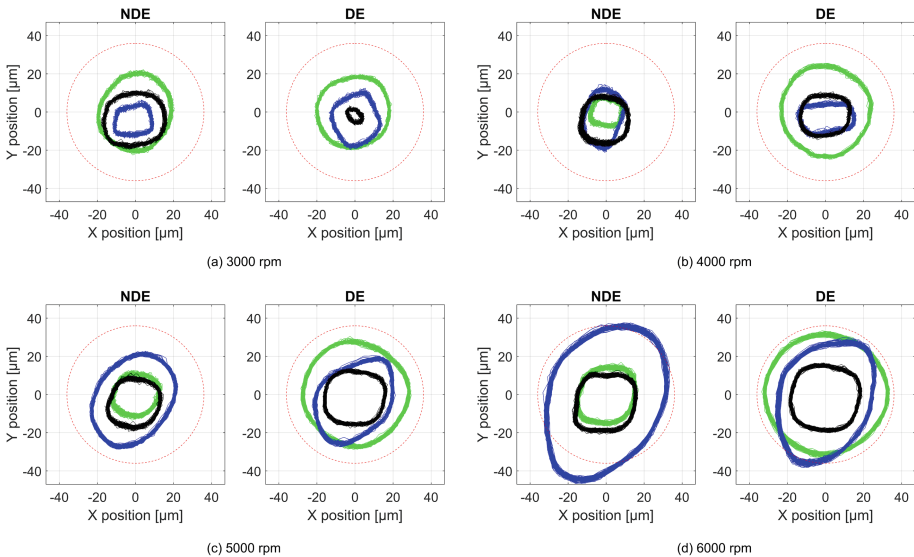


Fig. 14. Orbit plots at different speeds with PID controller (green), signal-based H_∞ controller (blue), mixed-sensitivity H_∞ controller (black), and design requirement (red) (Color figure online)

5 Conclusions

This paper investigated the application of genetic algorithm to weighting filter design in H_∞ control problem formulation for an AMB system with the first critical speed within the operating range. First, an analytical model of the system is constructed using classical techniques. Next, a benchmark PID controller is manually tuned and H_∞ controllers were synthesized using mixed-sensitivity and signal-based problem formulations where weighting filters are designed using GA to achieve desired performance. Validity of GA optimization is shown via the simulation results by comparing the achieved performances using traditional technique to GA for weighting filter design. The performances of manually tuned PID controller and H_∞ controllers designed using GA optimization are experimentally examined while the rotor was stationary as well as for running rotor at various speeds. Experimental results also confirm the validity of application of GA for synthesis of H_∞ controllers for AMB systems. Results also show relatively circular orbits with all controllers, which indicate all controllers result in isotropic bearing, which is expected considering same weights are used for each AMB axes. Out of the three controllers, mixed-sensitivity H_∞ controller outperformed the other two by resulting in smaller orbits in operating range.

References

1. Sawicki, J.T., Maslen, E.H., Bischof, K.R.: Modeling and performance evaluation of machining spindle with active magnetic bearings. *J. Mech. Sci. Technol.* **21**(6), 847–850 (2007)
2. Glover, K., McFarlane, D.: *Robust Controller Design Using Normalized Coprime Factor Plant Descriptions*. 138. Springer, Heidelberg (1990)
3. Kwakernaak, H.: Robustness optimization of linear feedback systems. In: *The 22nd IEEE Conference on Decisions and Control*, San Antonio, TX, USA, pp. 618–624 (1983)
4. Skogestad, S., Postlethwaite, I.: *Multivariable Feedback Control: Analysis and Design*, 2nd edn. Wiley, Chichester (2007)
5. Fujita, M., Hatake, K., Matsumura, F.: Loop shaping based robust control of a magnetic bearing. *IEEE Control Syst. Mag.* **13**(4), 57–65 (1993)
6. Sivrioglu, S., Nonami, K.: LMI approach to gain scheduled H_∞ control beyond PID control for gyroscopic rotor-magnetic bearing system. In: *Proceeding of the 35th Conference on Decision and Control*, Kobe, Japan, pp. 3694–3699 (1996)
7. Noshadi, A., Shi, J., Lee, S., Shi, P., Kalam, A.: System identification and robust control of multi-input multi-output active magnetic bearing systems. *IEEE Trans. Control Syst. Technol.* **24**(4), 1227–1239 (2016)
8. Lundstöröm, P., Skogestad, S., Wang, Z.Q.: Uncertainty weight selection for H-infinity and mu-control methods. In: *Proceedings of the 30th IEEE Conference on Decision and Control*, Brighton, UK, pp. 1537–1542 (1991)
9. Christiansson, A.K., Lennartson, B.: Weight selection for H_∞ control using genetic algorithm. *IFAC Proc. Vol.* **32**(2), 1043–1048 (1999)
10. Jastrzebski, R.P., Hynynen, K.M., Smirnov, A.: H_∞ control of active magnetic suspension. *Mechan. Syst. Sig. Process.* **24**(4), 995–1006 (2010)
11. Schweitzer, G., Maslen, E.H.: *Magnetic Bearing: Theory, Design, and Application to Rotating Machinery*. Springer, New York (2009)

12. ISO 14839-3: Mechanical vibration – Vibration of rotating machinery equipped with active magnetic bearings – Part 3: Evolution of stability margin. International Organization for Standardization ISO (2006)
13. Doyle, J.C.: Analysis of feedback systems with structured uncertainties. *IEEE Proc. D - Control Theory Appl.* **129**(6), 242–250 (1982)
14. Sawicki, J.T., Maslen, E.H.: Toward automated AMB controller tuning: progress in identification and synthesis. In: *Proceeding of 11th ISMB Conference*, Nara, Japan, pp. 68–74 (2008)
15. Goldberg, D.E.: *Genetic Algorithms in Search, Optimization & Machine Learning*. Addison-Wesley, Boston (1989)



An Active Elastic Support/Dry Friction Damper: New Modeling and Analysis for Vibration Control of Rotor Systems

Siji Wang^(✉), Mingfu Liao, Mingbo Song, and Yingge Xu

School of Power and Energy, Northwestern Polytechnical University,
Xi'an 710072, China
sjwang@nwpu.edu.cn

Abstract. This article introduces a new type of active damper—elastic support/dry friction damper (ESDFD) for vibration control of rotor systems and its performances. The basic operation principle of ESDFD in rotor system was introduced. In particular, a two-dimensional friction model-ball/plate model was proposed, by which a dynamic model of rotor systems with ESDFD was established and verified. The damping performance of the ESDFD has been studied numerically. The simulation results show that the damping performance of ESDFD is closely related to the characteristics of the rotor's mode. For obtaining the damper's best performance, the damper should be located at the elastic support in which the vibration energy is concentrated. And the damper not only provides external damping to the rotor system, but also increases extra stiffness into the rotor system. The stiffness of the stationary disk and the tangential contact stiffness of the contact interface are connected in series between the moving disk and the mounting base of the stationary disk. The larger of this combined stiffness, the better of the damper's damping performance. The application of ESDFD to the vibration suppression of a rotor system is investigated experimentally. A switch control scheme for the damper is introduced; the effectiveness and control characteristics with control scheme for attenuating the vibration of rotor systems are experimentally investigated.

Keywords: Active elastic support/dry friction damper
Ball/plate model of friction · P control · Rotor systems

1 Introduction

Traditional damper of rotor systems in aero engines, such as squeeze film dampers, is passive device because it cannot adjust its damping ratio in response to changes of unbalance response in the rotor system operating conditions. To overcome this deficiency, active dampers have been suggested as a means of control unbalance response of the rotating machine. The ESDFD is a new type of damper for active vibration

The present work is supported by the National Natural Science Foundation of China (Project No: 51405393).

control of rotor systems in aero engines [1]. It can active control unbalance response of the rotor system through active damping and stiffness. A magnetic bearing is one of promising type of active bearings and has been the subject of extensive research. It is well suited for high-speed rotating machine because of its non-contact nature and its unique ability to suspend loads with no friction. However, because of its low load-carrying capacity and heavy weight, relative to a mechanical bearing, a magnetic bearing is not suitable for vibration control in aero engines.

The ESDFD is one promising damper candidate for active vibration control in aero engines. It has been proven theoretically and experimentally that the damper can significantly attenuate the unbalance response of a rotor system. There are several older applications of such systems, Fan et al. [2] proposed that friction damping could be applied in rotor system. Wang et al. [3–5], designed an active elastic support/dry friction damper using an electromagnetic actuator or piezoelectric ceramic actuator, which can conveniently be actively controlled by adjusting the control voltage of the electromagnet or piezoelectric ceramic actuator. Usually, dry friction is disadvantageous in mechanical systems, such as in rubbing faults of rotor systems [6–8]. However, as external damping, dry friction has been widely used to increase the stability of mechanical systems, such as the dry friction damping blade of aero engines and turbines [9–15]. Figure 1 shows the operation principles of a rotor with ESDFDs. The rotor is supported by two elastic supports, and at the end cross section of each one, the dry friction damper is affixed. Each damper consists of three key components: the elastic support, the friction pairs (stationary disk and moving disk) and the actuator. The elastic supports redistribute the strain energy of the whole rotor-support system and concentrate the vibration, which is then dissipated by the dry friction between the friction pairs. The moving disk, which is fixed to the end cross section of the elastic support, is connected to the bearing outer ring and vibrates with the elastic support but does not rotate with the rotor. The stationary disk is fixed to the casing and can be moved in the axial direction by the actuator. The frictional force between the two disks can be changed by adjusting the pressure force from the actuator.

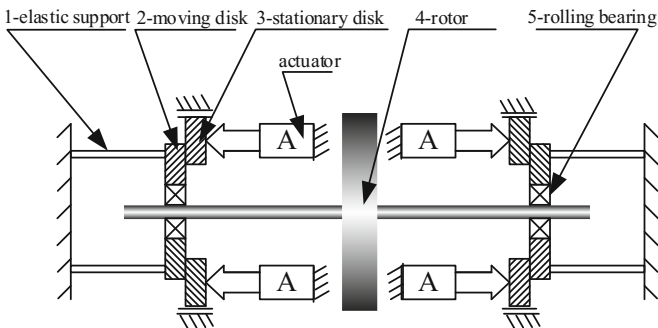


Fig. 1. The operation principles of the ESDFD

The work to propose the mechanism model of the ESDFD was Fan et al. [1, 2], in which the rotor was simplified to a single degree of freedom system, and dry friction model was the classic one-dimensional hysteretic. The classic one-dimensional hysteretic dry friction model was just for illustrating the friction damping mechanism of the dry friction damper, and was insufficient for the damper designing of rotor systems. There are two reasons. The first one is the axial location of the damper influences the damping performance of the elastic support/dry friction damper, which cannot be considered in the previous work; the second one is the relative motion between the friction pair is a two-dimensional motion, which is considered as one-dimensionally in the previous work.

This work departs from the existing hysteretic dry friction model, a two-dimensional friction model-ball/plate model is proposed by which dynamic model of a rotor system with ESDFDs was established and verified. According to the characteristics of the ESDFD, A control scheme was introduced; the effectiveness and control characteristics for the vibration control of the rotor system were experimentally investigated.

2 Damper and Rotor System Model

2.1 Two-Dimensional Friction and Ball/Plate Model

A two-dimensional friction model-ball/plate model (shown in Fig. 2) is proposed. The model was developed from the hysteretic dry friction model. As shown in Fig. 2, the stationary disk is represented by a rectangle and remains at rest. The moving disk consists of a ball and a plate. The plate (without considering its mass) represents the contact interface between the moving disk and the stationary disk, and the ball represents the moving disk. The ball and the plate are connected with ideal springs and linear damping in two directions. The ideal springs represent the tangential contact stiffness of the contact interface. The displacement between the ball and the plate represents the microscopic sliding in the state of stick. So if the applied force on the ball is greater than maximum stick, the ball will touch the edge of the plate, and the plate will begin to move.

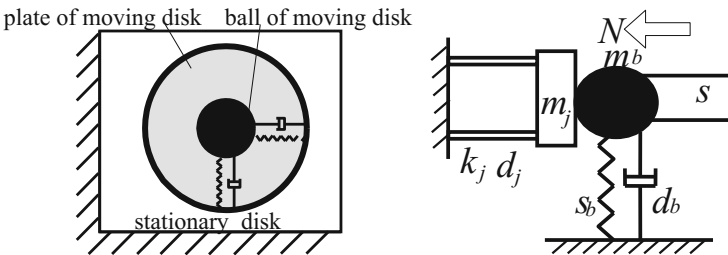


Fig. 2. Two-dimensional friction and ball/plate model

The ball/plate dry friction model is actually a type of two-dimensional hysteretic dry friction model. The frictional force between the stationary disk and the plate is Coulomb's friction force. The frictional force at any time depends on the motion state of the plate and the applied force with which the ball acts on the plate.

Without considering the mass of the plate, the resultant force acting on the plate will be 0 at any time. When the plate is stationary relative to the stationary disk, namely the friction pair is in the state of stick, the frictional force acting on the plate is

$$F_f = -[k(r_1 - r_2) + d(\dot{r}_1 - 0)] < \mu N \tag{1}$$

If $|k(r_1 - r_2) + d(\dot{r}_1 - 0)| \geq \mu N$, the plate will not remain stationary relative to the stationary disk, namely the friction pair is in the state of kinetic friction, and the frictional force acting on the plate is

$$F_f = -\frac{\dot{r}_2 - \dot{r}_j}{|\dot{r}_2 - \dot{r}_j|} \mu N \tag{2}$$

where $r_1 = x_1 + iy_1$ is the displacement of the ball; $r_2 = x_2 + iy_2$ is the displacement of the plate; $r_j = x_j + iy_j$ is the displacement of the stationary disk, its value is 0 when the stationary disk remains at rest; k is the stiffness coefficient between the ball and the plate; d is the damping coefficient between the ball and the plate; μ is the friction coefficient; and N is the pressure force.

2.2 Dynamics Model with the Rotor Systems

As shown in Fig. 3 is a single-disk flexible rotor with ESDFDs. The system consists of two parts: a rotor and two ESDFDs (in the dashed boxes). The rotor is a single offset disk with a flexible shaft that is supported by two elastic supports at both ends. The two ESDFDs can be set up at each elastic support, shown in the dashed boxes of Fig. 3.

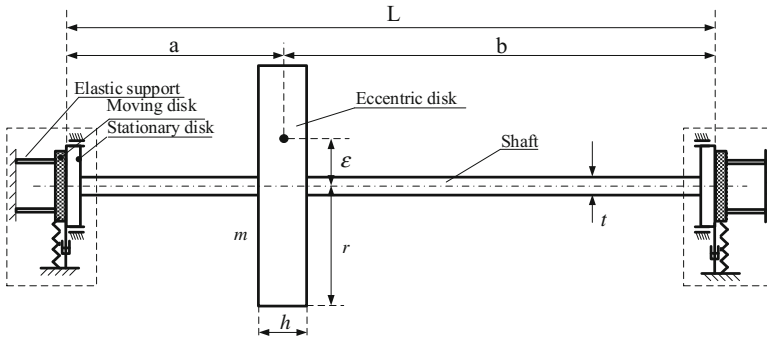


Fig. 3. A single-disk flexible rotor with ESDFDs

For the rotor disk, four coordinates are required to describe its motion. Two of them (x, y) describe its two-dimensional translation; the other two (φ_x, φ_y) describe its two-dimensional swing. For the left friction pair, six coordinates are required to describe the two-dimensional motion of the moving disk (the ball and the plate) and the stationary disk: x_{b1} and y_{b1} describe the motion of the ball; x_{d1} and y_{d1} describe the motion of the plate; and x_{j1} and y_{j1} describe the motion of the stationary disk. In the same way, another 6 coordinates describe the motion of the right friction pair. They are $x_{b2}, y_{b2}, x_{d2}, y_{d2}, x_{j2}, y_{j2}$. So in total, the whole rotor system is a system with 16 degrees of freedom (16-DOF system).

By means of Euler's laws of motion, the motion equations of the rotor disk, moving disk and stationary disk can be obtained as follows.

The rotor disk:

$$m\ddot{\mathbf{r}} + s_{11}\mathbf{r} - is_{12}\boldsymbol{\varphi} - \left(\frac{L-a}{L}s_{11} + \frac{1}{L}s_{12}\right)\mathbf{r}_{b1} - \left(\frac{a}{L}s_{11} - \frac{1}{L}s_{12}\right)\mathbf{r}_{b2} = m\varepsilon\Omega^2 e^{i\Omega t} \quad (3)$$

$$J_d\ddot{\boldsymbol{\varphi}} - iJ_p\Omega\boldsymbol{\varphi} + is_{21}\mathbf{r} + s_{22}\boldsymbol{\varphi} - i\left(\frac{L-a}{L}s_{21} + \frac{1}{L}s_{22}\right)\mathbf{r}_{b1} - i\left(\frac{a}{L}s_{21} - \frac{1}{L}s_{22}\right)\mathbf{r}_{b2} = 0 \quad (4)$$

The moving disk (the ball in the ball/plate model):

$$m_{b1}\ddot{\mathbf{r}}_{b1} + (d_{b1} + d)\dot{\mathbf{r}}_{b1} + A_1\mathbf{r} + A_2\boldsymbol{\varphi} + A_3\mathbf{r}_{b1} + A_4\mathbf{r}_{b2} = k\mathbf{r}_{d1} + d\dot{\mathbf{r}}_{d1} \quad (5)$$

$$\text{where } \begin{cases} A_1 = -\left(\frac{L-a}{L}s_{11} + \frac{1}{L}s_{21}\right) \\ A_2 = i\left(\frac{L-a}{L}s_{12} + \frac{1}{L}s_{22}\right) \\ A_3 = \left(\frac{L-a}{L}\right)^2 s_{11} + \frac{L-a}{L^2}s_{21} + \frac{L-a}{L^2}s_{12} + \frac{1}{L^2}s_{22} + (s_{b1} + k) \\ A_4 = \frac{(L-a)a}{L^2}s_{11} + \frac{a}{L^2}s_{21} - \frac{L-a}{L^2}s_{12} - \frac{1}{L^2}s_{22} \end{cases}$$

$$m_{b2}\ddot{\mathbf{r}}_{b2} + (d_{b2} + d)\dot{\mathbf{r}}_{b2} + B_1\mathbf{r} + B_2\boldsymbol{\varphi} + B_3\mathbf{r}_{b1} + B_4\mathbf{r}_{b2} = k\mathbf{r}_{d2} + d\dot{\mathbf{r}}_{d2} \quad (6)$$

$$\text{where } \begin{cases} B_1 = -\left(\frac{a}{L}s_{11} - \frac{1}{L}s_{21}\right) \\ B_2 = i\left(\frac{a}{L}s_{12} - \frac{1}{L}s_{22}\right) \\ B_3 = \frac{(L-a)a}{L^2}s_{11} - \frac{L-a}{L^2}s_{21} + \frac{a}{L^2}s_{12} - \frac{1}{L^2}s_{22} \\ B_4 = \left(\frac{a}{L}\right)^2 s_{11} - \frac{a}{L^2}s_{21} - \frac{a}{L^2}s_{12} + \frac{1}{L^2}s_{22} + (s_{b2} + k) \end{cases}$$

The stationary disk:

$$m_{j1}\ddot{\mathbf{r}}_{j1} + d_{j1}\dot{\mathbf{r}}_{j1} - d\dot{\mathbf{r}}_{b1} - k\mathbf{r}_{b1} + s_{j1}\mathbf{r}_{j1} = -k\mathbf{r}_{d1} - d\dot{\mathbf{r}}_{d1} \quad (7)$$

$$m_{j2}\ddot{\mathbf{r}}_{j2} + d_{j2}\dot{\mathbf{r}}_{j2} - d\dot{\mathbf{r}}_{b2} - k\mathbf{r}_{b2} + s_{j2}\mathbf{r}_{j2} = -k\mathbf{r}_{d2} - d\dot{\mathbf{r}}_{d2} \quad (8)$$

The plate of the moving disk (the plate in the ball/plate model):

$$\dot{\mathbf{r}}_{d1} = \begin{cases} \dot{\mathbf{r}}_{j1}, & |k(\mathbf{r}_{b1} - \mathbf{r}_{d1}) + d(\dot{\mathbf{r}}_{b1} - \dot{\mathbf{r}}_{j1})| < \mu N_1 \\ \dot{\mathbf{r}}_{b1} - \left[\frac{\mu N_1}{d} \frac{k(\mathbf{r}_{b1} - \mathbf{r}_{d1}) + d(\dot{\mathbf{r}}_{b1} - \dot{\mathbf{r}}_{j1})}{|k(\mathbf{r}_{b1} - \mathbf{r}_{d1}) + d(\dot{\mathbf{r}}_{b1} - \dot{\mathbf{r}}_{j1})|} - \frac{k}{d} (\mathbf{r}_{b1} - \mathbf{r}_{d1}) \right], & |k(\mathbf{r}_{b1} - \mathbf{r}_{d1}) + d(\dot{\mathbf{r}}_{b1} - \dot{\mathbf{r}}_{j1})| \geq \mu N_1 \end{cases} \quad (9)$$

$$\dot{\mathbf{r}}_{d2} = \begin{cases} \dot{\mathbf{r}}_{j2}, & |k(\mathbf{r}_{b2} - \mathbf{r}_{d2}) + d(\dot{\mathbf{r}}_{b2} - \dot{\mathbf{r}}_{j2})| < \mu N_2 \\ \dot{\mathbf{r}}_{b2} - \left[\frac{\mu N_2}{d} \frac{k(\mathbf{r}_{b2} - \mathbf{r}_{d2}) + d(\dot{\mathbf{r}}_{b2} - \dot{\mathbf{r}}_{j2})}{|k(\mathbf{r}_{b2} - \mathbf{r}_{d2}) + d(\dot{\mathbf{r}}_{b2} - \dot{\mathbf{r}}_{j2})|} - \frac{k}{d} (\mathbf{r}_{b2} - \mathbf{r}_{d2}) \right], & |k(\mathbf{r}_{b2} - \mathbf{r}_{d2}) + d(\dot{\mathbf{r}}_{b2} - \dot{\mathbf{r}}_{j2})| \geq \mu N_2 \end{cases} \quad (10)$$

Where $\mathbf{r} = x + iy$ is the displacement of the rotor disk; $\boldsymbol{\varphi} = \varphi_x + i\varphi_y$ is the swing angle of the rotor disk; $\mathbf{r}_{b1} = x_{b1} + iy_{b1}$ is the displacement of the left moving disk; $\mathbf{r}_{b2} = x_{b2} + iy_{b2}$ is the displacement of the right moving disk; $\mathbf{r}_{d1} = x_{d1} + iy_{d1}$ is the displacement of the left plate of the moving disk; $\mathbf{r}_{d2} = x_{d2} + iy_{d2}$ is the displacement of the right plate of the moving disk; $\mathbf{r}_{j1} = x_{j1} + iy_{j1}$ is the displacement of the left stationary disk; $\mathbf{r}_{j2} = x_{j2} + iy_{j2}$ is the displacement of the right stationary disk; m , m_{b1} , m_{b2} , m_{j1} , and m_{j2} respectively represent the masses of the rotor disk, the moving disks and the stationary disks; s_{11} , s_{12} , s_{21} and s_{22} represent the stiffness coefficients of the shaft at the rotor disk, where s_{11} is the displacement stiffness, s_{22} is the angle stiffness, s_{12} and s_{21} are cross stiffness; s_{b1} , s_{b2} , s_{j1} , and s_{j2} respectively represent the stiffness coefficients of the elastic support and the stationary disk; d_{b1} , d_{b2} , d_{j1} , and d_{j2} respectively represent the damping coefficients of the elastic support and the stationary disk; J_p and J_d respectively represent the polar moment of inertia and the moment of inertia about a diameter of the rotor disk; N_1 and N_2 respectively represent the pressing force between the moving disk and stationary disk of the two dampers; k and d are the tangential contact stiffness coefficient and damping coefficient of the contact interface introduced by the ball/plate model; L is the length between the two supports; a is the length between the left support and the rotor disk; ε is the eccentricity of the rotor disk; and Ω is the rotational speed of the rotor.

To solve the equations by numerical methods, the following variables are introduced:

$$\begin{cases} \mathbf{u}_1 = \{\mathbf{r}, \boldsymbol{\varphi}, \mathbf{r}_{b1}, \mathbf{r}_{b2}, \mathbf{r}_{j1}, \mathbf{r}_{j2}\}^T \\ \mathbf{u}_2 = \dot{\mathbf{u}}_1 \\ \mathbf{u}_3 = \{\mathbf{r}_{d1}, \mathbf{r}_{d2}\}^T \end{cases} \quad (11)$$

Equations (3)–(10) can be written in the following form:

$$\begin{bmatrix} \mathbf{E} & \mathbf{O} & \mathbf{O} \\ \mathbf{O} & \mathbf{M} & \mathbf{O} \\ \mathbf{O} & \mathbf{O} & \mathbf{E} \end{bmatrix} \begin{Bmatrix} \dot{\mathbf{u}}_1 \\ \dot{\mathbf{u}}_2 \\ \dot{\mathbf{u}}_3 \end{Bmatrix} + \begin{bmatrix} \mathbf{O} & -\mathbf{E} & \mathbf{O} \\ \mathbf{S} & \mathbf{D} & \mathbf{O} \\ \mathbf{O} & \mathbf{O} & \mathbf{O} \end{bmatrix} \begin{Bmatrix} \mathbf{u}_1 \\ \mathbf{u}_2 \\ \mathbf{u}_3 \end{Bmatrix} = \begin{Bmatrix} \mathbf{O} \\ \mathbf{f} \\ \mathbf{f}_d \end{Bmatrix} \quad (12)$$

where

$$\begin{aligned}
 [\mathbf{M}] &= \begin{bmatrix} m & & & & & \\ & J_d & & & & \\ & & m_{b1} & & & \\ & & & m_{b2} & & \\ & & & & m_{j1} & \\ & & & & & m_{j2} \end{bmatrix}; \\
 [\mathbf{S}] &= \begin{bmatrix} s_{11} & -is_{12} & -(\frac{L-a}{L}s_{11} + \frac{1}{L}s_{12}) & -(\frac{a}{L}s_{11} - \frac{1}{L}s_{12}) & 0 & 0 \\ is_{21} & s_{22} & -i(\frac{L-a}{L}s_{21} + \frac{1}{L}s_{22}) & -i(\frac{a}{L}s_{21} - \frac{1}{L}s_{22}) & 0 & 0 \\ A_1 & A_2 & A_3 & A_4 & 0 & 0 \\ B_1 & B_2 & B_3 & B_4 & 0 & 0 \\ 0 & 0 & -k & 0 & s_{j1} & 0 \\ 0 & 0 & 0 & -k & 0 & s_{j2} \end{bmatrix}; \\
 [\mathbf{D}] &= \begin{bmatrix} 0 & & & & & \\ & -iJ_p\Omega & & & & \\ & & d_{b1} + d & & & \\ & & & d_{b2} + d & & \\ & & & & -d & \\ & & & & & d_{j1} \\ & & & & & & -d & & & d_{j2} \end{bmatrix}; \\
 \{\mathbf{f}\} &= \begin{bmatrix} m\varepsilon\Omega^2 e^{i\Omega t} \\ 0 \\ k\mathbf{r}_{d1} + d\dot{\mathbf{r}}_{d1} \\ k\mathbf{r}_{d2} + d\dot{\mathbf{r}}_{d2} \\ -(k\mathbf{r}_{d1} + d\dot{\mathbf{r}}_{d1}) \\ -(k\mathbf{r}_{d2} + d\dot{\mathbf{r}}_{d2}) \end{bmatrix}; \\
 \{\mathbf{f}_d\} &= \begin{cases} \begin{cases} \dot{\mathbf{r}}_{j1}, & |k(\mathbf{r}_{b1} - \mathbf{r}_{d1}) + d(\dot{\mathbf{r}}_{b1} - \dot{\mathbf{r}}_{j1})| < \mu N_1 \\ \dot{\mathbf{r}}_{b1} - \left[\frac{\mu N_1}{d} \frac{k(\mathbf{r}_{b1} - \mathbf{r}_{d1}) + d(\dot{\mathbf{r}}_{b1} - \dot{\mathbf{r}}_{j1})}{|k(\mathbf{r}_{b1} - \mathbf{r}_{d1}) + d(\dot{\mathbf{r}}_{b1} - \dot{\mathbf{r}}_{j1})|} - \frac{k}{d} (\mathbf{r}_{b1} - \mathbf{r}_{d1}) \right], & |k(\mathbf{r}_{b1} - \mathbf{r}_{d1}) + d(\dot{\mathbf{r}}_{b1} - \dot{\mathbf{r}}_{j1})| \geq \mu N_1 \end{cases} \\ \begin{cases} \dot{\mathbf{r}}_{j2}, & |k(\mathbf{r}_{b2} - \mathbf{r}_{d2}) + d(\dot{\mathbf{r}}_{b2} - \dot{\mathbf{r}}_{j2})| < \mu N_2 \\ \dot{\mathbf{r}}_{b2} - \left[\frac{\mu N_2}{d} \frac{k(\mathbf{r}_{b2} - \mathbf{r}_{d2}) + d(\dot{\mathbf{r}}_{b2} - \dot{\mathbf{r}}_{j2})}{|k(\mathbf{r}_{b2} - \mathbf{r}_{d2}) + d(\dot{\mathbf{r}}_{b2} - \dot{\mathbf{r}}_{j2})|} - \frac{k}{d} (\mathbf{r}_{b2} - \mathbf{r}_{d2}) \right], & |k(\mathbf{r}_{b2} - \mathbf{r}_{d2}) + d(\dot{\mathbf{r}}_{b2} - \dot{\mathbf{r}}_{j2})| \geq \mu N_2 \end{cases} \end{cases}
 \end{aligned}$$

\mathbf{E} is the unit matrix, and \mathbf{O} is the zero matrix.

$$\text{Let } \begin{bmatrix} \mathbf{E} & \mathbf{O} & \mathbf{O} \\ \mathbf{O} & \mathbf{M} & \mathbf{O} \\ \mathbf{O} & \mathbf{O} & \mathbf{E} \end{bmatrix} = \mathbf{A}, \quad \begin{bmatrix} \mathbf{O} & -\mathbf{E} & \mathbf{O} \\ \mathbf{S} & \mathbf{D} & \mathbf{O} \\ \mathbf{O} & \mathbf{O} & \mathbf{O} \end{bmatrix} = \mathbf{B}, \quad \begin{Bmatrix} \mathbf{O} \\ \mathbf{f} \\ \mathbf{f}_d \end{Bmatrix} = \{\mathbf{p}\}, \quad \begin{Bmatrix} \mathbf{u}_1 \\ \mathbf{u}_2 \\ \mathbf{u}_3 \end{Bmatrix} = \{\mathbf{u}\}, \text{ then}$$

Eq. (12) can be transformed into

$$\{\dot{\mathbf{u}}\} = -\mathbf{A}^{-1} \cdot \mathbf{B} \cdot \{\mathbf{u}\} + \mathbf{A}^{-1} \cdot \{\mathbf{p}\} \quad (13)$$

Equation (13) can be solved by numerical method for ordinary differential equations.

3 Characteristics of a Rotor with ESDFDs

3.1 Rotor Systems with the ESDFDs

Figure 4 shows a rotor system with two ESDFDs. The rotor experimental apparatus consists of a bias disk rotor, two dampers, two self-aligning bearings, a flexible coupling, a motor and two amplifiers for driving the damper.

The amplitude-frequency characteristics of a rotor with ESDFDs under variable pressing force were tested. Two friction pairs were used in the experiments. One was brass/steel, and the other was steel/steel. The test results are shown in Figs. 5a and 6a.

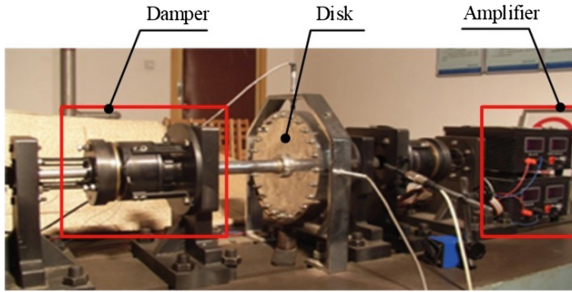


Fig. 4. The rotor system with the ESDFDs

Numerical simulations were carried out using the parameters of the rotor test rig shown in Fig. 4 and the model shown in Fig. 3. The geometrical dimensions of the rotor system are as follows:

$L = 700$ mm, $a = 250$ mm, $b = 450$ mm, $t = 28$ mm, $r = 120$ mm, $h = 40$ mm, and material parameters are $\rho = 7.8 \times 10^3$ kg/m³, $E = 2.1 \times 10^{11}$ N/m².

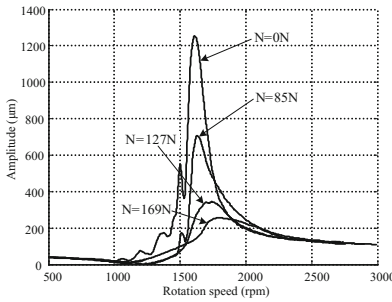
Based on the geometrical dimensions and material parameters above, the mass, stiffness, moment of inertia, etc., of the rotor can be obtained. In addition, in order to investigate the effect of mode shape on damping effect, m_{b2} is valued much larger than m_{b1} to make the vibration amplitude at the right elastic support higher than left on the second mod. The results are shown in Figs. 5b and 6b.

All of the basic Parameters are listed in Table 1.

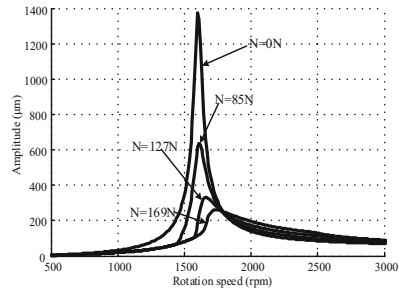
Figure 5 shows the amplitude-frequency characteristics when the friction pair is brass/steel, and Fig. 6 shows the amplitude-frequency characteristics when the friction pair is steel/steel. Comparing figure a with figure b in both figures, the calculation results show good agreement with the test results, not only regarding the trend but also the specific values with the damper. Figure 5 shows a significant mismatch for zero N pressure force is that nonlinearity response of rotor systems with a large unbalance.

Table 1. Parameters of the rotor for numerical analysis

Parameters	Values	Parameters	Values
m	15.7 kg	ε	3×10^{-5} m
J_p	0.113 kg m ²	J_d	0.0586 kg m ²
a	250 mm	L	700 mm
s_{11}	1.4251×10^6 N/m	s_{12}	2.1026×10^5 N/m
s_{21}	2.1026×10^5 N/m	s_{22}	1.1827×10^5 N/m
s_{b1}	7.38×10^5 N/m	s_{b2}	7.73×10^5 N/m
d_{b1}	250 Ns/m	d_{b2}	250 Ns/m
m_{b1}	1.6 kg	m_{b2}	12 kg
k	3×10^5 N/m	d	10 Ns/m
m_{j1}	2 kg	m_{j2}	2 kg
s_{j1}	1×10^7 N/m	s_{j2}	1×10^7 N/m
d_{j1}	134 Ns/m	d_{j2}	134 Ns/m
μ (brass/steel)	0.19	μ (steel/steel)	0.1

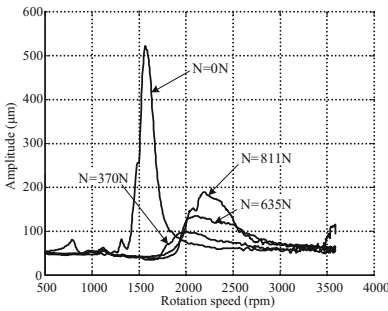


a. Test results

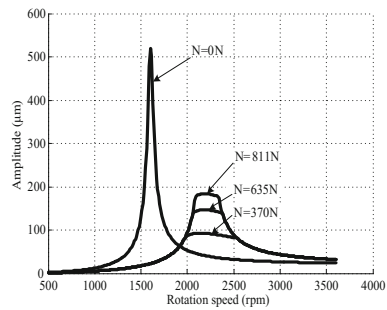


b. Calculation results

Fig. 5. Amplitude-frequency characteristics of the rotor, brass/steel



a. Test results



b. Calculation results

Fig. 6. Amplitude-frequency characteristics of the rotor, steel/steel

3.2 Characteristics of Damping Performance

Stiffness of the Elastic Support

The critical speed and mode shape can be affected by the elastic support. The performances of the ESDFD with respect to the stiffness of the elastic support are shown in Figs. 7 and 8. The friction force is applied simultaneously on the left and right elastic supports, $N_1 = N_2 = 20$ N.

Figure 7 is the mode shape of the rotor with the different stiffness of elastic supports, it is shown that the deflection of the disk increases in comparison to the deflection of the bearings with increase of stiffness. Its means that the smaller the stiffness coefficient of the elastic supports, the more vibration energy is concentrated in the elastic support.

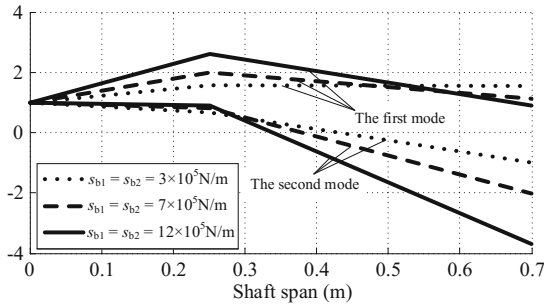


Fig. 7. Mode shape of the rotor

Figure 8 shows the simulation results of the unbalance response of the rotor with the different stiffness of elastic supports. It is shown that the damping performance of the ESDFD is closely related to the operating speed of the rotor and the characteristics of the rotor’s mode. Even the same dampers fixed on different rotors or different support locations can perform differently.

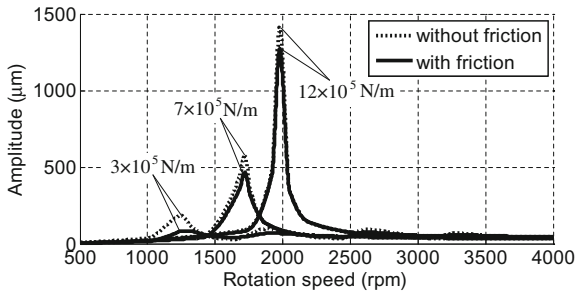


Fig. 8. Unbalance response of the rotor

Pressure Force and the Friction Coefficient

The damping provided by an ESDFD to a rotor is derived from the sliding friction force between the stationary and moving disks. So, as the product of the pressure forces N_1 and N_2 and the friction coefficient μ , the sliding friction forces μN_1 and μN_2 directly determine the damping performance of the damper.

Figure 9 is the simulation results of the unbalance response of the rotor with the different sliding friction forces.

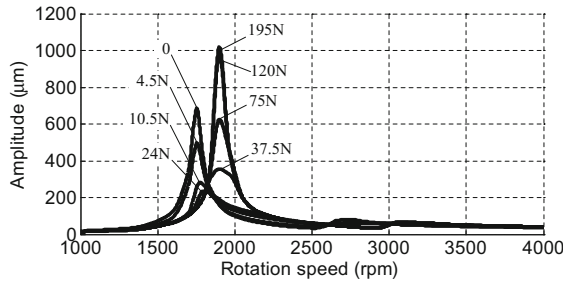


Fig. 9. Unbalance response of the rotor

It is shown in Fig. 9 that as the sliding friction forces μN_1 and μN_2 increase, the critical speed of the rotor system moves upward, and the peak amplitude of the rotor at the critical speed decreases and then increases. When the sliding friction forces are large enough, the peak amplitude of the rotor even exceeds the peak amplitude without friction. There must be an optimal sliding friction force under which the unbalance response of the rotor system will be smallest for all rotational speeds, and the rotor can pass through the critical speed smoothly. In this model, the optimal sliding friction force is between 24 N and 37.5 N.

Stiffness of the Stationary Disk and Tangential Contact Stiffness of the Contact Interface

Between the moving disk and the mounting base of the stationary disk, there is a combined stiffness that consists of the stiffness of the stationary disk and the tangential contact stiffness of the contact interface.

The Stiffness of the Stationary Disk

Figure 10 is the simulation results of the unbalance response of the rotor with the stiffness the stationary disk. The stiffness the stationary disks $s_{j1} = s_{j2}$, and the pressure forces of the two dampers, applied simultaneously $N_1 = N_2 = 150$ N. It is shown that as the stiffness coefficient of the stationary disk increases, the peak amplitude of the rotor decreases, while the damping performance of the elastic support/dry friction damper improves. When the stiffness coefficients s_{j1} and s_{j2} increase to some extent, the unbalance response curve is nearly constant and the damping performance of the damper no longer changes.

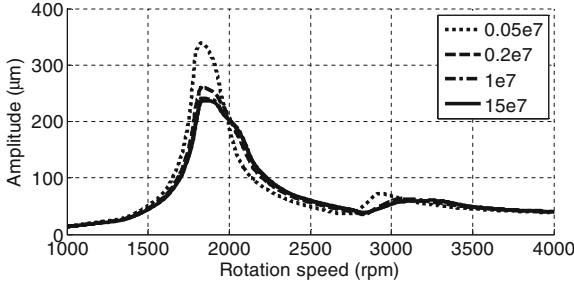


Fig. 10. Unbalance response of the rotor

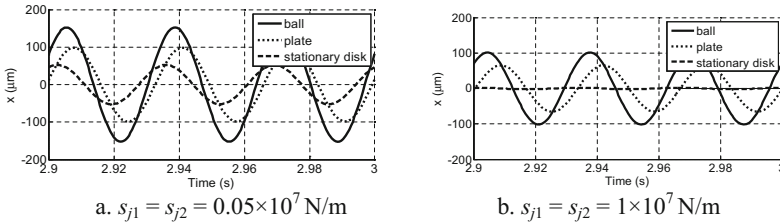


Fig. 11. Time domain waveform of the left support

Figure 11 is the simulation results of time domain waveform of the left support at 1800 rpm. As shown in Fig. 11a, when the stiffness coefficient is small, $s_{j1} = s_{j2} = 0.05 \times 10^7 \text{ N/m}$, the motion of the stationary disk under the traction of the moving disk is obvious, which makes the relative motion between the moving and stationary disks smaller, which is unfavourable for the damping performance of the elastic support/dry friction damper. In Fig. 11b, when the stiffness coefficient is large, $s_{j1} = s_{j2} = 1 \times 10^7 \text{ N/m}$, the stationary disk barely moves, which is very favorable for the damper.

The Tangential Contact Stiffness of the Contact Interface

Figure 12 is the simulation results of unbalance response of the rotor with the tangential contact stiffness k and the pressure forces of the two dampers, applied simultaneously $N_1 = N_2 = 150 \text{ N}$. It is shown that as the stiffness coefficient k increases, the peak amplitude of the rotor decreases and the damping performance of the elastic support/dry friction damper improves.

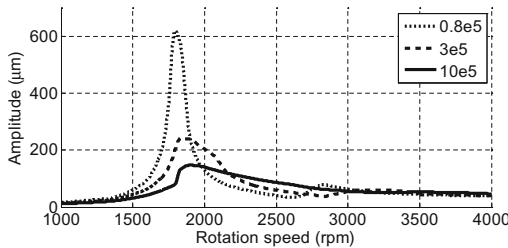


Fig. 12. Unbalance response of the rotor

In the ball/plate model, the plate moves under the traction of the ball. The damping comes from the relative motion between the plate and the stationary disk. When the tangential contact stiffness k is small, the relative motion between the plate and the stationary disk is small, so the damping will be small.

The stiffness of the stationary disk s_j and the tangential contact stiffness of the contact interface k are connected in series between the moving disk and the mounting base of the stationary disk. The larger this combined stiffness is, the better the damper's damping performance.

The Dampers are Applied Different Control Schemes

Due to the additional stiffness of the damper, the critical speed of the rotor system increases as the pressing force increases. This is not allowed for the rotor system. It is necessary to design a control scheme based on the characteristics of the damper, with which that rotor vibration control can be achieved without changing the critical speed of the rotor system. The switch control is one of the most basic control schemes. If the rotational speeds of rotor are within the critical speed regions, the damper is switched on, or the damper switched off. The optimal pressure force N are represented by the control voltage depending simulation results of the damper, or applied proportional (P) control based on the vibration amplitude feedback. The P controller is defined as

$$U = U_0 + k_p(PP_D - PP_{D0})$$

Where U is the control voltage, U_0 is the initial voltage, k_p is the proportional gain, PP_D and PP_{D0} are the amplitude of P-P and reference amplitude of P-P, respectively.

The experiments are conducted to investigate the vibration characteristics of the rotor system in switch control scheme. The control voltages are depending on the simulation results and P controller.

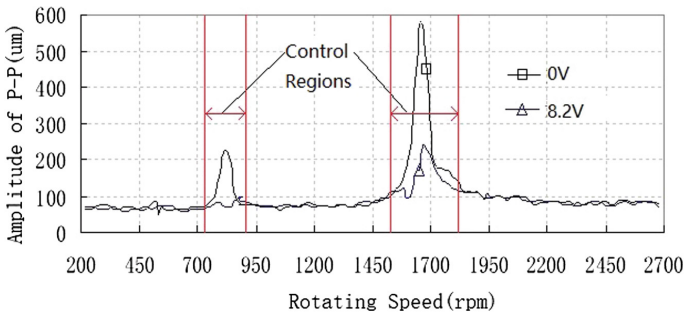


Fig. 13. Diagrams of bode while using switch control at 0 V and 8.2 V

Figure 13 is the amplitude-frequency characteristics of the rotor system at the disk while using switch control and without control in the vertical direction. According to the simulation results, the control voltage is 8.2 V. Comparing to without control, the vibration amplitude of disk is clearly decreased within the critical speed regions, and not changed out of the control regions. At the same time, there is also no change of the critical

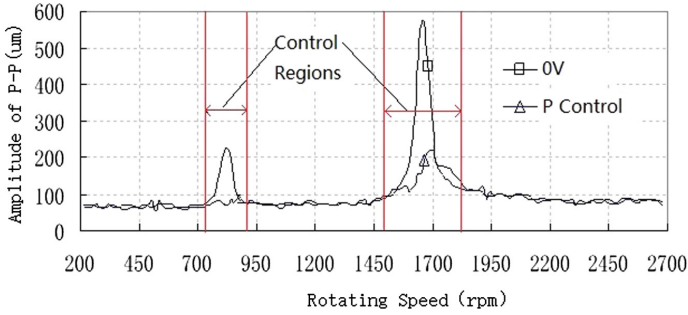


Fig. 14. Diagrams of bode while using switch control at 0 V and P control

speed of the rotor system. The reason is that the additional stiffness of the damper to rotor systems is removed when applied the switch control scheme out of critical regions.

Figure 14 is the amplitude-frequency characteristics of the rotor system at the disk while using switch control and without control in the vertical direction. The control voltages are depending on the P controller. Where U_0 is 3 V, k_p is 0.013, PP_{D0} is 200 μm . Comparing to the control voltage depended on the simulation results, There is the same effect of vibration reduction.

It is shown that switch control scheme is very suitable for the ESDFD to control the vibration of rotor systems actively. It is also possible to optimize vibration control of rotor systems with the ESDFD.

4 Conclusions

Conclusions can be drawn from the theoretical and experimental analysis of the rotor system with the ESDFD:

- (1) The ESDFD can effectively control unbalance response of rotor systems around the critical speed by adding the damping and stiffness to rotor systems.
- (2) The switch control scheme can effectively controls the ESDFD without changing the critical speed of rotor systems, and the control voltages can be obtained by simulation results or by P controller.
- (3) The two-dimensional friction and ball/plate model are very effective in analyzing the steady responses of unbalance. Theoretical results agree with the experimental results to a great extent.

References

1. Fan, T., Liao, M.: Dynamic behavior of a rotor with dry friction dampers. *Mech. Sci. Technol.* **22**, 743–745 (2003)
2. Fan, T: Vibration reduction by elastic support dry friction damper. Ph.D. thesis, Northwestern Polytechnical University (2006)

3. Wang, S., Liao, M.: Experimental investigation of an active elastic support/dry friction damper on vibration control of rotor systems. *Int. J. Turbo Jet Engines* **22**, 13–17 (2014)
4. Wang, S.: Vibration control techniques for rotor systems by an active elastic support/dry friction damper. Ph.D. thesis, Northwestern Polytechnical University (2008)
5. Liao, M., Song, M., Wang, S.: Active elastic support/dry friction damper with piezoelectric ceramic actuator. *Shock Vib. ID 712426*, 1–10 (2014)
6. Deng, X., Liao, M., Liebich, R., Gasch, R.: Experimental research of bending and torsional vibrations of a double disc rotor due to rotor-to-stator contacts. *J. Aerosp. Power* **17**, 205–211 (2002)
7. Abu-Mahfouz, I., Banerjee, A.: On the investigation of nonlinear dynamics of a rotor with rub-impact using numerical analysis and evolutionary algorithms. *Procedia Comput. Sci.* **20**, 140–147 (2013)
8. Oberst, S., Lai, J.C.S., Marburg, S.: Guidelines for numerical vibration and acoustic analysis of disc brake squeal using simple models of brake systems. *J. Sound Vib.* **332**(9), 2284–2299 (2013)
9. Ma, Y., Zhang, Q., Zhang, D., Scarpa, F., Liu, B., Hong, J.: Tuning the vibration of a rotor with shape memory alloy metal rubber supports. *J. Sound Vib.* **351**, 1–16 (2015)
10. Griffin, J.H., Menq, C.H.: Friction damping of circular motion and its implications to vibration control. *J. Vib. Acoust.* **113**, 225–229 (1991)
11. Menq, C.H., Bielak, J., Griffin, J.H.: The influence of microslip on vibratory response, part I: a new microslip model. *J. Sound Vib.* **107**, 279–293 (1986)
12. Menq, C.H., Griffin, J.H., Bielak, J.: The influence of microslip on vibratory response, part II: a comparison with experimental results. *J. Sound Vib.* **107**, 295–307 (1986)
13. Ding, Q., Chen, Y.: Analyzing resonant response of a system with dry friction damper using an analytical method. *J. Vib. Control* **14**(8), 1111–1123 (2008)
14. Liu, C.S., Hong, H.K., Liou, D.Y.: Two-dimensional friction oscillator: group-preserving scheme and handy formulae. *J. Sound Vib.* **266**, 49–74 (2003)
15. Breard, C., Green, J.S., Vahdati, M., Imregun, M.: A non-linear integrated aero elasticity method for the prediction of turbine forced response with friction dampers. *Int. J. Mech. Sci.* **43**, 2715–2736 (2001)



Identification of Crack and Internal Damping Parameters Using Full Spectrum Responses from a Jeffcott Rotor Incorporated with an Active Magnetic Bearing

Nilakshi Sarmah and Rajiv Tiwari^(✉)

Department of Mechanical Engineering,
Indian Institute of Technology Guwahati,
Kamrup, Assam 781039, India
rtiwari@iitg.ernet.in

Abstract. In smart rotor technology the active magnetic bearing plays a vital role in controlling vibration for safe and efficient running of high speed machineries, and for its condition monitoring or system identification. Researchers mostly investigated the dynamics of cracked rotors independent of the internal damping. Nevertheless, the internal damping is also influenced by the presence of crack in a rotating system because of rubbing of crack fronts during its opening and closing throughout the shaft whirling. The present work deals with the identification of rotor dynamic parameters in the cracked Jeffcott rotor considering both external and internal damping through a model based technique. The active control of vibration that is caused due to the transverse crack, unbalance and internal damping can be done by using the magnetic bearing. Numerical rotor responses and AMB currents are investigated using the full spectrum tool, which can reveal directional nature of the vibration signature in frequency domain. The response and current harmonics due to the excitation force of crack function, which is found from full spectrum analysis, are input to the proposed identification algorithm. It estimates the additive crack stiffness, unbalance in rotor, external damping, internal damping and AMB parameters such as the force-displacement and force-current coefficients. For different noise levels in responses and currents the proposed identification algorithm is tested for validating its robustness against measurement noise.

Keywords: Estimation of internal damping · Active magnetic bearing (AMB) Unbalance · Switching crack · Full spectrum

1 Introduction

In modern machinery control, the automated health monitoring of machines is becoming common, increasingly. Active magnetic bearing which is a mechatronic product has been more profound in using as a bearing or as a controller in high-speed rotating machineries for its safe operation and integrity. Towards the continuation and advancement of higher and higher speeds in rotating machineries, witnesses many mechanical side effects, which induces vibrations into it. The continuous monitoring of

performances of rotating machinery are done through vibration monitoring systems, and the information collected are used for more efficient scheduling of routine interruption [1]. The condition monitoring is a predictive maintenance measure of the health of a machine. The best way to prevent failure and measure reliability of a machine is to identify and eliminate the faults in early stage of its design [1].

Practical rotors experience mainly two common faults, among others, which influence vibrations in machines are basically unbalances and cracks. The breathing behavior of crack depends on the vibration due to out of balance force, while it is much smaller than the static deflection of the rotor due to gravity. Opening and closing of crack faces occur due to the rotation of the shaft and thus, based on this phenomenon various crack models have been developed [2, 3]. A paper on different types of cracks including crack initiation and its propagation as well as various diagnostics methods are reviewed by Sabnavis and Kirk [4]. The dynamics of the rotor system can be analyzed by identification of system parameters by the model based approach [5]. Bachschmid et al. [6] discussed an identification approach through modeling, based on least square fit to identify the multiple faults, simultaneously, in frequency domain. The experimental validation of the algorithm as well as effectiveness of the developed model in identifying faults' position, phase, have been elaborated.

Full spectrum is a handy tool as it provides the directional nature of signals by retaining all the phase information, which helps in identifying faults, correctly. Patel and Darpe [7] illustrated the effect of vibration response in the presence of rotor-stator rub, simultaneously, by introducing full spectrum approach. Shrivankumar and Tiwari [8] illustrated a model-based identification approach of the switching crack, where the crack was identified by the reduction in flexibility of the system. Full spectrum analysis was used to obtain the multi harmonics from the response to use in the developed identification algorithm.

In high speed rotating machineries the internal damping induces instability and results in excessive vibration, which actually affects the life of a system. In literature, the internal damping influences instability in supercritical speed ranges, while at subcritical speed it reduces amplitude of vibration [9]. The internal viscous damping introduces circulatory effect which causes destabilizing effects [9]. Many literatures on stability analysis of rotors due to internal damping have been discussed. Nelson and Zorzi [10], and Melanson and Zu [11] developed finite element formulations considering rotary inertia, both internal and external damping, and gyroscopic effect for the rotor bearing system.

Active magnetic bearing in modern days are in great use as active devices for fault detection and diagnosis. In modern rotating machineries, the major area of interest is its vibration-based condition monitoring through active devices. Quinn and Mani [12] illustrated an identification technique to detect crack using active magnetic bearings as an actuator. The rotating system is excited at a combination resonance, which describes the presence of breathing crack.

Lees et al. [13] overviewed the quantification of faults in rotating machinery through model based identification approach, which is less time consuming. Various fault parameter estimations, like of the bow, misalignment and crack, using mathematical models are discussed, which are for practical rotors have been a real challenge. Singh and Tiwari [14] worked on the identification of additive stiffness of crack and

AMB parameters using model based approach. Identification algorithm was developed, where the full spectrum based amplitudes and phases have been taken into consideration to estimate the parameters.

As internal damping force is rotating in nature, it causes severe problems by inducing instability in supercritical speed range of rotors. The internal damping effect is enhanced to a great extent due to the presence of crack in a rotor system. Thus, there is a need for accurate identification of these fault parameters so as to monitor the operational condition of rotating machinery. Thereby, warranting the longevity of the plant and safety of the personnel using the equipment. The active control of vibration is a promising solution to mitigate the failure of a system. This can be achieved with the usage of AMB as a controller. However, it can be seen from the literature survey that researchers have hardly touched upon the simultaneous consideration of rotor crack, internal damping and usage of AMB as controller. Therefore, the novelty of this research lies in,

- (1) simultaneous consideration of rotor crack, internal damping and AMB for vibration control and identification of fault parameters (like internal damping, additive stiffness) and AMB parameters, and
- (2) usage of full spectrum analysis to understand the directional nature, i.e. the forward as well as backward whirling directions of the rotor system of the generated response.

The work starts with developing equation of motion (EOM) of the Jeffcott rotor considering unbalance, crack, external damping, internal damping, and magnetic bearing force. The frequency response of the system is derived based on the developed EOM. This is further used for development of identification algorithm (regression based least-square fitting technique) to estimate the aforementioned parameters from the obtained harmonics.

2 Description of Cracked Jeffcott Rotor System

The Jeffcott rotor comprises of a rigid disc at mid-span of a cracked flexible shaft, and it is supported on two rigid bearings and an AMB is integrated with it as shown in Fig. 1. Vibrations emanating by the system and due to the presence of faults can be controlled by the AMB existing into the system itself. Weight dominance effect where the disc mass considered is heavy. According to the weight dominance effect, the vibration response due to static deflection of the system due to gravity is much higher than that of the dynamic response.

Motions in two orthogonal directions have been considered for the rotor-AMB model. Internal (rotating) damping effects, which often bring the rotor to dynamic unstable condition, are also considered in the mathematical modeling.

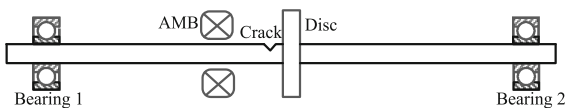


Fig. 1. Schematic of cracked Jeffcott rotor with disc at mid-span and integrated with an AMB

The crack present in the rotor system provides an additional flexibility into the shaft, which varies with time and thus alters the natural frequency of the system. In the proposed model, switching crack is used, where shifting from open to closed of the crack faces, and vice-a-versa is sudden. The switching crack model is based on the hinge model [15]. The non-rotating (external) viscous damping and rotating (internal) viscous damping, both are considered in the rotor system model.

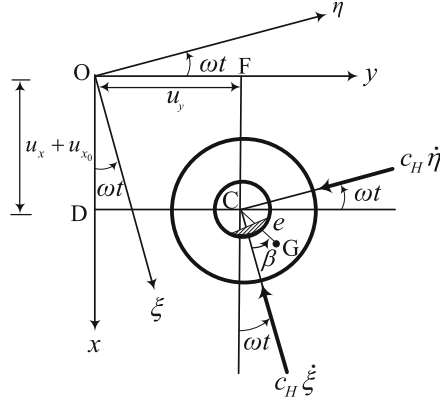


Fig. 2. Disc rotation of a Jeffcott rotor in rotating frame with reference to stationary coordinate system with the crack, unbalance and internal damping

In the rotor model, the inertial frame of reference is considered; where x and y are axes in the vertical and horizontal directions, respectively, and its origin O as shown in Fig. 2, is at the mid-span on the bearing center line. Displacements in rotating coordinate system (ξ - η) are represented by ξ and η . The spin speed of the shaft is defined by ω and t is the time. The product of spin speed and time is considered here as $\omega t = \theta$. The distance between the center of gravity (G) and center of mass (C), is denoted by eccentricity (e), m is the disc mass and k is the undamaged shaft stiffness.

2.1 Equations of Motion Considering Both External and Internal Damping

The equation of motion of the Jeffcott rotor considering both external and internal damping, however, without other excitation forces can be represented in rotating frame of reference in complex form by $\zeta = \xi + j\eta$, as, in [16]

$$m(\ddot{\zeta} + 2j\omega\dot{\zeta} - \omega^2\zeta) + c_V(\dot{\zeta} + j\omega\zeta) + c_H\dot{\zeta} + k\zeta = 0 \quad (1)$$

The equations of motion in complex form with $z = (u_x + u_{x_0}) + ju_y$ in stationary co-ordinate system as,

$$m\ddot{z} + (c_V + c_H)\dot{z} + (k - j\omega c_H)z = 0 \quad (2)$$

The transformation between the stationary and rotating coordinates are given as $\zeta = ze^{-j\omega t}$. Equation (2) can be split into two translation directions, as

$$m\ddot{u}_x + (c_V + c_H)\dot{u}_x + k(u_x + u_{x_0}) + \omega c_H u_y = 0 \quad (3)$$

$$m\ddot{u}_y + (c_V + c_H)u_y - \omega c_H(u_x + u_{x_0}) + ku_y = 0 \quad (4)$$

2.1.1 Modelling of Crack Force

The model of the crack force considered in the present case is the switching crack. The breathing behavior of the crack face depends on the speed and the orientation of the crack during shaft rotation. The switching crack excitation function based on the hinge model as illustrated by Gasch [15], has square periodic wave that comprises of multi-harmonics. The additive stiffness which comes into existence due to the presence of crack, is rotating in nature contributes reduction in stiffness. The stiffness matrix of the cracked shaft $\mathbf{K}(t)$ arises due to breathing crack which is time varying in nature is given as

$$\mathbf{K}(t) = \mathbf{K}_0 + \Delta\mathbf{K}(u(t), \theta(t)) \quad (5)$$

where \mathbf{K}_0 represents the diagonal stiffness matrix of an intact shaft assumed to be isotropic and $\Delta\mathbf{K}$ represents the additive stiffness matrix that describes the decrease in stiffness of shaft due to the presence of crack. The crack force in the rotating co-ordinate system is represented as,

$$\begin{Bmatrix} f_\xi \\ f_\eta \end{Bmatrix}_{rot} = \left(\begin{bmatrix} k_0 & 0 \\ 0 & k_0 \end{bmatrix} - s(t) \begin{bmatrix} \Delta k_\xi & 0 \\ 0 & 0 \end{bmatrix} \right) \begin{Bmatrix} \xi \\ \eta \end{Bmatrix}_{rot} \quad (6)$$

where, $s(t)$ is the crack excitation function for switching model of crack represented in [15] as,

$$s(t) = \frac{1}{2} + \frac{2}{\pi} \cos(\theta) - \frac{2}{3\pi} \cos(3\theta) + \frac{2}{5\pi} \cos(5\theta) - \frac{2}{7\pi} \cos(7\theta) + \dots \quad (7)$$

The stiffness matrix term in inertial frame of reference can be represented by transforming it from rotating co-ordinate system as,

$$\mathbf{K}_0 + \Delta\mathbf{K}(t) = \mathbf{T}^{-1}(t) (\mathbf{K}_{0,rot} + \Delta\mathbf{K}_{rot}(t)) \mathbf{T}(t) \quad (8)$$

where, the transformation matrix \mathbf{T} is defined as,

$$\mathbf{T}(t) = \begin{bmatrix} \cos \theta & \sin \theta \\ -\sin \theta & \cos \theta \end{bmatrix} \quad (9)$$

The whole stiffness matrix after transformation with additive stiffness parameter, Δk_ξ is given as,

$$K_0 + \Delta K(t) = \begin{bmatrix} k_0 & 0 \\ 0 & k_0 \end{bmatrix} - \frac{1}{2}s(t)\Delta k_\xi \begin{bmatrix} (1 + \cos 2\theta) & \sin 2\theta \\ \sin 2\theta & (1 - \cos 2\theta) \end{bmatrix} \quad (10)$$

2.1.2 Modelling of Unbalance Force

The unbalance excitation force acts in the rotor system is represented by

$$f_{umb} = me\omega^2 \begin{Bmatrix} \cos(\theta + \beta) \\ \sin(\theta + \beta) \end{Bmatrix} \quad (11)$$

2.1.3 Modelling of Magnetic Force

The magnetic bearing force can be expressed in the linear form near the operating point in terms of the force-displacement factor k_s and the force-current factor k_i as,

$$f_{AMB} = \begin{Bmatrix} -k_s u_x + k_i i_{cx} \\ -k_s u_y + k_i i_{cy} \end{Bmatrix} \quad (12)$$

Proportional-integral-derivative (PID) controller is practiced for stable operation of the system. The expression of the control current i_{cx} and i_{cy} of PID controller is expressed as,

$$i_c(t) = K_P z(t) + K_I \int z(t) dt + K_D \frac{dz(t)}{dt} \quad (13)$$

2.2 Overall Motion Equation of the Cracked Jeffcott Rotor Bearing System

All the excitation forces such as unbalance force, crack force and magnetic force after incorporation into Eq. (4), we get

$$\begin{aligned} & \begin{bmatrix} m & 0 \\ 0 & m \end{bmatrix} \begin{Bmatrix} \ddot{u}_x \\ \ddot{u}_y \end{Bmatrix} + \begin{bmatrix} c_V + c_H & 0 \\ 0 & c_V + c_H \end{bmatrix} \begin{Bmatrix} \dot{u}_x \\ \dot{u}_y \end{Bmatrix} + \begin{bmatrix} k_0 & \omega c_H \\ -\omega c_H & k_0 \end{bmatrix} \begin{Bmatrix} u_x \\ u_y \end{Bmatrix} = me\omega^2 \begin{Bmatrix} \cos(\theta + \beta) \\ \sin(\theta + \beta) \end{Bmatrix} \\ & + \frac{1}{2}s(t)\Delta k_\xi \begin{bmatrix} (1 + \cos 2\theta) & \sin 2\theta \\ \sin 2\theta & (1 - \cos 2\theta) \end{bmatrix} \begin{Bmatrix} u_{x_0} \\ 0 \end{Bmatrix} - \omega c_H \begin{Bmatrix} u_{x_0} \\ 0 \end{Bmatrix} - \begin{Bmatrix} -k_s u_x + k_i i_{cx} \\ -k_s u_y + k_i i_{cy} \end{Bmatrix} \end{aligned} \quad (14)$$

From equilibrium position in complex form introducing $z = u_x + ju_y$, and $i_c = i_{cx} + ji_{cy}$ for both displacement and current, respectively, into Eq. (14), as

$$m\ddot{z} + (c_V + c_H)\dot{z} + (k_0 - k_s - j\omega c_H)z = \frac{1}{2}s(t)\Delta k_\xi u_{x_0}(1 + e^{j2\theta}) + j\omega c_H u_{x_0} + me\omega^2 e^{j(\theta+\beta)} - k_i \left\{ K_P z(t) + K_I \int z(t)dt + K_D \frac{dz(t)}{dt} \right\} \quad (15)$$

The development of identification algorithm and numerical simulation has been done on the basis of the overall system's EOM.

3 Response Analysis in Both Time and Frequency Domain

The vibration response based on EOM (15) can be generated into both time and frequency domain. Equation (10) can be represented in summation form consisting of participation factor as p_i and i represent the harmonics number, as

$$f_{cr} = \Delta k_\xi u_{x_0} \sum_{i=-\infty}^{\infty} p_i e^{ji\theta} \quad (16)$$

where, switching crack multi harmonics crack excitation function can be implemented in the crack force, as

$$u_{x_0} \Delta k_\xi \left(\begin{array}{l} \dots + 0.009e^{-j5\theta} - 0.021e^{-j3\theta} + 0.106e^{-j\theta} + 0.25 + 0.319e^{j\theta} + 0.25e^{j2\theta} \\ + 0.106e^{j3\theta} - 0.021e^{j5\theta} + 0.009e^{j7\theta} + \dots \end{array} \right) = u_{x_0} \Delta k_\xi \sum_{i=-n}^n p_i e^{ji\theta} \quad (17)$$

Equation as a combination of all current harmonics can be represented by,

$$f_{AMB} = k_i \sum_{i=-\infty}^{\infty} I_i e^{ji\theta} \quad (18)$$

The assumed solution $Z(t)$ for a particular harmonic of crack force excitation is $Z(\omega)e^{ji\theta}$ and for control current $I(t)$ as $I(\omega)e^{ji\theta}$. The proposed system is assumed to be linear for which the principle of superposition can be used. The assumed solutions for each harmonic of the spectrum have been added up using superposition principle, as

$$z(t) = Z_{-n}e^{-nj\theta} + \dots + Z_{-5}e^{-5j\theta} + Z_{-3}e^{-3j\theta} + Z_{-1}e^{-1j\theta} + Z_0e^{0j\theta} + Z_1e^{j\theta} + Z_2e^{2j\theta} + Z_3e^{3j\theta} + Z_5e^{5j\theta} + Z_7e^{7j\theta} + \dots + Z_n e^{nj\theta} \quad (19)$$

Similarly, for the current, as

$$i_c(t) = I_{-n}e^{-nj\theta} + \dots + I_{-5}e^{-5j\theta} + I_{-3}e^{-3j\theta} + I_{-1}e^{-1j\theta} + I_0e^{0j\theta} + I_1e^{j\theta} + I_2e^{2j\theta} + I_3e^{3j\theta} + I_5e^{5j\theta} + I_7e^{7j\theta} + \dots + I_n e^{nj\theta} \quad (20)$$

The EOM (15) in frequency domain for multi-harmonics, as

For $i = 0$;

$$Z_0\{(-\omega^2)m + (j\omega)(c_V + c_H) + (k_0 - k_s - j\omega c_H)\} = \Delta k_\xi u_{x_0} p_0 - k_i I_0 + j\omega c_H u_{x_0} \quad (21)$$

For $i = 1$;

$$Z_1\{(-\omega^2)m + (j\omega)(c_V + c_H) + (k_0 - k_s - j\omega c_H)\} = \Delta k_\xi u_{x_0} p_1 + m e \omega^2 e^{j\omega t} - k_i I_1 \quad (22)$$

Similarly, for $i \neq 1$;

$$Z_i\{(-i^2 \omega^2)m + (j i \omega)(c_V + c_H) + (k_0 - k_s - j\omega c_H)\} = \Delta k_\xi u_{x_0} p_i - k_i I_i + j\omega c_H u_{x_0} \quad (23)$$

The frequency domain Eqs. (21), (22) and (23) will be used in the identification algorithm formulation.

4 Identification Algorithm for Parameter Estimation

Multi harmonics of frequency domain equations have been used for the development of identification algorithm in estimation of the external and internal damping, additive stiffness and AMB parameters. For identification of unknown system parameters, a linear regression method has been practiced, as

$$\mathbf{Ax} = \mathbf{b} \quad (24)$$

where $[A]$ is the the regressor or the regression matrix, $\{b\}$ is the vector consisting of known quantities and $\{x\}$ is the vector containing the unknowns to be determined in estimation. The regression matrix for displacement and current respectively are as follows,

$$\left. \begin{aligned} [A]_{n \times i} \{x_Z\}_{i \times 1} &= \{b_Z\}_{n \times 1} \\ [A]_{n \times i} \{x_I\}_{i \times 1} &= \{b_I\}_{n \times 1} \end{aligned} \right\} \quad (25)$$

The regression based harmonics for the displacement and the current in both forward and backward directions are represented, as

$$\left. \begin{aligned} \{x_Z\}_{n \times 1} &= \{Z_0(\omega) \quad Z_1(\omega) \quad Z_2(\omega) \quad Z_3(\omega) \quad Z_5(\omega) \quad \cdots \quad Z_{-1}(\omega) \quad Z_{-3}(\omega) \quad \cdots\}^T \\ \{x_I\}_{n \times 1} &= \{I_0(\omega) \quad I_1(\omega) \quad I_2(\omega) \quad I_3(\omega) \quad I_5(\omega) \quad \cdots \quad I_{-1}(\omega) \quad I_{-3}(\omega) \quad \cdots\}^T \end{aligned} \right\} \quad (26)$$

The regressor is defined in matrix form, as

$$\mathbf{A} = \begin{bmatrix} 1 & e^{j\theta_1} & e^{j2\theta_1} & e^{j3\theta_1} & e^{j5\theta_1} & \dots & e^{-j\theta_1} & e^{-j3\theta_1} & e^{-j5\theta_1} & e^{-j7\theta_1} & \dots \\ 1 & e^{j\theta_2} & e^{j2\theta_2} & e^{j3\theta_2} & e^{j5\theta_2} & \dots & e^{-j\theta_2} & e^{-j3\theta_2} & e^{-j5\theta_2} & e^{-j7\theta_2} & \dots \\ \vdots & \vdots & \vdots & \vdots & \vdots & \dots & \vdots & \vdots & \vdots & \vdots & \dots \\ 1 & e^{j\theta_n} & e^{j2\theta_n} & e^{j3\theta_n} & e^{j5\theta_n} & \dots & e^{-j\theta_n} & e^{-j3\theta_n} & e^{-j5\theta_n} & e^{-j7\theta_n} & \dots \end{bmatrix} \quad (27)$$

The known matrix is defined, as

$$\left. \begin{aligned} \{b_z\}_{n \times 1} &= \{z(t_1) \quad z(t_2) \quad z(t_3) \quad z(t_4) \quad \dots \quad z(t_{n-1}) \quad z(t_n)\}^T \\ \{b_{i_c}\}_{n \times 1} &= \{i_c(t_1) \quad i_c(t_2) \quad i_c(t_3) \quad i_c(t_4) \quad \dots \quad i_c(t_{n-1}) \quad i_c(t_n)\}^T \end{aligned} \right\} \quad (28)$$

Separating the real and imaginary quantities the developed algorithm in the regression form is represented as,

$$\begin{bmatrix} -\omega Z_{1,Im} & 0 & -u_{x_0} p_1 & -m\omega^2 & 0 & -Z_{1,Re} & I_{1,Re} \\ 0 & \omega Z_{0,Im} & -u_{x_0} p_0 & 0 & 0 & -Z_{0,Re} & I_{0,Re} \\ -2\omega Z_{2,Im} & -\omega Z_{2,Im} & -u_{x_0} \delta_w p_2 & 0 & 0 & -Z_{2,Re} & I_{2,Re} \\ -3\omega Z_{3,Im} & -2\omega Z_{3,Im} & -u_{x_0} p_3 & 0 & 0 & -Z_{3,Re} & I_{3,Re} \\ \vdots & \vdots & \vdots & \vdots & \vdots & \vdots & \vdots \\ \omega Z_{-1,Im} & 2\omega Z_{-1,Im} & -u_{x_0} p_{-1} & 0 & 0 & -Z_{-1,Re} & I_{-1,Re} \\ 3\omega Z_{-3,Im} & 4\omega Z_{-3,Im} & -u_{x_0} p_{-3} & 0 & 0 & -Z_{-3,Re} & I_{-3,Re} \\ \vdots & \vdots & \vdots & \vdots & \vdots & \vdots & \vdots \\ \omega Z_{1,Re} & 0 & 0 & 0 & -m\omega^2 & -Z_{1,Im} & I_{1,Im} \\ 0 & \omega(Z_{0,Re} + u_{x_0}) & 0 & 0 & 0 & -Z_{0,Im} & I_{0,Im} \\ 2\omega Z_{2,Re} & \omega Z_{2,Re} & 0 & 0 & 0 & -Z_{2,Im} & I_{2,Im} \\ 3\omega Z_{3,Re} & 2\omega Z_{3,Re} & 0 & 0 & 0 & -Z_{3,Im} & I_{3,Im} \\ \vdots & \vdots & \vdots & \vdots & \vdots & \vdots & \vdots \\ -\omega Z_{-1,Re} & -2\omega Z_{-1,Re} & 0 & 0 & 0 & -Z_{-1,Im} & I_{-1,Im} \\ -3\omega Z_{-3,Re} & -4\omega Z_{-3,Re} & 0 & 0 & 0 & -Z_{-3,Im} & I_{-3,Im} \\ \vdots & \vdots & \vdots & \vdots & \vdots & \vdots & \vdots \end{bmatrix} \begin{Bmatrix} c_V \\ c_H \\ \Delta k_\zeta \\ e_{Im} \\ k_s \\ k_i \end{Bmatrix} = \begin{Bmatrix} (\omega^2 m - k_0) Z_{1,Re} \\ -k_0 Z_{0,Re} \\ (4\omega^2 m - k_0) Z_{2,Re} \\ (9\omega^2 m - k_0) Z_{3,Re} \\ \vdots \\ (\omega^2 m - k_0) Z_{-1,Re} \\ (9\omega^2 m - k_0) Z_{-3,Re} \\ \vdots \\ (\omega^2 m - k_0) Z_{1,Im} \\ -k_0 Z_{0,Im} \\ (4\omega^2 m - k_0) Z_{2,Im} \\ (9\omega^2 m - k_0) Z_{3,Im} \\ \vdots \\ (\omega^2 m - k_0) R_{-1,Im} \\ (9\omega^2 m - k_0) Z_{-3,Im} \\ \vdots \end{Bmatrix} \quad (29)$$

Equation (29) can be expressed in a typical matrix form and estimated the identifiable parameters using least-squares regression as,

$$\mathbf{x} = (\mathbf{A}^T \mathbf{A})^{-1} \mathbf{A}^T \mathbf{b} \quad (30)$$

The identification with combined speed matrix as,

$$\left\{ \begin{array}{c} \mathbf{A}(\omega_1) \\ \mathbf{A}(\omega_2) \\ \vdots \\ \mathbf{A}(\omega_n) \end{array} \right\} \mathbf{x} = \left\{ \begin{array}{c} \mathbf{b}(\omega_1) \\ \mathbf{b}(\omega_2) \\ \vdots \\ \mathbf{b}(\omega_n) \end{array} \right\} \quad (31)$$

The system parameters can be estimated by simulating Eq. (31) for combined spin speeds. The effect of multiple speed conditions for the identifiable has been illustrated.

5 Numerical Simulation

The numerical simulation of the regression Eq. (31) in Matlab SIMULINK™ environment done has been illustrated in this section. The numerical model of the system is best described by SIMULINK™ environment as shown in Fig. 3, which provides the rotor displacement and AMB current at two orthogonal directions. The numerical simulation is done using the system's parameters from Table 1.

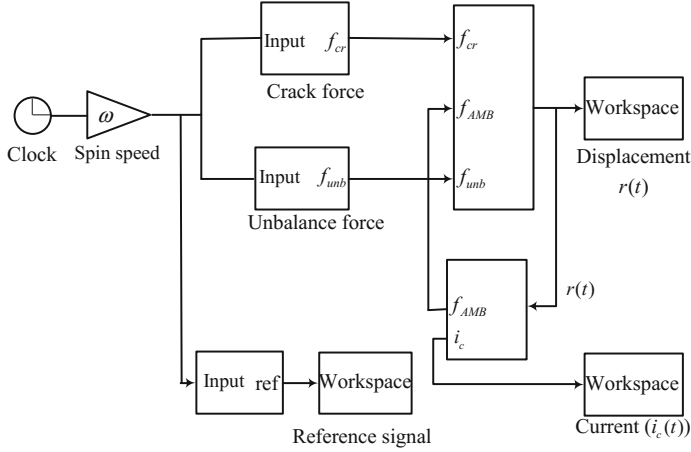


Fig. 3. SIMULINK™ Block of the Rotor system

5.1 Nyquist Stability Plot of the System

Nyquist plot stability criterion assessed the stability of a system with feedback through frequency response plot. As the proposed rotor system with AMB possess feedback control (closed) loop, system's closed-loop transfer function can be represented as in Ref. [16].

Rotor system parameters used for the numerical simulation is based on the existing laboratory rotor kit [17] and the internal damping values is chosen based on stability boundary graph [18]. The PID controller gains of the AMB are chosen based on the Routh-Hurwitz criterion and as illustrated by Parth [19].

$$G = \frac{G_{CMA}}{1 + G_{CMA}G_{sn}} \quad (32)$$

where, assuming G_{CMA} be the transfer function of the system containing controller, sensor and magnetic bearing in series and G_{sn} is the overall correction sensor gain.

$$G = \frac{s^2(K_P + \frac{K_I}{s} + K_D s)k_i k_s}{(\{ms^3 + (c_V + c_H + K_D k_i k_s k_{sn})s^2 + (k - j\omega c_H + k_x + K_P k_i k_s k_{sn})s\}) + K_I k_i k_s k_{sn}} \quad (33)$$

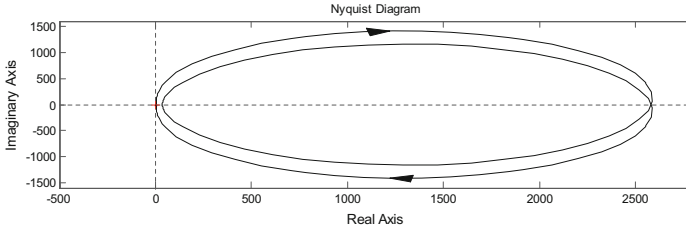


Fig. 4. Nyquist Plot for a speed of 157.07 rad/s of the cracked rotor system

The condition of Nyquist stability criterion as in Ref. [20]

$$N = Z - P \tag{34}$$

where the number of zeros of the characteristic equation, i.e. closed-loop transfer function is represented as Z . The number of poles in the open-loop characteristic equation is defined as P , and N is the number of encirclements of the $(-1 + j 0)$ point. The Nyquist plot of the rotor system is depicted Fig. 4.

It has been observed that the number of encirclement of $(-1, j 0)$ by the contour is zero. Since, here, P is zero (for the open loop stable system) and there are no closed-loop poles present in the right half of complex plane. Hence, according to the Nyquist stability criterion, the system is stable which best describes the chosen PID controller parameters, such as K_P , K_I and K_D values ability to stabilize the proposed rotor system.

5.2 Time Domain and Full Spectrum Responses

The numerical simulation has been performed for 5 s and data have been chosen for response generation for last 1 s to avoid numerical transients. The response generated at a rotational speed of 157.07 rad/s of two lateral displacements (x and y directions) and control current (i_{cx} and i_{cy}) and orbit plots are shown in Fig. 5.

Table 1. Parameters assumed for the proposed system

Parameters	Assumed values	Parameters	Assumed values
<i>Rotor</i>			
Disc mass, m	1.185 kg	Intact shaft stiffness, k_0	$3.84 \times 10^5 \text{ N m}^{-1}$
External damping, c_V	76 N s m^{-1}	Additive stiffness, Δk_ξ	$-1.158 \times 10^5 \text{ N s m}^{-1}$
Internal damping, c_H	25 N s m^{-1}	Disc eccentricity, e	$3 \text{ }\mu\text{m}$
<i>PID controller gains</i>		<i>Actuator factors</i>	
Proportional, K_P	$8 \times 10^3 \text{ A/m}$	Force-displacement coefficient, k_s	$1.052 \times 10^5 \text{ N/m}$
Integral, K_I	$1.34 \times 10^5 \text{ A/m-s}$	Force-current coefficient, k_i	42.1 N/A
Derivative, K_D	1 A-s/m		

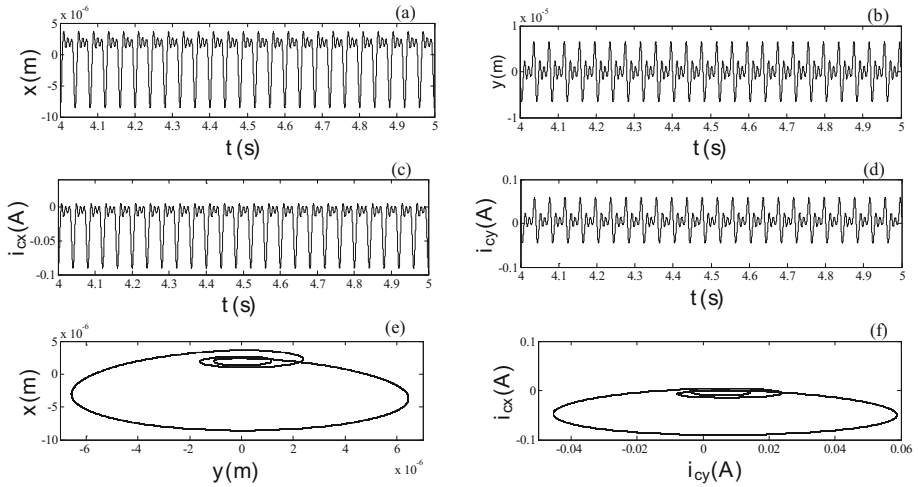


Fig. 5. Response generated for (a) displacement in vertical direction (b) displacement in horizontal direction (c) current in vertical direction (d) current in horizontal direction (e) orbit plot for displacements (f) orbit plots for currents

Similarly, the full spectrum amplitude and phase for the same spin speed as in time domain has been generated for both displacement and current as shown in Fig. 6.

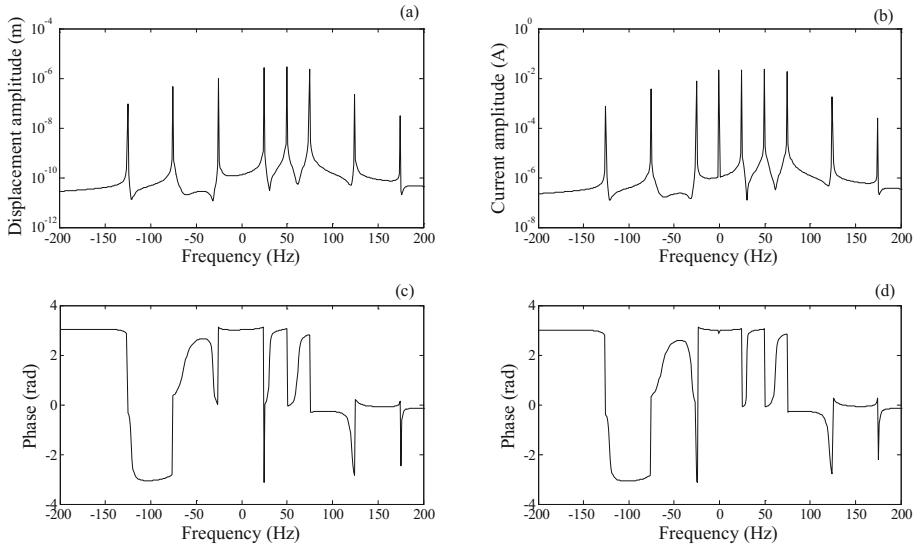


Fig. 6. Full spectrum generated for (a) displacement amplitude (b) current amplitude (c) phase for displacement (d) phase for current

The harmonics found from the full spectrum of displacement and current have been used in the developed algorithm to estimate system parameters.

6 Parameters Estimation

For the identification of parameters, the full spectrum amplitudes and the corrected phases of both forward and backward harmonics have been introduced in the developed algorithm. The amplitudes found from the regression matrix in frequency domain are similar with the amplitudes of FFT based full spectrum.

In the present identification process the basis of choosing multiple speeds is the critical speed of the system, which is 569.25 rad/s. The multiple speeds considered here are from 157.08 rad/s to 314.16 rad/s which comprises of 25 spin speeds. The spin speeds have been chosen in between the 2X harmonic and 5X harmonic of spin speed contributing spectrum.

Random noises have been added to the time domain signal with different level of percentage to correlate the algorithm with the real time simulation problem. From Table 2, it has been observed that the AMB force displacement parameter (k_s) is the most exposed to 5% noise effect with error percentage as 4.67. Whereas, the additive crack stiffness (Δk_ξ) is the least affected parameter with error of -0.83% with the assumed parameter. Using these random noises to the uncontaminated signal the robustness of the identification algorithm has been checked.

From Table 2, it has been observed that the AMB force displacement parameter (k_s) is the most exposed to 5% noise effect with error percentage as 4.67.

Table 2. Identifiable parameters with and without noise for multiple spin speeds

	Assumed values	Estimated parameters with various percentage of noise			
		0%	1%	3%	5%
c_V Ns m ⁻¹	76	76.012	75.744	75.207	74.672
	% error	0.02	-0.34	-1.04	-1.75
c_H Ns m ⁻¹	25	24.927	24.889	24.811	24.732
	% error	0.02	-0.45	-0.76	-1.07
Δk_ξ N m ⁻¹	-1.152×10^5	-1.152×10^5	-1.150×10^5	-1.146×10^5	-1.142×10^5
	% error	-0.03	-0.19	-0.51	-0.83
e μ m	3	2.998×10^{-6}	3.006×10^{-6}	3.021×10^{-6}	3.035×10^{-6}
	% error	-0.07	0.19	0.68	1.15
β deg.	30	30.01	29.88	29.64	29.40
	% error	0.04	-0.39	-1.22	-2.01
k_s N m ⁻¹	105210	1.0518×10^5	1.0618×10^5	1.0816×10^5	1.1013×10^5
	% error	-0.03	0.92	2.81	4.67
k_i NA ⁻¹	42.1	42.084	42.039	41.949	41.858
	% error	-0.04	-0.14	-0.36	-0.58

Whereas, the additive crack stiffness (Δk_ξ) is the least affected parameter with error of -0.834% with the assumed parameter. Using these random noises to the uncontaminated signal the robustness of the identification algorithm has been checked.

In real systems due to manufacturing as well as operational ambiguity and in the measurement of rotor properties like mass and moment of inertia of disc and the undamaged shaft stiffness may contain errors and due to assumptions taken for modelling simplified mathematical model influence in the parameter estimation. Thus, some modelling or bias errors also have been introduced into the model parameters such as the disc mass and the undamaged shaft stiffness. The generated response found from the new model parameters has been incorporated into the identification algorithm to estimate the parameters. The effects of modelling or bias errors in the estimated parameters have been shown in Table 3.

From the estimation it has been noticed that the modelling errors laid very less effect on the parameters. Likewise, the least affected parameter with 5% bias error is the AMB force current factor with deviation of -0.1% and highest affected on is the external damping parameter, with -0.3% deviation from the assumed one.

Table 3. Identifiable parameters with and without modelling or bias error for multiple spin speeds

Parameters	Assumed values	Estimated parameters with various percentage of modelling error			
		0%	1%	3%	5%
c_V Ns m^{-1}	76	75.7130	75.7089	75.7182	75.7385
	% error	-0.378	-0.383	-0.371	-0.344
c_H Ns m^{-1}	25	24.9673	24.9668	24.9678	24.9683
	% error	-0.131	-0.133	-0.129	-0.126
Δk_ξ N m^{-1}	-1.1518×10^5	-1.1506×10^5	-1.1456×10^5	-1.1574×10^5	-1.1728×10^5
	% error	-0.101	-0.169	0.087	-0.459
e μm	3	2.9927×10^{-6}	2.9926×10^{-6}	2.9928×10^{-6}	2.9931×10^{-6}
	%error	-0.244	-0.247	-0.240	-0.232
β deg.	30	30.0919	30.0935	30.0902	30.0851
	% error	0.307	0.312	0.301	0.321
k_s N m^{-1}	105210	1.0536×10^5	1.0536×10^5	1.0536×10^5	1.0536×10^5
	% error	0.147	0.147	0.148	0.148
k_i NA $^{-1}$	42.1	42.0562	42.0557	42.0568	42.0587
	% error	-0.104	-0.105	-0.107	-0.108

7 Conclusions

The present work introduces the mathematical model of cracked Jeffcott rotor with both external and internal damping incorporating AMB force. The identification algorithm has been developed based on frequency domain equations to estimate the system parameters, viz. the unbalance, additive crack stiffness, external and internal damping, force displacement and force current of AMB. To check the sensitivity of the algorithm, noise has been added to the response at different level of percentages for estimation. Lastly, modelling errors have been further added to show its effect in estimated system parameters. Implementation of the present methodology in a real rotor system

through experimentation would have been a challenging future work. In the experimentation the generated data can be used in developed aforesaid identification algorithm for demonstrating different crack models and their parameter estimation.

References

1. Muszynska, A.: Rotordynamics. CRC Press, Boca Raton (2005)
2. Gasch, R.: A survey of the dynamic behaviour of a simple rotating shaft with a transverse crack. *J. Sound Vib.* **160**(2), 313–332 (1993)
3. Mayes, I., Davies, W.: Analysis of the response of a multi-rotor-bearing system containing a transverse crack in a rotor. *J. Vib. Acoust. Stress Reliab. Des.* **106**(1), 139–145 (1984)
4. Sabnavis, G., Kirk, R.G., Kasarda, M., Quinn, D.: Cracked shaft detection and diagnostics: a literature review. *Shock Vib. Dig.* **36**(4), 287 (2004)
5. Soffker, D., Bajkowski, J., Muller, P.: Detection of cracks in turborotors—a new observer based method. *J. Dyn. Syst. Meas. Control* **115**(3), 518–524 (1993)
6. Bachschmid, N., Pennacchi, P., Vania, A.: Identification of multiple faults in rotor systems. *J. Sound Vib.* **254**(2), 327–366 (2002)
7. Patel, T.H., Darpe, A.K.: Vibration response of a cracked rotor in presence of rotor-stator rub. *J. Sound Vib.* **317**(3–5), 841–865 (2008)
8. Shrivankumar, C., Tiwari, R.: Identification of stiffness and periodic excitation forces of a transverse switching crack in a Laval rotor. *Fatigue Fract. Eng. Mater. Struct.* **36**(3), 254–269 (2013)
9. Genta, G.: On a persistent misunderstanding of the role of hysteretic damping in rotordynamics. *J. Vib. Acoust.* **126**(3), 459–461 (2004)
10. Zorzi, E., Nelson, H.: Finite element simulation of rotor-bearing systems with internal damping. *J. Eng. Power* **99**(1), 71–76 (1977)
11. Melanson, J., Zu, J.: Free vibration and stability analysis of internally damped rotating shafts with general boundary conditions. *J. Vib. Acoust.* **120**(3), 776–783 (1998)
12. Quinn, D.D., Mani, G., Kasarda, M., Bash, T., Inman, D.J., Kirk, R.G.: Damage detection of a rotating cracked shaft using an active magnetic bearing as a force actuator-analysis and experimental verification. *IEEE/ASME Trans. Mechatron.* **10**(6), 640–647 (2005)
13. Lees, A., Sinha, J., Friswell, M.: Model-based identification of rotating machines. *Mech. Syst. Signal Process.* **23**(6), 1884–1893 (2009)
14. Singh, S., Tiwari, R.: Model-based fatigue crack identification in rotors integrated with active magnetic bearings. *J. Vib. Control* **23**(6), 980–1000 (2017)
15. Gasch, R.: Dynamic behaviour of the Laval rotor with a transverse crack. *Mech. Syst. Signal Process.* **22**(4), 790–804 (2008)
16. Tiwari, R.: Rotor Systems: Analysis and Identification. CRC Press, Boca Raton (2017)
17. Goldman, P., Muszynska, A.: Application of full spectrum to rotating machinery diagnostics. *Orbit* **20**(1), 17–21 (1999)
18. Ehrlich, F.: Shaft whirl induced by rotor internal damping. *J. Appl. Mech.* **31**(2), 279–282 (1964)
19. Shah, P., Markert, R., Krishnapillai, S.: Design and implementation for controller of active magnetic bearing. Thesis (2007)
20. Chen, D., Seborg, D.E.: Design of decentralized PI control systems based on Nyquist stability analysis. *J. Process Control* **13**(1), 27–39 (2003)



Active Control of Rotor Supported by Faulting Journal Bearing

Matheus Freire Wu^(✉), Tiago Henrique Machado,
and Katia Lucchesi Cavalca

Faculty of Mechanical Engineering, University of Campinas, Campinas, Brazil
{matheusfw, tiagomh, katia}@fem.unicamp.br

Abstract. Although hydrodynamic bearings have minimum contact between solid parts, under particular circumstances they might be susceptible to abrasion and wear. In order to mitigate the problem, it is proposed to apply active control methods to reduce the vibration level at critical situations: fluid induced instability and the first bending mode. However, damage in the bearing surface have direct influence over the oil-film pressure and, consequently, in the bearings equivalent coefficients. Although, initially, small variations may lead to minor performance loss, when it becomes more significant close-loop stability may be affected. Therefore, in this paper it is conducted a preliminary study on the effect of journal bearing wear depth effects in active controlled rotors. A structured uncertain model is proposed to include the possible fault coefficients in the model allowing to perform robust stability analysis. Based on the uncertain formulation a robust control solution is designed guaranteeing rotor stability for a certain damage range.

Keywords: Robust control · Hydrodynamic journal bearing
Bearing wear damage

1 Introduction

During field operation every machine component is susceptible to wear, which, in the beginning, causes small changes in the system behavior, but in the absence of maintenance, eventually, can lead to failure. It is not different for hydrodynamic journal bearing. Although the oil film provides isolation between solid parts minimizing friction during operation, when the shaft comes to a full stop there is direct contact with the bearing. When starting-up there may occur abrasion of the bearing surface, generally made of materials softer than the shaft. Contact between solid parts is also possible in cases of extreme vibration amplitudes, which may occur due to operation at critical speed, or at fluid induced instability condition.

Detection, analysis and modeling the effects of journal bearing wear is a challenging task. Over the years, several researchers have studied the stability of a worn bearing, as well as evaluated its performance under different circumstances [1–4]. Considerable research has also been carried out for the development of various techniques for bearing fault detection and diagnosis. As described by Machado et al. [5], these techniques can be mainly classified into two categories: time domain [6–8] and frequency domain techniques [9, 10].

Considering a rotor supported by hydrodynamic bearings susceptible to wear, the goal of this paper is to analyze those effects in an active controlled rotor and design an auxiliary robust active controller that allows to mitigate the possibilities for the damage propagation by reducing the vibration at critical speed and stabilizing the system at fluid induced instability. With active control, the rotor should be able to sustain safe operation levels until further scheduled maintenance to repair the damaged component.

The control force is supposed to act in the system via a magnetic actuator with the sole objective of controlling the vibration, all the rotor load should still be supported by the journal bearings. Applying the magnetic actuator only as an auxiliary component requires less powerful magnets which can significantly reduce the cost, size and energy consumption of the system. Many studies regarding active rotor vibration control can be found in literature, such as [11–17]. Studies focused on controlling fluid-induced instability can be found in the works [18–20]. Other significant contributions can be found in studies regarding levitating active magnetic bearings (AMB) [21–23]. However, most of the literature is concerned to the main source of parametrical variation, the rotational speed, which has direct influence over gyroscopic effect and journal bearing parameters. Few references concerning controlling damaged rotors can be found, being mostly related to levitating AMB under critical failure such as sensor or coils malfunctioning [24, 25].

Here it is proposed to design and compare, via numerical simulation, two different active control methods to be applied in a rotor supported hydrodynamic bearing evaluating the effect of abrasion damage on the close-loop performance. Both are static gain-scheduled controllers obtained by solving the two-stage method proposed in [26], but one considers uncertainties due to bearing wear in its project. The general guideline of this paper starts with the presentation of the rotor and its modeling, followed by a brief description of worn journal bearing coefficients modeling. Then, in Sect. 2, it is presented the approximation used to create a model fitted for the LMI formulation. In Sect. 3 is described the main formulation for the controllers and uncertainties. Finally, in Sects. 4 and 5 are the main results, discussion and conclusions.

2 Rotor Modeling

2.1 Rotor

For this study, the adopted rotor, Fig. 1, consists in a steel (SAE 1030) shaft of 583 mm length and 12 mm diameter bi-supported by hydrodynamic journal bearings, with the wear effect acting over the bearing number 2. Nominally, both bearings have 18 mm length, 31 mm diameter and radial clearance of 90 μm , and are lubricated by ISO VG 32 oil. The other main components are the disc with 47.5 mm length and 95 mm diameter, which adds load and it is the main source of unbalance to the system, and the journal with 80 mm length and 40 mm diameter through which a magnetic actuator applies the control force. For control feedback are considered the displacements of the bearings nodes at Y and Z directions. This configuration presents its first critical speed at about 46 Hz, and fluid induced instability near 79 Hz. To analyze the most important operational conditions, it is considered the rotor operational speed

range between 20 Hz and 100 Hz spanning the situations: before, at and after the critical speed, and above the fluid-instability threshold.

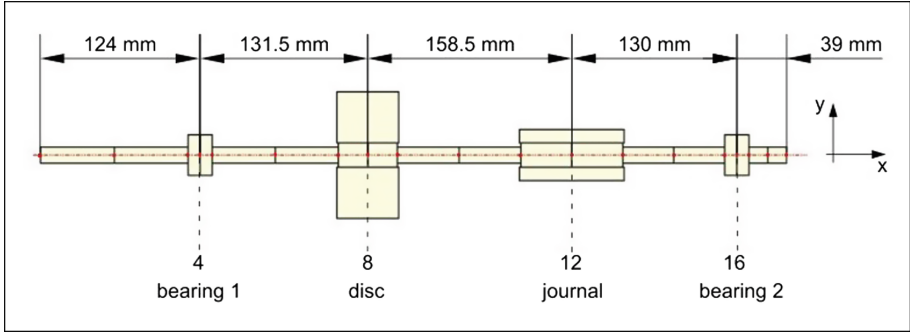


Fig. 1. Rotor FEM model, and main components and respective nodes.

The system is formulated following the finite element model (FEM) by Nelson [27], which allows to represent the set composed by the shaft, disc and journal as the classic second order equation of motion, Eq. (1), where \mathbf{M}_{fem} , \mathbf{D}_{fem} , \mathbf{K}_{fem} and \mathbf{G}_{fem} are respectively the global mass, damping, stiffness and gyroscopic matrices, Ω is the system rotational speed, and \mathbf{q} and \mathbf{f} are respectively the degrees of freedom (DOF) and external excitation vectors.

$$\mathbf{M}_{fem}\ddot{\mathbf{q}} + (\mathbf{D}_{fem} + \Omega\mathbf{G}_{fem})\dot{\mathbf{q}} + \mathbf{K}_{fem}\mathbf{q} = \mathbf{f}(t) \quad (1)$$

2.2 Bearing and Wear Models

For the cylindrical journal bearings, it is used the approach of equivalent linear coefficients of stiffness and damping, which are inserted in the finite element model in bearing position. The procedure for obtaining these coefficients is based on the solution of Reynolds equation, the basis of hydrodynamic lubrication theory. The solution of Reynolds equation gives the pressure field generated by the oil film, and the hydrodynamic forces supporting the rotor are obtained by integration of this pressure around the shaft circumference. These general nonlinear hydrodynamic forces are then expanded into a Taylor series and the resulting differential expressions are approximated by finite differences in order to calculate the bearing equivalent coefficients of stiffness and damping, as shown in Eq. (2), as an example, for the cross coupled stiffness coefficient (K_{yz}) and damping coefficient (C_{zy}). Δz and $\Delta \dot{y}$ are, respectively, small perturbations in the shaft equilibrium position for displacement and velocity.

$$K_{yz} = \frac{\partial F_y}{\partial z} = \frac{\Delta F_y}{\Delta z} \quad C_{zy} = \frac{\partial F_z}{\partial \dot{y}} = \frac{\Delta F_z}{\Delta \dot{y}} \quad (2)$$

For the numerical procedure to solve Reynolds equation, in the case when the oil-film thickness is discontinuous, it is used the approach presented by Machado and Cavalca [28]. In this procedure, the fluid-film is discretized in a uniform mesh of finite volumes, as shown in Fig. 2a. In the close vicinity of the discontinuous film thickness, the pressure has an abrupt variation, and to compensate that, this pressure variation is attributed to a fluid velocity variation by writing a generalized Bernoulli equation immediately before and after the discontinuity (see [28] for more details).

Regarding the wear region, it is based on the geometry initial proposed by Dufrane et al. [29] and adapted by Machado and Cavalca [28], assuming abrasive wear. This model considers that the wear has a uniform thickness in axial direction; it can have a variable depth and can be located in any region of the bearing circumference.

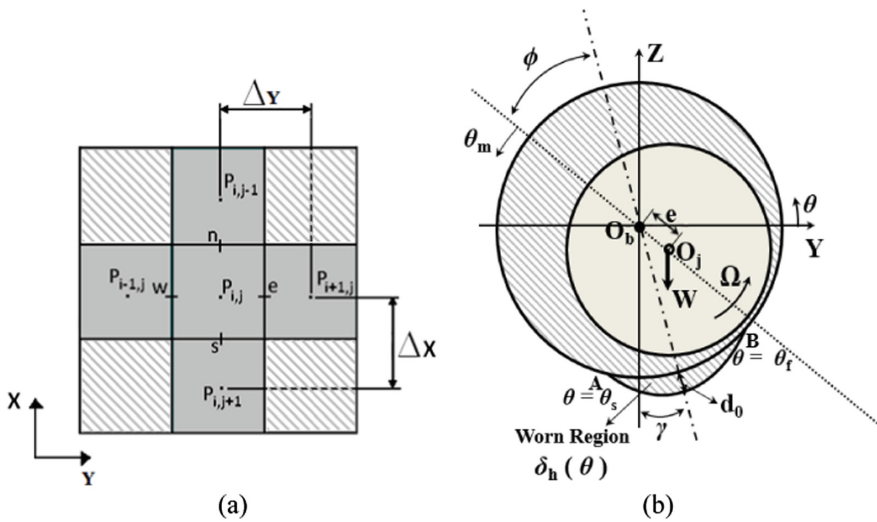


Fig. 2. Schematic representation: (a) finite volume mesh; (b) worn bearing geometry. (Adapted from Machado and Cavalca [28])

In the schematic draw of the worn bearing (Fig. 2b), it can be seen that the wear pattern introduces an additional oil layer with depth $\delta_h(\theta)$ in the region delimited by the angles θ_s and θ_f . Thus, the fluid-film thickness $h(\theta)$ in the presence of wear is given by Eq. (3), where $h_0(\theta)$ is the film thickness due to the shaft eccentricity.

$$h(\theta) = h_0(\theta) + \delta_h(\theta) \tag{3}$$

Equation (3) can also be written in the local reference system, denoted by θ_m in Fig. 2b:

$$\begin{aligned} h_0(\theta) &= Cr + e \cdot \cos(\theta_m) \\ \delta_h(\theta) &= d_0 - Cr \cdot (1 + \cos(\theta_m + \varphi)) \end{aligned} \tag{4}$$

Where Cr is the bearing radial clearance, e is the eccentricity of the shaft and d_0 is the maximum wear depth. Finally, the terms of Eq. (4) can be rewritten in the inertial reference system (Y, Z) through the eccentricity components e_y and e_z , respectively in the Y and Z coordinates:

$$\begin{aligned} h_0(\theta) &= Cr - e_z \cdot \cos(\theta - \pi/2) + e_y \cdot \sin(\theta - \pi/2) \\ \delta_h(\theta) &= d_0 - Cr \cdot (1 + \cos(\theta - \pi/2)) \end{aligned} \quad (5)$$

The depth $\delta_h(\theta)$ in the wear edges, $\theta = \theta_s$ and $\theta = \theta_f$, is zero. Consequently, the extreme points of wear are given by Eq. (6), where γ is the angular displacement of the center of wear, and the fluid-film thickness can be rewritten as Eq. (7).

$$\begin{aligned} \theta_s &= \pi/2 + \cos^{-1}(d_0/Cr - 1) + \gamma \\ \theta_f &= \pi/2 - \cos^{-1}(d_0/Cr - 1) + \gamma \end{aligned} \quad (6)$$

$$h(\theta) = \begin{cases} h_0, & 0 \leq \theta \leq \theta_s, \quad \theta_f \leq \theta \leq 2\pi \\ h_0 + \delta_h, & \theta_s < \theta < \theta_f \end{cases} \quad (7)$$

Equation (7) for the oil film thickness was then inserted into the Reynolds equation, which is solved using the finite volume method (see [28] for more details).

2.3 Model Reduction and Polynomial Approximation

Although the bearings coefficients come from a linearization of the Reynolds equation solution, they have a non-linear dependence on the rotational speed. Adding this variation to the system means that for each speed the system may present different linear (space-state) model. To control such system one possible strategy is to apply adapting controllers, which can variate according to a monitored parameter, e.g. the rotational speed. In this paper the adopted gain-scheduled control law requires describing the system in polynomial form. For that matter it is applied a least square second degree polynomial fit to approximate the dependence of each bearing coefficient to the rotational speed. The resultant bearing coefficients matrices can be described by Eq. (8). As a remark, most of the following polynomial formulation are depicted in second-degree but any degree would be applicable.

$$\begin{cases} \mathbf{K}_{br}(\Omega) = \mathbf{K}_{br0} + \mathbf{K}_{br1}\Omega + \mathbf{K}_{br2}\Omega^2 \\ \mathbf{D}_{br}(\Omega) = \mathbf{D}_{br0} + \mathbf{D}_{br1}\Omega + \mathbf{D}_{br2}\Omega^2 \end{cases} \quad (8)$$

The system is originally divided into 19 nodes, as in Fig. 1, of 4 degrees of freedom (DOF) each, totalizing 76 DOF. In space-state form the system has order 152, which is considerably high for LMI problems; therefore, reduction is necessary. Many reduction methods with different properties can be found in literature. Here is applied the Guyan reduction method [30], allowing to preserve the physical DOF, which makes easier to add the varying bearing coefficients based on the polynomial approximation and to include uncertainties, described in Sect. 3.2.

Firstly, the global matrices related to shaft, disc and journal are reduced using matrix \mathbf{T} of Eq. (9) [30] preserving only the key nodes for the problem (4, 8, 12 and 16), which are the disc, journal and bearings. The resulting model has order 32, which is more suitable for LMI formulation. Moreover, since the bearings nodes DOF are preserved, the coefficients matrices from Eq. (8) can be directly added to the global reduced matrices. Thus, the space-state can be written as the matrix polynomial from Eq. (10). Note that the gyroscopic matrix can be inserted in the polynomial first degree term.

$$\begin{cases} \mathbf{M}_{\text{red}} = \mathbf{T}^T \mathbf{M}_{\text{fem}} \mathbf{T} \\ \mathbf{D}_{\text{red}} = \mathbf{T}^T \mathbf{D}_{\text{fem}} \mathbf{T} \end{cases} \quad \begin{cases} \mathbf{K}_{\text{red}} = \mathbf{T}^T \mathbf{K}_{\text{fem}} \mathbf{T} \\ \mathbf{K}_{\text{red}} = \mathbf{T}^T \mathbf{K}_{\text{fem}} \mathbf{T} \end{cases} \quad (9)$$

$$\dot{\mathbf{x}} = \mathbf{A}(\Omega)\mathbf{x} + \mathbf{B}\mathbf{f} \quad (10)$$

Where,

$$\begin{aligned} \mathbf{A}(\Omega) = \mathbf{A}_0 + \mathbf{A}_1\Omega + \mathbf{A}_2\Omega^2 = & \begin{bmatrix} \mathbf{0} & \mathbf{I} \\ -\mathbf{M}_{\text{red}}^{-1}(\mathbf{K}_{\text{red}} + \mathbf{K}_{\text{br0}}) & -\mathbf{M}_{\text{red}}^{-1}(\mathbf{D}_{\text{red}} + \mathbf{D}_{\text{br0}}) \end{bmatrix} + \\ & \begin{bmatrix} \mathbf{0} & \mathbf{I} \\ -\mathbf{M}_{\text{red}}^{-1}\mathbf{K}_{\text{br1}} & -\mathbf{M}_{\text{red}}^{-1}(\mathbf{G}_{\text{red}} + \mathbf{D}_{\text{br1}}) \end{bmatrix} \Omega + \begin{bmatrix} \mathbf{0} & \mathbf{I} \\ -\mathbf{M}_{\text{red}}^{-1}\mathbf{K}_{\text{br2}} & -\mathbf{M}_{\text{red}}^{-1}\mathbf{D}_{\text{br2}} \end{bmatrix} \Omega^2 \end{aligned}$$

To facilitate the formulation of the controller it is possible to normalize the varying parameter as a unitary simplex Λ_2 , Eq. (11).

$$\begin{aligned} \mathbf{A}(\Omega) = \mathbf{A}(\alpha) = \mathbf{A}\mathbf{p}_0 + \mathbf{A}\mathbf{p}_1\alpha_1 + \mathbf{A}\mathbf{p}_2\alpha_1^2 = \\ [\mathbf{A}_0 + \mathbf{A}_1a + \mathbf{A}_2a^2] + [\mathbf{A}_1(b-a) + \mathbf{A}_22a(b-a)]\alpha_1 + [\mathbf{A}_2(b-a)^2]\alpha_1^2 \end{aligned} \quad (11)$$

Where,

$$\alpha = \Lambda_2 \Leftrightarrow \sum_{n=1}^2 \alpha_n, \alpha_n \geq 0 \text{ and } \alpha_1 = \frac{\Omega-a}{b-a}$$

a, b : minimum and maximum parameter variation, in this case, minimum and maximum rotational speed, respectively.

An important step to make the control design less conservative is to homogenize the polynomial, that is, making every term dependent on the same degree to the varying parameter. That can be done by using the unitary simplex property as in Eq. (12).

$$\begin{aligned} \mathbf{A}(\alpha) = \mathbf{A}\mathbf{p}_0(\alpha_1 + \alpha_2)^2 + \mathbf{A}\mathbf{p}_1\alpha_1(\alpha_1 + \alpha_2) + \mathbf{A}\mathbf{p}_2\alpha_1^2 = \\ \mathbf{A}\mathbf{p}_{20}\alpha_1^2 + \mathbf{A}\mathbf{p}_{11}\alpha_1\alpha_2 + \mathbf{A}\mathbf{p}_{02}\alpha_2^2 = \\ [\mathbf{A}\mathbf{p}_0 + \mathbf{A}\mathbf{p}_1 + \mathbf{A}\mathbf{p}_2]\alpha_1^2 + [2\mathbf{A}\mathbf{p}_0 + \mathbf{A}\mathbf{p}_1]\alpha_1\alpha_2 + \mathbf{A}\mathbf{p}_0\alpha_2^2 \end{aligned} \quad (12)$$

3 Control Formulation

3.1 Two-Stage Static Gain-Scheduled H_∞ Controller

Designing regulator H_∞ controllers generally follows a well-known framework [21, 31]. Firstly, an augmented plant, Eq. (13), based on state-space formulation, Eq. (10), is created separating the inputs in exogenous disturbances \mathbf{w} and control signal \mathbf{u} ; and the outputs in performance signal \mathbf{z} , usually composed by the actual objective (in this case disc displacement) and the control effort \mathbf{u} , and the feedback signal \mathbf{y} , which in most cases are the sensors readings.

$$\begin{cases} \dot{\mathbf{x}} = \mathbf{A}\mathbf{x} + \mathbf{B}_1\mathbf{w} + \mathbf{B}_2\mathbf{u} \\ \mathbf{z} = \mathbf{C}_1 + \mathbf{D}_{11}\mathbf{w} + \mathbf{D}_{12}\mathbf{u} \\ \mathbf{y} = \mathbf{C}_2 + \mathbf{D}_{21}\mathbf{w} + \mathbf{D}_{22}\mathbf{u} \\ \mathbf{u} = \mathbf{L}\mathbf{y} \end{cases} \quad (13)$$

There are many structures and methods for solving the H_∞ control problem. However, the majority relies on linear time invariant systems, which may not be applicable for rotating machinery since their dynamics are strongly dependent on the rotational speed. Since considering the whole possible variations as uncertainties might be excessively conservative, a very usual solution has been applying gain-scheduled techniques. This way, the control law $\mathbf{L}(\alpha)$ also variates according to the current operation condition. In this paper, to obtain $\mathbf{L}(\alpha)$ dependent on Ω , the two-stage technique proposed by Agulhari [26] is applied. The method is based on Lyapunov quadratic stability and consists on solving two consecutive linear matrix inequalities (LMI) as described by Theorems 1 and 2, respectively. The resulting control has guaranteed Lyapunov stability for the considered conditions and presents no dynamic part, being an attractive option for real-time applications.

Theorem 1. There is a state-feedback gain $\mathbf{K}(\alpha) = \mathbf{Z}(\alpha)\mathbf{X}^{-1}$ that stabilizes the system from Eq. (14), with $\mathbf{x} \in \mathbb{R}^n$ and $\mathbf{B}_2 \in \mathbb{R}^{n,ic}$, if there are $\mathbf{P}(\alpha) = \mathbf{P}^T(\alpha) > 0 \in \mathbb{R}^{n,n}$, $\mathbf{X} \in \mathbb{R}^{n,n}$, $\mathbf{Z} \in \mathbb{R}^{ic,n}$ for a given $\xi > 0 \in \mathbb{R}$ which fulfill the LMI from Eq. (15).

$$\dot{\mathbf{x}} = (\mathbf{A}(\alpha) + \mathbf{B}_2\mathbf{K}(\alpha))\mathbf{x} + \mathbf{B}_1\mathbf{w} \quad (14)$$

$$\begin{bmatrix} \mathbf{A}(\alpha)\mathbf{X} + \mathbf{X}^*\mathbf{A}(\alpha)^* + \mathbf{B}_2\mathbf{Z}(\alpha) + \mathbf{Z}(\alpha)^*\mathbf{B}_2^* & \mathbf{P}(\alpha) - \mathbf{X}^* + \xi\mathbf{A}(\alpha)\mathbf{X} + \xi\mathbf{B}_2\mathbf{Z}(\alpha) \\ * & -\xi\mathbf{X} - \xi\mathbf{X}^* \end{bmatrix} < \mathbf{0} \quad (15)$$

*: Conjugate transpose.

The proof for the Theorem 1 can be found in [32].

Theorem 2. There exists an output-feedback control gain $\mathbf{L}(\alpha) = \mathbf{H}^{-1}\mathbf{J}(\alpha)$ that stabilizes the system from Eq. (16) and minimizes it's H_∞ norm, with $\mathbf{x} \in \mathbb{R}^n$, $\mathbf{w} \in \mathbb{R}^i$, $\mathbf{B}_2 \in$

\mathbb{R}^{ic} , $\mathbf{C}_2 \in \mathbb{R}^{oc,n}$, if there are $\mathbf{P}(\alpha) = \mathbf{P}^T(\alpha) > \mathbf{0} \in \mathbb{R}^{n,n}$, $\mathbf{K}(\alpha) \in \mathbb{R}^{ic,n}$, $\mathbf{F}(\alpha) \in \mathbb{R}^{n,n}$, $\mathbf{G}(\alpha) \in \mathbb{R}^{n,n}$, $\mathbf{H} \in \mathbb{R}^{ic,ic}$, $\mathbf{J}(\alpha) \in \mathbb{R}^{ic,oc}$ and $\mu > \gamma^2 > 0 \in \mathbb{R}$ that fulfill the conditions in Eq. (17).

$$\begin{cases} \dot{\mathbf{x}} = (\mathbf{A}(\alpha) + \mathbf{B}_2\mathbf{L}(\alpha)\mathbf{C}_2)\mathbf{x} + \mathbf{B}_1\mathbf{w} \\ \mathbf{z} = (\mathbf{C}_1 + \mathbf{D}_{12}\mathbf{L}(\alpha)\mathbf{C}_2)\mathbf{x} \end{cases} = \begin{cases} \dot{\mathbf{x}} = \mathbf{A}_{CL}(\alpha)\mathbf{x} + \mathbf{B}_{CL}\mathbf{w} \\ \mathbf{z} = \mathbf{C}_{CL}(\alpha)\mathbf{x} \end{cases} \quad (16)$$

$$\inf \left(\mu : \begin{bmatrix} \Psi_{11} & \Psi_{12} & \Psi_{13} & \Psi_{14} & \Psi_{15} \\ & -\mathbf{G}(\alpha) - \mathbf{G}(\alpha)' & \mathbf{G}(\alpha)\mathbf{B}_1 & \mathbf{0} & \mathbf{G}(\alpha)\mathbf{B}_2 \\ & & -\mathbf{I} & \mathbf{0} & \mathbf{0} \\ & * & & -\mu\mathbf{I} & \mathbf{0} \\ & & & & -\mathbf{H} - \mathbf{H}' \end{bmatrix} < \mathbf{0} \right) \quad (17)$$

Where,

$$\begin{aligned} \Psi_{11} &= \mathbf{A}^T(\alpha)\mathbf{F}^T(\alpha) + \mathbf{F}(\alpha)\mathbf{A}(\alpha) + \mathbf{K}^T(\alpha)\mathbf{B}_2^T\mathbf{F}^T(\alpha) + \mathbf{F}(\alpha)\mathbf{B}_2\mathbf{K}(\alpha) \\ \Psi_{12} &= \mathbf{P}(\alpha) - \mathbf{F}(\alpha) + \mathbf{A}^T(\alpha)\mathbf{G}^T(\alpha) + \mathbf{K}^T(\alpha)\mathbf{B}_2^T\mathbf{G}^T(\alpha) & \Psi_{13} &= \mathbf{F}(\alpha)\mathbf{B}_1^T \\ \Psi_{14} &= \mathbf{C}_1^T + \mathbf{K}(\alpha)^T\mathbf{D}_{12}^T & \Psi_{15} &= \mathbf{F}(\alpha)\mathbf{B}_2 + \mathbf{C}_2^T\mathbf{J}(\alpha)^T - \mathbf{K}^T(\alpha)\mathbf{H}^T \end{aligned}$$

The proof for the Theorem 2 can be found in [26].

The conditions for the second stage, Eq. (17), are not linear since there are terms with two variable product ($\mathbf{K}(\alpha)$ and $\mathbf{F}(\alpha)$). In the proof of Theorem 2, one arrives at a condition where $\mathbf{K}(\alpha)$ is a stabilizing state-feedback gain. Thus, it is possible to utilize the first stage to generate generic gains $\mathbf{K}(\alpha)$ and apply it as a constant in the second-stage. Due to this linearization the method presents only a sufficient condition, that is, if no solution can be found doesn't mean it does not exist. Moreover, since it is also difficult to find a correlation between the first stage and the final performance, Agulhari et al. [32] propose testing different solutions for $\mathbf{K}(\alpha)$ (through the variation of ζ) to increase the chance of finding better results. Therefore, any other LMI condition that generates stabilizing gain would be fitting as a first stage.

3.2 Uncertainties

The problem of deviation from a linear time invariant model due to rotational speed variation is addressed by the gain-scheduled method. However, the problem of bearing wear presents a challenging approach, since it may be difficult to parametrize it during the machine operation. Although abrasive wear usually occurs gradually and is not as evident as variations due to rotational speed, it can reach levels in which the system dynamic is too distant from the nominal condition and, if not taken into account, may result in serious performance loss or even instability in close-loop. To address the effect of bearing wear, here it is proposed to include the possible variations, limited to a certain range, as structured uncertainties.

Supposing the uncertain bearings parameters Δp follows the model from Eq. (18), where the effect of the abrasion depth is expressed by the linear approximation δ_d and the rotational speed influence is expressed by the polynomial in Ω , as in Sect. 2.3. The state-space matrix \mathbf{A} becomes the uncertain matrix \mathbf{A}_{unc} , Eq. (19), where $\Delta \mathbf{K}$ and $\Delta \mathbf{C}$ are the uncertain bearing coefficients matrices composed by the terms from Eq. (18).

$$\Delta p_{jk} = p_{jk} + \delta_d(p_{jk2}\Omega^2 + p_{jk1}\Omega + p_{jk0}) \quad (18)$$

Where,

$$p = (k, d), j \text{ and } j \text{ and } k = (y, z).$$

$$\mathbf{A}_{\text{unc}}(\alpha) = \mathbf{A}(\alpha) + \begin{bmatrix} \mathbf{0} & \mathbf{I} \\ -\mathbf{M}_r^{-1}\Delta \mathbf{K}(\Omega, \delta_d) & -\mathbf{M}_r^{-1}\Delta \mathbf{D}(\Omega, \delta_d) \end{bmatrix} \quad (19)$$

It is possible to extract the uncertainties from \mathbf{A}_{unc} obtaining the augmented system from Eq. (20) with the auxiliary input (\mathbf{h}), output (\mathbf{g}) and structured uncertain matrix Δ . Note that since the uncertainties are dependent on the rotational speed, \mathbf{B}_u is dependent on Ω and can also be easily written in terms of α and homogenized. This augmented plant can be used as base for synthesizing robust controllers or analyzing robust stability. For example, if the H_∞ norm from \mathbf{h} to \mathbf{g} is smaller than one, the system is guaranteed to be stable for any possible considered uncertainty by the small gain theorem [31]. Even though the applied control in this paper focus on reducing the H_∞ norm, utilizing this metric for robust analysis may offer very conservative analysis. Therefore, it is proposed to apply μ -analysis [13, 23, 33] to evaluate the systems robustness.

$$\begin{cases} \dot{\mathbf{x}} = \mathbf{A}(\alpha)\mathbf{x} + \mathbf{B}_u(\Omega)\mathbf{h} + \mathbf{B}_1\mathbf{w} + \mathbf{B}_2\mathbf{u} \\ \mathbf{g} = \mathbf{C}_u\mathbf{x} \\ \mathbf{z} = \mathbf{C}_1\mathbf{x} + \mathbf{D}_{12}\mathbf{u} \\ \mathbf{y} = \mathbf{C}_2\mathbf{x} \end{cases} \quad (20)$$

$$\mathbf{u} = \mathbf{L}(\alpha)\mathbf{y}$$

$$\mathbf{h} = \Delta\mathbf{g}$$

3.3 Controllers and Weighting Filters

In this paper two controllers are compared: \mathbf{L} and \mathbf{Lu} are respectively static H_∞ gain-scheduled controller without and with uncertainties. That is, both are obtaining solving the two-stage LMIs from Sect. 3.1, however, \mathbf{Lu} also includes \mathbf{h} in the inputs and \mathbf{g} in the outputs. For \mathbf{Lu} the matrix \mathbf{B}_1 will be concatenated with \mathbf{B}_u and written as a polynomial in α . The resultant $\mathbf{B}_1(\alpha)$ can be applied to the two-stage method without any loss of generality.

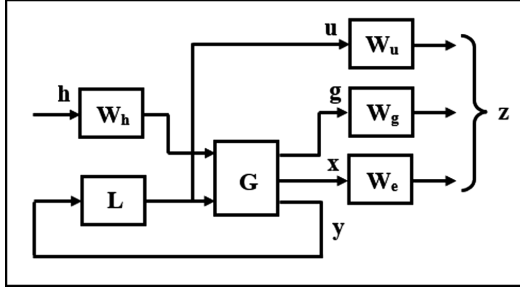


Fig. 3. Weighting filters

The final performance and feasibility of MIMO H_∞ are strongly related to weighting filters. They are functions that adjust the scale and priority between the outputs and inputs. Here are applied the filters according to Fig. 3 and Eq. (21).

$$\mathbf{W}_e(s) = \left(\frac{\frac{s}{\sqrt{M_e}} + \omega}{s + \sqrt{\epsilon_e} \omega} \right)^k \quad \mathbf{W}_u(s) = g_u \left(\frac{s + \frac{\omega}{\sqrt{M_u}}}{\sqrt{\epsilon_u} s + \omega} \right)^k \quad \mathbf{W}_h = \mathbf{W}_g = g_h \quad (21)$$

4 Results

The controllers' synthesis and simulations for the rotor described in Sect. 2 are done considering the frequency range from 20 to 100 Hz, an abrasive wear depth varying from 0 to 40 μm at 20° at the second bearing, and an unbalance momentum of 1×10^{-4} kg.m. The bearings coefficients are calculated as described in Sect. 2.2 and then approximated by a second order polynomial fit. For the $\mathbf{L}\mathbf{u}$ gain and μ -analysis, the bearing 2 coefficient is considered to be the mean value between the parameters without damage and 40 μm wear depth. And the polynomial regarding the uncertain is fitted to represent the difference between the mean and the nominal value, allowing the uncertain $\delta \in [-1,1]$ to cover most of the possible variations. The control gains are obtained in Matlab® using the ROLMIP package [34] to formulate and automatic homogenize the problem and the solver SDPT-3 [35].

The dynamic related to the magnetic actuator is neglected since it is usually much faster than the mechanical response, also no unity conversions are considered, therefore the control gains represent a direct relation between the bearings displacement readings (in meters) and control force (in Newtons).

This result section is organized starting by the polynomial approximation, followed by the utilized control parameters and final structures, then the system robustness is analyzed by means of μ norm, and finally, the achieved performance for each controller is compared.

4.1 Bearing Coefficients Approximation

The influence of different abrasive wear depth on the bearings parameters is shown in Fig. 4a. It is possible to notice that they have a non-linear behavior, therefore the adopted linear approximation for the depth uncertain may lack precision. One could try to express each parameter as an independent uncertainty. However, it would generate an excessively conservative result, since it would comprehend combinations between parameters related to different wear degrees for the same bearing.

The first step to design the controllers is finding the polynomial fit for the bearings coefficients which will be used to design the gain-scheduled controllers. Figure 4b shows the second order approximation for the first bearing stiffness utilized for both **L** and **Lu**. For the damping and the second bearing coefficients similar results are obtained. However, for **Lu** and μ -analysis the polynomial approximations for the second bearing are regarding the mean parametrical variation value, as explained before. Figure 4a shows the considered mean, and polynomial approximation for the second bearing stiffness uncertainty.

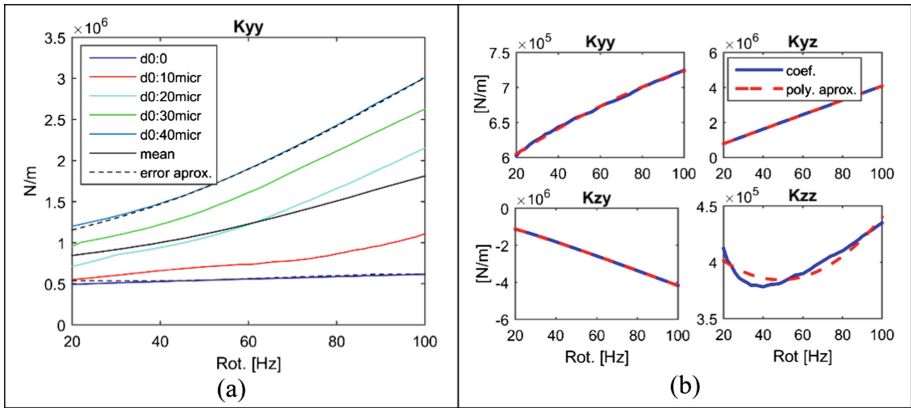


Fig. 4. (a) Bearing number 2 stiffness coefficient for different abrasive wear depths, utilized mean and second order polynomial error bounds. (b) Bearing number 1 stiffness coefficients and second degree polynomial approximation.

4.2 Control Parameters

As stated before, the weighting functions have strong relation to the final control performance. This section brings the utilized weighting parameters, Table 1. The weighting functions for **L** was adjusted aiming the maximum vibration attenuation at nominal condition. For **Lu** the adjustment also considered maintaining the resultant μ norm bellow one. It is important to remark that these configurations are suboptimum, since, as explained in Sect. 3.2, loss of necessity occurs. The final control function **Lu** is given by Eq. (22), and **L** follows the same structure. Note that the final **L** and **Lu**

control expressions consist in gains obtained by a weighted sum between matrices, which can be done without problems in real time.

$$\mathbf{Lu}(\alpha) = 10^6 \begin{bmatrix} -0.1909 & 2.3607 & -0.0822 & 0.0258 \\ -2.3272 & 0.1948 & -0.0359 & -0.0777 \end{bmatrix} \alpha_1 + 10^6 \begin{bmatrix} 0.1246 & 1.8734 & -0.0279 & 0.0076 \\ -2.0348 & 0.7281 & -0.0280 & -0.0117 \end{bmatrix} (1 - \alpha_1) \quad (22)$$

Table 1. Control parameters

	ω (Hz)	k	M_u	M_e	ε_u	ε_e	g_u	g_h
L	220	4	1	100	0.1	1	$2 \cdot 10^{-6}$	–
Lu	220	4	1	100	0.1	1	$5 \cdot 10^{-5}$	$4 \cdot 10^{-3}$

4.3 Robustness Analysis

To evaluate the robustness level of the systems the peak μ value for a set of speeds between 20 and 100 Hz is calculated and displayed in Fig. 5. Where OL is the open-loop system, and CL and CLu are the closed loops with **L** and **Lu**, respectively.

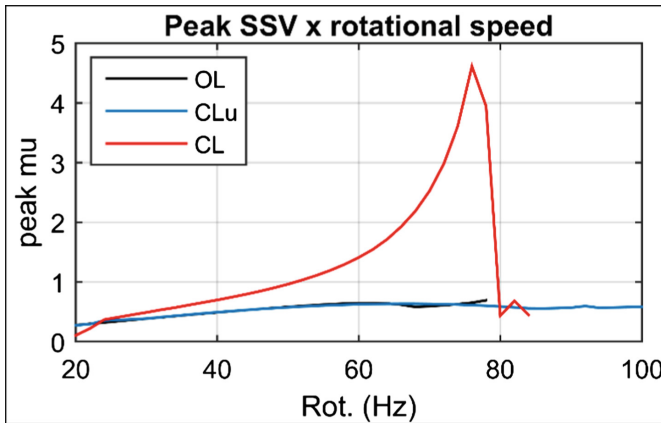


Fig. 5. μ -peak diagram.

Analyzing Fig. 5 it is possible to observe that the open-loop system does not cross one, therefore the bearing wear, in the considered range, is not expected to affect the system stability. However, it is expected instability near 80 Hz (line interruption when reaching eigenvalue positive real part), due to fluid-induced instability. For the **Lu** closed-loop the bearing wear is also expected to not destabilize the system, moreover, the fluid-induced instability is suppressed for the whole considered rotational speed range (continuous line). As for **L**, although in the diagram the line is

interrupted near 84 Hz suggesting that the controller cannot stabilize fluid-induced instability, it is important to remind that this diagram is based on the mean value for bearing number two (Fig. 4a), i.e. the system is not the nominal one. Therefore, it is expected some level of discrepancy. However, the analysis for the μ -value still holds, and since the line crosses 1, that indicates that \mathbf{L} does not guarantee stability when dealing with wear conditions.

4.4 Unbalance Response

To perform the unbalance response analysis a set of systems at different rotational speed for the nominal condition and 40 μm at 20° wear were generated. Their eigenvalue and frequency response at each respective speed were analyzed to define if the system is stable and what is the maximum amplitude of the orbit. The results for the responses at the bearing number 2 node are shown in Fig. 6 and Table 2. It is possible to notice the nominal \mathbf{OL} system presents its peak response near 45.9 Hz (critical speed), and instability at 79.2 Hz. It is interesting to observe that, as predicted in μ -analysis, the considered bearing wear does not cause the system instability to be anticipated but rather delayed to 81.6 Hz. However, it did cause a fairly amplification on the vibration level. As for the \mathbf{Lu} controller, it manages to considerably attenuate the vibration level and and, as expected by the μ -analysis, also guarantee stability for the whole frequency range even with damaged bearing. Regarding the \mathbf{L} controller, it does stabilize the system and reduces the vibration peak for the nominal condition, but under wear effects, it may lead the system to instability even before the nominal fluid-induced threshold (60.7 Hz).

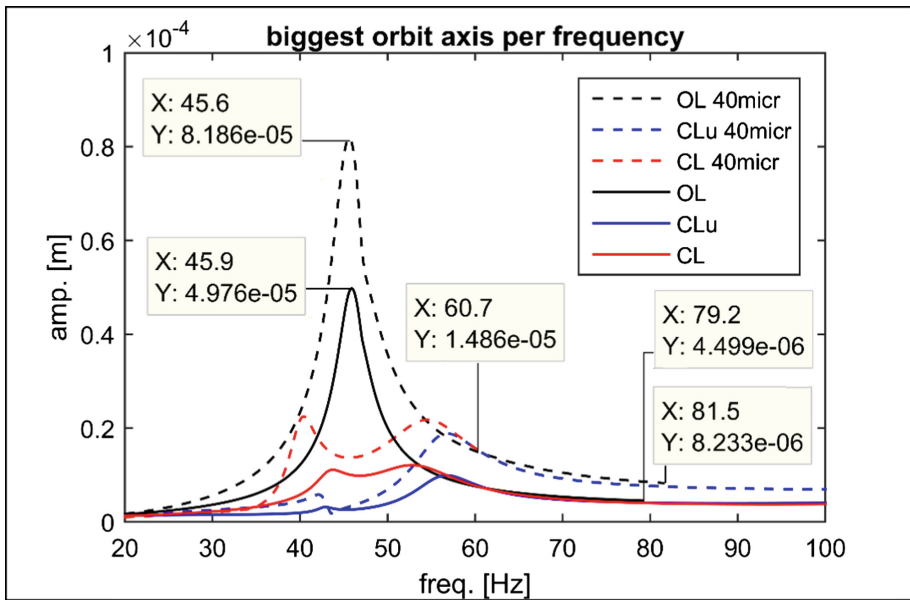


Fig. 6. Unbalance response at bearing number 2 for 0 and 40 μm depth.

Table 2. Main unbalance response parameters

Depth 0/40 μm	Peak freq. [Hz]	Peak amp. (μm)	Instab. freq. [Hz]
OL	45.9/45.6	49.76/81.86	79.2/81.5
CLu	56.4/56.8	9.83/18.81	–
CL	52.8/54.5	12.05/21.76	–/60.7

5 Conclusion

In this preliminary study about the wear effects of bearing wear on active controlled systems it was possible to observe that in open-loop condition, although the wear, for the considered range, does not destabilize the system, it does amplify the vibration levels in the bearing, which could lead to damage propagation. When in closed-loop, the vibration amplitude can be significantly attenuated, but stability can be critically compromised if the coefficients variation is not accounted for. To perform the robustness analysis and to synthesize a robust controller an uncertain model was proposed considering a linear approximation for the depth influence. Although the results were promising, accurately accusing instability risks due to bearing damage for CL while predicting stability for OL and CLu, further analysis is to be conducted to verify this approximation precision. If necessary, other degrees or other parameters may be included in the uncertain model providing a more accurate model in exchange for more computational requirements.

Acknowledgements. The authors would like to thank CAPES, CNPq and Grants # 2015/20363-6, # 2016/13059-1 and # 2017/07454-8 from the São Paulo Research Foundation (FAPESP) for the financial support to this research.

References

1. Suzuki, K., Tanaka, M.: Stability characteristics of worn journal bearing. In: Proceedings of the Asia-Pacific Vibration Conference, Kuala Lumpur, pp. 296–301 (1995)
2. Kumar, A., Mishra, S.: Stability of a rigid rotor in turbulent hydrodynamic worn journal bearings. *Wear* **193**, 25–30 (1996)
3. Bouyer, J.M., Fillon, M., Pierre-Danos, I.: Influence of wear on the behavior of a two-lobe hydrodynamic journal bearing subjected to numerous start-ups and stops. *J. Tribol.* **129**, 205–208 (2007)
4. Muzakir, S.M., Hirani, H., Thakre, G.D.: Experimental investigations on effectiveness of axial and circumferential grooves in minimizing wear of journal bearing operating in mixed lubrication regime. *Int. J. Curr. Eng. Technol.* **5**, 486–489 (2015)
5. Machado, T.H., Mendes, R.U., Cavalca, K.L.: Directional frequency response applied to wear parameter identification in hydrodynamic bearings. *Mech. Res. Commun.* **74**, 60–71 (2016)
6. Okac, H., Loparo, K.A., Discenzo, F.M.: Online tracking of bearing wear using wavelet packet decomposition and probabilistic modeling: a method for bearing prognostics. *J. Sound Vib.* **302**, 951–961 (2007)

7. Wu, T., Mao, J., Dong, G., Xu, H., Xie, Y.: Journal bearing wear monitoring via on-line visual ferrograph. *Adv. Mater. Res.* **44**, 189–194 (2008)
8. Chasalevris, A.C., Nikolakopoulos, P.G., Papadopoulos, C.A.: Dynamic effect of bearing wear on rotor-bearing system response. *ASME J. Vib. Acoust.* **135**(1), 011008–011008-12 (2013)
9. Papadopoulos, C.A., Nikolakopoulos, P.G., Gounaris, G.D.: Identification of clearances and stability analysis for a rotor-journal bearing system. *Mech. Mach. Theory* **43**, 411–426 (2008)
10. Machado, T.H., Cavalca, K.L.: Geometric discontinuities identification in hydrodynamic bearings. In: *Proceedings of 9th IFToMM International Conference on Rotor Dynamics*, vol. 1, pp. 1–10. Politecnico di Milano, Milan, Italy (2014)
11. Siqueira, A.A.G., Nicoletti, R., Norrick, N., Cavalca, K.L., Castro, H.F., Bauer, J., Dohnal, F.: Linear parameters varying control desing for rotating systems supported by journal bearings. *Elsevier J. Sound Vib.* **331**, 2220–2222 (2012)
12. Fittro, R.L., Knospe, C.R.: Rotor compliance minimization via mu-control of active magnetic bearings. *IEEE Trans. Control Syst. Technol.* **10**, 238–249 (2002)
13. Riemann, B., Sehr, M.A., Schittenhelm, R.S., Rinderknecht, S.: Real gyroscopic uncertainties in robust control of flexible rotors. In: *Proceedings of the IEEE Conference on Decision and Control*, pp. 3762–3769 (2013)
14. Riemann, B., Sehr, M.A., Schittenhelm, R.S., Rinderknecht, S.: Robust Control of Flexible High-Speed Rotors Via Mixed Uncertainties, pp. 2343–2350 (2013)
15. Schittenhelm, R.S., Rinderknecht, S.: Controllers for Attenuation of Lateral Rotor Vibration Part I: Controller Design, pp. 1753–1762 (2015)
16. Schittenhelm, R.S., Rinderknecht, S.: Controllers for Attenuation of Lateral Rotor Vibration Part II: Controller Optimization and Comparison, pp. 1763–1773 (2015)
17. Becker, F.B., Sehr, M.A., Rinderknecht, S.: Vibration isolation for parameter-varying rotor systems using piezoelectric actuators and gain-scheduled control. *J. Intel. Mater. Syst. Struct.* **28**(16), 1–12 (2017)
18. Dimitri, A.S., El-Shafei, A., Adly, A.A., Mahfoud, J.: Magnetic actuator control of oil whip instability in bearings. *IEEE Trans. Magn.* **51**, 1–4 (2015)
19. Riemann, B., Perini, E.A., Cavalca, K.L., Castro, H.F., Rinderknecht, S.: Oil whip instability control using μ -synthesis technique on a magnetic actuator. *Elsevier J. Sound Vib.* **332**, 654–673 (2013)
20. Wu, M.F., Mendes, R.U., Cavalca, K.L.: Vibration control of a journal-bearing supported rotor using gain-scheduled controller via LMI. In: *Proceedings of the XVII International Symposium on Dynamic Problems of Mechanics*, pp. 1–10 (2017)
21. Schweitzer, G., Maslen, E.H.: *Magnetic Bearings*. Springer, Berlin (2009)
22. Balini, H.M.N.K., Witte, J., Scherer, C.W.: Synthesis and implementation of gain-scheduling and LPV controllers for an AMB system. *Automatica* **48**, 521–527 (2012)
23. Kuseyri, İ.S.: Robust control and unbalance compensation of rotor/active magnetic bearing systems. *J. Vib. Control* **18**, 817–832 (2012)
24. Yu, J., Zhu, C.: A Sensor-fault tolerant control method of active magnetic bearing in flywheel energy storage system. In: *IEEE Vehicle Power and Propulsion Conference (VPPC)*, pp. 1–6 (2016)
25. Gouws, R., Schoor, G.: A comparative study of fault detection and correction techniques on active magnetic bearing systems. In: *IEEE*, pp. 1–10 (2007)
26. Agulhari, C.M., Oliveira, R.C.L.F., Peres, P.L.D.: Static output feedback control of polytopic systems using polynomial Lyapunov functions. *IEEE Conf. Decis. Control* **49**, 6894–6901 (2010)

27. Nelson, H.D., Mcvaugh, J.M.: The dynamics of rotor-bearing systems using finite elements. *J. Eng. Ind.* **98**, 593–600 (1976)
28. Machado, T.H., Cavalca, K.L.: Modelling of hydrodynamic bearing wear in rotor-bearing systems. *Mech. Res. Commun.* **69**, 15–23 (2015)
29. Dufrane, K.F., Kannel, J.W., McCloskey, T.H.: Wear of steam turbine journal bearings at low operating speeds. *J. Lubr. Technol.* **105**, 313–317 (1983)
30. Gyan, R.J.: Reduction of stiffness and mass matrices. *AIAA J.* **3**, 380 (1965)
31. Zhou, K.: *Essentials of robust control*. Prentice Hall, New York (1998)
32. Agulhari, C.M., Oliveira, R.C.L.F., Peres, P.L.D.: LMI relaxations for reduced-order robust H_∞ control of continuous-time uncertain linear systems. *IEEE Trans. Autom. Control* **57**, 1532–1537 (2012)
33. Doyle, J., Wall, J., Stein, G.: Performance and robustness analysis for structured uncertainty. In: 21st IEEE Conference on Decision and Control, pp. 629–636 (1982)
34. Oliveira, R.C.L.F., Peres, P.L.D.: Parameter-dependent LMIs in robust analysis: characterization of homogeneous polynomially parameter-dependent solutions via LMI relaxations. *IEEE Trans. Autom. Control* **52**, 1334–1340 (2007)
35. Toh, K.C., Todd, M.J., Tutuncu, R.H.: SDPT3—a Matlab Software Package for Semidefinite Programming. *Optimization Methods and Software* **11**, 545–581 (1999)



Control of Flexible Rotor Vibration with Flexibly Mounted Active Magnetic Bearings

Chris Lusty^(✉), Nicola Y. Bailey, and Patrick S. Keogh

Department of Mechanical Engineering, University of Bath, Bath BA2 7AY, UK
C.Lusty@bath.ac.uk

Abstract. Typical rotor/active magnetic bearing (AMB) system layouts involving large, external stator AMBs may be difficult or inconvenient to apply to some rotor systems. Where space in the machine working envelope is at a premium, the space required by traditional AMBs may preclude them from inclusion in the design.

To open up the possibility of using AMBs in next generation compact, high speed machines, a system topology whereby the magnetic bearing stators are positioned inside of hollow-shaft rotors is suggested. This leaves the entire rotor surface available for other machine elements. In such designs, it is probably that both the rotor and the secondary shaft may exhibit flexible behaviour, which adds complexities to the design of the AMB controller compared to the requirements in typical AMB systems. Satisfactory performance can only be achieved if the dynamic characteristics of both rotor and AMB support structure are considered. This paper investigates solutions to this control issue, particularly through the use of model based techniques.

A unique experimental facility based on this system topology is presented. The rotor is sufficiently unbalanced so as to be unable to pass its first critical speed without experiencing excessive vibration. It is demonstrated how an appropriately designed AMB controller can reduce the vibration to a level which allows the rotor to reach up to three times its first critical speed. This also includes the rotor speed (i.e. excitation frequency) exceeding the natural frequency of the AMB support structure.

Keywords: Active magnetic bearings · Vibration reduction
 H_∞ control · Homopolar

1 Introduction

When considering the use of mechatronic techniques to enhance the performance of rotating systems, active magnetic bearings (AMBs) are established as an important and versatile tool [1]. Published standards [2–5] exist offering guidelines to help ensure uniformity in describing, quantifying and implementing rotating systems which incorporate AMBs.

AMBs may be used either as the primary bearings of a system, in which case they are used to levitate a rotor in a contact free manner, or else they may be employed as secondary bearings in a system which is already supported by other (commonly passive) types of bearing. In the second case, the main function of the bearings is to improve the machine performance, for example by reducing rotor vibration levels.

Fundamental theoretical and practical work aimed at optimising the performance enhancing capacity which might be provided by an actuator such as an AMB was presented by Burrows et al. [6, 7]. Further practical examples of AMBs being used as secondary, performance enhancement bearings are presented by Gondhalekar and Holmes [8], Kasarda et al. [9] and Nonami et al. [10]. An analysis of using AMBs as a supplementary device to control instabilities arising in journal bearings is given by El-Shafei and Dimitri [11]. Mahfoud and Der Hagopian [12] investigate the open-loop use of an electromagnetic actuator to shift rotor critical speeds, and thus avoid resonant vibration peaks during rotor run-up or run-down.

Performance enhancement techniques can also be applied to systems where the rotor is fully levitated on the magnetic bearings. Cole et al. [13] consider controlling rotor vibration in the case when such a system is exposed to base-excitation, while Lauridsen and Santos [14] publish work on controlling a levitated rotor which is subject to varying and uncertain seal forces by a process fluid.

A commonality through all the published work relates to the basic layout of the rotor/AMB system. It is almost universal for the stator of the AMB to sit outside the rotor, with the poles facing inwards. This stator is then rigidly mounted to the machine base, such that it may be considered grounded for analysis purposes. However, there may be cases where it is not possible to locate the AMB stator on the outside of a rotor, for instance where the space is required by other machine components. Thus the authors have proposed [15, 16] a layout whereby an AMB stator is located inside of a hollow-shaft rotor, with the magnetic poles facing outwards.

A particular challenge associated with such a layout is that whatever structure is used to support the AMBs will very likely be flexible. Thus one is required to control the flexible behaviour of the rotor with a flexibly mounted actuator.

This paper presents an experimental facility specifically constructed to explore this concept, comments on relevant controller design considerations, and a set of experimental results demonstrating the capacity of the system to permit an imperfectly balanced rotor to safely pass its first critical speed.

2 Description of Experimental Facility

A rotor has been designed to explore the concept of flexibly-mounted internal-stator AMBs. In order to ensure a rotor which exhibits flexible behaviour at relatively low speeds suitable for use in a compact laboratory environment, a multi-section rotor design is used. The rotor is fabricated from steel, with large

diameter, open-ended hollow sections at each end, connected in the centre by a small diameter solid length. The hollow end sections allow accommodation of the internal-stator AMBs, while the slim central section introduces low-speed flexible behaviour. The rotor is supported by a pair of rolling element bearings, located one at each end. The rotor forms a stand-alone unit, with pairs of orthogonally mounted eddy current displacement sensors monitoring its external surface at two mid-span locations.

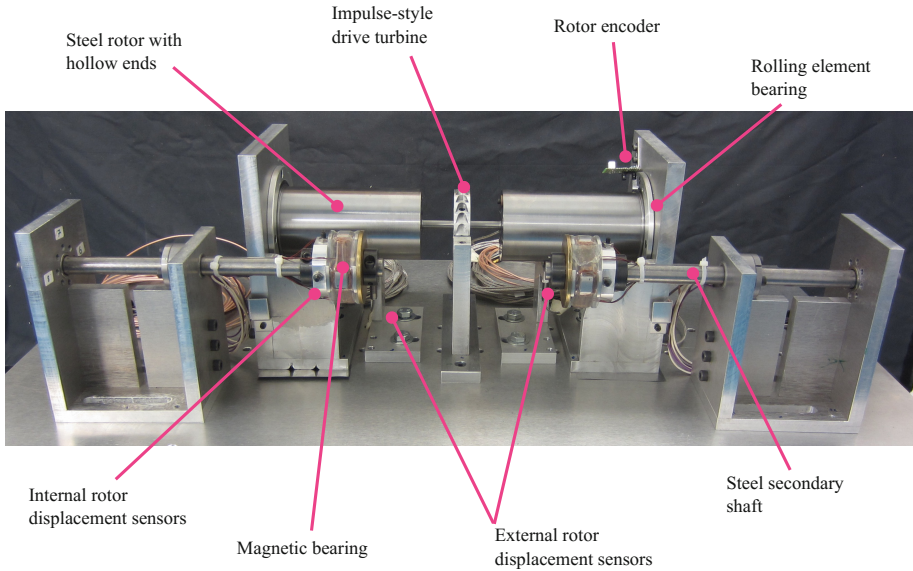


Fig. 1. Photograph of experimental facility with magnetic bearings shown before insertion into rotor

It is then required to locate the magnetic bearings inside the hollow rotor sections. Thus the AMBs are mounted at the ends of cantilevered steel beams, termed secondary shafts. There are two (nominally identical) secondary shaft subassemblies, one for each end of the rotor, and these are independently fixed to the machine base plate.

These various components are shown in Fig. 1. Note that, for illustration purposes, the photograph is taken before the final assembly, at which point the magnetic bearings, on their secondary shafts, are inserted into the rotor. A drive turbine can also be seen mounted at the shaft midspan in the figure - this is driven from a compressed air supply.

Figure 2 provides a close-up look at one of the AMB units. The AMB stator itself is of a four pole-pair homopolar design. The nature of the homopolar layout permits the bearing to act directly upon the inner surface of the rotor without the need for a laminated collar, due to the low levels of rotor eddy currents induced by this design. The geometry was also influenced by the need

to achieve as compact a form as possible, while still allowing sufficient space for coil winding. Ultimately this resulted in a design which is essentially four back-to-back E-shaped electromagnets.

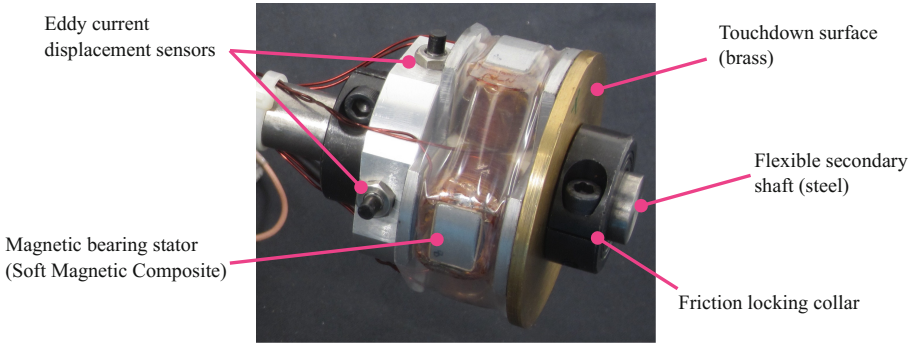


Fig. 2. Detail photograph of flexibly mounted, internal stator magnetic bearing unit

A further consideration, once this design had been established, was how it could be fabricated. It was observed that it would be extremely difficult to fabricate this design from laminated steel sheets (as is commonly done with AMBs). To do so would compromise either the compactness of the device or the pole/winding area (and thus the force capacity) available. This problem is generally easily solved with external-stator devices, as there is little in the way of upper limit on the space envelope available, and thus the stator can simply be made larger to allow for fabrication and assembly considerations. In this instance however, the solution was to use a Soft Magnetic Composite material, which is an iron powder based composite which exhibits excellent magnetic properties, while offering an omnidirectional electrical lamination effect. This allowed the AMB stator to be machined from a single piece of material, thus maintaining both its compact size, and its designed force capacity.

Adjacent to the bearing stator is a brass touchdown disk to protect the bearing in the event of contact with the rotor, and also a pair of orthogonally mounted eddy current displacement sensors. These sensors are used to provide the feedback signal to the controller which governs the AMB coil currents. Note that the displacement sensors previously shown which observe the external surface of the rotor are not used for feedback, and are present purely for monitoring purposes.

An unusual challenge is presented by the system topology under consideration, namely that the structures supporting the AMB stators and the feedback displacement sensors (i.e. the cantilever beams) are flexible. The vast majority of AMB system designs mount the AMB stators and the displacement sensors on a rigid structure. The goal in this work is to address the challenges presented by the flexible mounting structure in order to open the path to new, highly compact machine designs.

3 Controller Design

The focus of this paper is on demonstrating the capacity of the proposed system to control the rotor vibration as it passes its first critical speed, working within the limits set by using compact, flexibly-mounted internal stator AMBs. To this end, two separate controllers were developed and tested.

The first controller was a classical proportional/derivative (PD) controller. Note that integral action is not required in this case, due to the fact that no steady-state element is expected to contribute to the error signal. This is in contrast to AMBs which are used for levitation, where integral action is commonly used to offset the static weight of the rotor. The PD controller was tuned through iterative experimentation to achieve the best results possible without experiencing stability problems (encountered due to imperfectly concentric alignment between the rotor and the AMB). The chosen controller outputs a control current (I_c) as indicated in Eq. (1), where K_P is 10 N/mm, K_D is 0.012 Ns/mm and τ is 6×10^{-4} s. This is combined with a 2 A bias current (I_b) in an opposing pole pair in the usual way (2).

$$I_c = \left(K_P + \frac{K_D s}{1 + \tau s} \right) \times \text{displacement error} \quad (1)$$

$$I_{tot} = I_b \pm I_c \quad (2)$$

The second controller was designed based on H_∞ techniques. As a model based technique, generation of a successful H_∞ controller is dependent on having an accurate model to begin with. A finite element model of the experimental system was generated based on the standard techniques set out by Nelson and McVaugh [17, 18]. The construction of such a model generally initially requires estimates of certain parameters to be made; such parameters might include the stiffness provided by rolling element bearings and any damping present in the system. In order to refine this initial model to match its behaviour to that of the experimental apparatus, a parameter identification procedure was undertaken similar to that presented by Lauridsen et al. [19]. This resulted in a highly accurate model suitable for generating an H_∞ controller.

The controller generation used the Matlab `hinfsv` to output a state space controller based on the identified plant model and a set of weighting functions.

In the present system, a key advantage of employing a model based technique is the facility to impose performance goals on degrees of freedom which are not directly measured. In particular, this allows objective to be set both for the absolute vibration of the rotor relative to the ground, as well as for the relative motion between the rotor and the (flexibly supported) magnetic bearing.

4 Experimental Results

Rotating rundown test were performed with the rotor under three conditions:

1. Magnetic bearings inactive

2. Magnetic bearings operating under PD control
3. Magnetic bearings operating under H_∞ control

In each case, the rotor was spun up via the drive turbine to the maximum speed achievable. In the case of the uncontrolled and the PD controlled rotor, the maximum speed was determined by the speed at which excessive vibration caused contact to occur between the rotor and the AMB touchdown surfaces. In both cases, the magnitude of vibration prohibited the rotor from passing its first critical speed at approximately 3000 rpm (50 Hz).

In the case when the H_∞ controller was used, the system successfully reduced the vibration amplitudes such that the rotor was able to pass its first critical speed without touchdown occurring. In this case, the maximum achievable speed was dictated by the rated speed of the rolling element bearings at 10,000 rpm (165 Hz).

Figure 3 is a 3D orbit plot of the rundown behaviour of the rotor without any action from the magnetic bearings. It is clearly seen that at a rotational speed just over 50 Hz, the rotor exhibits resonant vibration. The magnitude of this vibration caused it to contact the touchdown disks protecting the magnetic bearing (radial clearance 0.25 mm), leading to a chaotic bouncing behaviour. The residual unbalance of the rotor was estimated at 50 g.cm.

The behaviour also displays two notable local vibration maxima at sub-critical rotation speeds, occurring at approximately 26 Hz and 18 Hz. These frequencies are approximately half and one third of the critical speed respectively. Fractional-frequency vibration peaks are a known phenomenon in rotor systems, and are attributed to nonlinear parameters in various elements of the system, such as bolted joints and imperfections in mechanical bearings and their housings.

The rundown test was repeated with the magnetic bearings operating under the PD control scheme presented above. The 3D rotor orbit plot under these conditions is presented in Fig. 4. It is seen that some limited performance improvement was possible with the PD control, including suppression of the sub-critical vibration peaks. It is also evident that the magnetic bearings have contributed an increased stiffness to the rotor, such that resonant frequency is increased by approximately 10 Hz. However, it was not found to be possible to control the vibration such as to avoid contact occurring with the AMB touchdown disk, and thus it was not possible to pass the critical speed.

As indicated above, the controller faces the challenge of attempting to minimise the absolute vibration of the rotor, while only being provided with a reading of the relative motion between the rotor and the secondary shafts, and applying control forces through a flexibly mounted actuator.

This challenge, and the limited capacity of the PD controller to provide satisfactory performance under these conditions, provided the motivation to seek a more advanced controller. As a model-based controller, the H_∞ controller embeds a model of the plant in its structure, thus allowing the controller to estimate how the entire system is behaving, even if provided with only limited measurement data. Furthermore, one is able to specify performance goals on any characteristic of the plant, whether or not it is directly measured.

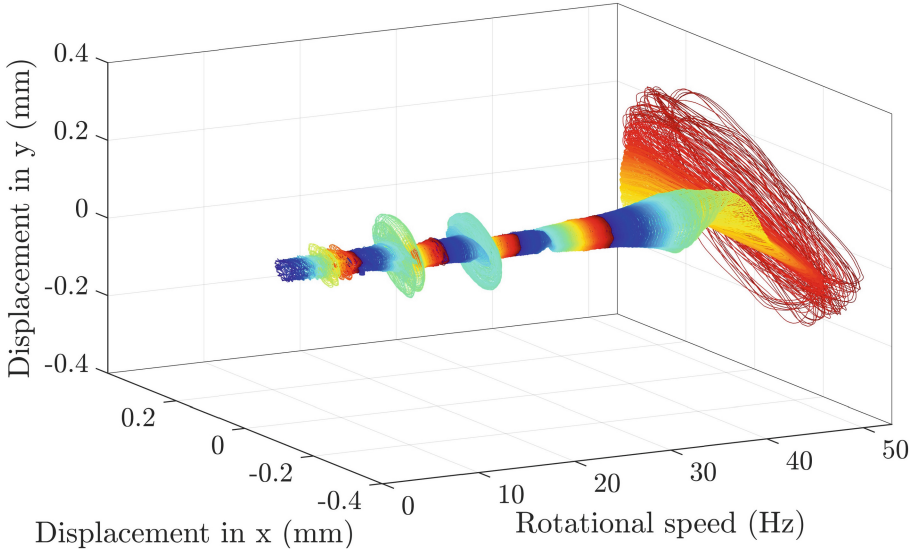


Fig. 3. Rotor orbits during unbalanced rotor run-down with no control active. The colours are for visual enhancement. (Color figure online)

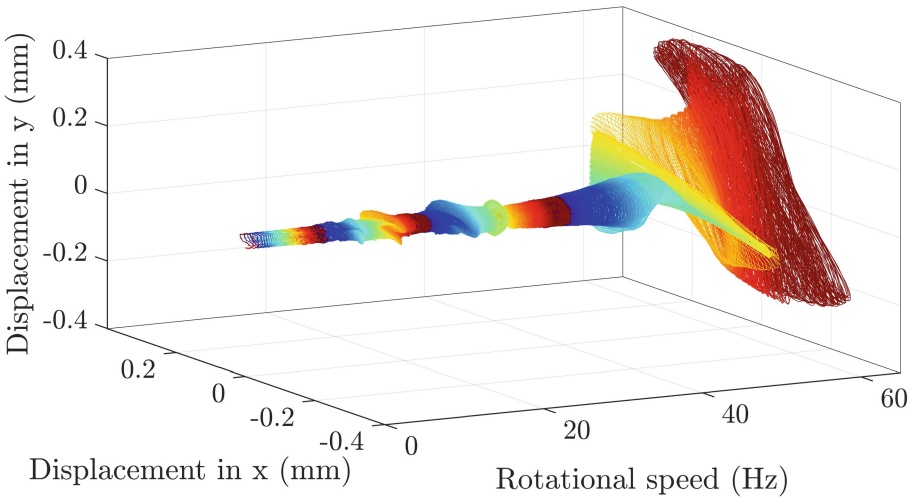


Fig. 4. Rotor orbits during unbalanced rotor run-down with PD control active. The colours are for visual enhancement. (Color figure online)

The rotor orbits from the third rundown test, with the magnetic bearings operating under H_∞ control, are presented in Fig. 5. It can clearly be seen that very significant performance gains are achieved with this controller. The vibration peak at the critical speed of around 50 Hz has a greatly reduced magnitude compared to the previous results, and contact between the rotor and AMB touch-down surfaces is prevented. Thus the rotor is able to reach supercritical speeds,

and in this case the test was stopped as the speed approached 10,000 rpm, which is the maximum specified speed of the rolling element bearings.

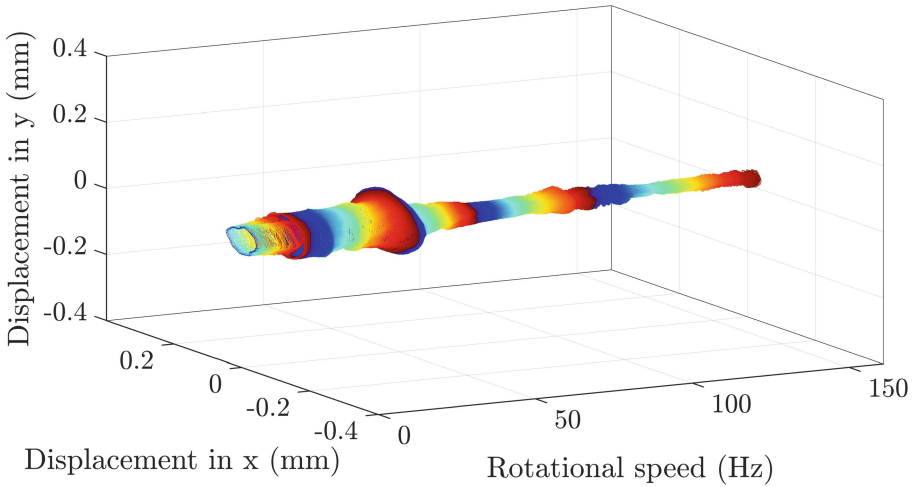


Fig. 5. Rotor orbits during unbalanced rotor run-down with H_∞ control active. The colors are for visual enhancement. (Color figure online)

5 Conclusions

This paper presents a potential pathway to enable novel machine designs which incorporate AMBs in compact, high speed systems. The concept of mounting AMBs inside of hollow shaft rotors is discussed, with consideration given to the unique challenges attendant to such a system compared to traditional AMB system designs. This includes the design and material choices for a compact bearing stator, and the implications of flexibility in the bearing support structure.

The requirements for successfully using such a system layout in terms of the AMB controller capabilities are examined, and H_∞ techniques are identified as offering inherent advantages in this situation compared to classical control techniques. Through a series of experimental rotor rundown tests, it is demonstrated that an unbalanced rotor can be augmented with flexibly mounted, internal stator AMBs under H_∞ control to allow the critical speed to be passed and supercritical rotation safely achieved.





References

1. Maslen, E., Schweitzer, G., Bleuler, H., Cole, M., Keogh, P., Larsonneur, R., Nordmann, R., Okada, Y., Traxler, A.: *Magnetic Bearings: Theory, Design, and Application to Rotating Machinery*. Springer, Berlin (2009). <https://doi.org/10.1007/978-3-642-00497-1>
2. *Mechanical vibration - vibration of rotating machinery equipped with active magnetic bearings*, ISO Standard, 14839 – 1:2002 Part 1: Vocabulary (2002)

3. Mechanical vibration - vibration of rotating machinery equipped with active magnetic bearings, ISO Standard, 14839 – 2:2004 Part 2: Evaluation of vibration (2004)
4. Mechanical vibration - vibration of rotating machinery equipped with active magnetic bearings, ISO Standard, 14839 – 3:2006 Part 3: Evaluation of stability margin (2006)
5. Mechanical vibration - vibration of rotating machinery equipped with active magnetic bearings, ISO Standard, 14839 – 4:2012 Part 4: Technical guidelines (2012)
6. Burrows, C., Sahinkaya, M.: Vibration control of multi-mode rotor-bearing systems. *Proc. R. Soc. London A Math. Phys. Sci.* **386**(1790), 77–94 (1983)
7. Burrows, C., Sahinkaya, M., Clements, S.: Active vibration control of flexible rotors: an experimental and theoretical study. *Proc. R. Soc. London A Math. Phys. Sci.* **422**(1862), 123–146 (1989)
8. Gondhalekar, V., Holmes, R.: Design of a radial electromagnetic bearing for the vibration control of a supercritical shaft. *Proc. Inst. Mech. Eng. Part C J. Mech. Eng. Sci.* **198**(4), 235–242 (1984)
9. Kasarda, M., Allaire, P., Humphris, R., Barrett, L.: A magnetic damper for first-mode vibration reduction in multimass flexible rotors. *ASME J. Eng. Gas Turbines Power* **112**(4), 463–469 (1990)
10. Nonami, K., Fan, Q., Ueyama, H.: Unbalance vibration control of magnetic bearing systems using adaptive algorithm with disturbance frequency estimation. *JSME Int. J. Ser. C Mech. Syst. Mach. Elem. Manuf.* **41**(2), 220–226 (1998)
11. El-Shafei, A., Dimitri, A.: Controlling journal bearing instability using active magnetic bearings. *J. Eng. Gas Turbines Power* **132**(1), 012502 (2010)
12. Mahfoud, J., Der Hagopian, J.: Investigations on the critical speed suppressing by using electromagnetic actuators. *Smarts Struct. Syst.* **9**(4), 303–311 (2012)
13. Cole, M., Keogh, P., Burrows, C.: Vibration control of a flexible rotor/magnetic bearing system subject to direct forcing and base motion disturbances. *Proc. Inst. Mech. Eng. Part C J. Mech. Eng. Sci.* **212**(7), 535–546 (1998)
14. Lauridsen, J., Santos, I.: Design of robust amb controllers for rotors subjected to varying and uncertain seal forces. *JSME Mech. Eng. J.* **4**(5) (2017). Advance publication, <https://doi.org/10.1299/mej.16-00618>)
15. Lusty, C., Sahinkaya, M., Keogh, P.: A novel twin-shaft rotor layout with active magnetic couplings for vibration control. *Proc. Inst. Mech. Eng. Part I J. Syst. Control Eng.* **230**(3), 266–276 (2016)
16. Lusty, C., Keogh, P.: Vibration reduction in a hollow-shaft rotor using flexibly-mounted internal-stator magnetic bearings. *JSME Mech. Eng. J.* **4**(5) (2017). Advanced publication, <https://doi.org/10.1299/mej.17-00008>
17. Nelson, H., McVaugh, J.: The dynamics of rotor-bearing systems using finite elements. *ASME J. Eng. Ind.* **98**, 593–600 (1976)
18. Nelson, H.: A finite rotating shaft element using timoshenko beam theory. *J. Mech. Des.* **102**, 793 (1980)
19. Lauridsen, J., Sekunda, A., Santos, I., Niemann, H.: Identifying parameters in active magnetic bearing system using LFT formulation and Youla factorization. In: 2015 IEEE Conference on Control Applications (CCA), pp. 430–435. IEEE (2015)



Reduction of Rotor Vibration Amplitude Using PID Tuning Methods

Leonardo Biagiotti Saint Martin^(✉) , Diogo Stuani Alves ,
Ricardo Ugliara Mendes , and Katia Lucchesi Cavalca 

Faculty of Mechanical Engineering, University of Campinas (UNICAMP),
Campinas, Brazil
{lbsmartin, dsalves, katia}@fem.unicamp.br,
rumqld@gmail.com

Abstract. Rotating machines present some common inherent operational problems, such as the critical amplitude of motion that the machine may experience when passing through one or more of its natural frequencies. High vibration levels can be harmful to the machine and its attenuation is important to maintain the system working healthily. In this context, the paper proposes a proportional-integral-derivative (PID) controller acting with two pairs of electromagnetic actuators to reduce the vibration amplitude of a flexible rotor, supported by hydrodynamic journal bearings, crossing its first resonance. The oil film behavior of the hydrodynamic bearings is modeled both through linear equivalent stiffness and damping coefficients and by the complete solution of the Reynolds equation applied to short bearings. Next, the relay feedback test (a frequency response method) is applied to estimate the ultimate gain and ultimate period of the respective PID controllers. Finally, five different tuning methods are proposed to adjust the PID: the Ziegler-Nichols traditional method, three Ziegler-Nichols modifications to obtain less aggressive controllers, and a fifth method, the Tyreus-Luyben method, whose objective is to improve the robustness of the controller.

Keywords: Rotating machine · Electromagnetic actuators · PID controller
Relay feedback test · Oil film forces · Identification

1 Introduction

Rotating elements are commonly found in several important industrial applications, being central components in a wide range of machines. From small pumps and compressors to complex power plant turbines and aircraft engines, they play a relevant economic role and it is a major concern that these machines work properly.

A proper operation of a rotating machine, however, demands some attention not just to the rotor itself, but also to other attached components (e.g. lumped masses and/or journals) and to connections of the rotor to some static supporting structure. From this point of view, a safe, stable and predictable dynamic behavior of the machine is aimed. Especially due to characteristics of modern design (such as lightweight and rotation at increased speeds), some resonances might occur within the machine operational range,

with inherent residual unbalances imposing high levels of vibration (bending modes) and compromising the machine aimed safety, stability and predictability.

A simple way to overcome excessive vibration issue is to increase the rotating machine damping, for example, by using hydrodynamic journal bearings to connect the rotor to the static support structure. Hydrodynamic journal bearings not only provide advantages of increased damping, but also allows the machine to operate at higher rotational speeds and higher loads when compared to ball bearings. However, since the hydrodynamic oil film behavior is dependent of the rotational speed [1], it is time varying and may be strongly nonlinear. The oil film may still lead the rotor to a fluid-induced instability condition, in which a self-excited sub-synchronous vibration may impose harmful high amplitudes of motion to the rotor [2–4].

In this context, aiming to take advantage of the hydrodynamic journal bearing benefits without compromising the machine safety and stability, active vibration control mechanisms and techniques have been studied [5–10]. In such techniques, one or more electromagnetic actuators were used to apply known and adjustable control forces to the rotor aiming: (1) to center the rotor around some reference position; (2) to stabilize the rotor (increasing the robustness against disturbances and assuring the machine healthy operation); and (3) to attenuate the rotor vibration amplitude (especially when crossing resonances or at fluid induced instabilities) [9, 10].

To accomplish the desired active control effectiveness, a controller is necessary to quantify the electromagnetic force applied by the actuators to the rotor [11]. There are several techniques that can be used to obtain a satisfactory controller, such as the μ -synthesis method [10], the H_∞ method [9] or the PID method [11–15]. In this work, the PID method was adopted due to its easy to tune and to implement characteristics; besides, PID controllers are widely used in industrial applications.

Therefore, this work focus on the applicability and efficiency of different PID controller tuning methods in reducing the unbalance vibration amplitude of a flexible rotor supported by hydrodynamic journal bearings when crossing its first resonance. The influence of the mathematical model used to represent the oil film dynamics (linear coefficients or the complete solution of the Reynolds equation for short bearings) in the PID tuning is also evaluated. Finally, the obtained PID controllers have their performances compared when subjected to an external disturbance.

2 Methodology

In this section, the entire system model is described in details. First, the finite element model (fem) of the rotor is described, and the system equation of motion containing the journal bearings and the control forces is presented. Next, two possible ways to represent the oil film forces within the hydrodynamic journal bearings are presented: (1) equivalent linear stiffness and damping coefficients; (2) solution of the Reynolds equation for short bearings. Finally, the relay feedback test is described and five PID tuning methods are presented.

2.1 Rotor Model

For the analyses, the flexible rotor of Fig. 1 is modeled using the finite element method. In the equation of motion (Eq. 1), \mathbf{M}_{fem} is the mass matrix, $\mathbf{C}_{fem} = \beta \mathbf{K}_{fem}$ is the proportional damping matrix, \mathbf{K}_{fem} is the stiffness matrix, and \mathbf{G}_{fem} is the gyroscopic matrix, according to [16, 17]. The proportionality coefficient β relates the stiffness and damping matrices, Ω is the rotation speed and $\mathbf{q}(t)$ is the generalized coordinate vector. The rotor is subjected to an unbalance exciting force \mathbf{F}_E , the bearing forces \mathbf{F}_B , and its own weight \mathbf{W}_{fem} .

$$\mathbf{M}_{fem} \ddot{\mathbf{q}}(t) + (\mathbf{C}_{fem} + \Omega \mathbf{G}_{fem}) \dot{\mathbf{q}}(t) + \mathbf{K}_{fem} \mathbf{q}(t) = \mathbf{F}_E(t) + \mathbf{F}_B(t) - \mathbf{W}_{fem} \quad (1)$$

The rotor is divided into 19 nodes and the shaft elements are modeled using the Timoshenko beam theory [18]. Each beam element contains eight degrees of freedom: four translational and four rotational. The disc elements are considered rigid and their effects are applied in a single node (the lumped mass, the bearing journals and the actuator journal are modeled as discs). No foundation or supporting structure influence on the rotor dynamics is considered.

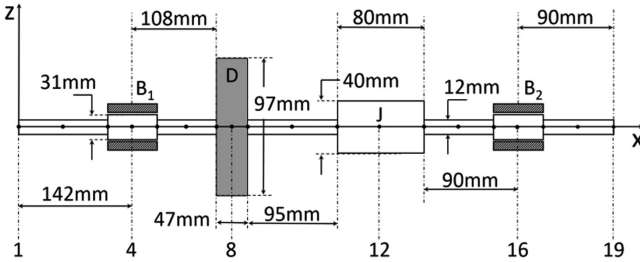


Fig. 1. Rotor finite element model. B_1 and B_2 are the first and second bearings. D is the lumped mass and J is the actuator journal.

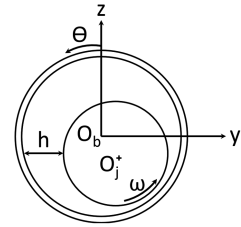


Fig. 2. Hydrodynamic bearing geometry.

2.2 Hydrodynamic Bearings

Hydrodynamic bearings, which allow relative movement between static and rotating parts, have their behavior described by Reynolds isoviscous equation, Eq. 2. The solution of this equation leads to the pressure field in the lubricant film of the bearings [19, 20].

$$\frac{1}{R^2} \frac{\partial}{\partial \theta} \left(\frac{h^3}{\mu} \frac{\partial p}{\partial \theta} \right) + \frac{\partial}{\partial x} \left(\frac{h^3}{\mu} \frac{\partial p}{\partial x} \right) = 6\Omega \frac{\partial h}{\partial \theta} + 12 \frac{\partial h}{\partial t} \quad (2)$$

In Eq. 2, p is the oil pressure; θ is the circumferential coordinate; x is the axial coordinate; μ is the lubricant viscosity; R is the bearing radius; and t is the time. The oil film thickness, h , is both function of the geometry of the bearing (the bearing radial clearance, C_R) and of the circumferential position of the rotor inside the bearing (the

horizontal and vertical coordinates, y and z , respectively, and the circumferential coordinate θ) as shown in Fig. 2 and Eq. 3.

$$h = C_R + y \sin \theta - z \cos \theta \quad (3)$$

Since the Reynolds equation is a second order differential equation, a numerical method must be applied to obtain the pressure field solution. In the present paper, a finite volume method is used to evaluate oil film forces by integration of the pressure distribution within the bearing area that effectively sustains the rotor [20, 21], as shown in Eqs. 4a and 4b.

$$F_{By} = R \int_{-\frac{1}{2}}^{\frac{1}{2}} \int_{\theta_1}^{\theta_2} p \sin \theta \, d\theta \, dx \quad (4a)$$

$$F_{Bz} = -R \int_{-\frac{1}{2}}^{\frac{1}{2}} \int_{\theta_1}^{\theta_2} p \cos \theta \, d\theta \, dx \quad (4b)$$

For adequate simulation of rotor dynamics, the oil film forces must be calculated for each time step. Consequently, the direct application of the Reynolds equation to this solution implies a very expensive computational time. Therefore, a first-order Taylor expansion is proposed to direct evaluation of bearing forces.

Linear Expansion. Linear bearing analysis can be done via expansion of bearing forces into a first-order Taylor series, as presented in Eqs. 5a and 5b [22]. This process leads to a total of eight direct and cross-coupled stiffness and damping coefficients (respectively, K_{lm} and C_{lm}).

$$F_{By} = F_{y0} + K_{yy}\Delta y + K_{yz}\Delta z + C_{yy}\Delta \dot{y} + C_{yz}\Delta \dot{z} \quad (5a)$$

$$F_{Bz} = F_{z0} + K_{zy}\Delta y + K_{zz}\Delta z + C_{zy}\Delta \dot{y} + C_{zz}\Delta \dot{z} \quad (5b)$$

In Eqs. 5a and 5b, F_{y0} and F_{z0} are bearing forces at the equilibrium position, while Δy , Δz , $\Delta \dot{y}$ and $\Delta \dot{z}$ are, respectively, relative displacements and velocities in both Y and Z axes around the equilibrium position. Consequently, the linear coefficients K_{lm} and C_{lm} in Eqs. 5a and 5b can be obtained from partial derivatives of bearing forces in both directions at the equilibrium position:

$$K_{lm} = \left(\frac{\partial F_m}{\partial l} \right)_0 \quad C_{lm} = \left(\frac{\partial F_m}{\partial \dot{l}} \right)_0 \quad (6)$$

A Newmark integrator was applied to solve the system of equations [23, 24].

2.3 PID Controller and Tuning Methods

The controller considered in this work is a PID (parallel form) controller with a derivative filter, N_D , whose transfer function is given by Eq. 7 [11].

$$\frac{V_C(s)}{X(s)} = K_P + \frac{K_I}{s} + N_D \frac{K_D s}{N_D + s} \quad (7)$$

In Eq. 7, K_P , K_I and K_D are, respectively, the proportional, integral and derivative gains of the PID controller. $X(s)$, the input of the controller, is the negative of the displacement signal taken in the corresponding degrees of freedom of the electromagnetic journal where control force is applied (collocated control). $V_C(s)$ is the output voltage of the controller (in terms of electromagnetic force).

An efficient PID controller relies on the proper choice of its parameters in Eq. 7. This adequate choice can be done by performing some tests to better determine the system over which the controller will act. A frequency response method called relay feedback test [11, 13–15] is applied to estimate the ultimate gain, K_u , and ultimate period, T_u , of the closed-loop system.

The relay feedback test consists in replacing the PID controller by a relay in the closed control loop. The gain of the relay should be adjusted to make the system respond with a sustained oscillation. The ultimate gain is obtained from this adjustment (Eq. 8) [15], and the ultimate period is the period from the oscillatory system response.

$$K_u = \frac{4\left(r - \frac{DB}{2}\right)}{\pi g} \quad (8)$$

In Eq. 8, r and g are, respectively, the relay and the plant output amplitudes. DB is the width of the relay dead band. From these ultimate gain and period, the PID controller can be tuned. In this work, five tuning methods are used for the PID [11, 14, 15]:

Ziegler-Nichols (ZN) method. A classic PID tuning method, characterized, in general, by aggressive controllers, with fast response and high overshoots [12];

Ziegler-Nichols modified method to allow Some-Overshoot (SO-OV). Modification of the ZN method to reduce the overshoot (by reducing the proportional gain of the ZN tune from $0.60K_u$ to $0.33K_u$ and increasing K_D) [25];

Ziegler-Nichols modified method for No-Overshoot (NO-OV). Another modification of the ZN classical method to completely attenuate the overshoot (via another K_P reduction, from $0.33K_u$ for the SO-OV to $0.20K_u$ in the NO-OV) [25];

Tyres-Luyben (TL) method. An interesting method whose objective is to improve the robustness of the controller (being remarkable for its high T_I value, which implies the smallest K_I among all tunes considered) [26];

Shinskey (SH) method. Another modification of the ZN method, whose objective is also to be less aggressive by reducing the value of the proportional gain to $0.25K_u$ (which results in the smallest K_D value among all tunes considered) [27].

Table 1 gives relations to predict PID parameters according to Eq. 9.

$$K_I = \frac{K_P}{T_I} \quad K_D = K_P T_D \quad (9)$$

Table 1. PID controller parameters for different tuning methods [11, 12, 14, 15, 24–26].

Tuning method	K_P	T_I	T_D	K_I	K_D
ZN	0.60 K_u	0.50 T_u	0.125 T_u	1.20 K_u/T_u	0.075 $K_u T_u$
SO-OV	0.33 K_u	0.50 T_u	0.330 T_u	0.66 K_u/T_u	0.109 $K_u T_u$
NO-OV	0.20 K_u	0.50 T_u	0.330 T_u	0.40 K_u/T_u	0.066 $K_u T_u$
TL	0.46 K_u	2.20 T_u	0.159 T_u	0.21 K_u/T_u	0.073 $K_u T_u$
SH	0.25 K_u	0.50 T_u	0.120 T_u	0.50 K_u/T_u	0.030 $K_u T_u$

The PID controller equation (Eq. 7) can be re-written in a state-space formulation as presented in Eq. 10a and 10b.

$$\dot{\mathbf{q}}_C(t) = \mathbf{A}_C \mathbf{q}_C(t) + \mathbf{B}_C [-\mathbf{q}(t) + \mathbf{u}_{\text{ref}}] \quad (10a)$$

$$\mathbf{F}_C(t) = \mathbf{C}_C \mathbf{q}_C(t) + \mathbf{D}_C [-\mathbf{q}(t) + \mathbf{u}_{\text{ref}}] \quad (10b)$$

In Eqs. 10a–10b, $\mathbf{q}_C(t)$ is the vector of control states, while $\dot{\mathbf{q}}_C(t)$ is the first time derivative of $\mathbf{q}_C(t)$ and \mathbf{u}_{ref} is the reference signal for the controller. $\mathbf{q}(t)$ is the displacement vector of all rotor degrees of freedom and $\mathbf{F}_C(t)$ is the vector of control forces. \mathbf{A}_C , \mathbf{B}_C , \mathbf{C}_C and \mathbf{D}_C are the respective controller state-space matrices, obtained as stated in Eqs. 11a–11b from the controller gains and the derivative filter.

$$\mathbf{A}_C = \begin{bmatrix} 0 & 1 \\ 0 & -N_D \end{bmatrix} \text{ and } \mathbf{B}_C = \begin{bmatrix} 0 \\ 1 \end{bmatrix} \quad (11a)$$

$$\mathbf{C}_C = [K_I N_D \quad K_I - K_D N_D^2] \text{ and } \mathbf{D}_C = [K_P + K_D N_D] \quad (11b)$$

When the control system is active, the rotor described initially by Eq. 1 is also subjected to the control force, $\mathbf{F}_C(t)$, as shows Eq. 12.

$$\mathbf{M}_{\text{fem}} \ddot{\mathbf{q}}(t) + \mathbf{C}_{\text{fem}} \dot{\mathbf{q}}(t) + \mathbf{K}_{\text{fem}} \mathbf{q}(t) = \mathbf{F}_E(t) + \mathbf{F}_B(t) - \mathbf{W}_{\text{fem}} + \mathbf{F}_C(t) \quad (12)$$

The system composed by Eqs. 10a, 10b and 12 can be rewritten in a single matrix equation:

$$\begin{bmatrix} \mathbf{M}_{\text{fem}} & \mathbf{0} \\ \mathbf{0} & \mathbf{0} \end{bmatrix} \begin{Bmatrix} \ddot{\mathbf{q}}(t) \\ \ddot{\mathbf{q}}_C(t) \end{Bmatrix} + \begin{bmatrix} \mathbf{C}_{\text{fem}} & \mathbf{0} \\ \mathbf{0} & \mathbf{I} \end{bmatrix} \begin{Bmatrix} \dot{\mathbf{q}}(t) \\ \dot{\mathbf{q}}_C(t) \end{Bmatrix} + \begin{bmatrix} \mathbf{K}_{\text{fem}} + \mathbf{D}_C & -\mathbf{C}_C \\ \mathbf{B}_C & -\mathbf{A}_C \end{bmatrix} \begin{Bmatrix} \mathbf{q}(t) \\ \mathbf{q}_C(t) \end{Bmatrix} = \begin{Bmatrix} \mathbf{F}_E(t) + \mathbf{F}_B(t) - \mathbf{W}_{\text{fem}} + \mathbf{D}_C \mathbf{u}_{\text{ref}} \\ \mathbf{B}_C \mathbf{u}_{\text{ref}} \end{Bmatrix}. \quad (13)$$

3 Simulation Results

Once the complete system model was established, a series of simulations was performed. First, a comparison between the models adopted to calculate the oil film forces was carried out considering both controlled and uncontrolled conditions, at three different rotation

speeds, within the first bearing. Next, the performances in the steady-state response of the tuned controllers were evaluated. Finally, a step signal was applied in the control-loop input in order to evaluate the controller performance in the transient response.

3.1 Linear Versus Reynolds Oil Film Modeling

In the first set of simulations, a comparison between the models adopted to describe the oil film behavior (i.e. oil film forces) was carried out. Since both bearings presented similar results, the orbits for the second bearing were omitted. For this comparison, both controlled and uncontrolled cases are shown (Figs. 3, 4 and 5) for three different rotation speeds: 25 Hz, 44 Hz and 52 Hz. The controller’s ultimate gain and ultimate period were, respectively, $8.1774 \cdot 10^5$ and 0.0208 for y direction and $6.3518 \cdot 10^5$ and 0.0208 for z direction.

From Figs. 3, 4 and 5 one may notice that the uncontrolled orbits (in black) present only subtle differences for the linear model and the complete nonlinear Reynolds solution. Therefore, all PID controllers (Figs. 3, 4 and 5) were calculated for the linear model of the oil film forces at a rotation speed of 25 Hz.

Tuning the PID controllers in a low rotational speed (25 Hz) simulates the real case where the uncontrolled rotor is not able to approximate the critical speed due to the high vibration level. The orbits of the controlled rotor are also compared for the rotational speed of 44 Hz, which is near the first critical speed at 46.6 Hz, and for 52 Hz, which represents a rotational speed above the critical speed.

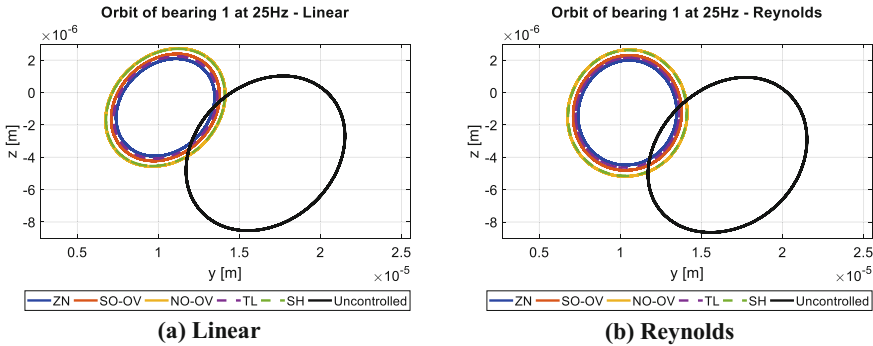


Fig. 3. First bearing orbits, with and without controller, for a rotation speed of 25 Hz.

After the application of the developed controllers (Figs. 3, 4 and 5), the rotor orbits also presented only subtle differences for the linear model and the complete nonlinear Reynolds solution. Therefore, it was concluded that nonlinear effects are small within forces and velocities considered (even close to the first critical speed).

Despite these subtle differences, all PID tunes have performed effectively, mainly for 25 Hz and 44 Hz rotation speeds, independent of the model for the oil film. For these two speeds, all PID tunes have almost the same efficiency. For 52 Hz, however, more differences emerge: while ZN, SO-OV and TL tunes remained effective, closely followed by the NO-OV, the SH tune almost lost its entire effectiveness. This result was somehow

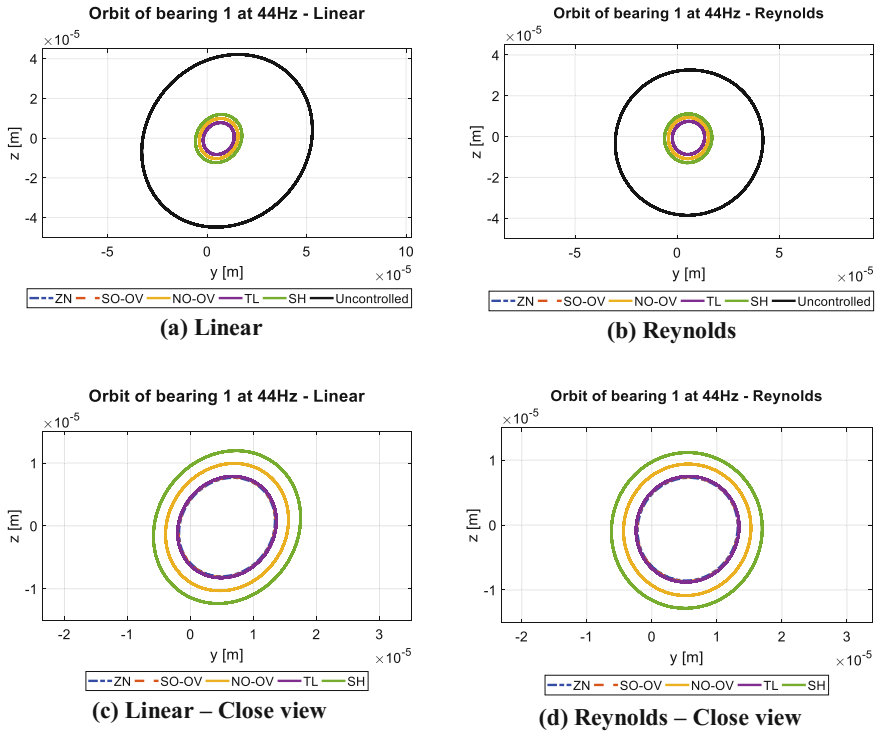


Fig. 4. First bearing orbits for a rotation speed of 44 Hz: (a)–(b) orbits with and without controller; (c)–(d) detail of the orbits with controller.

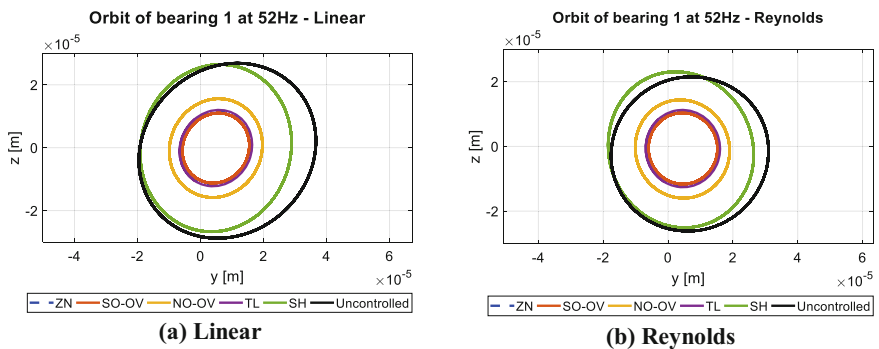


Fig. 5. First bearing orbits, with and without controller, for a rotation speed of 52 Hz.

expected since the NO-OV and SH tunes have the smallest K_P values, and therefore less contribute to the closed-loop system stiffness when compared to other tunes [11].

Once the analyzed operation conditions do not impose strong nonlinearities in the oil film behavior, the results of the following subsections were obtained using the equivalent linear damping and stiffness coefficients for the bearings.

3.2 Comparative PID Efficiency at Different Rotation Speeds

In the present subsection, the controller obtained for a rotation speed of 25 Hz is applied to other rotation speeds, namely: 44 Hz, 52 Hz and 75 Hz. Figure 6 presents a comparison of efficiency of the different tunes for different speeds in three positions along the rotor (at the first and second bearings and at the lumped mass).

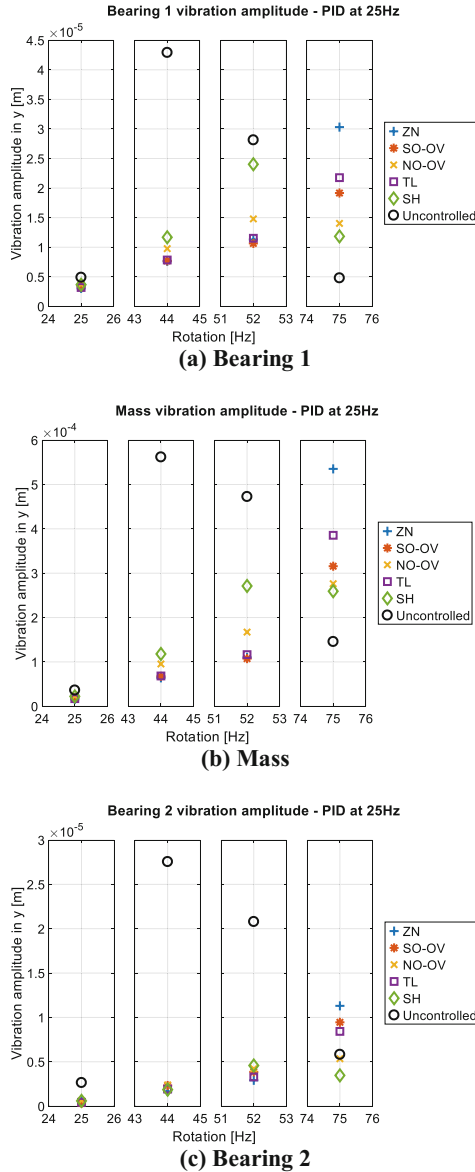


Fig. 6. Controlled and uncontrolled maximum displacement amplitude in y direction at different rotation speeds: (a) first bearing; (b) lumped mass; (c) second bearing.

The results obtained at the z direction were omitted due to the similarity to the results at the y direction in Fig. 6. Also, from Fig. 6, one may notice that at the disc position no tune could attenuate the motion of the rotor at 75 Hz. This fact will be addressed later, at Subsect. 3.4.

3.3 Transient Regime Analysis

In the present subsection a step signal of amplitude 3 mm is applied to the reference of the control-loop at $t = 3$ s. After that, the system is simulated until a new permanent regime is achieved. The simulations were carried out for a rotation speed of 52 Hz (Fig. 7). Only the results obtained for the y direction are presented due to the similarity with the results for the z direction.

The first harmonic (rotational frequency component) masks the transient analysis of the closed-loop system as it can be noted in Fig. 7. Therefore, the first harmonic was filtered from the system response using the DFT. The filtered results are presented in Fig. 8.

Initially, it must be remarked that despite efficiency differences among PID tunes, all of them could answer effectively to a new reference value. The small discrepancy of permanent regime position in all graphs of Fig. 8 to the new reference value (3 mm) may be attributed to the fact that the controller was not acting directly on the disc. It was acting on the journal (Fig. 1), where the new permanent regime position of all cases was at 3 mm.

In order to compare the transient response performance of each controller, the percentage of overshoot and the settling time were measured for each case and summarized in Table 2.

Table 2. Performance parameters of the tuned controllers.

Tuning method	Overshoot (%)	Settling time 5% (s)
ZN	24.9	0.057
SO-OV	4.6	0.065
NO-OV	-	0.094
TL	5.9	0.220
SH	-	0.102

As expected [11], the parameters extracted from the disc response to a variation in the reference signal of the controller agreed to the individual characteristics (values of proportional, integral and derivative gains) of each PID tune considered.

The biggest overshoot happened for the ZN tune, which has the biggest K_P and K_I values, followed almost in a linear relation by the TL and SO-OV tunes, in this order. The SH and NO-OV tunes, with the smallest values of K_P , did not produce any positive overshoot, as expected from the descriptions of the methods.

The smallest settling time also occurred for the ZN tune, the one with the highest K_I parameter, followed by the SO-OV, NO-OV, SH and TL tunes in this order. The poor performance of the TL tune when considering the settling time is due to its high value of $T_I = 2.20 T_u$ (Table 1), set intentionally to lead to a more robust controller.

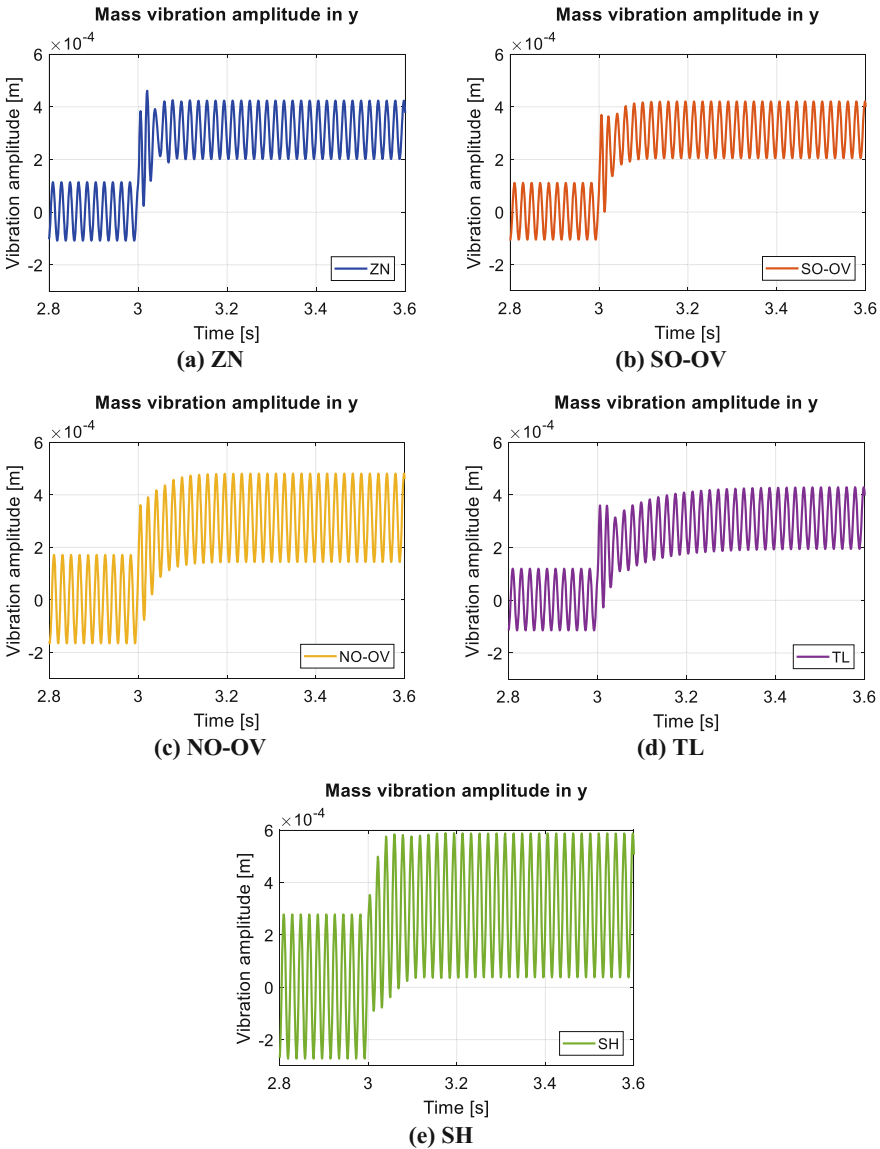


Fig. 7. Transient response of the closed-loop system at the mass position due to the application of a step signal.

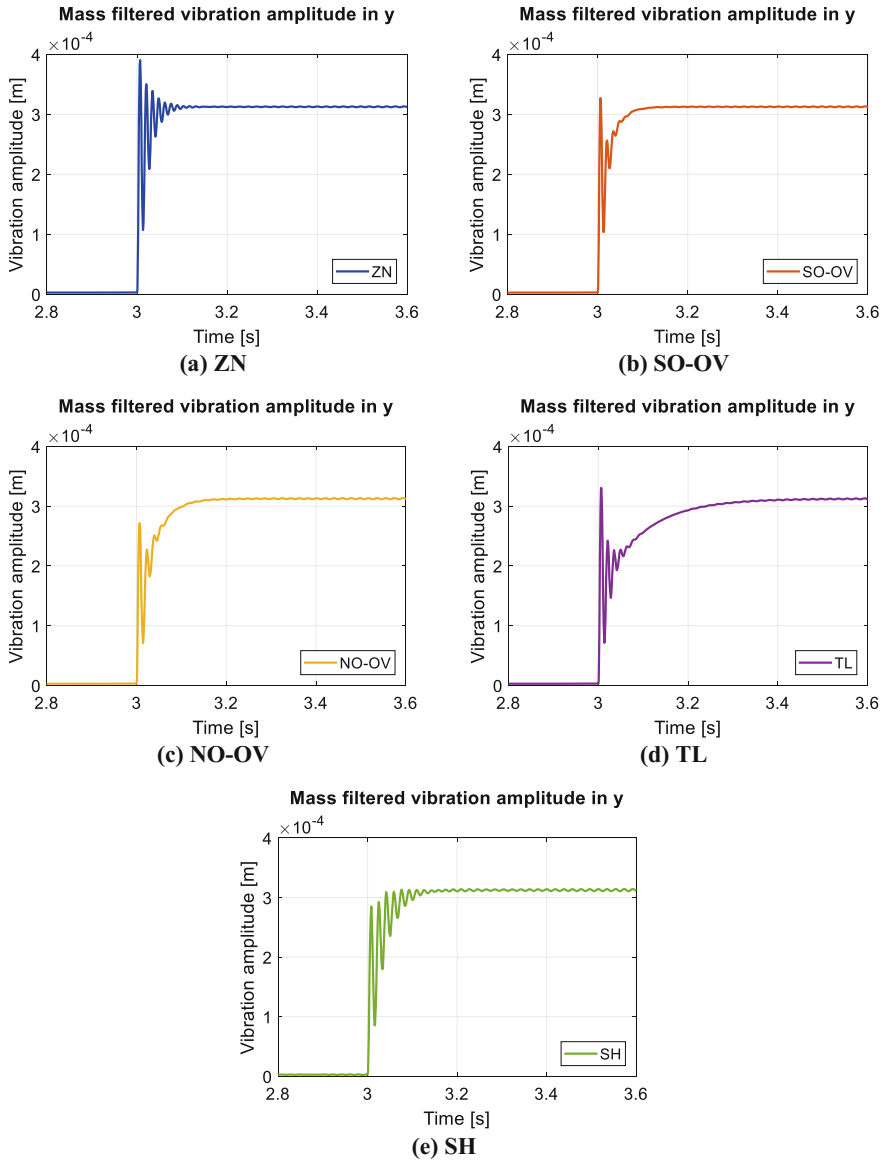


Fig. 8. Filtered transient ZN response of the closed-loop system at the mass position due to the application of a step signal.

3.4 Frequency Response Analysis

To obtain a better comprehension of the system behavior in the presence of the controller, the unbalance response of the system was calculated. Figure 9 presents the lumped mass response considering a harmonic excitation (due to unbalance) at the

lumped mass (which is where the unbalance was applied in the previous simulations). The results of Fig. 9 are summarized in Table 3.

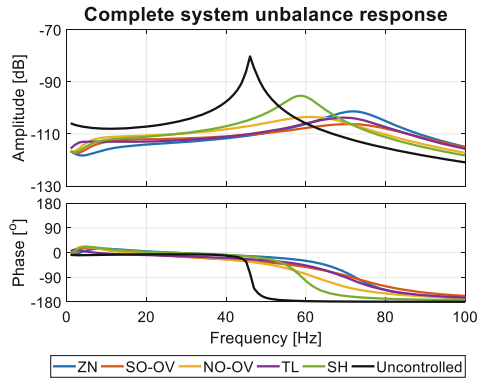


Fig. 9. Unbalance response of the complete system.

Table 3. Performance parameters of the system unbalance response.

Case	Critical speed (Hz)	Peak amp. (dB)	Modal damping
Uncontrolled	46	-80.26	0.013
ZN	72	-101.3	0.104
SO-OV	72	-106.2	0.222
NO-OV	63	-103.5	0.198
TL	70	-103.7	0.150
SH	59	-95.36	0.076

As expected, the critical speed of the system increased (Table 3) since the actuator behaves as another bearing adding stiffness to the system, which explains why the amplitudes of the controlled systems decrease in the rotational speed of 44 Hz but increase in the rotational speed of 75 Hz, as presented in the results of Fig. 6 (Subsect. 3.2). Nevertheless, comparing the vibration amplitudes at the critical speeds (peaks in Fig. 9 and Table 3), it can be seen that every tuning method is able to reduce the system orbit during the critical speed crossing. The resultant damping of the system is also increased for every controller as presented in Table 3.

4 Conclusions

In this work, two methods for modeling the hydrodynamic bearings were compared. Although a high unbalance was considered in the lumped mass attached to the rotor, no significant nonlinear effects arose when comparing the linear model (equivalent linear coefficients) to the nonlinear model (complete solution of the Reynolds equation). Therefore, the test used for tuning the PID controllers and the following performance

tests were conducted using the linear bearing model, due to its computational efficiency. The similarity of the rotor orbits, regarding the linear and non-linear bearing models, was observed even in the presence of the PID controllers.

The steady-state analysis of the PID controllers showed that the five tunings were capable of reducing the vibration amplitude of the rotor for three operating conditions: below the critical speed (25 Hz - condition in which the controllers were tuned), close to the critical speed (44 Hz), and above the critical speed (52 Hz). When the rotor was set to a rotational speed much higher than the critical speed (75 Hz), all controllers failed in reducing the vibration amplitude of the rotor.

The steady-state analysis of the PID controllers (unbalance response) has shown that the critical speed of the system increased (since the system stiffness is increased by the actuator). Nevertheless, the vibration amplitude of the critical speed is reduced and the system damping is increased for every tuning method.

Finally, a transient analysis was performed by injecting a step signal into the reference input of the closed-loop. All controllers could satisfactorily control attenuate the system response and the controllers performance were compared in terms of overshoot and settling time. The obtained performances were in agreement with the expected behavior of each tuning method.

Acknowledgements. The authors would like to thank CNPq and grant #2015/20363-6 from the São Paulo Research Foundation (FAPESP) for the financial support to this research.




References

1. Dubois, G.B., Ocvirk, F.W.: Analytical derivation and experimental evaluation of short bearing approximation for full journal bearings. *NACA* **1157**, 1199–1230 (1953)
2. Muszynska, A.: Whirl and whip – rotor bearing stability problems. *J. Sound Vib.* **110**, 443–462 (1986)
3. Muszynska, A.: Stability of whirl and whip in rotor bearing system. *J. Sound Vib.* **127**, 49–64 (1988)
4. Crandall, S.: From whirl to whip in rotordynamics. In: *Proceedings of the Third IFToMM International Conference on Rotordynamics*, Lyon, Franc, pp. 19–26 (1990)
5. Burrows, C., Sahinkaya, M., Clements, S.: Active vibration control of flexible rotors: an experimental and theoretical study. In: *Proceedings of the Royal Society of London A*, vol. 422, pp. 123–146 (1989)
6. Burrows, C., Sahinkaya, M., Clements, S.: Electromagnetic control of oil-film supported rotors using sparse measurements. *J. Vib. Acoust. Stress Reliab. Des.* **110**, 295–299 (1988)
7. Fürst, S., Ulbrich, H.: An active support system for rotors with oil-film bearings. In: *Proceedings of the IMechE International Conference*, Edinburgh, United Kingdom, pp. 61–68 (1988)
8. Dimitri, A., El-Shafei, A.: Instability control and unbalance compensation of flexible rotors supported on journal bearings using magnetic bearings. In: *Proceedings of the Eighth IFToMM International Conference on Rotor Dynamics*, Korea, pp. 657–664 (2010)
9. Siqueira, A.A.G., Nicoletti, R., Norrick, N., Cavalca, K.L., Castro, H.F., Bauer, J., Dohnal, F.: Linear parameter varying control design for rotating systems supported by journal bearings. *J. Sound Vib.* **331**, 2220–2232 (2012)

10. Rieman, B., Perini, E.A., Cavalca, K.L., Castro, H.F., Rinderknecht, S.: Oil whip instability using μ -synthesis technique on a magnetic actuator. *J. Sound Vib.* **332**, 654–673 (2013)
11. Saint Martin, L.B., Mendes, R.U., Cavalca, K.L.: Electromagnetic actuators for controlling flexible cantilever beams. *Struct. Control Health Monit.* **25**, 1–19 (2018). <https://doi.org/10.1002/stc.2043>
12. Ziegler, J.G., Nichols, N.B.: Optimum settings for automatic controllers. *Trans. ASME* **65**, 433–444 (1943)
13. Åström, K.J., Häggglund, T.: *PID Controllers: Theory, Design, and Tuning* (1994)
14. Anantachaisilp, P., Lin, Z., Allaire, P.: PID tuning methods for active magnetic bearing systems. In: *Proceedings of the 13th International Symposium on Magnetic Bearings*, Arlington, USA (2012)
15. Anantachaisilp, P., Lin, Z.: An experimental study on PID tuning methods for active magnetic bearing systems. *Int. J. Adv. Mechatron. Syst.* **5**(2), 146–154 (2013)
16. Nelson, H.D., McVaugh, J.M.: The dynamics of rotor-bearing systems using finite elements. *J. Eng. Ind.* **98**, 593–600 (1976). <https://doi.org/10.1115/1.3438942>
17. Childs, D.: *Turbomachinery Rotordynamics: Phenomena, Modeling, and Analysis*. Wiley-Intersciences, New York (1993). Article title. *Journal* **2**(5), 99–110 (2016)
18. Nelson, H.D.: A finite rotating shaft element using timoshenko beam theory. *J. Mech. Des.* **102**, 793–803 (1980). <https://doi.org/10.1115/1.3254824>
19. Pinkus, O., Sternlicht, B.: *Theory of Hydrodynamic Lubrication*. McGraw-Hill Book Company, New York (1961)
20. Machado, T.H., Cavalca, K.L.: Dynamic analysis of cylindrical hydrodynamic bearings with geometric discontinuities. In: *Proceedings of International Conference on Vibration Problems, ICoVP 2011, Prague, Czech Republic*, vol. 1, pp. 1–6 (2011)
21. Patankar, S., Pengairan, J., Van Rijn, L.C.: *Numerical Heat Transfer and Fluid Flow*, 1st edn. Hemisphere Publishing Corporation, New Jersey (1980)
22. Lund, J.W.: Review of the concept of dynamic coefficients for fluid film journal bearings. *J. Tribol.* **109**, 37–41 (1987). <https://doi.org/10.1115/1.3261324>
23. Bathe, K.J., Saunders, H.: *Finite Element Procedures in Engineering Analysis*. Prentice-Hall, New Jersey (1984). <https://doi.org/10.1115/1.3264375>
24. Dakel, M., Baguet, S., Dufour, R.: Nonlinear dynamics of a support-excited flexible rotor with hydrodynamic journal bearings. *J. Sound Vib.* **333**, 2774–2799 (2014)
25. Perry, R.H., Chilton, C.H.: *Chemical Engineers' Handbook*, 5th edn. McGraw-Hill, New York (1973)
26. Luyben, W.L.: Tuning proportional-integral-derivative controllers for integrator/deadtime process. *Ind. Eng. Chem. Res.* **35**(10), 3480–3483 (1996)
27. Shinskey, F.G.: *Process Control Systems: Application, Design and Tuning*. McGraw-Hill, New York (1996)



Experimental Validation of Angular Viscoelastic Dynamic Neutralizers Designed for Flexural Vibration Control in Rotating Machines

Danielle Raphaella Voltolini¹(✉) , Samuel Kluthcovsky² ,
Eduardo Márcio de Oliveira Lopes² ,
and Carlos Alberto Bavastrri² 

¹ WEG Group – Energy Division, Jaraguá do sul,
Santa Catarina 89256-900, Brazil
danieller@weg.net

² Mechanical Engineering Department, Federal University of Paraná,
Curitiba 81531-980, Brazil

Abstract. The installation of micro hydroelectric power plants has recently been growing in Brazil, where small hydraulic generators are combined with hydraulic turbines. Some technical solutions require different runaway factors, from 1.2 up to 3.0 times the synchronous speed of the generator, so that the mechanical design of them must be reinforced or changed to support this critical dynamic condition, affecting costs and reducing competitiveness. An effective technique to control vibration is the use of simple devices called ‘dynamic vibration neutralizers’. These devices can contain viscoelastic material to introduce high mechanical impedance onto the system to reduce its vibration levels. There is a special kind of neutralizer, called ‘angular viscoelastic dynamic neutralizer’ (angular VDN), which acts indirectly in slope degree of freedom controlling flexural vibration. They have the predicted ability to control more than one single mode once the device is assembled where the maximum slope happens. The aim of the current work is to present a methodology to design angular VDNs and validate it by using a simplified experimental rotor exploring two different geometries. The results show that, if well-tuned, this kind of control is effective not only for the frequency band of interest, but also over higher modes.

Keywords: Angular viscoelastic dynamic neutralizer
Flexural vibration control · Rotordynamics

1 Introduction

In order to make the most of the Brazilian hydraulic power capacity, the installation of micro hydroelectric power plants (MHPs) has been growing year after year. In Brazil, the plants with power capacity up to 5 MW are considered MHPs, using small hydraulic generators combined with hydraulic turbines to generate this amount of energy, where the turbine set depends on the fall height.

The design of the hydraulic generator is intimately related to the type of turbine, since it influences the generator runaway factor. Therefore, in applications concerning Pelton and Francis turbines, it is a common practice to use a runaway factor up to 2.0 times the nominal speed of the generator. However, for Kaplan turbines, this runaway factor usually grows from 2.3 up to 3.0, so that the mechanical design of the generator must be reinforced to support this critical dynamic condition.

These generators should be small and low-priced, so their construction employs roller bearings to support the rotor and turbine loads. So, if a generator is mechanically designed to operate at a runaway factor 2.0, and then one wishes to use it in an application with a higher runaway factor, it is necessary to modify the mechanical project by increasing the diameters of the shaft, the bearings, or even changing the roller bearings to hydrodynamic bearings, in order to comply with the API 541 vibration requirements. All these modifications impact the generator costs, reducing competitiveness.

When it comes to flexural vibration control, there are some techniques consolidated by the literature [1–7], most of them based on the addition of damping to the vibration control system. Another effective technique consists of using simple and relatively low-cost devices called ‘dynamic vibration neutralizers’ [8–13]. These devices can contain viscoelastic material - instead of spring and dashpot - introducing high mechanical impedance into the primary system (dynamic structures to be controlled), to reduce vibration levels in a frequency band of interest. That is, the neutralizers add not only damping, but they also introduce reaction forces into the primary system.

There is a special kind of neutralizer, called ‘angular viscoelastic dynamic neutralizer’ (angular VDN), which acts indirectly on slope degree-of-freedom (DOF) - as shown in Fig. 1 - controlling flexural vibration. It is attached near the bearings, where one finds the maximum angular displacement for the shaft regarding its neutral axis. Furthermore, the angular VDN has the predicted ability to control more than one single mode, since, for a simply supported beam, regardless of the mode shape, the DOF slope is never null close to the supports.

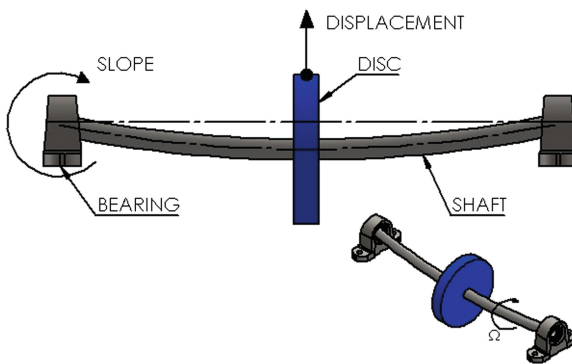


Fig. 1. Slope degree-of-freedom in rotating systems.

The aim of current study is to present a methodology to design angular VDNs – and validate it using a simplified experimental rotor – by exploring two different geometries. The studies and the results show that the auxiliary support has to be carefully designed in

order to ensure the angular degree of freedom control, since the neutralizer motion could be exposed, through this support, to the displacement and angular motion in all directions due to shaft whirling. The results show that, if well-tuned, this kind of control is effective not only for the frequency band of interest, but also over higher modes.

2 Viscoelastic Material Model

Viscoelastic materials are widely used in vibration and noise control applications due to their relative low cost and attractive physical properties: the dynamic behavior depends on their complex elasticity moduli, which are frequency and temperature dependent. The properties of a typical and thermorheologically simple viscoelastic material are detailed in [14, 15].

The four-parameter fractional derivative model for viscoelastic solid materials was introduced by [10, 15]. This simple model may numerically characterize a wide range of viscoelastic materials in engineering. So, in the frequency domain, the complex shear modulus ($\bar{G}(\Omega, T)$) is represented by:

$$\bar{G}(\Omega, T) = \frac{G_0 + G_\infty b_1 (i\Omega\alpha(T))^\beta}{1 + b_1 (i\Omega\alpha(T))^\beta} = G_r(\Omega, T)(1 + i\eta(\Omega, T)) \quad (1)$$

where $G_r(\Omega, T) = Re(\bar{G}(\Omega, T))$ is the dynamic shear modulus or storage modulus and $\eta(\Omega, T) = Im(\bar{G}(\Omega, T))/Re(\bar{G}(\Omega, T))$ is the loss factor; parameters G_0 and G_∞ represent the asymptotic values of the dynamic shear modulus at low and high frequencies, respectively; $b_1 = b^\beta$ is an experimental constant, where b is the relaxation time [10] and β is the fractional derivative power; Ω is the excitation frequency and i is the imaginary unit ($i = \sqrt{-1}$). Parameter $\alpha(T)$ is actually a function called ‘shift factor’ and represents the temperature influence in the dynamic behavior of viscoelastic materials. This factor was experimentally proposed by William–Landel–Ferry (WLF) and empirically equated by [16]:

$$\log\alpha(T) = -\theta_1 \frac{T - T_0}{\theta_2 + T - T_0} \quad (2)$$

where constants θ_1 and θ_2 may be experimentally determined, parameter T_0 is an arbitrary reference temperature, and T is the working temperature, both in Kelvin. For the sake of simplicity, parameter T will be suppressed from now on, since the present paper will fix a constant temperature for the system modelling.

3 Viscoelastic Dynamic Neutralizer Applied to Slope Degree of Freedom

The approach of the present paper is related to the angular VDN, i.e., the neutralizer works in slope DOF instead of the transversal displacement. Based on the methodology showed on [11], the generalized equivalent parameters model for slope degree-of-

freedom of a simple neutralizer is proposed in order to replace the classical one, as shown in Fig. 2. Then, the simple neutralizer attached on the primary system can be represented by an equivalent model compound just by an equivalent mass, $m_{es}(\Omega)$, and an equivalent damping, $c_{es}(\Omega)$. These equivalent dynamic parameters are found equating the dynamic stiffness on the base of the neutralizer of the both models presented in Fig. 2.

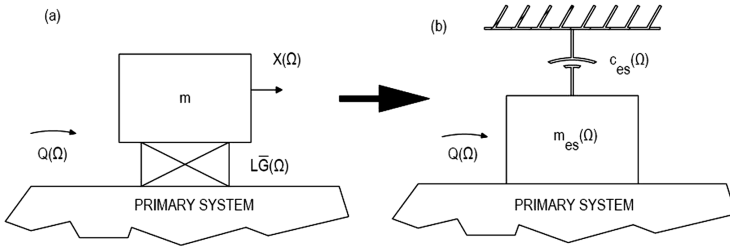


Fig. 2. Generalized equivalent model for a system with VDN – slope DOF.

The dynamic stiffness at the base of angular VDN ($\bar{K}_{bs}(\Omega)$) is calculated through the relation between the external moment applied to the base ($M_b(\Omega)$) and the slope displacement at base ($\theta_b(\Omega)$), as shown in Fig. 3. This figure shows a lateral view of a simplified model for the VDN, where is represented the shaft, as indicated, the arm of the neutralizer, with an inertia I_b , the viscoelastic blanket in blue, and the mass of neutralizer above the viscoelastic.

$$\bar{K}_{bs}(\Omega) = \frac{M_{ext}(\Omega)}{\theta_b(\Omega)} \tag{3}$$

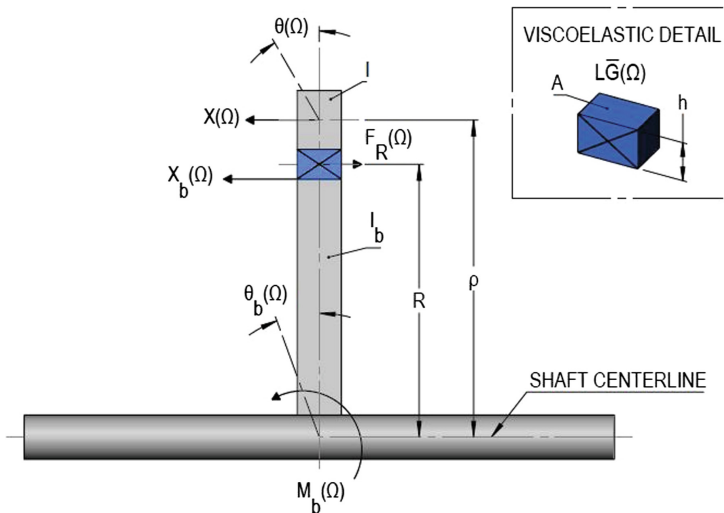


Fig. 3. Simplified physical model for angular VDN.

The lateral action force ($F_R(\Omega)$) of the viscoelastic element is obtained in the frequency domain, as shown by [13], as a relation between the dynamic stiffness and the displacements at base $X_b(\Omega)$ and at mass $X(\Omega)$. The free body diagram and Newton's second law are also applied to the bodies, and, by handling these equations, it is possible to obtain the dynamic stiffness for the angular VDN, as shown below. The relations are obtained as follows:

$$\bar{K}_{bs}(\Omega) = \frac{M_{ext}(\Omega)}{\theta_b(\Omega)} = \frac{\bar{K}(\Omega)R^2(-\Omega^2 I)}{-\Omega^2 I + \bar{K}(\Omega)R^2} - \Omega^2 I_b \quad (4)$$

where variables I and I_b are the mass inertias of the neutralizer mass and its base, respectively.

As shown in [17], handling Eq. (4) and comparing with the stiffness on the base of the simple neutralizer shown in Fig. 2b given by $\bar{K}_{bs}(\Omega) = -\Omega^2 m_{es}(\Omega) + i\Omega c_{es}(\Omega)$, the generalized equivalent mass and damping can be obtained taking the real and imaginary part of the Eq. (4) and dividing by $-\Omega^2$ and Ω , respectively. Then, these generalized equivalent parameters are defined as:

$$m_{es}(\Omega) = \frac{r(\Omega)R^2(I + I_b) \left[-\varepsilon(\Omega)^2 + r(\Omega)R^2(1 + \eta(\Omega)^2) \right] - \varepsilon(\Omega)^2 I_b \left[-\varepsilon(\Omega)^2 + r(\Omega)R^2 \right]}{\left[-\varepsilon(\Omega)^2 + r(\Omega)R^2 \right]^2 + r(\Omega)^2 \eta(\Omega)^2 R^4} \quad (5)$$

$$c_{es}(\Omega) = \frac{\Omega r(\Omega)R^2 \eta(\Omega) \varepsilon(\Omega)^2 I}{\left[-\varepsilon(\Omega)^2 + r(\Omega)R^2 \right]^2 + r(\Omega)^2 \eta(\Omega)^2 R^4} \quad (6)$$

where $r(\Omega) = LG_r(\Omega)/LG_r(\Omega_n)$, Ω_n is the natural frequency of the system given by $\Omega_n^2 = LG_r(\Omega_n)/m$ and $\varepsilon(\Omega) = \Omega/\Omega_n$.

To find the control frequency Ω_θ , it is necessary to equal the denominator of Eq. (4) to zero, as follows:

$$\Omega_\theta = \sqrt{\frac{LG_r(\Omega_n)R^2}{m\rho^2}} \quad (7)$$

The mass inertia of the neutralizer mass is defined by $I = m\rho^2$, where ρ is the distance between the center of the neutralizer mass and the centerline of the shaft (Fig. 3). So, the relation between the natural frequency of the system and the control frequency is given by:

$$\Omega_\theta = \Omega_n \frac{R}{\rho} \quad (8)$$

Based on Eq. (8) and Fig. 3, given that $R < \rho$, the relation between the frequencies will be $\Omega_\theta < \Omega_n$. So, it is possible to obtain a control frequency as low as necessary.

4 The Rotating System: Primary and Compound Systems

The rotating primary system may be discretized through the finite element method by using the beam finite element with three nodes and four degrees of freedom each, as shown in Fig. 4.

The equation of motion [18, 19] for a simple rotating system with multiple DOF, in the frequency domain, is expressed by:

$$[-\Omega^2[M] + i\Omega([C] + [G(\Omega_r)]) + [K]]\{Q(\Omega)\} = \{F(\Omega)\} \tag{9}$$

where $[M]$ is the global mass matrix defined by the kinetic energy of the system; $[C]$ is the global damping matrix; $[G(\Omega_r)]$ is the global gyroscopic effect matrix obtained by the kinetic energy as well; $[K]$ is the global stiffness matrix defined by the potential deformation; $\{Q(\Omega)\}$ is the generalized coordinate vector and $\{F(\Omega)\}$ is the generalized excitation vector. For the sake of simplification, the effects of rotating damping and stiffness were disregarded in Eq. (9).

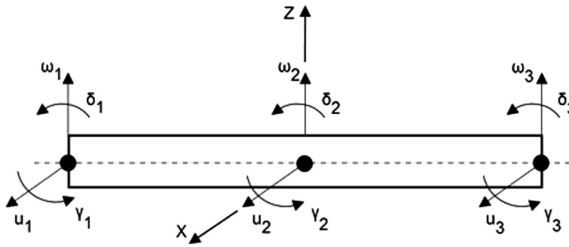


Fig. 4. Finite element method: discretization of a beam element.

The motion equation, in the state space, can be rewritten as follows:

$$\left(i\Omega \begin{bmatrix} [C] + [G(\Omega_r)] & [M] \\ [M] & 0 \end{bmatrix} + \begin{bmatrix} [K] & 0 \\ 0 & [-M] \end{bmatrix} \right) \{Y(\Omega)\} = \begin{Bmatrix} F(\Omega) \\ 0 \end{Bmatrix} = \{N(\Omega)\} \tag{10}$$

For the compound system (primary system plus angular VDV), the generalized equivalent parameters must be added to the primary system. These parameters are expressed in matrix terms by:

$$[C_e(\Omega)] = \begin{bmatrix} 0 & 0 & \dots & 0 & 0 \\ 0 & c_{es1}(\Omega) & \dots & 0 & 0 \\ \vdots & \vdots & \ddots & \vdots & \vdots \\ 0 & 0 & \dots & c_{esp}(\Omega) & 0 \\ 0 & 0 & \dots & 0 & 0 \end{bmatrix} \begin{matrix} \vdots \\ \leftarrow \theta_{j1} \\ \vdots \\ \leftarrow \theta_{jp} \\ \vdots \end{matrix} \tag{11}$$

$$[M_e(\Omega)] = \begin{bmatrix} 0 & 0 & \cdots & 0 & 0 \\ 0 & m_{es_1}(\Omega) & \cdots & 0 & 0 \\ \vdots & \vdots & \ddots & \vdots & \vdots \\ 0 & 0 & \cdots & m_{es_p}(\Omega) & 0 \\ 0 & 0 & \cdots & 0 & 0 \end{bmatrix} \begin{matrix} \vdots \\ \leftarrow \theta_{j1} \\ \vdots \\ \leftarrow \theta_{jp} \\ \vdots \end{matrix} \quad (12)$$

where parameters c_{es_j} and m_{es_j} are the j^{th} term, with $j = 1$ to p with p being the number of angular VDNs used.

Then, the motion equation for the compound system is given by:

$$[-\Omega^2([M] + [M_e(\Omega)]) + i\Omega([C] + [C_e(\Omega)] + [G(\Omega_r)]) + [K]]\{Q(\Omega)\} = \{F(\Omega)\} \quad (13)$$

In the state space, Eq. (13) can be rewritten as

$$i\Omega[\tilde{A}(\Omega, \Omega_r)]\{Y(\Omega)\} + [\tilde{B}(\Omega)]\{Y(\Omega)\} = \begin{Bmatrix} F(\Omega) \\ \cdots \\ 0 \end{Bmatrix} = \{N(\Omega)\} \quad (14)$$

where:

$$[\tilde{A}(\Omega, \Omega_r)] = [A(\Omega_r)] + [A_e(\Omega)] \quad (15)$$

$$[\tilde{B}(\Omega)] = [B] + [B_e(\Omega)] \quad (16)$$

the matrices $[A(\Omega_r)]$ and $[B]$ represent the primary system behavior and $[A_e(\Omega)]$ and $[B_e(\Omega)]$ represent the influence of the dynamic neutralizers attached to the primary system. These matrices are given by:

$$[A(\Omega_r)] = \begin{bmatrix} ([C] + [G(\Omega_r)]) & [M] \\ [M] & 0 \end{bmatrix} \quad (17)$$

$$[A_e(\Omega)] = \begin{bmatrix} [C_e(\Omega)] & [M_e(\Omega)] \\ [M_e(\Omega)] & [0] \end{bmatrix} \quad (18)$$

and

$$[B] = \begin{bmatrix} [K] & 0 \\ 0 & [-M] \end{bmatrix} \quad (19)$$

$$[B_e(\Omega)] = \begin{bmatrix} [0] & [0] \\ [0] & [-M_e(\Omega)] \end{bmatrix} \quad (20)$$

To solve the motion equation, it is necessary to transform Eq. (14), in the configuration system, into the modal or sub-modal space of the state space by using the right eigenvector matrix of the primary system $[\Theta](\lambda[A(\Omega_r)][\Theta]) = [B][\Theta]$.

$$\{Y(\Omega)\} = [\Theta]\{P(\Omega)\} \quad (21)$$

and, then, pre-multiplying Eq. (14) by the transpose left eigenvectors $[\Psi]^T(\lambda[A(\Omega_r)]^T[\Psi]) = [B]^T[\Psi]$, its adjoint problem, the motion equation can be solved as:

$$[i\Omega[\Psi]^T[\tilde{A}(\Omega, \Omega_r)]][\Theta] + [\Psi]^T[\tilde{B}(\Omega)][\Theta]]\{P(\Omega)\} = [\Psi]^T\{N(\Omega)\} \quad (22)$$

or, simplified as:

$$\{\bar{Y}(\Omega)\} = [\Theta][D(\Omega)][\Psi]^T\{N(\Omega)\} \quad (23)$$

with

$$[D(\Omega)] = [i\Omega([I] + [\Psi]^T[A_e(\Omega)][\Theta]) + ([A] + [\Psi]^T[B_e(\Omega)][\Theta])]^{-1} \quad (24)$$

For the angular VDN design, the subspace can be obtained by limiting the size of eigenvectors matrices $[\Theta]$ and $[\Psi]$ to the first $2\hat{n}$ modes, with $\hat{n} \ll n$, since the contribution of the higher order modes is insignificant and can be ignored. This significantly reduces the computational time, which is proportional in n^3 .

5 Optimization Problem

In the present work, the optimization problem consists of reducing the flexural vibration level for the primary system as much as possible. This control is made by the indirect reduction of the slope degree of freedom of the primary system obtained by using angular VDNs. For that, the angular VDN must be optimally designed, in other words, its natural frequency must be determined in an optimization environment.

To this end, it is suggested a non-linear optimization method, and the objective function f_{obj} is defined by:

$$f_{obj}(x) = \|\max_{\Omega_1 < \Omega < \Omega_2} |P(\Omega, x)|\| \quad (25)$$

where x is the design vector containing the natural frequencies of the p neutralizers ($x^T = [\Omega_{a1}, \Omega_{a2}, \dots, \Omega_{ap}]$); parameters Ω_1 and Ω_2 constitute the frequency band control related to the operation of the machine and its flexural modes; “max” is the maximum value for each component of vector $P(\Omega, x)$ and $\|\ \|\$ indicates the use of the Euclidian Norm.

When it comes to ensure the convergence of an optimization problem, it is advisable to use barrier functions, which are inequality functions defined by $\Omega_{ai}^L < \Omega_{ai} < \Omega_{ai}^U$ with $i = 1$ to p , and L and U are the lower and upper constrains, respectively.

The aim of this optimization problem is to find a vector with the frequencies for the angular VDNs that minimize function $P(\Omega, x)$.

The complete methodology used in the present paper is based on the following instructions:

1. the generalized equivalent parameters for the slope DOF are calculated (Eqs. (5) and (6)) based on the viscoelastic material selected and the rotor geometry studied;
2. matrix $[D(\Omega)]$ from Eq. (24) is assembled and equated;
3. the unbalance excitation and the matrix $[D(\Omega)]$ are solved to obtain vector $\{P(\Omega, x)\}$;
4. the absolute values of vector $\{P(\Omega, x)\}$ are evaluated for the optimization algorithm, and its maximum values are chosen;
5. the objective function is solved, and a new project vector is assembled;
6. steps 1 to 5 are repeated until the minimal value for vector $\{P(\Omega, x)\}$ is found; then, the optimal natural frequencies are finally obtained.

After having found the natural frequencies of the angular VDN, the other parameters can be found out to physically design the neutralizer. The mass inertia of the neutralizer was defined by [13] for the mode-to-mode control and is adapted for this application as follow:

$$\mu_j = \frac{I_a \sum_{s=1}^p |\phi_{k_{sj}}|^2}{I_j} \quad (26)$$

where $\phi_{k_{sj}}$ are the $k_{s,j}$ elements of the right modal matrix on state space; I_a is the neutralizer mass inertia considering it in modal space; p is the number of neutralizers; k_s is the position where the i^{th} neutralizer is fixed on the primary system with $s = 1$ to j , where j is the j^{th} mode to be controlled. Finally, μ_j is the relation between the mass moment of inertia of the neutralizer, considered in the modal space of the primary system, and the modal mass moment of inertia of the primary system and can typically go up 10% to 25%.

6 Numerical-Experimental Development and Results

The current work presents three different geometries performed to experimentally validate the methodology presented above. They are the compact angular VDN using E-A-R Isodamp C-1002 rubber (item 6.1), the same design by using butyl rubber (item 6.2), and the center of percussion of the angular VDN design (item 6.3).

The three types of angular VDN were designed for the same rotor geometry, as detailed in Fig. 5, and the same unbalance mass was used: 0.0002 kg m applied to the central disk, or 458 mm from the driven side of the shaft.

The neutralizers were assembled in the same position, as close as possible to the rear bearing, 50 mm away from the bearing in the shaft end direction, as presented in Figs. 7 and 14.

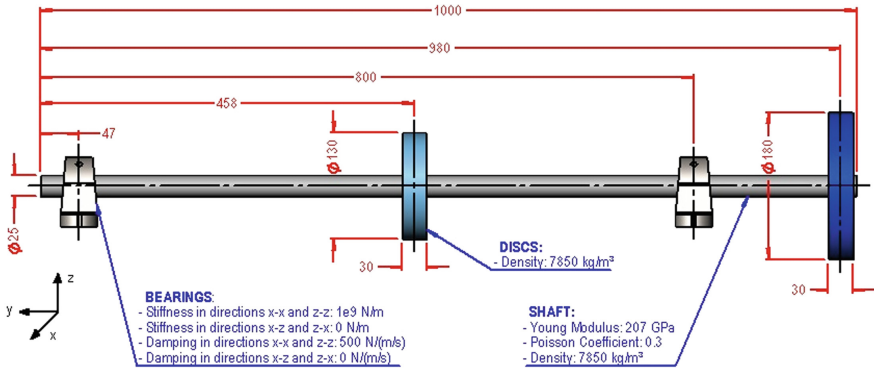


Fig. 5. Rotor geometry used for all types of angular VDN tested.

6.1 Compact Angular VDN – C-1002

The first geometry proposed was designed by using the E-A-R Isodamp C-1002, and the parameters of the four-parameter fractional derivative model are preset in Table 1.

Table 1. Rubber parameters.

E-A-R Isodamp C-1002			Butyl rubber		
T_0	286.341	K	T_0	273	K
T	298	K	T	293	K
θ_1	24.2078		θ_1	6.57	
θ_2	249.808		θ_2	68.0	
G_0	6.56e5	Pa	G_0	3.57e6	Pa
G_∞	8.61e8	Pa	G_∞	4.79e8	Pa
B	0.545		B	0.435	
b_1	6.46e-4		b_1	2.46e-3	

The design starts by modelling the rotor, as shown previously, and applying it to the optimization environment. So, for this case, the optimal natural frequency found was 24.9 Hz, as presented in Fig. 6. For other neutralizer geometries, the same unbalance frequency response shown in Fig. 6 is used, since the primary system is the same.

Based on that geometry, the modal inertia is obtained and, considering a μ_j equal to 10%, the neutralizer inertia is $I_a = 0.0077496 \text{ kg m}^2$. This inertia was divided into four identical devices, consisting of an aluminum base with three pieces of rubber glued to a steel sleeve; fixed on it by threading bars are two steel cylinders serving as the mass of the device, as presented on Fig. 7. The device is attached to a fake bearing by using a threading bar. This bearing consists of an aluminum sleeve mounted above the rolling bearing and anchored on the structure by steel wires.

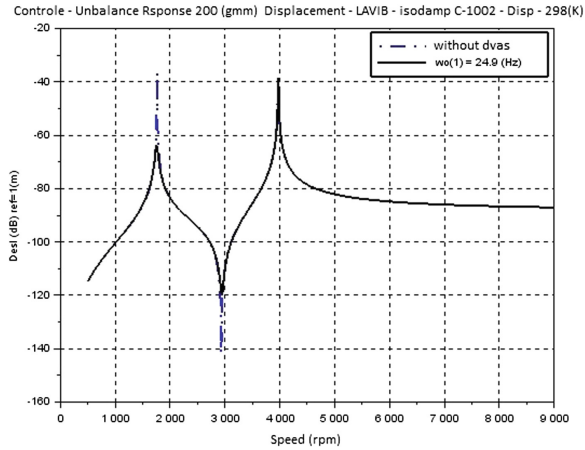


Fig. 6. Unbalance frequency response with and without compact angular VDN C-1002.

The experimental validation of the VDN natural frequency is presented in Fig. 8 and shows the inertance curve measured. The curve was obtained by fixing the accelerometer to the cylinder mass of the neutralizer (measuring point) and by applying an impact force near this point (exciting point). This curve presents a damped behavior due the physical properties of the material. The natural frequency presented was approximately 25 Hz, as expected.



Fig. 7. Rotor assembled with compact angular VDN compound with C-1002.

Two of the angular VDNs were positioned parallel to the faces of the disks, as shown in Fig. 7. Due to the size of the mass, the other two devices were assembled slightly misaligned in relation the other ones. From now on, this configuration will be called 'standard position'. The rundown test was conducted, and the unbalance frequency response (UFR) for 'X' direction, according Fig. 4, is shown in Fig. 9.

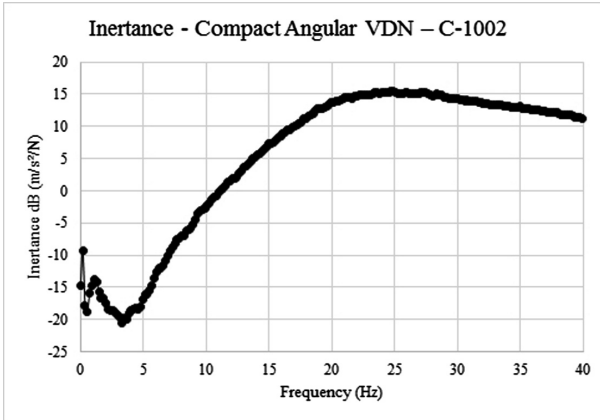


Fig. 8. Inertance to C-1002 VDN.

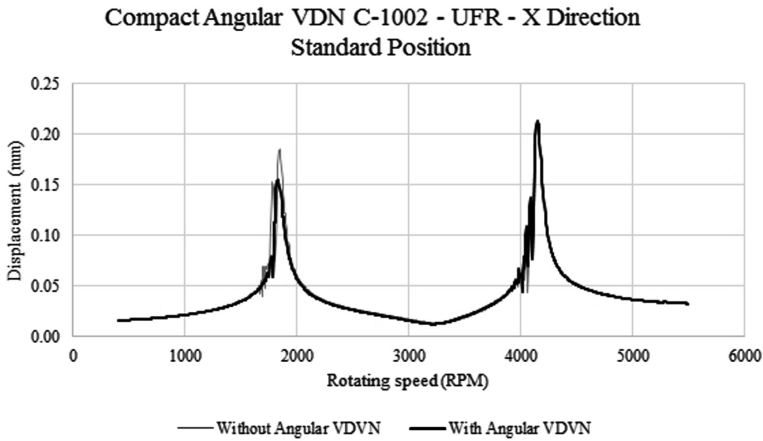


Fig. 9. UFR for standard position – angular VDN C-1002.

Based on Fig. 9, it is possible to note that the angular VDNs do not insert the necessary impedance to effectively control the vibration level of the primary system for the first mode, and barely had any effect on the second one. This behavior was initially associated to clearance in ball bearings. The hypothesis was rebutted after assembling a new hub using roller bearings, without a significant change in the results. Other tests were conducted by altering the angular position of neutralizers, as showed on Fig. 11, resulting in distinct dynamic behaviors, increasing or reducing control capacity, as presented in Fig. 10.

When comparing the curves in Figs. 9 and 11, there is a reduction in the amplitude of vibration for both modes, which is stronger for the case with variation of the angular positioning in relation to the standard position, showing the sensitivity of the device to

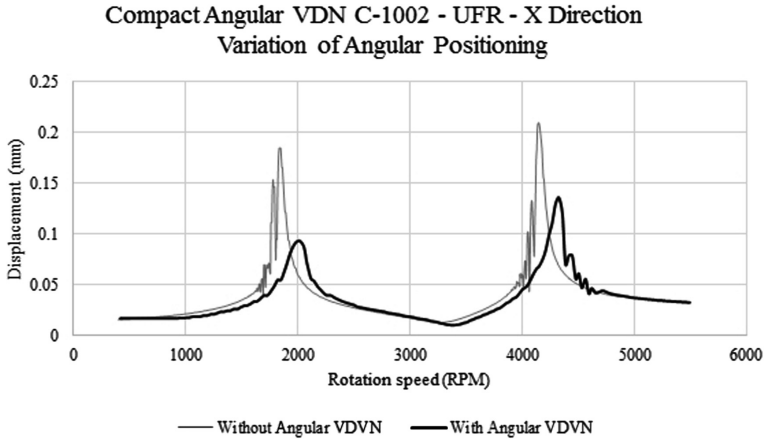


Fig. 10. UFR for variation of angular positioning – angular VDN C-1002.

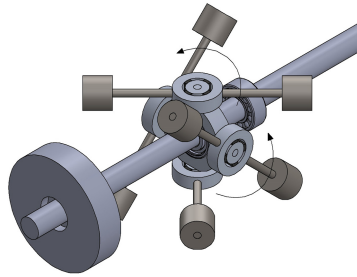


Fig. 11. Variation of angular positioning – angular VDN C-1002.

this design variable. This behavior seems to be due to the combined displacement presented in operation, that is, the rotor whirling combines translational (X and Z directions) and slope (δ and γ) displacements.

6.2 Compact Angular VDN – Butyl Rubber

The second geometry of angular VDN proposes to change only the viscoelastic material from C-1002 to a butyl rubber available in the laboratory where the tests were conducted. The parameters of the four-parameter fractional derivative model for this material are present in Table 1.

For the present case, the optimal natural frequency obtained was 28.8 Hz. The μ_j used to calculate the neutralizer inertia was changed to 25%, resulting in $I_a = 0.019374 \text{ kg m}^2$. The same geometry concept of the previous case was used, just changing the rubber blanks. Just to clarify: the device on the top of the figure is the C-1002 neutralizer, and the other four, at the bottom of the figure, are the butyl rubber ones. The device was positioned at the same point the C-1002 one was.

The inertance of this angular VDN was measured, and the curve is shown in Fig. 12. This curve can be compared the one shown in Fig. 8, presenting the difference in the dynamic behavior of the butyl rubber and compared to E-A-R Isodamp C-1002. The inspection of the inertance shows that the natural frequency of VDN with butyl rubber was not in accordance with the design ($25 \text{ Hz} \times 28.8 \text{ Hz}$). When this occurs, the temperature used in the project must have been different from that experienced in the laboratory during the tests. This shows the vulnerability of the project related to the use of some kinds of viscoelastic material, which are more susceptible to the influence of temperature in their dynamic behaviors.

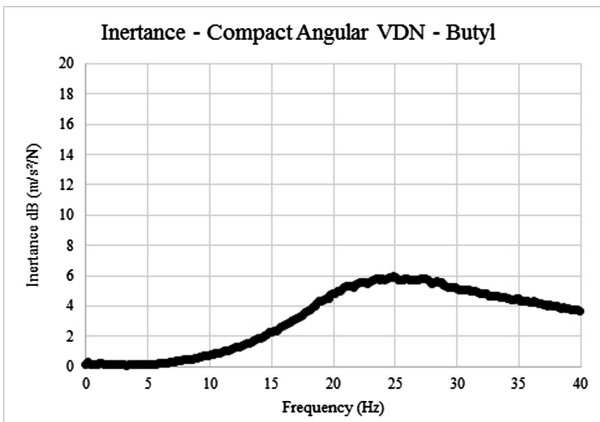


Fig. 12. Inertance curve to compact angular VDN butyl rubber.

Subsequently, the unbalance frequency response curves of the rotor, with and without neutralizer, were obtained by the rundown test. In a more detailed analysis of the rotor response curves, it was found that there was a region being controlled, below the first critical rotation. The hypothesis associated to this behavior was that the rotor was not exciting the design frequency of the neutralizer, in other words, the neutralizers were vibrating in a different way from that expected. To test this hypothesis, the natural frequency of the neutralizer was increased to coincide with the first critical rotation of the primary system. For this, the masses were approximated in increments of 10 mm of the neutralizer center until achieving a satisfactory control of the primary system. Figure 13 shows the unbalance frequency response curves with and without neutralizer, in the X direction.

Although rotor vibration was significantly controlled for the first mode, great difficulty was encountered in predicting the behavior of the neutralizer, that is, how the rotor will excite the neutralizer. This hinders the design and the correct tuning, the same problem faced on the C-1002 device.

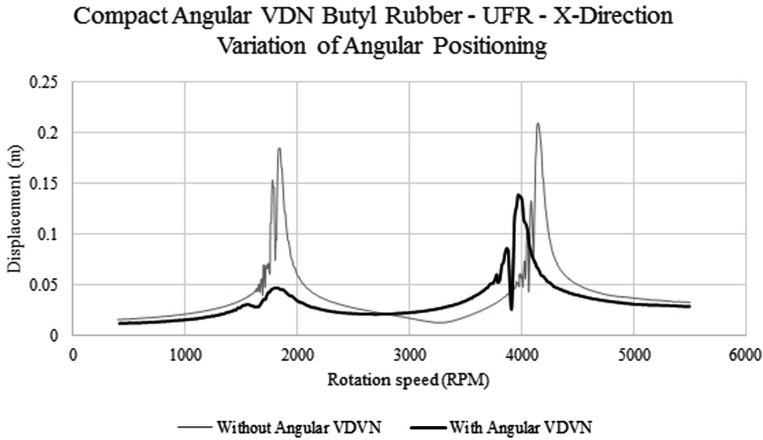


Fig. 13. UFR for Angular VDN butyl rubber.

6.3 Center of Percussion Angular VDN

The third angular VDN design used a butyl rubber material, the parameters of which are presented in Table 1. The primary system is the same as shown in Fig. 5.

In this case, the neutralizer was designed to control the second rotor vibration mode, since the higher the frequency of the neutralizer, the easier its physical construction due to the viscoelastic material form factor. Based on this, an optimum frequency of 62.2 Hz and a mass inertia of $I_a = 0.019374 \text{ kg m}^2$ were obtained for a $\mu_j = 25\%$.

This inertia was divided into four identical pieces with a different geometry, here called ‘center of percussion’. This geometry has been arranged in order to operate in shear as much as possible, and to obtain the minimal distance R possible and, then, minimize the influence of the other neutralizer modes.

However, this geometry proved to be very fragile, due to its form of assembly, with the viscoelastic material segments attached between the base of the mass and the hub of the fake bearing. In an attempt to measure the unbalance frequency response to runaway/rundown, the viscoelastic segments came loose, making it impossible to operate and take measurements. In addition, this geometry shown a tendency to move in the direction of traction/compression of the material, further altering the frequency of the device in operation. Figure 14 shows the neutralizer assembled on the rotor.

Since the natural frequency of the device was lower than the one designed, the thickness of the viscoelastic material was reduced until the frequency coincided with the calculated one. The inertance of the system without neutralizer - with a designed neutralizer for the 1st mode and for the 2nd mode - was measured, as shown in Fig. 15.

Evaluating Fig. 15, one observes that there was an expressive control for the mode corresponding to the designed mode of the VDN. This behavior presents potential regarding the control of the primary system, once the previously listed problems are eliminated.

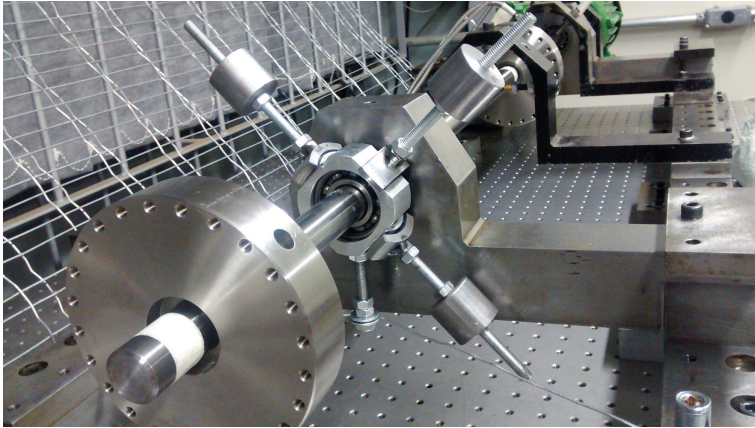


Fig. 14. Center of percussion angular VDN – experimental set.

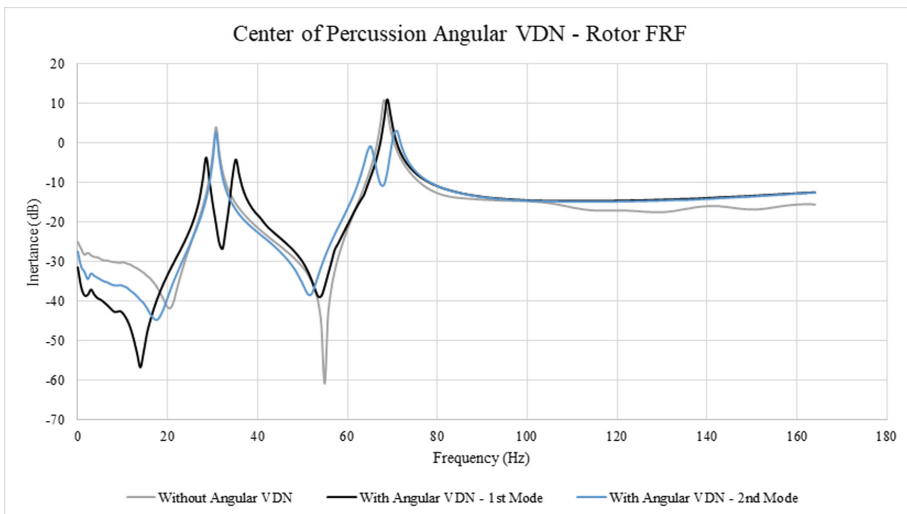


Fig. 15. Inertance for the center of percussion angular VDN.

7 Conclusions

The current paper presents a revision of the methodology on optimal design of angular viscoelastic dynamic neutralizers, as well as the experimental application of three different concepts in a controlled laboratory environment.

The results obtained were promising: the reduction of the response to the rotor unbalance frequency response of the primary system - by using angular VDNs - achieved 20 dB for the last geometry, for example.

However, several questions concerning the analytical design of the devices were identified in relation to the non-analytical prediction of the excitation behavior of the neutralizer by the rotor. Due to the rotor whirling, the angular VDN vibrates in different planes and not preferably in the one it was designed for, thus decreasing its effectiveness. These questions are being reviewed, and other geometries are under study for the neutralizer support.

References

1. Shabaneh, N.H.: Dynamic analysis of rotor-shaft systems with viscoelastic supported bearing. *Mech. Mach. Theory* **35**, 1313–1330 (2000)
2. Dutt, J.K., Toi, T.: Rotor vibration reduction with polymeric sectors. *J. Sound Vib.* **262**, 769–793 (2003)
3. Lee, Y., Kim, T., Kim, C., Lee, N., Cho, D.: Dynamic characteristics of a flexible rotor system supported by a viscoelastic foil bearing (VEFB). *Tribol. Int.* **37**, 679–687 (2004)
4. Bavastrri, C.A., Ferreira, E.M.S., Espindola, J.J., Lopes, E.M.O.: Modeling of dynamic rotors with flexible bearings due to the use of viscoelastic materials. *J. Braz. Soc. Mech. Sci. Eng.* **30**, 22–29 (2008)
5. Zhou, Q., Hou, Y., Chen, C.: Dynamic stability experiments of compliant foil thrust bearing with viscoelastic support. *Tribol. Int.* **42**, 662–665 (2009)
6. Varney, P., Green, I.: Rotordynamic analysis using complex transfer matrix: an application to elastomer supports using viscoelastic correspondence principle. *J. Sound Vib.* **333**, 6258–6272 (2014)
7. Ribeiro, E.A., Pereira, J.T., Bavastrri, C.A.: Passive vibration control in rotor dynamics: optimization of composed support using viscoelastic materials. *J. Sound Vib.* **351**, 43–56 (2015)
8. Snowdon, J.C.: Steady-state behavior of the dynamic absorber. *J. Acoust. Soc. Am.* **38**(8), 1096–1103 (1959)
9. Rogers, L.: Operators and fractional derivatives for viscoelastic constitutive equations. *J. Rheol.* **27**, 351–372 (1983)
10. Pritz, T.: Analysis of four-parameter fractional derivative model of real solid materials. *J. Sound Vib.* **195**, 103–115 (1996)
11. de Espíndola, J.J., Bavastrri, C.A., de Lopes, E.M.O.: On the passive control of vibrations with viscoelastic dynamic absorbers of ordinary and pendulum types. *J. Frankl. Inst.* **347**, 102–115 (2010)
12. Doubrawa Filho, F.J., Luersen, M.A., Bavastrri, C.A.: Optimal design of viscoelastic vibration absorbers for rotating systems. *J. Vib. Control* **17**(5), 699–710 (2010)
13. Voltolini, D.R., Kluthcovsky, S., Doubrawa Filho, F.J., Lopes, E.M.O., Bavastrri, C.A.: Optimal design of a viscoelastic vibration neutralizer for rotating systems: flexural control by slope degree of freedom. *J. Vib. Control*, 1–13 (2018)
14. Nashif, A.D., Jones, D.I.G., Henderson, J.P.: *Vibration Damping*. Wiley, New York (1985)
15. Jones, D.I.G.: *Handbook of Viscoelastic Vibration Damping*. Wiley, New York (2001)
16. Ferry, J.D., Fitzgerald, E.R., Grandine, L.D., Williams, M.L.: Temperature dependence of dynamic properties of elastomers; relation distributions. *Ind. Eng. Chem.* **44**(4), 703–706 (1952)

17. De Espíndola, J.J., Silva, H.P.: Modal reduction of vibrations by dynamic neutralizers: a generalized approach. In: 10th International Modal Analysis Conference, pp. 1367–1373. Society for Experimental Mechanics, San Diego (1992)
18. Genta, G.: Dynamic of Rotating Systems. Springer, New York (2005)
19. Lalanne, M., Ferraris, G.: Rotordynamic Prediction in Engineering, 2nd edn. Wiley, New York (1998)
20. Rathbun Associates. <https://www.rathbun.com/c-40-damping-isolation-materials.aspx>. Accessed 19 Jan 2018



Active Control of Rotating Machinery Under Rotor-Stator Contact Conditions

Patrick S. Keogh^(✉), Chris Lusty, Nicola Y. Bailey, and Fawaz Saket

Department of Mechanical Engineering, University of Bath, Bath BA27AY, UK
p. s. keogh@bath. ac. uk

Abstract. A rotor spinning within an active magnetic bearing (AMB) system will normally be levitated and hence operate without rotor-stator contact. External disturbances and inherent unbalance may be compensated with appropriate control to keep rotor deviations within the clearance gap. However, AMBs have limited dynamic load capacity due to magnetic material field saturation. Hence overload conditions may result in rotor-stator contact. A touchdown bearing (TDB) and rotor landing sleeve are usually included to protect the expensive rotor, magnetic bearing and sensor components from damage. Once rotor-TDB contact has been made, rotor dynamic conditions may ensue resulting in persistent rotor bouncing or rubbing limit cycle responses. Prolonged exposure to these severe dynamics will cause TDB degradation and require regular replacement. If possible, a clear aim should be to restore contact-free levitation through available control capability in an efficient manner. This paper is used to guide the control options that are available to restore contact-free levitation. The use of AMB control is appropriate if the required control forces are within saturation limits. It is also possible to actuate TDBs and destabilize persistent rotor dynamic contact conditions. For example, piezo-based actuation offers larger control forces than those from magnetic bearing systems. Hybrid control action involving both types of actuation system has the greatest potential for completely robust restoration of contact-free levitation.

Keywords: Magnetic bearings · Touchdown bearings · Contact-free levitation

1 Introduction

It is a current focus for the designers and manufacturers of active magnetic bearing (AMB) systems to give significant attention to the associated touchdown bearing (TDB) systems. The TDB is included to prevent damage to expensive rotor and stator components and to ensure that run-downs are safe. The sacrificial components are the replaceable TDB and rotor landing sleeve. During rotor-TDB contact, the TDB may be stressed mechanically and thermally, reducing TDB residual life significantly. It is therefore beneficial for the TDB to minimize contact periods to reduce losses of machine output and downtime.

Loss of levitation that causes rotor drop is the most severe duty experienced by a TDB [1, 2]. Larger scale drop tests are presented in [3–6]. Simulation of rotor drop includes the nonlinear study of [7]. Research in this area has continued to bring out the

finer details of the rotor dynamic and TDB responses [8–10]. Recently, significant further activity has also followed [11–20].

If a rotor/AMB system is still able to operate normally under closed loop control, the following scenarios may occur leading to rotor/TDB contact:

- (a) Feedback signal disturbances may lead to significant momentary rotor excursions.
- (b) Base accelerations or shock inputs may overload the AMBs, hence limiting rotor dynamic control.
- (c) Contact induced dynamics may become persistent or changed so much that the AMB closed loop control is unstable.

One course of action is to apply additional AMB control action to restore contact-free levitation [21, 22]. Alternatively, the TDB may be changed from being a passive component to an active component. This was achieved in [23–26].

Given the previous studies, it is useful to have a greater understanding of rotor contact dynamics. This would aid the design of control strategies that are able to restore contact-free levitation from a persistent condition of rotor-TDB contact. A distinction is made from standard controllers that are designed based on a contact-free rotor dynamic plant model. The reason is that under persistent contact, the rotor dynamic plant changes, hence the standard controllers may not respond appropriately or may induce rotor dynamic instability unintentionally. In order to ascertain the principles required for the restoration of contact-free levitation, the issues are assessed using an analytical model of a simple rotor supported in an AMB/TDB system. Conditions to destabilize persistent rub contact responses are derived. Simulations are then used to demonstrate how feedforward control of AMBs and TDBs may be used effectively. Feedforward AMB action may be appropriate if dynamic load capacity is available. Otherwise, feedforward TDB motions may be able to induce the rotor away from persistent contact.

2 Modeling of Rotor/TDB Contact

Figure 1 shows a simplified schematic of a section of rotor within an active magnetic bearing (AMB), which has made contact with a portion of a touchdown bearing (TDB). The TDB may have some degree of radial stiffness and damping in its mounting arrangement. Under standard proportional-integral-derivative (PID) control, the linearized AMB radial characteristics are isotropic and may be represented by stiffness and damping from the magnetic center. The purpose of the TDB is to prevent contact between the rotor and AMB magnetic poles, hence the rotor-AMB radial gap is designed to be less than the rotor-TDB radial gap. In practice, the AMB may have a significant axial dimension and the TDB is located adjacent to the AMB. Hence the TDB in Fig. 1 will be generally axially offset from the AMB. This non-collocation should be taken into account in the system design so that rotor tilt through the AMB, arising from conical and flexible rotor modes, does not allow rotor-AMB contact.

In the following section that considers an analytical approach to determine rotor/TDB rub responses, the AMB and TDB are considered to be axially aligned and the TDB rigidly mounted. This is an idealized representation. In Sect. 3.5, simulated

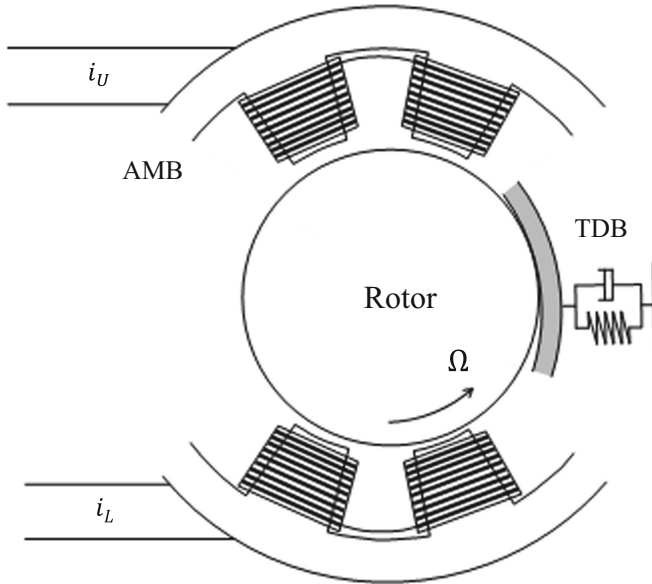


Fig. 1. Simulation of a rotor making contact with a touchdown bearing (TDB) within a functional AMB.

results are presented under compliant TDB mounting and it will be demonstrated that the analytical representations provide insight into the rotor rub response behavior. Relevant system parameters are shown in Table 1.

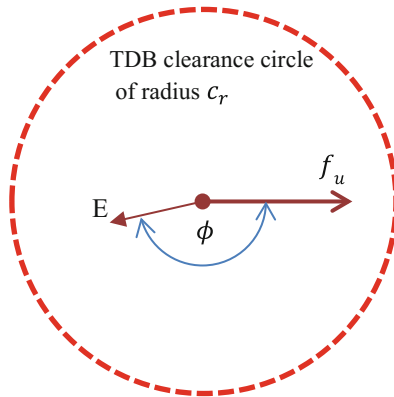


Fig. 2. Steady forward synchronous orbit representation of Eq. (4) viewed in a (u, v) rotating frame. The length of the displacement to E is r_E .

2.1 Synchronous Rotor Response

In this case the rotor is considered to be a simple unbalanced mass, m , that can rotate and translate in fixed axis x and y directions. In the following, E will denote the case of rotor motion that excludes rotor-TDB contact, while C will denote rotor motion with rotor-TDB contact. The orbit motions may be viewed in a fixed Cartesian (x, y) system or a synchronously rotating (u, v) system. The relation between the systems is

$$z = x + iy, \quad w = u + iv = ze^{-i\Omega t} \quad (1)$$

where Ω is the rotational speed. The AMB radial stiffness and damping characteristics may be specified through a natural frequency ω_n and damping ratio ξ so that

$$\ddot{z}_{E,C} + 2\xi\omega_n\dot{z}_{E,C} + \omega_n^2 z_{E,C} = \frac{f_u}{m} e^{i\Omega t} - \frac{f_c}{m} (1 + i\mu) \frac{z_C}{c_r} \quad (2)$$

or

$$\ddot{w}_{E,C} + (2\xi\omega_n + 2i\Omega)\dot{w}_{E,C} + (\omega_n^2 - \Omega^2 + 2i\xi\omega_n\Omega)w_{E,C} = \frac{f_u}{m} - \frac{f_c}{m} (1 + i\mu) \frac{w_C}{c_r} \quad (3)$$

where the subscripts E and C correspond with the orbit motions E and C, respectively. Also, c_r is the rotor-TDB radial clearance, f_u is the rotor unbalance amplitude, f_c is the normal contact force, and μ is the coefficient of friction between the rotor and TDB. Obviously, for orbit motions E, $f_c = 0$ always.

Under steady state forward synchronous motions, the non-contacting orbit corresponds with

$$w_E = r_E e^{-i\phi} = \frac{f_u}{m(\omega_n^2 - \Omega^2 + 2i\xi\omega_n\Omega)} \quad (4)$$

The force displacement relation of Eq. (4) may be represented in the (u, v) plane as shown in Fig. 2.

In the case of a steady forward synchronous rub orbit, $w_C = c_r e^{-i\psi}$ where ψ is some phase angle, it follows from Eq. (3) that

$$(\omega_n^2 - \Omega^2 + 2i\xi\omega_n\Omega)c_r e^{-i\psi} = \frac{f_u}{m} - \frac{f_c}{m} (1 + i\mu) e^{-i\psi} \quad (5)$$

With the inclusion of the contact components of force (normal and tangential friction), a resultant synchronous force of amplitude f_s must exist to drive the orbit at C in the same way that f_u drives the orbit at E (see Fig. 3). It follows from Eqs. (4) and (5) and the force equilibrium shown in Fig. 3 that

$$\frac{f_u c_r}{m r_E} e^{i(\phi-\psi)} = \frac{f_u}{m} - \frac{f_c}{m} (1 + i\mu) e^{-i\psi} = \frac{f_s}{m} e^{i(\phi-\psi)} \quad (6)$$

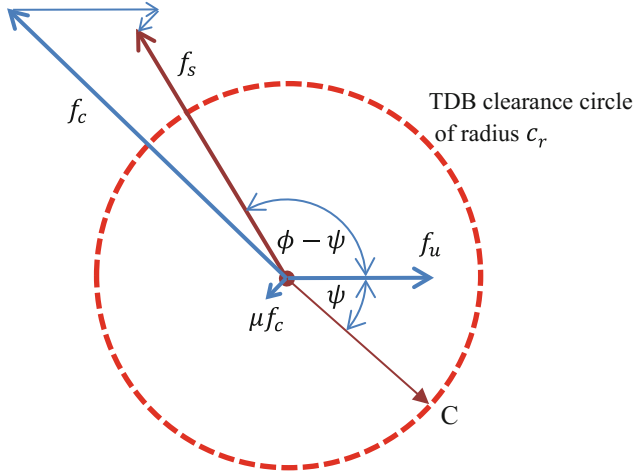


Fig. 3. Steady forward synchronous rub orbit, C, viewed in a (u, v) rotating frame. In order to drive the orbit to C, a synchronously rotating force of amplitude f_s must exist with a phase lead of ϕ on the vector to C.

Hence,

$$f_s = f_u \frac{c_r}{r_E} \quad (7)$$

and

$$f_c = \frac{f_u}{(1 + i\mu)} \left(e^{i\psi} - \frac{c_r}{r_E} e^{i\phi} \right) \quad (8)$$

Although the force expression in Eq. (8) is complex, if it is to be a genuine physical force amplitude arising from contact, then

$$\left. \begin{aligned} \text{Im}f_c &= \text{Im} \left(\frac{f_u}{(1 + i\mu)} \left(e^{i\psi} - \frac{c_r}{r_E} e^{i\phi} \right) \right) = 0 \\ \text{Re}f_c &= \text{Re} \left(\frac{f_u}{(1 + i\mu)} \left(e^{i\psi} - \frac{c_r}{r_E} e^{i\phi} \right) \right) > 0 \end{aligned} \right\} \quad (9)$$

In general, ψ should be varied until the conditions of Eq. (9) are satisfied to determine the rub orbit. Ultimately, in contrast with Eq. (4), the rubbing contact satisfies

$$w_C = c_r e^{-i\psi} = \frac{f_s e^{i(\phi - \psi)}}{m(\omega_n^2 - \Omega^2 + 2i\zeta\omega_n\Omega)} \quad (10)$$

3 Control for Contact-Free Levitation

3.1 AMB Synchronous Forcing

If AMB functionality exists, an obvious procedure to restore contact-free levitation is to apply AMB synchronous forcing at some phase angle α :

$$f_{AMB} = f_A e^{i\alpha} \quad (11)$$

For the simple rigid disk analysis considered in Sect. 2, this is simply superimposed onto the synchronous unbalance force, f_u .

3.2 Active TDB Synchronous Motion

Consider the TDB to be actuated under sufficiently strong control such that demand motions may be imposed. Suppose then that forward synchronous whirl motion of the TDB is enabled in the form

$$w_B = r_B e^{i\beta} \quad (12)$$

where β is some phase angle. When viewed in the (u, v) plane, this corresponds to a shift of the rotor-TDB clearance circle at an angle β relative to the unbalance vector. It is therefore of interest to evaluate the relative rotor to TDB displacement

$$w_{CB} = w_C - w_B \quad (13)$$

Equation (3) should then be modified to

$$\begin{aligned} \ddot{w}_{CB} + (2\zeta\omega_n + 2i\Omega)\dot{w}_{CB} + (\omega_n^2 - \Omega^2 + 2i\zeta\omega_n\Omega)w_{CB} \\ = \frac{f_u}{m} - \frac{f_c}{m} (1 + i\mu) \frac{w_{CB}}{c_r} - (\omega_n^2 - \Omega^2 + 2i\zeta\omega_n\Omega)w_B \\ = \frac{f_u}{m} \left(1 - \frac{r_B}{r_E} e^{i(\beta + \phi)} \right) - \frac{f_c}{m} (1 + i\mu) \frac{w_{CB}}{c_r} \end{aligned} \quad (14)$$

3.3 Criteria for Contact to Fail to Exist

Suppose that AMB synchronous forcing of Eq. (11) is applied simultaneously with the TDB motion of Eq. (12). Following through the analysis of Sect. 2.1, steady synchronous forward rubbing will exist if

$$\begin{aligned} \text{Im}f_c = \text{Im} \left(\frac{1}{(1+i\mu)} \left\{ f_A e^{i\alpha} + f_u \left(1 - \frac{r_B}{r_E} e^{i(\beta + \phi)} \right) \right\} \left(e^{i\psi} - \frac{c_r}{r_E} e^{i\phi} \right) \right) = 0 \\ \text{Re}f_c = \text{Re} \left(\frac{1}{(1+i\mu)} \left\{ f_A e^{i\alpha} + f_u \left(1 - \frac{r_B}{r_E} e^{i(\beta + \phi)} \right) \right\} \left(e^{i\psi} - \frac{c_r}{r_E} e^{i\phi} \right) \right) > 0 \end{aligned} \quad (15)$$

It follows that by violating these conditions for all cases of ψ , then no steady state rub condition is possible.

3.4 Practicalities for Contact Determination

If a control strategy to restore contact-free levitation is to be implemented, it would be useful to identify the following data as occurring in Eq. (15):

- (a) The unbalance amplitude, f_A , and a zero phase reference for the unbalance vector.
- (b) The contact-free orbit radius, r_E , and its phase, ϕ , relative to the unbalance vector.
- (c) The coefficient of friction, μ .

Note that the conditions of Eq. (15) have been derived assuming a zero phase reference for the unbalance. The required data could be obtained through periodic monitoring and updating using the AMB control system. If done, then this knowledge may be used to select appropriate control for contact-free restoration either through the AMB alone, the TDB alone or as a combination of both.

It would also be useful to have some trigger system to indicate when contact has occurred. This could be achieved using stator-mounted accelerometers to detect responses to contact force transmission. Displacement transducers that provide signals for feedback control of AMBs may also be used, though care is required to decide between a large non-contacting orbit and a real rub orbit, since there are significant phase differences between the two cases. Transducer systems that respond directly to contact forces may also have potential [27].

The results in the previous sections have been derived under steady state assumptions. In reality, the motion from a contact-free orbit E to a contact orbit C will involve some intervening transient motion involving possible bounce-like behavior. To assess the effectiveness of the analytical derivations, a series of dynamic simulations now follow.

3.5 Simulated Motions

Simulations were undertaken with a resiliently mounted TDB model (Fig. 1). Parameter values used are shown in Table 1.

Table 1. Parameters used for simulations.

Parameter	Value
k_B (TDB radial support stiffness)	6×10^6 N/m
c_B (TDB radial support damping)	2500 Ns/m
m_B (TDB mass)	0.18 kg
m (rotor mass)	4.25 kg
μ (coefficient of friction between rotor and TDB)	0.05
TDB inner radius	15 mm
TDB inner race material	Steel
Rotor material	Steel
AMB magnetic gap	0.8 mm
AMB under PD control rotor natural frequency	638 rad/s
AMB under PD control rotor damping ratio	0.086
Ω (rotor speed)	1000 rad/s

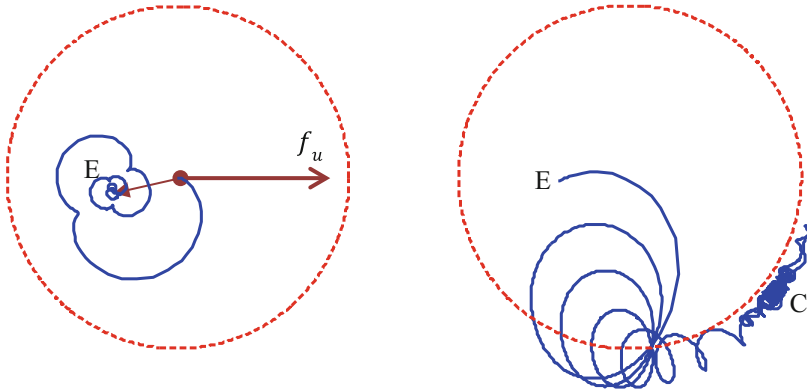


Fig. 4. Synchronous (u, v) rotating frame views. The left figure shows the effect of a step change of unbalance, which leads to the steady state position E after transient motion. The right figure shows the effect of a subsequent velocity input to the rotor, leading to the steady state contact response at C after transient motion that involves bouncing contact.

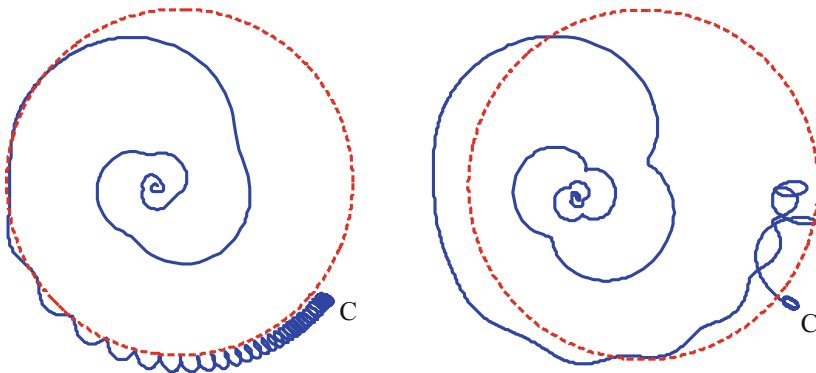


Fig. 5. Synchronous (u, v) rotating frame views. The left figure shows the effect of applying a ramped force at 180° phase to the unbalance, which leads to the restoration of contact-free levitation after transient motion. The right figure shows the effect of a synchronous TDB motion with -4.5° phase, which leads to the restoration of contact-free levitation after transient motion.

A Hertzian model was used to represent the normal contact stresses between the rotor and TDB. Starting from a rotor spinning precisely at the AMB magnetic center, a step change of unbalance (425 N) was applied. The left plot of Fig. 4 shows the transient response of the rotor, which does not involve any TDB contact, to the steady orbit at E. A sudden velocity input of 0.3 m/s (horizontal) was then imposed while the unbalance remained unchanged. The right plot of Fig. 4 shows that the rotor interacts with the TDB, undergoing several bounces, before settling on the rub orbit C. The red dashed clearance circles correspond with the centered TDB position (undeflected). The appearance of the rub orbit C lying outside the clearance circle indicates that the TDB has deflected on its resilient mount.

It is interesting to note that the simulated results of Fig. 4 show similar orbit positions for E and C from the analytical model results of Figs. 2 and 3. In the simulated case of Fig. 4, orbit C lies outside the nominal clearance circle of the TDB, a consequence of the fact that the compliantly mounted TDB experiences whirling with the contacting rotor. In effect, the final steady rub orbit would be similar to that of a rigidly mounted TDB having an appropriately larger rotor to TDB radial clearance.

Feedforward control was then applied as guided by the conditions of Eq. (15). The left plot of Fig. 5 shows how feedforward AMB control in the form of a ramped synchronous force was able to destabilize the rotor rub orbit at C. The right plot of Fig. 5 shows how a step change of synchronous TDB orbit motion was able to achieve a similar result.

4 Conclusions

Analytical expressions have been used to show how synchronous forward rubbing may coexist with a contact-free forward whirl under the same rotor dynamic unbalance. These bi-stable responses are differentiated by the relative orbit sizes and significant phase differences. The orbits were evaluated in a synchronously rotating reference frame in which the usual circular whirl orbits are represented as stationary points. A complex representation was used to evaluate contact forces and conditions were established to define whether a rub orbit was able to exist. These conditions were extended to include contributions from feedforward AMB synchronous forcing and feedforward TDB synchronous orbits. This enabled deductions to be made on how these feedforward motions could be used to destabilize a rotor-TDB contact orbit.

Simulations of rotor to TDB contact were also undertaken and these confirmed that the analytical results guide understanding of the nonlinear dynamics and the final rub orbit. The simulations were also extended to demonstrate how the feedforward control was also effective with a resiliently mounted TDB and the presence of significant transient motion in the transitions between steady state orbits.

References

1. Bartha, A.R.: Dry friction induced backward whirl: theory and experiment. In: Proceedings of the 5th IFToMM Conference on Rotor Dynamics, Darmstadt, Germany (1988)
2. Fumagalli, M., Varadi, P., Schweitzer, G.: Impact dynamics of high speed rotors in retainer bearings and measurement concepts. In: Proceedings of the 4th International Symposium on Magnetic Bearings (ISMB4), Zurich, Switzerland (1994)
3. Schmied, J., Pradetto, J.C.: Behavior of a one ton rotor being dropped into auxiliary bearings. In: Proceedings of the 3rd International Symposium on Magnetic Bearings (ISMB3), Alexandria, USA (1992)
4. Kirk, R.G., Ishii, T.: Transient response drop analysis of rotors following magnetic bearing power outage. In: Proceedings of the MAG 1993, Alexandria, USA (1993)
5. Kirk, R.G., Swanson, E.E., Kavarana, F.H., Wang, X.: Rotor drop test stand for AMB rotating machinery, part 1: description of test stand and initial results. In: Proceedings of the 4th International Symposium on Magnetic Bearings (ISMB4), Zurich, Switzerland (1994)

6. Swanson, E.E., Kirk, R.G., Wang, J.: AMB rotor drop initial transient on ball and solid bearings. In: Proceedings of the MAG 1995, Alexandria, USA (1995)
7. Foiles, W.C., Allaire, P.E.: Nonlinear transient modeling of active magnetic bearing rotors during rotor drop on auxiliary bearings. In: Proceedings of MAG 1997, Alexandria, USA, pp. 154–163 (1997)
8. Sun, G., Palazzolo, A.B., Provenza, A., Montague, G.: Detailed ball bearing model for magnetic suspension auxiliary service. *J. Sound Vib.* **269**(3), 933–963 (2004)
9. Helfert, M., Ernst, M., Nordmann, R., Aeschlimann, B.: High-speed video analysis of rotor-retainer-bearing-contacts due to failure of active magnetic bearings. In: Proceedings of the 10th International Symposium on Magnetic Bearings, Martigny, Switzerland (2006)
10. Hawkins, L., Filatov, A., Imani, S., Prosser, D.: Test results and analytical predictions for rotor drop testing of an active magnetic bearing expander/generator. *Trans. ASME J. Eng. Gas Turbines Power* **129**, 522–529 (2007)
11. Janse van Rensburg, J.J., van Schoor, G., van Vuuren, P.: The characterization of the severity of rotor delevitation events—a parametric study. In: Proceedings of the 13th International Symposium on Magnetic Bearings (ISMB 2013), Arlington, USA (2012)
12. Janse van Rensburg, J.J., Vanek, C., Worlitz, F.: Backup bearing modelling for turbo machines with high axial and radial loads. In: Proceedings of the 14th International Symposium on Magnetic Bearings (ISMB 2014), Linz, Austria (2014)
13. Collins, T., Masala, A., Shultz, R., Guo, Z.: Numerical and experimental results of auxiliary bearings testing on a high speed test rig. In: Proceedings of the 14th International Symposium on Magnetic Bearings (ISMB 2014), Linz, Austria (2014)
14. Denk, J., Köhler, B.-E., Siegle, G., Siebke, P.: Landing tests with a 6300 rpm, 9 t AMB rotor in rolling element back-up bearings. In: Proceedings of the 14th International Symposium on Magnetic Bearings (ISMB 2014), Linz, Austria (2014)
15. Siebke, P., Golbach, H.: A novel rolling element back-up bearing for a 9 t rotor application. In: Proceedings of the 14th International Symposium on Magnetic Bearings (ISMB 2014), Linz, Austria (2014)
16. Siegl, G., Tzianetopoulou, T., Denk, J.: Simulation and experimental validation of a 9 ton AMB rotor landing in rolling element back-up bearings. In: Proceedings of the 14th International Symposium on Magnetic Bearings (ISMB 2014) (2014). Linz, Austria and the J. Jpn. Soc. Mech. Eng. Article ID: 15-00136 (2016)
17. Yang, G., Shi, Z., Liu, X., Zhao, J.: Research and experiment of auxiliary bearings with no lubrication for helium blower of HTR-10. In: Proceedings of the 14th International Symposium on Magnetic Bearings (ISMB 2014), Linz, Austria (2014)
18. Lahriri, S., Santos, I.F.: Theoretical modelling, analysis and validation of the shaft motion and dynamic forces during rotor–stator contact. *J. Sound Vib.* **332**, 6359–6376 (2013)
19. Lee, J.L., Palazzolo, A.: Catcher bearing life prediction using a rainflow counting approach. *Trans. ASME J. Tribol.* **134**(3), 031101 (2012)
20. Anders, J., Leslie, P., Stacke, M.L.-E.: Rotor drop simulations and validation with focus on internal contact mechanisms of hybrid ball bearings. Paper GT2013-95816, ASME/IGTI Turbo Expo, San Antonio, USA (2013)
21. Keogh, P.S., Cole, M.O.T.: Rotor vibration with auxiliary bearing contact in magnetic bearing systems, Part I: synchronous dynamics. In: Proceedings of the Institution of Mechanical Engineers, Part C, vol. 217, pp. 377–392 (2003)
22. Cole, M.O.T., Keogh, P.S.: Asynchronous periodic contact modes for rotor vibration within an annular clearance. In: Proceedings of the Institution of Mechanical Engineers, Part C, vol. 217, pp. 1101–1115 (2003)

23. Ulbrich, H., Ginzinger, L.: Stabilization of a rubbing rotor using a robust feedback control, Paper-ID: 306. In: Proceedings of the 7th IFToMM Conference on Rotor Dynamics, Vienna, Austria (2006)
24. Cade, I.S., Sahinkaya, M.N., Burrows, C.R., Keogh, P.S.: On the design of an active auxiliary bearing for rotor/magnetic bearing systems. In: Proceedings of the 11th International Symposium on Magnetic Bearings (ISMB 2011), Nara, Japan (2008)
25. Keogh, P.S., Sahinkaya, M.N., Burrows, C.R., Cade, I.S.: Rotor/auxiliary bearing dynamic contact modes in magnetic bearing systems. In: Proceedings of the 11th International Symposium on Magnetic Bearings (ISMB 2011), Nara, Japan (2008)
26. Li, P., Sahinkaya, M.N., Keogh, P.S.: Active touchdown bearing control for recovery of contact-free rotor levitation in AMB systems. In: Proceedings of the 14th International Symposium on Magnetic Bearings (ISMB 2014), Linz, Austria (2014)
27. Saket, F.Y., Sahinkaya, M.N., Keogh, P.S.: Experimental assessment of touchdown bearing contact forces in magnetic bearing systems. In: 9th IFToMM International Conference on Rotor Dynamics, Milan, Italy (2014)

Blades, Bladed Systems and Impellers



Applying Compressed Sensing to Blade Tip Timing Data: A Parametric Analysis

Raphael P. Spada^(✉) and Rodrigo Nicoletti

Department of Mechanical Engineering, São Carlos School of Engineering,
University of São Paulo, Trabalhador São Carlense Ave. 400,
São Carlos 13566-590, Brazil
raphael.spada@usp.br

Abstract. Monitoring the behavior of rotating blades is a critical procedure to ensure safety and proper performance of turbomachinery. For a long time strain gages have been the only solution to measure blade vibrations in a rotating scenario, but with the advances in software and hardware over the last decades, the research on blade tip timing (BTT) data analysis, a non-intrusive technique has gained momentum. A major drawback comes with this approach: undersampling. Several methodologies can be found in the literature do deal with this undersampled signal and this work presents a parametric study of the most recent type of approach that has gained momentum in the BTT research: compressed sensing (CS). The results show what are the best conditions to apply CS on BTT data, in terms of probe placement, amount of sensors and number of rotations.

Keywords: Blade tip timing · Blade vibrations
Compressed sensing · Signal reconstruction · Spectral analysis

1 Introduction

Blades are a fundamental component in turbomachinery and they are often subjected to induced vibrations. For a typical gas turbine, these vibrations are originated through mainly four types of stresses [1], but the alternating stresses, that are originated by forced response to excitations at multiples of the rotating speed, are the most common cause of high cycle fatigue. These vibrations will diminish the fatigue life and the performance of the blades, which can ultimately lead to catastrophic results. Therefore, carrying on-line vibration monitoring is an intrinsic duty when dealing with turbomachinery.

For a long time strain gages have been the only solution to measuring flexible blade vibrations in rotating machinery. However, the installation of such sensors consists in a very tedious, laborious, costly and time consuming task. This is due specially to the number of blades per stage of the turbine and the requirement of having telemetry or slip rings to acquire the signals. On top of these disadvantages, the sensors can alter the blade dynamics and, more importantly,

this monitoring system tends to not be very durable due to the harsh working conditions [2]. In light of these issues, the development of non-intrusive vibration measuring system for rotating blades was boosted.

Describing it in a simple manner, the Blade Tip-Timing (BTT) methodology consists in monitoring blade vibrations by measuring passing times of the blades' tip with static sensors, usually optic, located at the turbine casing. Since the blades are vibrating, the deformation induced will alter these passing times, known as arrival times, when compared with the arrival times of the blades in a non-vibrating referential. This referential can be obtained by placing a sensor on the shaft to measure the actual rotating speed, and by knowing the angular position of the blades, the non-vibrating signal can be generated. This sensor is known as the Once Per Revolution (OPR) sensor.

Despite being a simplistic and straightforward methodology with several advantages over the strain gage measuring procedure, the technique suffers from bad sampling, since the sampling frequency is directly related to the rotating speed and the number of sensors used. To ensure a sampling frequency that attends to the Nyquist criterion, the quantity of sensors involved can be quite substantial. As a result, a significant effort in the BTT scope was devoted to the development and application of techniques capable of identifying vibration properties from a under sampled signal.

Recently, Compressed Sensing (CS), a digital signal reconstruction technique, has gained momentum in the field of BTT data analysis. The idea behind the theory of Compressed Sensing consists in a search for the reconstruction of sparse signals with a number of samples that is way lower than the number of samples required by the classic methodologies that need to attend to the Nyquist criterion. This methodology is being explored for some time, especially in the field of image compression, in which the image is recovered directly by a compressed representation, instead of capturing the whole image to then compress it and decompress it in a computer, eliminating an entire step and reducing the amount of data that was needed to be stored. The pioneer work on this technique can be found in [3–5]. The motivation for utilizing this methodology on the BTT scenario comes from the fact that if some criteria is met, that will be shown in the next section, it is possible to perfectly reconstruct a signal with a sampling frequency lower than the Nyquist rate.

The goal of this present work is to produce a parametric analysis of a CS implementation on BTT data. To achieve this goal, the frequency spectrum of a simulated vibration signal, obtained by BTT, is reconstructed in the frequency domain by the CS methodology, and several parameters of the BTT system are altered so that it is possible to identify its effects on the frequency spectrum obtained.

2 BTT Data

A BTT measuring system scheme is presented in Fig. 1 and to extract the information of blade tip deflection, it is necessary to first generate a virtual signal,

based on the OPR sensor, that corresponds to the expected passing times of the blades in a non-vibrating referential. The non-vibrating time sequence, $\hat{t}(i, n, k)$, can be described as

$$\hat{t}(i, n, k) = \frac{\alpha_i + 2\pi n - \theta_k}{2\pi\Omega}, \quad (1)$$

where α_i is the angular position of the i th probe, θ_k is the initial angular position of the k th blade, n is the rotation number and Ω is the constant rotating speed of the assembly, in Hz.

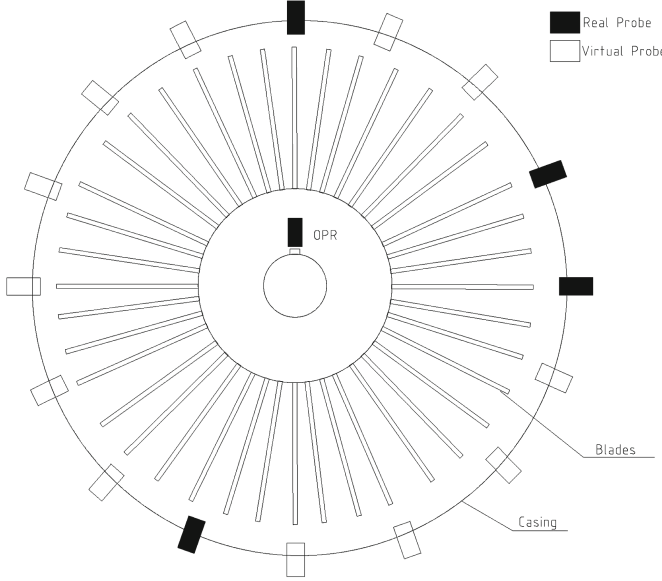


Fig. 1. Representation of the BTT measuring system.

Due to the fact that the blades are vibrating, the real measured time sequence will be distorted by the angular deflection of the blade's tip, $\delta(i, n, k)$, altering the real timing sequence $t(i, n, k)$ to

$$t(i, n, k) = \frac{\alpha_i + 2\pi n - \theta_k - \delta(i, n, k)}{2\pi\Omega}. \quad (2)$$

Subtracting Eqs. (2) from (1) and knowing the distance between the rotating center and the tip of the blade, R , the linear displacement can be obtained by

$$\mathbf{d}(i, n, k) = \delta(i, n, k)R = 2\pi\Omega R[t(i, n, k) - \hat{t}(i, n, k)] = 2\pi\Omega R\Delta t. \quad (3)$$

With the obtained \mathbf{d} signal, the vibration amplitude of each blade, measured at each sensor, in each rotation is extracted, but the sampling rate of this signal is directly related to the amount of probes used, and the rotating speed of the

assembly. To exemplify the typical sampling obtained with a BTT system, Fig. 2 presents a 30 Hz vibration signal on a 10 Hz rotating speed assembly and it shows the collection of samples obtained by four probes. This case shows an Engine Order (EO) excitation, since the vibrating frequency is an integer multiple of the rotating frequency. The bad sampling can clearly be seen due to the fact that each probe needs to wait three entire periods (3 EO) of the vibrating signal to collect new information, for each blade.

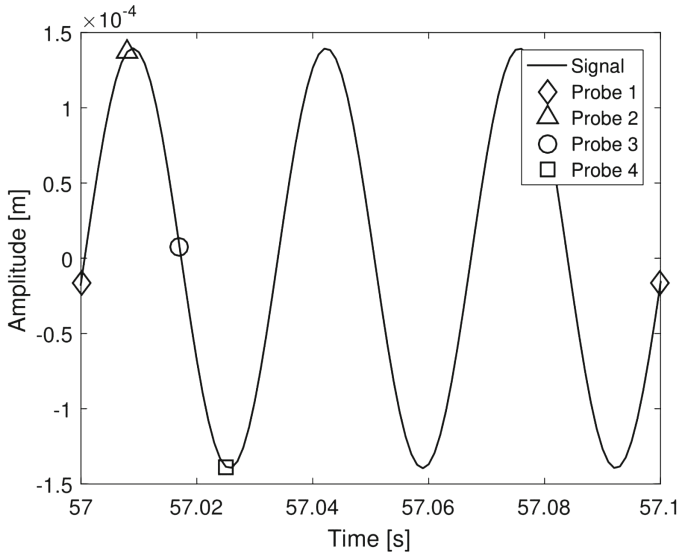


Fig. 2. Example of a BTT signal sampled with 4 probes.

Several techniques are being utilized and explored in the context of BTT undersampled data. A new approach that has gained track in recent years is the Compressed Sensing methodology.

3 CS Theory

The CS methodology consists in recovering a signal, sparse in some domain, with fewer samples than the classic methodologies that are based on the Shannon-Nyquist criterion. The motivation for this approach is to recover the signal directly from compressed samples (lower sampling rate) instead of firstly sampling the signal at a high rate to then compress it, eliminating a stage of compression and decompression [6]. This problem can be formulated in mathematical form through an optimization task, searching for the sparsest solution to the problem:

$$\min_{\mathbf{x}} \|\mathbf{x}\|_{\ell_0} \quad \text{s.t.} \quad \mathbf{Ax} = \mathbf{b}, \quad (4)$$

where \mathbf{x} is the sparse signal with N samples, sampled above the Nyquist rate; ℓ_0 is the “0-norm”, a quasi-norm that represents the amount of non zero elements in a vector, indicating the quantity k of sparse elements. The vector \mathbf{b} is the M observations vector, where $M \ll N$, while \mathbf{A} is the $M \times N$ sensing matrix.

The sensing matrix \mathbf{A} is usually formed by the multiplication of two matrices, Φ and Ψ^{-1} . The matrix Φ consists in the sensing part of the matrix, i.e., the relationship between the selected samples and the reconstructed signal, while Ψ^{-1} consists in the sparse basis of the signal. In most cases the signal in time is not sparse, so the matrix Ψ^{-1} is usually the inverse Fourier basis, so that the signal in time can be represented in the sparse frequency domain.

Despite being a straightforward and well defined approach, finding the sparsest solution is a non trivial task, in fact it is known as a NP-hard problem, being computationally unsolvable even for modest values of k , M and N . Fortunately, [3] proposed a substitution of ℓ_0 by the norm ℓ_1 , defined as

$$\|\mathbf{x}\|_1 = \sum_{n=0}^{N-1} |x(n)|, \tag{5}$$

making the optimization problem convex and linear. Despite not being the same exact solution to the ℓ_0 problem, a graphic representation of different norms in \mathbb{R}^2 shows that the closest solution to the sparsest search, is the ℓ_1 norm, as seen in Fig. 3. The optimization task of Eq. (4) with the norm ℓ_1 instead of ℓ_0 is called Basis Pursuit (BP).

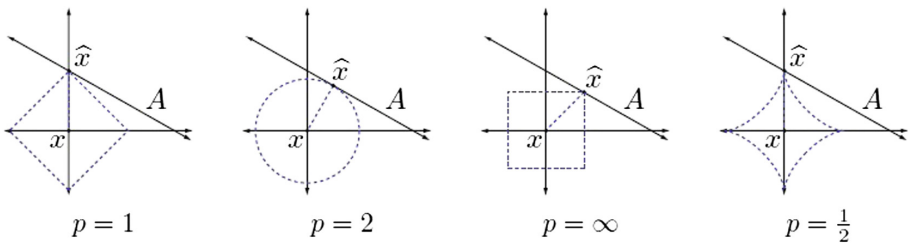


Fig. 3. Approximation of a point in \mathbb{R}^2 by a one-dimensional subspace for ℓ_p norms, with $p=1, 2, \infty$ and $\frac{1}{2}$. Source:[6].

To ensure unique solution to the BP problem, the matrix \mathbf{A} needs to respect the Restricted Isometry Property (RIP) described in [7]. This property basically requires that the columns of \mathbf{A} to be quasi-orthonormal. Another way of ensuring the unique solution is to have minimal coherence between the matrices Φ and Ψ^{-1} . Since $\mathbf{A} = \Phi\Psi^{-1}$ the coherence is defined as

$$\mu(\mathbf{A}) = \max_{1 \leq i < j \leq N} \frac{|\langle a_i, a_j \rangle|}{\|a_i\|_2 \|a_j\|_2}, \tag{6}$$

where $a_{i,j}$ are the column vectors of \mathbf{A} .

Usually random Φ matrices with a fixed Ψ^{-1} basis attend to this property with a high probability, and to exemplify the potential of this approach, a signal composed by three sinusoids of frequencies 50, 75 and 100 Hz, with unitary amplitudes, is reconstructed with this technique. The original time signal to be reconstructed, $x(t)$, is 512 samples long with a sampling frequency higher than the Nyquist rate, while the observed signal, $y(t)$, is made of 128 random samples. The results are shown in Fig. 4 and it can be seen perfect reconstruction of the signal.

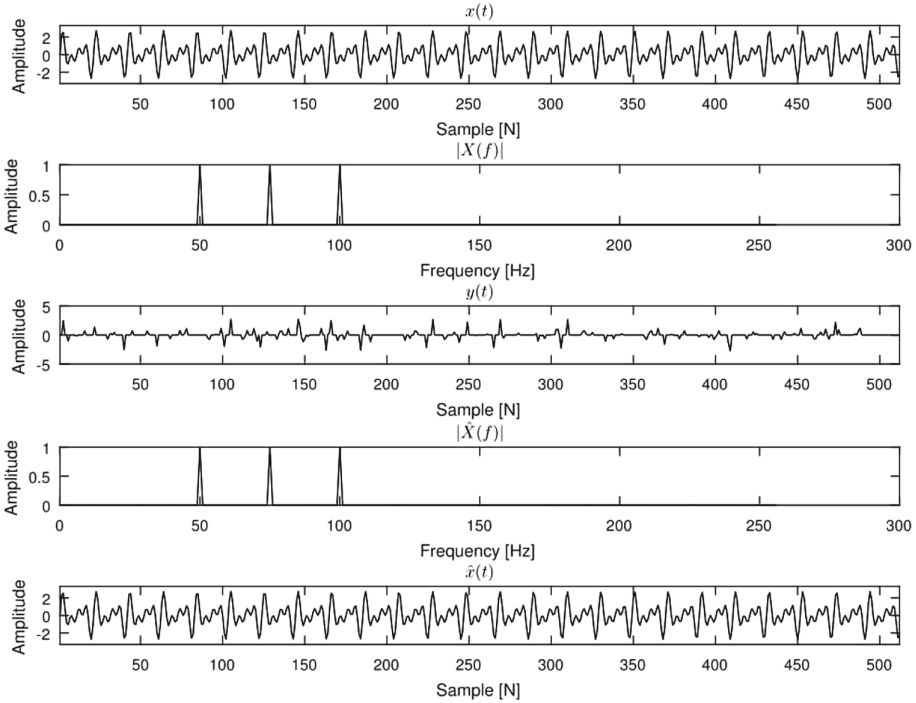


Fig. 4. Example of CS reconstruction with random sensing matrix.

4 Applying CS on BTT Data

As presented before, the CS consists in retrieving a sparse signal with N samples through an optimization task based only on M observations, usually $M \ll N$. To reproduce this conditions in the BTT context, the number N of samples of the sparse vector, in this case the frequency spectrum sampled over the Nyquist rate, is produced through placing a number L of imaginary probes equispaced around the casing and rotating the blade assembly for N_r revolutions, resulting in $N = LN_r$. The real measurements made are obtained through the real probes, positioned in any of the possible virtual positions L . This results in a real amount

of data $M = lN_r$, where l is the number of real probes placed around the casing. From this, observations it is easy to see that the ratio $\frac{M}{N}$ is always defined by the ratio of the number of real sensors in respect with the number of virtual sensors ($\frac{l}{L}$). The idea behind this formulation is to retrieve a frequency spectrum of a scenario of L probes, that attends to the Nyquist sampling rate, with only l real probes being utilized.

In this context, the matrix Ψ^{-1} will be the inverse Fourier basis $N \times N$, since the signal is not sparse in the time domain, but it is in the frequency domain. With respect to the sensing matrix Φ , it is constructed as

$$\Phi = \begin{bmatrix} 1 & 0 & \dots & \dots & \dots & 0 \\ 0 & \dots & 1 & 0 & \dots & 0 \\ \vdots & \dots & \dots & \dots & \dots & \vdots \\ 0 & \dots & \dots & 1 & \dots & 0 \end{bmatrix}_{M \times N}, \quad (7)$$

that is determined by the sampling sequence of the probes throughout the N_r revolutions. Each row contains a unitary value on a single column $j = \frac{\alpha_i L}{2\pi} + nL$, where α_i is the angular position of the i th probe and n is the current rotation number.

With these matrices assembled, it is seen that the observations made by l probes are:

$$\mathbf{y} = \Phi \Psi^{-1} \mathbf{X}, \quad (8)$$

where \mathbf{X} is the FFT of length N of the signal sampled by the L imaginary probes, which will be recovered through the BP algorithm.

As described in the last section, the matrix $\mathbf{A} = \Phi \Psi^{-1}$ needs to comply with the RIP condition, and, as noted before, it complies, with high probability, if the matrix is random. From the direct formulation of the CS on BTT data, it is seen that this matrix is not random, since the real probes are fixed throughout the revolutions. To deal with this problem [8] proposes the realization of an orthogonalization preprocessing procedure, in which the matrix \mathbf{A} is reformulated as an orthogonal basis for the range of \mathbf{A}^T , as in $\mathbf{Q} = [\text{orth}(\mathbf{A}^T)]^T$. The procedure results in

$$\mathbf{Q} \mathbf{A}^\dagger \mathbf{y} = \mathbf{Q} \mathbf{A}^\dagger \mathbf{A} \mathbf{X}, \quad (9)$$

where † denotes the pseudoinverse. From [8] it is also described that $\mathbf{Q} \mathbf{A}^\dagger \mathbf{A} = \mathbf{Q}$ and renaming $\mathbf{z} = \mathbf{Q} \mathbf{A}^\dagger \mathbf{y}$ results in the formulated BP problem:

$$\min_{\mathbf{X}} \|\mathbf{X}\|_{\ell_1} \quad \text{s.t.} \quad \mathbf{Q} \mathbf{X} = \mathbf{z}. \quad (10)$$

It is worth noticing that the optimization task can be quite demanding, computationally, since the amount of variables N are directly related to the amount of virtual probes L and the number of revolutions N_r . In some cases it can easily be in the range of 10^3 – 10^4 variables.

5 Results

To make the analysis, two scenarios were created, with signals in the form of $\sum_{i=1}^p a(i) \sin(2\pi f(i) \frac{n}{N} + \phi(i))$, whose parameters are described in the Table 1.

Scenario 1 consists of a signal with three close frequencies, all asynchronous (not integer multiples of the rotating speed Ω). The reconstruction of the signal is made from cases of two to six probes. For scenario 2 a synchronous frequency of 75 Hz replaces the 88 Hz frequency, so that it is possible to verify a hybrid vibration case and in this situation only five and six probes were utilized, due to the results seen in scenario 1.

Table 1. Simulated signals.

Scenario	$\mathbf{a}(\mathbf{i})$	$\mathbf{f}(\mathbf{i})$ [Hz]	$\phi(\mathbf{i})$ rad	Ω [Hz]	# Probes
1	$\begin{bmatrix} 3 & 2 & 1 \end{bmatrix}$	$\begin{bmatrix} 88 & 89 & 90 \end{bmatrix}$	$[0 - 2\pi]$	25	2-6
2	$\begin{bmatrix} 3 & 2 & 1 \end{bmatrix}$	$\begin{bmatrix} 75 & 89 & 90 \end{bmatrix}$	$[0 - 2\pi]$	25	5-6

For both cases evaluated, the number of virtual probes was fixed in $L = 10$. The rotating speed was also fixed at 25 Hz. This conditions implicate that the signal to be reconstructed had a $F_s = L\Omega = 250$ Hz sampling frequency, being over the Nyquist rate for both scenarios. The parametric analysis is based on the amount of sensors and the amount of revolutions utilized in the analysis.

Firstly, as pointed in Eq. (6), the coherence of \mathbf{Q} should be closer to 0 to ensure the RIP condition. With that in mind, the minimal coherence for all the combinations of probes, from two probes up to six are calculated and shown in Table 2, for $L = 10$ to 25 imaginary probes. It can be seen that increasing the number of real probes elevates the incoherence in the matrix \mathbf{Q} , but increasing the amount of virtual probes and maintaining the number of real ones results in lower incoherence. The amount of possible probe arrangements also increase with a higher number of virtual probes as it is given by the total $\binom{L}{l}$ combinations of probe placement.

Table 2. Minimal $\mu(Q)$ for different amount of real and virtual probes.

Probes	$\mu(\mathbf{Q})$			
	$L = 10$	$L = 15$	$L = 20$	$L = 25$
2	0.95	0.98	0.99	0.99
3	0.72	0.76	0.83	0.86
4	0.54	0.50	0.56	0.69
5	0.43	0.48	0.53	0.50
6	0.36	0.40	0.44	0.47

5.1 Scenario 1

Even though the phase of the signals is generated randomly, between 0 and 2π radians, the expected results throughout the course of 50 reconstructions with the BP algorithm are expected to be the same. If they are different it means that the proposed sensing matrix does not attend the RIP condition, resulting in a poor recovery. Using two sensors resulted in extremely poor results, same as the case of three probes, presented in the Fig. 5, that was obtained with $N_r = 300$ revolutions, resulting in 900 observations to reconstruct a 3000 samples long signal. The probe positioning was $p = [1 \ 2 \ 4]$, one of the optimal arrangements that give minimal $\mu(\mathbf{Q})$.

In the Fig. 5 and for the others to follow, the criteria utilized to analyze the results were the energy of the signal. E_T stands for the total energy of the signal, E_f is the energy of the correct frequency components and E_R is the real energy of the correctly sampled signal. The wanted results are those in which the ratio $\frac{E_f}{E_T}$ is 100%, meaning that all the energy of the reconstructed signal is located only on the correct frequencies. The ratio $\frac{E_T}{E_R}$ is also wanted to be 100% meaning that the amount of energy in the reconstructed signal is equal to the desired correctly sampled signal. It is obvious from Fig. 5 that three probes are not enough to assure proper reconstruction, there are even cases that the energy of the correct frequency components surpass the total energy. This occurs due to the fact that the E_f calculation is made as twice the energy of the positive frequencies, which means that the situations that $E_f > E_T$ are those that the reconstructed signal is complex, not having the symmetry property of the frequency spectrum.

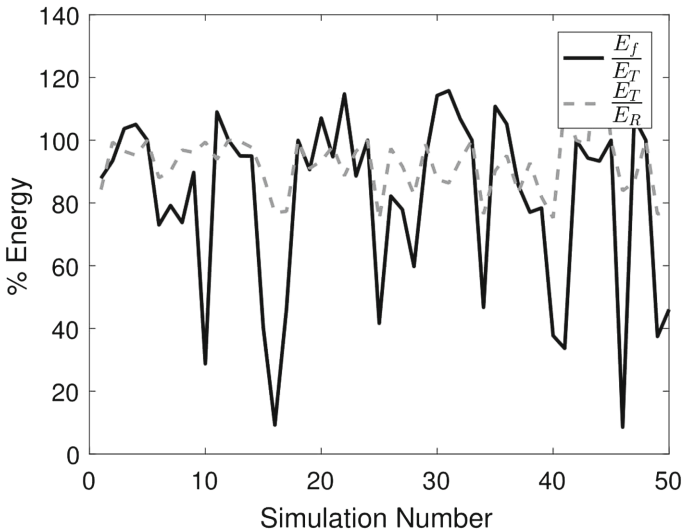


Fig. 5. Ratio of signal energy for the reconstructed signal of scenario 1 using 3 probes and 50 revolutions through 50 simulations.

Seeing that three probes were insufficient for perfect reconstruction, the amount of sensors was increased to four, in the locations $p = [1 \ 3 \ 4 \ 9]$ with a $N_r = 50$ revolutions. It can be seen from Fig. 6 that the results are much improved, but there are still cases of poor reconstruction. In an attempt to improve this results the amount of revolutions was increased to $N_r = 300$ resulting in 1200 observations to reconstruct a 3000 samples long signal. From Fig. 7 it is clear that augmenting the amount of data did not improve the results.

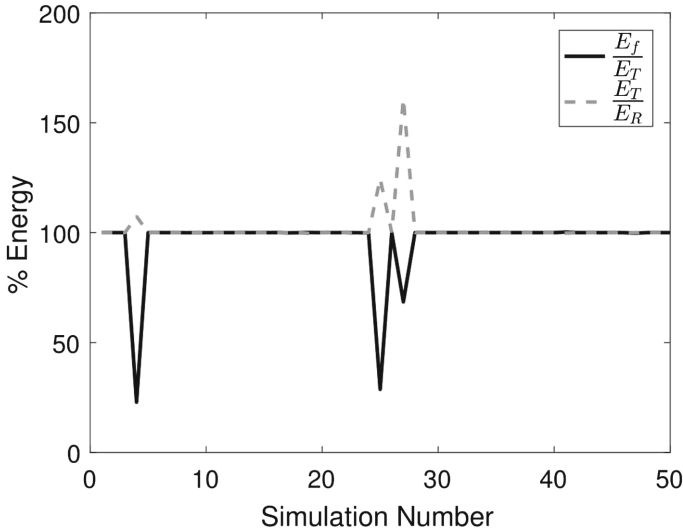


Fig. 6. Ratio of signal energy for the reconstructed signal of scenario 1 using 4 probes and 50 revolutions through 50 simulations.

Now, the number of probes was raised to five and the results from Fig. 8, with only $N_r = 50$ revolutions and with the probes at $p = [1 \ 2 \ 6 \ 9 \ 10]$, were extremely satisfactory, showing that perfect reconstruction was achieved, since through the 50 simulations the ratio was around 100%. The same can be said by the results with six probes on Fig. 9 with probes at $p = [1 \ 2 \ 3 \ 4 \ 6 \ 8]$, for the same number of revolutions.

5.2 Scenario 2

Scenario 2 is expected to be more complicated, because of the presence of a synchronous vibration in the signal. From the results of Scenario 1, utilizing less than five probes is not recommended, since the perfect reconstruction was not ensured.

From Fig. 10 it becomes clear that the introduction of the synchronous frequency has a negative impact on the reconstruction of the frequency spectrum. To elucidate an example of what is happening, Fig. 11 presents the reconstructed

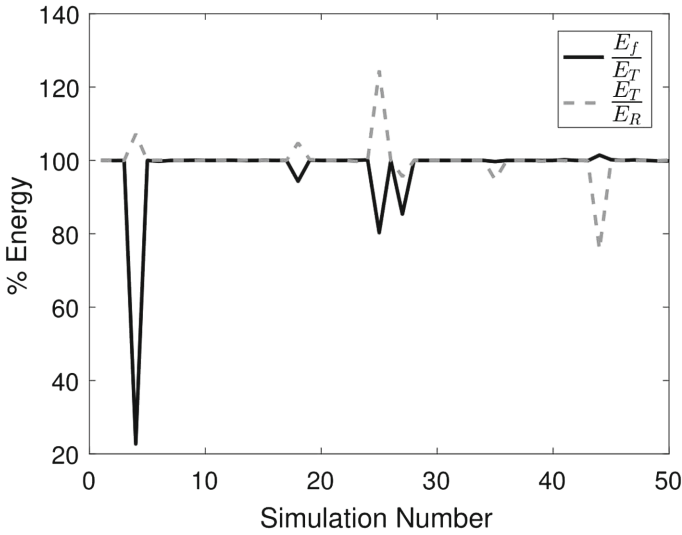


Fig. 7. Ratio of signal energy for the reconstructed signal of scenario 1 using 4 probes and 300 revolutions through 50 simulations.

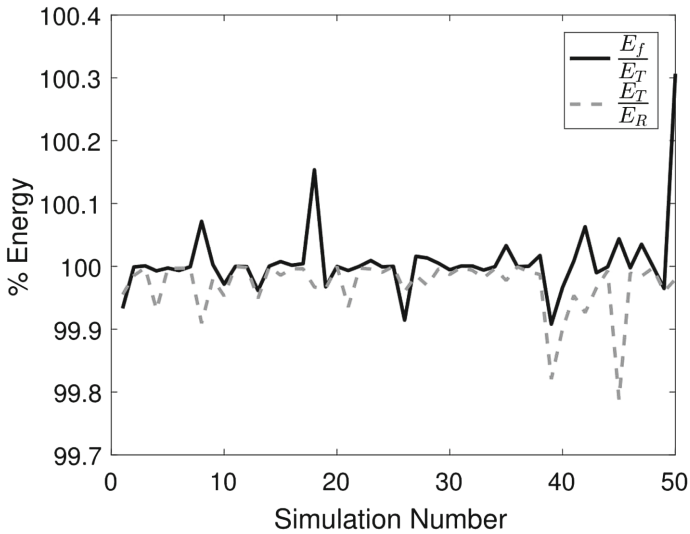


Fig. 8. Ratio of signal energy for the reconstructed signal of scenario 1 using 5 probes and 50 revolutions through 50 simulations.

frequency spectrum of the simulation 25 from Fig. 10. It can be seen that the synchronous frequency started to replicate around multiples of the rotating speed, at 25 and 50 Hz, while the asynchronous frequencies of 89 and 90 Hz were perfectly reconstructed.

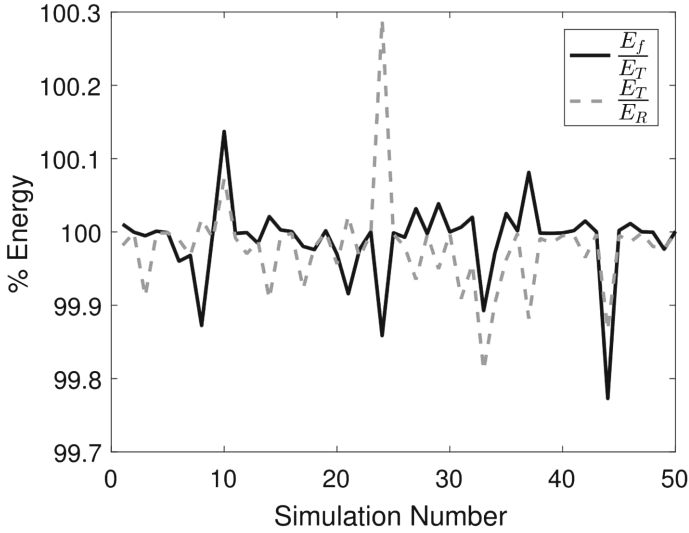


Fig. 9. Ratio of signal energy for the reconstructed signal of scenario 1 using 6 probes and 50 revolutions through 50 simulations.

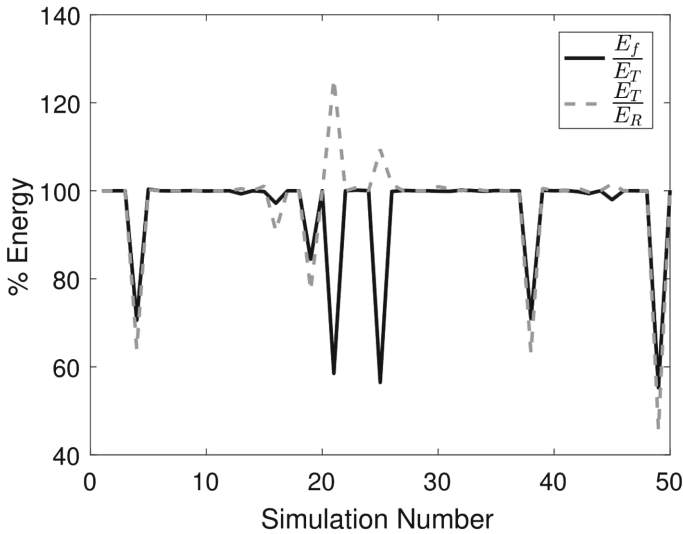


Fig. 10. Ratio of signal energy for the reconstructed signal of scenario 2 using 5 probes and 50 revolutions through 50 simulations.

Meanwhile, the same results were not observed on the six probes case of Fig. 12, that was capable of performing in the same manner as in the asynchronous case, with perfect reconstruction throughout the test.

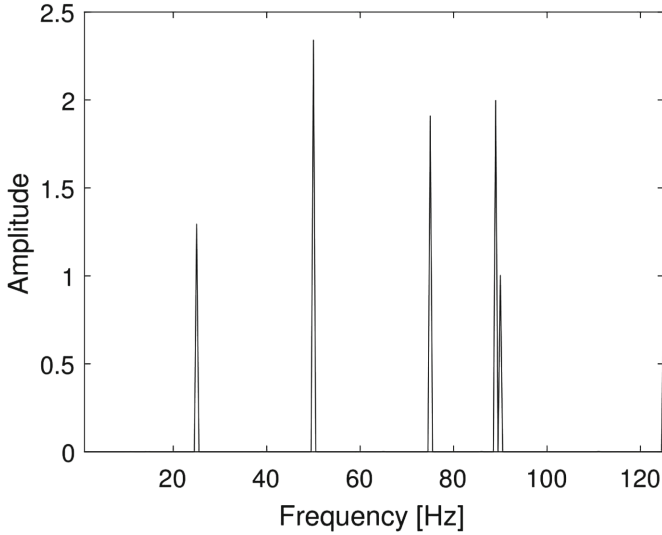


Fig. 11. Reconstructed frequency spectrum for simulation 25 of scenario 2 using 5 probes and 50 revolutions.

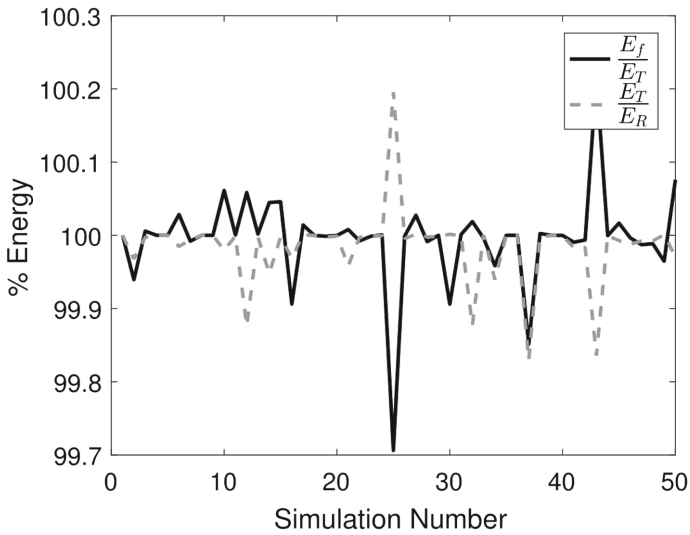


Fig. 12. Ratio of signal energy for the reconstructed signal of scenario 2 using 6 probes and 50 revolutions through 50 simulations.

6 Conclusions

This work proposed the evaluation of several conditions for the application of Compressed Sensing (CS) on Blade Tip Timing (BTT) data. It was described

both methodologies and how to produce the reconstruction of signals through undersampled and non uniform data.

From the results of the present research, it was possible to conclude that the CS has potential of performing well on BTT data. It was shown that some special probe positioning impact in the results of the analysis and those are the ones that indicate minimal coherence of the sensing matrix. Furthermore, it was shown that for asynchronous vibrations, five probes are sufficient to ensure perfect reconstruction of the signal generated by BTT sampling. For cases that include synchronous vibrations, six probes were determined as a reliable proposition for perfect recovery.

It is worth noticing that the high number of probes required to retrieve a frequency spectrum of an asynchronous vibration signal is possibly related to the amount of frequencies presented in the simulated signal and due to the fact that increasing the amount of observations did not result in improvements on the reconstruction, surprisingly.

Even though the predominant amplitude of vibration, in real cases, are identified as the result of EO excitations, it is still valid to pursue reconstruction of multi frequency signals, because instabilities, that originates asynchronous excitation, can still occur even when the dominant frequency of vibration has an EO nature.

For future works it is interesting to investigate the ratio of real to virtual probes $\frac{l}{L}$, for increased values L . It was shown that less incoherence comes with higher L which will affect negatively on the reconstruction, but perhaps an optimal ratio can be found while varying L .

Acknowledgments. This project was supported by the Brazilian research foundation CNPq (Conselho Nacional de Desenvolvimento Científico e Tecnológico).

References

1. Carrington, I.B.: Development of blade tip timing data analysis techniques, Ph.D. thesis, University of Manchester, Manchester, United Kingdom (2002)
2. McCarty, P.E., Thompson Jr, J.W.: Development of a Noninterference Technique for Measurement of Turbine Engine Compressor Blade Stress, No. AEDC-TR-79-78, Arnold Engineering Development Center (1980)
3. Cands, E.J., Romberg, J., Tao, T.: Robust uncertainty principles: exact signal reconstruction from highly incomplete frequency information. *IEEE Trans. Inf. Theory* **52**(2), 489509 (2006)
4. Candes, E.J., Tao, T.: Near-optimal signal recovery from random projections: universal encoding strategies? *IEEE Trans. Inf. Theory* **52**(12), 54065425 (2006)
5. Donoho, D.L.: Compressed sensing. *IEEE Trans. Inf. Theory* **52**(4), 12891306 (2006)
6. Davenport, M.A., et al.: Introduction to Compressed Sensing, vol. 93, no. 1, p. 2 (2011, preprint)
7. Candes, E.J., Tao, T.: Decoding by linear programming. *IEEE Trans. Inf. Theory* **51**(12), 42034215 (2005)
8. Pan, M., et al.: Sparse representation based frequency detection and uncertainty reduction in blade tip timing measurement for multi-mode blade vibration monitoring. *Sensors* **17**(8), 1745 (2017)



Nonlinear Transverse and In-Plane Vibrations of a Thin Rotating Disk

Xiang-lin Wu, Ying-hou Jiao^(✉), Zhao-bo Chen, and Wen-sheng Ma

Harbin Institute of Technology, Harbin, China
jiaoyh@hit.edu.cn

Abstract. An analytical method is presented to investigate nonlinear transverse and in-plane vibrations of a thin rotating disk by using a theory of geometrically nonlinear thin plate. The nonlinear wave solutions of the rotating disk are obtained by Galerkin analysis. The disk is assumed to be isotropic and rotating at the constant speed. The influence of amplitude ratios and rotating speed on natural frequency is studied. Natural frequency and static waves for different nodal-diameter numbers are also calculated. This analytical method not only takes into account the vibration perpendicular to the middle surface of the disk but also the vibration in the middle surface of the disk. In addition, this analytical method provides a more accurate way to solve the severe vibration problems in rotating disks of turbine engine rotors.

Keywords: Nonlinear vibration · Rotating disk · Dimensionless speed
Dimensionless natural frequency · Amplitude ratios · Nodal diameters

1 Introduction

Thin rotating disks are frequently applied in engineering, from gas turbine rotors to computer memory disks. Since the turbine disks are important components of gas turbine rotors, the vibrations of turbine disks have an important effect on the behavior of the entire rotors. This kind of periodic motion of rotating disks has been investigated widely.

von Karman [1] first established a nonlinear plate theory when the nonlinear stretch effects in the transverse, equilibrium balance were considered. The first nonlinear analysis of transverse vibration in a spinning disk is due to Nowinski [2], he analyzed the large amplitude vibrations of a spinning disk by using the von Karman field equations. But he only analyzed the transverse vibration of the rotating disk without analyzing the in-plane vibration of the disk. Later Nowinski [3] analyzed the thermal stability of the rotating membrane disk. Maher and Adams [4] investigated the influence of coupling between in-plane displacements and transverse deflections considering the effects of bending stiffness and of the air flow between the disk. The von Karman equations have also been used to investigate the nonlinear vibration of a spinning disk by Renshaw and Mote [5], Hamidzadeh [6, 7] and Luo [8]. It should be noted that professor Hamidzadeh's work was based on the research of Nowinski, he expanded Nowinski's research and got some meaningful results. Luo [9, 10] developed a more accurate theory of thin plates. In his theory, the exact geometry of the deformed middle surface is used to derive the physical strains of plates and equilibrium equations

in the plate was established based on the exact geometry of the deformed middle surfaces. By using his own theory, he analyzed the response and natural frequencies for the nonlinear vibrations of a rotating thin disk. Koo and Lesieutre [11] analyzed the transverse vibration of a composite-ring disk for data storage, they calculated its natural frequencies and critical speeds. Maretic, Glavardanov, Milosevic-Mitic [12] studied the frequencies of transverse vibrations of a disk assembled from two rings of two different materials, they analyzed the influence of angular velocity, moduli of elasticity, the volume densities of the materials and the radius of the connection on the vibration frequencies of the rotating disk. Pei, Wang and Yang [13] analyzed the natural frequency, dynamic stability, critical speeds and steady state response amplitude of a rotating disk under several boundary conditions.

This research work is based on the work of Nowinski and Hamidzadeh, the presented work get the solutions of the nonlinear transverse and in-plane vibrations of a thin rotating disk and the static waves for different nodal-diameter numbers are presented, also, the variations of dimensionless natural frequency versus dimensionless speed and amplitude ratio are analyzed.

2 Equations of Motions

The vibration of a thin elastic rotating disk of radius a and thickness h is considered. The disk rotates about its central axis at a constant angular velocity Ω . The thin rotating disk is shown in the following Fig. 1.

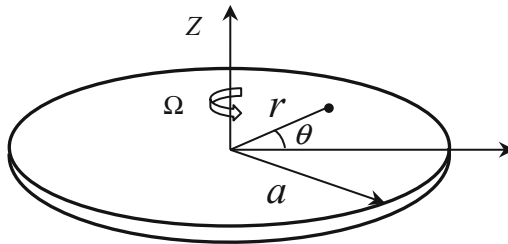


Fig. 1. A thin rotating disk

The transverse deflection of the rotating disk is large compared with its thickness h . According to the nonlinear plate theory, the strain-displacement relationship in polar coordinate system is as follows:

$$\varepsilon_{rr} = \frac{\partial u}{\partial r} + \frac{1}{2} \left(\frac{\partial w}{\partial r} \right)^2 - z \frac{\partial^2 w}{\partial r^2} \quad (1a)$$

$$\varepsilon_{\theta\theta} = \frac{1}{r} u + \frac{1}{r} \frac{\partial v}{\partial \theta} + \frac{1}{2r^2} \left(\frac{\partial w}{\partial \theta} \right)^2 - z \left(\frac{1}{r} \frac{\partial w}{\partial r} + \frac{1}{r^2} \frac{\partial^2 w}{\partial \theta^2} \right) \quad (1b)$$

$$\varepsilon_{r\theta} = \frac{1}{r} \frac{\partial u}{\partial \theta} + \frac{\partial v}{\partial r} - \frac{1}{r} v + \frac{1}{r} \frac{\partial w}{\partial r} \frac{\partial w}{\partial \theta} - 2z \left(\frac{1}{r} \frac{\partial^2 w}{\partial r \partial \theta} - \frac{1}{r^2} \frac{\partial w}{\partial \theta} \right) \quad (1c)$$

Where ε_{rr} , $\varepsilon_{\theta\theta}$ and $\varepsilon_{r\theta}$ are radial, hoop, and shear strains. u , v and w are the displacements in cylindrical coordinates. The stress-strain relation is expressed as follows:

$$\sigma_{rr} = \frac{E}{1 - \mu^2} (\varepsilon_{rr} + \mu \varepsilon_{\theta\theta}) \quad (2a)$$

$$\sigma_{\theta\theta} = \frac{E}{1 - \mu^2} (\varepsilon_{\theta\theta} + \mu \varepsilon_{rr}) \quad (2b)$$

$$\sigma_{r\theta} = \frac{E}{2(1 + \mu)} \varepsilon_{r\theta} \quad (2c)$$

Where σ_{rr} , $\sigma_{\theta\theta}$ and $\sigma_{r\theta}$ are radial, hoop, and shear stress. Also E and μ are Young's modulus and Poisson ratio. The unit thickness membrane forces of the disk can be calculated by using the following equations:

$$\begin{aligned} N_r &= \int_{-\frac{1}{2}}^{\frac{1}{2}} \sigma_{rr} dz & N_\theta &= \int_{-\frac{1}{2}}^{\frac{1}{2}} \sigma_{\theta\theta} dz & N_{r\theta} &= \int_{-\frac{1}{2}}^{\frac{1}{2}} \sigma_{r\theta} dz \\ M_r &= \int_{-\frac{1}{2}}^{\frac{1}{2}} \sigma_{rr} z dz & M_\theta &= \int_{-\frac{1}{2}}^{\frac{1}{2}} \sigma_{\theta\theta} z dz & M_{r\theta} &= \int_{-\frac{1}{2}}^{\frac{1}{2}} \sigma_{r\theta} z dz \end{aligned} \quad (3)$$

By substituting Eqs. (1a), (1b), (1c) and (2a), (2b), (2c) in (3), one can get membrane forces which are presented by displacements:

$$N_r = \frac{E}{1 - \mu^2} \left\{ \frac{\partial u}{\partial r} + \frac{1}{2} \left(\frac{\partial w}{\partial r} \right)^2 + \mu \left[\frac{1}{r} u + \frac{1}{r} \frac{\partial v}{\partial \theta} + \frac{1}{2r^2} \left(\frac{\partial w}{\partial \theta} \right)^2 \right] \right\} \quad (4a)$$

$$N_\theta = \frac{E}{1 - \mu^2} \left\{ \frac{1}{r} u + \frac{1}{r} \frac{\partial v}{\partial \theta} + \frac{1}{2r^2} \left(\frac{\partial w}{\partial \theta} \right)^2 + \mu \left[\frac{\partial u}{\partial r} + \frac{1}{2} \left(\frac{\partial w}{\partial r} \right)^2 \right] \right\} \quad (4b)$$

$$N_{r\theta} = \frac{E}{2(1 + \mu)} \left(\frac{\partial v}{\partial r} + \frac{1}{r} \frac{\partial u}{\partial \theta} - \frac{1}{r} v + \frac{1}{r} \frac{\partial w}{\partial r} \frac{\partial w}{\partial \theta} \right) \quad (4c)$$

$$M_r = -D \left[\frac{\partial^2 w}{\partial r^2} + \mu \left(\frac{1}{r} \frac{\partial w}{\partial r} + \frac{1}{r^2} \frac{\partial^2 w}{\partial \theta^2} \right) \right] \quad (4d)$$

$$M_\theta = -D \left(\frac{1}{r} \frac{\partial w}{\partial r} + \frac{1}{r^2} \frac{\partial^2 w}{\partial \theta^2} + \mu \frac{\partial^2 w}{\partial r^2} \right) \quad (4e)$$

$$M_{r\theta} = -(1 - \mu) D \left(\frac{1}{r} \frac{\partial^2 w}{\partial r \partial \theta} - \frac{1}{r^2} \frac{\partial w}{\partial \theta} \right) \quad (4f)$$

Where D is the stiffness for the disk, $D = E/12(1 - \mu^2)$.

Because the in-plane vibration displacement amplitudes are much smaller than that of transverse vibration, so the inertia terms in equations of in-plane motions are ignored. The equilibrium equations of motions in terms of membrane forces for the disk can be written as:

$$\frac{\partial N_r}{\partial r} + \frac{1}{r} \frac{\partial N_{r\theta}}{\partial \theta} + \frac{1}{r} (N_r - N_\theta) + \rho \Omega^2 r = 0 \quad (5a)$$

$$\frac{\partial N_{r\theta}}{\partial r} + \frac{1}{r} \frac{\partial N_\theta}{\partial \theta} + \frac{2}{r} N_{r\theta} = 0 \quad (5b)$$

$$\frac{1}{r} \frac{\partial}{\partial r} \left[r \left(N_r \frac{\partial w}{\partial r} \right) + N_{r\theta} \cdot \frac{\partial w}{\partial \theta} + r \cdot Q_r \right] + \frac{1}{r} \frac{\partial}{\partial \theta} \left[\frac{1}{r} \left(N_\theta \frac{\partial w}{\partial \theta} \right) + N_{\theta r} \frac{\partial w}{\partial r} + Q_\theta \right] + q = 0 \quad (5c)$$

$$\frac{\partial M_r}{\partial r} + \frac{1}{r} \frac{\partial M_{\theta r}}{\partial \theta} + \frac{1}{r} (M_r - M_\theta) - Q_r = 0 \quad (5d)$$

$$\frac{\partial M_{r\theta}}{\partial r} + \frac{1}{r} \frac{\partial M_\theta}{\partial \theta} + \frac{2}{r} M_{r\theta} - Q_\theta = 0 \quad (5e)$$

The in-plane stress function ϕ is introduced in order to satisfy Eqs. (5a) and (5b) by introducing the following expressions [12]:

$$N_r = \frac{1}{r} \frac{\partial \phi}{\partial r} + \frac{1}{r^2} \frac{\partial^2 \phi}{\partial \theta^2} - \frac{1}{2} \rho \Omega^2 r^2 \quad (6a)$$

$$N_\theta = \frac{\partial^2 \phi}{\partial r^2} - \frac{1}{2} \rho \Omega^2 r^2 \quad (6b)$$

$$N_{r\theta} = - \frac{\partial}{\partial r} \left(\frac{1}{r} \frac{\partial \phi}{\partial \theta} \right) \quad (6c)$$

The von Karman equation of the rotating disk is obtained by inserting Eqs. (4a), (4b), (4c), (4d), (4e), (4f) and (5d–5e) into Eq. (5c). Under the hypothesis of free vibration, the governing equation of the rotating disk in the polar coordinate system becomes:

$$\begin{aligned} \frac{D}{h} \nabla^4 w + \rho \frac{\partial^2 w}{\partial t^2} &= \frac{\partial^2 w}{\partial r^2} \left(\frac{1}{r} \frac{\partial \phi}{\partial r} + \frac{1}{r^2} \frac{\partial^2 \phi}{\partial \theta^2} \right) + \left(\frac{1}{r} \frac{\partial w}{\partial r} + \frac{1}{r^2} \frac{\partial^2 w}{\partial \theta^2} \right) \frac{\partial^2 \phi}{\partial r^2} \\ &- 2 \frac{\partial}{\partial r} \left(\frac{1}{r} \frac{\partial w}{\partial \theta} \right) \frac{\partial}{\partial r} \left(\frac{1}{r} \frac{\partial \phi}{\partial \theta} \right) - \frac{1}{2} \rho \Omega^2 r^2 \nabla^2 w - \rho \Omega^2 r \frac{\partial w}{\partial r} \end{aligned} \quad (7)$$

The compatibility equation is also obtained:

$$\frac{1}{E} [\nabla^4 \phi - 2(1 - \mu) \rho \Omega^2] = - \frac{1}{r} \left(\frac{\partial w}{\partial r} + \frac{1}{r} \frac{\partial^2 w}{\partial \theta^2} \right) \frac{\partial^2 w}{\partial r^2} + \left(\frac{1}{r} \frac{\partial^2 w}{\partial r \partial \theta} - \frac{1}{r^2} \frac{\partial w}{\partial \theta} \right)^2 \quad (8)$$

3 Approximate Solution

An approximate solution was proposed by Nowinski [2], Hamidzadeh [7] analyzed the case of no nodal circles but any number of nodal diameters, but they only analyzed the transverse vibration of the disk and ignored the in-plane vibration of the disk, this research work expands their work to analyze the transverse and in-plane coupling vibrations of the disk. According to the work of Hamidzadeh [7], the displacement of transverse direction is:

$$w(r, \theta, t) = W_0 T(t) r^n \cos(n\theta + \varphi) \quad (9)$$

Where $w(r, \theta, t)$ is the transverse deflection of the disk in polar coordinates, ' W_0 ' is a constant, ' φ ' is the phase constant, ' $T(t)$ ' is a time function respecting that ' w ' varies with time, and ' n ' is the number of nodal diameters.

The stress function ' ϕ ' is obtained by substituting Eq. (9) into (8) according to Nowinski [2]. The stress function is as follows:

$$\phi = k \frac{a_1}{c_1} r^{2n} + \frac{1-\mu}{32} \Omega^2 \rho r^4 + Ar^2 + (Cr^{2n} + Dr^{2(n+1)}) \cos 2(n\theta + \varphi) \quad (10)$$

Where A , C , and D are constants and

$$k = \frac{E}{2} W_0^2 T^2 \quad (11)$$

$$a_1 = 2n^2(n-1)^2 \quad (12a)$$

$$c_1 = 16n^2(n-1)^2 \quad (12b)$$

Substitute (10) into (6a), (6b), (6c), one can get the following equations:

$$\begin{aligned} N_r = & \frac{2kna_1}{c_1} r^{2(n-1)} - \frac{\mu+3}{8} \Omega^2 \rho r^2 + 2A \\ & + [2Cn(1-2n)r^{2(n-1)} + 2D(n-2n^2+1)r^{2n}] \cos 2(n\theta + \varphi) \end{aligned} \quad (13)$$

$$\begin{aligned} N_\theta = & \frac{2kn(2n-1)a_1}{c_1} r^{2(n-1)} - \frac{1+3\mu}{8} \Omega^2 \rho r^2 + 2A \\ & + [2Cn(2n-1)r^{2(n-1)} + 2D(n+1)(2n+1)r^{2n}] \cos 2(n\theta + \varphi) \end{aligned} \quad (14)$$

$$N_{r\theta} = 2n [C(2n-1)r^{2(n-1)} + D(2n+1)r^{2n}] \sin 2(n\theta + \varphi) \quad (15)$$

Constants A , C , and D can be determined by satisfying the stress boundary conditions at $r = a$, which will be presented in the later analysis. According to Nowinski [2], apply the procedure of Galerkin to the Eq. (7), then substitute Eqs. (9) and (10)

into (7) and integrate the result over the domain of the disk result in the following second-order non-linear time equation:

$$\frac{d^2T}{dt^2} + \alpha T + \beta T^3 = 0 \tag{16}$$

The α and β are given by

$$\alpha = -\frac{s_4}{2s_1} \Omega^2 \tag{17a}$$

$$\beta = -\frac{EW_0^2 a^{2(n-2)}}{\rho s} \left(s_2 C' + s_3 a^2 D' + \frac{1}{2} s_5 \right) \tag{17b}$$

Where

$$C' = \frac{C}{EW_0^2 T^2} \tag{18a}$$

$$D' = \frac{D}{EW_0^2 T^2} \tag{18b}$$

and

$$s_1 = \frac{1}{2(n+1)} \tag{19a}$$

$$s_2 = -2n^2(n-1) \tag{19b}$$

$$s_3 = -n(n-1)(2n+1) \tag{19c}$$

$$s_4 = -\frac{n}{n+1} \left[1 + \frac{n-1}{4} (1-\mu) \right] \tag{19d}$$

$$s_5 = -\frac{n^2(n-1)^2}{4(2n-1)} \tag{19e}$$

The solution to Eq. (13) is a Jacobian elliptical function:

$$T(t) = cn(qt, \lambda) \tag{20}$$

Where

$$q = \sqrt{\alpha + \beta} \tag{21a}$$

$$\lambda = \sqrt{\frac{\beta}{2(\alpha + \beta)}} \quad (21b)$$

Obviously, $cn(qt, \lambda)$ is a periodic function with the period $T_0 = 4K/q$, and K is the first kind of complete elliptic integral [16].

4 Free Nonlinear Vibration

In order to identify unknown constants A , C , and D , two stress boundary conditions need to be satisfied. The two boundary conditions are that the radial and tangential stresses on the outer radius of the disk are zero:

$$N_r(r = a, \theta) = 0 \quad (22a)$$

$$N_{r\theta}(r = a, \theta) = 0 \quad (22b)$$

By satisfying the stress boundary conditions, ones yield:

$$Cn(1 - 2n) + D(n - 2n^2 + 1)a^2 = 0 \quad (23a)$$

$$C(2n - 1) + D(2n + 1)a^2 = 0 \quad (23b)$$

Solve Eqs. (23a), (23b), ones obtain:

$$C = D = 0 \quad (24)$$

Substitute (24) into (13), A becomes:

$$A = \frac{\mu + 3}{16} \Omega^2 \rho a^2 - kn \frac{a_1}{c_1} a^{2(n-1)} \quad (25)$$

Since C and D are zero, Eq. (15) yields $N_{r\theta} = 0$.

Thus, with (11), ones obtain:

$$N_r = \frac{En}{8} W_0^2 T^2 \left[r^{2(n-1)} - a^{2(n-1)} \right] + \frac{\mu + 3}{8} \Omega^2 \rho (a^2 - r^2) \quad (26)$$

$$N_\theta = \frac{En}{8} W_0^2 T^2 \left[(2n - 1)r^{2(n-1)} - a^{2(n-1)} \right] - \frac{1 + 3\mu}{8} \Omega^2 \rho r^2 + \frac{\mu + 3}{8} \Omega^2 \rho a^2 \quad (27)$$

$$N_{r\theta} = 0 \quad (28)$$

In order to calculate in-plane vibration displacements u and v , the relationship between u , v and N_r , N_θ are obtained, subtracting Eq. (4b) multiplied by μ from Eq. (4a) yields:

$$\frac{\partial u}{\partial r} = \frac{N_r - \mu N_\theta}{E} - \frac{1}{2} \left(\frac{\partial w}{\partial r} \right)^2 \quad (29a)$$

Similarly, subtracting Eq. (4a) multiplied by μ from Eq. (4b) yields:

$$\frac{u}{r} + \frac{1}{r} \frac{\partial v}{\partial \theta} = \frac{N_\theta - \mu N_r}{E} - \frac{1}{2r^2} \left(\frac{\partial w}{\partial \theta} \right)^2 \quad (29b)$$

Substitute (27), (28) to (29a), (29b), ones obtain:

$$\begin{aligned} \frac{\partial u}{\partial r} = & \frac{nW_0^2 T(t)^2}{8} \left\{ [1 - (2n - 1)\mu] r^{2(n-1)} + (\mu - 1)a^{2(n-1)} \right\} + \frac{3(\mu^2 - 1)}{8E} \Omega^2 \rho r^2 \\ & + \frac{(\mu + 3)(1 - \mu)}{8E} \Omega^2 \rho a^2 - \frac{1}{2} [nW_0 T(t) \cos(n\theta + \varphi)]^2 r^{2n-2} \end{aligned} \quad (30)$$

$$\begin{aligned} u + \frac{\partial v}{\partial \theta} = & \frac{nW_0^2 T(t)^2}{8} \left[(2n - 1 - \mu) r^{2n-1} + (\mu - 1)a^{2(n-1)} r \right] + \frac{\mu^2 - 1}{8E} \Omega^2 \rho r^3 \\ & + \frac{-\mu^2 - 2\mu + 3}{8E} \Omega^2 \rho a^2 r - \frac{1}{2} n^2 W_0^2 T(t)^2 r^{2n-1} \sin^2(n\theta + \varphi) \end{aligned} \quad (31)$$

Integrate (30) and (31), ones obtain:

$$\begin{aligned} u = & \frac{nW_0^2 T(t)^2}{8} \left\{ \frac{1 - (2n - 1)\mu}{2n - 1} r^{2n-1} + (\mu - 1)a^{2(n-1)} r \right\} + \frac{(\mu^2 - 1)}{8E} \Omega^2 \rho r^3 \\ & + \frac{(\mu + 3)(1 - \mu)}{8E} \Omega^2 \rho a^2 r - \frac{n^2}{2(2n - 1)} W_0^2 T(t)^2 r^{2n-1} \cos^2(n\theta + \varphi) + f(\theta, t) \end{aligned} \quad (32)$$

$$v = \frac{n^2}{4(2n - 1)} W_0^2 T(t)^2 r^{2n-1} \sin 2(n\theta + \varphi) - \int f(\theta, t) d\theta + R(r, t) \quad (33)$$

To calculate unknown functions $f(\theta, t)$ and $R(r, t)$, the displacement boundary conditions need to be satisfied. the displacement boundary conditions are:

$$u(r = 0, \theta) = 0 \quad (34a)$$

$$v(r = 0, \theta) = 0 \quad (34b)$$

$$\left. \frac{\partial u}{\partial \theta} \right|_{r=0} = 0, \quad \left. \frac{\partial v}{\partial r} \right|_{r=0} = 0 \quad (34c)$$

By imposing the above conditions on Eqs. (32) and (33), and with Eq. (9), the transverse deflection and in-plane displacements of the non-linear vibration rotating disk are finally obtained:

$$u = \frac{nW_0^2 T(t)^2}{8} \left\{ \frac{1 - (2n-1)\mu}{2n-1} r^{2n-1} + (\mu-1)a^{2(n-1)} r \right\} + \frac{(\mu^2-1)}{8E} \Omega^2 \rho r^3$$

$$+ \frac{(\mu+3)(1-\mu)}{8E} \Omega^2 \rho a^2 r - \frac{n^2}{2(2n-1)} W_0^2 T(t)^2 r^{2n-1} \cos^2(n\theta + \varphi)$$
(35)

$$v = \frac{n^2}{4(2n-1)} W_0^2 T(t)^2 r^{2n-1} \sin 2(n\theta + \varphi)$$
(36)

$$w = W_0 T(t) r^n \cos(n\theta + \varphi)$$
(37)

5 Results and Discussion

In order to do the analysis and show the results, the following dimensionless parameters are introduced

$$\text{Amplitude ratio:} \quad W = \frac{W_0 a^n}{h}$$
(38)

$$\text{Dimensionless rotating speed:} \quad \Omega_1 = \frac{\Omega a}{\sqrt{E/\rho}}$$
(39)

$$\text{Dimensionless period:} \quad T^* = \frac{4K}{qa} \sqrt{\frac{E}{\rho}}$$
(40)

$$\text{Dimensionless frequency:} \quad \Omega_2 = \frac{2\pi}{T^*}$$
(41)

The presented results in this research work are for the disk with the following parameters: Young's modulus $E = 2.1 \times 10^{11}$ Pa, Poisson ratio $\mu = 0.33$, density $\rho = 7.85 \times 10^3$ kg/m³, outer radius $a = 0.5$ m, thickness $h = 0.02$ m, rotating speed $\Omega = 100\pi$ rad/s.

Let time-relative terms vanish, for $W = 0.2$, $n = 3$, the displacements of static waves in the three-directions from Eqs. (35), (36) and (37) are plotted in Fig. 2(a)–(c).

Figure 2 shows that the in-plane displacements are much smaller than the deflection in the transverse direction. The results also show that the nodal diameters number of circumferential mode is always twice that of the transverse vibration. The frequency associate to this mode is 1438.3 rad/s.

From Eqs. (35), (36) and (37), we can see that the in-plane vibrations of the rotating disk are affected by rotating speed and nodal diameters number. So the variation of radial displacement amplitude u on the outer radius versus rotating speed for different numbers of nodal diameters is presented in Fig. 3 for a dimensionless amplitude ratio of $W = 0.2$.

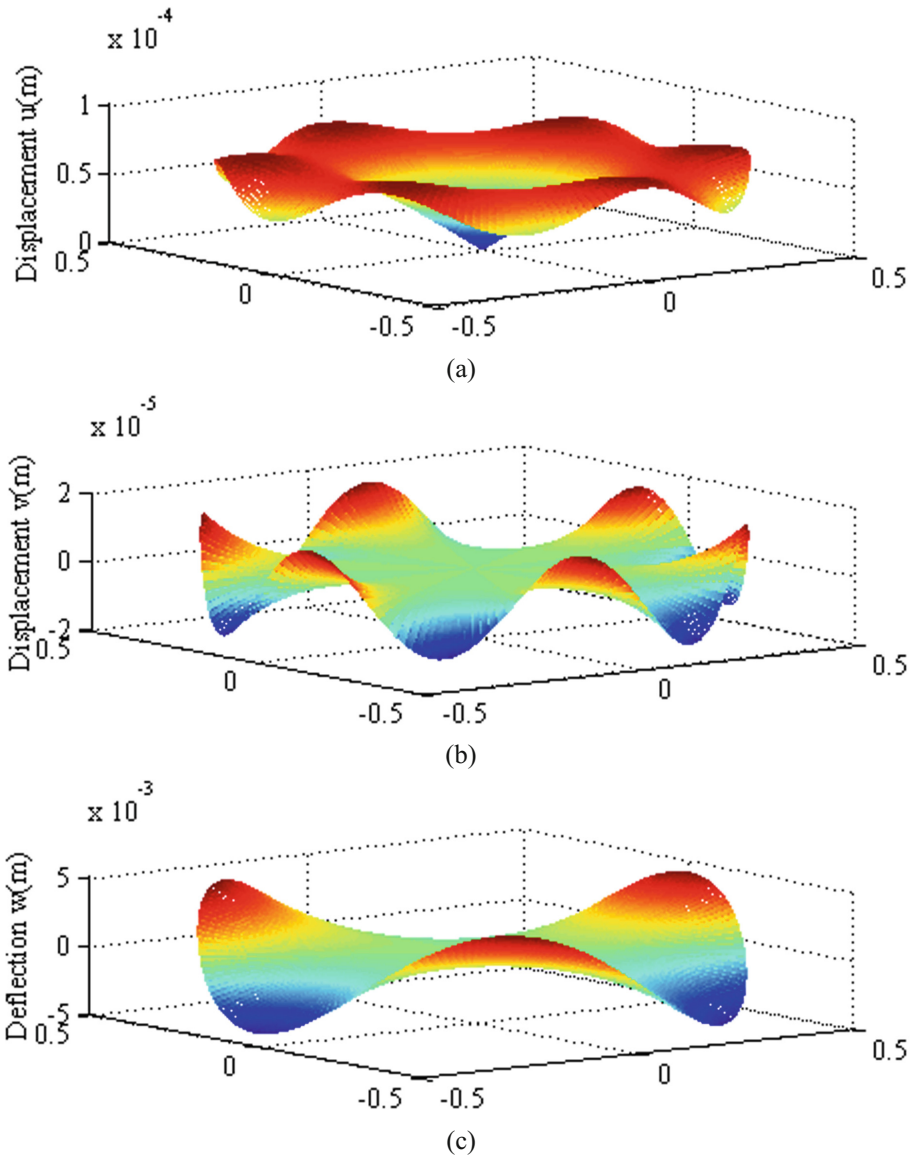


Fig. 2. Static waves in rotating disk: (a) radial displacement u , (b) circumferential displacement v , (c) transverse deflection w

The results indicate that the value of the radial displacement amplitude on the outer radius is negative when the rotating speed is zero and increases with rotating speed for different numbers of nodal diameters. The radial vibration disappears at a certain rotating speed. The radial displacement amplitude on the outer radius is also increases with the number of nodal diameters.

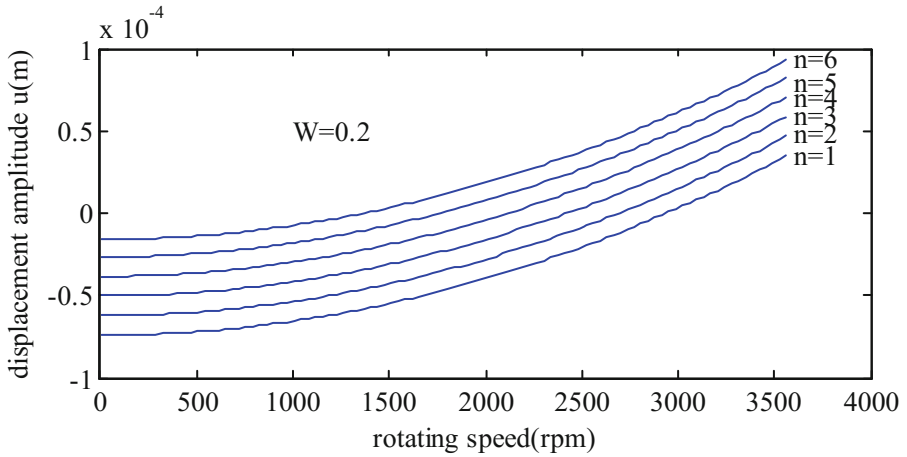


Fig. 3. Variation of radial displacement amplitude u on the outer radius versus rotating speed for different numbers of nodal diameters

The nonlinear and linear dimensionless natural frequencies of the rotating disks versus a wide range of rotating speeds are calculated. For a dimensionless amplitude ratio of $W = 2$, the variations of dimensionless natural frequencies for different numbers of nodal diameters is presented in Fig. 4. Presented results show that the natural frequencies in both the nonlinear analysis and linear analysis depend on nodal diameter, and have no difference when $n = 1$. Nonlinear natural frequencies and linear natural frequencies are mainly distinguished at lower speed, at higher speed, the nonlinear dimensionless frequencies of different nodal diameters numbers approach the corresponding linear dimensionless frequencies.

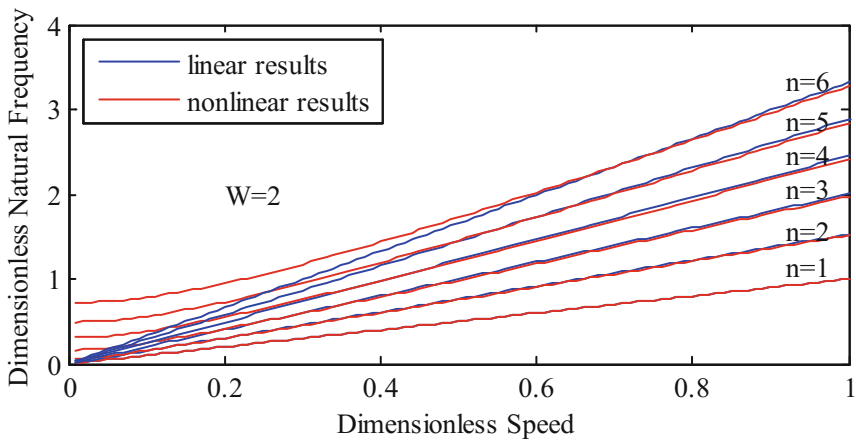


Fig. 4. Variation of dimensionless natural frequency versus dimensionless speed for different numbers of nodal diameters

The nonlinear and linear dimensionless natural frequencies of the rotating disks versus amplitude ratios at different dimensionless speeds for $n = 6$ are also calculated and presented in Fig. 5. The results show that the natural frequencies in the nonlinear analysis are dependent of amplitudes, and the effect of speeds on natural frequency at small amplitudes is higher than that at large amplitudes, and the relationship between natural frequencies and amplitudes gradually become linear at large amplitudes. But the dimensionless natural frequencies in the linear analysis are independent of amplitudes for all speeds.

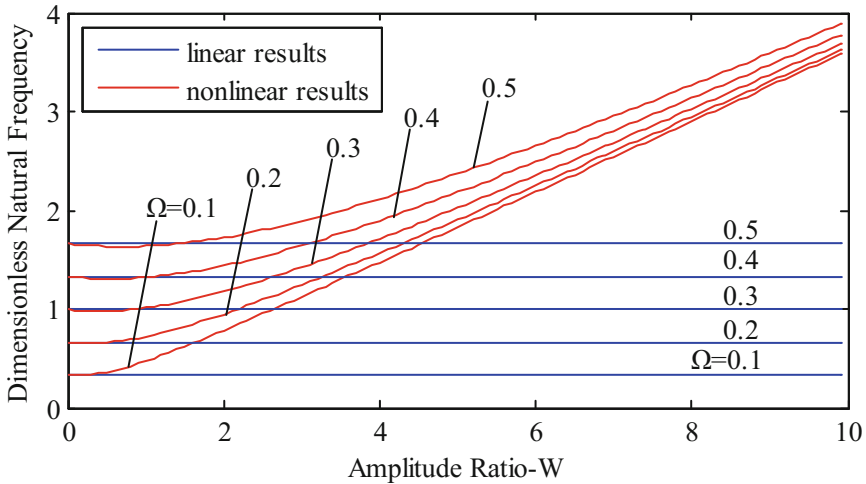


Fig. 5. Dimensionless natural frequency versus amplitude ratio at different dimensionless speeds for $n = 6$

6 Conclusion

An analytical method is presented to investigate nonlinear transverse and in-plane vibrations of a thin rotating disk, the solutions of the nonlinear transverse and in-plane vibrations of the thin rotating disk are finally obtained, the static waves, natural frequency for nonlinear transverse vibrations of the rotating disk are also determined. The provided modal analysis is valid for thin rotating disks with any number of nodal diameters without nodal circles. The results show that the in-plane displacements of the vibration are much smaller than the deflection in the transverse direction. Analysis indicates that the natural frequencies provided by nonlinear analysis are different from that of linear analysis. The nonlinear natural frequencies are highly dependent on amplitude of vibration and nodal diameters. The presented results provide the designer an analytical method for analyzing vibrations in three directions of a thin rotating disk.

Acknowledgements. This research is funded by the National Natural Science Foundation of China (Grant No. 11672083).

References

1. von Karman, T.: Festigkeitsprobleme im mashinenbau. *Encyklopadie der Mathematischen Wissenschaften* **4**(4), 348–352 (1910)
2. Nowinski, J.L.: Nonlinear transverse vibrations of spinning disk. *J. Appl. Mech.* **31**, 72–78 (1964)
3. Nowinski, J.L.: Stability of nonlinear thermos elastic waves in membrane-like spinning disks. *J. Therm. Sci.* **4**, 1–11 (1981)
4. Maher, J.F., Adams, G.G.: Effect of displacement dependent membrane stresses on the axisymmetric configuration of a spinning flexible disk. *ATLE Tribol. Trans.* **34**(4), 597–603 (1991)
5. Renshaw, A.A., Mote Jr., C.D.: A perturbation solution for the flexible rotating disk: nonlinear equilibrium and stability under transverse loading. *J. Sound Vib.* **183**, 309–326 (1995)
6. Hamidzadeh, H.R., Nepal, N., Dehghani, M.: Transverse vibration of thin rotating disks–nonlinear modal analysis. In: *ASME International Mechanical Engineering Congress and Exposition, Anaheim, California*, pp. 219–225 (1998)
7. Hamidzadeh, H.R.: Non-linear free transverse vibration of thin rotating discs. In: *20th Biennial Conference on Mechanical Vibration and Noise, Long Beach, CA*, vol. 221, pp. 467–473 (2005)
8. Luo, A.C.J., Mote Jr., C.D.: An analytical solution of the non-linear vibration of rotating disks. In: *ASME 17th Biennial Conference on Mechanical Vibration and Noise, Las Vegas, Nevada, DETC99/VIB-8150* (1999)
9. Luo, A.C.J.: Approximate theory for geometrically-nonlinear, thin plates. *Int. J. Solids Struct.* **37**, 7655–7670 (2000)
10. Luo, A.C.J., Mote Jr., C.D.: Nonlinear vibration of rotating, thin disks. *ASME J. Vib. Acoust.* **122**(4), 376–383 (2000)
11. Koo, K.-N., Lesieutre, G.A.: Vibration and critical speeds of composite-ring disks for data storage. *J. Sound Vib.* **329**, 833–847 (2010)
12. Maretic, R., Glavardanov, V., Milosevic-Mitic, V.: Vibration and stability of rotating annular disks composed of different materials. *Arch. Appl. Mech.* **85**(1), 117–131 (2015)
13. Pei, Y., Wang, J., Yang, F.: Dynamics comparison of rotating flexible annular disk under different edge boundary conditions. *Int. J. Mech. Sci.* **137**, 121–132 (2018)
14. Novozhilov, V.V.: *Foundations of the Nonlinear Theory of Elasticity*, 3rd edn. Graylock Press, Rochester (1953)
15. Timoshenko, S.: *Theory of Plates and Shells*. McGraw-Hill Book Company, New York (1940)
16. Ye, Q., Shen, Y.: *Handbook of Mathematical Functions*, 2nd edn. Science Press, Beijing (2013)



Stiffening Effect and Dry-Friction Damping of Bladed Wheel Model with “Tie-Boss” Couplings - Numerical and Experimental Investigation

Luděk Pešek^(✉), Ladislav Půst, Petr Šulc, Pavel Šnábl,
and Vitězslav Bula

Institute of Thermomechanics AS CR, v.v.i.,
Dolejskova 5, Prague 8, Czech Republic
pesek@it.cas.cz

Abstract. Bladed wheel model with tie-boss couplings for numerical and experimental investigation of stiffening and friction damping between tie-bosses is introduced. The modal behavior of FE numerical models of the wheel for two contact limit states, i.e. open and bonded contacts, was ascertained. The experimental modal analysis of the wheel both for open and pre-stressed contacts were performed, too. For detail stiffening and damping effect investigation the physical model of three-blade-bundle was elaborated. The experiments were performed for different excitation forces, excitation frequencies and contact prestresses. The dynamics of the bundle with respect to different contact states was evaluated from vibration attenuation after short resonant excitation. It was observed that if the macroslips arise in contacts that eigen-frequencies of the bundle are very close to the eigen-frequencies of open contact model bundle and high damping effect is achieved. If the macroslips arise in contacts the eigen-frequencies are close to eigen-frequencies of the bond contact model and low damping is achieved. Hence the stiffening effect is high only in the case of macroslips. The slip transition is conditioned by the level of adhesion that must be exceeded by excitation force. The FE model of the wheel and blade triple model with dynamic frictional contacts in the tie-boss couplings were developed and calculated results are compared with experiment.

Keywords: Bladed wheel · Dry-friction contacts · Damping
Tie-boss couplings

1 Introduction

Blades of bladed wheels coupled by a disk and inner couplings show much more complicated dynamic behavior than single blades. Eigenmodes and eigen-frequencies are influenced by vibration of neighboring blades, mass and stiffening of the coupling elements. Therefore stiffening and dissipation of mechanical energy by means of slip damping in platforms [1] or shrouds [2] or by tie wires [3] are still under investigation. The damping effect of the friction damping and snubbing mechanism is studied for

reduction of turbine blade vibration in [4–6]. Besides traditional approaches based on the Hertzian theory and Coloumb’s law [7, 8] the new numerical approaches appear based on the finite element technology. The non-holonomic couplings of contact forces are computed by e.g. the Penalty or the Augmented Lagrangian method [9, 10]. However, due to possible space and time discretization inaccuracies and numerical errors, an experimental validation is still needed.

The bladed wheel model with “tie-boss” couplings was designed and fabricated for numerical and experimental investigation of the dry-friction damping and the stiffening effect [11]. Modal analysis of the full bladed disk for two contact limit states, i.e. (I) bonded contacts and (II) open contacts, shows large dynamic stiffening effect for bonded contacts with respect to the open contact wheel case. Bonded contacts arise when high pre-stress and adhesive forces in contacts prevent a complete sliding (macroslips) because dynamic excitation is not sufficiently high. Then only a stick-slip state (microslip) in contacts appears. To deal with these phenomena in more detail, we fabricated also three-blade-bundle physical model and we use it for evaluation of influence of excitation amplitude level and the pre-stress in contacts on its dynamics. The numerical solution of this system based on 3D finite element model with dynamical friction contacts together with results for selected excitation parameters and contact pre-stresses are herein presented.

Description of the bladed wheel design with “tie-boss” couplings is in the first part of the paper, then numerical and experimental modal analysis of full bladed disk with limit contact states are presented. The stiffening and damping effects of the tie-bosses are discussed on our experimental results of three-blade-bundle dynamical test. The modelling of three-blade-bundle with dynamical friction contacts by finite element (FE) method and the computed results of dynamical response of this system for one typical excitation case and pre-stress conditions in contacts are shown, too. Besides the steady state modal and transient tests, the rotary tests of the bladed wheel excited by synchronized electromagnets are in progress. Therefore the last part of this paper is dedicated to a description of the experimental set-up, electromagnetic excitation system and dynamical behavior of the wheel with open contacts between tie-bosses.

2 Description of Bladed Wheel Model with “Tie-Boss” Couplings

The model disk is equipped with thirty prismatic blades. Picture of a design of bladed wheels with so-called “tie-boss” couplings and additional weights is shown in Fig. 1. The tie-bosses are shoulders of blades whose ends are in a contact with shoulders of the neighboring blades. The ends of the shoulders are cut so that its areas, i.e. contact areas, are parallel to a direction of the flexural vibration of a single blade.

Because of setting up the pre-stress in the contacts between the tie-bosses of the neighboring blades, the tie-bosses were consisted of extensible shoulders screwed with left (right side) and right (left side shoulder) winding into the suspension bolt that was fixed to the blade by two nuts. By screwing the bolt in the nuts the shoulders extend simultaneously on both sides. The detail of the tie-boss structure is in Fig. 1, too. Each blade is fixed to the disk by the system of two small finger consoles. Bottom console is

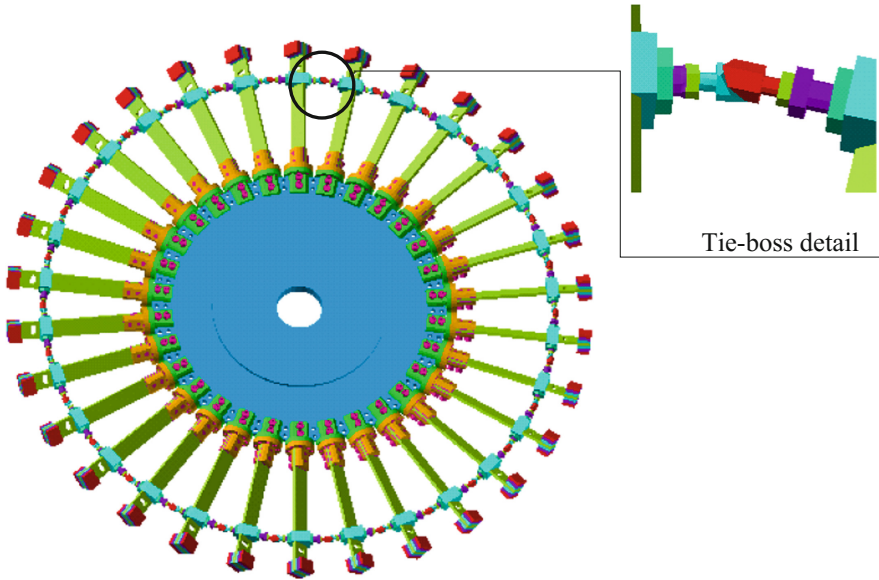


Fig. 1. Bladed wheel model with inter-blade tie-boss couplings.

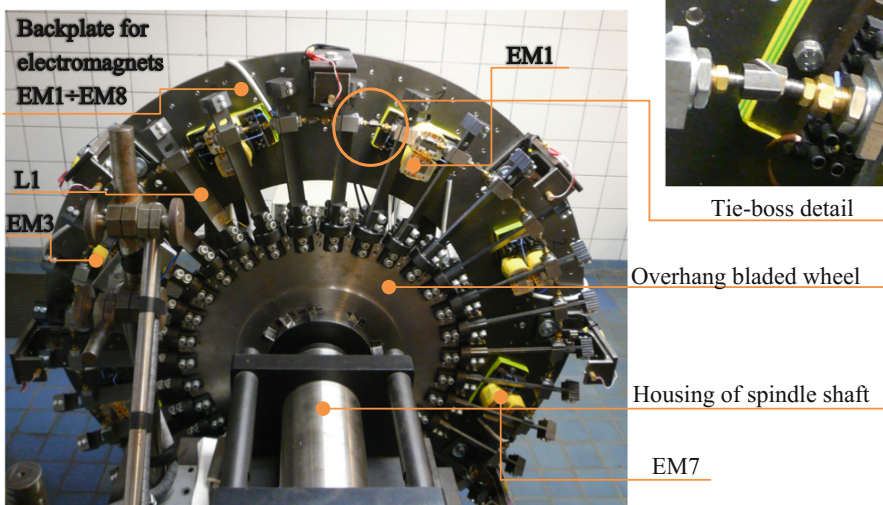


Fig. 2. Experimental set-up of the bladed wheel and test rig.

bolted down to the disk and upper console is bolted to the blade. The consoles are bolted together and their mutual position is set by angle 45° before their bolting together. At the end of the blades an additional mass is bolted to lower its first flexural eigen-frequency. Experimental set-up of rotary test rig of the designed bladed wheel with denotation of the particular components is in the Fig. 2.

3 Numerical and Experimental Modal Analysis of Full Bladed Disk

The three-dimensional FE model of the designed bladed disk was developed in the program ANSYS 15.0. Modal analysis of the numerical bladed disk were computed for two contact limit states, i.e. (I) bonded contacts (i.e. contact surfaces stuck together) and (II) open contacts (i.e. no coupling between contact surfaces) between tie-bosses. The dependences of the eigen-frequencies of flexural eigen-modes on number of nodal diameters (ND) are depicted for both contact cases in Fig. 3 as so-called SAFE diagram. The open contact model approximates the “eigen-frequency” of the wheel at large relative displacements (macroslips) in contacts. The eigen-frequencies of the open contact model monotonously increase with a number of ND and its value converges to a limit 50.3 Hz that is defined by the first flexural mode of a clamped blade. The highest possible number of ND for 30 blades is 15. At this case the inter-blade angle reaches 180° . The model with bonded contacts served for mapping of modal behavior of the wheel under high pre-stress in contacts and low amplitudes of excitation when only a stick-slip state (microslip) in contacts appear. For this case it can be seen large stiffening effect at modes with a higher number of ND.

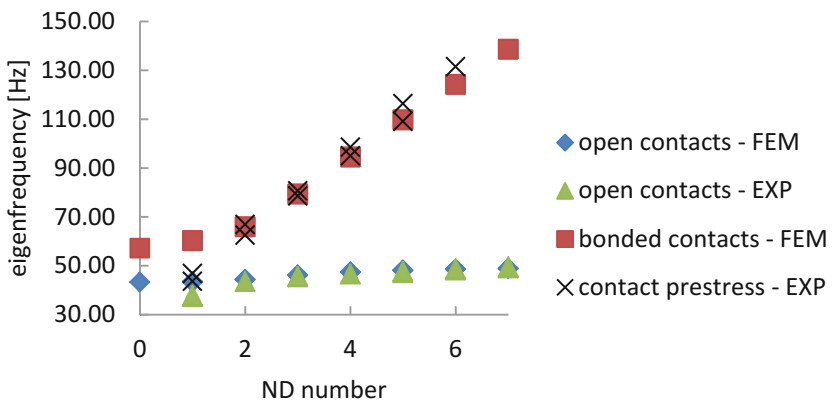


Fig. 3. Eigen-frequencies versus number of nodal diameters for the wheel with (I) bonded and (II) open contacts – FEM model tuned to the experiment.

To attune the numerical modal model of the bladed wheel to the experiment we performed experimental modal analysis (Table 1) both for (A) open contacts and (B) pre-stress contact states between tie-bosses. The pre-stresses in contacts between the tie-bosses were set manually by extensions of length of their arms. The values of the pre-stresses were evaluated indirectly after releasing the pre-stresses by the magnetic torque sensor Active-3 Lite that enabled to register the torque moment of each blade. The normal forces in the contacts were estimated from a size of the torque moment applied to the blade by contact pre-stresses. Normal forces were relatively high, i.e. about 50 N with a slight variation along the circumference. Excitation of the

bladed wheel was electromagnetic. The electromagnet placed against the top of the blade L1 (see Fig. 2) was excited by the high power pulse in case A and by harmonic frequency sweep function in case B.

Table 1. Results of modal analysis of the bladed wheel for cases: (A) open contacts (FEM, experiment) and (B) bonded contacts (FEM) and pre-stress states (experiment) between tie-bosses.

ND	Open contacts FEM	Open contacts EXP		Bonded contacts FEM	Contact prestress EXP	
	Freq. (Hz)	Freq. (Hz)	Damp. r. (%)	Freq. (Hz)	Freq. (Hz)	Damp. r. (%)
0	43.32	-	-	57.17	-	-
1	43.37	37.34	0.32	60.24	43.66	1.29
1	43.47	37.71	0.28	60.35	46.85	1.73
2	44.32	43.51	0.15	65.88	62.51	0.51
2	44.39	-	-	65.99	66.92	0.85
3	46.14	45.43	0.18	79.36	78.58	1.04
3	46.20	45.65	0.12	79.44	80.63	0.24
4	47.37	46.59	0.08	94.48	94.98	1.57
4	47.42	-	-	94.53	98.56	0.28
5	48.10	47.08	0.06	109.65	109.11	0.50
5	48.22	47.67	0.08	109.74	116.38	0.21

The wheel model with open contacts (A) was tuned to the experimental results of modal analysis. The results of both numerical and experimental modal analysis are depicted in the Fig. 3. It shows good agreement. Furthermore, the results of numerical modal analysis with bonded couplings between tie-bosses are depicted in the Fig. 3, too. And finally there are also results of experimental modal analysis of the wheel with pre-stresses between tie-bosses (case B). The figure clearly shows that the eigen-frequencies of the case (B) are found between the eigen-frequencies of two contact limit states. The position of each eigen-frequency within the limit eigen-frequencies are given by the level of pre-stress and level of excitation that define rate of microslips and macroslips during the vibration. Since the open contact model approximates the blade “eigen-frequency” at macroslips it means the closer is the pre-stressed state to the open contact model eigen-frequency the higher relative displacements are excited. Since the experimental eigen-frequencies are close to bonded contacts it shows that the pre-stresses in contacts were relatively high with respect to a force excitation capacity and microslips aroused only in contacts. The differences of 1ND mode measured eigen-frequencies from the numerical counterparts are caused by differences in boundary conditions (bearing of the wheel hub) of physical and numerical model. The influence of the bearing diminishes for higher number of ND.

4 Measurement of Dynamical Behaviour of Three-Blade-Bundle

The experimental setup of the blade triple is shown in Fig. 4. This bundle is constructed to correspond to the section of the designed bladed disk. The measurement setup is shown in Fig. 5. Blades A, B and C are clamped by the fixing console into the steel block by bolts. Because of the smooth friction, one tie-boss end is made of brass and the second of steel in each contact pair. The contact surfaces were polished by compound of the second degree. The normal contact forces were measured by the direct level of strain-gauge signals. The excitation was performed by electromagnet (EM) acting to the blade B.

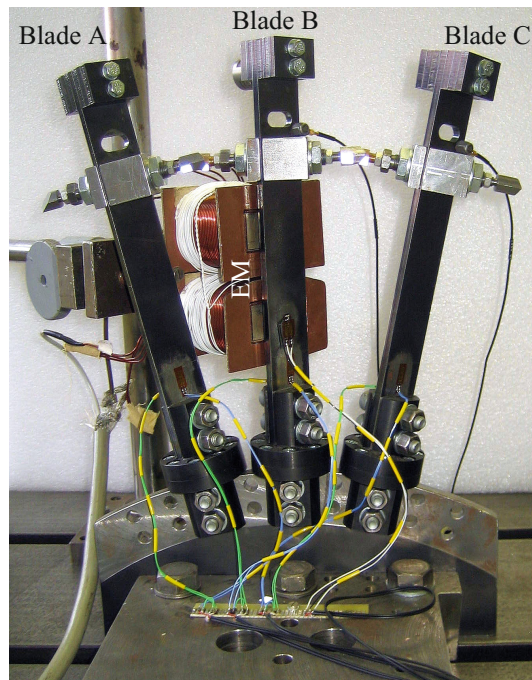


Fig. 4. Picture of experimental set-up of the three-blade-bundle.

For stiffening and friction coupling analysis a short block of harmonic excitation with resonant flexural frequency either 47 Hz (high excitation force level) or 69 Hz (low excitation force level) by electromagnet was performed. These excitation frequencies were ascertained for different excitation levels experimentally by attuning the resonant conditions. The time length of excitation was chosen to achieve a stationary resonant vibration. Then the excitation was switched-off. The damping effect was evaluated from vibration amplitude decay of blades after switching-off the excitation. Damping ratios were identified from amplitude logarithmic decrement by Hilbert's transformation.

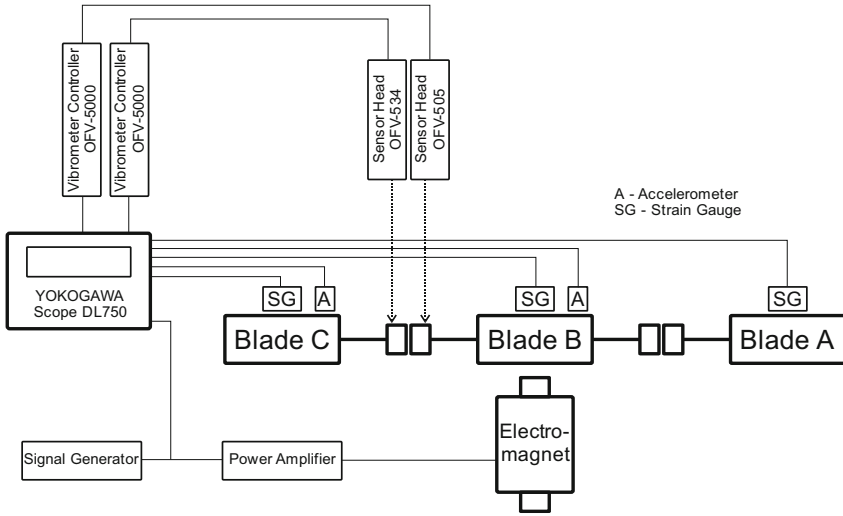


Fig. 5. Schema of the measurement up of the three-blade-bundle.

Each blade displacements u_A , u_B resp. u_C were picked up by strain-gauges and at the same time velocities v_B of the tie-boss end of blade B and v_C of tie-boss of blade C by POLYTEC laser vibrometers. Electromagnet was supplied by LDS power amplifier and controlled by signal of generator HP 33120A. Time characteristics of generator signal, blades and two tie-boss heads responses were registered in Scope Recorder YOKOGAWA DL750 for different force levels and three contact pre-stresses, i.e. 3.25 N, 4.5 N and 9 N.

The value of damping ratios of the blade B vibration was designated for estimation of the friction damping effect in the tie-bosses' contacts. The graph (Fig. 6) shows the dependence of identified damping ratios on amplitudes of forced responses of the blade B for excitation frequency 47 Hz and macroslips in contacts. The typical results of the blade B vibration are shown in the Figs. 7, 8, 9 and 10 for different excitation frequencies 47 Hz (Figs. 7 and 8), 69 Hz (Figs. 9 and 10) and different level of forced amplitudes of the blade B. The top graphs of these figures depict the displacement of the blade B with evaluated damping ratios at the attenuation after switch off of the electromagnet current supply. Bottom graphs show relative displacement of tie-boss ends of the blade B and C (contact BC). The relative displacement was evaluated from the difference of measured velocities v_B and v_C after their integrations. From practical reasons, the linear amplitude decay that is typical for Coulomb's friction law is approximated here by the logarithmic decrement. As seen from the Fig. 7 the resulting exponential function (green line) describes satisfyingly the amplitude decay in the selected narrow time interval. The error of the evaluation of damping ratio is estimated about 10%.

From the Figs. 6, 7, 8, 9 and 10 we can draw these observations:

- (a) At higher excitation force of the blade B and higher response of the blade B and excitation frequency 47 Hz, the adhesion forces in contacts are exceeded, the

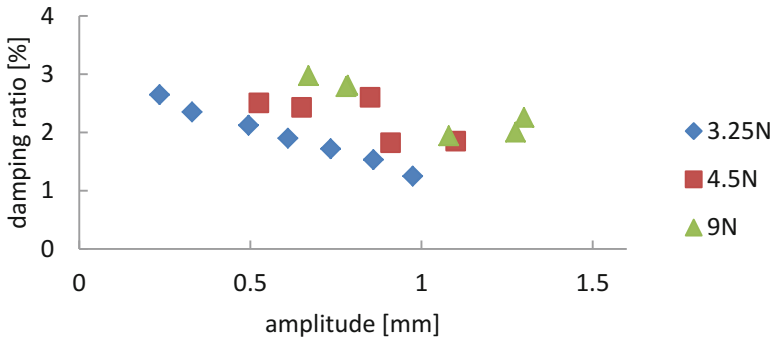


Fig. 6. Macroslip damping ratios for different maximal amplitudes of forced response.

contacts gets into the macroslips and damping ratios is range 1.2–3% (Fig. 7), the size of damping ratio drops with increase of forced amplitudes. The blades vibrate on the same frequency as excitation frequency that corresponds to eigenfrequency of the single contact-free blade. It means that there is no stiffening but only damping effect of the contact with the rest of the bundle.

- (b) At low excitation force of the blade B and excitation frequency 47 Hz, the adhesion forces in contacts are not exceeded, the contacts are in the microslips (relative motions $\approx 1e-3$ mm, Fig. 8) and damping ratios are low around 0.14%. Yet the excitation is 47 Hz, the vibration frequency 69 Hz prevails at the vibration attenuation when amplitudes decay. This frequency approaches to the eigenfrequency of the blade triple with bond contacts (76.4 Hz). It means that there is stiffening but damping effect is low.

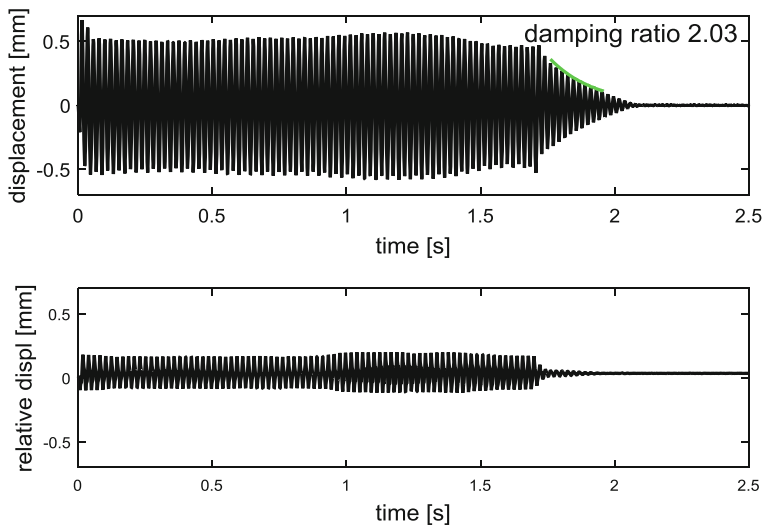


Fig. 7. Measured signals of blade B displacement (top) and relative displacement in contact BC (bottom) during the harmonic excitation with frequency 47 Hz and maximal amplitude 0.6 mm - contact pre-stress 3.25 N.

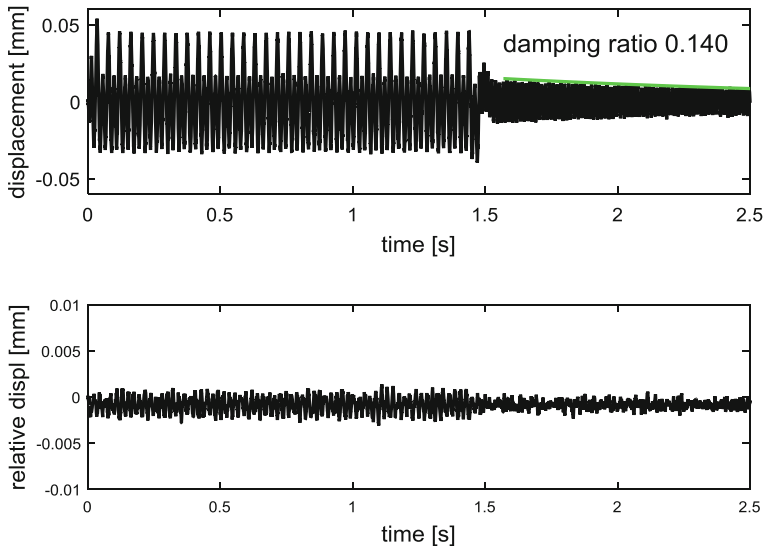


Fig. 8. Measured signals of blade B displacement (top) and relative displacement in contact BC (bottom) during the harmonic excitation with frequency 47 Hz and maximal amplitude 0.05 mm - contact pre-stress 9 N.

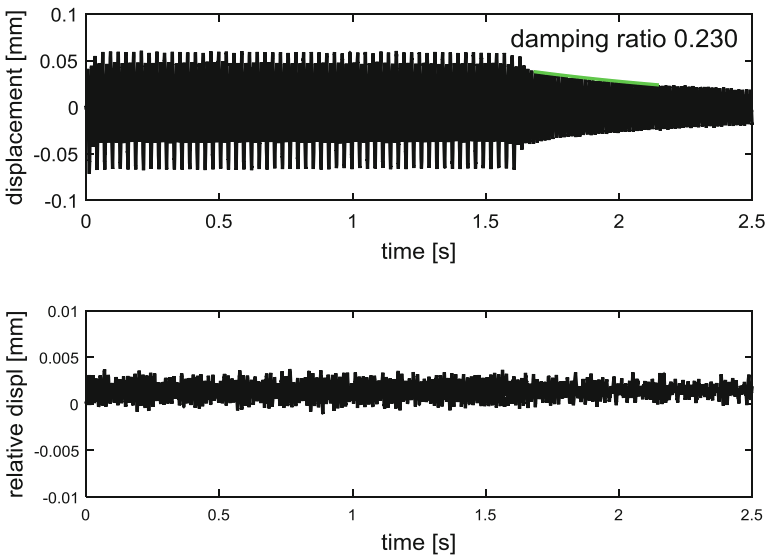


Fig. 9. Measured signals of blade B displacement (top) and relative displacement in contact BC (bottom) during the harmonic excitation with frequency 69 Hz and maximal amplitude 0.06 mm - contact pre-stress 9 N.

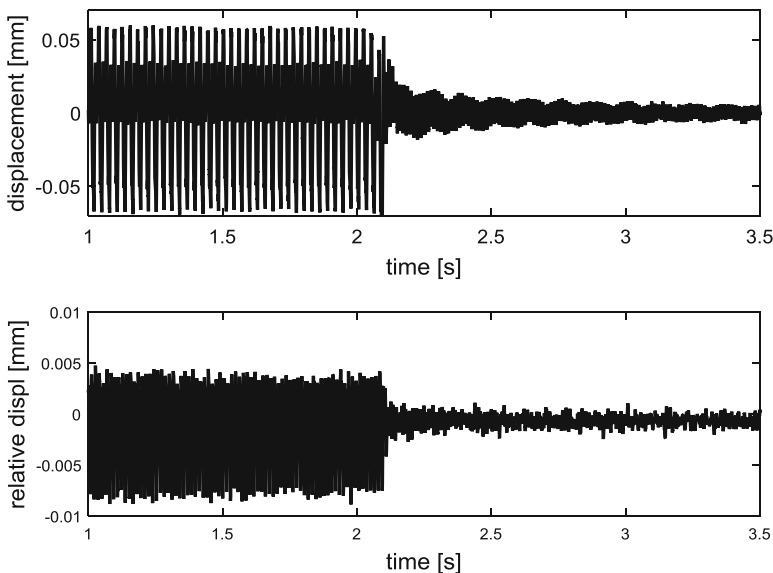


Fig. 10. Measured signals of blade B displacement (top) and relative displacement in contact BC (bottom) during the harmonic excitation with frequency 69 Hz and maximal amplitude 0.05 mm - contact pre-stress 9 N.

- (c) At lower excitation force of the blade B and excitation frequency 69 Hz, the adhesion forces in contacts are not exceeded, the contacts are in the microslips (relative motion $\approx 1e-3$ mm) and damping is low (Fig. 9). By a certain increase of the force the adhesion is exceeded abruptly and the vibration level is decreased and though the excitation was 69 Hz, the vibration attenuation is modulated by frequency 47 Hz (Fig. 10). It means that at the macroslips the decrease of amplitudes is caused not only by damping but mainly by over tuning the system that changes its eigen-frequency to 47 Hz due to macroslips.

It is general feature that the transition from microslips to macroslips and change of dynamical behavior of the system comes very abruptly by achievement of the critical excitation amplitudes.

5 Numerical Results of Three-Blade Finite Element Model

Because of long computational times of the full bladed wheel in case of the non-linear solution due to the friction contacts, we decided to aim at the dynamics of bundle of three blades [12]. Three-dimensional FE model of the bundle with surface-to-surface dynamical friction contacts was developed in the program ANSYS 15.0. The Augmented Lagrangian method was used to compute contact normal pressures and friction stresses. The friction coupling was modeled by the Isotropic Coulomb's law. For a description of the friction coefficient, its dependence on relative velocity was

considered. The pre-stress in contacts was modeled by contact surface offset $2e-5$ m. The resulting normal force in contacts was 4.9 N.

The blade bundle, the global reference system x, y, z and directions of displacements u_x, u_y, u_z are shown in Fig. 11. The detail of the mesh in the vicinity of the contact surfaces is depicted in the Fig. 11. Resonance frequencies of the first flexural eigen-mode of the blade triple for open and bonded contact cases resulted 47.9 Hz and 76.3 Hz, respectively. Then finally a transient non-linear analysis of blade triple with friction contacts was performed for loading cases: force amplitude $A = 28.2$ N, excitation frequency $f_E = 47.9$ Hz corresponding to the eigen-frequency of the first flexural mode of the open contact blade triple. Excitation force is applied at the head of the middle blade in direction perpendicular to a plane of the blade.

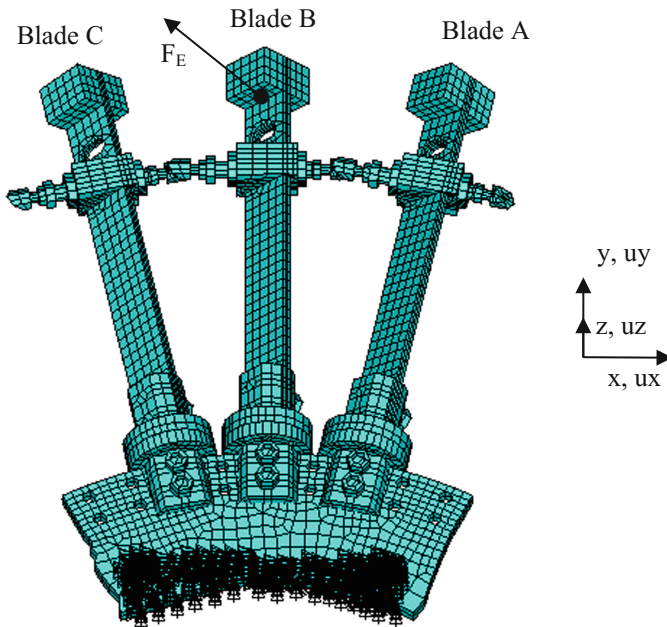


Fig. 11. FE mesh of triple blade model with excitation force F_E .

The computed contour maps of the total displacements and a detail of the contact states (sliding-sticking) are depicted in the Fig. 12a, b for a selected computational time. The contact states are very time and space variable. In most times the contact is concentrated in small areas of the contact surfaces and is in a sliding state due to higher vibrational amplitudes.

The time characteristic of the vector sum both of displacement of the blade B at its end (node N166200) and excitation force are shown in the Fig. 13. From the force course it can be seen that after five periods the excitation is switched off. The damping ratio was evaluated at this period from the amplitude attenuation by the envelope method (green line, Fig. 13). Fast decrease of amplitudes with high damping ratio 1.98% is achieved. Blade displacements u_x is the same but opposite to u_z what means that a plane of vibration

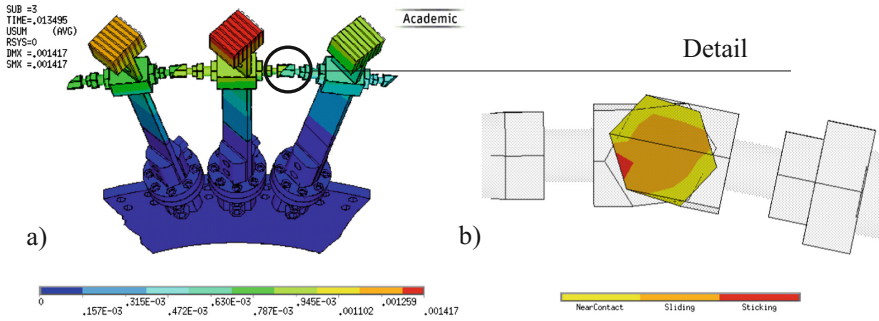


Fig. 12. Computed contour maps of (a) total displacement; (b) detail of contact status (sliding, sticking) in a computational time 0.013495 s.

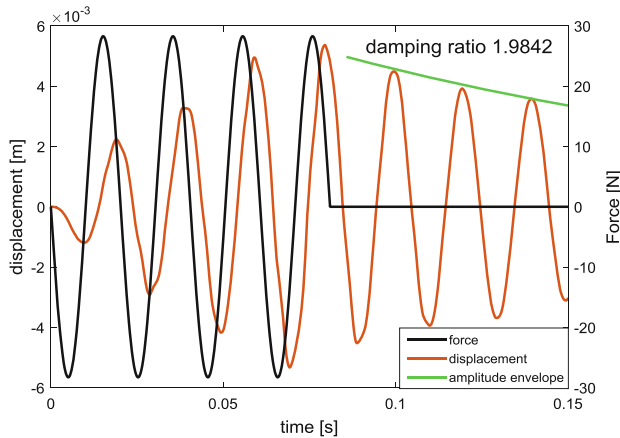


Fig. 13. Time characteristics of vector sum of (a) displacements (red line) of the blade B; (b) excitation force (black line).

of the blade B lies perpendicular to the plane of the blade. The displacements of blades A and C are mutually very similar and phase-shifted to the displacements of the blade B. It means that there is relative motion in the contacts between blade pair A, B and B, C and the motion of blades A, C to the blade B is almost symmetric.

6 Dynamical Tests of Bladed Wheel Under Revolutions

Experimental tests under revolutions were performed on the rotary test stand of the Institute [12]. The model wheel is driven by the three-phase synchronous engine ABB (10 kW) supplied by a current from the frequency converter ACSM1. The bladed wheel excited by eight exciting electromagnets EM1 ÷ EM8 distributed along the circumference of the wheel. Strain gauges were glued on three blades for measurement of the blade vibration. The absolute encoder ECN1313 was used for the angular speed detection.

To obtain maximal amplification of the bladed wheel vibration the control algorithm of exciting electromagnets was developed [13]. The algorithm generates narrow force pulses of magnetic field of electromagnets at the moment of blade passage around the electromagnet. On the other hand a maximum amplification of the vibration arises when the blade moves in the direction of the attractive pulse magnetic force. Since an impulse excitation causes, in general, transient oscillations of many superposed eigenmodes of the wheel we used herein a strategy of interconnections of electromagnets into groups. For by more-magnetic pulse excitations with the same force orientation and intensity a more uniform distribution of the excitations on the wheel is provided. Electromagnets were grouped to pairs (EM1, EM5) and (EM3, EM7). The blades L1 (see Fig. 2) and L16 (diametrically opposed to L1) were simultaneously excited by the pairs of synchronized electromagnets. Vibration modes with 2ND, 4ND vibration modes were mainly ascertained practically in whole range of revolutions.

The result of the test under revolution of the open contact wheel model is shown in the Campbell diagram (Fig. 14). This colored map spectrogram of amplitude-frequency dependences on revolutions was evaluated in the automatized data acquisition system PULSE, B&K at a slow run up (60 up to 450 rpm in 250 s) of the driving engine.

The Campbell diagram was evaluated from the strain-gauge signal of blade L1. The sloping lines of the vibration with a revolution frequency and its multiples and vertical branch of the flexural vibration (2ND, 4ND) are visible in the diagram. The engine order lines were mainly generated by revolution dependent deflections of blades from unbalances and gravitation forces.

The same electromagnetic excitation system will be used for study of stiffening and damping effects of the wheel model with pre-stressed contacts. The same evaluation method will be used as in the case of the blade triple. Electromagnet excitation will pull the wheel into the resonance. Then the excitation will be switched off and the eigenfrequencies and damping ratios will be evaluated from the free attenuation.

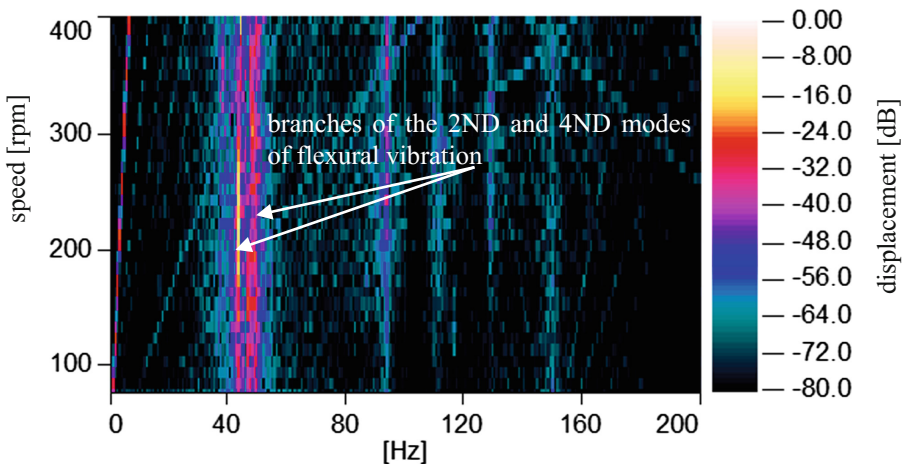


Fig. 14. Campbell diagram of the blade wheel vibration - open contacts.

7 Conclusion

Bladed wheel model with tie-boss couplings for numerical and experimental investigation of stiffening and friction damping in tie-bosses was herein introduced. The modal behavior of FE numerical model for two contact limit states was ascertained. The experimental modal analysis of the wheel both for open contacts and for contacts in pre-stress were performed, too.

For detail stiffening and damping effect investigation the physical model of blade triple was elaborated. The experiments were performed for different excitation forces, excitation frequencies and contact pre-stresses. The dynamics of the bundle with respect to contact states was analyzed from vibration attenuation after short resonant excitation.

It was observed that if the macroslips arise in contacts that eigen-frequencies of the blade bundle are very close to the eigen-frequencies of bundle with open contacts with high damping effect (about 2–3%). If the macroslips arise in contacts the eigen-frequencies are close to eigen-frequencies of the bundle with the bond contacts with low damping (about 0.2%). Hence the stiffening effect is high in the case of macroslips but the stiffening is eliminated after transition into the macroslips. The transition is conditioned by level of adhesion forces that must be exceeded by excitation force. The transition is very narrow and arises abruptly at small increase of the excitation force level.

The FE model of the wheel and blade triple model with dynamic frictional contacts in the tie-boss couplings were developed. Due to long computation time of non-linear dynamical responses of the full bladed disk, first the triple model was dealt with. The results of dynamical response of the triple for one typical excitation case and pre-stress condition in contacts is shown and discussed. The evaluated stiffening and damping results are in a good accordance with our experimental observations. The full bladed wheel is going to be computed at the national super-computer center in Ostrava (IT4Innovations) and the results will be included in the conference presentation.

Acknowledgements. This work was supported by the research project of the Czech Science Foundation No. 16-04546S “Aero-elastic couplings and dynamic behaviour of rotational periodic bodies”.

References

1. Drozdowski, R., Volker, L., Hafele, D., Vogt, D.M.: Experimental and numerical investigation of the nonlinear vibrational behavior of steam turbine last stage blades with friction bolt damping elements. In: Proceedings of the ASME Turbo Expo 2015, Canada, 15–19 June, vol. 8 (2015)
2. Pešek, L., Hajžman, M., Půst, L., Zeman, V., Byrtus, M., Brůha, J.: Experimental and numerical investigation of friction element dissipative effects in blade shrouding. *J. Nonlinear Dyn.* **79**(3), 1711–1726 (2015)
3. Pešek, L., Půst, L., Bula, V., Cibulka, J.: Investigation of dry friction effect of shroud damping wire on model test bladed wheel. In: Proceedings of ASME 2013, IDETC/CIE 2013, DETC2013-12851, Portland, Oregon, USA, p. 7 (2013)

4. Pennacchi, P., Chatterton, S., Bachschmid, N., Pesatori, E., Turozzi, G.: A model to study the reduction of turbine blade vibration using the snubbing mechanism. *Mech. Syst. Sig. Process.* **25**(4), 1260–1275 (2011)
5. Rizvi, A., Smith, C.W., Rajasekaran, R., Evans, K.E.: Dynamics of dry friction damping in gas turbines: literature survey. *J. Vib. Control* **22**(1), 296–305 (2016)
6. Pešek, L., Půst, L.: Blade couple connected by damping element with dry friction contacts. *J. Theor. Appl. Mech.* **52**(3), 815–826 (2014)
7. Sextro, W.: *Dynamic Contact Problems with Friction*. Springer, Berlin (2002)
8. Voldřich, J., Lazar, J., Polach, P., Morávka, Š.: Finding the stiffnesses of interface contact elements for the computational model of steam turbine blading. In: *Proceedings of ASME IDETC/CIE 2017 Conference*, Cleveland, Ohio, USA, p. 12 (2017)
9. Petrov, E.P.: Method for direct parametric analysis of non-linear forced response of bladed disks with friction contact interfaces. *ASME J. Turbomach.* **126**, 654–662 (2004)
10. Yamashita, Y., Shiohata, K., Kudo, T., Yoda, H.: Vibration characteristics of a continuous cover blade structure with friction contact surfaces of a steam turbine. In: *Proceedings of 10th International Conference on Vibrations in Rotating Machinery (VIRM)*, pp. 323–332 (2012)
11. Pešek, L., Půst, L., Bula, V., Cibulka, J.: Numerical analysis of dry friction damping effect of tie-boss couplings on three blade bundle. In: *Proceedings of ASME IDETC/CIE 2017 Conference*, Cleveland, Ohio, USA, p. 7 (2017)
12. Pešek, L., Vaněk, F., Procházka, P., et al.: Dynamics of rotating blade disk identified by magneto-kinematic measuring system. In: *Proceedings of the International Conference on Noise and Vibration Engineering (ISMA)*, KU Leuven, pp. 1097–1112 (2008)
13. Pešek, L., Půst, L., Bula, V., Cibulka, J.: Development of laboratory tip-timing optical measurement system of rotating bladed wheel excited by electromagnetic pulses. In: Rzadkowski, R., Szczepanik, R. (eds.) *Proceedings of VETOMAC-XII Conference*, Warszawa, pp. 119–128 (2016)



Parametric Study of the Effects of Varying the Airfoil Section, the Chord and Pitch Distributions Along the Propeller Blade

Kamal A. R. Ismail and Célia V. A. G. Rosolen^(✉)

School of Mechanical Engineering, Department of Energy,
University of Campinas, Rua Mendeleiev, 200,
Cidade Universitária “Zeferino Vaz”, Campinas, SP 13083-860, Brazil
kamal@fem.unicamp.br, c.rosolen@uol.com.br

Abstract. The flow through the rotor of a propeller is complex and cannot be solved by pure analytical methods. Varieties of numerical methods were used to handle this problem including the momentum theory, blade element theory, lifting line theory, panel methods and CFD analysis. The objective of this study is to look into the possible use of alternative airfoils (Joukowski and Göttingen) for use in small propellers calculated by a simple validated home-built FORTRAN code based on the momentum theory and blade element theory. This code was then used to investigate the effects of the airfoil section, chord and pitch angle distributions along the blade. The linear pitch distribution in blades of propeller reduced the coefficients of thrust and power and indicated higher blade loading at the intermediate region and lower loading at the tip region in comparison with the Göttingen 796 propeller with the reference pitch distribution. With reference to the two investigated airfoils sections, Göttingen 796 and generalized Joukowski, it was found that the thrust and the power coefficients and the efficiency of the generalized Joukowski propeller are greater than the respective coefficients of Göttingen 796 propeller for advanced ratio $J = 0.85$ and higher. The predicted results indicated that the use of the elliptical chord distribution instead of tapered blade reduces the blade loading at the tip region and increases it at the intermediate region of the blade, but also reduces the coefficient of thrust, torque and power in comparison with the blade having the reference chord distribution.

Keywords: Small propeller · Momentum theory · Blade element theory
Blade aerodynamics · Airfoil section

1 Introduction

Small and medium size rotors are used in many recent applications as in propulsion of small airplanes, unmanned aerial vehicles (UAV), autonomous underwater vehicle (AUV), and small wind turbines and ducted propellers. Understanding rotor action and interaction with wake flow field are important aspects to better formulate and predict the performance of propeller rotors and wind turbines. Momentum theory applied to rotors and blade element theory were widely used for light loaded blades. Theodorsen [1] developed the propeller theory with ideal load distribution from the dynamics of the

wake vortex sheet. This condition of maximum propeller efficiency occurs when the wake vortex sheets are helicoidal without any deformation.

The flow over the rotors is very complex due to the circular movement of the blades and the strong interaction with the wake. For this reason, the precise calculation of the aerodynamic behavior of the rotor depends on the correct modeling of the rotor wake, whose complex structure limits pure analytical methods and hence the numerical methods are inevitably necessary [2].

Dumitrescu and Cardoso [2] used a lifting line method to replace the wind turbine blades with the trailing vortices shed along the turbine blade. The model is nonlinear and was solved iteratively. The performance parameters were calculated by the Biot–Savart law and the Kutta–Joukowski theorem.

Palmiter and Katz [3] used a three-dimensional potential flow based panel code to model the flow over rotating propeller blades. They modified an existing panel code and studied the wind turbine and propeller flows and validated their predictions with available results.

Bohorquez, Pines and Samuel [4] developed a low cost computational methodology to design and optimize hovering rotors for small-scale vehicles using circular arc airfoils. Detailed experimental investigation on rectangular and tapered blades generated the data necessary to identify performance trends and the effect of planform modifications. A blade element momentum theory was implemented. Validation showed that the model predictions improved with the empirical correlations and the methodology used proved is adequate to optimize the blade geometry and operating conditions following imposed constraints within a defined design space.

Khan and Nahon [5] presented a slipstream model which uses simple analytical and semi-empirical equations. The numerical predictions were found to agree with experimental data.

Morgado *et al.* [6] used the software JBLADE for the design and optimization of a new propeller. The airfoil characteristics were obtained from coupling of a BEM formulation module and XFOIL. The inverse design methodology, due to Adkins and Liebeck method, was used to calculate the chord and twist angle of the blades. The approach based on the concept of maximum $L^{3/2}/D$ generated bigger pressure differences between upper and lower surfaces with less friction which mean more thrust than the blade designed with the concept of maximum L/D .

The objective of this study is to investigate the possible use of alternative airfoils (Joukowski and Göttingen) for the rotors of small propellers calculated by a simple a home-built FORTRAN code based on the momentum theory and blade element theory and validated against available experimental and numerical results. The numerical code was then used to investigate the effects of the airfoil section, the distributions of chord and pitch angle along the blade.

2 Formulation

The propeller develops an axial force called thrust T at an advance V for a rotational n due to a torque Q . In this manner the propeller efficiency is the ratio of the useful power to the power input P

$$\eta = TV/(2\pi n Q) \quad (1)$$

The aerodynamic characteristics are usually expressed by dimensionless forms which depend on the Reynolds and Mach numbers based on the blade tip velocity and the advance ratio J . The advance ratio is defined as

$$J = V/(nD) \quad (2)$$

while the tip velocity is given by

$$V_{tip} = \pi n D \quad (3)$$

The thrust k_T , torque k_Q and the power k_P coefficients are defined as

$$k_T = T/(\rho n^2 D^4) \quad (4)$$

$$k_Q = Q/(\rho n^2 D^5) \quad (5)$$

$$k_P = P/(\rho n^3 D^5) = 2\pi k_Q \quad (6)$$

In terms of these coefficients the efficiency of the propeller can be alternatively written as

$$\eta = J k_T / k_P \quad (7)$$

As mentioned before, the calculation routine to predict the general performance of the propeller associates the momentum theory due to Rankine and Froude [7] with Glauert blade element theory [8]. The Froude momentum theory treats the propeller as a disc with an axial velocity in relation to the disc given by the advance velocity V corrected by the inflow factor a ,

$$V_0 = V(1 + a) \quad (8)$$

From the linear momentum conservation and the pressure difference across the disc, the velocity component well behind the disc V_S is

$$V_S = V(1 + 2a) \quad (9)$$

Glauert's blade element theory for propellers indicates that the velocity component in the plane of rotation V_w can be calculated from

$$V_w = 2\pi n(1 - b)r \quad (10)$$

where b is the swirl factor which accounts for the effects of the wake vortex system on the flow angular velocity in the rotor plane.

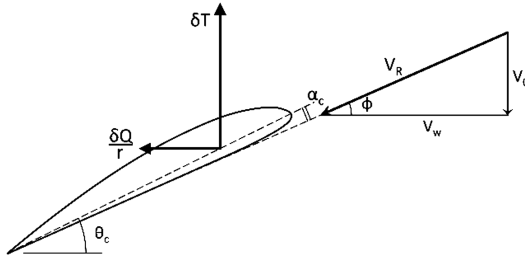


Fig. 1. Cross section of the rotor blade at radius r indicating the velocity components and the acting forces.

Applying the principle of conservation of linear momentum to the flow in an infinitesimal radial ring one can determine the elementary thrust as

$$dT = 4\pi\rho rV^2a(1+a)dr \tag{11}$$

Similarly, the elementary torque is given by

$$dQ = 4\pi\rho r^3 V b(1+a)2\pi ndr \tag{12}$$

The elementary thrust and torque can be obtained alternatively from the lift and drag acting on the blade element as below

$$dT = Bc\frac{1}{2}\rho V_R^2(C_\ell \cos\phi - C_d \sin\phi)dr \tag{13}$$

$$dQ = Bcr\frac{1}{2}\rho V_R^2(C_\ell \sin\phi + C_d \cos\phi)dr \tag{14}$$

where B is the number of blades, V_R is the resultant velocity with reference to the blade and ϕ is the angle of the vector V_R with the plane of rotation of the propeller, Houghton *et al.* [9].

The local resultant velocity V_R is given by

$$V_R = V_0/\sin\phi = V_w/\cos\phi \tag{15}$$

while the angle ϕ is calculated from

$$\phi = \tan^{-1}\left[\frac{V_0}{V_w}\right] = \tan^{-1}\left[\frac{J}{2\pi(r/D)}\left(\frac{1+a}{1-b}\right)\right] \tag{16}$$

The angle of attack α_c is the angle between the resultant velocity V_R and the chord, calculated as the difference between the pitch angle (twist) of the blade section θ_c and the angle ϕ of the resultant velocity (Fig. 1). The pitch angle θ_c is defined as the angle

between the local chord and the plane of rotation of the propeller. The geometric pitch p of the blade section is related to the pitch angle θ_c by the expression $p = 2\pi r \tan \theta_c$.

The geometry of the blade is usually given by the distributions of chord, thickness and the geometrical pitch as function of radius. The pitch angle of the blade is defined as the pitch angle of the blade section localized at $r = 0.75R$, where R is the radius of the blade tip, $R = D/2$.

Equating Eqs. (11) to (13) and Eqs. (12) to (14) one can obtain

$$a = (1 + a) \frac{\sigma}{4 \sin^2 \phi} (C_\ell \cos \phi - C_d \sin \phi) \quad (17)$$

$$b = (1 + a) \frac{\sigma}{4 \sin^2 \phi} (C_\ell \sin \phi + C_d \cos \phi) \frac{J}{2\pi (r/D)} \quad (18)$$

where σ is the solidity defined as $\sigma = (Bc)/(2\pi r)$.

Equations (17) and (18) can be used to calculate the factors a and b iteratively.

The thrust loading coefficient δk_T of the blade element δr at r is given by

$$\delta k_T = \frac{\frac{dT}{dr}}{B\rho n^2 D^4} \delta r = \frac{1}{2} c \left[\frac{J(1+a)}{D \sin \phi} \right]^2 (C_\ell \cos \phi - C_d \sin \phi) \delta r \quad (19)$$

While the torque loading coefficient of the blade δk_Q is given by

$$\delta k_Q = \frac{\frac{dQ}{dr}}{B\rho n^2 D^5} \delta r = \frac{1}{2} c \left[\frac{J(1+a)}{D \sin \phi} \right]^2 (C_\ell \sin \phi + C_d \cos \phi) \frac{r}{D} \delta r \quad (20)$$

The coefficients of thrust k_T and the torque k_Q of the propeller can be obtained by integrating Eqs. (19) and (20) from the root of the blade to the tip and then multiplying the result by the number of blades B .

One can see that the radial loading coefficients of the blade δk_T and δk_Q depend on the airfoil geometry, its aerodynamic characteristics and the advance ratio J . This also applies to the coefficients of thrust k_T , torque k_Q and power k_P of the propeller. The specification of the value of the advance velocity V or the rotation n determines the Reynolds number of the propeller Re_{75} and allows calculation the global values of thrust T , torque Q and power P . The calculations can be repeated for new values of C_ℓ and C_d coefficients of the local blade chord of the airfoil section, according to the local Reynolds number.

2.1 Validation

To establish the validity of this method and its viability in calculating the propeller performance and/or its pre dimensioning, the numerical predictions from the present method are compared with experimental results [10] and numerical predictions based on panel method [3]. The available experimental results are for the propeller Clark Y 5868-9, with airfoil Clark Y, 3.048 m diameter, two blades and for two blade pitch

angles of 25° and 35° [10]. Palmiter and Katz [3] realized recent numerical results for the same propeller, they used three-dimensional panel method.

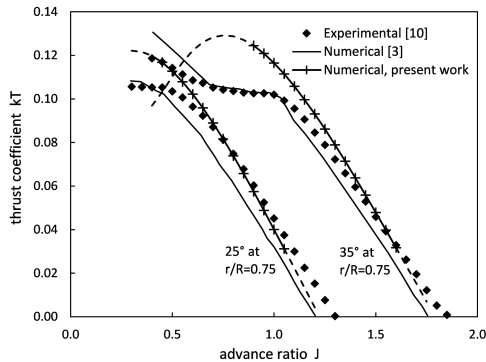


Fig. 2. Variation of the thrust coefficient with the advance ratio for propeller Clark Y 5868-9.

Figure 2 shows a comparison of coefficient of thrust k_T predicted from the present method compared with the experimental results and with the numerical predictions calculated by the panel method. As can be seen the agreement is good for the case of pitch angle of 25° . When the pitch angle is increased to 35° , there is noticeable divergence between the present predictions and the experimental results for low advance ratios due to possible flow separation [3], which is not accounted for in the both numerical methods.

3 Results and Discussion

The reference propeller used here for comparison is the Clark-Y 5868-9 propeller for which Hartman and Biermann [10] presented the geometry and the experimental results. It has Clark-Y airfoil for the blades, two blades, 3.048 m diameter and pitch of 25° . The present code used the data available in Lyon *et al.* [11] for Reynolds number of 3.0×10^5 .

The validated code was used to calculate a propeller with a new airfoil Göttingen 796 similar to the original airfoil Clark-Y but has a higher value of the ratio Cl/Cd . The characteristics of Göttingen 796 were determined from XFOIL [12] for Reynolds numbers of 0.50×10^6 , 0.75×10^6 , 1.00×10^6 , 1.25×10^6 , 1.50×10^6 , 1.75×10^6 and 2.00×10^6 . The curves of the lift and drag coefficients were obtained in terms of the angle of attack for increments of 0.25° , and incorporated in the numerical code.

Göttingen 1 propeller has exactly the same geometry and operational conditions as the reference propeller except that the airfoil section is Göttingen 796.

Figure 3 shows a comparison of the predicted thrust and power coefficients and efficiency of the Göttingen 1 and the reference propellers. As can be seen the Göttingen 1 propeller shows higher values due to the differences in the aerodynamic characteristics of the two airfoils.

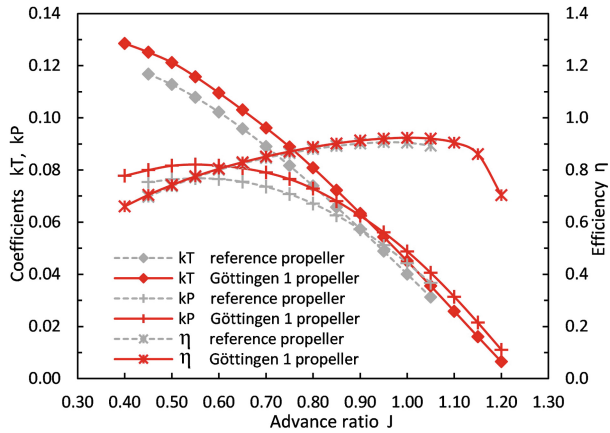


Fig. 3. Comparison of aerodynamic coefficients of Göttingen 1 and reference propellers.

Figure 4 shows the spanwise distribution of blade loading for both propellers for the advance ratio $J = 1$ corresponding to maximum efficiency. The root region is defined between $r/R = 20\%$ and $r/R = 40\%$, while the tip region is defined between $r/R = 80\%$ and the blade tip. The respective local contributions of the three regions of Göttingen 1 propeller to the total thrust are: -1.3% for root region, 48.3% for the intermediate region and 52.9% for the tip region. In the case of the reference propeller the contributions are: -1.6% for root region, 48.4% for the intermediate region and 53.2% for the tip region.

Similar results were obtained for the Joukowski airfoil and were omitted for the sake of brevity.

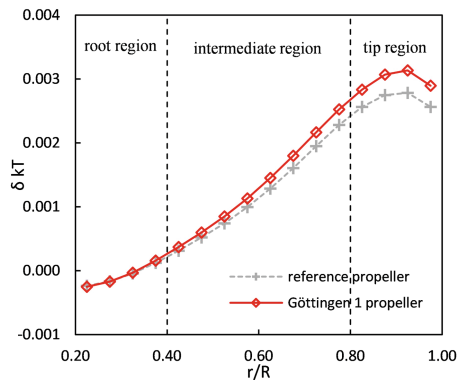


Fig. 4. Comparison of thrust loading distribution of Göttingen 1 and reference propellers.

3.1 Distribution of Pitch Angle

The reference and the Göttingen 1 propellers have the same reference distribution of pitch angle along the blade as presented in Hartman and Biermann [10] for the Clark-Y 5868-9 propeller, shown in Fig. 5(a).

To investigate the effect of the pitch distribution on the performance of the propeller we introduce Göttingen 2 propeller which is exactly the same as the Göttingen 1 propeller except it has linear pitch angle distribution along the blade, as in Fig. 5(a). The values of the angles of attack for each section of the blade calculated according to Sect. 2 are shown in Fig. 5(b).

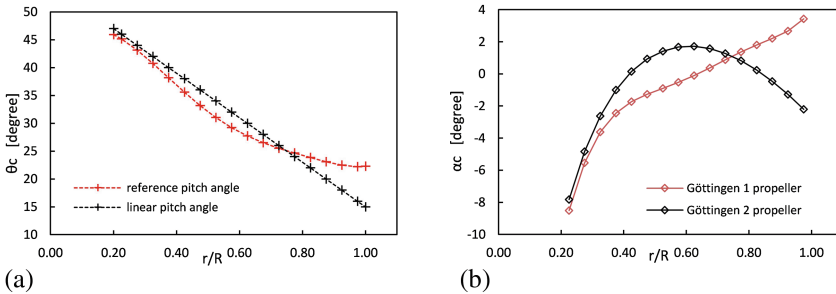


Fig. 5. Comparison of proposed linear pitch angle distribution and reference pitch angle distribution: (a) pitch angle distribution; (b) local angle of attack for advance ratio $J = 1.0$.

Figure 6 shows the predicted results of the thrust and power coefficients as well as the efficiency for the Göttingen 1 propeller and the Göttingen 2 propeller. One can observe that Göttingen 2 propeller shows lower coefficients of thrust and power with nearly the same efficiency, than Göttingen 1 propeller.

Figure 7 shows that Göttingen 2 propeller (based on assuming linear distribution of pitch angle) results in higher blade loading at the intermediate region and lower blade loading at the tip region in comparison with Göttingen 1 propeller (based on the reference distribution as shown in Fig. 5(a)). Also one can observe that the linear distribution of pitch angle favors reduced loading at the tip region which helps reducing mechanical loads at the root region. As can be seen from Fig. 5(b), the use of the linear pitch angle distribution of the blade produces larger local angles of attack in the intermediate blade region and smaller in the blade tip region than those produced by the reference distribution of pitch angle.

The respective local contributions of the three regions of Göttingen 2 propeller to the total thrust are: 0.8% for root region, 73.5% for the intermediate region and 25.7% for the tip region. In the case of the Göttingen 1 propeller the contributions are: -1.3% for root region, 48.3% for the intermediate region and 52.9% for the tip region.

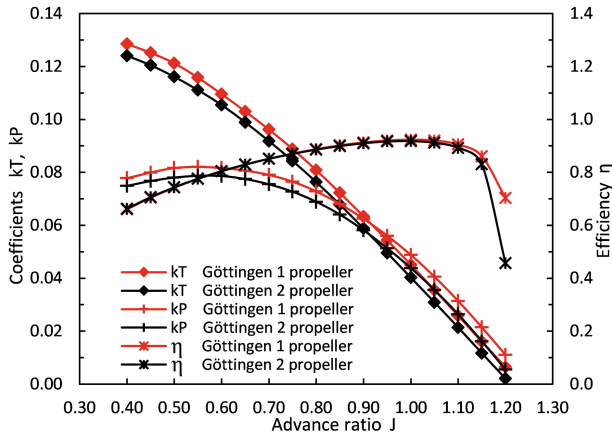


Fig. 6. Comparison of aerodynamic coefficients of Göttingen 2 and Göttingen 1 propellers.

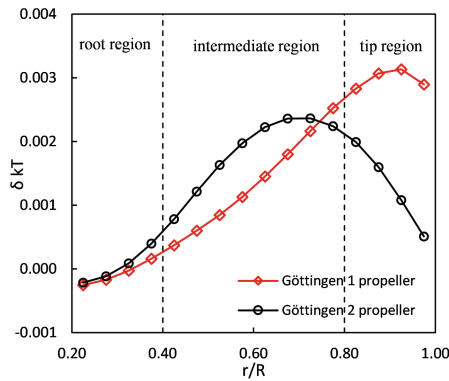


Fig. 7. Comparison of thrust loading distribution of Göttingen 2 and Göttingen 1 propellers for advance ratio $J = 1.0$.

3.2 Effect of Airfoil Section

To investigate the effect of airfoil section two families of airfoils were selected that is Göttingen and Joukowski. The traditional Joukowski airfoil has a thin trailing edge which makes it unsuitable for the present application. Glauert [13] presented a method to obtain generalized airfoils more suitable for practical use by using the conformal transformation $[(\zeta - nc)/(\zeta + nc)] = [(z - c)/(z + c)]^n$. Details of this transformation can be found in [13]. The generalized Joukowski generated for this study has general characteristics similar to those of Göttingen 796 as can be seen in Table 1.

Joukowski 2 propeller has exactly the same geometry and operational conditions as the Göttingen 2 propeller except that the airfoil section is a generalized Joukowski airfoil.

Figure 8 indicates that the thrust and the power coefficients and the efficiency of the Joukowski 2 propeller are greater than the respective coefficients of Göttingen 2 propeller for advanced ratio $J = 0.85$ or higher.

Table 1. Characteristics of Göttingen and generalized Joukowski airfoils.

Airfoil Section	Maximum thickness/chord (%)	Maximum camber/chord (%)	Trailing edge angle (radians)
Göttingen 796 airfoil	12.0 at 30% chord	3.6 at 40% chord	–
Generalized Joukowski airfoil ($k = 1.060, \beta = 4.5^\circ, n = 1.920$)	12.3 at 36.8% chord	3.8 at 51.8% chord	0.2513

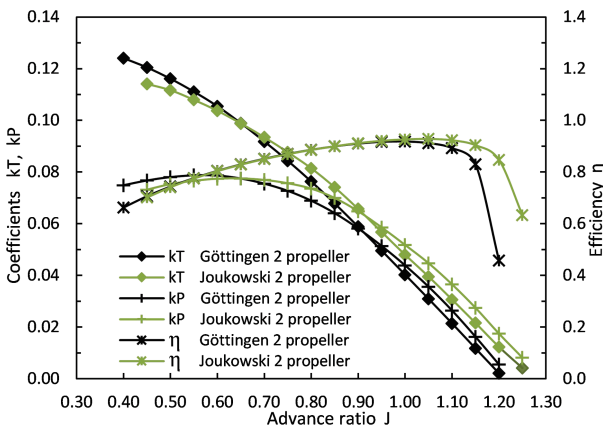


Fig. 8. Comparison of aerodynamic coefficients of Joukowski 2 propeller and Göttingen 2 propeller, both propellers with the same reference chord and linear pitch angle distributions.

Figure 9 indicates that the blade thrust loading of the Joukowski 2 propeller is higher but follows the same trend as the loading of Göttingen 2 propeller. Both propellers have well-loaded intermediate region and less loaded blade-tip region due to the linear pitch angle distribution.

The respective local contributions of the three regions of Joukowski 2 propeller to the total thrust are: 2.1% for root region, 69.6% for the intermediate region and 28.3% for the tip region. In the case of the Göttingen 2 propeller the contributions are: 0.8% for root region, 73.5% for the intermediate region and 25.7% for the tip region.

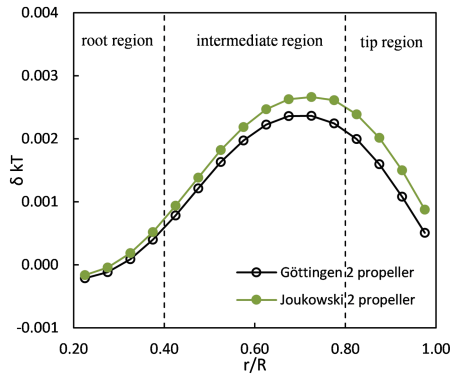


Fig. 9. Comparison of thrust distribution of Joukowski 2 propeller and Göttingen 2 propeller for advance ratio $J = 1.0$.

3.3 Effect of Chord Distribution

Further calculations were realized to investigate the effects of chord distribution on the blade loading and on the performance characteristics of the propeller.

Propeller with Göttingen Airfoil. In this case the propellers have exactly the same geometry, same operational conditions, and the same airfoil Göttingen 796 and have linear pitch angle distribution along the blade, as the Göttingen 2 propeller, but the chord distribution is modified according to the taper ratios $\lambda = 1.0$, $\lambda = 0.75$, $\lambda = 0.50$, $\lambda = 0.30$ and for elliptical chord distribution along the blade. The blade loading is calculated for the above taper ratios.

Figure 10 shows that tapered blade reduces the local loading at the tip region of the blade in comparison with the reference chord distribution. This change becomes more noticeable with the increase of the blade taper or decrease of λ . However, the taper does not increase the blade loading at intermediate region of the blade as much as the reference chord distribution does.

One can also observe that the elliptical chord distribution resulted in severe loading reduction in comparison with the reference chord distribution and the tapered blades. The results for elliptical chord are close to those of the blade with taper ratio of 0.30. Effects of varying the chord distribution for advance ratio $J = 1.0$ are shown in Table 2 and Fig. 10.

The numerical predictions show that the reduction of the blade loading at the tip region and its increase in the middle part of the blade can be obtained by adopting linear distribution of the pitch angle or by using tapered blade. In the case of tapered blades these effects are intensified by the increase of the blade taper ratio. It is also possible to observe from the predicted results that the use of the elliptical chord distribution instead of tapered blade accentuates these effects. However, the changes in the geometry of the blade reduce the blade loading near the tip but also reduce the coefficient of thrust, torque and power at nearly constant efficiency, in comparison with the blade having the reference chord distribution.

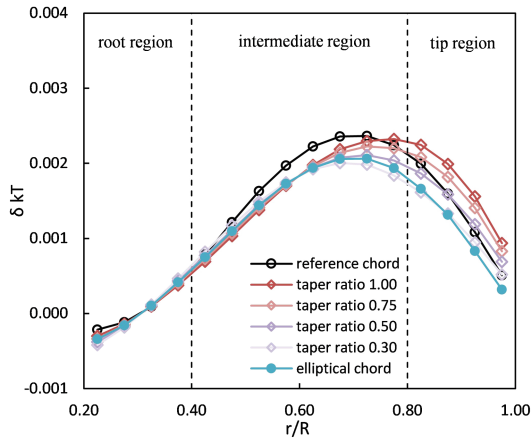


Fig. 10. Comparison of thrust distribution of propellers using airfoil Göttingen 796 and different chord distributions along the blade, for advance ratio $J = 1.0$ (all propellers have linear pitch angle distribution).

Table 2. Performance characteristics and blade loadings of the propellers with Göttingen 796 airfoil and different chord distributions on the blade for $J = 1.0$ (linear pitch angle distribution).

Chord	η	$T(N)$	$Q(Nm)$	Thrust loading of the blade (%)		
				Root	Intermediate	Tip
Reference	0.9182	1183	625	0.79	73.47	25.74
Straight $\lambda = 1.00$	0.9154	1195	633	0.15	66.78	33.07
Tapered $\lambda = 0.75$	0.9169	1151	609	0.07	68.61	31.32
Tapered $\lambda = 0.50$	0.9182	1090	576	-0.02	71.31	28.71
Tapered $\lambda = 0.30$	0.9194	1020	538	-0.12	74.72	25.40
Elliptical	0.9222	1008	530	0.13	75.84	24.03

Propeller with Generalized Joukowski Airfoil. A similar study is also made for the propellers with generalized Joukowski airfoil section.

The propellers have exactly the same geometry and operational conditions as the Joukowski 2 propeller, with generalized Joukowski airfoil and linear pitch angle distribution along the blade, except that the chord distribution is modified. The chord length in the middle of the blade height is keeping equal to the value corresponding to that of the reference propeller. The blade loading is calculated for taper ratio $\lambda = 1.0$, $\lambda = 0.75$, $\lambda = 0.50$, $\lambda = 0.30$ and for elliptic blade.

The results shown in Table 3 indicate that blades with linear taper ratio of 0.3 reduce the tip loading, while keeping the intermediate region as loaded as that of the elliptic blade and increase slightly the loading at the root region (Fig. 11). These aspects can help to achieve possible improvements in blade design, performance and weight reduction etc.

Table 3. Performance characteristics and blade loadings of the propellers with generalized Joukowski airfoil and different chord distributions on the blade for $J = 1.0$ (linear pitch angle distribution).

Chord	η	$T(N)$	$Q(Nm)$	Thrust loading of the blade (%)		
				Root	Intermediate	Tip
Reference	0.9265	1409	738	2.09	69.64	28.28
Straight $\lambda = 1.00$	0.9257	1456	763	1.65	61.88	36.47
Tapered $\lambda = 0.75$	0.9272	1400	732	1.78	63.72	34.50
Tapered $\lambda = 0.50$	0.9287	1320	689	1.99	66.41	31.60
Tapered $\lambda = 0.30$	0.9298	1229	641	2.25	69.95	27.80
Elliptical	0.9311	1201	626	2.17	71.74	26.09

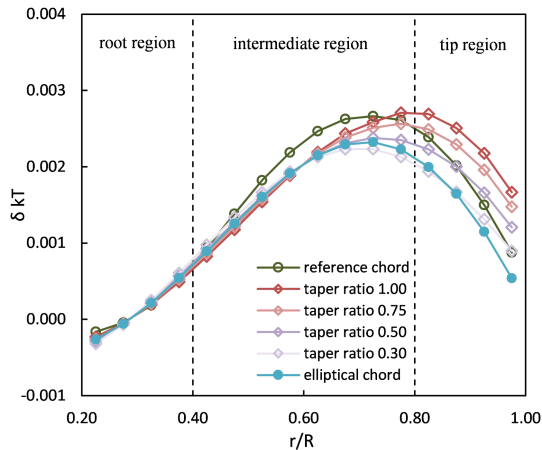


Fig. 11. Comparison of thrust distribution of propellers with generalized Joukowski airfoil for different chord distributions along the blade, for advance ratio $J = 1.0$ (all propellers have linear pitch angle distribution).

4 Conclusions

The home-built numerical code based on the momentum theory and blade element theory calculates the performance parameters of the propeller including thrust loading, blade thrust, torque and power coefficients, and efficiency of the propeller as functions of the advance ratio. Predictions from the present method for the reference propeller Clark Y 5868-9 are in agreement with both experimental results and numerical calculations by the panel method.

The predicted thrust and power coefficients and efficiency of the Göttingen 1 propeller showed higher values in comparison with the reference propeller due to the differences in the aerodynamic characteristics of the two airfoils.

The spanwise distribution of blade loading for Göttingen 1 propeller is higher in the intermediate and tip regions in comparison with the reference propeller for the advance ratio $J = 1$ corresponding to maximum efficiency.

Göttingen 2 propeller based on linear pitch angle distribution along the blade shows lower coefficients of thrust and power with nearly the same efficiency, higher blade loading at the intermediate region and lower blade loading at the tip region in comparison with Göttingen 1 propeller. This result indicates that the linear pitch distribution is better than the reference distribution.

To investigate the effect of airfoil section two rotors were calculated based on the airfoils Göttingen 796 and generalized Joukowski, respectively. It was found that the thrust and the power coefficients and the efficiency of the generalized Joukowski propeller are greater than the respective coefficients of Göttingen 796 propeller for advanced ratio $J = 0.85$ and higher.

The numerical predictions showed that the reduction of the blade loading at the tip region and its increase in the middle part of the blade can be obtained by adopting linear distribution of the pitch angle or by using tapered blade. In the case of tapered blades these effects are intensified by the increase of the blade taper ratio. It is also possible to observe that the use of the elliptic chord distribution accentuates these effects. However, the changes in the geometry of the blade reduce the blade loading near the tip and also reduce the coefficient of thrust, torque and power at nearly constant efficiency, in comparison with the blade having the reference chord distribution.

Acknowledgements. The first author wishes to thank the National Research Council (CNPq) for the PQ research grant.

References

1. Theodorsen, T.: *Theory of Propellers*, Chap. II. McGraw-Hill, New York (1948)
2. Dumitrescu, H., Cardos, V.: Wind turbine aerodynamic performance by lifting line method. *Int. J. Rotat. Mach* **4**(3), 141–149 (1998). <https://doi.org/10.1155/S1023621X98000128>
3. Palmiter, S.M., Katz, J.: Evaluation of a potential flow model for propeller and wind turbine design. *J. Aircr.* **47**(5), 1739–1746 (2010)
4. Bohorquez, F., Pines, D., Samuel, P.D.: Small rotor design optimization using blade element momentum theory and hover tests. *J. Aircr.* **47**(1), 268–283 (2010). <https://doi.org/10.2514/1.45301>
5. Khan, W., Nahon, M.: Development and validation of a propeller slipstream model for unmanned aerial vehicles. *J. Aircr. AIAA Early Edition* (2015). <https://doi.org/10.2514/1.c033118>
6. Morgado, J., Abdollahzadeh, M., Silvestre, M.A.R., Páscoa, J.C.: High altitude propeller design and analysis. *Aerosp. Sci. Technol.* **45**, 398–407 (2015). <https://doi.org/10.1016/j.ast.2015.06.011>
7. Wald, Q.R.: The aerodynamics of propeller. *Prog. Aerosp. Sci.* **42**(2), 85–128 (2006)
8. Glauert, H.: *The Elements of Aerofoil and Airscrew Theory*, Chaps. XV, XVI. Cambridge University Press, Cambridge (1926)

9. Houghton, E.L., Carpenter, P.W., Collicott, S.H., Valentine, D.T.: *Aerodynamics for Engineering Students*, Chap. 10, vol. Sixth. Elsevier, London (2013)
10. Hartman, E.P., Biermann, D.: *The Aerodynamic Characteristics Full-Scale Propellers Having 2, 3 and 4 Blades of Clark Y and R.A.F. 6 Airfoil Sections*. NACA Report No. 640. Langley Memorial Aeronautical Laboratory, National Advisory Committee for Aeronautics, Langley Field, VA, USA (1938)
11. Lyon, C.A., Broeren, A.P., Giguère, P., Gopalarathnam, A., Selig, M.S.: *Summary of Low-Speed Airfoil Data*, vol. 3. Department of Aeronautical and Astronautical Engineering, University of Illinois at Urbana-Champaign, SoarTech Publications, Virginia Beach, VA, USA (1998)
12. Drela, M.: *XFOIL Subsonic Airfoil Development System*, XFOIL 6.99. Massachusetts Institute of Technology, Cambridge, MA, USA (2013). <http://web.mit.edu/drela/Public/web/xfoil/>. Accessed 12 Apr 2016
13. Glauert, H.: *A Generalised Type of Joukowski Aerofoil*. ARC RM No. 911 (1924)



Stability Analysis of a Cracked Blade Coupled with a Rigid Rotor

Bruno R. F. Rende^(✉), Izabela B. da Silva, Tobias S. Morais,
Aldemir Ap. Cavalini Jr., and Valder Steffen Jr.

LMEst - Structural Mechanics Laboratory, School of Mechanical Engineering,
Federal University of Uberlândia, Av. João Naves de Ávila, 2121, Uberlândia,
MG 38408-196, Brazil
brunorende@ufu.br

Abstract. Flexible blades coupled to rotating systems are commonly used in industrial machines, such as compressors, exhausters, and turbines. These components are usually exposed to different operating conditions, including high speed, large centrifugal forces, high temperatures, and pressure. Considering the inevitable manufacturing flaws, cracks can emerge and grow particularly in blades of these systems. Thus, investigations on the dynamic behavior of cracked blades become mandatory to prevent failures. In this work, the development, solution, and instability analysis of a system composed of four flexible blades coupled to a flexible shaft are presented. The flexible blades are modeled as Euler-Bernoulli beams with tip masses attached at their ends. Their deformations are obtained by considering second order nonlinear terms to ensure that the centrifugal stiffness is correctly represented, thus characterizing a second order linearized model. The equations of motion are obtained by applying the so-called Newton-Euler-Jourdain method. The crack presence brings an additional flexibility to the blades, which is introduced in the model by using a torsional spring. The resulting blade stiffness is obtained through the beam elastic equation. The Newmark time integration method is associated with the Newton-Raphson iteration procedure to integrate the equations of motion. The system was evaluated for different situations, regarding the depth of the crack in the blades, as well as the operating condition of the rotor-blade system. Finally, the instability map and the vibration responses of the system is determined. The obtained results indicate the instability condition of the rotor-blade system for a certain combination of rotating speed, angular position of the blades, and crack depth.

Keywords: Rotor-blade system · Second order linearized model
Crack · Instability map

1 Introduction

Flexible blades coupled to rotating shafts are widely used in industrial machines, such as compressors, exhausters, and turbines. These components are usually exposed to different operating conditions, including high-speed situations, large centrifugal forces, high temperatures, and high pressures [1]. Thus, associated with the inevitable

manufacturing flaws and with the possible presence of a foreign object in the system, damage in the system may occur. One of the most dangerous damages is the growth a crack in the blades. This occurs mainly near the attachment between the rotor and the blade. If the crack is not identified it can lead to failure, even to catastrophic consequences. In these cases, the application of predictive maintenance is mandatory.

Nowadays, there are various methods used for crack detection, such as the ultrasonic, X-rays, and acoustic emission [2]. These methods have not proved to be efficient in some situations due to the required detailed periodic inspection, which is very costly [3]. Thus, this problem justified investigations on a class of crack detection methods based on vibration analysis through either frequency or time domain responses.

There are contributions in literature devoted to the modeling of flexible blades. Legrand [4] modeled the blades of a rotor-blade system by using the finite element method, where each finite element was described as Euler-Bernoulli beam. Santos et al. [5] and Saracho [6] used an alternative approach based on the Newton-Euler-Jourdain method to obtain the equations of motion of a rotor-blade system. The authors pointed out that the deformation of the blades cannot be neglected because the coupling between their displacement and deformation causes an effect known as centrifugal stiffening. This effect makes the natural frequencies of the beam increase according to the rotating speed, which is the main characteristic observed in the dynamic behavior of this kind of system.

The dynamic behavior of cantilever beams with transversal cracks was extensively discussed in various papers. Wu and Huang [2] employed an energy approach followed by the Extended Hamilton principle in conjunction with a weighted residual method to obtain the equations of motion of a cracked beam. Dimarogonas [7] and Chondros [8] explained that the crack generates a new local flexibility in the beam. The authors used the linear fracture mechanics theory to represent the crack. Dimarogonas, Rizos, and Aspragathos [9] also observed that the most important effect introduced by cracks on beams is a new local flexibility that changes the dynamical behavior of the system. The authors formulated a model composed of two beams connected by a torsional spring to represent this effect, whose stiffness coefficient represents the crack. The crack strain energy function was used to determine the additional local flexibility on the beam [10]. Mayes and Davies [11] proposed a finite element model to include the new local flexibility in the shaft, in which the diameter of the shaft finite element was reduced at the crack position according to the crack flexibility.

In this context, the present work aims to investigate the influence of cracks on the dynamic behavior of a rotor-blade system based on its vibration responses. In this case, the adopted model for the rotor-blade system is similar to the one described in Saracho [6]. The model is composed of a mass-spring system that represents the rotor and four rotating beams with tip masses attached to them. The blades are modeled as Euler-Bernoulli beams [5] and their deformations were obtained by considering second order non-linear terms to ensure that the centrifugal stiffness is correctly represented [12]. Then, a second order-linearized model was obtained. The Newton-Euler-Jourdain method was applied to determine the equations of motion of the rotor-blade system. The crack is represented by an additional local flexibility of the blade according to the formulation presented in [9].

The equations of motion were solved by using the Newmark time integration method and Newton-Raphson iteration technique by considering different damage scenarios. The first one evaluated the rotor-blade system without crack (pristine condition) and the others considered a crack in one of the blades with different depths. The obtained results indicated the instability condition of the rotor-blade system for a certain combination of rotating speed and crack depth.

2 Mathematical Model

2.1 Rotor-Blade Model

The model used to represent the coupling between the rotor and the four flexible blades is shown in Fig. 1. The system is composed of a rotor with mass m_0 and radius r , which is elastically supported by the stiffness k_0 , and four blades with lengths L_i , thickness h_i , and stiffness k_i ($i = 1, 2, 3, \text{ and } 4$). Tip masses m_{pi} are attached to the blades, presenting length L_{ii} and width b_{ii} . The distance between the extremity and the centroid of the tip mass is given by r_{ii} . The system has five degrees of freedom $z(t) = \{z_0(t) \ z_1(t) \ z_2(t) \ z_3(t) \ z_4(t)\}^T$, where $z_0(t)$ represents the horizontal displacement of the rotor (point C in Fig. 1) and $z_i(t)$ describes the displacements of the blades.

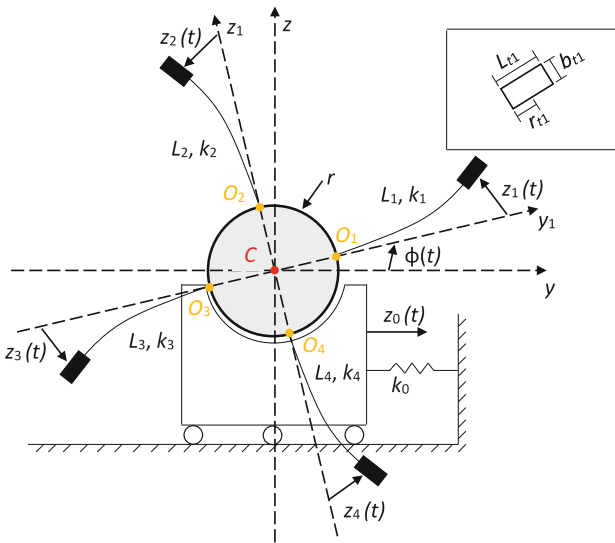


Fig. 1. Model illustrating the rotor-blade system. (Adapted from Santos et al. [5]).

Three reference frames are used to obtain the equations of motion of the rotor-blade system [6], as follows: the inertial frame $B_I(x, y, z)$, the rotating frame $B_1(x_1, y_1, z_1)$ centered at point C (defining the angular position ϕ through the y_1 axis), and the frame $B_{pi}(x_{pi}, y_{pi}, z_{pi})$ fixed to each tip mass.

According to Santos et al. [5], the reference frame B_{pi} facilitates the description of the beam deformation field. Therefore, this frame was employed to find the displacements and the external forces of each blade pi . The displacements of the blades are interpolated by using a cubic polynomial form to minimize the number of degrees of freedom of the model and to approximate only the first bending mode of the blade [6]. The displacements are shown in Eq. (1).

$${}_{B_{pi}}\mathbf{u}_{pi} = \begin{pmatrix} 0 \\ 0 \\ \psi_i(\xi_i)z_i(t) \end{pmatrix} \quad \psi_i(\xi_i) = \frac{3}{2}\left(\frac{\xi_i}{L_i}\right)^2 - \frac{1}{2}\left(\frac{\xi_i}{L_i}\right)^3 \quad (1)$$

Then, the absolute velocity and the acceleration of each blade are given by Eqs. (2) and (3), respectively.

$${}_{B_{pi}}\mathbf{v}_{pi} = {}_{B_{pi}}\mathbf{v}_{O_i} + \frac{d}{dt}({}_{B_{pi}}\mathbf{u}_i) + {}_{B_{pi}}\boldsymbol{\omega} \times ({}_{B_{pi}}\mathbf{L}_i + {}_{B_{pi}}\mathbf{u}_i) \quad (2)$$

$$\begin{aligned} {}_{B_{pi}}\mathbf{a}_{pi} = & {}_{B_{pi}}\mathbf{a}_{O_i} + \frac{d^2}{dt^2}{}_{B_{pi}}\mathbf{u}_i + 2{}_{B_{pi}}\boldsymbol{\omega} \times {}_{B_{pi}}\mathbf{u}_i \\ & + {}_{B_{pi}}\dot{\boldsymbol{\omega}} \times ({}_{B_{pi}}\mathbf{L}_i + {}_{B_{pi}}\mathbf{u}_i) + {}_{B_{pi}}\boldsymbol{\omega} \times {}_{B_{pi}}\boldsymbol{\omega} \times ({}_{B_{pi}}\mathbf{L}_i + {}_{B_{pi}}\mathbf{u}_i) \end{aligned} \quad (3)$$

where ${}_{B_{pi}}\mathbf{v}_{pi}$ and ${}_{B_{pi}}\mathbf{a}_{pi}$ ${}_{B_{pi}}\boldsymbol{\omega}$ are the velocity and acceleration of the point where the blade is fixed to the rotor (point O_i in Fig. 1), respectively, ${}_{B_{pi}}\boldsymbol{\omega}$ and ${}_{B_{pi}}\dot{\boldsymbol{\omega}}$ represent the angular speed and acceleration of the rotor, respectively. These vectors are shown in Eq. (4). It is important to note that the only external force applied to the system is the weight.

$${}_{B_{pi}}\boldsymbol{\omega} = \begin{Bmatrix} \dot{\varphi} \\ 0 \\ 0 \end{Bmatrix} \quad {}_{B_{pi}}\dot{\boldsymbol{\omega}} = \begin{Bmatrix} \ddot{\varphi} \\ 0 \\ 0 \end{Bmatrix} \quad {}_{B_{pi}}\mathbf{L}_i = \begin{Bmatrix} 0 \\ L_i \\ 0 \end{Bmatrix} \quad (4)$$

In the rotor-blade model, the rotatory inertia was taken into account. Thus, an equivalent mass is estimated as follows:

$$\begin{aligned} \bar{m}_i &= m_i\psi(L_i)^2 + (I_{ti} + m_i r_{ti})\psi'(L_i)^2 + 2m_i r_{ti}\psi(L_i)\psi'(L_i) \\ I_{ti} &= m_i \left(\frac{L_{ti}^2 + h_{ti}^2}{12} \right) \end{aligned} \quad (5)$$

where $\psi(L_i)$ is the cubical polynomial showed in Eq. (1) and h_{ti} is the height of the tip mass, which will be considered the same height of the blade.

The energy stored in the system was separated in two terms, π_0 that represents the energy of the elastic support and π_{pi} , which is the potential energy of the blades. In this case, $\pi_{pi} = \pi_{li} + \pi_{gi}$, where π_{li} is associated with the blades deformation and π_{gi} is the

energy related to the blade geometrical stiffness. The energy π_{gi} ensures that the second order non-linear terms of the deformation vector are not neglected (see Eqs. (6) to (9)).

$$\pi_0 = \frac{1}{2} k_0 z_0^2 \tag{6}$$

$$\pi_{li} = \frac{1}{2} \int_0^{L_i} EI \left\{ \frac{\partial^2}{\partial \xi_i^2} [\psi_i(\xi_i) z_i] \right\}^2 d\xi_i = \frac{1}{2} k_i z_i^2 \quad k_i = \frac{3EI}{L_i} \tag{7}$$

$$\pi_{gi} = \frac{1}{2} \int_0^{L_i} N_{pi}(\xi_i) \left\{ \frac{\partial^2}{\partial \xi_i^2} [\psi_i(\xi_i) z_i] \right\}^2 d\xi_i = \frac{3}{5L_i} N_{pi}(\xi_i) z_i^2 \tag{8}$$

$$\pi_{pi} = \pi_{li} + \pi_{gi} \tag{9}$$

where N_{pi} is the normal force acting on each blade. The expression of the normal force can be approximated by using Eq. (10) [13].

$$N_{pi}(\xi_i) = m_{pi} \dot{\phi}^2 (L_i + r) \tag{10}$$

The Newton-Euler-Jourdain method is applied to obtain the system equations of motion, as given by Eq. (11). In this case, an eccentricity ε in a given angular position Φ is considered in the model.

$$\mathbf{M} \ddot{\mathbf{q}} + [\mathbf{C}_1 + \mathbf{C}_p] \dot{\mathbf{q}} + [\mathbf{K} + \mathbf{K}_\Omega + \mathbf{K}_\alpha + \mathbf{K}_g] \mathbf{q} = \mathbf{f}_\Omega + \mathbf{f}_\alpha + \mathbf{f}_p \tag{11}$$

in which \mathbf{M} is the mass matrix, \mathbf{C}_1 is the Coriolis matrix, \mathbf{K} represents the structural stiffness matrix, \mathbf{K}_Ω is the stiffness matrix due to the angular speed, \mathbf{K}_α is the stiffness matrix due to the angular acceleration, \mathbf{K}_g is the geometric stiffness, \mathbf{f}_Ω is the force vector associated with angular speed, \mathbf{f}_α is the force vector due to angular acceleration, and \mathbf{f}_p is the weight force vector. A proportional damping matrix \mathbf{C}_p was added to the system, as shows Eq. (12).

$$\mathbf{C}_p = \alpha \mathbf{M} + \beta \mathbf{K} \quad \alpha = 5 \quad \beta = 1 \times 10^{-5} \tag{12}$$

2.2 Crack Model

The structural stiffness \mathbf{K} presented in Eq. (11) should be modified due to the local flexibility introduced by the crack. Following Dimarogonas, Rizos, and Aspragathos [9], the blade was separated into two beams (see Fig. 2b) with lengths $L_{B1} = L_1$ and $L_{B2} = L - L_{B1}$. These new beams are also modeled as Euler-Bernoulli beams, linked by a torsional spring with stiffness coefficient k_T .

Equations (13) and (14) present the stiffness coefficient k_T determined according to the crack depth a and position L_{B1} along the blade. In this case, it was considered that the beams had only bending movement.

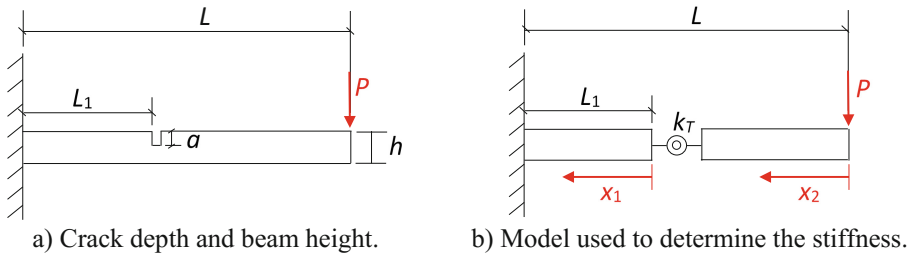


Fig. 2. Schematic model used to represent the crack.

$$k_T = \frac{1}{c} \quad c = \left(\frac{5.346h}{EI} \right) I \left(\frac{a}{h} \right) \quad (13)$$

$$I \left(\frac{a}{h} \right) = 1.8624 \left(\frac{a}{h} \right)^2 - 3.95 \left(\frac{a}{h} \right)^3 + 16.375 \left(\frac{a}{h} \right)^4 - 37.226 \left(\frac{a}{h} \right)^5 + 76.81 \left(\frac{a}{h} \right)^6 - 126.9 \left(\frac{a}{h} \right)^7 + 172 \left(\frac{a}{h} \right)^8 - 143.97 \left(\frac{a}{h} \right)^9 + 66.56 \left(\frac{a}{h} \right)^{10} \quad (14)$$

where c is the compliance, h is the beam height, E and I are, respectively, the Young's modulus of the material and the moment of inertia of the blade cross section. $I(a/h)$ is the dimensionless local compliance.

As can be seen in Fig. 2, the blade was divided into two beams with lengths L_{B1} and L_{B2} , connected by the angular stiffness k_T to represent the cracked blade. Thus, an equivalent stiffness coefficient was determined by considering the scheme presented in Fig. 2b, as shows Eq. (15).

$$k_{eq} = \frac{1}{\frac{1}{k_{B1}} + \frac{1}{k_{B2}} + \frac{1}{k_T}} \quad (15)$$

where k_{B1} is the stiffness of the beam with length L_{B1} (beam #1) and k_{B2} is the stiffness of the beam with length L_{B2} (beam #2). It is worth mentioning that the coefficients k_{B1} and k_{B2} were obtained by using the Euler-Bernoulli theory through the elastic line equation, as given by:

$$\frac{d^2 y_1}{dx_1^2} = \frac{M}{EI} \quad M = Px_1 + PL_{B2} \quad (16)$$

where y is the deflection of the beam, M is the bending moment applied to the beam, and P is a force applied in the end of the beam (see Fig. 2).

Integrating Eq. (16) twice with respect to x_1 ($0 \leq x_1 \leq L_1$), the vertical displacement y_1 and the deflection α_1 of the beam #1 are obtained as follows:

$$y_1 = \frac{Px_1^3}{6EI} + \frac{PL_{B2}x_1^2}{2EI} + C_1x_1 + C_2 \quad \frac{dy_1}{dx_1} = \alpha_1 = \frac{Px_1^2}{2EI} + \frac{PL_{B2}x_1}{EI} + C_1 \quad (17)$$

where C_1 and C_2 are constants that can be evaluated by considering $\alpha_1 = 0$ and $y_1 = 0$ at $x_1 = L_{B1}$. Thus,

$$C_1 = -\frac{P}{EI} \left(\frac{L_{B1}^2}{2} + L_{B1}L_{B2} \right) \quad C_2 = \frac{P}{EI} \left(\frac{L_{B2}L_{B1}^2}{2} + \frac{L_{B1}^3}{3} \right) \quad (18)$$

At $x_1 = 0$, $k_{B1} = P/y_1$. Consequently,

$$k_{B1} = \frac{EI}{\left(\frac{L_{B2}L_{B1}^2}{2} + \frac{L_{B1}^3}{3} \right)} \quad (19)$$

The stiffness k_{B2} of the beam #2 can be found by using a similar procedure through Eq. (16). Then, for the beam #2 (Fig. 2b), with $0 \leq x_2 \leq L_2$:

$$\frac{d^2y_2}{dx_2^2} = \frac{M}{EI} \quad M = Px_2 \quad (20)$$

Integrating Eq. (20) twice with respect to x_2 , the displacement y_2 and deflection α_2 can be obtained as follows:

$$\begin{aligned} y_2 &= \frac{Px_2}{2EI} + C_3x_2 + C_4 \\ \frac{dy_2}{dx_2} &= \alpha_2 = \frac{Px_2}{2EI} + C_3 \end{aligned} \quad (21)$$

The constants C_3 and C_4 in Eq. (22) are determined by using the boundary conditions associated with the beam #2. At $x_2 = L_{B2}$, $y_2(L_{B2}) = y_1(0)$ and the resulting deflection at the same point is given by:

$$\alpha_2(L_{B2}) = \alpha_1(0) + \phi \quad \phi = \frac{PL_{B2}}{k_T} \quad (22)$$

where ϕ is the deflection due to the torsional spring. Thus,

$$\begin{aligned} C_3 &= \frac{PL_{B2}}{k_T} - \frac{P}{EI} \left(\frac{L_{B2}^2}{2} + \frac{L_{B1}^2}{2} + L_{B1}L_{B2} \right) \\ C_4 &= \frac{P}{EI} \left(L_{B1}^2L_{B2} + \frac{L_{B1}^3}{3} + \frac{L_{B2}^3}{3} + L_{B1}L_{B2}^2 \right) - \frac{PL_{B2}^2}{k_T} \end{aligned} \quad (23)$$

At $x_2 = 0$, $k_{B2} = P/y_2$. Consequently,

$$k_{B2} = \frac{1}{\frac{1}{EI} \left(L_{B1}^2L_{B2} + \frac{L_{B1}^3}{3} + \frac{L_{B2}^3}{3} + L_{B1}L_{B2}^2 \right) - \frac{L_{B2}}{k_T}} \quad (24)$$

Substituting Eqs. (24), (20), and (13) into Eq. (15), the equivalent stiffness of the blade with crack is obtained.

3 Numerical Application

The goal of this work was to analyze the influence of a crack on the dynamic behavior of a rotor-blade system. Equation (11) was solved by considering two structural conditions, namely healthy blades (pristine condition) and a crack placed in the blade #1 distant $L_{B1} = 0.05 L_1$ from its root (i.e., the point where the blade is attached to the rotor). Table 1 presents the parameters of the considered rotor-blade system.

Table 1. Parameters of the rotor-blade system.

Rotor			Blades ($i = 1, 2, 3, 4$)		
m_r	1.907	kg	θ_i	$(i - 1)\pi/2$	rad
k_y	2.16×10^4	N/m	m_{pi}	0.1*	kg
r	0.04	m	k_i	1012	N/m
E	2×10^{11}	N/m ²	L_i	0.2	m
ε	1×10^{-5}	m	b_{ti}	0.006	m
Φ	0	rad	h	0.003	m
			L_{ti}	0.03	m
			r_{ti}	0.015	m
			I_{ti}	7.575×10^{-6}	kg m ²
			E	2×10^{11}	N/m ²
			I_i	1.35×10^{-11}	m ⁴

*Tip mass attached to the blade.

Figure 3 shows the vibration modes and corresponding natural frequencies of the healthy rotor-blade system. Note that the fourth and fifth modes are associated with the coupling between the rotor and the blades. The remaining vibration modes are associated with the blades motion.

Table 2 presents the parameters of the crack included in blade #1. This configuration was chosen aiming at emphasizing the effect of the crack brings on the dynamic behavior of the system. Figure 4 presents waterfall diagrams for which frequency responses functions were obtained in blade #1 according to the rotation speed of the rotor-blade system. Curves A and C represent the natural frequencies for the blade #1 with 25% and 50% crack depths, respectively. Curves B and D correspond to the same natural frequencies associated with the healthy system. As expected, the crack presence results in smaller natural frequencies as compared with the pristine condition. Additionally, the difference between the curves increases according to the crack depth. It is worth mentioning that the crack presence leads to a classic case of mistuning since the natural frequencies of the healthy and damaged blades become different [14]. Thus, unstable behavior may happen.

In this context, it is interesting to perform an instability analysis to evaluate the influence of the crack presence. The real parts of the system eigenvalues were analyzed [15], in which positive values indicate unstable condition. This study was performed by varying the rotation speed from 0 to 2500 RPM (in steps of 10 RPM) and the crack depth from 0 to 50% (in steps of 5%) of the blade height. In the present work, two different cases were analyzed. The first one is associated with the open crack (always-open crack during the simulation process - constant stiffness reduction of the blade #1). In the second case, the crack was able to open and close abruptly (breathing crack), according to the displacement of the blade #1 tip (see $z_I(t)$ in Fig. 1).

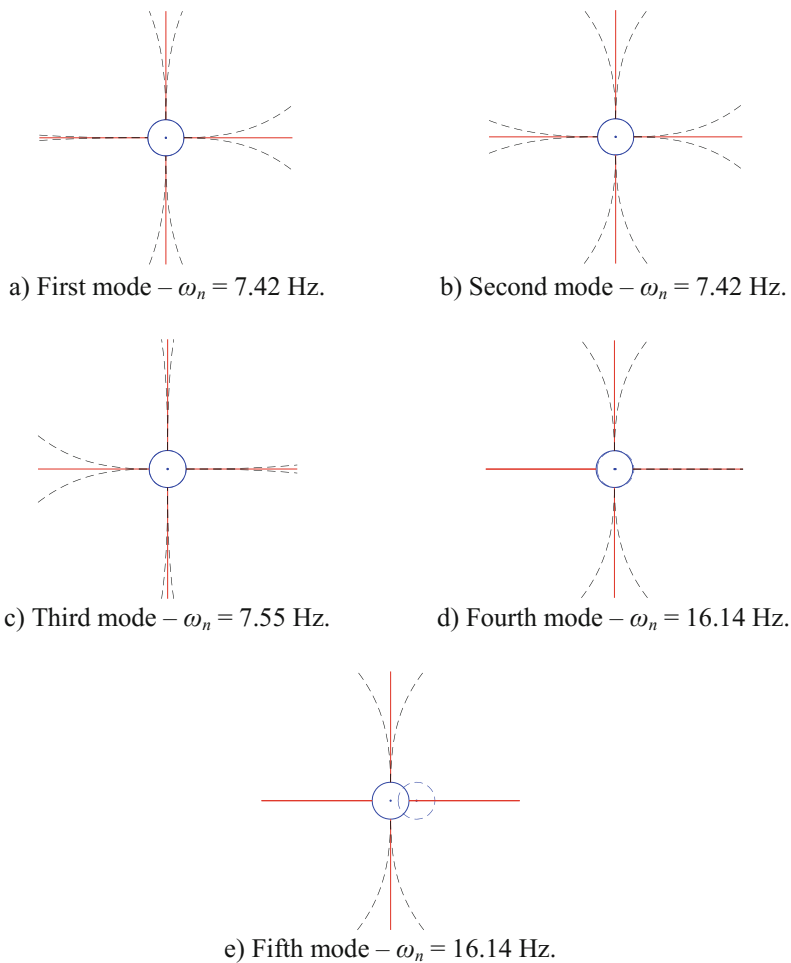
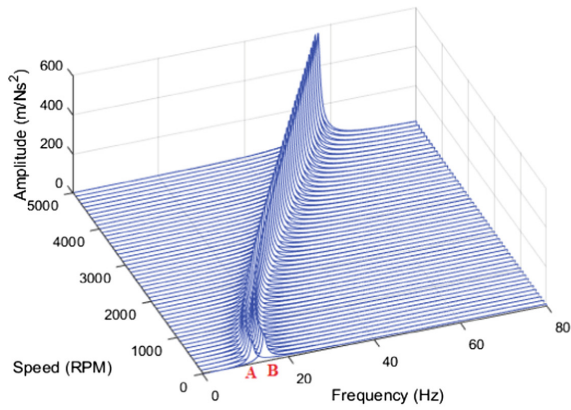


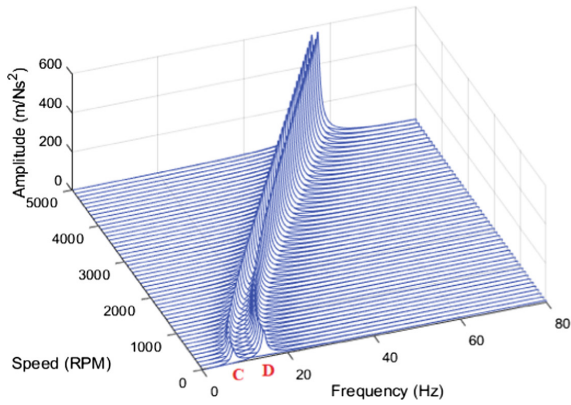
Fig. 3. Vibration modes and corresponding natural frequencies of the healthy system.

Table 2. Parameters of the crack model.

Pristine condition			25% crack depth			50% crack depth		
k_{eq}	1012	N/m	k_{eq}	650	N/m	k_{eq}	261	N/m
a/h	0		a/h	0.25		a/h	0.5	
L_{B1}	0.2	m	L_{B1}	0.01	m	L_{B1}	0.01	m
L_{B2}	0	m	L_{B2}	0.19	m	L_{B2}	0.19	m



a) 25% crack depth.



b) 50% crack depth.

Fig. 4. Waterfall diagrams for the blade #1 by considering two crack depths.

To introduce the breathing in the model was considered in Eq. (11), Positive displacements indicate a full closed crack (pristine condition) and negative values leads to a full open crack (stiffness reduction). Regarding the results for the instability regimes, for both cases (open crack and breathing crack) a new eigenvalue problem was solved for each time-step. Then, the real part of the eigenvalues were checked as a criterion for stability. For the breathing crack condition, the crack changes from closed (healthy blade) to open along the simulation. The unstable condition was observed only when the breathing crack is open. Thus, regarding the stability of the system, it is expected that the same result be obtained for both crack conditions, as can be seen in Fig. 5.

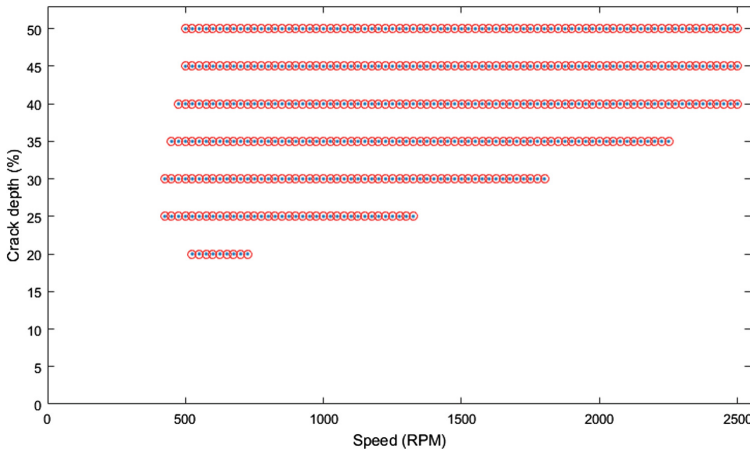


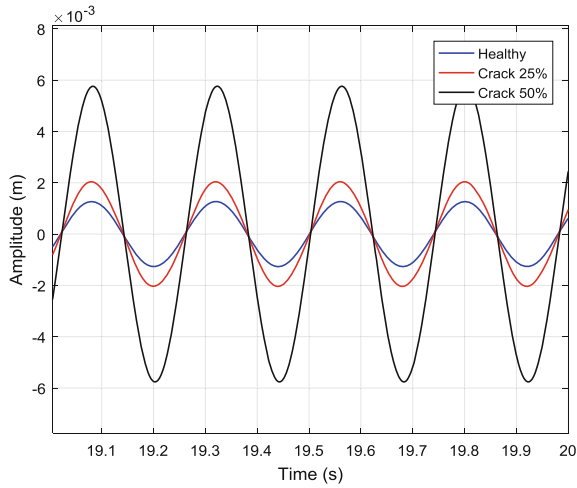
Fig. 5. Stability map of the rotor-blade system by considering the full open (*) and the breathing crack (o).

It is important to highlight that the unstable condition was associated only to the fourth and fifth vibration modes (see Fig. 3; positive real part obtained only in the eigenvalues of the fourth and fifth modes), and these conditions were obtained for crack depths above 20%.

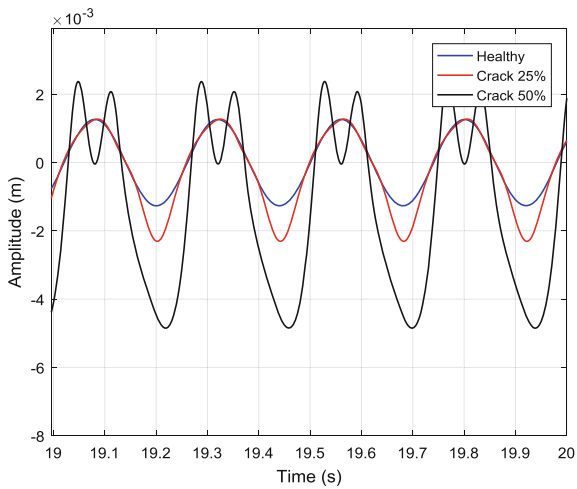
Figures 6, 7 and 8 show the displacement of the blade #1 tip (see $z_1(t)$ in Fig. 1) with the system operating at 250 RPM, 970 RPM, and 2000 RPM, respectively, where 25% and 50% crack depths in blade #1 are considered, as well as its pristine condition. Stable and unstable conditions were achieved for these cases, as presented by Table 3 (see Fig. 5). The rotor-blade system was simulated for 20 s. Note that the vibration responses obtained by considering the full open and breathing cracks are different for 250 RPM and 970 RPM, mainly for the lower speeds for which a 50% breathing crack introduce a new peak in the response. However, similar results were obtained with the rotor-blade system operating at 2000 RPM, which agrees with the waterfall diagram,

Table 3. Stable and unstable conditions according to the rotation speed.

Crack depth	25%	50%
250 RPM	Stable	Stable
970 RPM	Unstable	Unstable
2000 RPM	Stable	Unstable

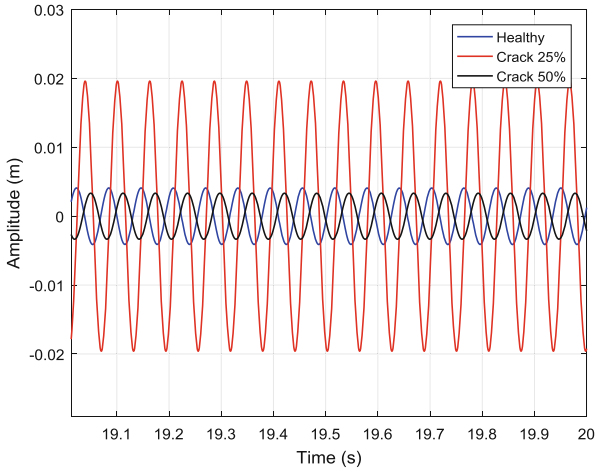


a) full open crack.

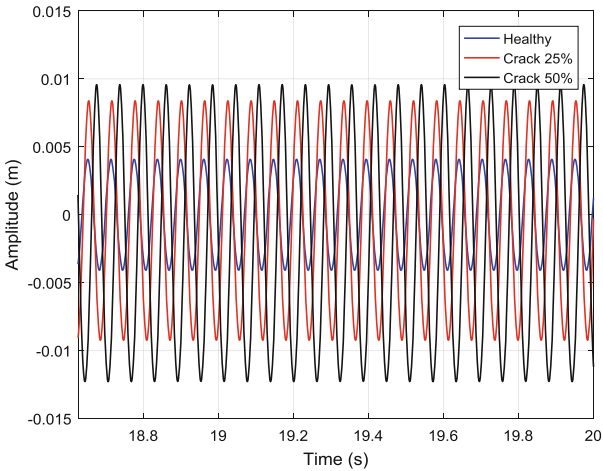


b) breathing crack.

Fig. 6. Vibration responses obtained with the system operating at 250 RPM.



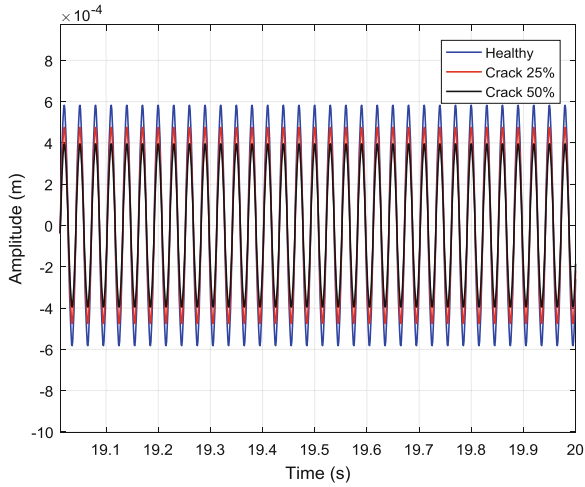
a) full open crack.



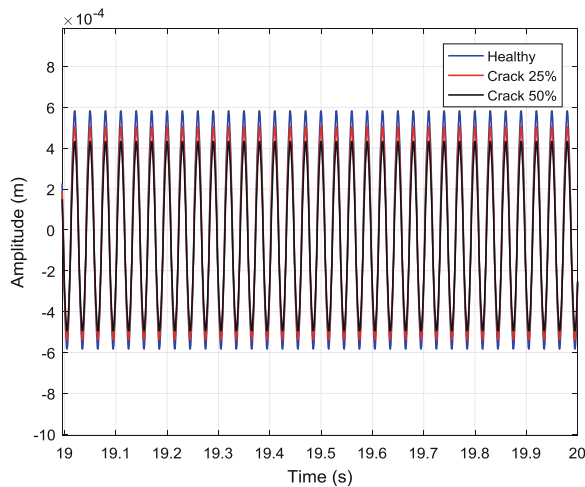
b) breathing crack.

Fig. 7. Vibration responses obtained with the system operating at 970 RPM.

since the two curves shown in Fig. 4 get closer due to the rotation increase. Additionally, it can be observed that the vibration amplitude does not increase necessarily with the crack depth (see Figs. 7a and 8a, b).



a) full open crack.



b) breathing crack.

Fig. 8. Vibration responses obtained with the system operating at 2000 RPM.

4 Conclusions

It is well known that rotating machines coupled with blades may operate under certain conditions that can lead to the growth of cracks. The presence of cracks is undesirable since it may lead to the failure of the system.

Thus, it is necessary to apply predictive maintenance techniques as based on vibration responses to ensure safety operating conditions of these machines. In this context, this contribution demonstrated the effects that a crack introduced in a blade presents on the dynamic behavior of a rotor-blade system. From the results, it was

observed that the crack introduced local flexibility in the blade, which makes the system unstable. Full open and breathing crack behaviors were analyzed. It was demonstrated that the resulting stability map is the same for both crack conditions. The time vibration responses of the system were also evaluated, revealing that the full open and breathing crack induce different dynamic behaviors on the system. Further research effort will be dedicated to the experimental verification of the presented results.

Acknowledgments. The authors are thankful to the Brazilian Research Agencies CAPES, CNPq (574001/2008-5/304546/2017-8) and FAPEMIG (TEC-APQ-022284-15/TEC-APQ-307609) for the financial support provided to this research effort. The authors are also thankful to the companies CERAN, BAESA, ENERCAN, and Foz do Chapecó for the financial support through the R&D project *Robust Modeling for the Diagnosis of Defects in Generating Units* (02476-3108/2016).

References

1. Xu, H., Chen, Z., Xiong, Y., Yang, Y., Tao, L.: Nonlinear dynamic behaviors of rotated blades with small breathing cracks based on vibration power flow analysis. *J. Shock Vib.* **2016** (2016)
2. Wu, M.C., Huang, S.C.: On the vibration of cracked rotating blade. *J. Shock Vib.* **5**, 317–323 (1998)
3. Saavedra, P.N., Cuitiño, L.A.: Crack detection and vibration behavior of cracked beams. *J. Comput. Struct.* **79**(2001), 1451–1459 (2001)
4. Legrand, M.: Modèles de prédiction de l'interaction rotor/stator dans un moteur d'avion. Doctorat, thesis, L'École Centrale de Nantes et l'Université de Nantes, Nantes (2005)
5. Santos, I.F., Saracho, C.M., Smith, J.T., Eiland, J.: Contribution to experimental validation of linear and non-linear dynamics models for representing rotor-blade parametric coupled vibrations. *J. Sound Vib.* **271**, 883–904 (2004)
6. Saracho, C.M.: Numerical and experimental analysis of flexible blade dynamic behavior. Campinas State University. Thesis (Doctorate), Campinas (2002)
7. Dimarogonas, A.D.: *Vibration Engineering*. St. Paul, West Publishers (1976)
8. Chondros, T.G.: Dynamic response of a cracked beam. University of Patras, Greece. M.Sc. thesis (1977)
9. Dimarogonas, A.D., Rizos, P.F., Aspragathos, N.: Identification of crack location and magnitude in a cantilever beam from the vibration modes. *J. Sound Vib.* **138**, 331–338 (1990)
10. Dimarogonas, A.D., Paipetis, S.A.: *Analytical Methods in Rotor Dynamics*. Elsevier, London (1983)
11. Mayes, I.W., Davies, W.G.R.: Analysis of the response of a multi-rotor-bearing system containing a transversal crack in a rotor. *J. Vib. Acoust. Stress Reliab. Des.* **106**, 139–146 (1984)
12. Simo, J.C., Vu-Quoc, L.: On the dynamics of flexible beams under large overall motion—the plane case. Part I and II. *ASME J. Appl. Mech.* **53**, 849–863 (1986)
13. Kane, T.R., Ryan, R.R., Banerjee, A.K.: Dynamics of a cantilever beam attached to a moving base. *J. Guid. Control Dyn.* **10**(2), 139–151 (1987)
14. Choi, Y.S., Gottfried, D.A., Fleeter, S.: Analysis of structural mistuning effects on bladed disc vibrations including aerodynamic damping. In: *International Compressor Engineering Conference*. Paper 1627 (2004)
15. Ogata, K.: *Modern Control Engineering*, 4th edn. Prentice Hall, Upper Saddle River (2002)



Effects of Twist Angle on Rubbing Induced Vibration Responses of Blade

Hui Ma^{1,2(✉)}, Tong Yang¹, Shiyu Liu¹, Qi Sun¹, and Bangchun Wen¹

¹ Northeastern University, Shenyang,
Liaoning 110819, People's Republic of China
mahui_2007@163.com

² Key Laboratory of Vibration and Control of Aero-Propulsion System Ministry of Education, Northeastern University, Shenyang,
Liaoning 110819, People's Republic of China

Abstract. In rotating machinery, such as axial-flow compressor, gas turbine and aero-engine, the small clearance between the rotational blade and casing can increase the system efficiency, but may also lead to the rubbing between the blade and casing. The severe rubbing can bring about damages of the blade or casing. In this paper, two mathematical models of blade: a uniform-thickness-shell (UTS) model and a uniform-thickness-twisted-shell (UTTS) model, are established to compare the effects of the blade twist angle on the rubbing-induced vibration responses. The natural characteristics obtained from the two models are compared. Dynamic behaviors obtained from two models considering the combined effects of centrifugal force and aerodynamic force are also compared. Moreover, considering the effects of the misalignment angle and radial misalignment, the transient responses caused by rubbing using the two models are discussed. The results exhibit that the resonance in the radial direction cannot be observed when the blade twist angle is ignored (using UTS model). However, this resonance can be observed using the UTTS model, i.e., taking the influences of twist angle into account.

Keywords: Rotating blade · Blade-casing rubbing · Twist angle
Super-harmonic resonance

1 Introduction

In aero engine, the small rotor-stator clearance can improve the system efficiency, but can also bring out the blade-casing rubbing. The rubbing may cause severe vibration of the engine and can decrease the system capability. The rotor-stator rubbing has aroused wide concern, and Jacquet-Richardet et al. [1] and Ma et al. [2] presented a detailed review related to this topic. Generally, the rotor-stator contact (interaction) can be regarded as rubbing in Refs. [3–5], modal interaction in Refs. [6–8] and whirl and whip in Ref. [9]. For the sake of obtaining a deep understanding of the dynamic characteristics during rubbing, some theoretical and experimental researches [3, 4, 10–13] were presented, and some numerical methods are proposed by Batailly et al. [14] and Parent et al. [15].

According to the different requirement of simulation modeling, the blade can be regarded as beam, thin plate and three-dimensional solid model in many studies. The

three-dimensional blade is simplified as a beam model [3, 4, 8]. It is clear that the beam model cannot accurately analyze the vibration response in the chord wise direction. For improving the precision of the beam model, the plate models are also widely adopted [11]. Adopting the thin shell theory, Sun et al. [16] established a new dynamic model of a rotational blade with stagger angles, and analyzed the dynamic characteristics of the blade systems. Yoo et al. [17] proposed a new method to carry out the modal analysis of a rotational cantilever plate, and discussed the modal behaviors of the plate under different structural and load parameters, such as the aspect ratios and the angular speeds. Sinha and Zylka [18] developed a dynamic model using thin shell theory to analyze the transverse vibration of a rotational blade.

Many researchers adopted three dimensional finite element models due to their accuracy, especially for complicated structures. A three-dimensional finite element model for a partial blade-disk with dovetail is established, and the dynamic behaviors of the blade and contact characteristics of dovetail are analyzed in Ref. [12]. It is obvious that the numerical simulation is time-consuming adopting a three-dimensional finite element model with large sizes.

From the above literatures, it can be observed that the dynamic characteristics of blade considering the effects of twist angle were investigated, however, the influences of blade twist angle on the responses caused by rubbing are not involved. In order to make up for this deficiency, in this paper, two finite element models of blade, i.e., uniform-thickness shell (UTS), and uniform-thickness-twisted shell (UTTS) models, are established to compare the influences of twist angles of blade on the system vibration responses during rubbing.

2 Finite Element Models of Blade and Blade-Casing Rubbing Model

2.1 Finite Element Model of Blade

For the UTS model, the simulation parameters are shown in Table 1. Compared with the UTS model, the UTTS model considers the effects of twist angle of the blade γ_L (see Fig. 1a, $\gamma_L = 10^\circ$ in this paper), and other parameters are all the same as those of the UTS model. It should be noted that the geometry of the UTTS model is shaped by extruding the rectangle along the Z axis with a constant rate γ' of the twist angle, such that the twist angle along the Z axis can be expressed as $\gamma(Z) = \gamma' Z = \frac{\gamma_L}{L} \times Z$. The UTTS is built by 9 mid-curves related to the profiles, as shown in Fig. 1b, where the thickness h is calculated by the blade surface data. The detailed modelling process can be found in Ref. [19].

Table 1. Blade simulation parameters

Material parameters	Values	Parameters of disk and blade	Values
Young's modulus E (GPa)	125	Radius of the disk R_d (mm)	216.52
Density ρ (kg/m ³)	4370	Blade length L (mm)	88.6
Poisson's ratio ν	0.3	Blade width b (mm)	56.7
		Stagger angle β_2 ($^\circ$)	35.32

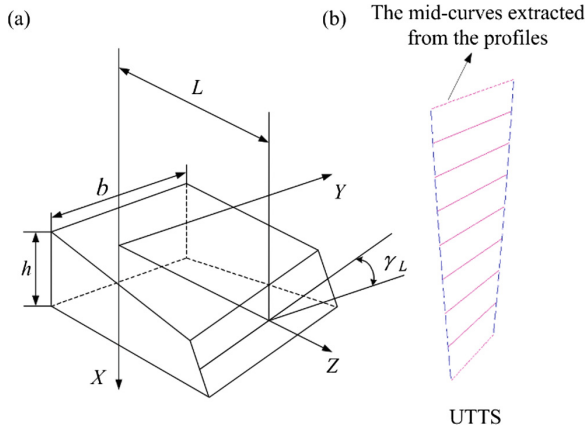


Fig. 1. Schematic diagram of the geometry: (a) schematic diagram of twist angle, (b) modeling schematic diagram for UTTS

Based on ANSYS, two finite element models are established, where the UTS and the UTTS FE models are established by Shell181 elements. For the UTS and the UTTS models, 20 elements (21 nodes) are divided on the blade-tip. It is worth noting that in the UTS and the UTTS model, the blade width (chord length) is set as the distance between the leading edge and trailing edge (see Fig. 2).

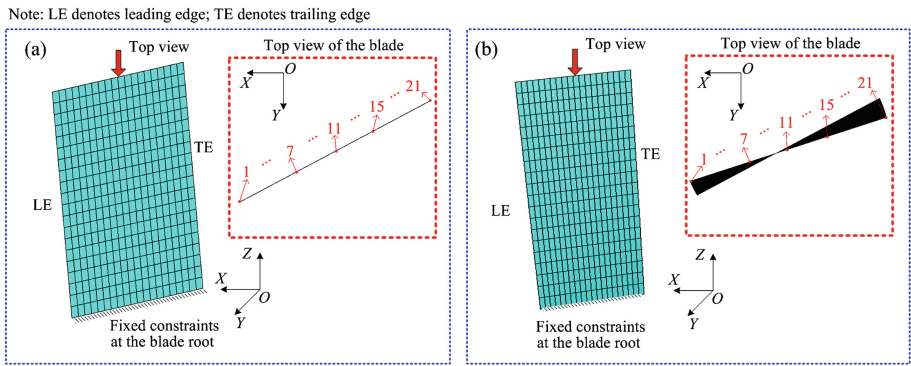


Fig. 2. Finite element models of blades: (a) UTS model, (b) UTTS model

The motion equations of the blade are

$$\mathbf{M}\ddot{\mathbf{u}} + [\mathbf{D} + \mathbf{G}(\Omega)]\dot{\mathbf{u}} + [\mathbf{K}_e + \mathbf{K}_c(\Omega) + \mathbf{K}_s(\Omega) + \mathbf{K}_{acc}(\dot{\Omega})]\mathbf{u} = \mathbf{f} \quad (1)$$

The detailed introduction about \mathbf{M} , \mathbf{D} , $\mathbf{G}(\Omega)$, \mathbf{K}_e , $\mathbf{K}_c(\Omega)$, $\mathbf{K}_s(\Omega)$, $\mathbf{K}_{acc}(\dot{\Omega})$, \mathbf{u} and \mathbf{f} can be found in Ref. [19].

2.2 Blade-Casing Rubbing Model

Considering the effects of angle misalignment β_1 and radial misalignment, blade-casing rubbing model is established (see Fig. 3). The detailed introduction of the showed parameters can be found in Ref. [19].

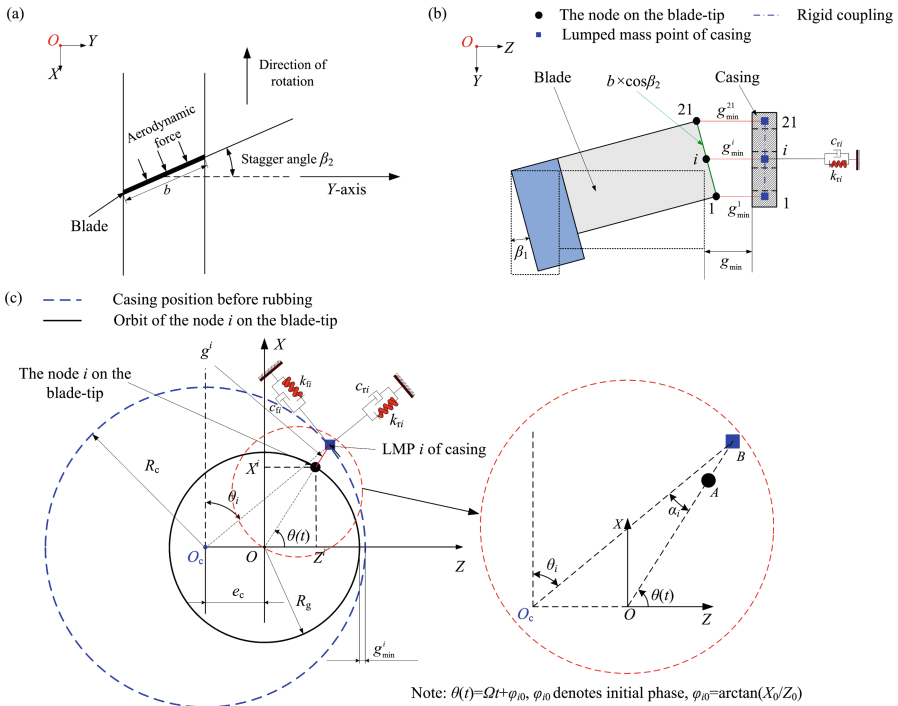


Fig. 3. (a) blade top view (b) blade-casing clearance (c) the clearance between blade-tip node i and LMP i of casing.

The clearance g_{rub}^i can be written as

$$g_{rub}^i = g^i - u_{Zb}^i + u_{Zc}^i \tag{2}$$

where u_{Zb}^i and u_{Zc}^i are radial displacements of blade-tip node i and LMP i of the casing, respectively. For the UTS and the UTTS models, $i = 1, 2, \dots, 21$. Here, it should be noted that the influences of the bending vibration of the casing on g_{rub}^i are not considered. g^i can be written as

$$g^i = \begin{cases} R_c \sin(\pi/2 - \theta_i(t)) / \sin \theta(t) - R_g & \theta(t) \neq n\pi \\ g_{min}^i & \theta(t) = 2n\pi \\ 2R_c - 2R_g - g_{min}^i & \theta(t) = (2n + 1)\pi \end{cases}$$

where n denotes positive integer; $R_c = l_{O,B}$; $\theta_i(t) = \pi/2 - \theta(t) + \alpha_i(t)$ (see Fig. 3c), $\varphi_{i0} = \arctan(Z_0^i/X_0^i)$, here, Z_0^i and X_0^i denote the initial Z and X coordinates of the node i on the blade-tip. $\alpha_i(t)$ can be written as

$$\alpha_i(t) = \arcsin((R_c - g_{\min}^i - R_g) \sin \theta(t)/R_c) \quad (4)$$

where $g_{\min}^i = g_{\min 1} + (21 - i) \times b \times \cos \beta_2/20 \times \sin \beta_1$. $g_{\min 1}$ is

$$g_{\min 1} = g_{\min} - (R_g \cos \beta_1 + b \cos \beta_2 \times \sin \beta_1 - R_g) \quad (5)$$

The penetration depth δ_i of the blade-tip node i is

$$\delta_i = \begin{cases} -g_{\text{rub}}^i & g_{\text{rub}}^i < 0 \\ 0 & g_{\text{rub}}^i \geq 0 \end{cases} \quad (6)$$

The equivalent normal rubbing force F_{Zb}^i of blade-tip node i is

$$F_{Zb}^i = f_n \frac{\delta_i}{\delta} \quad (7)$$

where δ denotes the penetration depth sum of each blade-tip node, and it can be written as:

$$\delta = \sum_{i=1}^n \delta_i \quad (8)$$

Assuming that the casing stiffness is linear [19], the rubbing force is

$$f_{\text{elastic}} = k_{ri} u_c, \quad (9)$$

where k_{ri} and u_c are the equivalent casing stiffness and the casing radial displacement. The force balance relation is shown the following expression.

$$f_n = f_{\text{elastic}}, \quad (10)$$

The tangential rubbing force of blade-tip node i is

$$F_{Xb}^i = \mu F_{Zb}^i \quad (11)$$

where μ is the coefficient of friction.

3 Dynamic Characteristics of Two Blade Models Without Rubbing

The section will firstly analyze the natural characteristics of rotational blade adopting two finite element models. Taking the effects of the stress stiffening, spin softening and Coriolis force into account, the first two natural frequencies and their mode shapes are

displayed in Figs. 4 and 5. In the figure, 10Ω represents the aerodynamic force frequency. The intersections of 10Ω line and the first natural frequency are defined as critical speeds, and they are 3999 RPM for UTS model and 3998 RPM for UTTS model, respectively. The first two natural frequencies are also shown in Table 2, which shows a light error (smaller than 0.4%) between natural frequencies obtained from two models.

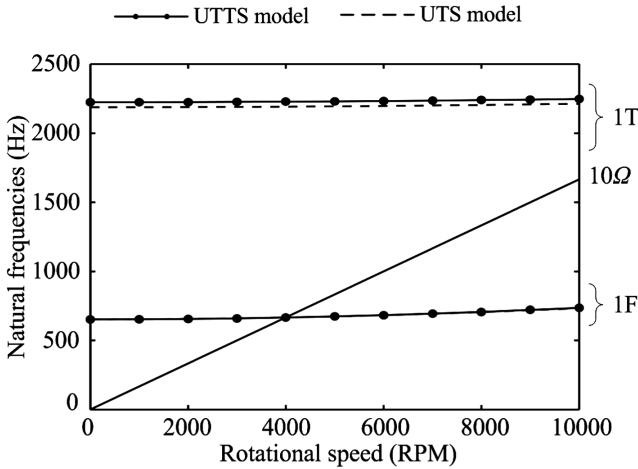


Fig. 4. Natural frequencies of the blade

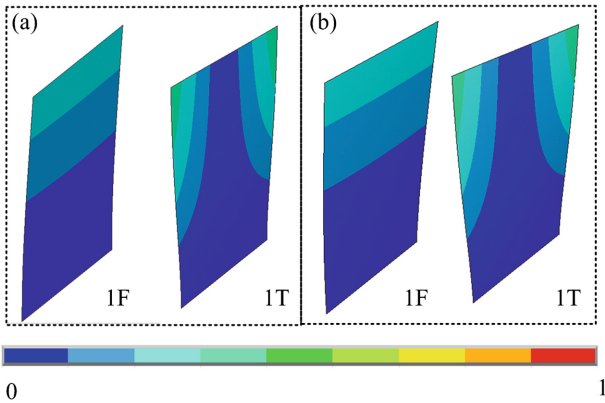


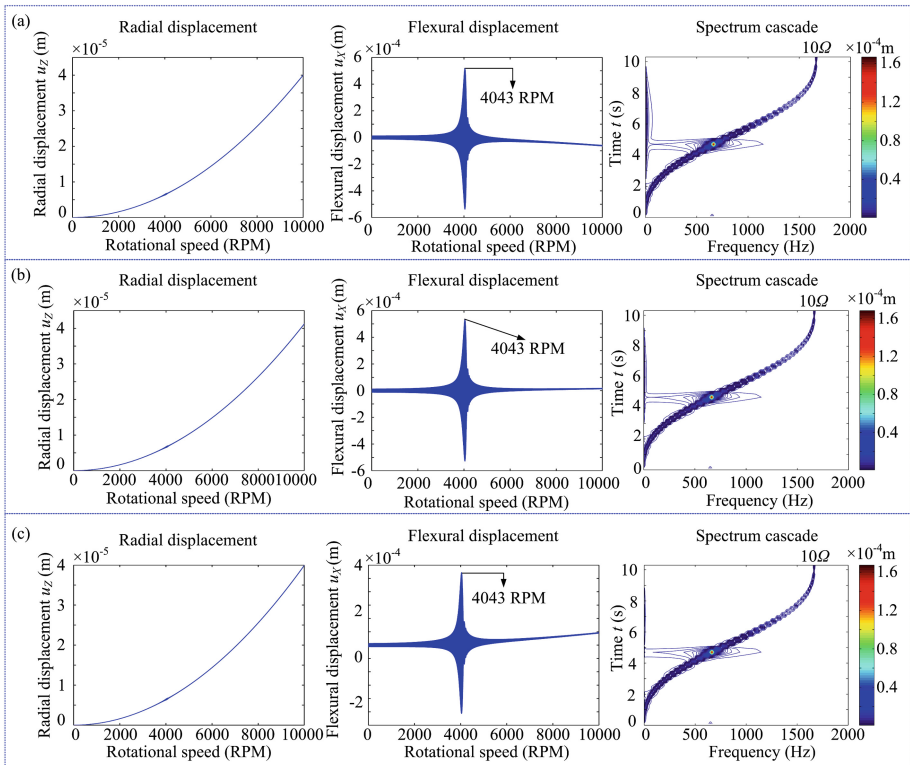
Fig. 5. Mode shapes obtained from two finite models at rest: (a) UTS model, (b) UTTS model

Comparison on the vibration responses of different blade-tip nodes are displayed in Figs. 6 and 7. In these figures, the nodes 1, 11, and 21 are used to describe the vibration of the leading edge, the blade-tip middle point and trailing edge.

Table 2. Natural frequencies obtained from two finite element models

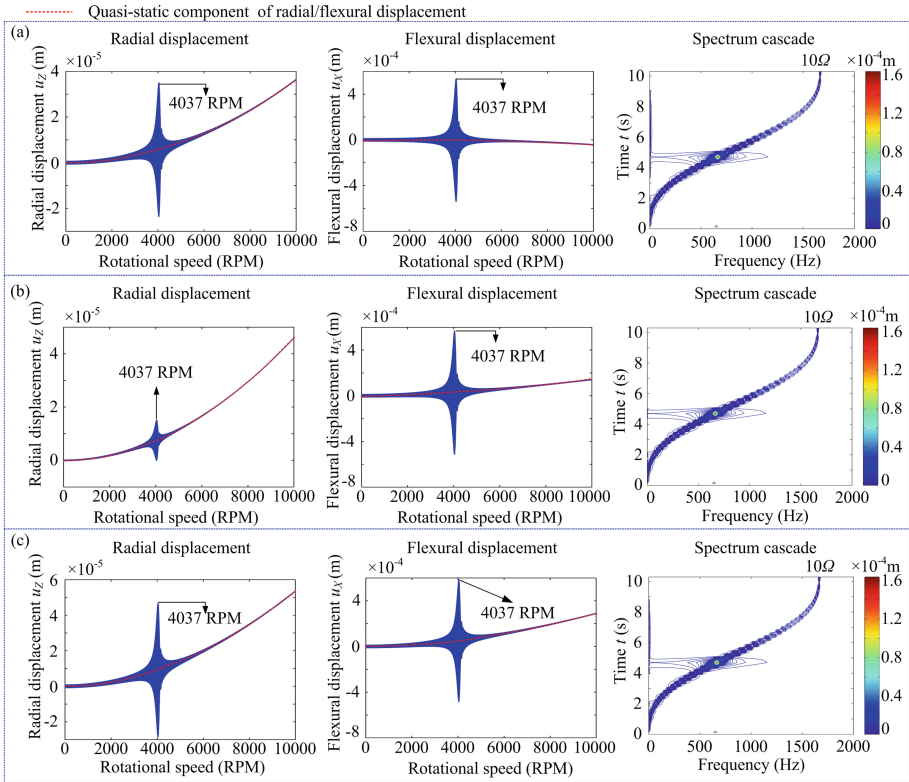
Mode	Models	Rotational speeds (RPM)					
		0	2000	4000	6000	8000	10000
1F	UTS (Hz)	652.875	656.292	666.436	682.997	705.508	733.402
	UTTS (Hz)	652.197	655.871	666.411	683.741	707.269	736.384
1T	UTS (Hz)	2188.227	2189.248	2192.311	2197.404	2204.514	2213.620
	UTTS (Hz)	2232.554	2233.543	2236.509	2241.441	2248.328	2257.149

The run-up response in the radial direction shows that for the UTS model, the radial displacements include only a static component due to the centrifugal force (see radial displacement in Fig. 6). For the UTTS models, the radial displacements include two distinct components: static component related to the centrifugal force and a high frequency component caused by aerodynamic force. Moreover, for the UTTS model, the radial-direction resonance peaks (the first order resonance) can be observed because the blade twist angles have an effect on the radial vibration (see Fig. 7).



Note: The relationship between rotational speed Ω (RPM) and time t (s) can be expressed as: $\Omega(t) = \frac{3000}{\pi}t - \frac{5000}{\pi} \sin(\frac{3}{5}t)$

Fig. 6. Vibration responses of blade-tip nodes without rubbing (UTS model): (a) node 1, (b) node 11, (c) node 21.



Note: The relationship between rotational speed Ω (RPM) and time t (s) can be expressed as: $\Omega(t) = \frac{3000}{\pi}t - \frac{5000}{\pi}\sin(\frac{3}{5}t)$

Fig. 7. Vibration responses of blade-tip nodes without rubbing (UTTS model): (a) node 1, (b) node 11, (c) node 21.

The flexural displacement also includes the static component and the high frequency component. The static components have different change trend for different blade-tip positions (see Figs. 6 and 7).

4 Vibration Responses of Blade and Casing Under Rubbing

When the rotor speeds up from Ω_0 to Ω_{end} , vibration responses of the blade-tip nodes (node 21) and casing based on two finite element models, are displayed in Figs. 8 and 9.

Except for the aerodynamic loads induced primary resonances, many rubbing induced super-harmonic resonances also appear when the multiple of the rotating speed is close to the blade natural frequency. For example, the resonance peaks obtained from the UTS model can be observed at 6994 RPM (see Fig. 8b) which are excited due to six times of rotating frequencies 6Ω ($6\Omega = f_{n1}$ Hz, f_{n1} denotes the first natural frequency of blade) and five times of rotating frequencies 5Ω ($5\Omega = f_{n1}$ Hz) approaching f_{n1} . More super-harmonic resonance peaks can be observed when using the UTTS

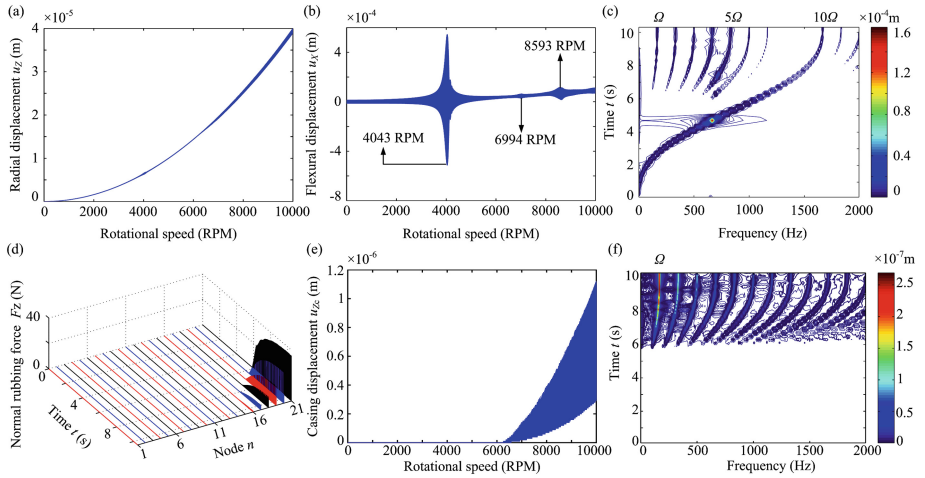


Fig. 8. Vibration responses of node 21 (UTS model): (a) radial displacement, (b) flexural displacement, (c) spectrum cascade, (d) normal rubbing forces, (e) radial displacement of the casing, (f) spectrum cascade of the casing

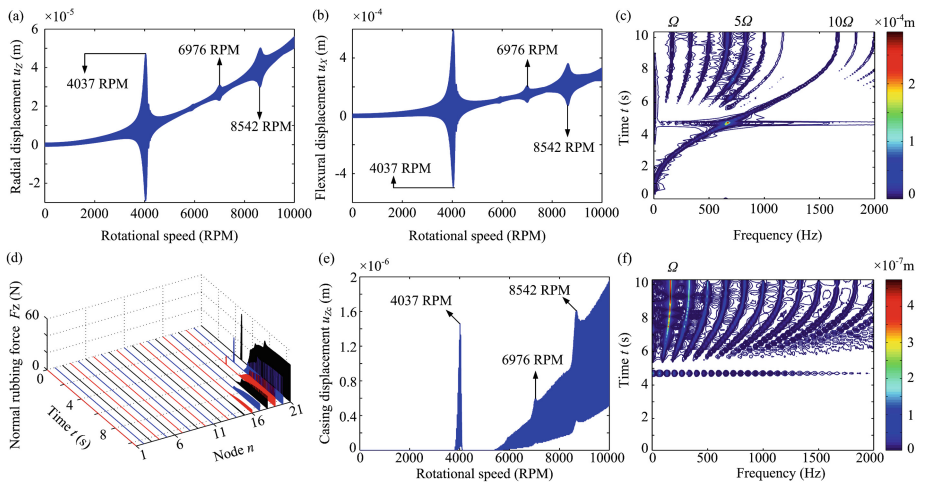


Fig. 9. Vibration responses on node 21 (UTTS model): (a) radial displacement, (b) flexural displacement, (c) spectrum cascade, (d) normal rubbing forces, (e) radial displacement of the casing, (f) spectrum cascade of the casing

model than those of the UTS model, and the super-harmonic resonance phenomena become even more abundant, compared with the UTTS model.

For the UTTS model, the first blade-tip rubbing occurs near 4037 RPM because the radial-direction resonance peak of the blade appears at 4037 RPM under the action of aerodynamic and centrifugal loads. With the increasing rotational speed, the radial elongation of the blade-tip increases, the rubbing appears again (see Fig. 9d).

The time history, frequency spectra and displacement nephograms obtained from the speed-up process (near $5\Omega = f_{n1}$ Hz) are discussed (see Figs. 10, 11, 12 and 13). It should be noted that in the time-domain waveforms (see Figs. 10a and 12a), the left-hand vertical ordinate axis (blue line) shows the flexural displacement of the node 21, and the right-hand vertical ordinate axis (green line) shows the normal rubbing force. The time segments for frequency spectra are in the interval of [7.3215 s, 7.4685 s] for the UTS and the UTTS models. The displacement nephograms of the blade at four typical moments A, B, C and D (see Figs. 10a and 12a) are shown in Figs. 11 and 13. Compared the vibration obtained from the UTS and the UTTS models, it is obvious that the vibration increases sharply due to the effect of the twist-shape of the blade (see Figs. 10 and 12). The results also show that the vibration response is predominant near f_{n1} in comparison with that near f_{n2} , as shown in Figs. 10b and 12b. It should be noted that for the UTS and the UTTS models, $15\Omega \approx f_{n2}$. In the displacement nephograms, the bending-torsion coupled vibrations of blade can be observed under $5\Omega \approx f_{n1}$ (see Figs. 11a and 13a) because the twist angle leads to the stiffness coupling in radial and flexural directions.

Note: A, B, C and D denote four typical moments

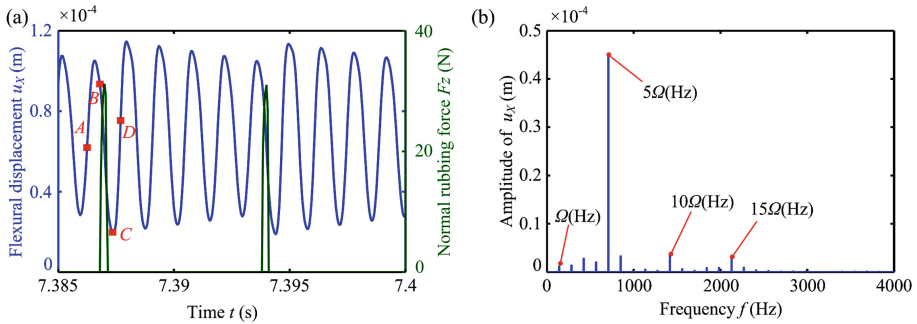


Fig. 10. Vibration responses of the node 21 near 8593 RPM (UTS model): (a) flexural displacement waveform, (b) frequency spectrum

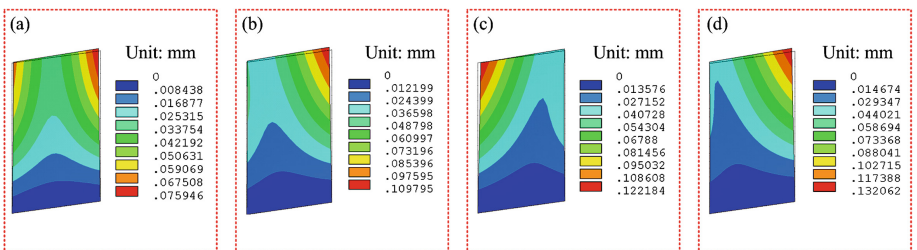


Fig. 11. Displacement nephograms near 8593 RPM (UTS model): (a) moment A, (b) moment B, (c) moment C, (d) moment D

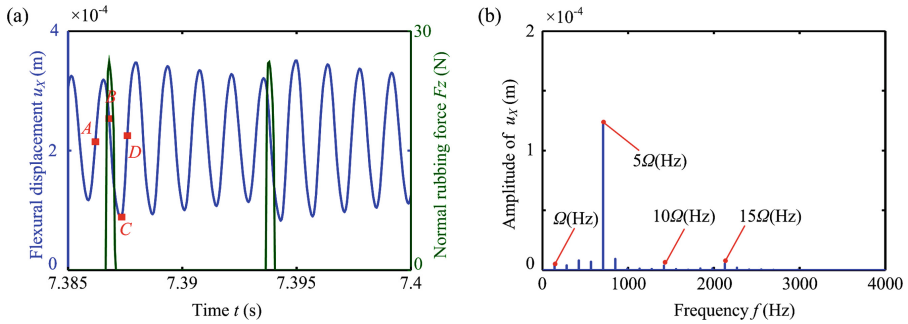


Fig. 12. Vibration responses of the node 21 near 8542 RPM (UTTS model): (a) flexural displacement waveform, (b) frequency spectrum

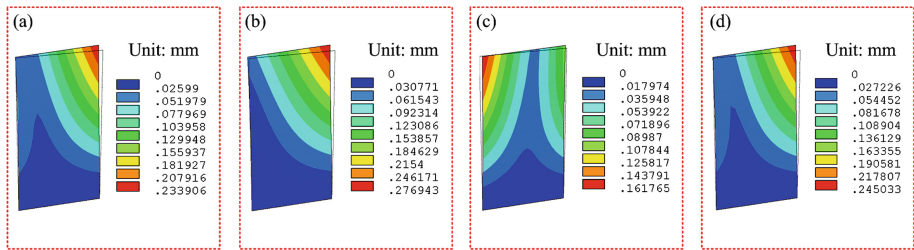


Fig. 13. Displacement nephograms near 8542 RPM (UTTS model): (a) moment A, (b) moment B, (c) moment C, (d) moment D

5 Conclusions

In this paper, the influences of blade twist angle on the vibration responses caused by rubbing are analyzed using two finite element models, i.e., the uniform-thickness shell (UTS) and uniform-thickness-twisted shell (UTTS) models. The casing is simulated by a lumped mass with spring and damping. By rubbing force to couple the blade can casing models, the blade-casing rubbing phenomena are simulated. Mainly conclusions are listed as follows:

The simulated results show that the twist angle can not affect the rubbing induced super-harmonic resonance phenomena in flexural direction. The vibration response is predominant near the first dynamic frequency compared with that near the second dynamic frequency. The rubbing can excite the blade bending-torsional coupled vibration.

The twist angle affects the resonance in the radial direction, and this resonance can be observed for the blade with twist angle. In addition, the twist angle also affects the active sets of rubbing nodes due to different blade-tip deformations.



Acknowledgment. This project is supported by the China Natural Science Funds (NSFC, Grant no. 11772089) and the Fundamental Research Funds for the Central Universities (Grant nos. N160313004 and N160312001).

References

1. Jacquet-Richardet, G., Torkhani, M., Cartraud, P., et al.: Rotor to stator contacts in turbomachines. *Rev. Appl. Mech. Syst. Signal Process.* **40**, 401–420 (2013)
2. Ma, H., Yin, F.L., Guo, Y.Z., Tai, X.Y., Wen, B.C.: A review on dynamic characteristics of blade-casing rubbing. *Nonlinear Dyn.* **84**(2), 437–472 (2016)
3. Ma, H., Yin, F.L., Wu, Z.Y., et al.: Nonlinear vibration response analysis of a rotor-blade system with blade-tip rubbing. *Nonlinear Dyn.* **84**(3), 1225–1258 (2016)
4. Sinha, S.K.: Non-linear dynamic response of a rotating radial Timoshenko beam with periodic pulse loading at the free-end. *Int. J. Non-Linear Mech.* **40**(1), 113–149 (2005)
5. Turner, K.E., Dunn, M., Padova, C.: Airfoil deflection characteristics during rub events. *J. Turbomachinery* **134**(1), 011018-1–011018-8 (2012)
6. Schmiechen, P.: Travelling wave speed coincidence. Ph.D. thesis, Imperial College of Science, Technology and Medicine—University of London (1997)
7. Legrand, M., Pierre, C., Cartraud, P., Lombard, J.P.: Two-dimensional modeling of an aircraft engine structural bladed disk-casing modal interaction. *J. Sound Vib.* **319**(1–2), 366–391 (2009)
8. Batailly, A., Legrand, M., Cartraud, P., et al.: Assessment of reduced models for the detection of modal interaction through rotor stator contacts. *J. Sound Vib.* **329**(26), 5546–5562 (2010)
9. Childs, D.W., Bhattacharya, A.: Prediction of dry-friction whirl and whip between a rotor and a stator. *J. Vib. Acoust.* **129**(3), 355–362 (2007)
10. Sinha, S.K.: Dynamic characteristics of a flexible bladed-rotor with Coulomb damping due to tip-rub. *J. Sound Vib.* **273**(4–5), 875–919 (2004)
11. Yuan, H.Q., Kou, H.J.: Contact-impact analysis of a rotating geometric nonlinear plate under thermal shock. *J. Eng. Math.* **90**(1), 119–140 (2015)
12. Ma, H., Wang, D., Tai, X.Y., Wen, B.C.: Vibration response analysis of blade-disk dovetail structure under blade tip rubbing condition. *J. Vib. Control* **23**(2), 252–271 (2017)
13. Almeida, P., Gibert, C., Thouverez, F., et al.: Experimental analysis of dynamic interaction between a centrifugal compressor and its casing. *J. Turbomachinery* **137**(3), 031008-1–031008-10 (2014)
14. Batailly, A., Legrand, M., Pierre, C.: Full three-dimensional rotor/stator interaction simulations in aircraft engines with time-dependent angular speed. *J. Eng. Gas Turbines Power* **139**(3), 031202-1–031202-7 (2017)
15. Parent, M.O., Thouverez, F., Chevillot, F.: Whole engine interaction in a bladed rotor-to-stator contact. In: *ASME Turbo Expo 2014: Turbine Technical Conference and Exposition*. American Society of Mechanical Engineers, 2014
16. Sun, J., Arteaga, I.L., Kari, L.: General shell model for a rotating pretwisted blade. *J. Sound Vib.* **332**(22), 5804–5820 (2013)
17. Yoo, H.H., Kim, S.K., Inman, D.J.: Modal analysis of rotating composite cantilever plates. *J. Sound Vib.* **258**(2), 233–246 (2002)
18. Sinha, S.K., Zylka, R.P.: Vibration analysis of composite airfoil blade using orthotropic thin shell bending theory. *Int. J. Mech. Sci.* **121**, 90–105 (2017)
19. Sun, Q., Ma, H., Zhu, Y.P., et al.: Comparison of rubbing induced vibration responses using varying-thickness-twisted shell and solid-element blade models. *Mech. Syst. Sig. Process.* **108**, 1–20 (2018)



Blade Modal Analysis by Means of Continuous Optical Fiber Sensors

Paolo Pennacchi^(✉), Gabriele Cazzulani^(iD), Martina Chieppi,
and Andrea Colombo

Department of Mechanical Engineering, Politecnico di Milano,
Via G. La Masa 1, 20145 Milan, Italy
paolo.pennacchi@polimi.it

Abstract. A new method for blade modal analysis is introduced in this paper by using continuous optical fiber sensors and optical backscatter reflectometer technology. The main advantage is that the sensor is few invasive and does not affect substantially system parameters. Moreover, the optical fiber sensor can be embedded in composite blades, for instance directly woven in carbon fiber fabric. This allows the sensor to be always installed and ready to use for continuous condition monitoring of the blade.

Differently from classical sensors, which can be placed independently from the others, in this case, all the measurement points are placed on the same wire (the fiber itself), characterized by a finite length. Furthermore, due to the physical characteristics of the fiber, some constraints on how the fiber is placed, such as maximum fiber curvature, must be considered. Moreover, strain measurements are collected and precise positioning is required to reconstruct correctly the displacement modal shapes from the strains.

In the literature, many optimal placement methods for sensors are proposed, but they are all referred to independent sensors. An optimal method for optical sensor placing on the blade for modal analysis is first introduced in the paper. Then, numerical and experimental tests performed on some blades are shown.

Keywords: Optical fiber · Blade mode shape reconstruction
Blade modal analysis · Optimal sensor arrangement · Rotordynamics

1 Introduction

Experimental modal analysis (EMA) is well-known and material tool for the identification of the dynamic characteristics of a structure [1, 2], including also blades employed in rotating machines [3]. In this case, the analysis is aimed at:

- predicting the locations of possible energy introduction. This permits the determination of fluid-structure interactions, which could be critical for the blade structure, and the design of devices for vibration damping [4–7];
- identifying the presence of possible cracks from the mode shapes and, with a suitable real-time system, controlling fatigue crack growth [8, 9];
- validating FE models, when complex geometries or inhomogeneous materials are used.

To completely decouple EMA from the use of numerical models, a high number of sensors is required to properly fit the different mode shapes of the structure and to distinguish between them, avoiding the so-called *spillover effect* [10].

One of the most promising solutions for this purpose is the use of optical fiber sensors [11–13], like the well-known fiber Bragg grating (FBG) sensors. Recently, other measurement techniques based on optical fiber sensors have been developed, allowing a continuous strain measurement along the fiber. This is the case, for example, of the optical backscatter reflectometer (OBR) technology, which is considered in this paper.

Anyway, the great potential of this kind of sensors must be exploited by suitably placing the sensor on the structure. Indeed, differently from classical sensors, which can be placed independently from the others, in this case all the measurement points are placed on the same wire (the fiber itself) and this wire is characterized by a finite length. Moreover, due to the physical characteristics of the fiber, some constraints on how the fiber is placed, such as the maximum allowed fiber curvature, must be considered, especially for highly twisted blades. Moreover, blade strains are measured and a proper position is required to be able to properly reconstruct the displacement modal shapes from strain measurements.

Many optimal placement methods for sensors have been proposed in the literature [14–18], but they are generally referred to independent sensors, like accelerometers, strain gauges, etc., while no methods can be found for this kind of continuous sensors, to the best knowledge of the authors. Aim of this paper is to propose an optimal method for continuous optical sensor placing on the structure for modal analysis.

After a brief recall of the optical sensing technology considered here (Sect. 2), the paper describes the optimal placement method, based on genetic algorithms (Sect. 3). Finally, Sect. 4 shows some significant numerical and experimental tests, which prove the good results obtained by using the proposed approach.

2 Optical Backscatter Reflectometry Sensors

Fiber optic sensors are an excellent solution for embedding in composite materials, thanks to their reduced cross-section and the consequent negligible load effect on the structure. Moreover, they can be embedded inside the structure during the manufacturing process, thus avoiding any surface alteration that may compromise the correct working of the structure, for example when a specific surface shape is required for fluid-structure interaction (e.g. turbine blades), or a free surface is necessary for the interaction with other components (e.g. mechanisms or joints).

Many different sensing technologies based on optical fibers are available, each one suitable for a range of applications depending on many parameters like the number of sensors, the fiber length or the frequency range. Among them, one interesting solution for vibration monitoring and modal analysis purposes is represented by OBR sensors [19, 20].

OBR fiber optics relies on the optical backscatter reflectometry physical principle: when an electromagnetic radiation, like a light beam or a laser, propagates in a medium, it collides and interacts with the incident atoms causing secondary electromagnetic

waves, called “*scattered*”, which are coherent and interact in a constructive way defining a weak, but detectable signal (see Fig. 1). If the medium is not homogeneous in terms of density (thus, in terms of refraction index), as a real fiber, the propagating wave gets scattered and then a back scattered wave is created. This phenomenon is called *spontaneous Rayleigh scattering*.

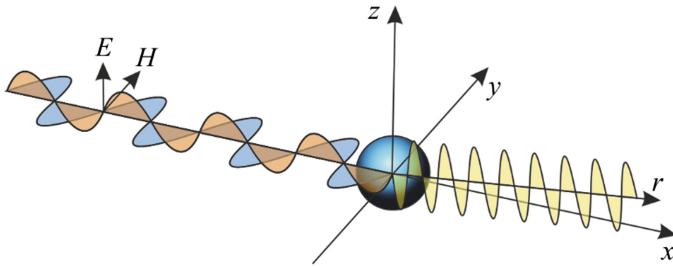


Fig. 1. Spontaneous Rayleigh scattering.

By varying the frequency of the laser wave, a periodic signal is created at the light sensor, whose frequency depends on the location of the respective fiber segment that scatters the light back. The further the segment away from the light sensor, the greater the frequency of the interference signal. As the light sensor receives the backscattered signal from all the segments simultaneously, the total signal must be split into its frequency components using a Fourier transform technique. The frequencies then correspond to the signal location along the fiber. The amplitude of each frequency component indicates the strength of the respective reflection.

The scanning of a commercial segment of optical fiber causes an oscillating intensity pattern of the Rayleigh scattering, which can be detected by a suitable detector. The measured pattern is stationary while repeating the measurements without applying any load. This characteristic is the fingerprint of the given optical fiber segment. Indeed, Rayleigh scattering is characterized by this phenomenon, which is due to both the elastic scattering and the variation of the index of refraction caused by local imperfections. The fingerprint is deformed in the space when a mechanical load or a temperature gradient is applied to the optical fiber segment. This is the fundamental principle of working of the OBR technology: local strain or temperature can be obtained from local pattern of Rayleigh scattering.

3 Optimal Sensor Placement Method

3.1 From Strain Measurements to Displacement Estimation

The procedure for optimal placement of continuous sensors should allow reconstructing the displacement modal shape of the structure starting from the available measurements.

Being the measurement output a strain measure, a strain-to-displacement procedure has to be implemented to obtain the structure displacements. In the literature, this is typically obtained by using the so-called DST-matrix method [21], which is based on a full a-priori knowledge of the modal shapes of the structure (displacement and strain modal shapes are linked by the numerical model itself). Anyway, for the purpose of this work, the modal shape estimation should rely on the model as less as possible. For this reason, the reconstruction of the displacement field of the structure must be obtained from the measurement of the strain in a number of points and in a given direction (i.e. the fiber direction in that points).

Considering the strain theory for thin plates, the surface strain of the plate can be expressed as

$$\epsilon_{xx} = \frac{\partial u}{\partial x} = -z \frac{\partial^2 u}{\partial x^2}, \quad \epsilon_{yy} = \frac{\partial v}{\partial y} = -z \frac{\partial^2 v}{\partial y^2} \tag{1}$$

$$\epsilon_{xy} = \frac{1}{2} \left(\frac{\partial u}{\partial y} + \frac{\partial v}{\partial x} \right) = \frac{1}{2} \left(-z \frac{\partial^2 w}{\partial x \partial y} - z \frac{\partial^2 w}{\partial x \partial y} \right) = -z \frac{\partial^2 w}{\partial x \partial y} = -\frac{1}{2} \gamma_{xy} \tag{2}$$

where x , y and z represent the reference system (see Fig. 2), u , v and w are the displacements along x , y and z respectively, ϵ_{xx} and ϵ_{yy} are the axial strain along x and y , while γ_{xy} represents the planar shear strain at 45°. All the other strain terms generally present in 3-D structures are equal to zero for thin plates.

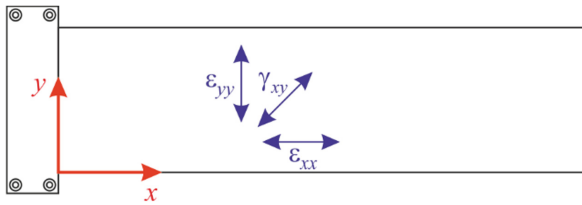


Fig. 2. Reference system for the thin plate under analysis.

Under a theoretical point of view, to obtain the displacement field (w), a few surface strain measurements with any direction are sufficient, since the displacement field can be obtained by double-integrating the strain field based on one of the two expressions in Eq. (1). In practice, this leads to non-robust results, because “information” from one direction only is employed, without considering what happens along the other ones.

For this reason, a different approach is adopted with the aim at considering strain information coming from different directions. Starting from

$$\begin{Bmatrix} \epsilon_{xx} \\ \epsilon_{yy} \\ \gamma_{xy} \end{Bmatrix} = \begin{bmatrix} \cos^2 \theta_1 & \sin^2 \theta_1 & \cos \theta_1 \sin \theta_1 \\ \cos^2 \theta_2 & \sin^2 \theta_2 & \cos \theta_2 \sin \theta_2 \\ \cos^2 \theta_3 & \sin^2 \theta_3 & \cos \theta_3 \sin \theta_3 \end{bmatrix}^{-1} \begin{Bmatrix} \epsilon_{\theta 1} \\ \epsilon_{\theta 2} \\ \epsilon_{\theta 3} \end{Bmatrix} \tag{3}$$

where $\varepsilon_{\theta i}$ represents the axial strain along a general i -th direction in a certain structure point, the shear strain γ_{xy} can be computed in the same structure point. Then, once the shear strain is known, the displacement w is computed by integrating twice the

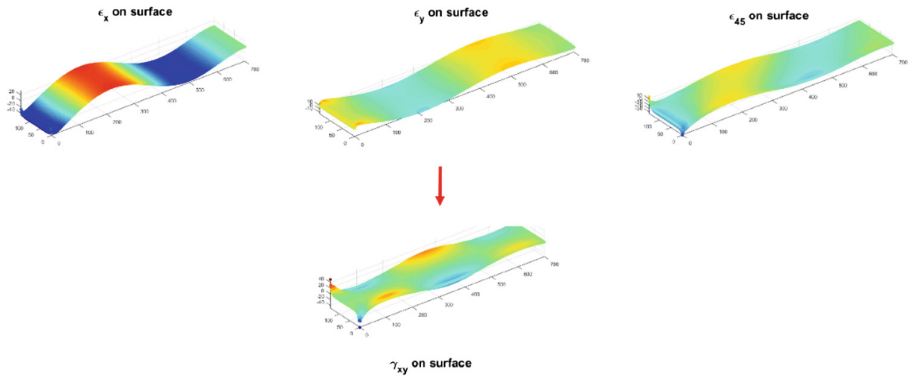


Fig. 3. Computation of the shear strain field from axial strain measurements.

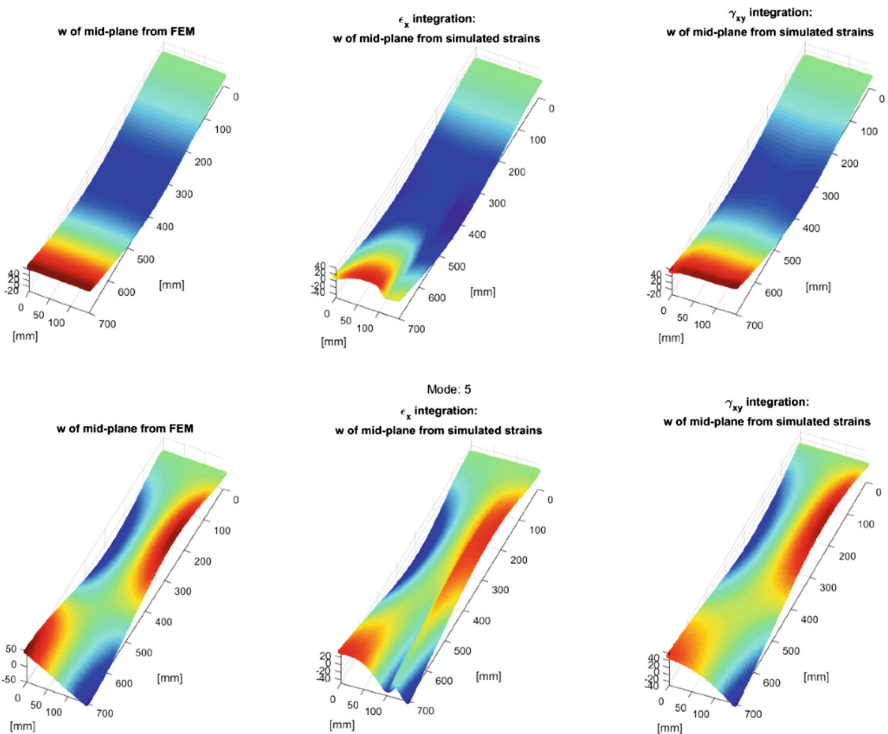


Fig. 4. Computation of the displacement field from axial strain along x (center) and from shear strain (right) compared with the correct displacement (left): lower order mode (on the top) and higher order mode (on the bottom)

expression in Eq. (1). To do that, the complete strain field along at least three directions must be known. By placing the optical fiber sensors along three directions, it is possible to interpolate them, obtaining the complete axial strain field along these directions and then to calculate γ_{xy} by using Eq. (2). An example of this procedure is shown in Fig. 3, while Fig. 4 shows an example comparing the displacement reconstruction obtained with this approach and using the axial strain measurements along the x -axis only. Both results are obtained considering 20 “virtual” sensors placed randomly on the structure.

3.2 Optimal Sensor Placing Algorithm

The optimal placing algorithm proposed in this paper is based on genetic algorithms (GA) [22]. Unlike FBG optical sensors, for which some optimal sensor placement methods can be found in the literature [14], OBR optical-fiber contains a huge number of embedded gauges. GA has to place the fiber dealing with a physically constrained continuous device. The continuity of the fiber-sensor is a tricky constraint to be dealt with. No kind of suggestion has been found in the literature concerning how to manage this specific aspect. Therefore, some new procedures have been implemented according to this fact.

It is necessary to develop a fiber-placement algorithm that works in the GA framework and tracks a potentially valid path for the fiber starting from a reduced number of encoded design variables (DVs). This approach permits producing valid sensor arrangements at each generation, depending on a fixed logic. As a matter of fact, too many constraints exist to allow the survival of whichever valid configuration, after a crossover if the whole fiber-path is encoded. For these reasons, the genetic coding and crossover procedure will not involve the whole fiber arrangement, but just a set of *outstanding* positions. These points, namely their position and orientation, represent the genes of each individual and build the chromosome, as represented in Fig. 5. The position is described by a number univocally representing a structure point, while orientation is described by another number representing the possible orientations allowed. In this example three possible orientations, identified by numbers 1, 2, and 3, are considered.

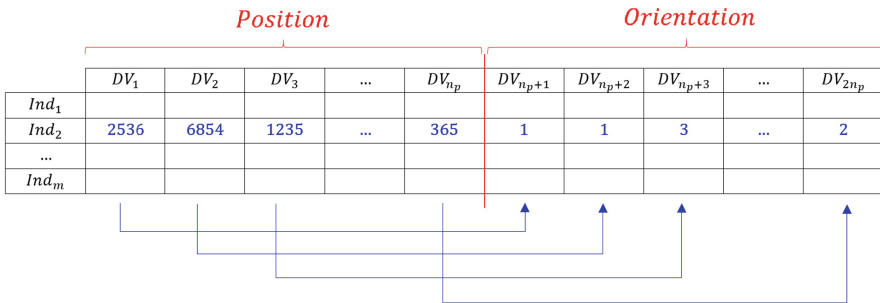


Fig. 5. Structure of the individual chromosome.

To obtain the full fiber path, these points will be connected in deterministic manner, providing the complete configuration of the fiber. Then, the individual fitness is computed accounting for the information available by the complete configuration. If the configuration exceeds the maximum fiber length, it is excluded by setting the corresponding fitness function to zero. Being the connection strategy deterministically dependent on the relative position and orientation of the *outstanding* locations, the genetic heritability of fiber arrangement is guaranteed among generations. Figure 6 resumes how the fitness function of the GA is calculated, as described above.

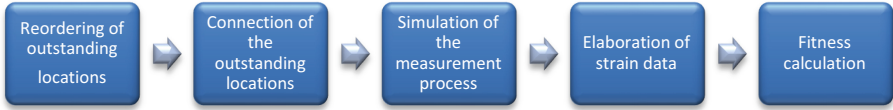


Fig. 6. Procedure for the definition of the fitness function of the genetic algorithm.

The fitness function, to be maximized by the GA, has been defined based on the scope of the algorithm and on the physical constraints the OBR sensor is subject to:

$$Fitness = \left\{ MSE_{weighted} \left[1 + \left(1 - \frac{\det FIM_{fiber}}{\det FIM_{global}} \right) + AutoMAC + \left(1 - \frac{bends_{min}}{bends_{fiber}} \right) \right] \right\}^{-1} \quad (4)$$

The fitness function is composed by:

- a main contribution ($MSE_{weighted}$), representing the mean square error between the estimated and real modal shape for all the considered modes. The weight is an user-defined coefficient that can be introduced to provide more importance to some modes;
- a penalty function ($\det FIM_{fiber}$) able to drive the optimization procedure to those points containing more significant strain information if compared to the global strain information of the structure;
- a penalty function, based on $AutoMAC$, to avoid fiber configurations for which two different modes cannot be distinguished one from the other;
- a penalty function ($bends_{fiber}$) to penalize configurations containing more fiber curves along the path than the minimum required ones.

While the first three elements of the fitness function depend on the target of the optimization procedure, the last one is strongly sensor-dependent and it is due to the fact that OBR sensors are characterized by a strong reduction of the measurement quality if the fiber is placed with many low-radius bends. The same optimization method can be used for any other kind of continuous sensor without losing generality, just removing this last penalty element.

4 Experimental Tests

4.1 Test Rig Setup with a Simple Plate

The optimal placement method proposed in the previous section has been tested on a PVC thin plate equipped with a LUNA OBR optical fiber. Figure 7 shows the gluing of the optical fiber on the structure, while Fig. 8 shows the experimental setup, where the plate has been mounted on a shaker to excite its modes. Two different mounting conditions have been used to excite both torsional and bending modes with the same unidirectional shaker.

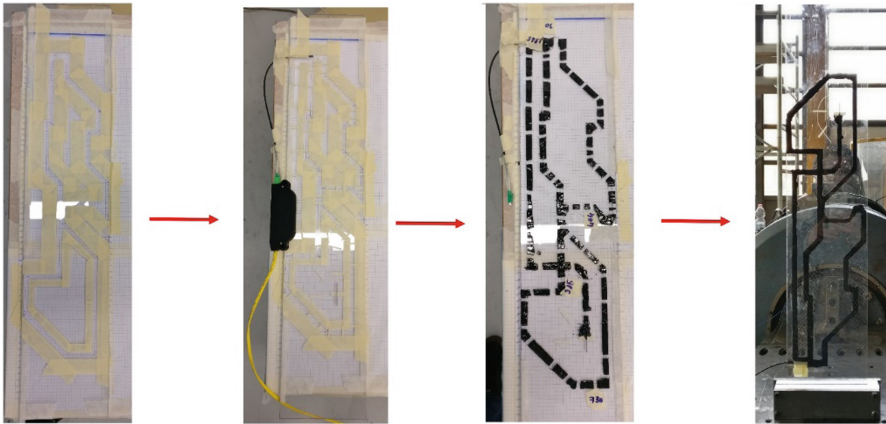


Fig. 7. Application of the optical fiber on the structure following the path identified by the optimal placing method.

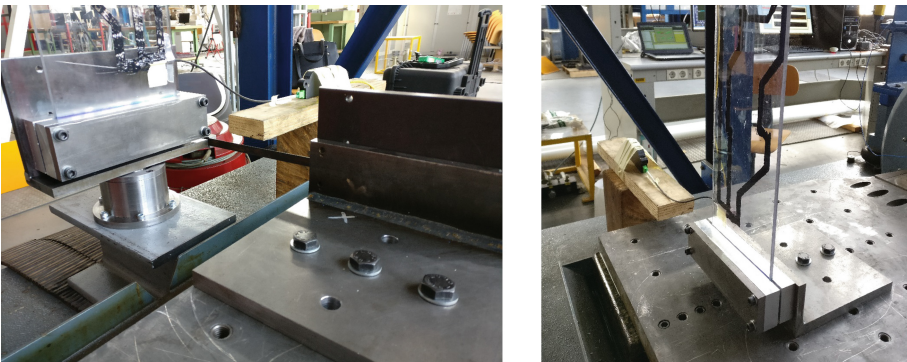


Fig. 8. Plate mounting on the shaker to excite the torsional modes (on the left) and the bending modes (on the right).

4.2 Optimal Sensor Placement Results

The following parameters have been considered as input for the placing algorithm:

- optical fiber length equal to 1.5 m;
- targeted modes from the 2nd to the 9th except to the 8th: the algorithm will optimize the fiber position to optimally identifying these modes;
- minimum fiber radius equal to 10 mm;
- three possible sensor directions (0°, 45° and 90° with respect to the x -axis).

Moreover, 100 individuals and mutation probability of 0.4 have been considered for the genetic algorithm.

Figure 9 shows the result obtained for the algorithm in this case. The segments of the fiber along the three allowed directions, representing the portions of the optical fiber that is used for the mode estimation, are represented with dots having different colors, namely blue for 0°, black for 45° and yellow for 90° with respect to the x -axis. The thin red lines represent the parts of the fiber used to connect the active measuring portions.

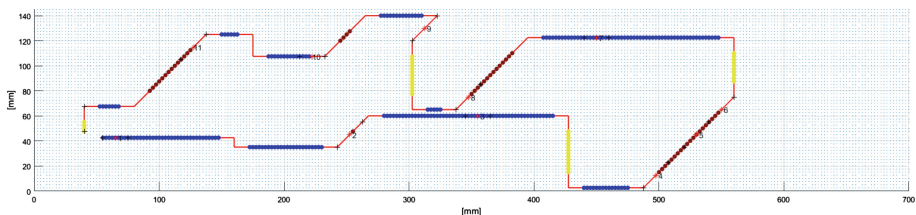


Fig. 9. Fiber configuration provided by the optimization algorithm.

4.3 Numerical and Experimental Mode Estimation Results

The optimal fiber configuration provided by the algorithm for the analyzed case study has been tested by means of numerical and experimental tests. The experimental ones have been done by forcing the structure on different resonances using the shaker and acquiring the fiber signals, while the numerical ones are obtained by simulating the fiber output on a FEM of the plate.

Due to the simplicity of the structure, the numerical and experimental results are expected to be similar, due to the very small differences between model and real structure. Anyway, a significant difference is related to the sensor measurement. Indeed, while numerical tests are performed under the assumption of ideal sensors (no noise, no measurement uncertainty, no signal quantization), the real output of OBR sensors is characterized by a poor signal quality and, as a consequence, by a potential loss of performance of the algorithm.

To reduce this effect on the final output of the modal analysis, an averaging among multiple vibrations cycles becomes necessary. Thus, the modal analysis of the structure cannot be performed punctually (i.e. a point-by-point estimation cannot be performed unless a high estimation error is accepted), but it must be performed on an acquisition window. Anyway, it must be underlined that the general validity of the proposed

procedure is not nullified by this issue, being it a characteristic of the particular fiber type used in this test setup.

For the sake of brevity, in the following only the results obtained on some significant modes are reported. For each represented mode, the ideal displacement modal shape (left), that estimated numerically (center) and that estimated from the experimental data (right) are reported.

In particular, Figs. 10 and 11 show the estimation result for 5th mode (second torsional mode) and 6th mode (fourth bending mode). It can be observed that in both cases the modal shape reconstruction provided by both numerical and experimental data are able to reproduce the real characteristics of the mode.

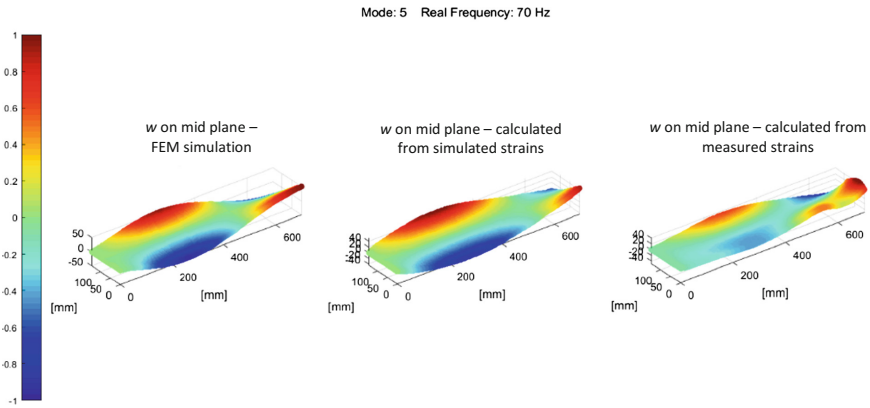


Fig. 10. Reconstruction of 5th mode: actual mode (left) and mode reconstructed by numerical data (center) and experimental data (right).

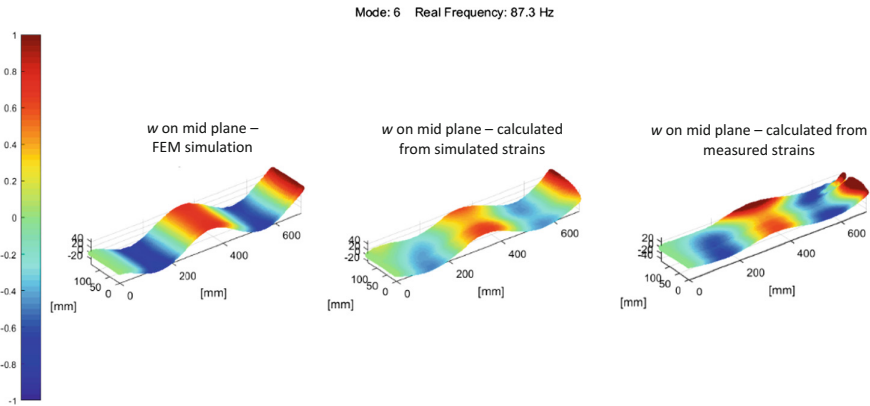


Fig. 11. Reconstruction of 6th mode: actual mode (left) and mode reconstructed by numerical data (center) and experimental data (right).

Different considerations can be drawn when analyzing the reconstruction of 8th mode (see Fig. 12). It is evident that in this case the mode shape reconstruction is not satisfactory, neither in the case it is computed from simulated strains, neither in the case of experimental measurements. Anyway, for the algorithm validation, this is a very good result, confirming the effectiveness of the fiber-placement. Indeed, 8th mode was not included as target mode in the optimization process and, for this reason, the capability of the sensor to properly identify this mode is poor.

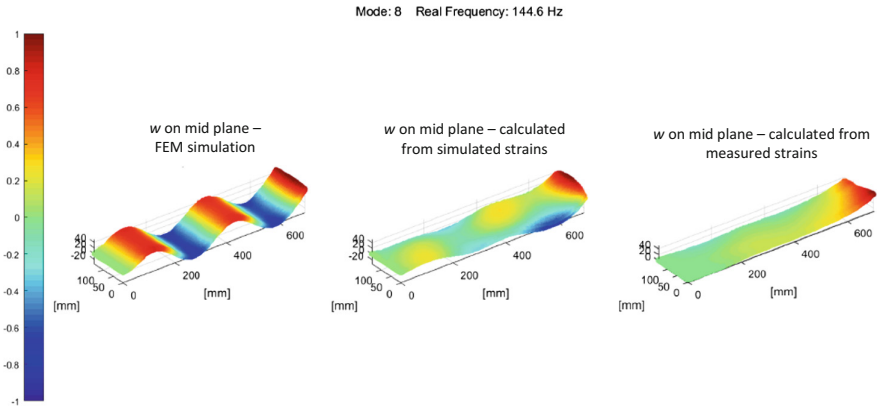


Fig. 12. Reconstruction of 8th mode: actual mode (left) and mode reconstructed by numerical data (center) and experimental data (right).

4.4 Tests on a Composite Blade

Once the good results obtained by the placing algorithm and by the measurement technique has been verified by means of the simple thin plate, a second test set-up, more substantial from the point of view of the application on the turbine blades, has been prepared.

For reasons related to simplicity of construction and mounting on the shaker, the blade used for the tests was made of ABS by additive manufacturing. The blade geometry was reproduced by means of the 3D reconstruction of a standard steam turbine blade (see Fig. 13). Obviously, given the elastic modulus of ABS lower than the steel one, the blade frequencies are scaled with respect to actual blade. For reasons of confidentiality, the original frequencies cannot be communicated.

Moreover, in the case of the blade, the accentuated 3D geometry due to the twist, involves two remarkable differences with respect to the thin plate case described in Sect. 4.1. The first one is relative to the reconstruction of the modal displacements starting from the 3D strain measurements: in this case, the strain theory for 3D solids requires a radical, even if not conceptual, modification of the contents of Sect. 2. The second is relative to the precise 3D reference for the positioning of the optical fiber on the blade. This fact has required the development of a suitable blade mapping algorithm. Also in this case, the optical fiber sensor has been glued to the blade surface,

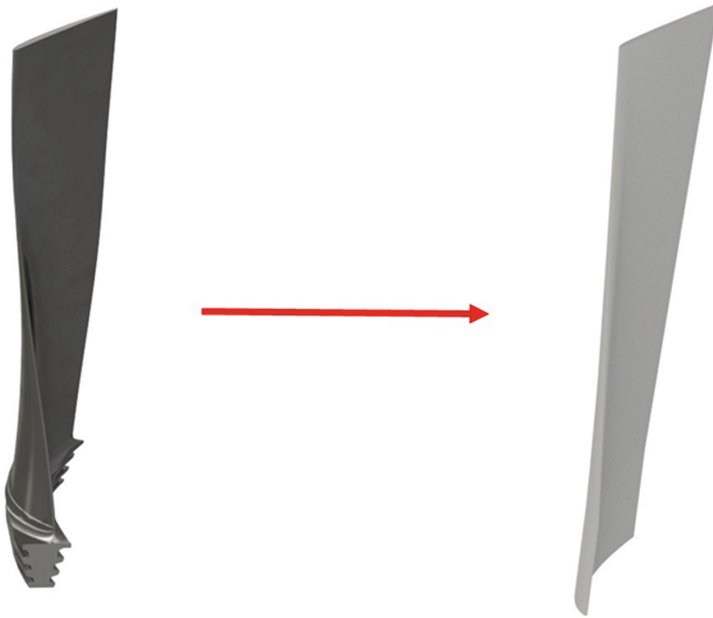


Fig. 13. Comparison among real blade and 3D ABS model.

optimizing its arrangement according to the algorithm introduced in Sect. 3.2. For the sake of brevity, it is not possible to illustrate all the theoretical details in this paper, but both these problems have been solved to allow the experimental tests to be carried out.

In the case of the ABS blade, a single mounting was used on the shaker, since it was not necessary a specific one for the excitation of bending or torsional modes. The results are shown in Figs. 14 and 15 for the first two blade modes and for the

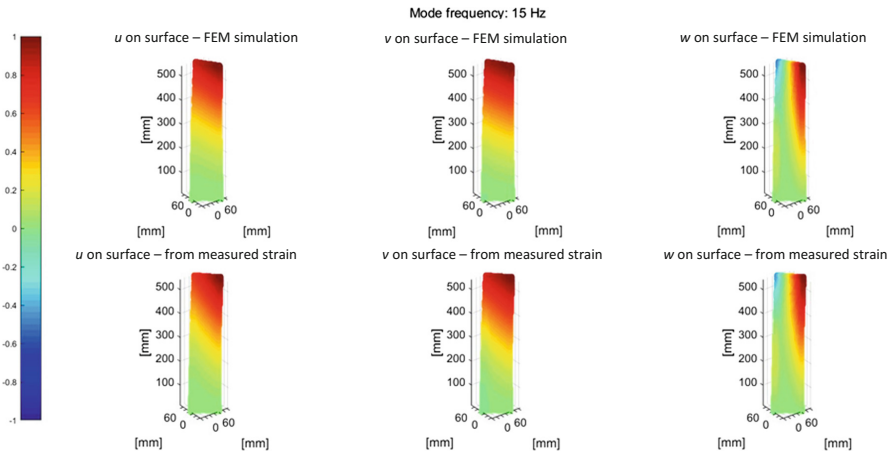


Fig. 14. 3D-blade experimental 1st mode-shape at 15 Hz.

displacements along the three reference axes and are compared with those obtained with the FEM model of the blade.

It is worth noting the good fitting between the FEM simulations of the modal displacements and the measurements obtained by OBR. Further tests are underway, by using a composite blade, in which the sensor is directly embedded in the structure.

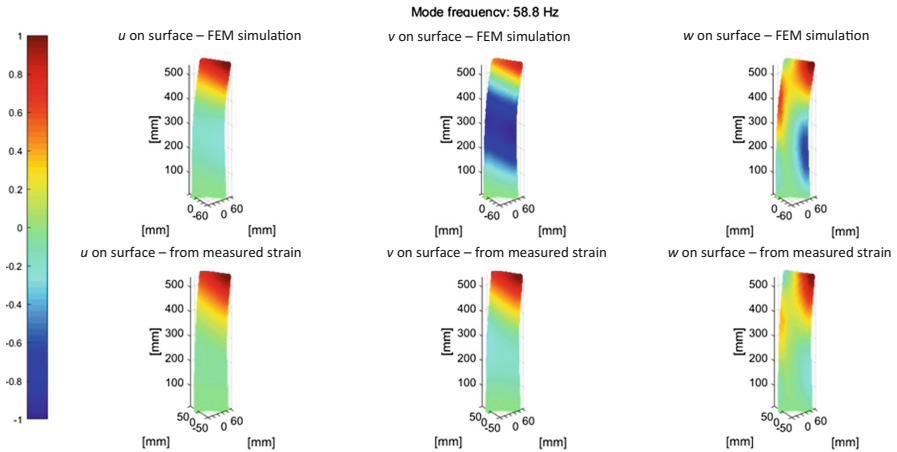


Fig. 15. 3D-blade experimental 2nd mode-shape at 58.8 Hz.

5 Conclusions

This paper proposed a new method to optimally place a continuous sensor, like an optical fiber one, on a structure for modal analysis purpose. The method is based on a genetic algorithm optimization able to find the best fiber configuration to correctly identify a number of structural modes under some constraints related to the fiber length and its measuring characteristics.

The proposed method has been first numerically and experimentally tested on a structure represented by a thin plate. The results obtained by placing the fiber based on the optimization algorithm have been compared to those obtained by placing the fiber in generic configurations, showing a strong improvement on the estimation of structural modal shapes. The second test has been performed on a 3D blade specimen: also in this case, the measured displacements fit well with those of FEM modal analysis.

Thanks to the advantages of optical fiber sensors, this approach can be used in several of applications, such as vibration monitoring of composite structures.

References

1. Ewins, D.J.: Modal testing: theory and practice. Wiley, New York (1984)
2. Friswell, M., Mottershead, J.E.: Finite Element Model Updating in Structural Dynamics. Springer, Berlin (1995)

3. Kuts, V.A., Nikolaev, S.M., Voronov, S.A.: The procedure for subspace identification optimal parameters selection in application to the turbine blade modal analysis. *Procedia Eng.* **176**, 56–65 (2017)
4. Pennacchi, P., Chatterton, S., Bachschmid, N., Pesatori, E., Turozzi, G.: A model to study the reduction of turbine blade vibration using the snubbing mechanism. *Mech. Syst. Signal Process.* **25**(4), 1260–1275 (2011)
5. Madhavan, S., Jain, R., Sujatha, C., Sekhar, A.S.: Vibration based damage detection of rotor blades in a gas turbine engine. *Eng. Fail. Anal.* **46**, 26–39 (2014)
6. Firrone, C.M., Zucca, S.: Underplatform dampers for turbine blades: the effect of damper static balance on the blade dynamics. *Mech. Res. Commun.* **36**(4), 515–522 (2009)
7. Zhang, D., Hong, J., Ma, Y., Chen, L.: A probability method for prediction on high cycle fatigue of blades caused by aerodynamic loads. *Adv. Eng. Softw.* **42**(12), 1059–1073 (2011)
8. Ciang, C.-C., Lee, J.-R., Bang, H.-J.: Structural health monitoring for a wind turbine system: a review of damage detection methods. *Meas. Sci. Technol.* **19**(12), 1–20 (2008)
9. Schroeder, K., Eckel, W., Apitz, J., Lembke, E., Lenschow, G.: A fibre Bragg grating sensor system monitors operational load in a wind turbine rotor blade. *Meas. Sci. Technol.* **17**(5), 1167–1172 (2006)
10. Yuan, Y.: Structural dynamics model updating with positive definiteness and no spillover. *Math. Probl. Eng.* **2014**, 1–6 (2014)
11. Cusano, A., Capoluongo, P., Campopiano, S., Cutolo, A., Giordano, M., Felli, F., Paolozzi, A., Caponero, M.: Experimental modal analysis of an aircraft model wing by embedded fiber Bragg grating sensors. *IEEE Sens. J.* **6**(1), 781–800 (2006)
12. Rapp, S., Kang, L.-H., Mueller, U.C., Hana, J.-H., Baier, H.: Displacement field estimation for a two-dimensional structure using fiber Bragg grating sensor. *Smart Mater. Struct.* **18**, 534–542 (2009)
13. Kang, L.-H., Kim, D.-K., Han, J.-H.: Estimation of dynamic structural displacements using fiber Bragg grating strain sensors. *J. Sound Vib.* **305**, 534–542 (2007)
14. Geng, L., Zhu, X., Zhang, H., Gao, Z., Liu, K.: Optimal placement of FBG sensors for reconstruction of flexible plate structures using modal approach. In: 34th Chinese Control Conference (2015)
15. Castro-Triguero, R., Murugan, S., Friswell, M.I., Gallego, R.: Optimal sensor placement for structures under parametric uncertainty. In: Proceedings of the 31st IMAC, Garden Grove, CA, USA (2012)
16. Meo, M., Zuppano, G.: On the optimal sensor placement techniques for a bridge structure. *Eng. Struct.* **27**, 1488–1497 (2005)
17. Papadimitriou, C., Beck, J.L., Au, S.K.: Entropy-based optimal sensor location for structural model updating. *J. Vib. Control* **6**, 781–800 (2000)
18. Tong, K.H., Bakhary, N., Kueh, A.B.H., Mohd Yassin, A.Y.: Optimal sensor placement for mode shapes using improved simulated annealing. *Smart Struct. Syst.* **13**(3), 389–406 (2013)
19. Huang, K.-Y., Carter, G.M.: Coherent optical frequency domain reflectometry (OFDR) using a fiber grating external cavity laser. *IEEE Photonics Technol. Lett.* **6**(12), 1466–1468 (1994)
20. Soller, B.J., Gifford, D.K., Wolfe, M.S., Froggatt, M.E.: High resolution optical frequency domain reflectometry for characterization of components and assemblies. *Opt. Express* **13**, 666–674 (2005)
21. Rapp, S., Kang, L.-H., Han, J.-H., Mueller, U.C., Baier, H.: Displacement field estimation for a two-dimensional structure using fiber Bragg grating sensors. *Smart Mater. Struct.* **18**(2), 1–12 (2009)
22. Zhang, H., Lennox, B., Goulding, P.R., Leung, A.Y.T.: Float-encoded genetic algorithm technique for integrated optimization of piezoelectric actuator and sensor placement and feedback gains. *Smart Mater. Struct.* **9**(4), 552–557 (2000)

Modal Testing and Identification



Identification of Coupling Parameters in Flexibly Coupled Jeffcott Rotor Systems with Angular Misalignment and Integrated Through Active Magnetic Bearing

R. Siva Srinivas¹, R. Tiwari¹(✉), and Ch. Kannababu²

¹ Indian Institute of Technology Guwahati, Guwahati 781039, India
rtiwari@iitg.ernet.in

² Aero Engine Research and Design Centre, Hindustan Aeronautics Limited,
Bangalore 560093, India

Abstract. In the present work, a rotor train system is connected by a flexible coupling and integrated with an auxiliary active magnetic bearing. Due to angular misalignment that exists between the shafts, coupling stiffness varies with shaft rotation. A mathematical function that is time-dependent and which can yield integer harmonics has been chosen to numerically model coupling additive stiffness. The equations of motion have been obtained from Lagrange's equation. The amplitude and phase of peaks of rotor vibration and AMB current signatures have been obtained in time and frequency domains using least-squares regression technique and full spectrum technique, respectively. They are eventually utilized to identify the intact and additive stiffness of coupling, viscous damping, unbalance magnitude and phase, and the AMB displacement and current stiffness. A SIMULINK™ has been built to generate time domain responses of discs and AMB current. From the EOM of rotors regression equations have been formed in frequency domain to create an inverse problem. The identification algorithm has been found to be robust against noise levels up to 5%.

Keywords: Rotor-train · Misalignment · Active magnetic bearing
Full spectrum

1 Introduction

Among the faults that are encountered in field operation of rotating system, misalignment is the one of the predominant faults. It arises due to loss of co-axiality between rotors and bearings, which is caused due to improper assembly and deformation caused due to thermal effects. It leads to decrease in transmission efficiency, bearing wear, noise and reduction of life in bearings.

Gibbons [1] made study on parallel misalignment and gave expressions for forces and moments generated in the coupling. Sekhar and Prabhu [2] and Rao and Sekhar [3] considered both parallel and angular misalignment in flexible coupling and set up formulae for reaction forces and moments. Prabhu [4] studied the influence of

misalignment on various harmonics of vibration response in rotor system with multiple disks supported on journal bearings. It was concluded that with increase in misalignment the amplitude of 2nd harmonic initially decreased and then increased. Rao et al. [5] studied parallel misalignment in a coupled Jeffcott rotor test rig. Higher vibrations and loopy orbits were noticed at one-half and one-third of the first critical speed. Numerical studies done in [6] on rigidly coupled rotors indicated that parallel misalignment could produce both translational and angular excitations.

In [7] rigid coupling stiffness is considered to be a sum of static and fluctuating components. The effect of parallel offset in a rotor system is considered in the presence of torsional excitation. In [8], the parallel and angular misalignments were introduced in a test set up, fluctuating forces and moments were then measured at the bearing location with a 6-axis load cell and input as force terms in the finite element model. The FFT of the vibration responses yielded all the integer harmonics. Jalan and Mohanty [9] identified unbalance and misalignment by comparing the equivalent forces generated due to faults obtained from both experiment and theoretical fault model. Avendano and Childs [10] used CosmosTM solid modeling tool to create three types of disc-pack couplings. The forces and moments obtained from FE analysis for various misalignment conditions were fit into Fourier series expansion. Verma et al. [11] used both vibration and motor current signals for misalignment detection in machinery fault simulator. In [12], it was reported that the spectral characteristics of torque sensor measurements for the parallel and angular misalignments differ from each other. Moreover, wavelets are found to be more sensitive than FFT to the presence of misalignment. Lal and Tiwari [13, 14] studied the numerical and experimental identification of coupling parameters in rigid and flexible rotor systems from run-down data.

Works on misalignments broadly deal with the following methods (i) numerical and experimental identification of static forces and moments, (ii) experimental identification/diagnosis using techniques such as orbits, spectral plots, thermal imaging [15], stator current analysis [11]. For more information on diagnostics of misalignment, apart from the numerous papers, the readers are referred to the books by [16, 17, 18, 19, 20] For information on applications of AMB in condition monitoring and vibration suppression, readers are requested to refer to [21].

This work aims to study the static and more importantly time dependent coupling misalignment forces in coupled rotor systems using an AMB. AMB current has been used for suppressing vibration and identification of unbalance magnitude and phase, coupling stiffness parameters, displacement and current constants of AMB. The mathematical formulation of coupled rotor-AMB system has been developed. The development of SimulinkTM model is then described. The equations used for the identification of harmonics of displacement of the two rotors and the AMB current using time domain regression technique have been developed. The application of full spectrum to the present problem has been explained. Finally, the equations used for the identification of system parameters have been developed and tested numerically.

2 System Configuration

2.1 Introduction

Coupled rotor systems are widely used in industrial gas turbines, compressors, and turbo generators. Power is transmitted from driving unit to driven unit across multiple stages of rotors through couplings. The coupling used can be of rigid or flexible type, the choice depending upon the rpm, power transmitted and application. Rigid couplings offer better power transmission with not much allowance for misalignment, while flexible couplings allow significant misalignment between the bearing centers of rotating units.

Coupled Rotor-Bearing-AMB System. A motor drives a coupled rotor bearing system through a drive coupling. The drive is transmitted from rotor-1 to rotor-2 by an intermediate flexible coupling (see Fig. 1). The behavior of intermediate coupling alone is considered in this work. The unbalance force is defined by a residual mass located at an angle from the reference x axis (see Fig. 2).

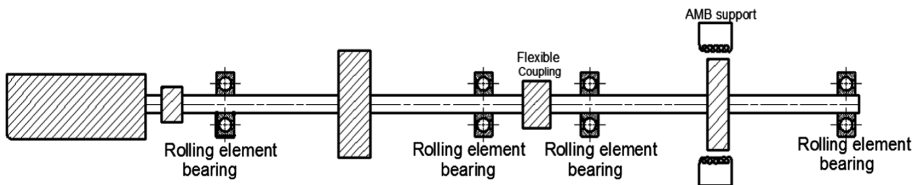


Fig. 1. Coupled rotor bearing system supported on auxiliary AMB

3 Assumptions

1. Coupling is modeled as a torsion spring since only angular misalignment is considered in the present study (see Fig. 3). The cross-coupled stiffness of coupling is less than direct stiffness.
2. Since the formulation uses Jeffcott rotors, the slopes at coupling and support are assumed to be equal. Putting it differently, it is assumed that coupling is near to support axially.
3. Coupling is assumed to be flexible and disc is assumed to be heavy. These are the crucial assumptions in the development of mathematical model for the present problem.
4. The previous assumptions lead to a linear mathematical relation between the deflection of central disc and coupling slope. This is on account of the fact that the slope of shaft at coupling location is due to the central heavy disc.
5. In other words, the linear and angular deflections of rotors produced by coupling forces and moments are less than that due to their self-weight, i.e. weight dominance is assumed. Similar assumption has been made by [4].

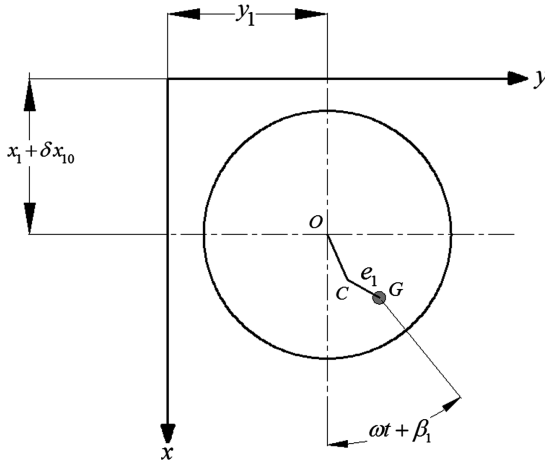


Fig. 2. Angular position of unbalance

- 6. Since the coupling is flexible, reaction moments and the corresponding slopes due to misalignment are small compared to that caused by the heavy disc at the shaft center. This assumption does not hold good for the rigid coupling model.

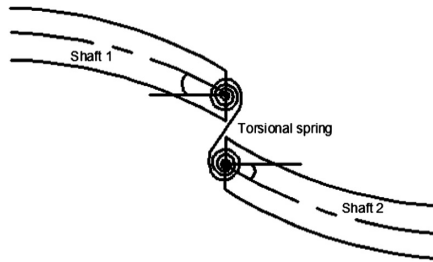


Fig. 3. Flexible coupling replaced by helical torsion spring

4 Mathematical Modeling

Translational displacements at 2 disc locations, i.e. x_1, y_1, x_2, y_2 , are the generalized coordinates of the coupled rotor system. The slopes at coupling locations for shafts are given by $\varphi_{x_1}, \varphi_{y_1}, \varphi_{x_2}, \varphi_{y_2}$. With heavy central disc assumption, there is a linear relation between disc deflections and shaft slopes at coupling locations. From the relations for deflection and slope of a simply supported shaft with point load at center, the following relation applies

$$\varphi_{x_1} = \frac{3y_1}{l}; \quad \varphi_{x_2} = \frac{3y_2}{l}; \quad \varphi_{y_1} = \frac{3x_1}{l}; \quad \varphi_{y_2} = \frac{3x_2}{l} \tag{1}$$

The expressions for kinetic energy and potential energy are given by

$$KE = \frac{1}{2}m_1\dot{x}_1^2 + \frac{1}{2}m_1\dot{y}_1^2 + \frac{1}{2}m_2\dot{x}_2^2 + \frac{1}{2}m_2\dot{y}_2^2 \quad (2)$$

$$PE = \frac{1}{2}k_1x_1^2 + \frac{1}{2}k_1y_1^2 + \frac{1}{2}k_1x_2^2 + \frac{1}{2}k_1y_2^2 + \frac{1}{2}k_{\varphi_x}(\varphi_{y_1} + \varphi_{y_2}) + \frac{1}{2}k_{\varphi_y}(\varphi_{x_1} + \varphi_{x_2}) \quad (3)$$

Since there is no slope at the central span disc the rotational kinetic energy term about transverse axes is zero. The equations of motion for rotor-1 and rotor-2 are obtained by applying Lagrange's equation. Since AMB acts as auxiliary support for rotor-2, the corresponding terms appear on the RHS of Eq. 2. To reduce computational complexity the equations are written in complex form by introducing, $r = x + iy$. The FFT of the complex form also helps in the extraction of harmonics, which shall be discussed in later sections

$$m_1\ddot{r}_1 + c_1\dot{r}_1 + (k_1 + k_{t_o})r_1 - k_{t_o}r_2 = f_{unb_1} + f_{mis_1} - F_{const_1} \quad (4)$$

$$m_2\ddot{r}_2 + c_2\dot{r}_2 + (k_2 + k_{t_o} - k_s)r_2 - k_{t_o}r_1 = f_{unb_2} + f_{mis_2} - f_{cur} - F_{const_2} \quad (5)$$

where

$$k_{t_x} = (3/l)^2k_{\varphi_x} \quad \text{and} \quad k_{t_y} = (3/l)^2k_{\varphi_y} \quad (6)$$

Complex unbalance forces for rotors are given by

$$f_{unb_i} = m_i e_i \omega^2 e^{j(\omega t + \beta_i)} \quad (7)$$

Complex coupling misalignment forces for rotors are given by

$$f_{mis_1} = f_{mis_2} = (1/2)s(t)\Delta k(\delta x_1 + \delta x_2)(1 + e^{2j\omega t}) \quad (8)$$

Constant coupling force is given by

$$F_{const_1} = F_{const_2} = k_{t_0}(\delta x_1 + \delta x_2) \quad (9)$$

Complex AMB current force is given by

$$f_{cur} = k_l \sum_{i=-n}^{+n} I_i e^{ij\omega t} \quad (10)$$

4.1 Coupling Excitation Function

Experimental data on the misalignment published by [8] have shown the presence of all integer harmonics on either side of full-spectrum. Hence, it is essential that a suitable

coupling stiffness function, which generates integer harmonics in the response, is chosen as a steering function in the mathematical model.

40% duty cycle pulse waveform with (see Fig. 4) is used to represent coupling misalignment. The Fourier expansion is shown below

$$s(t) = 0.5 + 0.6055 \cos(\omega t) + 0.1871 \cos(2\omega t) - 0.1247 \cos(3\omega t) - 0.1514 \cos(4\omega t) + 0.1009 \cos(6\omega t) + 0.0535 \cos(7\omega t) \tag{11}$$

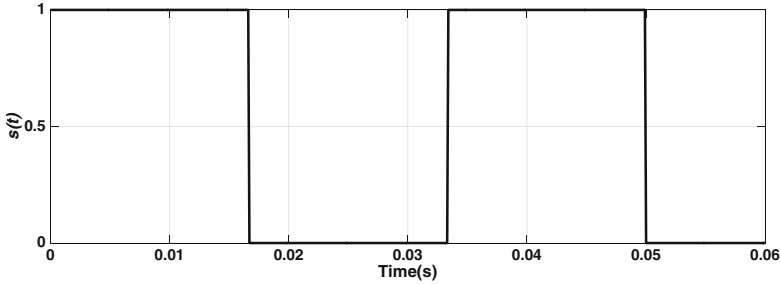


Fig. 4. Time domain signal of 40% duty cycle square wave

The expanded form of complex coupling misalignment forces is then given by

$$f_{mis_1} = f_{mis_2} = \Delta k(\delta x_1 + \delta x_2) \{ 0.25 + 0.3027e^{j\omega t} + 0.1201e^{-j\omega t} + 0.2967e^{2j\omega t} + 0.0089e^{-2j\omega t} + 0.1202e^{3j\omega t} - 0.0312e^{-3j\omega t} + 0.0089e^{4j\omega t} - 0.0037e^{-4j\omega t} - 0.0312e^{5j\omega t} - 0.0133e^{-5j\omega t} + \dots \} \tag{12}$$

The above Fourier expansion from [22] shall be used in the derivation of time dependent coupling excitation force caused by bearing misalignment.

Numerical Experiment with Simulink™ Model. The simplified model of the Simulink™ block that has been built from Eqs. (4) and (5) (see Fig. 5). Assumed values used for the generation of responses in time domain are shown in Table 1.

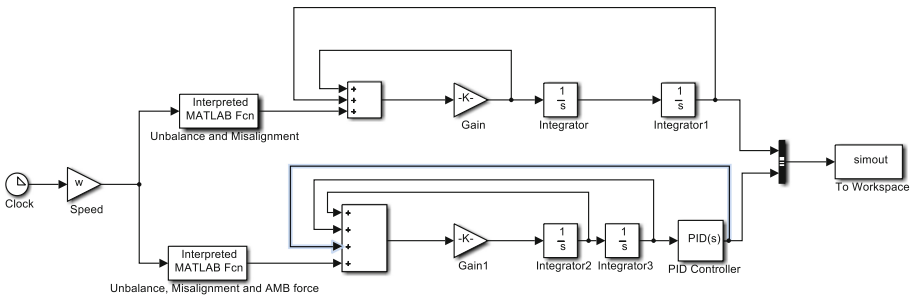


Fig. 5. Simulink model of coupled rotor – AMB system

The model generates complex displacement of rotor-1, rotor-2, complex AMB current and a multi-harmonic reference signal in time domain. The role and necessity of reference signal shall be discussed in Sect. 5.

Table 1. Assumed parameters of rotor system

m_1, kg	2	$k_2, \text{N/m}$	7.5e5
m_2, kg	2.5	$k_\varphi, \text{Nm/rad}$	300
$c_1, \text{N/m-s}$	75	$k_I, \text{N/m}$	10800
$c_2, \text{N/m-s}$	50	$\Delta k, \text{N/m}$	5000
$k_1, \text{N/m}$	7.5e5	$\delta_{x_1}, \mu\text{m}$	26
$k_I, \text{A/m}$	42.1	$\delta_{x_2}, \mu\text{m}$	30
$e_1, \mu\text{m}$	2.40	$k_p, \text{A/m}$	12200
$e_2, \mu\text{m}$	1.92	$k_i, \text{A/m-s}$	2e3
β_1, rad	$\pi/6$	$k_d, \text{A-s/m}$	3
β_2, rad	$\pi/4$	$k_S, \text{N/m}$	105210

5 Estimation of Coefficients of Harmonics in Time Domain: Least Squares Regression Method

Complex vibration responses of rotor-1 which are caused by misalignment at various instants of time and obtained from SimulinkTM model are multi-harmonic in nature and are given by

$$(\mathbf{A}_1)_{n \times i} (\mathbf{X}_{R_1})_{i \times 1} = (\mathbf{b}_{r_1})_{n \times 1} \quad (13)$$

with

$$(\mathbf{A}_1)_{n \times i} = \begin{bmatrix} 1 & e^{j\omega t_1} & \dots & e^{j(5\omega)t_1} & \dots & e^{j(-\omega)t_1} & \dots & e^{j(-5\omega)t_1} & \dots \\ 1 & e^{j\omega t_2} & \dots & e^{j(5\omega)t_2} & \dots & e^{j(-\omega)t_2} & \dots & e^{j(-5\omega)t_2} & \dots \\ \vdots & \vdots & \vdots & \vdots & \vdots & \vdots & \vdots & \vdots & \vdots \\ \vdots & \vdots & \vdots & \vdots & \vdots & \vdots & \vdots & \vdots & \vdots \\ 1 & e^{j\omega t_n} & \dots & e^{j(5\omega)t_n} & \dots & e^{j(-\omega)t_n} & \dots & e^{j(-5\omega)t_n} & \dots \end{bmatrix} \quad (14)$$

$$(\mathbf{b}_{r_1})_{n \times 1} = \{ r_{1c}(t_1) \quad r_{1c}(t_2) \quad r_{1c}(t_3) \quad \dots \quad \dots \quad r_{1c}(t_n) \}^T \quad (15)$$

And the vectors of unknowns are given by

$$(\mathbf{X}_{R_1})_{i \times 1} = \{ R_{10}(\omega) \quad R_{11}(\omega) \quad \dots \quad R_{15}(\omega) \quad \dots \quad R_{-11}(\omega) \quad \dots \quad R_{-15}(\omega) \quad \dots \}^T \quad (16)$$

Analogous matrix relations exist for rotor-2 vibration response and AMB current. All three relations are combined in to a single matrix equation. The complex harmonics of vibration and current are obtained by solving this equation

$$[\mathbf{X}_{R_1} \quad \mathbf{X}_{R_2} \quad \mathbf{X}_I] = (\mathbf{A}_1^T \mathbf{A}_1)^{-1} \mathbf{A}_1^T [\mathbf{b}_{r_1} \quad \mathbf{b}_{r_2} \quad \mathbf{b}_i] \tag{17}$$

where \mathbf{A} is the regression matrix, \mathbf{X} is the vector of unknowns (complex harmonics, in this case) to be determined and \mathbf{b} is the vector of known quantities.

6 Estimation of Coefficients of Harmonics in Frequency Domain: Full Spectrum FFT

The frequencies contained in the time domain current and displacement signals can be extracted using Fast Fourier Transform (FFT) algorithm. Since both positive and negative frequencies are contained in the signal, a full spectrum plot needs to be used to understand the qualitative nature of fault the time domain signal represents. A comprehensive treatment of the mathematical procedure to obtain full spectrum and its application to rotating machinery diagnostics has been given in [23]. Coefficients of harmonics from -5 to $+5$ can be seen in the full spectrum amplitude plot of rotor-1 complex displacement (see Fig. 6). The phase plot shows the phase angle of each harmonic with reference to the timing marker on the shaft.

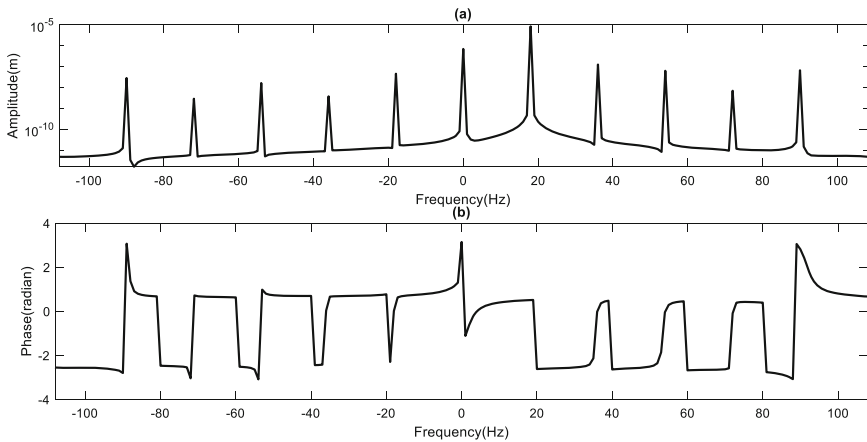


Fig. 6. Full spectrum of amplitude and phase of rotor-1 complex displacement

6.1 Phase Correction and Its Necessity

It has been noticed that as the time instants of signal acquisition change, a variation in phase information takes place. The amplitude information of harmonics, on the other hand, remains unaffected by this time shift. To account for this phase variation,

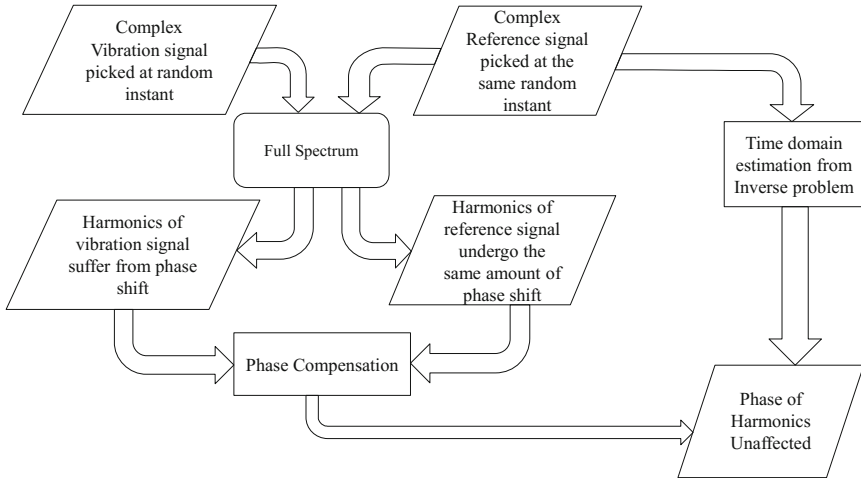


Fig. 7. Flow chart of phase compensation procedure

a complex multi-harmonic reference signal has been envisaged by Singh and Tiwari [24], who were the first to utilize this technique for the identification of phase of the harmonics of current and displacement of a cracked Laval rotor (see Fig. 7). Table 2 shows the comparison of amplitudes and phases of harmonics obtained from time domain and full spectrum with phase compensation. It can be seen that the full spectrum shows good similarity to the values obtained from time domain inverse problem. Using full spectrum technique with “peak finding algorithm”, the coefficients of harmonics of interest can be obtained quicker than it can be done with time domain analysis.

Table 2. Comparison of harmonics obtained from time domain and full spectrum with phase compensation

Rotor 1 Harmonic	Complex amplitude		Phase	
	Time domain	Full spectrum	Time domain	Full spectrum
0	6.9723E-07	6.9721E-07	3.1415	3.1415
1	8.3553E-06	8.3553E-06	0.5023	0.5023
2	1.2485E-07	1.2483E-07	-0.0256	-0.0257
3	6.2611E-03	6.2599E-08	-0.0477	-0.0478
4	6.9469E-09	6.9379E-09	-0.0958	-0.0965
5	6.6242E-08	6.6247E-08	2.8065	2.8065
-1	4.5310E-08	4.5322E-08	0.0115	0.0117
-2	3.7451E-09	3.7524E-09	0.0261	0.0271
-3	1.6252E-08	1.6246E-08	-3.0940	-3.0942
-4	2.8879E-09	2.8834E-09	-3.0462	-3.0469
-5	2.8238E-08	2.8233E-08	-2.8065	-2.8065

7 Identification of Rotor, Coupling and AMB Parameters in Frequency Domain by Least Squares Regression Method

The expressions for complex displacement, velocity, acceleration and complex current are substituted in Eqs. (4) and (5). After writing the equations of rotor-1 and rotor-2 for $i = 0, i = 1, i \neq 1$, real and imaginary parts are separated from equations. The equations are later grouped into identifiable parameters and known parameters and grouped in regression matrix form as shown below.

$$\mathbf{A}_2 \mathbf{X}_2 = \mathbf{b}_2 \tag{18}$$

The system parameters or identifiable parameters are grouped in the column vector \mathbf{X}_2 . They can be obtained by solving

$$\mathbf{X}_2 = \left[(\mathbf{A}_2)^T (\mathbf{A}_2)^{-1} \right]^{-1} (\mathbf{A}_2)^T \mathbf{b}_2 \tag{19}$$

The values of \mathbf{X}_2 and \mathbf{b}_2 can be obtained from n number of spin speeds, which improves the condition number of regression matrix, thereby yielding closer estimates.

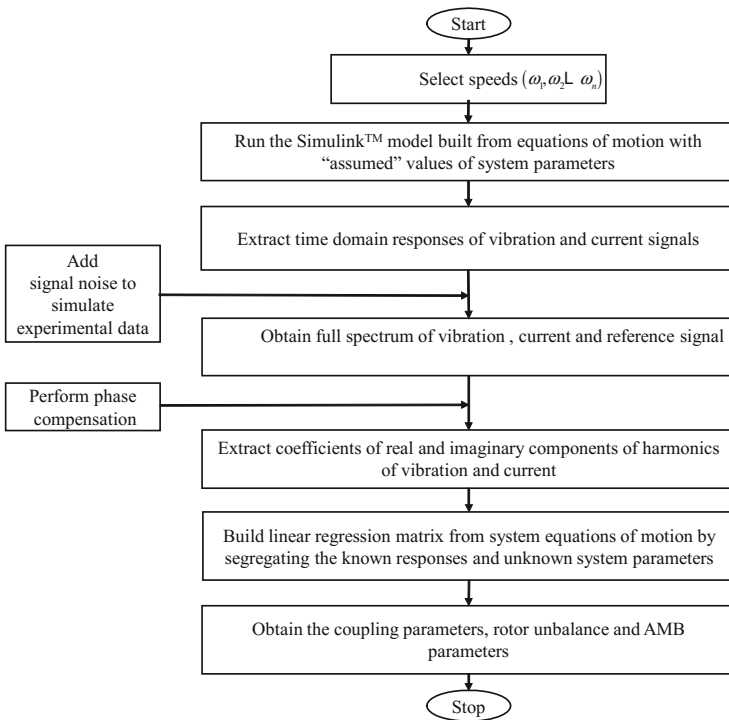


Fig. 8. Sequence of steps in rotor-coupling-AMB parameter identification

$$\begin{Bmatrix} \mathbf{A}_2(\omega_1) \\ \mathbf{A}_2(\omega_2) \\ \vdots \\ \mathbf{A}_2(\omega_n) \end{Bmatrix} \mathbf{X}_2 = \begin{Bmatrix} \mathbf{b}_2(\omega_1) \\ \mathbf{b}_2(\omega_2) \\ \vdots \\ \mathbf{b}_2(\omega_n) \end{Bmatrix} \tag{20}$$

The sequence of steps followed right from mathematical modeling till parameter identification is shown in the flow chart (see Fig. 8).

8 Results and Discussion

Table 3 shows the estimates of rotor-coupling-AMB parameters obtained from the inverse problem (17) at 18 Hz spin speed. The estimates obtained from clean signal are almost identical to the assumed values with error % less than -1%.

Table 3. Error percentage in identified parameters at various levels of noise at 18 Hz

	Assumed values	Estimated values			
		0%	1%	2%	5%
c_1	75	75.00	75.01	74.99	74.99
		0.0	0.02	-0.02	-0.01
c_2	50	49.82	49.32	48.65	48.72
		-0.95	-1.36	-2.70	-2.56
k_t	10800	10800.00	10805.56	10725.78	10793.31
		0.00	0.05	-0.69	-0.06
Δk_ξ	5000	5000.00	2001.07	1985.95	1998.52
		0.0	0.05	-0.70	-0.07
e_1	240E-6	239.99E-06	2.41E-04	2.42E-04	2.43E-04
		0.00	0.47	0.72	1.32
β_1	30	30.00	30.00	30.00	30.00
		0.00	0.00	0.00	0.01
e_2	240E-6	240E-06	1.93E-04	1.93E-04	1.95E-04
		0.0	0.46	0.76	1.34
β_2	45	44.99	45.00	44.99	44.99
		-0.01	-0.01	-0.01	-0.01
k_s	105210	104987	104189.74	104139.42	104200.22
		-0.98	-0.97	-1.02	-0.96
k_i	42.1	42.08	41.98	40.69	40.42
		-0.16	-0.30	-3.35	-3.98

Rotor-2's equivalent viscous damping, AMB constants undergo comparatively higher deviations compared to other estimates. Gaussian noise at various levels (1, 2, and 5%) has been added to the clean signal and estimation was carried out. Rotor-2

damping and AMB current stiffness have been underestimated by as much as 2.56 and 3.98%, respectively, at 5% noise level. The variation in static and additive coupling stiffness values stands at a reasonable 0.7%. Next the error percentages in the estimation of system parameters for a range of speeds are performed. The rotor system is ramped up with an angular acceleration of $20\pi \text{ rad/s}^2$ to identify the critical speed. The Hilbert envelope of vibration response of rotor-1 in x direction reveals the peaks in response, which correspond to critical speeds (see Fig. 9). The speeds on the either side of half power points can be taken for estimation (20 to 30 Hz). Here AMB displacement stiffness has displayed considerable variation from the assumed value by as much

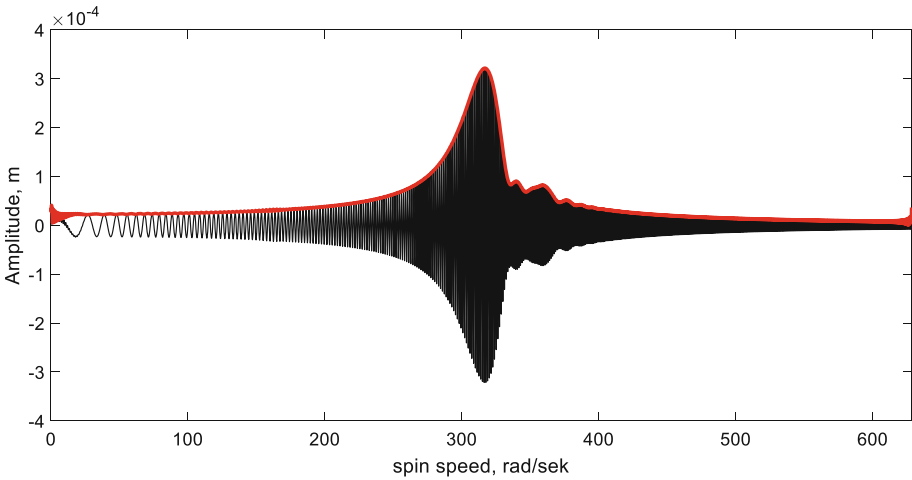


Fig. 9. Hilbert envelope of Rotor-1 X displacement during ramp-up ($\alpha = 20\pi \text{ rad/s}^2$)

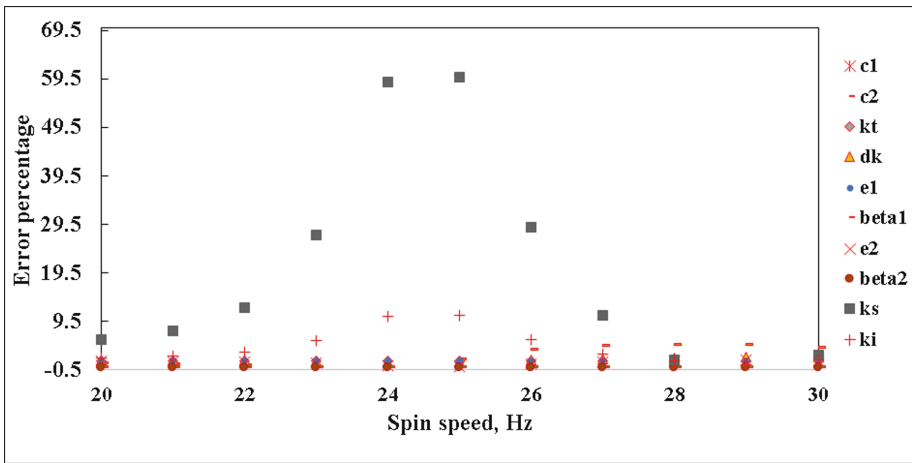


Fig. 10. Error percentage in identified parameters at various individual spin speeds (20–30 Hz)

as 59.96%, while AMB current stiffness displayed a variation of about 10% (see Fig. 10). Even though the speed range is sufficiently away from half power points, a large variance is observed at 24 and 25 Hz. This can be explained by the fact that the aforesaid speeds are half the 1st critical speed, which is 316 rad/s. This can be resolved by considering the accumulated data from many speeds and feeding them to Eq. (18). When collective data from the same speed range (20 to 30 Hz) is considered, the estimates show very good closeness to the assumed values (see Table 4). This exercise adequately justifies the usefulness of including multiple speeds in the identification algorithm.

Table 4. Parameters estimated after considering collective data from 20 to 30 Hz in the identification algorithm

Parameter	Assumed values	Estimated values
c_1	75	74.99
c_2	50	50.6
k_r	10800	10800
Δk_{ξ}	5000	5000
e_1	240E-06	239.99E-06
β_1	30	29.99
e_2	240E-06	240E-06
β_2	45	45
k_s	105210	105196
k_i	42.1	42.09

9 Conclusions

A mathematical model of coupled rotor system has been developed from Jeffcott rotor formulation. A Simulink™ model has been constructed from complex equations of motion. The model has been used to perform numerical experiments to generate vibration and current data in time domain. A reference signal which is multi-harmonic in nature has been used to correct the anomaly of phase variation that happens to the coefficients of vibration and current when signals are picked at different instants of time which would adversely affect the parameter identification if left uncorrected. A modal based identification algorithm has been developed that utilizes the coefficients of amplitude and phase harmonics of rotor vibration and AMB current, obtained either from inverse problem in time domain or from full spectrum, to estimate the flexible coupling, rotor and AMB parameters. The algorithm has been found to be robust to noise levels up to as much as 5%. The algorithm can be tested with data obtained from experimental data. The mathematical model can be extended to the case of Jeffcott rotor with offset disc to incorporate gyroscopic effects also.

References

1. Gibbons, C.B.: Coupling misalignment forces. In: Proceedings of the Fifth Turbo Machinery Symposium, pp. 111–116. Gas Turbine Laboratories, Texas A&M University (1976)
2. Sekhar, A.S., Prabhu, B.S.: Effects of coupling misalignment on vibrations of rotating machinery. *J. Sound Vib.* **185**(4), 655–671 (1995)
3. Rao, A.S., Sekhar, A.S.: Vibration analysis of rotor-coupling-bearing system with misaligned shafts. In: ASME International Gas Turbine and Aero Engine Congress and Exhibition, Birmingham, 8 p. (1996)
4. Prabhu, B.S.: An experimental investigation on the misalignment effects in journal bearings. *Tribol. Trans.* **40**(2), 235–242 (1997)
5. Rao, J.S., Sreenivas, R., Chawla, A.: Experimental investigation of misaligned rotors. In: Proceedings of ASME Turbo expo: Power for Land, Sea, and Air, New Orleans, Louisiana, 8 p. (2001)
6. Al-Hussain, K.M., Redmond, I.: Dynamic response of two rotors connected by rigid mechanical coupling with parallel misalignment. *J. Sound Vib.* **249**(3), 483–498 (2002)
7. Lees, A.W.: Misalignment in rigidly coupled rotors. *J. Sound Vib.* **305**(1–2), 261–271 (2007)
8. Patel, T.H., Darpe, A.K.: Experimental investigations on vibration response of misaligned rotors. *Mech. Syst. Signal Process.* **23**(7), 2236–2252 (2009)
9. Jalan, A.K., Mohanty, A.R.: Model based fault diagnosis of a rotor-bearing system for misalignment and unbalance under steady state condition. *J. Sound Vib.* **327**(3–5), 604–622 (2009)
10. Avendano, R.D., Childs, D.W.: One explanation for 2 N response due to misalignment in rotors connected by flexible couplings. In: Proceedings of ASME Turbo Expo, GT 2012, Copenhagen, Denmark, pp. 563–573 (2012)
11. Verma, A.K., Sarangi, S., Kolekar, M.H.: Experimental investigation of misalignment effects on rotor shaft vibration and on stator current signature. *J. Fail. Anal. Prev.* **14**(2), 125–138 (2014)
12. Reddy, M.C.S., Sekhar, A.S.: Detection and monitoring of coupling misalignment in rotors using torque measurements. *Measurement* **61**, 111–122 (2015)
13. Lal, M., Tiwari, R.: Multi-fault identification in simple rotor-bearing-coupling systems based on forced response measurements. *Mech. Mach. Theory* **51**, 87–109 (2012)
14. Lal, M., Tiwari, R.: Experimental estimation of misalignment effects in rotor-bearing-coupling systems. In: Proceedings of the 9th IFToMM International Conference on Rotor Dynamics, pp. 779–789. Springer, Milan (2015)
15. Mohanty, A.R., Fatima, S.: Shaft misalignment detection by thermal imaging of support bearings. *IFAC-PapersOnline* **48**(121), 554–559 (2015)
16. Taylor, J.I.: *The Vibration Analysis Handbook*, 2nd edn. Vibration consultants Inc., Tampa (2003)
17. Mohanty, A.R.: *Machinery Condition Monitoring: Principles and Practices*, 2nd edn. CRC Press, Taylor and Francis Group, Boca Raton (2014)
18. Tiwari, R.: *Rotor Systems: Analysis and Identification*, 1st edn. CRC Press, Taylor and Francis Group, Boca Raton (2017)
19. Giridhar, P., Scheffer, C.: *Practical Vibration Analysis and Predictive Maintenance*, 1st edn. Elsevier, Burlington (2004)
20. Macmillan, R.B.: *Rotating machinery: Practical Solutions to Unbalance and Misalignment*. Fairmont Press, Lilburn (2003)

21. Siva Srinivas, R., Tiwari, R., Kannababu, Ch.: Application of active magnetic bearings in flexible rotordynamic systems—a state-of-the-art review. *Mech. Syst. Signal Process.* **106**, 537–572 (2018)
22. Kreyszig, E.: *Advanced Engineering Mathematics*, 9th edn. Wiley, Hoboken (2011)
23. Goldman, P., Muszynska, A.: Application of full spectrum to rotating machinery diagnostics. In: *Orbit, First Quarter*, pp. 17–21 (1999)
24. Singh, S., Tiwari, R.: Model-based fatigue crack identification in rotors integrated with magnetic bearings. *J. Vib. Control* **23**(6), 980–1000 (2015)



Model-Based Identification of Rotor-Bearing System Parameters Employing Adaptive Filtering

Eduardo Moraes Coraça^(✉) and Milton Dias Junior

Structural and Machinery Dynamics Laboratory - LDEM,
School of Mechanical Engineering, University of Campinas - UNICAMP,
Campinas, SP 13083-860, Brazil
eduardocoraca@gmail.com, milton@fem.unicamp.br

Abstract. Instability issues and excessive vibration amplitudes are common problems encountered in large rotating machinery applications. In order to predict problems and overcome them, reliable rotor models are required. In the previous decades there has been a great improvement on finite element modeling, which was extensively used in rotordynamics problems. However, there is a great difficulty when bearings have to be considered, and the unbalance present in the machine must be known for good response prediction. This paper proposes a method of bearing and unbalance parameter estimation from measured responses at the bearings and considering a Finite Element model of the shaft. The proposed algorithm utilizes the adaptive filtering technique known as the RLS filter employing the QR decomposition. Simulations were conducted and good results were achieved for both stationary and speed-dependent bearing parameters.

Keywords: Rotor dynamics · System identification
Adaptive filtering · Bearings · Unbalance

1 Introduction

In modern rotating machinery applications, such as turbines, pumps and compressors, the delivery of large amounts of energy in small-sized equipment is possible due to high rotating speeds. Serious problems come accompanied with the high speeds, such as instability issues and excessive vibration due to mass unbalance. In the previous decades, mathematical tools allied with increasing computational power allowed the development of complex rotordynamics models, which have been used for problems prediction and solving. Although accurate models for the shaft and disk dynamics were developed, good foundation and bearing models are impractical, which is a problem as these components play important roles in the overall system dynamic performance.

Many authors proposed methods for the experimental identification of bearing and foundation parameters employing a model of the rotor and disks, known

as model-based identification. The techniques can be categorized with respect to the type of model employed (modal or physical), to the method of determining operational forces and to the measuring system used [10]. The mathematical foundations for modal analysis of asymmetric rotors, presenting time-varying matrices, has been proposed [6], and also for the case when there are periodically varying parameters [14]. For the identification of physical parameters, there are several methods employing known modal or physical parameters to estimate physical properties of bearings, foundation and unbalance [9, 13, 15, 16]. Although the basis for the methods is the same, involving a model of the rotor and vibration measurements at specific locations, different ways of tackling the mathematical problem were presented, since it is of an ill-posed nature.

Adaptive filtering techniques may be employed as a mathematical tool for solving the estimation problem. In rotating machinery applications the RLS filter has been used for order tracking [1, 17]. In the field of structure health monitoring (SHM), the same filter was employed for damage identification of structures [2]. As a parameter estimation tool for structural vibration, the RLS with QR decomposition was employed for the identification of the modal parameters of a structure when it was excited by an harmonic unwanted force [5], and also for the identification of natural frequencies of rotors in run-up conditions [4]. The Kalman filter has also been used for identification purposes in rotating machinery applications [11].

In this paper a model-based identification method is presented and applied to a rotor system modeled by the Finite Element Method. The goal is to extract dynamic bearing parameters, stiffness and damping, by taking its dynamic stiffness matrix as an unknown. Unbalance parameters, amplitude and phase angle, are also identified in the process, while assuming the foundation is rigid. To do so, an accurate model of the rotor is needed, as well as the unbalance response functions at the bearings locations, obtainable in a real situation. In order to estimate the parameters, adaptive filtering is employed. A RLS filter with QR decomposition, which ensures good numerical properties, is presented and reformulated based on the equations used in the identification process.

2 Adaptive Filtering Algorithm

In this section the RLS adaptive filtering algorithm is presented, which will be applied to the identification of rotor bearing parameters in the following sections. In order to present the concepts, a general FIR filter is employed as a basis filter, which will have its coefficients varied following an adaptive algorithm [3].

The output $y(n)$ of a FIR filter of length M at the discrete time n is related to the input $u(n)$ and its previous values through the filter coefficients w_k , $k = 1, 2, \dots, M-1$. Equation 1 shows the filter difference equation, where w_k^* denotes the complex conjugate of w_k , \mathbf{w} is a vector containing each w_k , \mathbf{w}^H denotes the Hermitian (conjugate transpose of \mathbf{w}) and $\mathbf{u}(n)$ is a vector containing the previous values of the input.

$$y(n) = \sum_{k=0}^{M-1} w_k^* u(n-k) = \mathbf{w}^H \mathbf{u}(n) \tag{1}$$

In the context of signal estimation, the filter coefficients should be tuned such that the output follows a reference, or desired, signal $d(n)$. An adaptive filter can be used to adjust \mathbf{w} in real-time according to an algorithm.

2.1 RLS Algorithm

The RLS algorithm is derived by minimizing the squared error of the filter estimation. Figure 1 shows a block diagram of the RLS filter acting in the context of system identification. The desired signal $d(n)$ is the output of a system to be identified and the error $e(n)$ is given by Eq. 2.

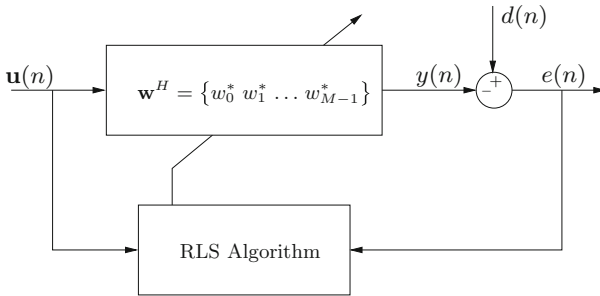


Fig. 1. RLS filter block diagram.

$$e(n) = d(n) - y(n) = d(n) - \mathbf{w}^H \mathbf{u}(n) \tag{2}$$

Considering that the signals were acquired from time M to N and by minimizing the squared error with respect to the filter coefficients, it is possible to derive an expression for the set of w_k coefficients that provides the best estimate of $d(n)$ from the input $\mathbf{u}(n)$. This is known as the Normal Equations, given by Eq. 3, where Φ is the autocorrelation matrix of the input of dimension $M \times M$, given by Eq. 4, and \mathbf{z} is the cross-correlation vector of the input of dimension $M \times 1$ and the desired signal, given by Eq. 5.

$$\mathbf{z} = \Phi \mathbf{w} \tag{3}$$

$$\Phi = \sum_{n=M}^N \mathbf{u}(n) \mathbf{u}^H(n) \tag{4}$$

$$\mathbf{z} = \sum_{n=M}^N \mathbf{u}(n) d^*(n) \tag{5}$$

The previous equations provide the filter coefficients that best adjust the input to the desired signal in a least squares sense. In order to implement it in real-time, Eq. 3 must be solved for each time-step, and Eqs. 4 and 5 must be modified. A forgetting factor λ is introduced, which lies in the interval $0 \leq \lambda \leq 1$. It is responsible for forgetting past values when its value is lesser than unity or considering all the acquired data when it is equal to the unit. The second modification is the recursive calculation of Φ and \mathbf{z} , which enables the computation of its values based on their previous values and the new acquired data. Equations 6 and 7 indicate the new set of expressions.

$$\Phi(n) = \lambda\Phi(n-1) + \mathbf{u}(n)\mathbf{u}^H(n) \quad (6)$$

$$\mathbf{z}(n) = \lambda\mathbf{z}(n-1) + \mathbf{u}(n)d^*(n) \quad (7)$$

From past values and new data at time n , it is possible to solve Eq. 3 for \mathbf{w} through matrix inversion. However, this would be impractical to solve in real time, as the numerical cost would be too large. In order to solve this problem, the matrix inversion lemma can be employed. For a non-singular matrix \mathbf{A} that can be written as a function of matrices \mathbf{B} , \mathbf{C} and \mathbf{D} according to Eq. 8, its inverse is given by Eq. 9.

$$\mathbf{A} = \mathbf{B}^{-1} + \mathbf{C}\mathbf{D}^{-1}\mathbf{C}^H \quad (8)$$

$$\mathbf{A}^{-1} = \mathbf{B} - \mathbf{B}\mathbf{C}(\mathbf{D} + \mathbf{C}^H\mathbf{B}\mathbf{C})^{-1}\mathbf{C}^H\mathbf{B} \quad (9)$$

Defining $\mathbf{P}(n) = \Phi^{-1}(n)$ and $\mathbf{A} = \Phi(n)$, $\mathbf{B} = \lambda\Phi(n-1)$, $\mathbf{C} = \mathbf{u}(n)$, $\mathbf{D} = \mathbf{I}$, the propagation equation for $\mathbf{P}(n)$ is given in Eq. 10, where $\mathbf{k}(n)$ is a gain vector, given in Eq. 11.

$$\mathbf{P}(n) = \lambda^{-1}\mathbf{P}(n-1) - \lambda^{-1}\mathbf{k}(n)\mathbf{u}^H(n)\mathbf{P}(n-1) \quad (10)$$

$$\mathbf{k}(n) = \mathbf{P}(n)\mathbf{u}(n) = \frac{\lambda^{-1}\mathbf{P}(n-1)\mathbf{u}(n)}{1 + \lambda^{-1}\mathbf{u}^H\mathbf{P}(n-1)\mathbf{u}(n)} \quad (11)$$

The filter coefficients at time n can be finally calculated through Eq. 13, where $\zeta(n)$ is an *a priori* error, given by Eq. 12.

$$\zeta(n) = d(n) - \hat{\mathbf{w}}^H(n-1)\mathbf{u}(n) \quad (12)$$

$$\mathbf{w}(n) = \mathbf{w}(n-1) - \mathbf{k}(n)\zeta^*(n) \quad (13)$$

Equations 10 to 13 define the RLS algorithm, which requires an initial condition for $\mathbf{P}(0)$. In a practical scenario, numerical errors and noise may lead a bad conditioning of matrix \mathbf{P} , which makes the estimator unstable.

2.2 QRD/RLS Algorithm

The QRD/RLS algorithm can be used to avoid instabilities. This method uses the QR decomposition to turn the normal equations into an upper triangular problem. Then, the filter coefficients can be determined through back-substitution.

The QR decomposition of a matrix \mathbf{M} returns two matrices: an unitary matrix \mathbf{Q} , such that $\mathbf{Q}\mathbf{Q}^H = \mathbf{I}$, and an upper triangular matrix \mathbf{R} , as shown in Eq. 14.

$$\mathbf{Q}\mathbf{M} = \begin{bmatrix} \mathbf{R} \\ \mathbf{0} \end{bmatrix} \tag{14}$$

A positive-definite matrix \mathbf{A} can be written as the product of an upper triangular matrix \mathbf{R} and its Hermitian, which is known as the Cholesky decomposition [12]. The application of this technique to $\Phi(n)$ leads to Eq. 15 and the normal equations can be written as Eq. 16.

$$\Phi(n) = \mathbf{R}(n)\mathbf{R}^H(n) \tag{15}$$

$$\mathbf{R}(n)\mathbf{R}^H(n)\mathbf{w}(n) = \mathbf{z}(n) \tag{16}$$

The propagation equations of the QRD/RLS algorithm can be written as the QR decomposition given by Eq. 17, where $\zeta(n)$ is the *a posteriori* error, $\gamma(n)$ is a conversion factor, $\mathbf{u}(n)$ is the input data vector and $\mathbf{p}(n) = \mathbf{R}^H(n)\mathbf{w}(n)$ [3].

$$\mathbf{Q} \begin{bmatrix} \lambda^{1/2}\mathbf{R}^H(n-1) & \lambda^{1/2}\mathbf{p}(n-1) & \mathbf{0} \\ \mathbf{u}^H(n) & d^*(n) & 1 \end{bmatrix} = \begin{bmatrix} \mathbf{R}^H(n) & \mathbf{p}(n) & \mathbf{R}^{-1}(n)\mathbf{u}(n) \\ \mathbf{0}^T & \zeta^*(n)\gamma^{*1/2}(n) & \gamma^{*1/2}(n) \end{bmatrix} \tag{17}$$

In the present work, the QR decomposition of the first matrix in Eq. 17 is accomplished through MATLAB's command `qr`. Matrix \mathbf{R} is initialized according to Eq. 18, where δ is a regulating parameter.

$$\mathbf{R}(0) = \delta^{1/2}\mathbf{I} \tag{18}$$

2.3 Vector QRD/RLS Algorithm

The previous algorithm can be extended to the MIMO case, where there are N input and N outputs. The input is now a data matrix $\mathbf{U}(n)$, of dimension $N \times M$ and the desired response is a vector $\mathbf{d}(n)$, of dimension $N \times 1$, which are related with the filter coefficients according to Eq. 19.

$$\mathbf{d}(n) = \mathbf{U}(n)\mathbf{w}(n) \tag{19}$$

The propagation equations are now given by Eq. 20, where ϵ is a normalized vector of dimension $N \times 1$, $\mathbf{\Lambda}$ is a conversion factor vector of dimension $N \times 1$ and Δ is a vector of dimension $N \times 1$ given by Eq. 21.

$$\mathbf{Q} \begin{bmatrix} \lambda^{1/2}\mathbf{R}^H(n-1) & \lambda^{1/2}\mathbf{p}(n-1) & \mathbf{0} \\ \mathbf{U}(n) & \mathbf{d}(n) & \Delta \end{bmatrix} = \begin{bmatrix} \mathbf{R}^H(n) & \mathbf{p}(n) & \mathbf{R}^{-1}(n)\mathbf{U}(n) \\ \mathbf{0}^T & \epsilon(n) & \mathbf{\Gamma}^{1/2}(n) \end{bmatrix} \tag{20}$$

$$\Delta = [0 \dots 0 1]^T \tag{21}$$

3 Rotor Modeling and Identification Procedure

In the previous section the QRD/RLS adaptive filter algorithm was presented, which will be used to identify the unbalance present in rotating machinery and the stiffness and damping coefficients of the bearings. In this section, a rotor model will be presented using the Finite Element Method (FEM), which will be used for simulating different machines. The unbalance response will be discussed, then the identification procedure will be presented.

3.1 Rotor Model

The rotating structure is modeled by dividing the system into four sub-systems: shaft, disks, bearings and foundation. In this work a rigid foundation was considered, hence the fourth sub-system is not taken into account. The shaft is modeled employing unidimensional beam elements, each one having two nodes. Each node contains two translation degrees of freedom (DOF), y and z , and two rotation DOFs, ϕ_y and ϕ_z . The equations of motion of the i -th shaft element are given by Eq. 22, where $\mathbf{M}_S^{(i)}$ is the shaft mass matrix, $\mathbf{K}_S^{(i)}$ the shaft stiffness matrix, $\mathbf{G}_S^{(i)}$ the shaft gyroscopic matrix, $\mathbf{C}_S^{(i)}$ the shaft internal damping matrix and Ω is the rotating speed. Vector $\mathbf{f}_S^{(i)}$ contains the shaft internal forces connecting the elements and vector $\mathbf{q}_S^{(i)}$ contains the 8 DOFs of the i -th element, given in Eq. 23 [8].

$$\mathbf{M}_S^{(i)} \ddot{\mathbf{q}}_S^{(i)} + \left(\mathbf{C}_S^{(i)} + \Omega \mathbf{G}_S^{(i)} \right) \dot{\mathbf{q}}_S^{(i)} + \left(\mathbf{K}_S^{(i)} + \Omega \mathbf{C}_S^{(i)} \right) \mathbf{q}_S^{(i)} = \mathbf{f}_S^{(i)} \quad (22)$$

$$\mathbf{q}_S^{(i)} = \left\{ y^{(i)} \ z^{(i)} \ \phi_y^{(i)} \ \phi_z^{(i)} \ y^{(i+1)} \ z^{(i+1)} \ \phi_y^{(i+1)} \ \phi_z^{(i+1)} \right\}^T \quad (23)$$

The disks are modeled as rigid bodies and, for the k -th element, the equations of motion are given in Eq. 24, where $\mathbf{M}_D^{(k)}$ is the disk mass matrix, $\mathbf{G}_D^{(k)}$ the disk gyroscopic matrix, $\mathbf{f}_D^{(k)}$ the internal forces connecting the disk to the shaft and the external unbalance forces. $\mathbf{q}_D^{(k)}$ contains the 4 DOFS of the k -th element. given in Eq. 25.

$$\mathbf{M}_D^{(k)} \ddot{\mathbf{q}}_D^{(k)} + \Omega \mathbf{G}_D^{(k)} \dot{\mathbf{q}}_D^{(k)} = \mathbf{f}_D^{(k)} \quad (24)$$

$$\mathbf{q}_D^{(k)} = \left\{ y^{(k)} \ z^{(k)} \ \phi_y^{(k)} \ \phi_z^{(k)} \right\}^T \quad (25)$$

The bearings Finite Element model utilizes a stiffness matrix \mathbf{K}_B and a damping matrix \mathbf{C}_B that, for the m -th bearing element, are given by Eqs. 26 and 27, respectively. Terms with subscripts yy and zz represent direct stiffness and damping coefficients, while subscripts yz and zy represent cross stiffness and damping coefficients. These terms are the unknowns of the identification procedure. Equation 28 represents the equations of motion for the m -th bearing element, where $\mathbf{q}_B^{(k)}$ contains the 2 DOFS of the m -th element, given in Eq. 29.

$$\mathbf{K}_B^{(m)} = \begin{bmatrix} k_{yy}^{(m)} & k_{yz}^{(m)} \\ k_{zy}^{(m)} & k_{zz}^{(m)} \end{bmatrix} \quad (26)$$

$$\mathbf{C}_B^{(m)} = \begin{bmatrix} c_{yy}^{(m)} & c_{yz}^{(m)} \\ c_{zy}^{(m)} & c_{zz}^{(m)} \end{bmatrix} \quad (27)$$

$$\mathbf{C}_B^{(m)} \dot{\mathbf{q}}_B^{(m)} + \mathbf{K}_B^{(m)} \mathbf{q}_B^{(m)} = \mathbf{f}_B^{(m)} \quad (28)$$

$$\mathbf{q}_B^{(m)} = \{y^{(m)} \ z^{(m)}\}^T \quad (29)$$

In order to assemble the equations of motion before, a global displacement vector \mathbf{q} is defined, which contains the displacement, y and z , and rotations, ϕ_y and ϕ_z , of all nodes. The global mass \mathbf{M} , damping \mathbf{C} , gyroscopic \mathbf{G} and stiffness \mathbf{K} matrices can then be assembled. Equation 30 indicates the global equation of motion of the Finite Element model, where $\mathbf{f}(t)$ is the external force vector. Note that the shaft internal damping is not considered, hence matrix \mathbf{C} contains only bearing parameters.

$$\mathbf{M}\ddot{\mathbf{q}} + (\mathbf{C} + \Omega\mathbf{G})\dot{\mathbf{q}} + \mathbf{K}\mathbf{q} = \mathbf{f}(t) \quad (30)$$

3.2 Unbalance Response

In the presence of unbalance, which may occur in the disks and also in the shaft, the rotor will vibrate. For the k -th node, the unbalance force is given by Eq. 32, where vector \mathbf{g} is given in Eq. 31 and has zero values in the nodes where there is no unbalance. Product $m_k e_k$ is the unbalance amplitude of the k -th node [7].

$$\mathbf{g} = \{ \{ \dots m_k e_k e^{j\alpha_k} \dots \} \{ \dots -j m_k e_k e^{j\alpha_k} \dots \} \mathbf{0}^T \mathbf{0}^T \}^T \quad (31)$$

$$\mathbf{f}_u(t) = \Omega^2 \mathbf{g} e^{j\Omega t} \quad (32)$$

When $\mathbf{f}(t) = \mathbf{f}_u(t)$, Eq. 30 can be solved by assuming that the response can be written as $\mathbf{q} = \mathbf{q}_u e^{j\Omega t}$, where \mathbf{q}_u is the unbalance amplitude response vector. By substituting this expression into Eq. 32, it is possible to demonstrate that the response due to unbalance can be determined by solving Eq. 33, where \mathbf{Z} is the dynamic stiffness matrix, given in Eq. 34.

$$\mathbf{Z}\mathbf{q}_u = \mathbf{g} \quad (33)$$

$$\mathbf{Z} = -\Omega^2 \mathbf{M} + j\Omega (\mathbf{C} + \Omega\mathbf{G}) + \mathbf{K} \quad (34)$$

3.3 Identification Procedure

In order to identify the bearing parameters and the unbalance amplitude in a running machine, it is assumed that the vibration is measured in the y and z directions in the bearing nodes. The proposed procedure also assumes that a Finite Element model of the remaining of the rotor is available.

Vector \mathbf{q}_u from Eq. 33 can be separated in four groups, containing the shaft inner DOFs ($\mathbf{q}_{R,i}$), connection DOFs between shaft and bearings ($\mathbf{q}_{R,B}$), connection DOFs between bearings and foundation ($\mathbf{q}_{F,B}$) and the inner DOFs of the foundation ($\mathbf{q}_{F,i}$) [13]. Since the foundation is assumed rigid, vectors $\mathbf{q}_{F,B}$

and $\mathbf{q}_{\mathbf{F},i}$ are null. Matrix \mathbf{Z} can be divided following the same approach, which leads to Eq. 35.

$$\begin{bmatrix} \mathbf{Z}_{\mathbf{R},ii} & \mathbf{Z}_{\mathbf{R},iB} \\ \mathbf{Z}_{\mathbf{R},Bi} & \mathbf{Z}_{\mathbf{R},BB} + \mathbf{Z}_{\mathbf{B}} \end{bmatrix} \begin{Bmatrix} \mathbf{q}_{\mathbf{R},i} \\ \mathbf{q}_{\mathbf{R},B} \end{Bmatrix} = \begin{Bmatrix} \mathbf{f}_{\mathbf{R},i} \\ \mathbf{0} \end{Bmatrix} \quad (35)$$

Matrices $\mathbf{Z}_{\mathbf{R},ii}$, $\mathbf{Z}_{\mathbf{R},iB}$, $\mathbf{Z}_{\mathbf{R},Bi}$ and $\mathbf{Z}_{\mathbf{R},BB}$ are known, because they only contain information about the shaft, which is known if the FEM matrices are known. Matrix $\mathbf{Z}_{\mathbf{B}}$ is unknown as it contains information about the bearings. Vector $\mathbf{f}_{\mathbf{R},i}$ contains the unbalance amplitude driving the system, which is also unknown. Equations 36 and 37 can be written from Eq. 35.

$$\mathbf{Z}_{\mathbf{R},ii}\mathbf{q}_{\mathbf{R},i} + \mathbf{Z}_{\mathbf{R},iB}\mathbf{q}_{\mathbf{R},B} = \mathbf{f}_{\mathbf{R},i} \quad (36)$$

$$\mathbf{Z}_{\mathbf{R},Bi}\mathbf{q}_{\mathbf{R},i} + (\mathbf{Z}_{\mathbf{R},BB} + \mathbf{Z}_{\mathbf{B}})\mathbf{q}_{\mathbf{R},B} = \mathbf{0} \quad (37)$$

Isolating $\mathbf{q}_{\mathbf{R},i}$ from Eq. 36 and substituting in 37, Eq. 38 can be written, where matrix \mathbf{Y} is given by Eq. 39.

$$(\mathbf{Z}_{\mathbf{R},BB} - \mathbf{Y}\mathbf{Z}_{\mathbf{R},iB})\mathbf{q}_{\mathbf{R},B} = -\mathbf{Z}_{\mathbf{B}}\mathbf{q}_{\mathbf{R},B} - \mathbf{Y}\mathbf{f}_{\mathbf{R},i} \quad (38)$$

$$\mathbf{Y} = \mathbf{Z}_{\mathbf{R},Bi}\mathbf{Z}_{\mathbf{R},ii}^{-1} \quad (39)$$

The unbalance force k -th plane can be expressed through Eq. 40 by modifying Eq. 32. Vector \mathbf{t}_k is a distribution vector, containing only 1 and $-j$ for the planes where unbalance is present and zeros otherwise. Term a_k is given in Eq. 41 and it contains the unbalance parameters for the k -th plane.

$$\mathbf{f}_{\mathbf{u}k} = \Omega^2 \{ \{0 \dots 1 \dots 0\} \{0 \dots -j \dots 0\} \mathbf{0}^T \mathbf{0}^T \}^T a_k = \Omega^2 \mathbf{t}_k a_k \quad (40)$$

$$a_k = m_k e_k e^{j\alpha_k} \quad (41)$$

Considering N_p unbalance planes, vectors $\mathbf{f}_{\mathbf{u}k}$ must be assembled. This can be achieved by considering a matrix \mathbf{T} , where each column is a \mathbf{b}_k vector, and a vector \mathbf{a} , where each entry is an a_k element. Hence, the unbalance force can be written according to Eq. 42.

$$\mathbf{f}_{\mathbf{u}} = \Omega^2 \mathbf{T} \mathbf{a} \quad (42)$$

For matrix $\mathbf{Z}_{\mathbf{B}}$, it can be expanded according to Eq. 43 in terms of the bearings stiffness and damping matrices, $\mathbf{K}_{\mathbf{B}}$ and $\mathbf{C}_{\mathbf{B}}$ respectively. In order to provide better identification performance, this matrix is written in terms of matrices $\mathbf{Z}_{\mathbf{0}}$ and $\mathbf{Z}_{\mathbf{1}}$, as shown, which will be identified and, from them, it is possible to reconstruct $\mathbf{Z}_{\mathbf{B}}$.

$$\mathbf{Z}_{\mathbf{B}} = \mathbf{K}_{\mathbf{B}} + j\Omega\mathbf{C}_{\mathbf{B}} = \mathbf{Z}_{\mathbf{0}} + \Omega\mathbf{Z}_{\mathbf{1}} \quad (43)$$

Substituting Eqs. 43 and 42 into 38, it is possible to write Eq. 44, which will be directly used with the adaptive filter algorithm to predict the unbalance and

bearing parameters. The vectors and matrices shown are expanded for the N_b bearings and N_p unbalance planes.

$$\begin{aligned}
 & (\mathbf{Z}_{\mathbf{R},\mathbf{BB}} - \mathbf{Y}\mathbf{Z}_{\mathbf{R},\mathbf{iB}}) \mathbf{q}_{\mathbf{R},\mathbf{B}} \\
 &= - \left\{ \begin{array}{c} \mathbf{Z}_0^{(1)} \mathbf{q}_{\mathbf{B}}^{(1)} \\ \vdots \\ \mathbf{Z}_0^{(N_B)} \mathbf{q}_{\mathbf{B}}^{(N_B)} \end{array} \right\} - \left\{ \begin{array}{c} \mathbf{Z}_1^{(1)} \Omega \mathbf{q}_{\mathbf{B}}^{(1)} \\ \vdots \\ \mathbf{Z}_1^{(N_B)} \Omega \mathbf{q}_{\mathbf{B}}^{(N_B)} \end{array} \right\} - \Omega^2 \mathbf{Y} \mathbf{T} \left\{ \begin{array}{c} a_1 \\ \vdots \\ a_{N_p} \end{array} \right\} \quad (44)
 \end{aligned}$$

Matrices $\mathbf{Z}_{\mathbf{R},\mathbf{BB}}$, $\mathbf{Z}_{\mathbf{R},\mathbf{iB}}$ and \mathbf{Y} are known from the finite element model of the shaft. Vector $\mathbf{q}_{\mathbf{b}}^{(k)}$ contains the unbalance response amplitude at the k -th bearing of the rotor and it must be measured for each speed Ω . Finally, the user must set the number of unbalance planes N_p and their location, hence matrix \mathbf{T} is also known.

The vector QRD/RLS algorithm can be applied in order to solve Eq. 44 for \mathbf{Z}_0 , \mathbf{Z}_1 and \mathbf{a} . The desired response vector $\mathbf{d}(n)$ is given by Eq. 45, which is equal to the left side of Eq. 44. Here, instead of performing tasks for each time step n , the algorithm is run for each speed $\Omega(n)$.

$$\mathbf{d}(n) = [\mathbf{Z}_{\mathbf{R},\mathbf{BB}}(\Omega(n)) - \mathbf{Y}(\Omega(n))\mathbf{Z}_{\mathbf{R},\mathbf{iB}}(\Omega(n))] \mathbf{q}_{\mathbf{R},\mathbf{B}}(\Omega(n)) \quad (45)$$

Data matrix $\mathbf{U}(n)$ is given by Eq. 46, and the filter coefficients are written in terms of several vectors containing the entries of \mathbf{Z}_0 , \mathbf{Z}_1 and \mathbf{a} , as shown in Eqs. 47 and 48. Note that matrices \mathbf{Z}_0 and \mathbf{Z}_1 are composed of N_b sub-matrices of dimension 2×2 containing direct (yy and zz) and cross components (yz and zy).

$$\mathbf{U}(n) = \left[\begin{array}{cccccccc} \mathbf{q}_{\mathbf{B}}^{(1)} & \Omega \mathbf{q}_{\mathbf{B}}^{(1)} & 0 & 0 & \dots & 0 & 0 & 0 & 0 \\ 0 & 0 & \mathbf{q}_{\mathbf{B}}^{(1)} & \Omega \mathbf{q}_{\mathbf{B}}^{(1)} & \dots & 0 & 0 & 0 & 0 \\ \vdots & \vdots & \vdots & \vdots & \ddots & \vdots & \vdots & \vdots & \vdots \\ 0 & 0 & 0 & 0 & \dots & \mathbf{q}_{\mathbf{B}}^{(N_b)} & \Omega \mathbf{q}_{\mathbf{B}}^{(N_b)} & 0 & 0 \\ 0 & 0 & 0 & 0 & \dots & 0 & 0 & \mathbf{q}_{\mathbf{B}}^{(N_b)} & \Omega \mathbf{q}_{\mathbf{B}}^{(N_b)} \end{array} \right] (-\Omega^2 \mathbf{Y} \mathbf{T}) \quad (46)$$

$$\mathbf{w}(n) = \left(\mathbf{v}^{(1)T} \dots \mathbf{v}^{(N_b)T} \mathbf{a}^T \right)^T \quad (47)$$

$$\mathbf{v}^{(m)} = \left(Z_{0yy}^{(m)} \ Z_{0yz}^{(m)} \ Z_{1yy}^{(m)} \ Z_{1yz}^{(m)} \ Z_{0zy}^{(m)} \ Z_{0zz}^{(m)} \ Z_{1zy}^{(m)} \ Z_{1zz}^{(m)} \right)^T \quad (48)$$

From the identified values it is possible to determine the physical parameters through Eqs. 41 and 43.

4 Simulation Results and Discussion

In this section a rotor will be studied utilizing a Finite Element model. Two cases will be analyzed: one with fixed bearing properties and one with speed-dependent parameters. The shaft has an Young’s modulus $E = 200 \times 10^9 \frac{N}{m}$, density $\rho = 7800 \frac{kg}{m^3}$, Poisson’s coefficient $\nu = 0.3$, length $L = 1.3$ m, diameter $D = 0.1$ m and presents no unbalance. The disks have an outer diameter of $D_o = 0.12$ m, thickness of $t = 0.05$ m, the same material as the shaft and its inner diameter matches the shaft’s diameter.

4.1 Fixed Bearing Properties

The model shown in Fig. 2(a) will be used. There is a total of 27 nodes and 31 elements. Bearings are located at nodes 1 (Bearing 1) and 27 (Bearing 2), and three disks are located at nodes 5, 11 and 21. Bearing and unbalance properties are given in Tables 1 and 2, respectively.

Table 1. Bearings properties

Bearing	$k_{yy} (\frac{N}{m})$	$k_{yz} (\frac{N}{m})$	$k_{zy} (\frac{N}{m})$	$k_{zz} (\frac{N}{m})$	$c_{yy} (\frac{Ns}{m})$	$c_{yz} (\frac{Ns}{m})$	$c_{zy} (\frac{Ns}{m})$	$c_{zz} (\frac{Ns}{m})$
1	5×10^7	0.5×10^7	1×10^7	7×10^7	500	50	100	700
2	5×10^7	1×10^7	0.5×10^7	7×10^7	500	100	50	700

From the Finite Element model with the previously specified parameters, the unbalance response of each bearing node was obtained. The speed range was set from 0 rpm to 15000 rpm. The Campbell Diagram is shown in Fig. 2(b), where f_n are the natural frequencies of the rotor as a function of the speed Ω . The dashed line indicates where the natural frequencies are equal to the shaft speed, and the intersections of this line with the full one represent the critical speeds.

The measured unbalance responses at the bearings are indicated in Figs. 3(a) and 3(b).

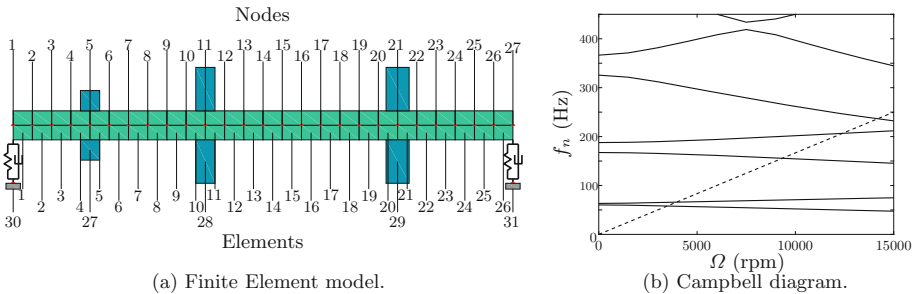


Fig. 2. Finite Element model of the rotor under study and its respective Campbell Diagram.

The unbalance responses at the bearing nodes are processed by the algorithm described in the previous section. The chosen filter parameters were $\lambda = 0.999$ and $\delta = 1 \times 10^{-7}$, and the initial guess for the filter weights was set to zero. The estimated stiffness k_{yy}, k_{yz}, k_{zy} and k_{zz} are shown in Fig. 4(a), and the estimated damping coefficients c_{yy}, c_{yz}, c_{zy} and c_{zz} are shown in Fig. 4(b).

The estimated properties change as the speed of rotation changes, since the filter coefficients is recursively updated for each speed sample. The parameters

Table 2. Unbalance properties

Node	me (kg.m)	α (°)
5	0.004	0
11	0.003	15
21	0.007	23

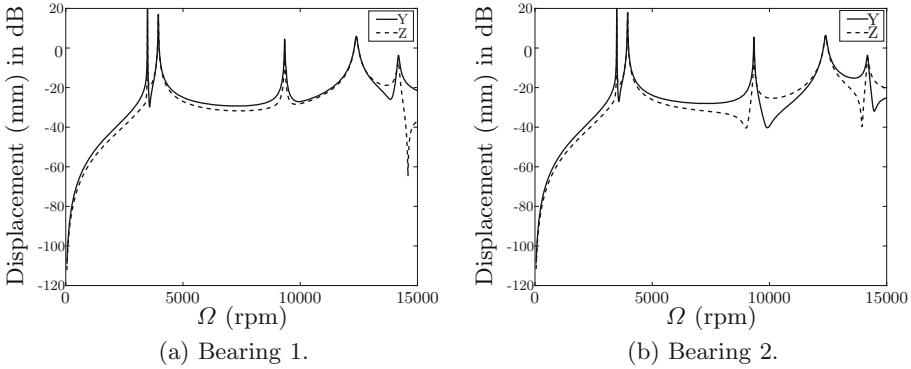


Fig. 3. Unbalance responses measured at the bearings.

converged to the correct values and, since the largest estimation error relative to the true parameters was from the order of 0.0001%, their values are not shown here. Although the converged properties are correct, filter convergence was very slow, which happened because the method is sample-based. Thus, more samples of unbalance response leads to a faster convergence. One possible method to improve results would be to employ a constant rotation during a number of samples before moving to the next speed. Unbalance parameters were perfectly estimated and are not shown here.

4.2 Speed-Dependent Bearing Properties

Considering the same rotor, bearing properties are now given by Eq. 49, where subscript (SD) indicates speed-dependent parameters and $ij = yy, yz, zy, zz$. Damping and unbalance remained constant and are equal to the previous case.

$$k_{ij}^{(SD)} = \frac{k_{ij}}{2.25 \times 10^8} \Omega^2 \tag{49}$$

As there are speed-dependent parameters, forgetting factor was set to $\lambda = 0.99$. The identified stiffness are shown in Fig. 5(a), where the reference values are given by the discrete points and the identified ones are given by the full lines. The identified parameters followed the reference with minor discrepancies. Figure 5(b) shows the identified damping parameters which clearly did not converge to the expected values.

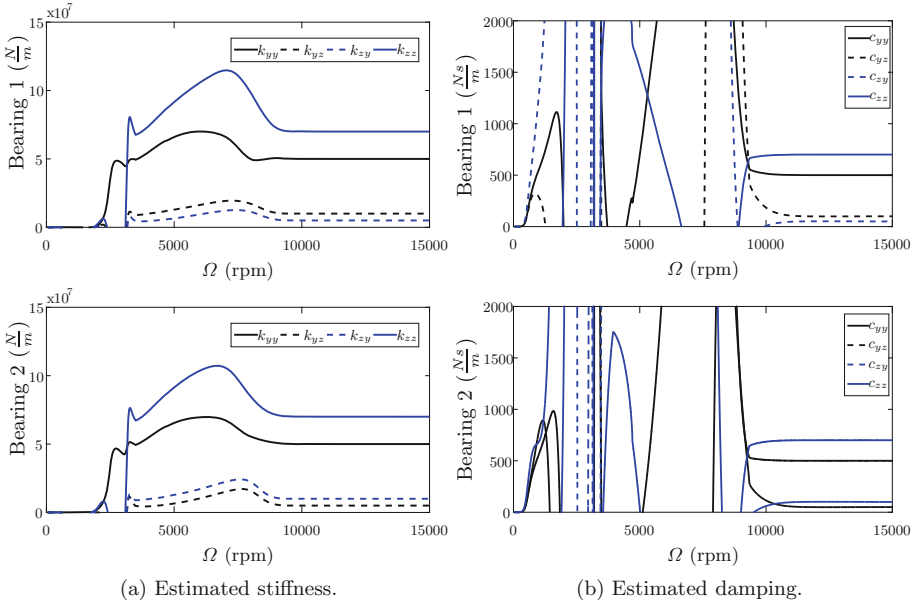


Fig. 4. Bearings estimated properties.

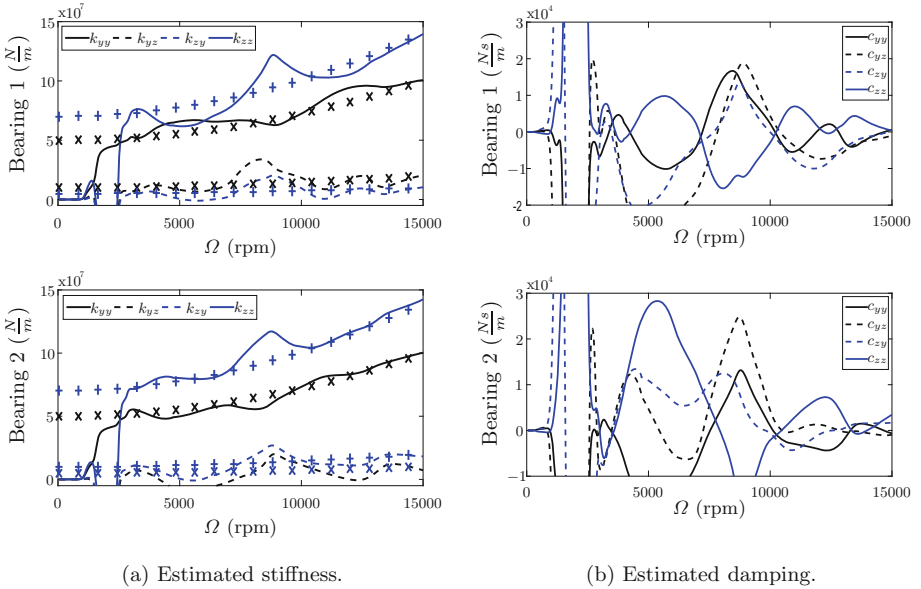


Fig. 5. Bearings estimated speed-dependent properties.

Table 3. Estimated unbalance parameters at 15000 rpm

Node	me (kg.m)	α ($^\circ$)
5	0.0042	-0.309
11	0.0030	17.760
21	0.0073	23.250

Table 3 shows the estimated unbalance parameters at 15000 rpm and it can be seen that they are very close to the reference values from Table 2. Figure 6(a) presents a comparison between the Campbell Diagrams of the fixed and speed-dependent situations, where it can be seen the stiffness influence at higher speeds. From the estimated parameters it was possible to estimate natural frequencies, indicated by the discrete points in Fig. 6(b), where the dashed line represents the 1x speed component. The natural frequencies could be well estimated, even the ones that were not excited by the rotor.

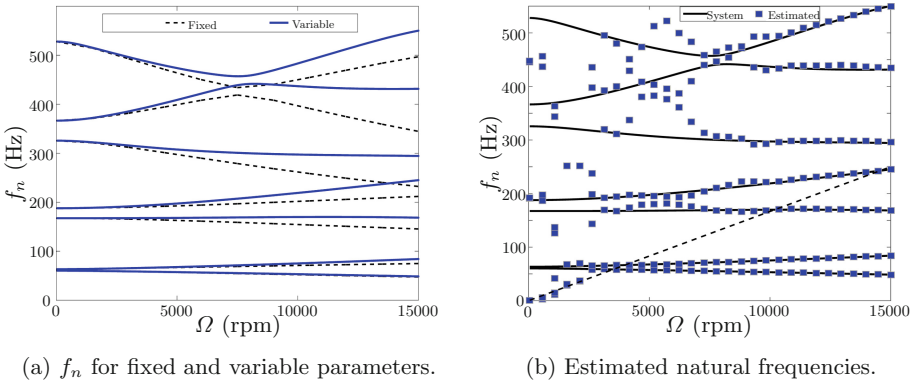


Fig. 6. Campbell diagram and identified natural frequencies.

By analyzing the presented results it can be seen that the proposed method is very useful for the identification of rotating machinery bearing and unbalance parameters. Although damping was not well estimated, the remaining parameters could be characterized, providing good natural frequencies estimates. It is important to note that the method relies upon the format specified for the dynamic stiffness of the bearings, given by Eq. 43. A linear model with respect to Ω was used but different formats should be employed, as a higher order polynomial, which could lead to better estimates.

5 Conclusions

In this paper an estimation algorithm was presented for the bearing and unbalance parameters of rotor systems. The method, which relies on the use of an

adaptive filter algorithm, was employed considering the use of a Finite Element model of the rotor and unbalance response measurement at the bearings. Simulations were conducted including both fixed and speed-dependent bearing properties. In the former case, the method provided good estimates, except for the bearing damping, while for the latter the technique was able to perfectly identify all properties. As the studies conducted so far included simulations only, the authors would like to emphasize the need of experimental testing in future studies. Also, the use of different equation format for the bearings dynamic stiffness should be evaluated.

References

1. Bai, M.R., Jeng, J., Chen, C.: Adaptive order tracking technique using recursive least-square algorithm. *J. Vibr. Acoust.* **124**(4), 502–511 (2002)
2. Da Silva, S., Gianini Gonzalez, C., Lopes Jr., V.: Adaptive filter feature identification for structural health monitoring in an aeronautical panel. *Struct. Health Monit.* **10**(5), 481–489 (2011)
3. Haykin, S.O.: *Adaptive Filter Theory*. Pearson Higher Education, London (2013)
4. Idehara, S.J.: Identificação de parâmetros modais de estruturas e máquinas rotativas através da filtragem adaptativa (2007)
5. Idehara, S.J., Junior, M.D.: Modal analysis of structures under non-stationary excitation. *Eng. Struct.* **99**, 56–62 (2015)
6. Irretier, H.: Mathematical foundations of experimental modal analysis in rotor dynamics. *Mech. Syst. Sig. Process.* **13**(2), 183–191 (1999)
7. Lalanne, M., Ferraris, G.: *Rotordynamics Prediction in Engineering*. Wiley, Hoboken (1998)
8. Lee, C.W.: *Vibration Analysis of Rotors*, vo. 21. Springer Science & Business Media (1993)
9. Lees, A., Friswell, M.: The evaluation of rotor imbalance in flexibly mounted machines. *J. Sound Vibr.* **208**(5), 671–683 (1997)
10. Lees, A., Sinha, J., Friswell, M.: Model-based identification of rotating machines. *Mech. Syst. Sig. Process.* **23**(6), 1884–1893 (2009)
11. Provasi, R., Zanetta, G.A., Vania, A.: The extended Kalman filter in the frequency domain for the identification of mechanical structures excited by sinusoidal multiple inputs. *Mech. Syst. Sig. Process.* **14**(3), 327–341 (2000)
12. Sayed, A.H.: *Adaptive Filters*. Wiley, Hoboken (2011)
13. Smart, M., Friswell, M., Lees, A.: Estimating turbo generator foundation parameters: model selection and regularization. In: *Proceedings of the Royal Society of London A: Mathematical, Physical and Engineering Sciences*, vol. 456, pp. 1583–1607. The Royal Society (2000)
14. Suh, J.-H., Hong, S.-W., Lee, C.-W.: Modal analysis of asymmetric rotor system with isotropic stator using modulated coordinates. *J. Sound Vibr.* **284**(3), 651–671 (2005)
15. Tiwari, R., Lees, A., Friswell, M.: Identification of speed-dependent bearing parameters. *J. Sound Vibr.* **254**(5), 967–986 (2002)
16. Ubinha, J.A.: *Estudo de metodo de identificação dos parametros de desbalanceamento e de fundação de maquinas rotativas* (2005)
17. Wu, J.D., Bai, M.R., Su, F.C., Huang, C.W.: An expert system for the diagnosis of faults in rotating machinery using adaptive order-tracking algorithm. *Expert Syst. Appl.* **36**(3), 5424–5431 (2009)



Problems of Rotordynamic Modeling for Built-Up Gas Turbine Rotors with Central Tie Rod Shaft

Konstantin Shaposhnikov¹(✉) and Chuang Gao²

¹ Helan Turbines Co., Ltd., No. 1180 Xingxian Road,
Shanghai 201815, People's Republic of China
kvshaposhnikov@helanturbines.com

² Shanghai Advanced Research Institute, Chinese Academy of Sciences,
No. 99 Haike Road, Pudong New Area,
Shanghai 201210, People's Republic of China

Abstract. Tie rod built-up rotor structures are widely used in power machinery for different types of gas turbine engines. Typical tie rod rotor structure consists from several disks and intermediate parts that are tightened together by central tie rod shaft. This type of construction allows assembling together compressor or turbine disks made from high strength materials whose welding is impossible or hard. Another benefit over solid cast rotor of the same size is lighter weight and possibility to replace damaged parts/disks during repair or retrofit. However modeling of this type of rotors is more complicated, time consuming and different from modeling of solid cast rotors or rotors with shrink fit disks/parts, since multiple interfaces between the built-up rotor components can reduce the shaft stiffness significantly. Fine meshed solid models are known to get a very accurate and close value with natural frequencies of real structures, however significant amount of time usually is required to get solution for them and further application of these models for rotordynamic simulations is not convenient. Thus beam models are still widely used, but cautions must be taken when preparing them, since obtained beam rotor model might be much more rigid than the real structure. Current paper is focused on rotordynamic modeling of typical built-up gas turbine rotor with central tie rod shaft. Paper describes a method how to correct beam model in order to achieve a better matching with fine meshed solid model. Described method was further used for rotor modeling of real 2 MW gas turbine rotor. Obtained simulation results were compared with experimental results from modal testing and good agreement was achieved.

Keywords: Built-up rotor · Tie-rod shaft · Rotordynamics · Modal testing
Natural frequencies · Free-free modes

1 Introduction

Tie rod built-up rotors are widely used by engineers for design of rotors working in different industries. Example of built-up rotors with central tie rod shafts can be found in stationary gas turbines used for power generation [1], in aviation and aircraft engines [2, 3], among turbocharger rotors [4]. Application of built-up rotors usually helps

designers to increase speed of machine manufacturing due to parallel processing of all assembled parts. Work pieces for single disks usually have a quality advantage over the work pieces for solid-forged rotors. Built-up rotors have possibility to have a lighter weight over the same size solid rotors and allow assembling the rotor from components manufactured from materials which are hard to weld or impossible. Another benefit of their application is that built-up rotors are easier for integration of cooling system in structure design. Moor and Lerche pointed out in [5] that multiple interfaces between the built-up rotor components can reduce the shaft stiffness, depending on the interface diameter and design used. API standard recognizes built-up rotors [6] and recommends to approximate joints being an integral piece of metal when creating a rotor model for rotor dynamic simulation, however there is no detail description for rotordynamic modeling of built-up rotors with central tie rod. This brings to difficulties in modeling of such rotors especially on design stage when exact values of connection stiffness between rotor components are not known. Despite of tendency to more and more use of solid finite element models for rotordynamic analysis [7–10], beam models are still widely used [5, 11, 12] due to significant gain in time used for simulation. However cautions must be taken during preparation of beam model since obtain beam rotor model might be much more rigid than the real structure. Books on rotordynamics [13–16] usually give a general guide for rotor modeling: nodal points must be placed at each location along the rotor with the step change in the diameter and each location with inertia disk, bearing, seal and any other source of external disturbance force. These guidelines are well working for heavy industrial cast rotors or rotors with shrunk disks, but bring to difficulties when implementing for modeling of disks in gas turbine engines which are usually integrated in rotor structure and significantly influence on its bending stiffness. In addition complex geometries such as disks used in aircraft engines are hard to model with single layer beam elements. To increase accuracy of modeling Lalanne [17] recommended to divide the disk on more lumped elements with addition of inertia properties for each element. Vance et al. [18] showed another approach of modeling disks which eliminates the need to add concentrated masses: to model the core structure of each disk with beam elements. This method is efficient for modeling of turbomachinery rotors with huge impeller disks. Hence stiffness and inertia properties of impeller disks are provided by element definition. However the bending stiffness of the structure is not able to change as sharp as its diameter, hence choice of inner and outer diameters of rotor elements depends a lot from experience of the user and may influence the obtained result significantly. In such a way application of solid models built from CAD becomes more and more popular, since meshing features in commercial codes make obtained mesh very accurate and accomplish in very little time compared to procedures in beam modeling [19]. Though, significant size of the solid model meshed with lots of elements, and huge memory slot required to store it are the other side of medal. Therefore beam models are still widely used due to their fast speed solution (what is very important on the design stage, when final design is not chosen yet and engineer should perform multiple analysis to develop it), small size and possibility to cooperate with different bearing codes. Current paper is focused on rotordynamic modeling of typical built-up gas turbine rotor with central tie rod shaft. Paper also describes a method how to correct beam model in order to achieve a better matching with fine meshed solid model.

2 Numerical Simulation

2.1 Modeling of Built-Up Rotors with Central Tie Rod Shaft

Before performing rotordynamic analysis of the engine its rotor model should be created and verified. As mentioned by Vance and Murphy [20] identification of rotor free-free modes using modal analysis is an excellent way of checking the accuracy of the mass-elastic model without involving uncertainties in the bearing parameters. For prediction of rotor free-free modes the problem is reduced to eigenvalue problem:

$$[\mathbf{K} - \lambda\mathbf{M}]\{\mathbf{u}\} = 0, \quad (1)$$

where $\lambda = \omega_i^2$ – are eigenvalues ($i = 1, 2, \dots, n$); ω_i – are natural frequencies; $\{\mathbf{u}\}$ – eigenvector; $[\mathbf{K}] = [\mathbf{K}_s] + [\mathbf{K}_{\text{bear}}]$ – rotor stiffness matrix, which consists from shaft and bearing stiffness matrix; $[\mathbf{M}] = [\mathbf{M}_T^s + \mathbf{M}_R^s] + [\mathbf{M}_T^d + \mathbf{M}_R^d]$ – rotor mass matrix which includes translational mass and rotational inertia matrices for shaft and disk components. Since the structure is assumed to be freely supported stiffness matrix is positive singular matrix where some eigenvalues become zero and are associated with rigid body modes, while the others are positive and associated with bending modes.

Simplified model of overhang gas turbine rotor with central tie rod shaft was used for study in the current paper, Fig. 1. For simplicity blades were not taken into account. In the same manner, for simplification all components for model were set to be made of steel ($\rho = 7800 \text{ kg/m}^3$, $E = 2.0\text{E}+11 \text{ N/m}^2$, $G = 7.7\text{E}+10 \text{ N/m}^2$). Spline joint was assumed to be used for coupling shaft connection and Curvic coupling joints for shaft-turbine disk connection and disks connection. Assembled condition is achieved with help of central tie rod shaft which has 3 steps and goes through the main shaft. Front nut is tightened from the coupling side to implement tie rod shaft pretension. Model was prepared from 3D geometry in ANSYS using solid elements (Solid 186), Fig. 2.

The main difficulty for creation of this type of model consists from correct understanding of applied boundary conditions between rotor components and parts. Some of these values are hard to obtain experimentally, but they have significant

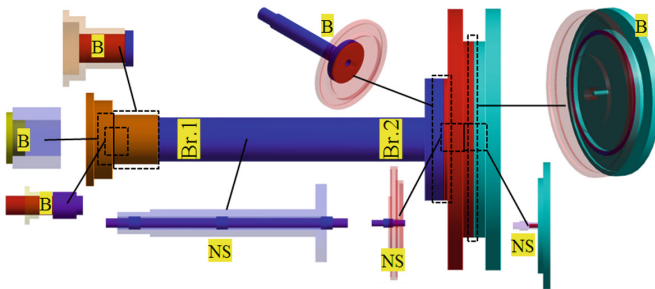


Fig. 1. Model of overhang built-up gas turbine rotor with central tie rod shaft with highlighted boundary conditions used for simulation in ANSYS: B-bounded; NS-no separation

influence on rotor free-free bending mode natural frequencies and mode shapes. On the design stage for the rotor which is assumed to be well assembled two types of contact connections can be used in ANSYS: bounded contact and no separation contact. Bounded contact is a contact when two contacting surfaces are not allowed to separate (assumed to be glued) or slide. No separation is similar to bounded type of connection, but connected parts are allowed to slide slightly.

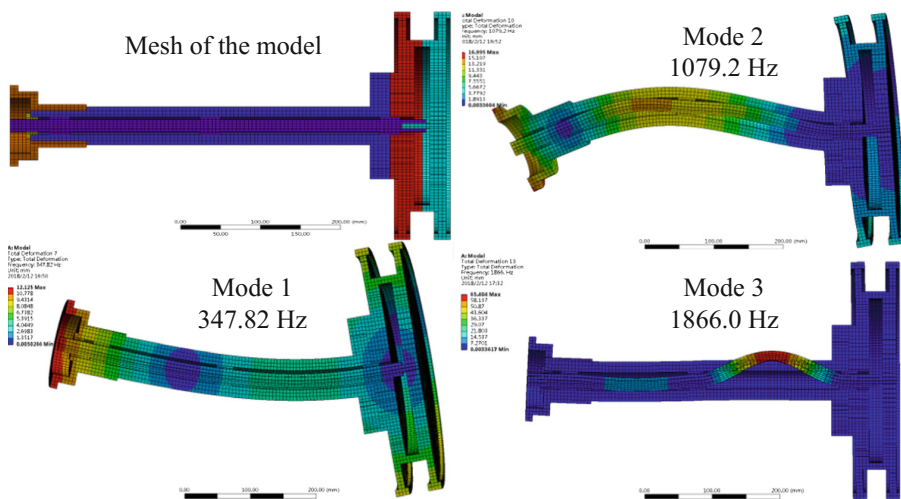


Fig. 2. Simulation results for solid rotor model – free-free bending modes

In addition, several beam models for the same type of rotor were prepared in XLRotor rotordynamic code for comparison with solid model. Consistent mass option was used for formulation of mass matrix of each model and solver based on finite element method was used for eigenanalysis. Model No. 1 is a multi-level model where each component (coupling, shaft, tie rod shaft, turbine disks) were modeled as separate parts connected by user-defined spring elements with 16 input columns: 4 translational (K_T) and 4 rotational stiffness (K_R). Damping was set to zero. Connection elements were highlighted in Fig. 3. For initial model high translational ($1E+12$ N/mm) and rotational ($1E+12$ N-mm/rad) stiffness were set. Inner and outer diameters for the beams were set to follow component geometry obtained from CAD. Model No. 2 is a 2 level model where coupling, shaft and turbine disks were modeled as one structure, assuming that joints between parts are stiff and approximated as integral piece of metal as recommended in [6]. Tie rod shaft was modeled as separate rotor connected with the main shaft using the same user-defined spring elements. Model 3 is a single level model built using beam layers. During eigenvalue and response calculations XLRotor automatically merges layers for beams which are at the same station [21]. Element number used for this model is twice less than for Model No. 1. Comparison of mass properties for all obtained models is shown in Table 1. All models had mass properties close to exact 3D model. Obtained simulation results for first 3 ordinal free-free bending modes for all beam models were summarized in Fig. 4.

Table 1. Mass properties for model

3D model	Solid model (51294 elements), kg	Beam models, kg		
		Model No. 1 (101 elements)	Model No. 2 (92 elements)	Model No. 3 (53 elements)
44.193	44.193	44.172	44.172	44.172

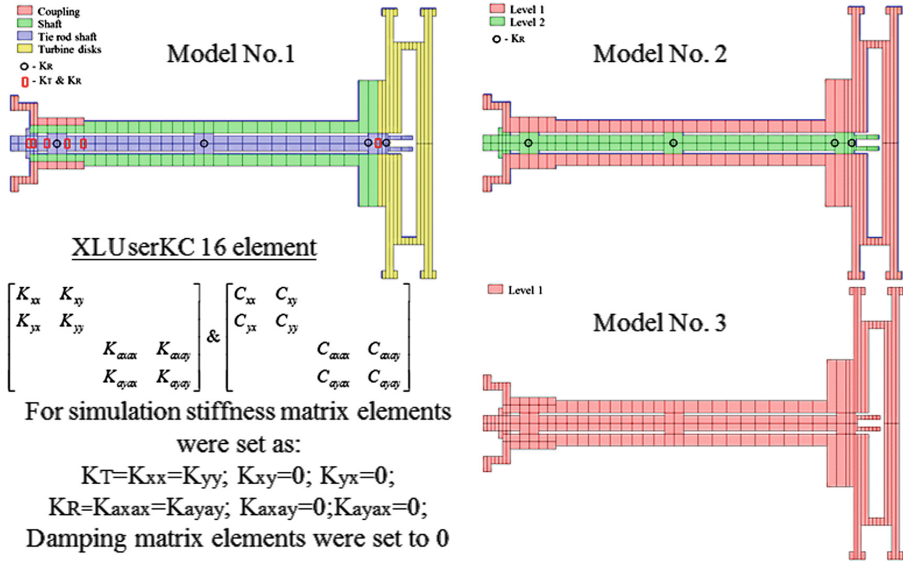


Fig. 3. Beam models for overhang built-up gas turbine rotor with central tie rod shaft

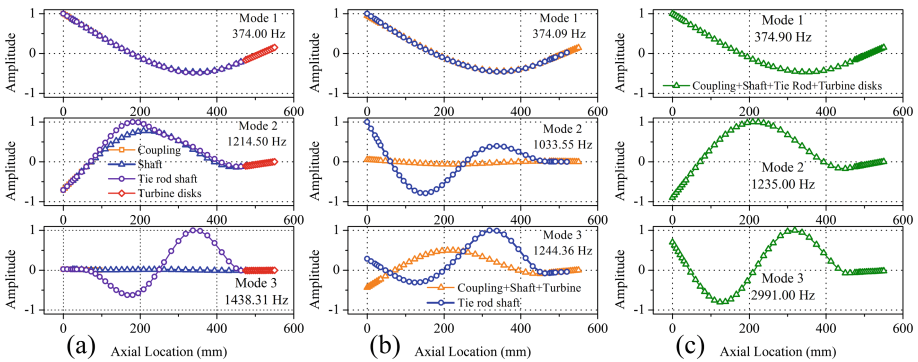


Fig. 4. Simulation results for beam models - free-free bending modes: (a) Model No. 1; (b) Model No. 2; (c) Model No. 3

Simulation results revealed that only for Model No. 1 all 3 ordinal bending modes, Fig. 4(a), were close with solid model results, Fig. 2. Model No. 2 and No. 3 were able to repeat first and second shaft bending modes but failed to present tie rod shaft bending mode. In addition they had shown much higher natural frequency in comparison with Model No. 1. Hence modeling of the structure using beam layers should be performed with caution and requires experience. When components are modeled as integral piece, beam element properties (OD and ID) should be set reasonably in order not to obtain much rigid structure. Model No. 1 in this case has an advantage over the other beam models described in this paper. Although natural frequencies for it also didn't match well with solid model (mode 1 difference - $\Delta = 7.52\%$, mode 2 - $\Delta = 12.54\%$, mode 3 - $\Delta = 22.92\%$), a good matching in mode shapes was reached. For natural frequencies a better matching can be achieved by setting the connection stiffness between model components and method for its implementation will be described in next section of this paper.

2.2 Method for Correction of Beam Model for Built-Up Rotor with Central Tie Rod Shaft

During free-free modal testing structure is freely supported and its bearing stiffness are set to zero, but internal connections between rotor components exist and influence on $[K_{\text{bear}}]$ component of matrix $[K]$ in Eq. (1). Rotor structure in Model No. 1 has only 10 connection elements but more complicated models may have much more internal connections, hence the question is how to understand which connection should be chosen and set to get a better matching for exact rotor mode shape.

The answer could be found with help of vibration energy analysis. Industrial application of energy distribution method in lateral analysis for rotor modeling was described by Gunter and Gaston [22]. Various forms of energy, work and their contribution to the dynamics of the system were also described by Chen [23]. Vibration energy analysis is currently integrated in all advanced rotordynamic commercial codes [15]. For this purpose the system damping is neglected and supports are considered as isotropic. Obtained shaft whirl modes are circular and energy distribution remains constant through the orbit. Since the amplitude of a free whirl mode is arbitrary, energy distribution is usually displayed as percentage of total energy of the system for the mode of interest. Potential energy of rotating shaft element in matrix form could be written as:

$$V = \frac{1}{2} q^T (K_b + K_\beta + K_a) q, \quad (2)$$

where q – is the displacement vector for rotor elements; K_b – bending stiffness; K_β – shear stiffness; K_a – geometric stiffness due to axial force. Ehrich pointed out in [13] that energy maps are very useful on the design stage, especially in preliminary design, but they also can be used for model refining to increase its accuracy and get better matching with experiment when rotor model is going to be prepared for further rotordynamic analysis. Evaluation of rotor potential energy distribution for Model No. 1 revealed that modes 1–2 were pure shaft bending modes since more than 90% of

energy was concentrated on the shaft, Fig. 5(a). However small concentration of potential energy for turbine disks - shaft connection element brought to conclusion that natural frequency of these modes can be changed by decreasing the stiffness for identified dominate element. Reduction of rotational stiffness for turbine disks - shaft connection element can help to achieve better matching between beam and solid model. When rotational stiffness was reduced to $5E+10$ N-mm/rad simulation results can match closer with experiment: Mode 1 - $\Delta = 0.08\%$; Mode 2 - $\Delta = 0.09\%$, Fig. 5(c).

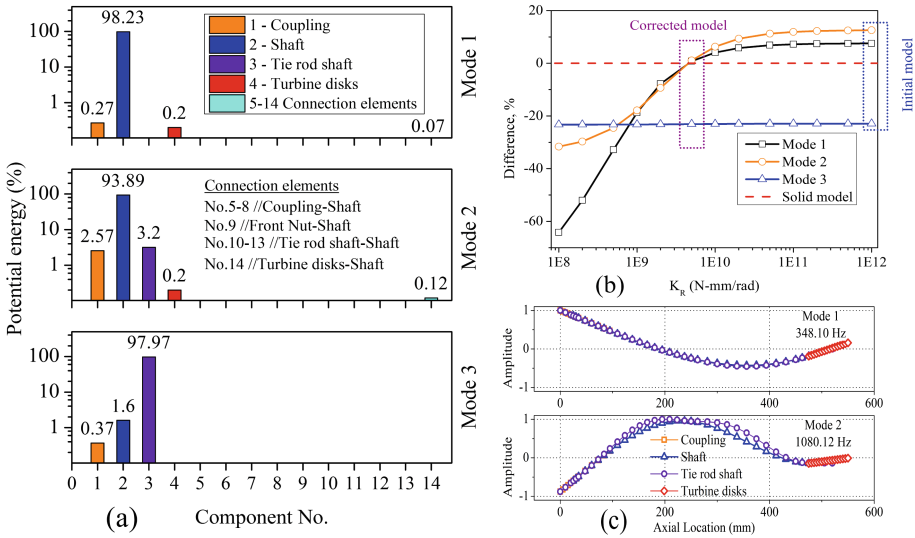


Fig. 5. (a) Potential energy map for initial Model No. 1 (b) Influence of rotational stiffness used for shaft-turbine connection on natural frequencies of beam model (c) Modes 1–2 mode shapes and natural frequencies for corrected beam model

Meanwhile for mode 3 most of potential energy was concentrated on the tie rod shaft and inspection of the plot in Fig. 5(a) from the first glance didn't bring to conclusion which connection was dominant for this mode. However comparison of the mode shapes obtained for solid and beam models revealed that tie rod central step in solid model had much larger area of contact surface with the rotor shaft. As a results additional connection element with only translational stiffness K_T was added to the beam model in area of tie rod central step. Influence of translational stiffness for added connection element on natural frequencies of mode 3 is shown in Fig. 6. A better matching with solid model was achieved when translational stiffness for additional connection element at the central step of tie rod shaft was increased to $K_T = 1.7E+07$ N/mm. Influence of this connection element on mode 3 natural frequency is clear from potential energy map obtained for rotor model when all bending modes were corrected to be close to solid model result, Fig. 6(c). Comparison of the obtained simulation results for initial (Model No. 1), corrected beam model and solid model was summarized in form of Table 2.

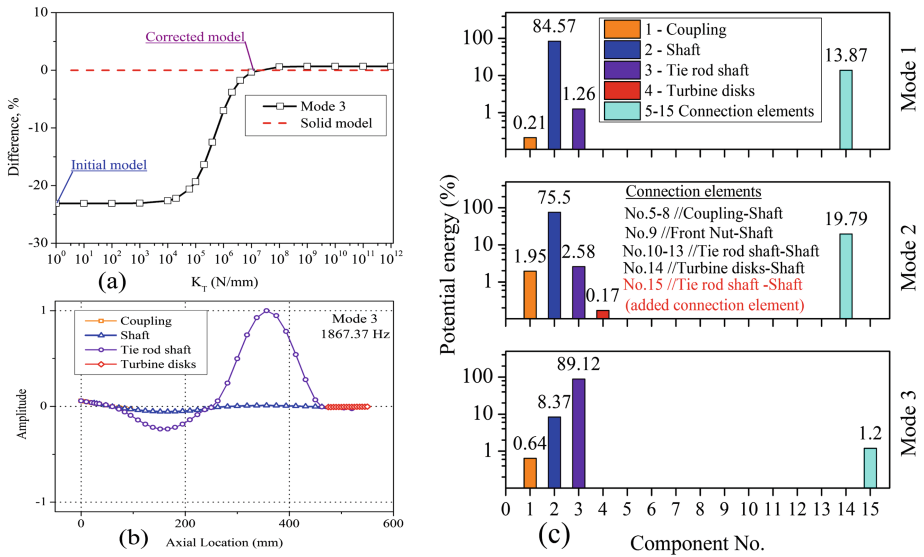


Fig. 6. (a) Influence of translational stiffness for added connection element on mode 3 for beam model; (b) Mode 3 mode shape and natural frequency for corrected beam model; (c) Potential energy map for corrected beam model

Table 2. Comparison of natural frequencies for solid and beam models

Mode No.	Natural frequency, Hz		
	Solid model	Model No. 1 (initial)	Model No. 1 (corrected)
1	347.82	374.00 ($\Delta = 7.53\%$)	348.10 ($\Delta = 0.08\%$)
2	1079.20	1214.50 ($\Delta = 12.54\%$)	1080.12 ($\Delta = 0.09\%$)
3	1866.00	1438.31 ($\Delta = 22.92\%$)	1867.37 ($\Delta = 0.07\%$)
Average difference, %		$\Delta = 14.33\%$	$\Delta = 0.08\%$

2.3 Influence of Axial Load on Natural Frequencies of Built-Up Rotor with Central Tie Rod

Tightening of the front nut for tie rod shaft helps to achieve assembled condition for the built-up rotor described in Sect. 2.1, Fig. 1. At the same time it brings to appearance of tension load in the tie rod shaft. Importance of bolt pretension incorporation in simulations for assembled built-up rotors was highlighted in [5, 11, 15, 24]. Influence of pre-tightening force on modal parameters for simplified rod-fastened rotors was also confirmed by experimental modal testing in [25].

In the current paper effect of axial load on natural frequencies for free-free bending modes was also studied for built-up rotor with central tie rod shaft on the base of beam corrected model described in Sect. 2.2. Based on ISO 898 [26] the minimum ultimate tensile load for M20 thread diameter of the tie rod shaft was identified to be 299 kN (for 12.8 property class). Pretension force was applied on beam model of tie rod shaft in form of axial load. At the same time equal value of compression load was applied on rotor

components which were held together by tie rod shaft. Simulation results revealed that increase of pretension force applied on tie rod shaft in comparison with non-loaded condition had a minor effect on modes 1–2, but on mode 3 natural frequencies influence was considerable, Fig. 7. With maximum applied pretension force natural frequencies: for mode 1 – decreased on 0.07% (due to compression load on the shaft), for mode 2 – increased on 0.05%, for mode 3 – increased on 10.2%. Influence of increase of pretension force on natural frequencies for modes 1–2 in comparison with mode 3 was smaller, since modes 1–2 were identified as full structure bending modes, Fig. 4(a), while mode 3 was a tie rod shaft bending mode. Thus, received simulation results confirmed necessity to include axial load from bolt pretension for assembled structures when preparing rotor model for rotordynamic simulations, since neglect of it may lead to additional decrease of accuracy of obtained model when it is going to be compared with experimental results from modal testing, especially for bending modes associated with tie rod shaft.

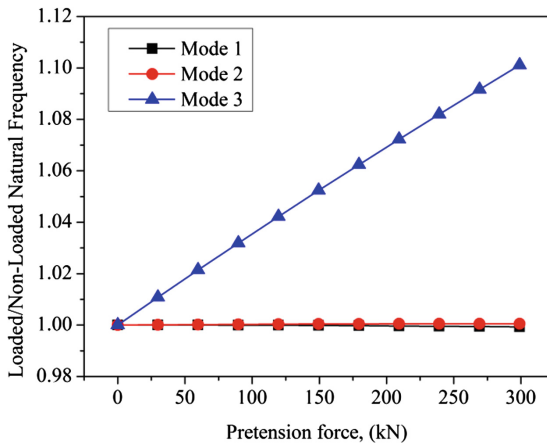


Fig. 7. Influence of applied pretension force on natural frequencies for first 3 ordinal free-free bending modes of built-up rotor with central tie rod shaft

3 Experimental Results

3.1 Modal Testing for Components of Built-Up Rotor with Central Tie Rod Shaft

Experimental modal testing was performed for components (tie rod shaft and rotor shaft) of real 2 MW built-up gas turbine rotor of ZK2000 engine in order to identify structure free-free bending modes and to compare them with simulation results. Both shafts were hanged using knitted ropes. Schematic view of used data acquisition system for modal testing is shown in Fig. 8. For every shaft 5 acceleration probes (Type 8774B050A Kistler) were used for measurements. Probes location is shown in Fig. 9. DASP software was used for processing of experiment results. Impact testing helped to get frequency response functions (FRF) for each rotor shaft. Mode shapes were obtained from FRF by measuring the peak amplitudes for its imaginary parts.

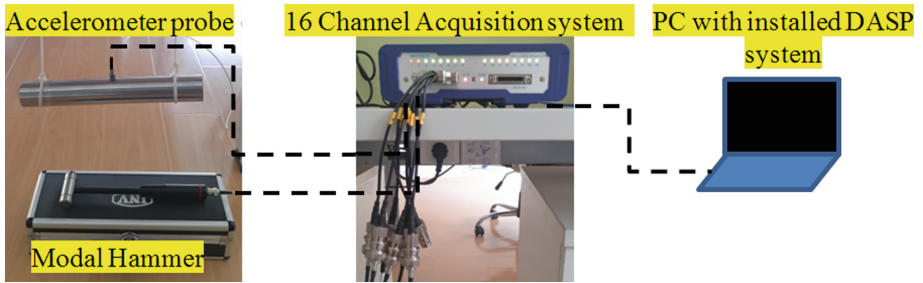


Fig. 8. Scheme of data acquisition system used for modal testing

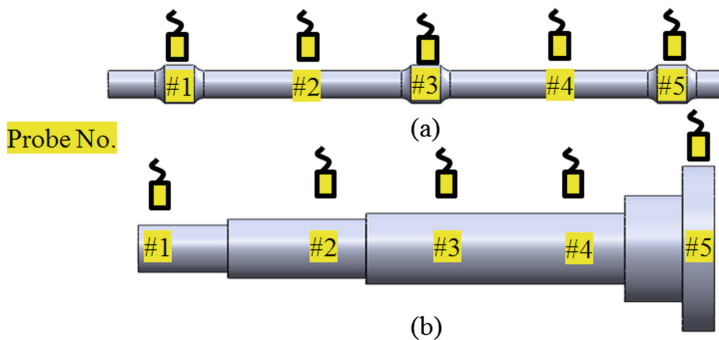


Fig. 9. Schematic view on probes location for components of built-up 2 MW gas turbine rotor: (a) Tie rod shaft; (b) Rotor shaft

Obtained experimentally mode shapes for the first 3 ordinal free-free bending modes are shown in Fig. 10, and were in agreement with obtained simulation results from beam models. Due to company regulations exact values of natural frequencies could not be presented in the paper, but difference for obtained simulation results with experimental was summarized in Table 3. Results revealed that for the first 3 ordinal free-free bending modes average difference between simulation and experiment for tie rod rotor shaft beam model was about $\Delta = 1\%$. For the rotor shaft beam model $\Delta = 1.3\%$.

Table 3. Comparison of simulation results with experiment for beam models of components of built-up 2 MW gas turbine rotor

Mode No.	Difference with experiment Δ , %	
	Tie rod shaft	Rotor shaft
1	-1.41	-0.60
2	-1.17	0.96
3	-0.53	2.23
Average Δ , %	1.04	1.26

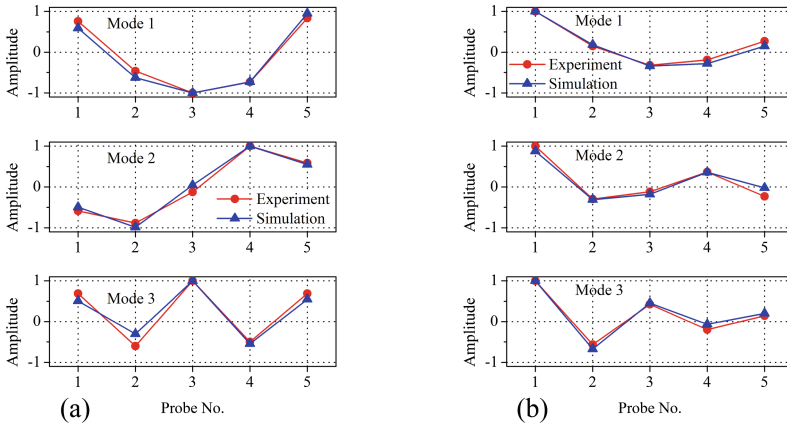


Fig. 10. Mode shapes comparison – experiment vs. simulation: (a) Tie rod shaft; (b) Rotor shaft

3.2 Modal Testing for Assembled Built-Up Rotor with Central Tie Rod Shaft

In the same manner as in previous section experimental modal testing was performed for assembled built-up gas turbine rotor of ZK2000 engine. The rotor was hung using single rope. Rope was girding the rotor in the zone between compressor-impeller and turbine disks, close to its center of gravity, what made the shaft silent and balanced during experimental modal testing. Eleven acceleration probes were used for measurements, Fig. 11. Impact excitation with modal hammer and measurements were performed in horizontal plane in order to reduce influence of the rope on natural frequencies.

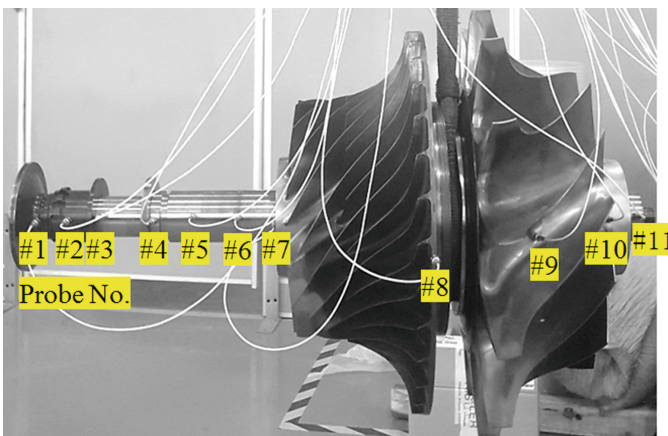


Fig. 11. Probes location for modal testing of built-up gas turbine rotor of ZK2000 engine

Obtained experimentally mode shapes for the first 3 ordinal free-free bending modes are shown in Fig. 12(a). Beam model for assembled built-up rotor of ZK2000 with included pretension load at tie rod shaft was also prepared. In general obtained by simulation mode shapes were in agreement with experimental results, Fig. 12(b). However due to complexity of the assembled rotor consisting from multiple parts and substitution of continuous structure on model with discrete elements with connections between components, matching was worse in comparison with results obtained for modal testing of single components, Fig. 10. In addition, natural frequencies of the initially constructed beam model didn't match easily, with average difference $\Delta = 12\%$ with experiment for the first 3 ordinal modes. However using the method described in Sect. 2, identifying dominate connection elements for each mode of interest beam model for built-up rotor was corrected and better matching was obtained with average difference $\Delta = 1.25\%$ for the first 3 ordinal modes, Table 4.

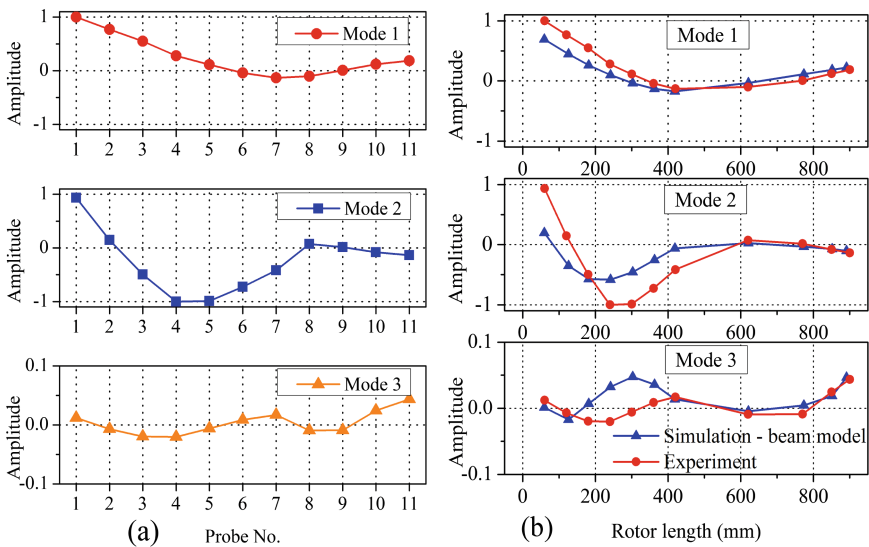


Fig. 12. (a) Experimentally obtained mode shapes for ZK2000 rotor (b) Comparison of simulation results for beam model of ZK2000 rotor with experiment

Table 4. Comparison of simulation results with experiment for different beam models of built-up 2 MW gas turbine rotor

Mode No.	Difference with experiment Δ , %	
	Initial beam model	Corrected beam model
1	12.69	1.36
2	10.56	-1.09
3	-13.15	1.32
Average Δ , %	12.13	1.25

4 Conclusion

It can be summed up in the conclusion:

- Existence of multiple interface surfaces inside built-up rotors can significantly reduce bending stiffness of the assembled rotor structure, what makes rotordynamic modeling of such rotors more complicated and time consuming. Application of modeling method when components are modeled as integral piece using beam elements and method when components are modeled using beam layers requires experience and should be performed with caution. When beam element properties (OD and ID) are not set reasonably, much rigid structure can be obtained. Solid models obtained from CAD and meshed in commercial codes can help to obtain a very accurate and close with experiment result. In this case for creation of beam models, when experimental results are not available, solid models can be used as a reference;
- Rotor model built with multi-level method where components are connected with user-defined elements is usually more convenient for further rotordynamic analysis, since tuning of connection stiffness between components can help to get better matching with experimental results obtained from modal testing. However, when connection stiffness between rotor components are not properly set model can have significant difference both with experiment and solid model;
- Inspection of potential energy maps for beam model of assembled rotor structure for each mode of interest can point out which connection element has a dominate influence on certain mode. Changing connection stiffness in dominate connection element can help to get a better matching with experimental results for certain mode;
- Simulation results revealed that increase of pretension force applied on tie rod shaft in comparison with non-loaded condition brings to increase of natural frequencies for tie rod shaft mode and confirmed necessity to include axial load from bolt pretension for assembled structures when preparing rotor model for rotordynamic simulations. Bending modes of the rotor structure may decrease slightly due to negative axial load from compression when assembled condition is modeled;
- Described in paper method for model tuning using inspection of potential energy maps was successfully implemented for creation of beam model for real gas turbine rotor. Further correction of the beam model helped to get good agreement with experimentally obtained mode shape and reduce difference in natural frequencies with experiment for numerical model to almost 1%;
- Performed experimental modal testing had shown that for single rotor parts like rotor shaft and tie rod shaft very close matching in natural frequencies for free-free bending modes between simulation and experimental results can be achieved for initially created beam models. Once the rotor is assembled, connection stiffness between rotor components and parts may influence the results matching significantly both for mode shapes and natural frequencies. Thus initially created beam model could have difference with experiment and will require further correction.

Acknowledgements. This work is funded by the Key Programs of Chinese Academy of Sciences (Project No. ZDRW-CN-2017-2) & National Natural Science Foundation (No. 51306199).

References

1. Soares, C.: *Gas Turbines: A Handbook of Air, Land and Sea Application*. Elsevier, New York City (2011)
2. Hunecke, K.: *Jet Engines*. Motorbooks International, Minneapolis (1997)
3. Rolls Royce: *The Jet Engine*. Wiley, Hoboken (2015)
4. Nguyen-Schafer, H.: *Rotordynamics of Automotive Turbochargers*. Springer, Heidelberg (2016)
5. Moore, J.J., Lerche, A.H.: Rotordynamic comparison of built-up versus solid rotor construction. In: *ASME Turbo Expo 2009: Power for Land, Sea and Air*, pp. 779–784. American Society of Mechanical Engineers (2009)
6. API Standard Paragraphs Rotordynamics Tutorial: Lateral Critical Speeds, Unbalance, Response, Stability, Train Torsionals, and Rotor Balancing, 2nd edn. American Petroleum Institute, Washington (2005)
7. Hong, J., Chen, M., Liu, S.: Application of whole engine finite element models in aero-engine rotordynamic simulation analysis. In: *ASME Turbo Expo 2007: Power for Land, Sea and Air*, pp. 771–778. American Society of Mechanical Engineers (2007)
8. Shuguo, L., Yanhong, M., Dayi, Z., Jie, H.: Studies on dynamic characteristics of the joint in aero-engine rotor system. *Mech. Syst. Signal Process.* **29**, 120–136 (2012)
9. Liu, S., Wang, J., Hong, J., Zhang, D.: Dynamics design of the aero-engine rotor joint structures based on experimental and numerical study. In: *ASME Turbo Expo 2010: Power for Land, Sea and Air*, pp. 49–60. American Society of Mechanical Engineers (2010)
10. Zhang, D., Ma, Y., Liang, Z., Hong, J.: Evaluation method on whole engine structural design structural efficiency. *J. Aerosp. Power* **25**(10), 2170–2176 (2010)
11. Jam, J.E., Meisami, F., Nia, N.G.: Vibration analysis of tie rod/tie-bolt rotor using FEM. *Int. J. Eng. Sci. Technol.* **3**, 7292–7300 (2011)
12. Yuan, Q., Gao, R., Feng, Z., Wang, J.: Analysis of dynamic characteristics of gas turbine rotor considering contact effect and pre-tightening force. In: *Proceedings of ASME Turbo Expo 2008: Power for Land, Sea and Air*, pp. 983–988. American Society of Mechanical Engineers (2008)
13. Ehrich, F.F.: *Handbook of Rotordynamics*. McGraw-Hill Inc., New York City (1992)
14. Vance, J.M.: *Rotordynamics of Turbomachinery*. Wiley, Hoboken (1988)
15. Chen, W.J., Gunter, E.J.: *Introduction to Dynamics of Rotor-Bearing Systems*. Eigen Technologies Inc., New York (2007)
16. Young, S., Lin, Z., Allaire, P.E.: *Control of Surge in Centrifugal Compressors by Active Magnetic Bearings*. Springer, London (2013)
17. Lalanne, M., Ferraris, G.: *Rotordynamics Prediction in Engineering*, 2nd edn. Wiley, Hoboken (1998)
18. Vance, J., Zeidan, F., Murphy, B.: *Machinery Vibration and Rotordynamics*. Wiley, Hoboken (2010)
19. Rao, J.S., Sreenivas, R.: Dynamic of a three level rotor system using solid elements. In: *Proceedings of ASME Turbo Expo 2003: Power for Land, Sea and Air*, pp. 1–6. American Society of Mechanical Engineers (2003)

20. Vance, J.M., Murphy, B.T., Tripp, H.A.: Critical speeds of turbomachinery: computer predictions vs. experimental measurements. In: Proceedings of the 13th Turbomachinery Symposium. Texas A&M University Turbomachinery Laboratories (1984)
21. XLRotor Reference Guide. Version 5.1. Rotating Machinery Analysis, Inc. (2016)
22. Gunter, E.J., Gaston, C.G.: CRITSPD-PC User's Manual: A Program for Undamped Critical Speed Analysis of Flexible Rotor-Bearing Systems. RODYN Vibration, Inc. (1987)
23. Chen, W.J.: Energy analysis to the design of rotor-bearing systems. *J. Eng. Gas Turbines Power* **119**(2), 1–9 (1995)
24. Wagner, N., Helfrich, R.: Static and dynamic analysis of a rod-fastened rotor. In: Proceedings of NAFEMS World Congress (2017)
25. Zhang, Y., Du, Z., Shi, L., Liu, S.: Determination of contact stiffness of rod-fastened rotors based on modal test and finite element analysis. *J. Eng. Gas Turbines Power* **132**(9), 094501 (2010)
26. ISO, P. 898-1: Mechanical properties of fasteners made of carbon steel and alloy steel—Part 1 (2013)



A Preliminary Experiment to Excite and Identify Modal Frequencies of a Rotor in the Rotating Frame of Reference

Sudhakar Gantasala^(✉) and Jan-Olov Aidanpää

Department of Engineering Sciences and Mathematics,
Luleå University of Technology, 97187 Luleå, Sweden
{sudhakar.gantasala,jan-olov.aidanpaa}@ltu.se

Abstract. The current work uses two types of excitation on a rotating shaft to identify its modal frequencies. The first one is a non-contact excitation where an oscillating magnet is placed near the shaft, eddy currents generated by the oscillating magnetic field excites vibrations in the shaft. In the second type of excitation, a miniature electrodynamic exciter powered by a decoder amplifier board is placed on the shaft to excite vibrations with predefined frequencies in a signal (mp3 format) stored on the USB flash drive connected to the board. The shaft is rotated at different speeds and vibration accelerations are measured using a small data logger placed on the shaft while excited using these two excitation systems. These two types of asynchronous excitation on the shaft excites both forward and backward whirl vibration modes of the rotor system. The modal frequencies are identified at the peak amplitudes in the waterfall plots of the measured vibration accelerations to a chirp excitation of the shaft. A Campbell diagram is plotted with the identified modal frequencies of the shaft in the rotating frame of reference.

Keywords: Modal frequency · Rotor · Excitation
Campbell diagram · Rotating frame of reference

1 Introduction

Rotating systems consisting several components like shafts, bearings, couplings, seals, foundations etc. are commonly used in many industries. Their reliable operation is crucial to avoid any breakdown or production losses. Manufacturing tolerances of the rotating system components and their assembling induces unbalance and causes vibrations. For a reliable operation under various operating conditions (like rotational speed, loads, temperature etc.), the rotating system components need to be designed appropriately to limit vibrations within a safe limit through detailed simulations for predicting their dynamic behavior. The rotating system components like bearings, couplings, and seals are modeled using mathematical models. Many researchers have derived simplified models

for such subsystems so that they can be coupled with rotating system models for simulating their dynamic behavior. However, the validity of such models can be verified if it is possible to extract modal frequencies of the rotating system experimentally. The modal frequencies of a rotating system are dependent on its rotational speed due to the speed and load dependent bearing properties and gyroscopic effects. These modal frequencies can be calculated using a numerical model (Finite Element Method, FEM) of the rotating system, but their extraction from its vibrations in the experiments is cumbersome. Conventional vibration exciters cannot be directly used to excite rotating systems due to their rotational motion. They need to be either non-contact or portable excitation systems that can be directly mounted on the rotating shaft. The literature on such vibration excitations are discussed in the following text.

Sinou et al. [1] supported bearing housing of a rotating system through four beams connected to a stationary rigid mass and excited the bearing housing using a shaker to identify natural frequencies of the first vibration mode. This asynchronous excitation at different rotational speeds of the shaft excited forward and backward whirl modes of the rotating system. Sodano [2] used a permanent magnet on the electromagnetic shaker to apply non-contact force generated by the eddy currents induced in a conductor due to the movement of the magnet relative to it. This force is proportional to the velocity of the magnet and depends on the distance between the magnet and the conductor. Nandi et al. [3] used two permanent magnets placed on a piezoelectric stack and excited a cantilever beam using the non-contact force generated by the moving magnetic field. Other non-contact excitations, like speaker [4], ultrasound radiation [5], laser [6], PZT patches [7] are used for exciting light and delicate structures. Esu [8] used a Visaton Ex 45 S electrodynamic exciter [9] to identify natural frequencies of a stationary small-scale wind turbine blade. This exciter resembles a loudspeaker without membrane. It consists of an oscillating mass whose movement is controlled by an input signal to the exciter. The mounting plate of the exciter is placed on the target surface which needs to be excited. This exciter is portable with dimensions $45 \times 45 \times 15$ mm and it only weighs 60 g.

Out of all the excitations discussed before, the authors chose eddy current excitation and Visaton Ex 45 S electrodynamic exciter as relevant for exciting rotating systems without making major changes in the rotor system. A simple rotor system supported on ball bearings is excited with these two excitations and vibration accelerations are measured using a MIDE Slam Stick X data logger [10] placed on the rotating shaft. The vibrations are measured in a rotating frame of reference. The modal frequencies are identified at different rotational speeds from the waterfall plots of the measured vibration signals.

2 Test Rig

A Spectraquest Rotordynamic Simulator is used in this work to carry out experiments and the schematic of the test rig is shown in Fig. 1. It consists of a steel shaft with diameter \varnothing 0.01905 m and length 0.914 m and it is supported by two

ball bearings at distances of 0.099 m and 0.824 m respectively from the end of the shaft connected to coupling. An aluminum disc of mass 1.322 kg is located at the half way between two bearing supports. The eddy current excitation is applied at 0.27 m from the Bearing 1 location. The speaker and accelerometer are placed on the outer periphery of a small cylinder clamped on the shaft at 0.535 m from the Bearing 1 location. The test rig with these excitation systems is shown in the Fig. 2. More details about the excitation and measurement systems are discussed in the following text.

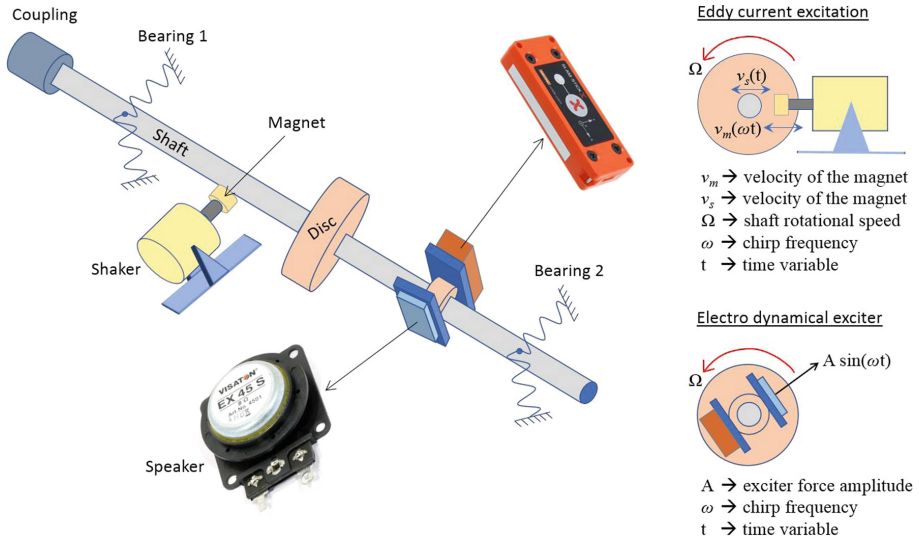


Fig. 1. Schematic of the test rig and excitation systems

2.1 Eddy Current Excitation

A neodymium magnet with dimensions \varnothing 15 mm, height 8 mm is placed on the TIRA vib S-50018 shaker’s moving surface as shown in the Figs. 1 and 2. This magnet is located at around 6 mm from the shaft surface, any closer distance than this can lead to a risk of contact with the rotating shaft. A chimp signal is given as an input to the shaker. Then, the magnet moves with a velocity $v_m(\omega t)$ and the shaft vibrates with a velocity $v_s(t)$ as shown in the Fig. 1. The moving magnetic field of the magnet is opposed by the magnetic field generated by eddy currents induced in the shaft. This results in a force between the magnet and the shaft. This force depends on the distance between the magnet and shaft, and the net velocity between the magnet and shaft. Sodano [2] theoretically modelled these forces and compared them with the values measured in an experiment. He also performed a modal analysis of the cantilever beam and compared frequency response function (FRF) calculated using the impact and eddy current excitations.

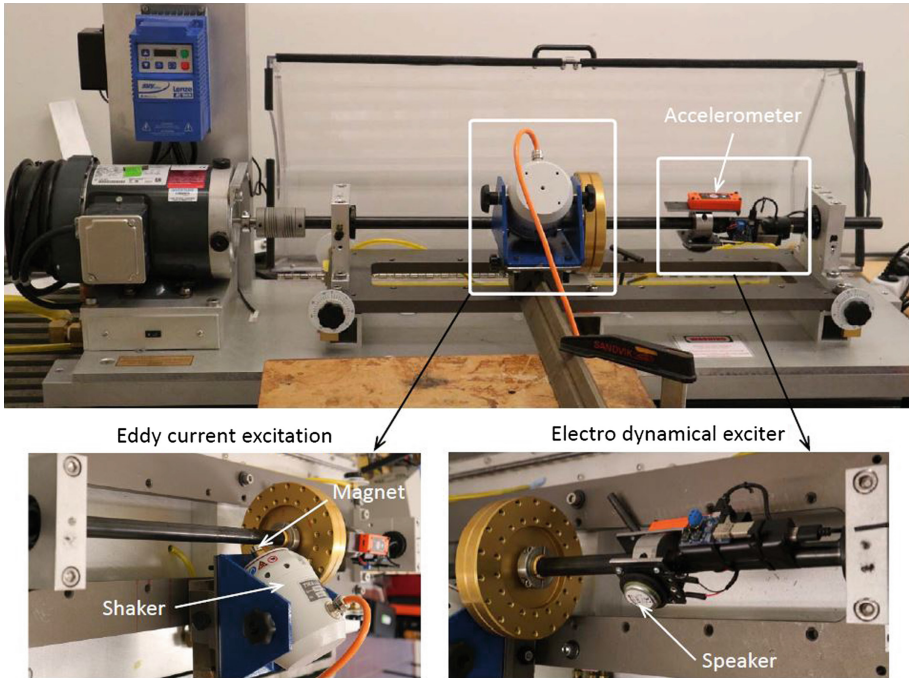


Fig. 2. Experimental setup

2.2 Electrodynamic Exciter

The Visaton Ex 45 S electrodynamic exciter needs signal amplification using an audio power amplifier and the authors used an mp3 format decoder amplifier board [11] for this purpose. A chirp signal is generated using MATLAB and converted to mp3 format and stored in a flash drive connected to the amplifier board. A small power bank is used to power this board. All these components are portable and light weight, which makes their use feasible as shown in the Fig. 2 for rotor excitation.

2.3 MIDE Slam Stick X

The MIDE Slam Stick X [10] is a data logger that measures accelerations in three axes with a sampling rate up to 20 kHz using a piezoelectric sensor and stores the data in its internal memory. It weighs about 40 g with dimensions $76 \times 30 \times 8$ mm and it can be attached to the target surface using bolts or adhesive tape. The light and miniature design of the data logger make it suitable for measuring vibration accelerations on the rotating shaft. It measures vibrations in the rotating frame of reference. In the current work, vibrations are measured using a sampling rate of 4096 Hz.

3 Results and Discussion

An acceleration frequency response function (FRF) of the stationary shaft is calculated after an impact test of the test rig (refer Fig. 2) and it is shown in the Fig. 3. Two vibration modes can be identified within the 300 Hz frequency range. Their frequency values in the current case (which only has structural damping) are estimated with better accuracy, using a circle fit method to FRF in the Nyquist plane [12], these values are estimated in this study as 46.797 and 205.55 Hz using the *DEWESoftTM FRF* [13] module. The speaker excitation system increased mass and stiffness of the original shaft. As a result its natural frequencies are changed and the percentage change (with respect to the natural frequencies of the original shaft) in the natural frequencies due to the speaker excitation system is -3.28% for the first mode and -19.18% for the second mode. The influence of asymmetry introduced by the placement of speaker and accelerometers on the periphery of a circular fixture clamped on the shaft is very small (change in natural frequencies are observed to be less than 1%).

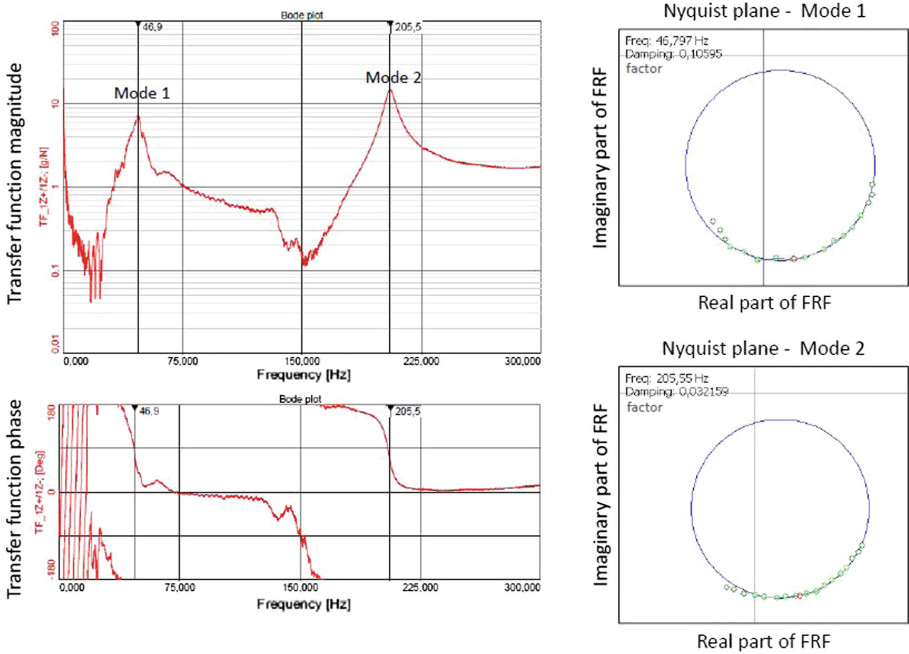
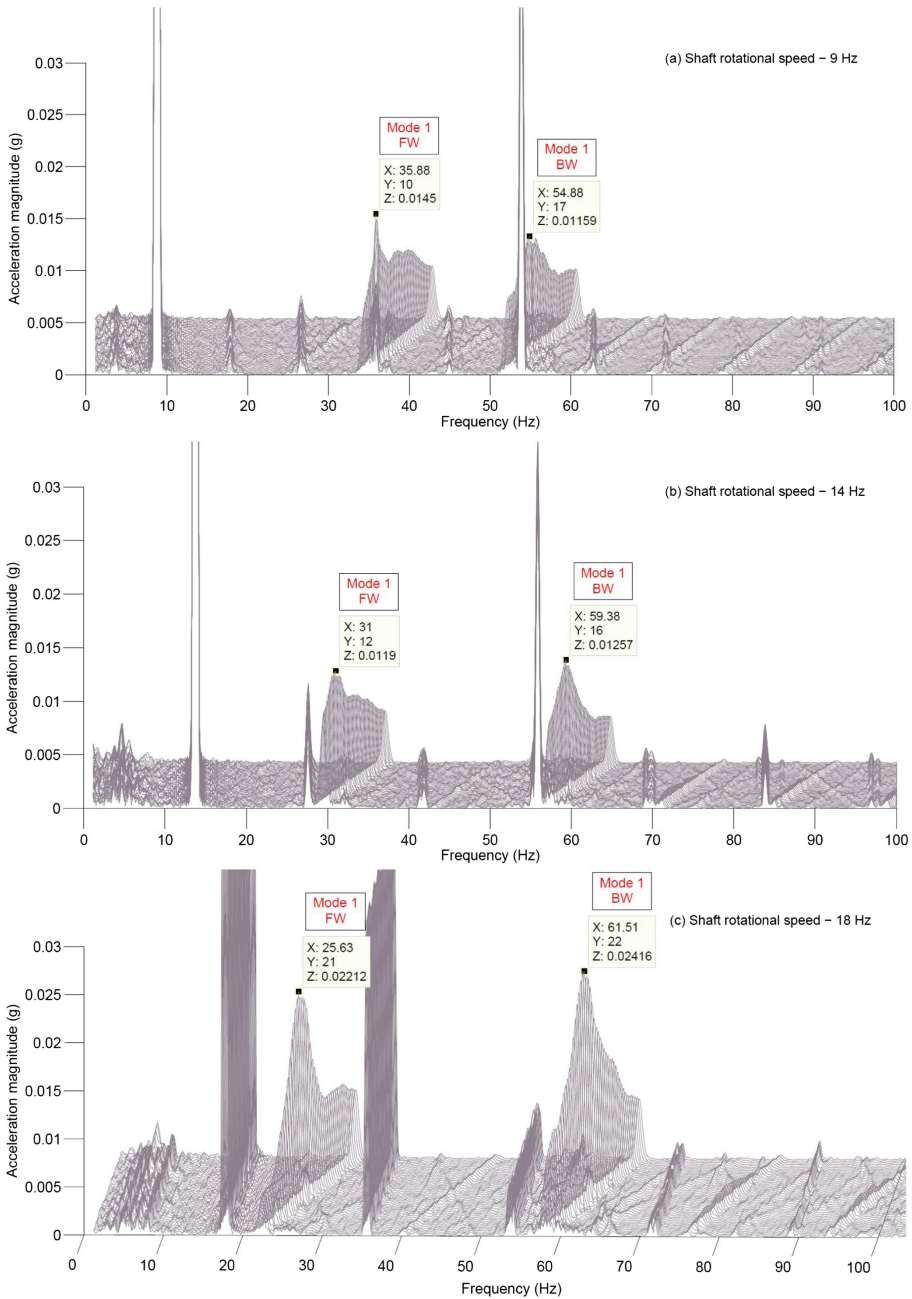


Fig. 3. Accelerance frequency response function

The shaft is rotated at three different speeds 9, 14 and 18 Hz and excited with eddy current and electrodynamic excitations described in the previous section. The locations of these excitations on the shaft can be moved flexibly. The excitation forces are not measured in this study, but the dynamic behavior



Note: FW and BW refers to forward and backward whirling in the rotating frame of reference

Fig. 4. Waterfall plots of vibration accelerations with eddy current excitation

of the shaft to these excitations is recorded. The frequencies in the chirp signal vary from 0 to 300 Hz in 50 s.

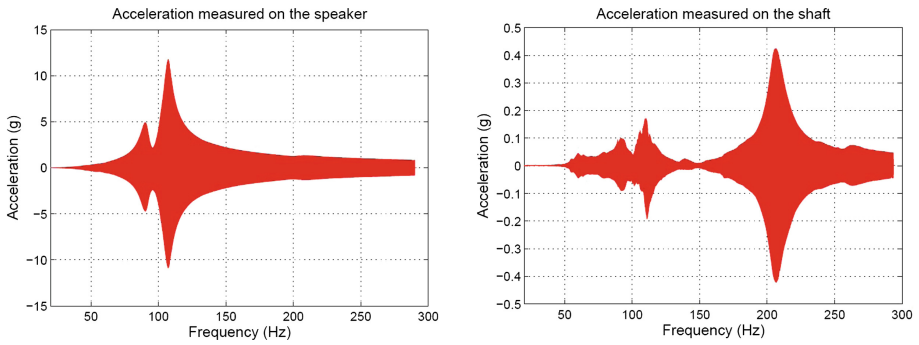
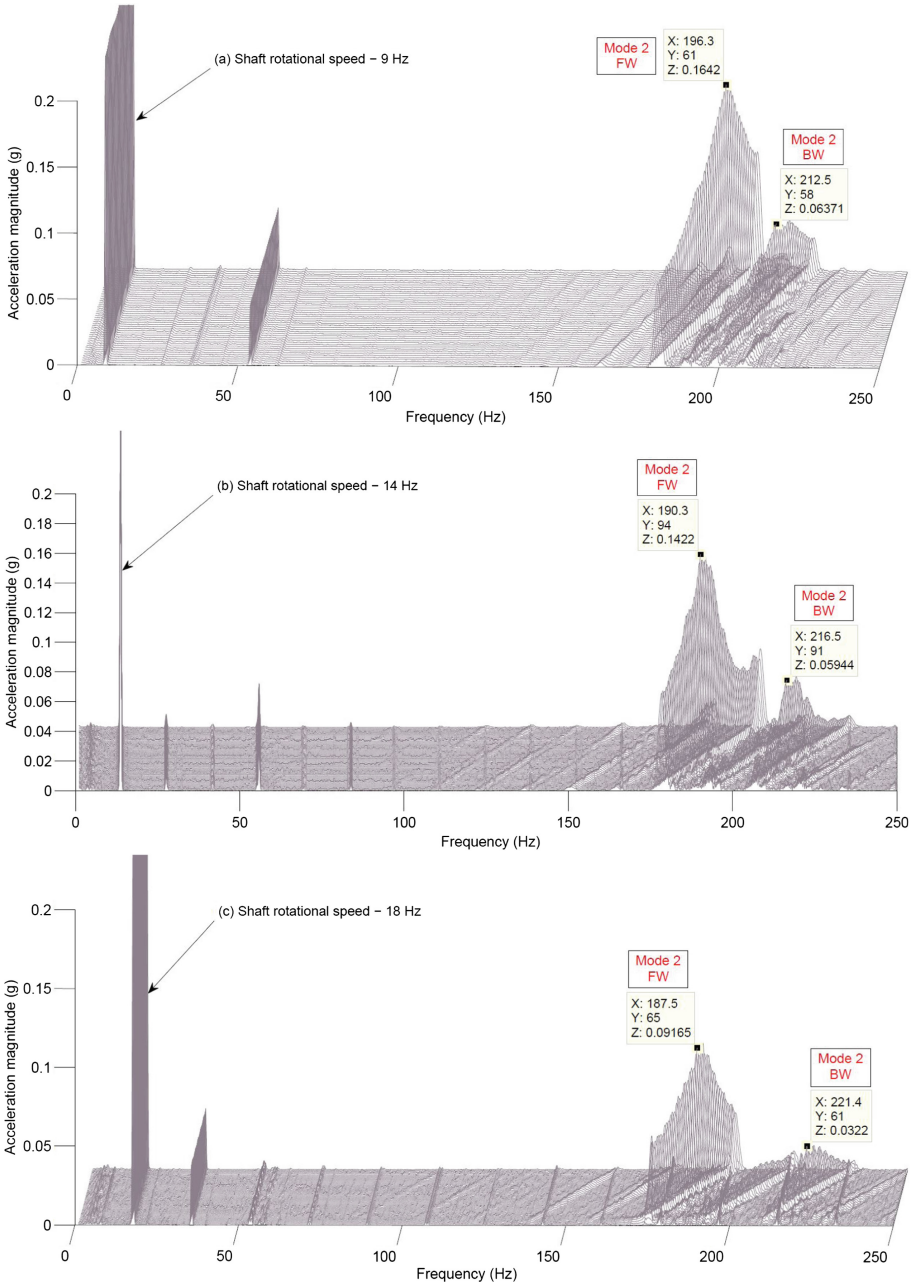


Fig. 5. Measured vibration accelerations to speaker excitation

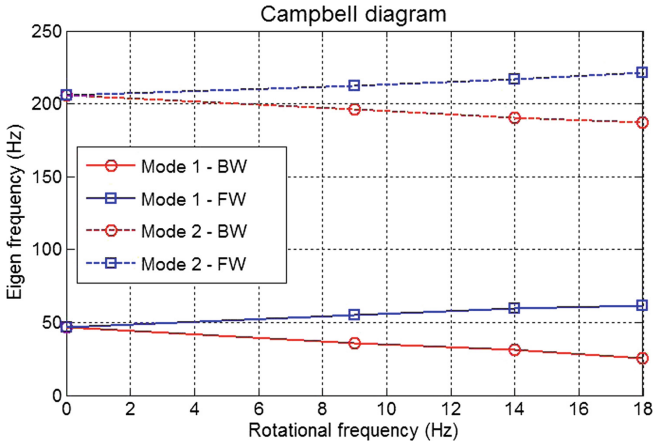
The waterfall plots generated using vibrations measured on the shaft while in rotation and excited by the eddy currents generated by the moving magnet currents are shown in the Fig. 4. The acceleration magnitude axis of the figure is zoomed in to clearly show the frequencies of vibrations generated in the shaft due to this excitation. The asynchronous excitation to the shaft excited both forward and backward whirl bending vibration modes. The vibration response reaches maximum amplitude when the excitation frequency matches with the modal frequencies of the shaft. The forward and backward modal frequencies of the first vibration mode are identified in Fig. 4 at the peak amplitudes in waterfall plots. The vibrations at higher excitation frequencies (above the first mode natural frequency) are not noticed in the waterfall plots. The forces generated by eddy currents are observed to be very small in comparison to the unbalance forces as the peak amplitude at the resonance condition is much smaller than the vibration amplitude at rotational frequency. The location chosen for eddy current excitation is close to the midpoint of the shaft between bearing supports which matches with the anti-node (i.e. maximum deformation point) in first vibration mode and a node in the second vibration mode. The weaker excitation force closer to node location could be the reason for not noticing second vibration mode in the waterfall plots. As the modal frequencies of the test rig are not calculated using a numerical model (FEM), the modal frequencies of a simple rotor are derived in the rotating frame of reference (refer Chap. 7 in [14]) in Appendix to show their dependency on the rotational frequency.

The accelerations measured on the speaker and the shaft to an excitation by the speaker are shown in Fig. 5. The speaker and its supporting structure have two resonances between 85 and 110 Hz and they are faraway from the first two natural frequencies of the shaft (refer Fig. 3). The amplitudes of these resonances are reduced significantly in the acceleration measurements on the shaft and the resonance peak corresponding to second vibration mode appears dominant. The



Note: FW and BW refers to forward and backward whirling in the rotating frame of reference

Fig. 6. Waterfall plots of vibration accelerations with electrodynamic excitation



Note: FW and BW refers to forward and backward whirling in the rotating frame of reference

Fig. 7. Campbell diagram plotted with eigen frequencies identified in the experiments

speaker is not able to excite first vibration mode of the shaft. So, the vibration accelerations for speaker excitation frequencies above 110 Hz are only used to identify the second vibration mode of the shaft.

The waterfall plots generated using the vibration response of the shaft subjected to electrodynamical excitation at different rotational speeds are shown in the Fig. 6. As the electrodynamical exciter used in this study can be regarded as a loudspeaker without membrane, the speaker frequency response function at low frequencies will generally have lower magnitude if those frequencies are around the lower limit of the human hearing frequency range. The location of the Visaton electrodynamical exciter is close to antinode of the second vibration mode and in the midway between antinode and node of the first vibration mode. The vibrations at lower frequencies (around the first vibration mode natural frequency) are not appearing in the waterfall plots may be due to these two reasons, whereas, the second vibration mode is clearly excited by this exciter. However, these postulates can be confirmed with the measurement of forces generated by the exciter with respect to frequency. This asynchronous excitation excites both forward and backward whirl modes and these frequencies are also changing with the rotational frequency. A Campbell diagram is plotted with the identified forward and backward whirl frequencies of the first and second vibration modes of the test rig in Fig. 7.

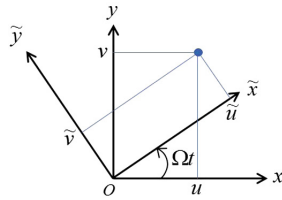
4 Conclusions and Future Work

A preliminary experiment to use eddy current excitation and a miniature electro-dynamical exciter for identifying modal frequencies of the rotor in the rotating frame of reference is carried out in this study. Neither of these two excitations can excite both first and second vibration modes of the test rig. A further study

experimenting with the locations of excitation and response is to be carried out like any other modal analysis to ascertain their suitability for exciting modal frequencies of the rotating systems. The strength of excitation forces can be enhanced using a stronger magnet and choosing a high power electrodynamical exciter. The authors planned these activities for the future work along with the comparison of frequencies identified in experiments with those calculated using a numerical model. However, a Campbell diagram with the first two vibration modes of the test rig is generated in this preliminary study using two new types of excitations to the rotating shaft. The idea of using these excitation systems in real machinery is not matured at this stage and it has the limitation of weak excitation forces and also need access to the shaft for its excitation.

Acknowledgments. The research work presented in this paper was carried out as a part of “Swedish Hydropower Centre - SVC”. SVC (www.svc.nu) has been established by the Swedish Energy Agency, Elforsk and Svenska Kraftnät together with Luleå University of Technology, The Royal Institute of Technology, Chalmers University of Technology and Uppsala University.

Appendix



The transformation between stationary (xy) and rotating $(\tilde{x}\tilde{y})$ coordinate systems shown in the above figure is obtained as follows. The coordinates of a point in the stationary frame are denoted by u, v and in the rotating frame they are denoted by \tilde{u}, \tilde{v} . The relation between stationary and rotating frame coordinates is given by

$$\begin{Bmatrix} u \\ v \end{Bmatrix} = \begin{bmatrix} \cos(\Omega t) & -\sin(\Omega t) \\ \sin(\Omega t) & \cos(\Omega t) \end{bmatrix} \begin{Bmatrix} \tilde{u} \\ \tilde{v} \end{Bmatrix} = [T] \begin{Bmatrix} \tilde{u} \\ \tilde{v} \end{Bmatrix}$$

Then, the differentiation with respect to time gives

$$\begin{Bmatrix} \dot{u} \\ \dot{v} \end{Bmatrix} = [T] \begin{Bmatrix} \dot{\tilde{u}} \\ \dot{\tilde{v}} \end{Bmatrix} + [\dot{T}] \begin{Bmatrix} \tilde{u} \\ \tilde{v} \end{Bmatrix},$$

$$\begin{Bmatrix} \ddot{u} \\ \ddot{v} \end{Bmatrix} = [T] \left(\begin{Bmatrix} \ddot{\tilde{u}} \\ \ddot{\tilde{v}} \end{Bmatrix} - \Omega^2 \begin{Bmatrix} \tilde{u} \\ \tilde{v} \end{Bmatrix} \right) + 2[\dot{T}] \begin{Bmatrix} \dot{\tilde{u}} \\ \dot{\tilde{v}} \end{Bmatrix}$$

where,

$$[\dot{T}] = \Omega \begin{bmatrix} -\sin(\Omega t) & -\cos(\Omega t) \\ \cos(\Omega t) & -\sin(\Omega t) \end{bmatrix}$$

The eigenvalues of a simple rotor in the rotating frame of reference are derived here using these transformations. The rotor system consists of a light flexible asymmetric shaft (stiffness in \tilde{x} and \tilde{y} directions are different) supported in isotropic bearings and a thin, rigid axisymmetrical disc of mass m is located at the mid-span. The elastic forces acting on the disc in terms of the shaft deformation variables in the rotating frame attached to it and the shaft stiffnesses k_x, k_y are given as

$$\begin{Bmatrix} f_{\tilde{x}} \\ f_{\tilde{y}} \end{Bmatrix} = \begin{bmatrix} k_x & 0 \\ 0 & k_y \end{bmatrix} \begin{Bmatrix} \tilde{u} \\ \tilde{v} \end{Bmatrix}$$

Using the Newton's second law, the equation of motion of the disc in stationary coordinates is expressed as

$$m \begin{Bmatrix} \ddot{u} \\ \ddot{v} \end{Bmatrix} = \begin{Bmatrix} f_x \\ f_y \end{Bmatrix}$$

Using the transformation matrices derived before, the above equation is rewritten as

$$m[T] \left(\begin{Bmatrix} \ddot{\tilde{u}} \\ \ddot{\tilde{v}} \end{Bmatrix} - \Omega^2 \begin{Bmatrix} \tilde{u} \\ \tilde{v} \end{Bmatrix} \right) + 2m[\dot{T}] \begin{Bmatrix} \dot{\tilde{u}} \\ \dot{\tilde{v}} \end{Bmatrix} = [T] \begin{Bmatrix} f_{\tilde{x}} \\ f_{\tilde{y}} \end{Bmatrix}$$

Premultiplying both sides of the above equation with $[T]^T$ and using the orthogonality property of the matrix $[T]$, i.e. $[T][T]^T = I$, we get

$$m \begin{Bmatrix} \ddot{\tilde{u}} \\ \ddot{\tilde{v}} \end{Bmatrix} + 2m\Omega \begin{bmatrix} 0 & -1 \\ 1 & 0 \end{bmatrix} \begin{Bmatrix} \dot{\tilde{u}} \\ \dot{\tilde{v}} \end{Bmatrix} - m\Omega^2 \begin{Bmatrix} \tilde{u} \\ \tilde{v} \end{Bmatrix} + \begin{bmatrix} k_x & 0 \\ 0 & k_y \end{bmatrix} \begin{Bmatrix} \tilde{u} \\ \tilde{v} \end{Bmatrix} = \begin{Bmatrix} 0 \\ 0 \end{Bmatrix}$$

Dividing the above equation by m , we get

$$\begin{Bmatrix} \ddot{\tilde{u}} \\ \ddot{\tilde{v}} \end{Bmatrix} + 2\Omega \begin{bmatrix} 0 & -1 \\ 1 & 0 \end{bmatrix} \begin{Bmatrix} \dot{\tilde{u}} \\ \dot{\tilde{v}} \end{Bmatrix} + \begin{bmatrix} \omega_{nx}^2 - \Omega^2 & 0 \\ 0 & \omega_{ny}^2 - \Omega^2 \end{bmatrix} \begin{Bmatrix} \tilde{u} \\ \tilde{v} \end{Bmatrix} = \begin{Bmatrix} 0 \\ 0 \end{Bmatrix}$$

where, $\omega_{nx}^2 = k_x/m$ and $\omega_{ny}^2 = k_y/m$ are the natural frequencies of the stationary shaft in \tilde{x} and \tilde{y} directions respectively.

To obtain free vibration response of the above equation, a solution of the form $\tilde{u} = \tilde{u}_0 e^{st}$ and $\tilde{v} = \tilde{v}_0 e^{st}$ is assumed. Then, we get

$$\begin{bmatrix} s^2 + \omega_{nx}^2 - \Omega^2 & -2\Omega s \\ 2\Omega s & s^2 + \omega_{ny}^2 - \Omega^2 \end{bmatrix} \begin{Bmatrix} \tilde{u}_0 \\ \tilde{v}_0 \end{Bmatrix} = \begin{Bmatrix} 0 \\ 0 \end{Bmatrix}$$

The eigenvalues of the system in rotating coordinates are obtained from the below equation.

$$\begin{vmatrix} s^2 + \omega_{nx}^2 - \Omega^2 & -2\Omega s \\ 2\Omega s & s^2 + \omega_{ny}^2 - \Omega^2 \end{vmatrix} = 0$$

It produces a quartic equation in s ,

$$s^4 + (\omega_{nx}^2 + \omega_{ny}^2 + 2\Omega^2)s^2 + (\omega_{nx}^2 - \Omega^2)(\omega_{ny}^2 - \Omega^2) = 0$$

with roots,

$$s_{1,2}^2 = \frac{1}{2} \left\{ -(\omega_{nx}^2 + \omega_{ny}^2 + 2\Omega^2) \pm \sqrt{(\omega_{nx}^2 - \omega_{ny}^2) + 8\Omega^2 (\omega_{nx}^2 + \omega_{ny}^2)} \right\}$$

For the Jeffcott rotor, i.e. $\omega_{nx} = \omega_{ny} = \omega_n$, the roots will be reduced to

$$s_{1,2}^2 = -(\omega_n^2 + \Omega^2) \pm 2\Omega\omega_n = -(\Omega \pm \omega_n)^2$$

The four roots in the case of Jeffcott rotor are,

$$s_{1,3} = \pm i(\Omega - \omega_n), s_{2,4} = \pm i(\Omega + \omega_n)$$

Two eigenvalues in the stationary reference frame, i.e. ω_n (natural frequencies in \tilde{x} and \tilde{y} directions are equal for Jeffcott rotor) are transformed to $(\Omega - \omega_n)$ and $(\Omega + \omega_n)$. These eigenvalues change with rotational speed, whenever the rotational speed matches with the natural frequency, a condition known as resonance is reached. This can be identified from the Campbell diagram, when this eigenvalue approaches the Ω axis, i.e. $(\Omega - \omega_n) = 0$. The eigenvalues of the Jeffcott rotor in stationary frame can be calculated using the relation, $s' = s - i\Omega$. This relation is not applicable in the case of a complex rotor. The eigenvalues of complex rotors can be calculated using the numerical models like FEM where the element matrices are derived for the shafts, disk elements in the rotating frame. Friswell et al. [14] derived these matrices and calculated eigenvalues in the rotating frame.

References

1. Sinou, J.J., Villa, C., Thouverez, F.: Experimental and numerical investigations of a flexible rotor on flexible bearing supports. *Int. J. Rotating Mach.* **2005**(3), 179–189 (2005)
2. Sodano, H.A.: Non-contact eddy current excitation method for vibration testing. *Exp. Mech.* **46**(5), 627–635 (2006)
3. Nandi, A., Neogy, S., Bhaduri, S.: Analysis of a Lorentz force based vibration exciter using permanent magnets mounted on a piezoelectric stack. *Sadhana* **36**(1), 87 (2011)
4. Weaver, H.J., Burdick, R.: Modal parameter estimation via shaker vs speaker excitation. Technical report, Lawrence Livermore National Laboratory, CA, USA (1984)
5. Huber, T.M., Hagemeyer, S.D., Ofstad, E.T., Fatemi, M., Kinnick, R.R., Greenleaf, J.F.: Noncontact modal excitation of small structures using ultrasound radiation force. In: *Proceedings of the SEM Annual Conference and Exposition on Experimental and Applied Mechanics*, Springfield, pp. 604–610 (2007)
6. Huda, F.: Structural health monitoring by vibration measurement with non-contact laser excitation (2014)
7. Presas, A., Valentin, D., Egusquiza, E., Valero, C., Egusquiza, M., Bossio, M.: On the use of PZT-patches as exciters in modal analysis: application to submerged structures. In: *Multidisciplinary Digital Publishing Institute Proceedings*, vol. 1, p. 32 (2016)

8. Esu, O.O.: Vibration-based condition monitoring of wind turbine blades. Ph.D. thesis, © Ozak-Obazi Oluwaseyi Esu (2016)
9. Visaton: Basic principles of exciter-technology. http://www.visaton.de/downloads/pdf/visaton_exciter_principles.pdf. Accessed 14 Feb 2018
10. MIDE: Slam Stick X - Plastic Data Logger datasheet. <http://info.mide.com/hubfs/slam-stick-vibration-data-loggers-datasheet.pdf?hsCtaTracking=c32024f3-178f-4f3b-bbf1-6ec4d131432f%7Cbba56a47-81d6-4103-a678-76dc75b24772>. Accessed 14 Feb 2018
11. MP3format: Decoder amplifier board. <https://www.ebay.com/itm/5262-TF-card-U-disk-MP3-Format-decoder-board-amplifier-amplificateur-decodeur-/172772701973?var=&hash=item283a0e3715>. Accessed 14 Feb 2018
12. Fu, Z.F., He, J.: Modal Analysis. Butterworth-Heinemann, Oxford (2001)
13. DEWESoft: FRF modal testing manual v1.1. www.dewesoft.com/download?file=FRF_Modal_Manual_v1.1.pdf, Accessed 14 Feb 2018
14. Friswell, M.I.: Dynamics of Rotating Machines. Cambridge University Press, Cambridge (2010)



Auto Resonance Based Identification of Rotating Systems

Netanel Ariel^(✉), Eyal Setter^(✉), Adi Minikes^(✉), Solomon Davis^(✉),
and Izhak Bucher^(✉)

Dynamics Laboratory, Mechanical Engineering,
Technion - Israel Institute of Technology, Haifa 3200003, Israel
netanelrel@gmail.com, eyalsetter.es@gmail.com,
minikes@gmail.com, solomondavis1987@yahoo.com,
bucher@me.technion.ac.il

Abstract. Rotating structures exhibit speed dependent natural frequencies and mode shapes that play an important role in the overall dynamics. Accurate experimental identification of these phenomena is of great importance for validating uncertainties in numerical models and for detecting potentially dangerous asynchronous frequencies, often obscured by the imbalance synchronous vibrations. As the speed dependent natural frequencies cannot be assessed experimentally without actually rotating the structure at the vicinity of these speeds, the task of exciting and measuring asynchronous frequencies during rotation without risking the integrity of the machine, becomes a great challenge.

The present paper proposes an automatic and efficient method to excite a rotating structure at a selected modeshape, while controlling the vibration amplitude, such that a non-destructive test takes place.

Automatic excitation of marginally stable vibration occurs upon introducing a phase shifting filter and a nonlinear feedback element. A digital signal processor carries out the latter, therefore the system behavior and the vibration levels are fully controllable.

Theoretical analysis, based on the describing function method and modal filtering, is carried out and verified by numerical simulations. Finally, some experimental results are described and analyzed. The experimental system exhibits different modes of vibration that are excited selectively, at any desired speed of rotation and at any desired magnitude. This approach effectively reconstructs the Campbell diagram with only basic knowledge of the system's modal behavior. It is also shown that one can switch, in situ while rotating the system, between modes of vibration in the presence of large imbalance forces.

Keywords: Autoresonance · Self-excited vibration
Synchronous demodulation · Modal filtering · Campbell diagram
Describing function

1 Introduction

Rotating systems exhibit some unique dynamical phenomena. One of the most significant phenomena, which this research deals with, is that the system natural frequencies of a rotating system may vary with the rotation speed mainly as a result of

gyroscopic effects and stress stiffening [1]. This speed dependence becomes even more significant in high-speed rotors. Such rotors store a large amount of kinetic energy and the conversion of only 1% of this energy into strain energy would most likely cause them to fail [2]. Therefore, careful modeling of such systems, anticipating dangerous operating modes is essential.

The vibration of rotating system is mostly driven by synchronous unbalance forces, which always exist at some level. Resonance or critical speed in rotating systems occurs when the rotor speed equals to one of the system natural frequencies (critical speed), which is speed dependent. Consequently, predicting critical speeds from a static experiment is impractical. On the other hand, reaching rotational speed close to critical speed endanger the system integrity. The method presented here seeks to overcome some of these challenges by experimentally anticipating the critical speeds while rotating below them.

The map of natural frequencies vs. speed, the Campbell diagram, can be computed analytically [1, 3], with sufficient accuracy for simple rotor models, or by using numerical or FEM (Finite Element Model) simulation, [4], for more complicated cases. Still, none of these methods produces an accurate and sometimes even not good enough prediction of the system's critical speeds due to two main reasons: (a) model simplification with physical assumptions that do not take place in reality, (b) model uncertainties (due to manufacturing and assembly imperfections, unknown material properties, joints stiffness and friction and other non-linearities). Therefore, reconstructing the Campbell diagram experimentally is an important tool for identifying the actual critical speeds, predicting suspected instability zones in non-axisymmetric rotors, and for verifying and calibrating computational models.

The currently employed experimental approaches [2, 4, 5] are limited to identification of the system only at the speed of rotation, while most of the non-synchronous dynamics remains obscured by the unbalance response. The ability to extract weakly excited non-synchronous forward and backward modes requires most often complicated hardware arrangement employing an array of sensors [6] and advanced signal processing tools, but these cannot overcome the lack of information at low rotation speeds.

The novel method presented in this paper allows the detectability of otherwise hidden non-synchronous natural frequencies and modes of vibration, which are inherently rotation-speed dependent, while doing so with minimal interference on the system and only basic knowledge of its modal behavior is required. The method seeks to enhance the ability to construct a physical model, enable comparison and validation of analytic models and detect structural faults by injecting suitable test signals.

This paper presents the model and tools used to applying the proposed method as well as analyzing the results of simulations and experiments performed on a laboratory test rig. The first part contains a general explanation of the research method and its applying principles. The second part presents the experimental system and analyzes the results of simulations and experiments that demonstrate the main phenomena and emphasize the usability of the proposed method. This part also includes analysis and estimation of the excited oscillations amplitude and frequency by means of a descriptive function. This is followed by explanation about detection and subtraction of the output signal synchronous content in order to excite and detect asynchronous

frequencies. Next, a rotating systems oriented method for controlling whirl direction modes is described and the simulation scheme includes the basic blocks is presented. Last, comparison of numerical to experimental results is being executed.

2 Auto Resonance Based Identification

The method, which extends the work in [5], employs a, phase shifted negative feedback to induce limit cycle (LC) oscillations. The oscillation amplitude is bounded due to a nonlinear discontinuous element, mostly a relay-like element in the closed loop, see Fig. 2. The LC oscillations are then used to estimate the physical parameters of the system. The parameter identification is carried out with a describing-function approach type of analysis to achieve limit cycle stability at a desired resonance, while maintaining a controlled magnitude of oscillations. This method enables the system to self-tune and lock on resonance of a desired mode shape (or combinations of mode shapes), and consequently revealing the system's natural characteristics.

The main principle is to make the system marginally stable at resonance and hence to improve dramatically the signal to noise ratio and the detectability of parameters related to high-speed dynamics. The idea is to use the system output for auto-resonating, also known as self-excitation, the system by feeding it negatively, phase shifted and amplitude limited back to the system input. With this method there is no need to know much about the system in advance.

Using negative feedback is compatible with Nyquist criterion. This criterion leans on the Nyquist plot which introduces both the system's amplitude and phase of the steady-state frequency response. Nyquist determined that a system is marginally stable if the plot crosses the real axis at the value $(-1, 0)$ in the complex plain [2]. The method can be heuristically described as rotation and expansion (applying gain) of the Nyquist plot so it would match the marginally stable state as illustrated at Fig. 1.

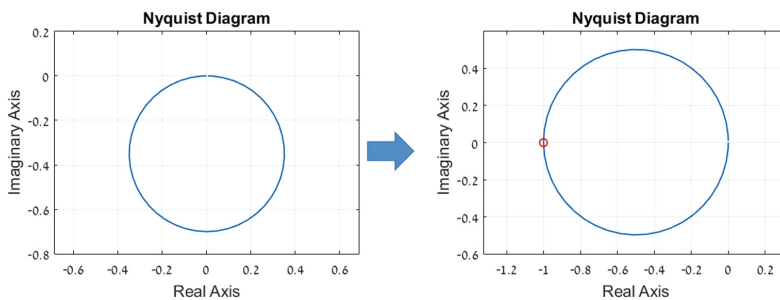


Fig. 1. Illustration of Nyquist plot, for positive frequencies, change. Left: system response, right: phase shifted response.

The feedback phase shift relates to the system input-output phase at the critical speed of the desirable mode to be excited. The required phase shift can be found from the system's phase in the open loop. As will be explained below for rotating systems, a

90° input-output phase shift can be achieved either by applying an integrator to the feedback or by feeding a signal measured at spatial 90° location with respect to the actuator.

To achieve a marginally stable limit cycle, while avoiding divergence of the system [6], a limiter is added before the system input, Fig. 2. Moreover, the limiter allows controlling the limit cycle's amplitude. The common manner to apply such constraints is to use a relay that converts the signal to a limited amplitude square wave. The relay can be implemented via hardware or as a software algorithm. Among other forms of a relay-like limiting functions is the hyperbolic tangent function.

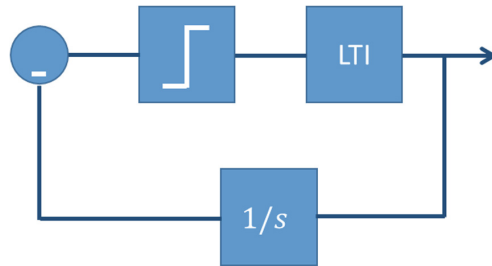


Fig. 2. A basic scheme of the method causing autoresonance of the linear-time-invariant (LTI) oscillating system. Integration is represented by $1/s$.

3 Numerical and Experimental Study

In order to examine the implementation of the method and the validation of the analytical development, several experiments were executed on an existing experimental system [7]. This chapter contains description of the experimental system structure modeling and some simulation and experiments results comparison and analysis.

3.1 Experimental System Description

The system described in Fig. 3 consists of a rigid rotor lying on two ball bearings mounted on a plate, free to move only in the horizontal plane by four elastic supports (round beams), subjected to two externally controlled forces (linear voice-coils) and rotated by a brushless DC motor. The test procedure program code that operates the motor and controls the actuators was written in Matlab® Simulink and realized by a dSPACE™ controller. Two current controllers translate voltage signal commands from the dSPACE™ into actuation current, driving the voice coils (f_1 , f_2).

The motion of the plate (x_1 , x_2 Fig. 3) was measured by laser displacement sensors (Fig. 4) and the shaft's rotational velocity, controlled by the DC motor, was measured by a magnetic encoder at the shaft's end. On the shaft, there are two discs with co-radial threads for balancing the rotor or implement a known imbalance.

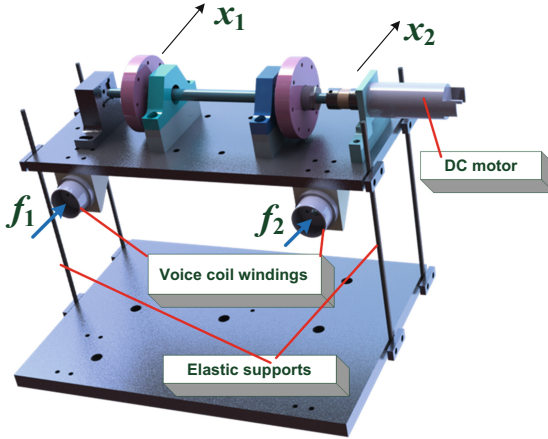


Fig. 3. Rigid rotor balancing demonstrator, consisting of rotating shaft and discs, flexible foundation supports, electromechanical voice-coil actuators at which the two forces f_1 , f_2 are applied and elastic supports, [7]

In order to excite oscillations of an individual modeshape of this system, it is sufficient to use only one actuator and an accordingly designed operating scheme controls only voice coil 1.

The experimental parameters common to the entire series of experiments are the rotation speed and the imbalance.

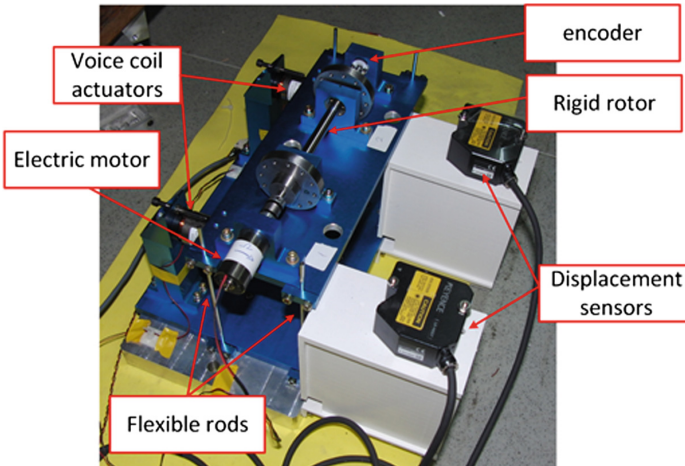


Fig. 4. Test rig showing the laser displacement sensors, electrical motor and the voice coil actuators

3.2 Mathematical Model and Numerical Scheme Description

In order to simulate the system and the algorithm numerically and analytically, a model derived from an identification process carried out as described in [7] was employed. Figure 5 shows a schematic dynamic model of the system. This is an asymmetric model with respect to the stiffness and center of gravity position (G). The system two degrees of freedom (DOF) are x, θ and the measurement and actuation coordinates are x_1, x_2 . The springs represent the flexible beams bending stiffness, which are located at distances L_{k1}, L_{k2} from G, respectively. The measurement and actuation points are positioned at distances L_{x1}, L_{x2} from G. Actuators excitation forces are noted f_1, f_2 , and imbalance forces due to asymmetric rotating shaft are f_{ib_1}, f_{ib_2} . The distances of the imbalance forces from the center of gravity are l_1, l_2 .

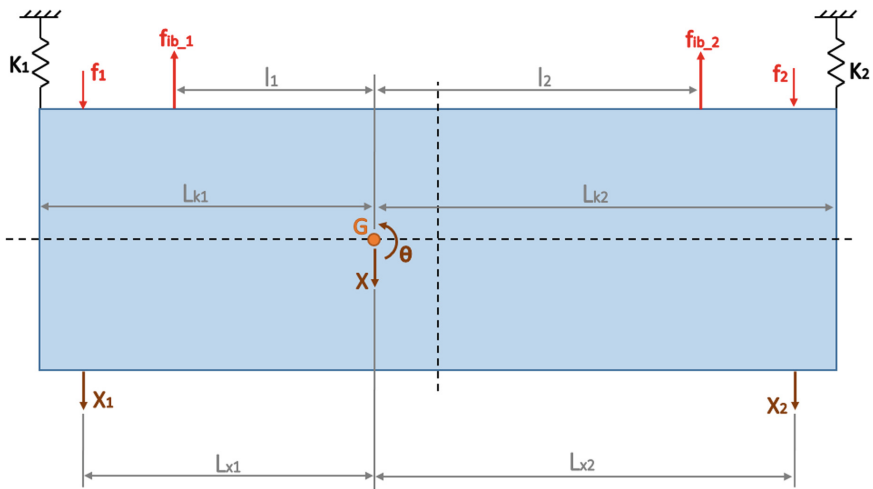


Fig. 5. Test rig scheme model

The system identification parameters are the system mass and stiffness matrix that describes the equations of motion at x_1, x_2 coordinates. In addition, modal damping, system frequencies, and imbalance are also evaluated in this process.

Amplitude Estimation of the Excited Oscillation (Limit Cycle). The Describing Function (DF) analysis allows us to estimate the limit cycle (LC) amplitude and frequency of the marginally stable closed loop. This is an important and useful analytical tool for the simulation validation and future test rig design [6].

According to the Nyquist theorem, a LC exists when the negative feedback open loop response crosses the real axis at -1 . Thus, the basic equation to be solved is:

$$N(A)G(s) = -1 \tag{1}$$

Where $N(A)$ is the DF of the non-linear block (a limiter), and $G(s)$ is the system transfer function. For a relay, as has been used here, the DF is [6]:

$$N(A) = \frac{4D}{\pi A}, \quad (2)$$

where D is the relay magnitude and A is the yet unknown LC Amplitude.

Substituting Eq. (2) into Eq. (1) leads to expression of the amplitude of vibration at steady state:

$$|A| = \frac{4D}{\pi} |G(s)|. \quad (3)$$

From Eq. (3) one can also learn about the ability of restrict the LC amplitude using the controllable relay threshold level, D .

Synchronous Detection. In rotating systems, there is an inherent spectral content at the synchronous frequency, caused by forces synchronous to the rotation speed (e.g. imbalance and shaft bow). Consequently, synchronous physical phenomena is most likely to obscure all other non-synchronous phenomena. Since this research is aiming to reconstruct non-synchronous natural frequencies in the Campbell diagram, a method for extracting the non-synchronous part of the measurement signal is essential. The measured non-synchronous signals of the identified natural frequencies are used for auto-resonating the system. Improving signal to noise ratio by extracting the non-synchronous measurement can be achieved by the *synchronous detection* method that realizes a lock-in amplifier equivalent. This method is widely used for low-level signals measurements [8] and for signals demodulation in effective radio transmission [9].

A block diagram scheme, which includes the *synchronous detection*, is shown in Fig. 6. The “synchronous subtraction” block receives the system output signal as input, detects and subtracts the synchronous content and passes as an output only the synchronous content. Simulated implementation example, for Jeffcott rotor model [1], is shown at Fig. 7. The example demonstrates the different between the system oscillation content with respect to amplitude and frequency before and after activation of the synchronous detection. The synchronous component of the signal due to imbalance obviously exists at all times, at the amplitude of the system imbalance response, but only after applying the synchronous subtraction it is able to excite the desired, non-synchronous, such that the response is according to the desired modeshape.

Controlling Whirl Direction Using Virtues of Rotating Systems. A rotating system at steady state is mainly excited by unbalance forces, which are synchronous and mostly in-phase with the shaft rotation (apart from special cases of non-axisymmetric bearings). For this reason, excitation of backward whirl is a non-trivial task, as well as controlling whirl direction. In identification problems, knowing the backward whirl frequencies helps to better estimate the system dynamical parameters, especially in gyroscopic systems where the backward natural frequencies differ from the forward ones.

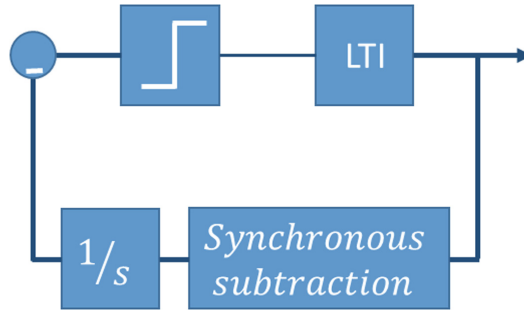


Fig. 6. Block diagram scheme – including synchronous detection

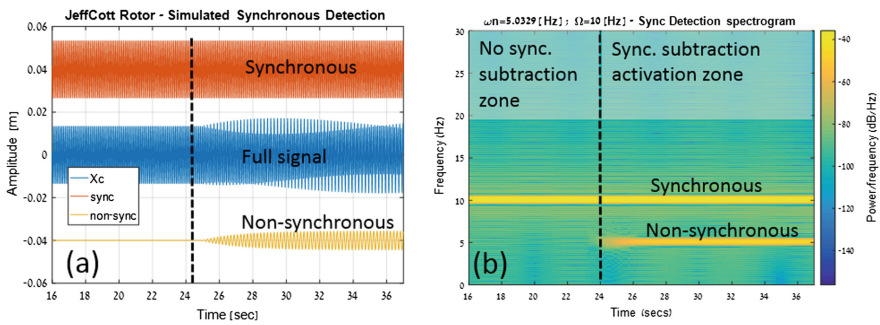


Fig. 7. Simulated Jeffcott rotor response before and under synchronous detection implementation. (a) system vibration and the two, synchronous and non-synchronous, content (at offset). (b) response frequencies spectrum

In the simulations conducted so far (considering a Jeffcott rotor model), it was demonstrated that with the proposed method, exciting forward or backward whirl can be achieved in a quite simple way. The concept, so called “cross coordinates”, is to use the nature of rotating system that includes inherently two perpendicular degrees of freedom (x , y). Exciting forward whirl is accomplished by injecting the negative y output into the x coordinate feedback and the y coordinate feedback is the positive x output. Backward whirl is excited by switching the feedback signs. Figure 8 shows the changing of the phase between the two outputs at the switching moment from forward to backward whirl.

Although controlling whirl direction can be achieved also with integrator phase shift, instead of the cross coordinates, and feedback sign changing, the “Cross coordinates method” uses the nature of rotating systems and eliminates the need to use an integrator that may add integration errors and undesired low frequency gain.

Simulation Scheme. In accordance with the executed experiments, several simulations were carried out for analytical examination of the phenomena examined in the experiments. The simulation scheme, as shown in Fig. 9, includes the basic blocks of the proposed method. These blocks are the system model (state space representation),

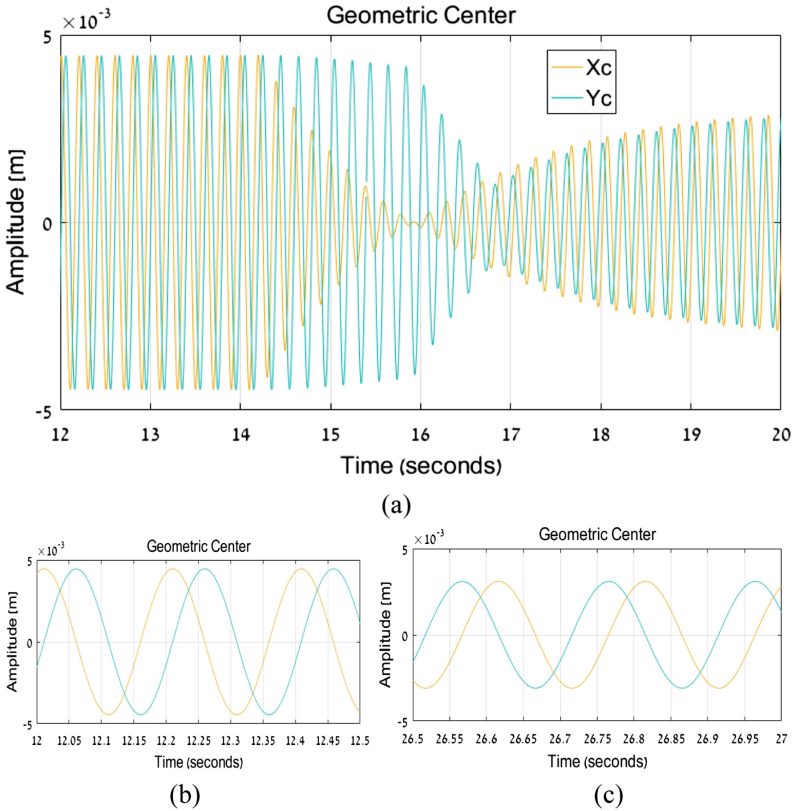


Fig. 8. Simulated response in the x, y directions, during whirl direction controlling simulation. (a) response during switching from forward to backward by reversing the sign of the feedback, (b) forward whirl, (c) backward whirl.

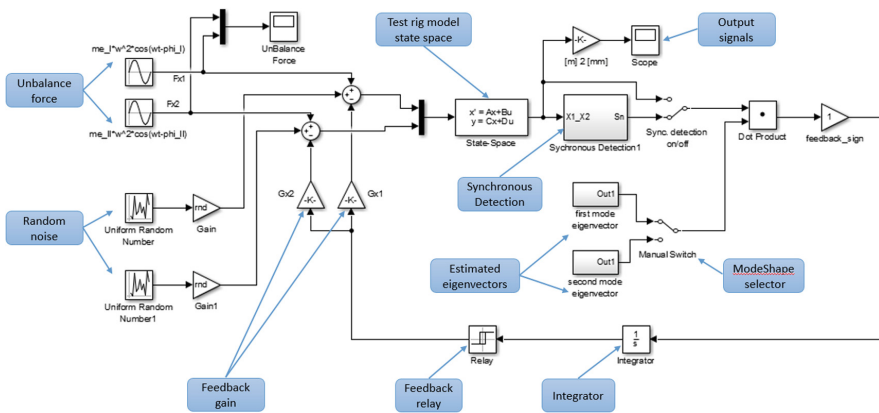


Fig. 9. Simulation scheme (Simulink™).

synchronous detection that isolates the frequency of rotation, modal filter weighting the response vector according to a desired spatial response, an integrator and a relay. Imbalance forces and random noise can be added artificially in the simulation.

3.3 Comparison of Numerical to Experimental Results

In this chapter, the major results of the experiments and simulations are presented graphically. The graphs present the relevant region of interest for the examined phenomenon. Later on, an analysis of the results and their comparison to the experiments are performed in order to draw conclusions about the study’s hypothesis.

Vibration amplitude control by changing the relay threshold. This experiment was performed in order to examine the ability of controlling the limit cycle amplitude by changing the relay threshold (from 0.1 to 0.2). Figure 11 shows the results at transition range for experiment (left) and simulation (right).

According to analytical analysis, Eq. (3), the relationship between the relay threshold and the limit cycle amplitude is a linear. The simulated Nyquist plot of the system, see Fig. 10, includes two circles, each have a zero Real value at different frequency (natural frequencies). Numerical calculation of the limit cycle amplitude at the different modes of vibration for X_1 DOF is performed by placing the experimental parameters and the relevant imaginary value of the frequency response as described before to Eq. (3). From doing so for the two DOF (X_1, X_2) one can estimate the system response at the experiments.

An analysis of the results reveals a difference of about 10% in the LC amplitude between the analytic evaluation and the experimental measurements. This estimation is needed only to ensure safety and protect the test rig, and inaccurate estimation doesn’t damage the ability of applying the method.

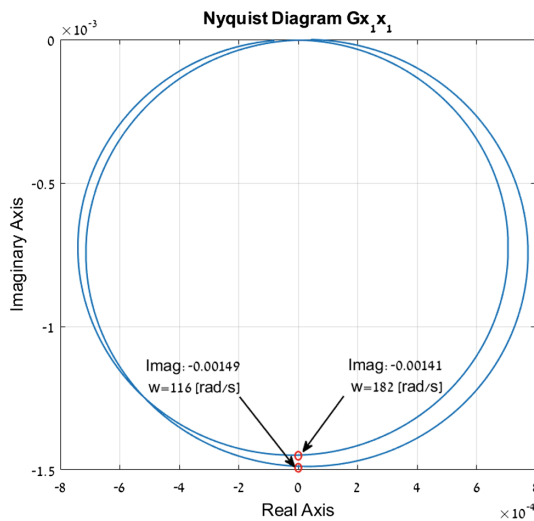


Fig. 10. Nyquist plot of $G_{X_1, X_1}(s)$ frequency response

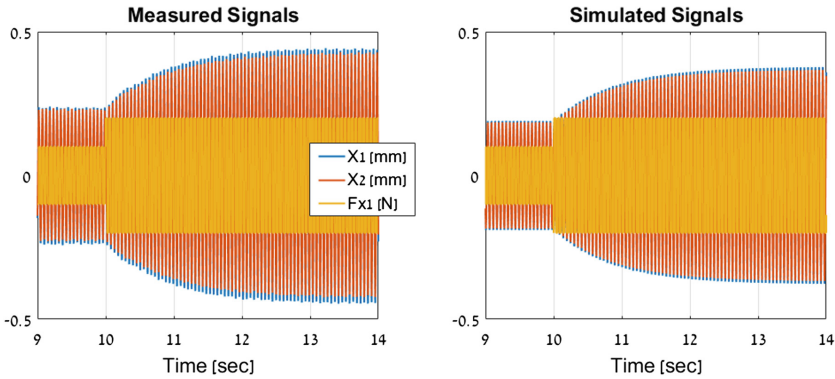


Fig. 11. Relay threshold change from $D = 0.1$ to $D = 0.2$

Real Time Vibration Modes Switching. The purpose of this simulation and test is to examine the ability to control the excited modeshape during experiment using the modal filter [5, 10]. The modal filter is applied throughout the simulation but the input eigenvector changes in the middle of the run from the first mode estimated eigenvector, $[1 \ 1]$, to the second mode estimated eigenvector, $[1 \ -1]$. As shown in Fig. 12, the system's response varies from first mode to the second and the vibration frequency changes accordingly.

The experiments and a simulations were performed such that the transition between different modes of excitation was performed continuously by changing the input vector to the modal filter.

The experiment and simulation results indicate that it is possible to switch between the oscillations modeshape of the system in a reasonable time manner. It should be noted that the transition between the system's natural frequencies occurs much faster than the limit cycle amplitude development.

Another experiment examined the essentiality of a modal filter in the feedback loop. Here, the modeshape which the system is aimed to be locked on using the modal filter is the second modeshape. It is shown, from the experiment and the simulations results, that the system's response without applying modal filter is a LC vibration at the lower natural frequency because the system's stiffness is lower at this modeshape direction. With the operation of the modal filter (at around $t = 10$ s, Fig. 12) the system is locked on the second modeshape, according to the input vector, $[1 \ -1]$, assigned to the modal filter in this experiment.

Another important thing one can learn from this experiment is that the estimated eigenvector can be used as input to the modal filter to control the excited modeshape. That is, there is no need to know system modeshapes precisely in advance. This fact is another significant advantage to the characterization method proposed in this research because it does not require a complicated calculation or a preliminary system identification.

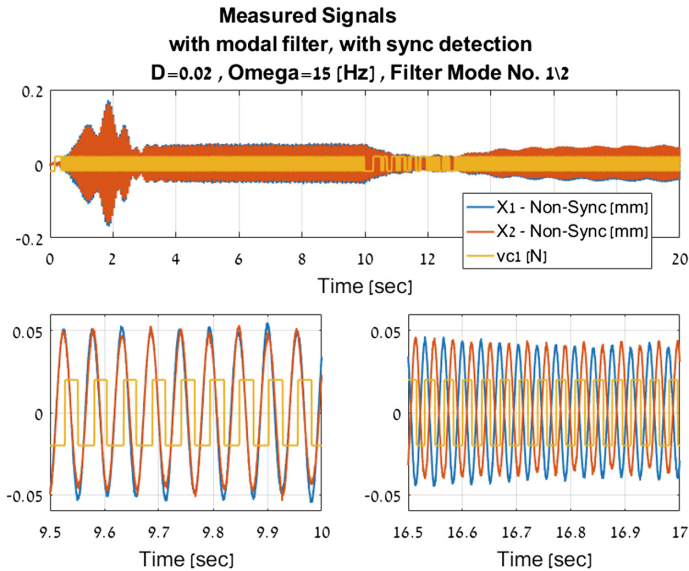


Fig. 12. Response during switching of the excited mode goal. (a) - first mode steady vibration, (b) - second mode, steady vibration (after transient has ceased)

4 Summary and Conclusions

Identification of the natural frequencies as a function of rotational speed is of great interest in characterizing rotating systems, identifying dynamic phenomena and calibrating simulations. This is not a trivial task to perform experimentally with current standard tools and in a way that does not endanger the system. This study proposes an auto-resonance based method that allows to excite an asynchronous frequency at a selected modeshape and controlled intensity. Thus identifying the natural frequencies of the different modes of vibration depending on the rotation speed automatically and safely.

In order to implement the method, several tools were used as followed. The Describing Function analysis was used to develop a closed form solution for estimating the LC amplitudes and frequencies. Resonance excitation was shown to be excited by using either integrator or the cross coordinate method. The later can be useful, elegant feature for whirl direction control. The response amplitude was kept limited and controllable using a relay and its threshold level respectively. Subtracting the synchronous content of the measured signal in order enabled the excitation of asynchronous frequency and improve the signal to noise ratio is done with synchronous detection. Locking to a desired mode of vibration and switching between modeshapes at real time was found practical by changing the modal filter. It was shown that educated guess of the system modeshapes were enough for applying successfully the proposed method.

This paper presented the principles of auto-resonance based identification, theoretical background, numerical investigation and experiments performed on a laboratory test rig. The work performed so far showed practical feasibility for implementing this detection method for building the full natural frequency – rotation speed map in experiment. The experiments verified the theory, and were compared with simulations with good agreement. Thus, we can use these analytical tools for parameters sensitivity analysis and system design.

References

1. Genta, G.: *Dynamics of Rotating System*. Springer, Heidelberg (2005)
2. Crandall, S.H., Dahi, N.C., et al. (eds.) *An Introduction to the Mechanics of Solids* (1959)
3. Irretier, H.: Experiments and calculations on the vibrations of rotating radial impellers. *2*(2), 601–606 (1987)
4. Arias-Montiel, M., Silva-Navarro, G.: Active unbalance control in a two disks rotor system using lateral force actuators. In: *CCE* (2010)
5. Davis, S., Bucher, I.: Automatic mode selection and excitation ; how to combine modal filtering with autoresonance
6. Gelb, A., Vander Velde, W.E.: *Multiple-input Describing Functions and Nonlinear System Design*. (1967)
7. Tresser, S., Dolev, A., Bucher, I.: Dynamic balancing of super-critical rotating structures using slow-speed data via parametric excitation. (2017)
8. Gruber, M.: Synchronous detection of AM signals, ARRL Labs (1992)
9. Orozco, L.: Use synchronous detection to make precision, low level measurements. Technical article, pp. 1–8 (2014)
10. Meirovitch, L., Baruh, H.: Control of self-adjoint distributed-parameter systems. *J. Guid. Control Dyn.* *5*(1), 60–66 (1982)



Modal Testing of a Full-Scale Rotating Woven Composite Fan Using Piezoelectric Excitation

Antoine Mabilia^{1,2}(✉), Claude Gibert¹, Fabrice Thouverez¹,
Edouard De Jaeghere², Lionel Sanchez¹, and Laura Giovannoni¹

¹ École Centrale de Lyon, LTDS, UMR CNRS 5513, Écully, France

² Safran Aircraft Engines, Moissy-Cramayel, France

antoine.mabilia@doctorant.ec-lyon.fr

Abstract. An experimental facility for testing full-scale bladed disks in vacuum conditions and under centrifugal load is described in this paper. The special feature of the PHARE#1 test rig is its multichannel excitation system which allows to excite woven composite fan blades with any spatial and phase distribution as well as synchronous or non-synchronous vibration forcing with respect to rotation speed. The configuration of the excitation system allows each blade to be excited independently and therefore nodal diameter excitations can be performed with traveling (forward, backward or mixed) or standing waves. First rotations of the PHARE#1 test rig produced results at different rotation speeds, for several modes, nodal diameters and excitation levels. Typical results analysis and findings are presented in this paper.

Keywords: Modal testing · Full-scale woven composite fan
Traveling and standing waves · Nodal diameter excitations
Piezoelectric actuators · Vacuum conditions

1 Introduction

Bladed disks are key components of turbojet engines. It is also one of the most prolific subjects of research and development in the aeronautical field, as evidenced by latest bladed disk technological advances such as shape (wide-chord blade) or material (composite material) evolutions. These innovations have allowed to increase by-pass ratio and reduce greatly the whole turbojet mass. However, they involve changes in fan dynamic behavior and sensitivity to vibrations. It is then essential to understand and control their vibration behavior to make sure they do not lead to their early fatigue failure. To improve comprehension of latest-generation bladed disk dynamics, a first step is to collect experimental data on these structures under conditions closest to operating conditions.

The PHARE#1 (standing for: rotAting macHinery Platform for control of Environmental Risks) facility has been developed in the last few years at the

École Centrale de Lyon in the perspective of mastering bladed disk vibratory phenomena. PHARE#1 is a research test rig dedicated to vibration tests of full-scale rotating industrial systems at their actual operating speed conditions. The entire test rig is highly instrumented, which allows a very large area of scientific investigations. Main research themes associated with the PHARE#1 facility are forced vibrations on bladed disks [1–4], contact instabilities between blades and carter [5–8], friction and wear effects [9, 10] and passive [11–13] or active vibration [14, 15] control methods.

The first testing campaign of the PHARE#1 test rig focuses on forced responses of a complete full-scale fan in rotation and more specifically on structural damping and friction induced damping studies. The blades incorporate a new generation of 3D woven composite materials and molded resin injection, this technology is also known as RTM (Resin Transfer Molding) [16]. This fan is similar to those used in the latest generation of fans, like the LEAP. Fluid-structure interactions are, in the case of a turbojet engine, the major source of vibrations brought to bladed disks. However, to study their vibration behavior in a pure solid mechanical and structure dynamic point of view, they are studied in vacuum conditions. Thanks to these conditions, actual fans can be rotated at nominal speed with a reasonable driving power in a free-aerodynamic disturbance environment. To dynamically force blades with realistic vibration amplitudes, an excitation system based on piezoelectric actuators [17] has been developed. Each blade is equipped with a network of several piezoelectric patches allowing it to be actuated independently by means of a software developed in the Laboratory of Tribology and Systems Dynamics. This very versatile excitation method can provide any spatial and/or temporal excitation distribution to the rotating test piece independently of the rotation speed.

This paper is divided in three parts. The first part includes a description of the PHARE#1 capability and its instrumentation. The following part focuses on the excitation system design and its associated control software. To conclude this paper, some first successful results, obtained for several rotating speeds, nodal diameters and excitation levels, are presented and discussed.

2 PHARE#1 Facility

The PHARE#1 test rig has been designed in order to perform full-scale vibration studies on fan units as well as High Pressure Compressor (HPC) stage units of modern civil aircraft in vacuum conditions at nominal speed (Figs. 1 and 2).

2.1 Test Rig

The main element of the bench is the vacuum chamber (Fig. 1 ①) which allows rotating systems to be placed in conditions close to total vacuum. Chamber useful dimensions are 3 m diameter for 4 m axial length. A double stage rotating vane vacuum pump extracts air from the chamber. The front part is reinforced with thick armor plates to protect from impact in case of accidental element loss.

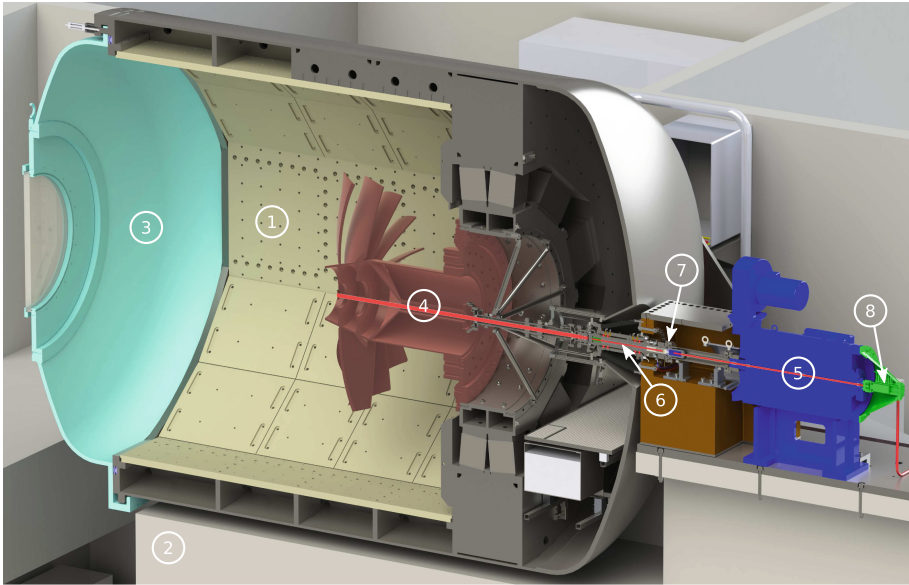


Fig. 1. CAD cross-section view of the PHARE#1 test rig

The vacuum chamber is strongly attached to a heavy concrete inertia block (Fig. 1 ②). The seismic block is designed to prevent machine and machine's foundations from critical vibration levels in case of accidental blade loss.

A retractable door (Fig. 1 ③), covering the chamber entire surface, allows to install the test vehicle (Fig. 1 ④) and the fan in the front side. An inflatable seal ensures airtightness when the door is closed.

A 700 kW electric driving motor (Fig. 1 ⑤) allows fast ramp up and down in vacuum and driving speeds up to 8000 RPM for Low Pressure stage applications or 25000 RPM (using a speed multiplier) for High Pressure stage applications. The motor is regulated by a powerful electric speed drive in order to achieve accurate rotating conditions.

In order to drive the tested structure inside the vacuum chamber, a sealed spindle (Fig. 1 ⑥) ensures connection between the driving motor and the main shaft. It is able to transmit the maximum torque provided by the motor as well as rotate at high speed for future HPC applications thanks to its bearings and its air-oil own lubrication technology. This unit features a circumferential carbon ring seal in order to drive the rotating shaft through the vacuum chamber wall. It also supports the telemetry unit and feed-through wiring for piezoelectric actuators as described in Subsect. 2.2.

Lubrication of the test vehicle's bearings is provided by means of a particular hydraulic unit able to return and cool lubricating oil from vacuum to the main oil tank at ambient pressure.

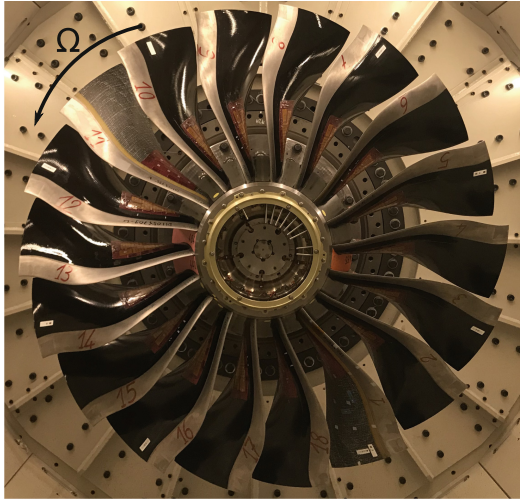


Fig. 2. Fan installed inside vacuum chamber

2.2 Instrumentation

All parts of the test rig mentioned in Subject. 2.1 are monitored with numerous sensors (vibration, speed, thermal and fluid parameters measurement, ...) in order to ensure proper functioning of each unit as well as monitoring experimental conditions.

The test vehicle is also heavily instrumented for balancing and monitoring purposes. Accelerometers, shaft contactless displacement sensors, strain gages and key phaser give global behavior of the test vehicle. Most of these sensors, operating inside the chamber, are connected via sealed cable glands to conditioning and data acquisition systems.

The telemetry system (Fig. 1 Ⓣ) carries out measurements (strain gages and thermocouples) from the rotating frame to the stationary one. This telemetry has a capacity of 44 channels mixing static or dynamic strain measurements and 8 channels for temperature measurements.

A total of more than 150 sensors monitor the test bench and the rotating structure.

3 Piezoelectric Excitation System

To provide necessary dynamic excitation for modal testing in vacuum, each fan blade is actuated by several piezoelectric patches distributed on pressure and suction sides of the blades. Piezoelectric actuators allow to convert electrical energy into mechanical energy even in rotating conditions and to excite the fan regardless of its rotation speed. Moreover, flexibility and non-intrusiveness are their major advantages.

3.1 Excitation Circuit

An overview of the needed circuitry for blade actuation is presented Fig. 3.

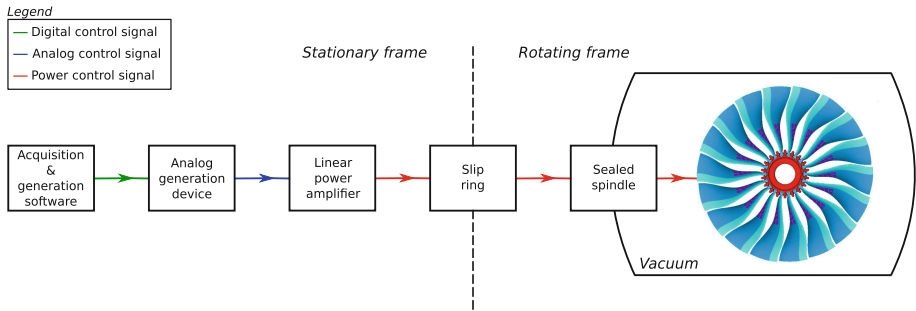


Fig. 3. Piezoelectric excitation set-up

Digital signals are generated by means of a software developed on LabView™ in the laboratory. Among other functionalities, this software allows frequency and interblade phase control of the excitation of each blade. A National Instrument™ analog output device generates analog signals for each of the eighteen blades. These signals are amplified by a linear power amplifier of 1500 W specially designed for this application.

In order to ensure transmission of the eighteen power signals delivered by the amplifier from the stationary frame to the rotating frame, a slip ring (Fig. 1 ©) is mounted at the rear of the shaft line. Power cables run inside the shaft line before reaching connection to piezoelectric actuators. These are shielded and constituted by twisted pairs in order to limit the risk of ElectroMagnetic Compatibility issue (EMC).

Piezoelectric actuators chosen for this application are made of Lead Zirconate Titanate (PZT-5H). These patches are a good compromise between flexibility (to fit the blade surface curvature) and excitation performance (high piezoelectric coupling factor).

Piezoelectric patches are most effective when positioned in blade higher strain areas [18]. A preliminary study was carried out to optimize the number of piezoelectric patches to be installed and their location on the blades (Fig. 4). As the aim is to study influence of several parameters on blade dynamics, patch location results from a compromise between maximum strain zones of the target modes (first bending mode: 1B and second bending mode: 2B) for several rotation speeds (Fig. 4a). It has been shown that, as rotation speed increases, dynamic strain distribution changes [18]. Eighteen piezoelectric actuators were finally bonded to each blade: 8 on the suction side and 10 on the pressure side (Fig. 4b). Piezoelectric patches are wired in parallel to deliver the same voltage to all actuators. Actuators on each side of the blade are connected out of phase for maximizing their effect on bending modes. A total of 324 piezoelectric patches are installed on the fan.

Figure 4a represents modal equivalent Von Mises strain contours of 1B mode on suction and pressure sides of the composite fan blade. Figure 4b provides pictures of a blade equipped with piezoelectric actuators and two strain gages at blade's foot.

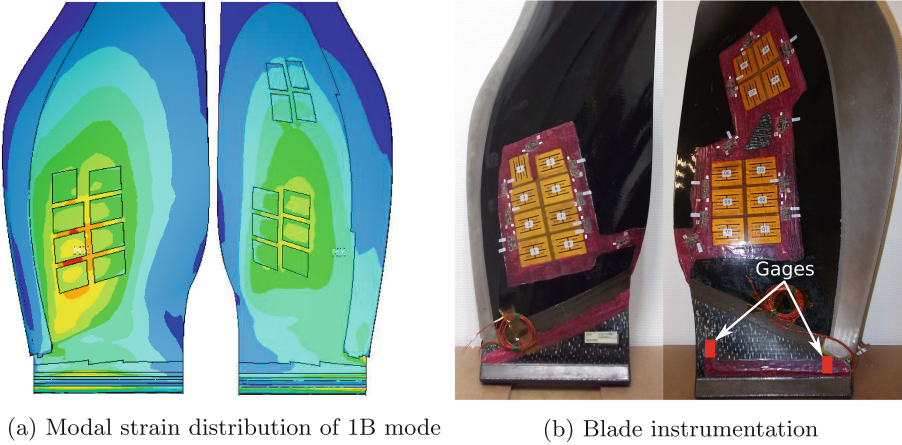


Fig. 4. Location of piezoelectric actuators

3.2 Excitation Signal

The configuration of the excitation system allows to excite each blade independently allowing generation of different spatial excitation patterns. It is then possible to constrain a particular nodal diameter (ND) mode (Fig. 5a) of the bladed disk. Standing or traveling wave excitations are generated for this purpose [1, 19] (1). It should be noted that traveling directions are both related to rotation direction and blade numbering (Fig. 2) in order to avoid some possible confusions.

$$\mathbf{v}_k(t) = \mathbf{v}_f \sin(\omega t - \varphi_{k_{ini}}) + \mathbf{v}_b \sin(\omega t + \varphi_{k_{ini}}) \tag{1}$$

With $\varphi_{k_{ini}} = \frac{kN_d 2\pi}{N}$ and $\omega = 2\pi f$

The notations \mathbf{v}_k , \mathbf{v}_f and \mathbf{v}_b are the k-blade excitation amplitude and excitation amplitudes of the forward and backward traveling wave components, respectively. ω , $\varphi_{k_{ini}}$ and f are the forcing angular frequency, the initial interphase blade angle and the excitation frequency of each traveling wave, respectively. N_d is the number of nodal diameters of the excitation pattern, $N_d \in [0, \frac{N}{2}]$ if N pair or $N_d \in [0, \frac{N}{2} - 1]$ if N odd. N is the number of fan blades.

All mentioned excitation waves can be generated using (1)

- A standing wave (SW) : $\mathbf{v}_f = \mathbf{v}_b$
- A forward wave (FW) : $\mathbf{v}_b = 0$
- A backward wave (BW) : $\mathbf{v}_f = 0$
- A mixed forward and backward wave (MW) : $\mathbf{v}_b \neq 0$, $\mathbf{v}_f \neq 0$ and $\mathbf{v}_f \neq \mathbf{v}_b$

Figure 5 gives three representations of a 2B-2ND forward traveling wave response. The same spatial characterization can be used for both wave excitation pattern and wave response by means of nodal diameter concept. Figure 5a is a spatial representation of the computed displacement field at $t = 0$. Figure 5b is a time history of each blade amplitude response. Figure 5c is a full spectrum amplitude performed on the time series of Fig. 5b and then reversed to display BW in the negative part of the diagram and FW in the positive part.

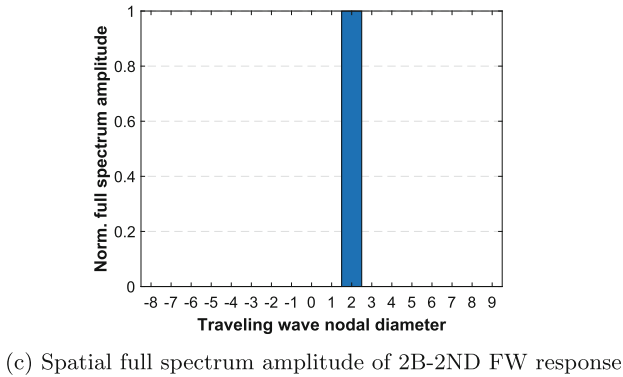
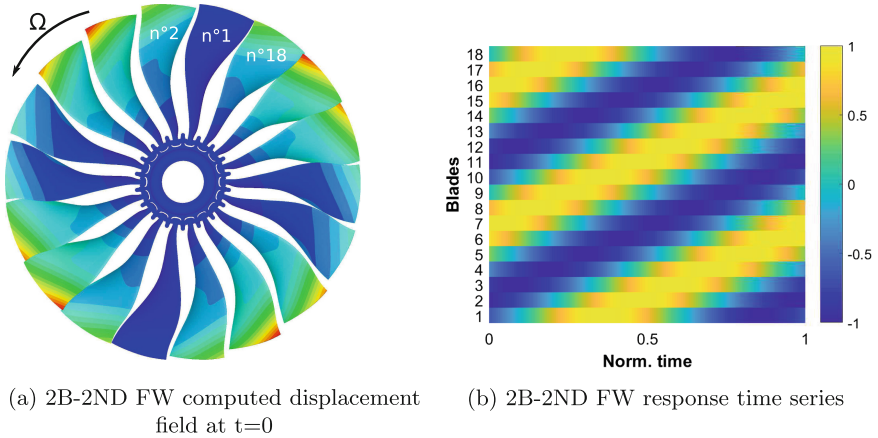


Fig. 5. Traveling wave response

4 Experimental Results

The fan tested here is a full-scale fan composed by eighteen woven composite blades with titanium leading edges.

The main objective of the first test campaign is to evaluate fan structural damping. The fan is tested under vacuum conditions allowing to concentrate only on structural damping. In addition, forces generated by piezoelectric actuators

allow to estimate friction induced damping at blade's attachment while mastering forces applied to the fan. During this campaign, several vibration modes of different fan configurations will be tested, for multiple rotation speeds, nodal diameter excitations (standing and traveling waves) and excitation levels.

Two strain gages are installed at the bottom of each blade capturing blade vibrations. Two gages are required to distinguish torsional from flexural vibration modes. Four thermocouples are distributed on the fan near the contact area between blades and disk in order to evaluate thermal conditions at the blade/disk interface.

Resonance excitations are performed using a stepped sine with increased frequencies through mode resonances. Like a swept sine [20], distortion effects may be brought to the estimation of steady-state response if the sweeping is too fast. A sufficient laps time must then be waited after each increment of the stepped sine forcing frequency in order to let the transient part of the response to vanish.

4.1 Testing of the 2B-2ND Mode

2ND forward traveling wave excitations are performed to excite the 2B mode for several excitation voltages (Fig. 6) and rotation speeds (Fig. 9). Rotation speeds are expressed in term of a percent of the fan nominal speed (%Nn). Figure 6's diagrams represent normalized strain forced responses amplitude and phase of the fan subjected to a 2ND forward traveling wave excitation for a rotation speed of 50% Nn. Each forced responses includes only the first harmonic and all forced responses have the same phase reference: the excitation signal measured for blade 1.

A slight frequency shift of the resonance peaks appearing with the increase in excitation voltage may be noticed on Fig. 6 and on all the blades. Moreover, two resonance peaks can be distinguished, notably on Fig. 6b.

A multichannel linear modal identification using least-squares rational function estimation method [21] is performed on each forced response to evaluate natural frequencies, damping ratios and mode shapes. The steady-state model of the response for modal parameter extraction is governed by Eq. (2) [22].

$$\mathbf{u}_k(w) = \sum_{j=1}^n \left(\frac{r_{k,j}}{\omega_j \xi_j + i(\omega - \omega_j \sqrt{1 - \xi_j^2})} + \frac{r_{k,j}^*}{\omega_j \xi_j + i(\omega + \omega_j \sqrt{1 - \xi_j^2})} \right) \quad (2)$$

where the subscripts \bullet_k and \bullet_j refer to the blade number and to the number of modes assumed in frequency band. \mathbf{u}_k is the k-blade frequency response and the sum of modal participations coming from each mode. \mathbf{r} is a residual vector ($\in \mathbb{C}$) which is proportional to the mode shape and \mathbf{r}^* , his conjugate complex. Here, residual vector is defined as $r_{k,j} = z_{k,j} \mathbf{z}_j \cdot \mathbf{v}$ where \mathbf{z}_j is the j-mode shape contribution and \mathbf{v} represents the excitation vector operating on the blades. ω and ω_j are the forcing frequencies and the j^{th} modal frequency respectively. ξ_j is the viscous damping ratio. The system exhibiting slight non-linearities, this linear approach is therefore an approximation.

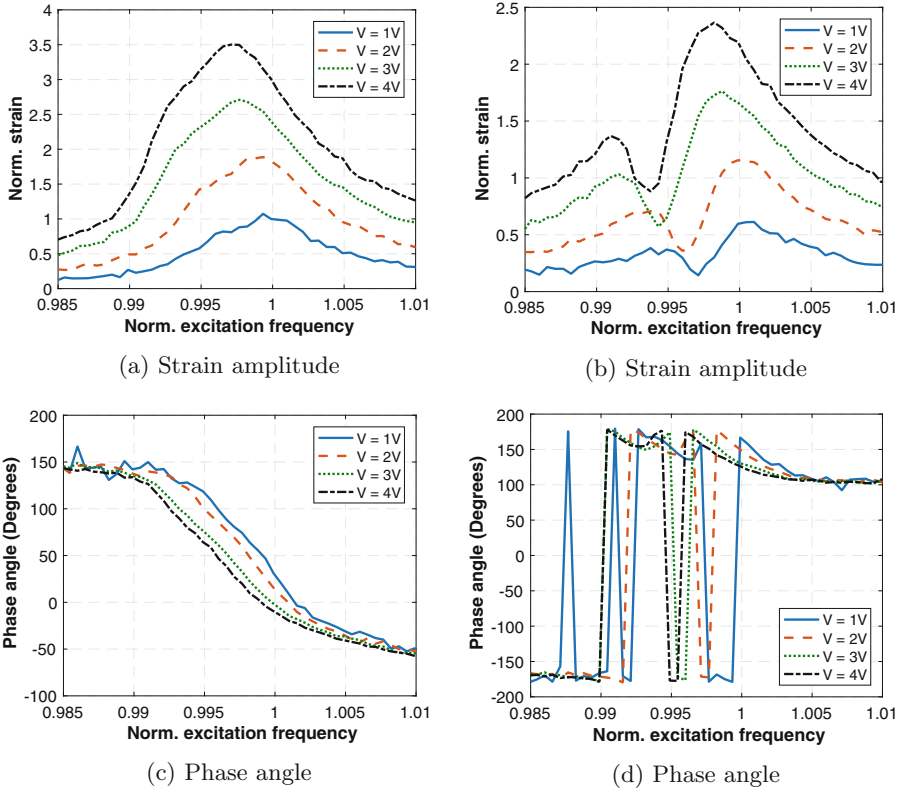


Fig. 6. 2B mode forced responses at 50% Nn excited by a 2ND FW (left: 6th blade, right: 13th blade)

Figure 7 shows a superposition of the experimental forced responses of the blade 8, the forced response synthesized using modal parameters and the modal participation of each mode, an amplitude (Fig. 7a) and a phase (Fig. 7b) diagrams are presented. Two modes are identified on forced responses of the 2B-2ND mode at 50%Nn and for a 2 V excitation (Fig. 7). A full spectrum is performed on the two extracted modal participation vectors for a 2 V excitation (Fig. 8).

The full spectrum spatial analysis put in evidence that each identified mode shape has a backward and a forward two nodal diameter component. Although, it can be seen that the 2ND mode shape n°1 corresponding to the lower modal frequency is predominantly backward and on the other hand that the higher modal frequency mode is mostly forward. The participation amplitude of the second mode is twice as high as the first mode, which is logical since the excitation provided is a forward traveling wave.

Figure 9 represents the modal parameter evolution as fonction of the maximal modal participation of the fan blades.

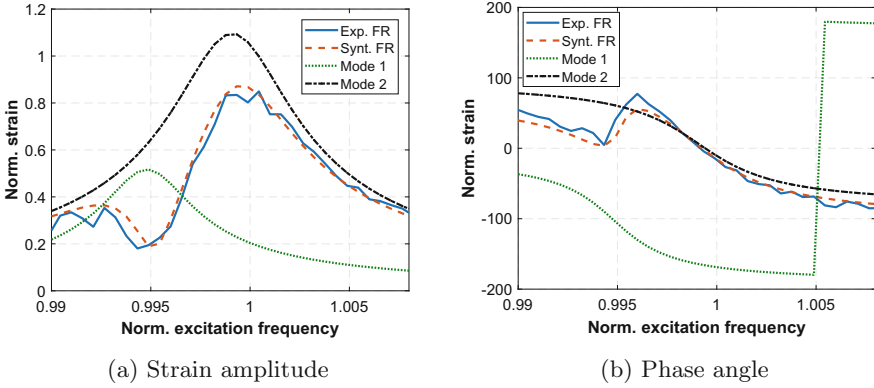


Fig. 7. Modal synthesis of blade 8's experimental forced response at 50% Nn

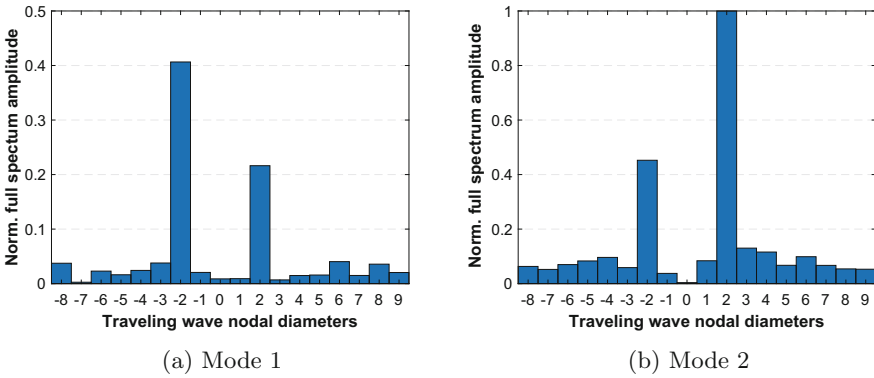


Fig. 8. 2B-2ND mode spatial full spectrum amplitude of modal participation vectors

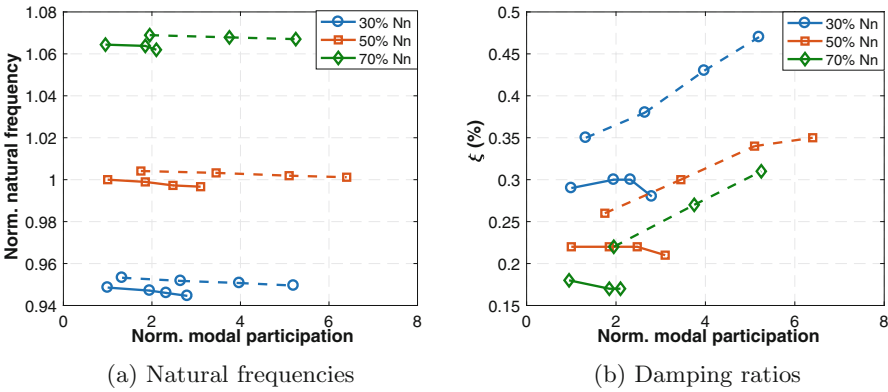


Fig. 9. 2B-2ND mode influence of speed and modal amplitude on modal parameters. 1st mode (—), 2nd mode (- - -)

Figure 9a confirms that a slight frequency shift depending on the modal participation amplitude of each mode is observable for the two modes. Moreover, Fig. 9b shows an increase of the damping ratio as the first mode maximal modal participation amplitude of all blades increases. These variations in natural frequency and damping ratio reflect a friction behavior [9]. Figure 9b indicates that the damping ratio of the first mode has a poor sensitivity to modal amplitude most certainly due to the low modal amplitude of mode 1 participation.

Figure 9 also reveals an increase in natural frequencies and a decrease in damping ratios with rotation speed which is a typical behavior for rotating bladed disks [9, 11].

4.2 Testing of the 2B-3ND Mode

3ND forward traveling wave excitations are performed to excite the 2B mode family at 70% Nn for several excitation voltages as shown in Fig. 10. Figure 10’s diagrams represent normalized strain forced responses amplitude and phase of the fan subjected to a 3ND forward traveling wave excitation for a rotation speed of 70% Nn.

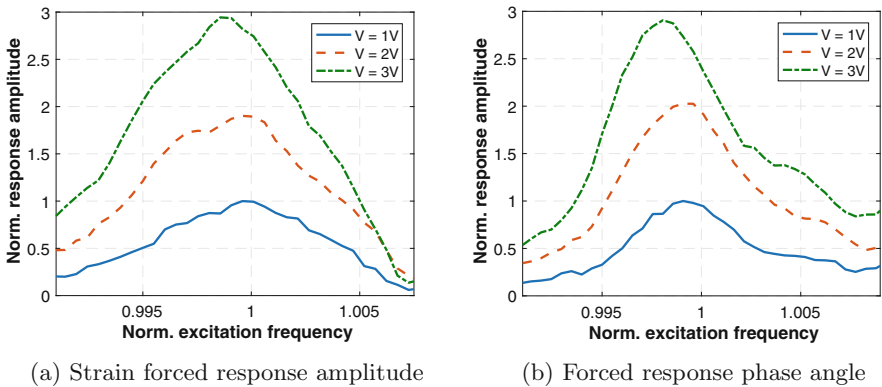


Fig. 10. 2B mode forced responses at 70% Nn excited by a 3ND FW (left: 6th blade, right: 13th blade)

For the same blades, the forced responses differ between 2ND (Fig. 6) and 3ND (Fig. 10) modes. The same conclusions can be derived from the evolution of the forced responses according to modal participation amplitude for 2ND or 3ND excitation, i.e. the existence of two modes and the presence of a frequency shift.

A full spectrum is performed on the two extracted 3ND modal participation vectors for a 2 V excitation.

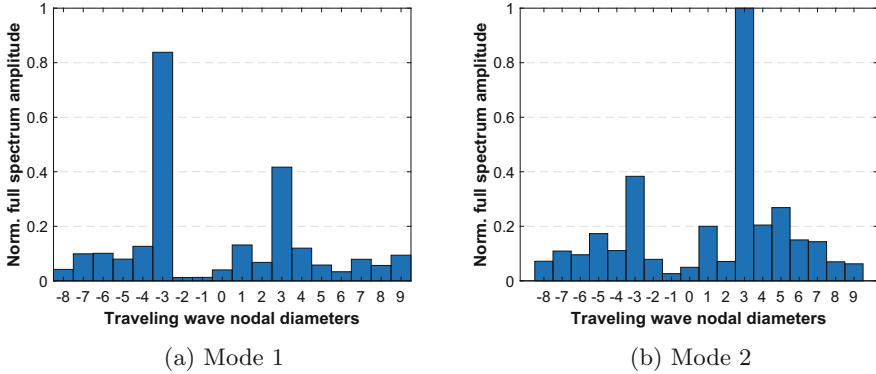


Fig. 11. 2B-3ND mode spatial full spectrum amplitude of mode shapes

Like the 2ND excitation, the first mode corresponds to a backward traveling wave (Fig. 11a) while the second mode corresponds to a forward traveling wave (Fig. 11b). Nevertheless, contribution of other traveling waves are higher than those of the 2ND excitation.

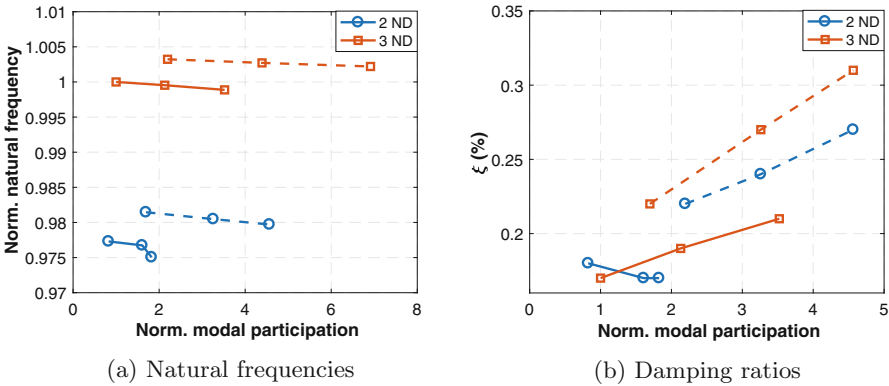


Fig. 12. Influence of nodal diameter and modal amplitude on modal parameters. 1st mode (—), 2nd mode (- - -)

Figure 12 represents the modal parameter evolution as function of the maximal modal participation of the fan blades.

Figure 12a indicates that 3ND mode natural frequencies are higher than those of the 2ND modes. and that the frequency shift is similar between the two nodal diameter modes. Furthermore, the natural frequency difference between the first and the second mode is constant as a function of the modal participation amplitude.

Figure 12b shows different behaviors for the two modes. For the first mode, the 2ND mode damping ratio does not vary while the 3ND mode damping ratio increases as a function of the modal participation amplitude. For the second mode, the 3ND damping ratio increases but the 2ND mode evolution is greater. Numerical simulations performed on a complete fan will allow to draw a full comparison with all the experimental observations reported in this paper.

5 Conclusion

The PHARE#1 test rig has been developed in the perspective of studying bladed disk vibratory phenomena. The test rig allows a very large area of scientific topics from forced vibrations on bladed disks to contact instabilities. This test rig is worldwide unique as far as it is equivalent in term of size, power and features to testing means found in industrial companies with the originality that it is surrounded by a close academic environment.

The first bladed disk tested is a complete full-scale fan composed by eighteen woven composite blades. The main objectives of the test campaign is to estimate the damping (structural and induced by friction at blade attachment) of the fan. First results of the PHARE#1 test rig presented on this paper are quite convincing as they show evolutions of modal characteristics that are generally found in turbomachines (increased natural frequency and decreased damping when the rotation speed increases). The response magnitudes reached make it possible to observe nonlinear friction highlighted by a decrease in natural frequencies and an increase in damping ratios as a function of the excitation level. In addition, two modes has been identified for each forced response: the mode corresponding to the lower modal frequency is mostly backward whereas the higher modal frequency mode is predominantly forward.

These first tests will be followed shortly by new ones, with different configurations in order to test the influence on structural and friction induced damping of particular fan components such as foils or platforms.

These tests may be correlated with numerical simulations of a mistuned fan under centrifugal loads [23] and excited by piezoelectric actuators in order to draw a full comparison with the experimental observations reported in this paper.

Acknowledgments. The PHARE#1 test-rig was set up as part of the French Future Investment Program (10-EQPX-0043) and implemented by the French National Research Agency (ANR).

The authors are also grateful to Safran Aircraft Engines for providing the financial support allowing to carry out this study and for their assistance during the project.

The authors would like to extend special thanks to Sandra Dubois, Cécile Esteves, Marie-Océane Parent, Xavier Leblanc, Stéphane Lemahieu and Alain Dravet for their contribution to the PHARE#1 project.

References

1. Gibert, C., Kharyton, V., Thouverez, F., Jean, P.: On forced response of a rotating integrally bladed disk: predictions and experiments. In: ASME Paper No. GT2010-23610 (2010)
2. Kielb, J.J., Abhari, R.S., Dunn, M.G.: Experimental and numerical study of forced response in a full-scale rotating turbine. In: ASME Paper (2001)
3. Belz, J., May, M., Siemann, J., Seume, J.R., Voigt, C., Böhmer, H., Grüber, B.: Excited blade vibration for aeroelastic investigations of a rotating blisk using piezo-electric macro fiber composites. In: Proceedings of the ASME Turbo Expo 2013: Power for Land, Sea and Air (2013)
4. Goltz, I., Böhmer, H., Nollau, R., Belz, J., Grüber, B., Seume, J.: Piezo-electric actuation of rotor blades in an axial compressor. In: ETC 2009 - 8th European Conference on Turbomachinery (2009)
5. Almeida, P., Gibert, C., Thouverez, F., Leblanc, X., Ousty, J.P.: Experimental analysis of dynamic interaction between a centrifugal compressor and its casing. *J. Turbomach.* **137**(3), 031008 (2015)
6. Padova, C., Barton, J., Dunn, M.G., Manwaring, S., Young, G., Adams, M., Adams, M.: Development of an experimental capability to produce controlled blade tip/shroud rubs at engine speed. *J. Turbomach.* **127**(4), 726–735 (2005)
7. Millecamps, A., Brunel, J.F., Dufrenoy, P., Garcin, F., Nucci, M.: Influence of thermal effects during blade-casing contact experiments. In: ASME Paper No. DETC2009-86842 (2009)
8. Jacquet-Richardet, G., Torkhani, M., Cartraud, P., Thouverez, F., Baranger, T.N., Herran, M., Gibert, C., Baguet, S., Almeida, P., Peletan, L.: Rotor to stator contacts in turbomachines. Review and application. *Mech. Syst. Sig. Process.* **40**(2), 401–420 (2013)
9. Charleux, D., Gibert, C., Thouverez, F., Dupeux, J.: Numerical and experimental study of friction damping blade attachments of rotating bladed disks. *Int. J. Rotat. Mach.* **2006**, 13 p. (2006). Article ID 71302
10. Jean, P., Gibert, C., Dupont, C., Lombard, J.P.: Test-model correlation of dry-friction damping phenomena in aero-engines. In: ASME Turbo Expo 2008: Power for Land, Sea, and Air. American Society of Mechanical Engineers (2008)
11. Laxalde, D., Gibert, C., Thouverez, F.: Experimental and numerical investigations of friction rings damping of blisks. In: ASME Paper No. GT2008-50862 (2008)
12. Szwedowicz, J., Gibert, C., Sommer, T., Kellerer, R.: Numerical and experimental damping assessment of a thin-walled friction damper in the rotating setup with high pressure turbine blades. *J. Eng. Gas Turbines Power* **130**(1), 012502 (2008)
13. Zhou, B., Thouverez, F., Lenoir, D.: Essentially nonlinear piezoelectric shunt circuits applied to mistuned bladed disks. *J. Sound Vib.* **333**(9), 2520–2542 (2014)
14. Choi, B., Kauffman, J., Duffy, K., Provenza, A., Morrison, C.: Active vibration reduction of titanium alloy fan blades (FAN1) using piezoelectric materials. In: Propulsion-Safety and Affordable Readiness (P-SAR) Conference (2010)
15. Botta, F., Marx, N., Gentili, S., Schwingshackl, C., Mare, L.D., Cerri, G., Dini, D.: Optimal placement of piezoelectric plates for active vibration control of gas turbine blades: experimental results. In: Sensors and Smart Structures Technologies for Civil, Mechanical, and Aerospace Systems, vol. 8345. International Society for Optics and Photonics (2012)
16. Dambrine, B., Molinari, O., Coupe, D.: Turbomachine blade, in particular a fan blade, and its method of manufacture. US Patent 7,241,112 B2 (2007)

17. ANSI/IEEE: IEEE standard on piezoelectricity. IEEE Standard 176-1987 (1987)
18. Duffy, K.P., Choi, B.B., Provenza, A.J., Min, J.B., Kray, N.: Active piezoelectric vibration control of subscale composite fan blades. *J. Eng. Gas Turbines Power* **135**(1), 011601 (2013)
19. Judge, J., Pierre, C., Mehmed, O.: Experimental investigation of mode localization and forced response amplitude magnification for a mistuned bladed disk. In: *ASME Turbo Expo 2000: Power for Land, Sea, and Air*. American Society of Mechanical Engineers (2000)
20. Gloth, G., Sinapius, M.: Analysis of swept-sine runs during modal identification. *Mech. Syst. Sig. Process.* **18**(6), 1421–1441 (2004)
21. Ozdemir, A.A., Gumussoy, S.: Transfer function estimation in system identification toolbox via vector fitting. *IFAC-PapersOnLine* **50**(1), 6232–6237 (2017)
22. Ewins, D.J.: *Modal Testing: Theory and Practice*, vol. 15. Research Studies Press, Letchworth (1984)
23. Joannin, C., Chouvion, B., Thouverez, F., Ousty, J.P., Mbaye, M.: A nonlinear component mode synthesis method for the computation of steady-state vibrations in non-conservative systems. *Mech. Syst. Sig. Process.* **83**, 75–92 (2017)



Kriging-Based Surrogate Modeling for Rotordynamics Prediction in Rotor-Bearing System

Mateus P. F. Barbosa^(✉) and William M. Alves^(✉)

Embraer S.A., São José dos Campos, São Paulo, Brazil
{mateus.barbosa, william.alves}@embraer.com.br

Abstract. In this work, it was proposed to use Kriging surrogate models for rotordynamics prediction in rotor-bearing systems. The motivation is to significantly reduce computation effort when evaluating the design space. First, fundamentals of rotordynamics are reviewed and the rotor-bearing system is modeled using the Finite Element (FE) method. Modal analysis is used to determine whirl frequencies and critical speeds while system dynamic behavior is evaluated in terms of the unbalance response. Subsequently, approximations of the input/output relationships created by the FE simulations are obtained by applying the Kriging interpolating method. The derived models work as fast-running surrogates for the full model. Comparison of the results from Kriging surrogates obtained using different training samples shows that the proposed methodology provides a computationally efficient and low-dimension mathematical relationship that can accurately predict rotor-bearing system outputs with considerably low training effort.

Keywords: Kriging surrogate modeling · Rotor-bearing systems
Rotordynamics prediction

1 Introduction

In engineering design, surrogate modeling techniques are of particular interest when high-fidelity, thus computationally expensive analysis are required, such as rotordynamics analysis. The dynamic behavior of complex rotor systems is usually solved by means of computational models such as the Finite Element (FE), where the complexity of the model increases with the wealth of information it contains.

Also, computational cost increases when the values of system parameters are indeterminate, i.e. they may vary within particular ranges, what is called uncertainty.

Although the recurrent call of the deterministic computational model for processing uncertain quantities through Monte Carlo sampling is robust and independent of the model dimension, it has remarkably slow convergence rate and requires large number of time-consuming simulations to guarantee an accurate and efficient coverage of the design space, which is sometimes impractical for rotordynamics analysis in most rotating machinery design.

In this context, the use of an adequate approximation of the system response appears as an effective way to accomplish reasonable reduction of numerical effort. Surrogate models, or metamodels, are analytic relationships that approximate the multivariable input/output dynamic behavior of higher order models, based on a limited set of computationally expensive simulations. A surrogate is built from sampled data obtained by intelligently exploring the design space. It only requires tens to a few hundreds of full computational model runs for the training. Once validated, the surrogate model becomes a very effective low cost substitute of the original model for a wide variety of purposes, such as robust optimization, design automation, parametric studies and uncertainty analysis [1].

There are several surrogate models techniques available in the literature, such as polynomial response surface models, radial basis functions, Kriging, support vector regression and artificial neural networks [2].

Here, the method known as Kriging surrogate modeling is approached. Kriging is a statistics-based interpolating technique capable of handling deterministic noise-free data, which drew a lot of attention during the past decade.

It was first used in mining and geostatistical applications and has been increasingly used, especially in structural and aerodynamic optimization. Kriging-based surrogate provides an explicit function to represent the relationship between the inputs and outputs with a small initial training sample set in linear or nonlinear system.

The purpose of this work is to evaluate the use Kriging-based surrogate modeling for rotordynamics prediction (natural frequencies and unbalance response) of rotor-bearing systems. Results of Kriging surrogates are compared for different training samples and the efficiency of the Kriging model for rotordynamics prediction is further analyzed.

Section 2 brings the fundamentals of rotor-bearing system modeling and an overview of the Kriging surrogate modeling. The application of Kriging interpolation to the rotordynamics system is described in Sect. 3, followed by the assessment of the accuracy of the Kriging surrogate. The main conclusions are finally presented in Sect. 4.

2 Mathematical Modeling and Kriging Surrogates: A Brief Description

2.1 Rotor-Bearing Model

The dynamic behavior of rotor-bearing systems depends considerably on the geometry and properties of the rotor and bearing parameters, which in the sense of dynamics have corresponding inertial, elastic, gyroscopic and damping forces [3].

A rotor-bearing system model is typically composed of three essential components: the shaft, the disks and the bearings. In most cases, a common source of rotor excitation resultant from a mass unbalance is also present on the rotor, which must also be considered [4].

In current industry practice, each component of the rotating systems is discretized using the Finite Element method in order to model and predict its dynamic behavior

and bearing performance. A common approach for discretization is to use a shaft-line model, in which the mesh is created by simply choosing nodes at key locations along the shaft line [5].

The shaft with distributed mass and elasticity is represented as a set of two-node circular cross-section Timoshenko beam elements, each with eight degrees of freedom, and characterized by both strain and kinetic energies.

Disks represent the rotating components, either attached to the shaft or an integral part of the shaft, with relatively short axial length and large diameter (e.g., compressor impellers, turbine wheels and balancing rings). They are characterized by the kinetic energy, and modeled as rigid elements when studying its effects on rotordynamics [6]. Usually present on disks, mass unbalance is also defined in terms of the kinetic energy.

The elements that support the shaft are the bearings, which may be classified into rigid or elastic. In practice, a rigid bearing is equivalent to a high stiffness bearing whereas an elastic bearing is characterized by finite stiffness properties and by viscous damping properties [7]. In this work, we use hydrodynamic journal bearings as the shaft elastic support elements. These fluid-film bearings have noticeable speed-dependent properties, which has to be incorporated in the rotor-bearing model by changing the linear stiffness and damping elementary matrices as the shaft speed varies [5].

The speed-dependent linearized stiffness and damping coefficients for the journal bearing can be calculated analytically as a function of the journal eccentricity and the modified Sommerfeld number, assuming Ocvirk's short-bearing approximation [5, 8–10]. As expected, the stiffness matrix is not symmetric, introducing anisotropy into the model.

Rotor-bearing system time-domain equations of motion, including the effects of rotatory inertia, gyroscopic moments and damping, are obtained by assembling element matrices derived from Lagrange's equations and is written in matrix form as:

$$M\ddot{q}(t) + C\dot{q}(t) + Kq(t) = F(t) \quad (1)$$

where q are the generalized coordinate displacement vector, M is the inertia matrix, C contains the linearized bearing damping matrix and the gyroscopic matrix, K is the stiffness matrix and F is the force vector.

This matrix equation represents a set of n second-order ordinary differential equations. This system is solved for two different cases: first for eigenvalues and eigenvectors (i.e., natural frequencies and mode shapes) using modal analysis and lately for frequency response to harmonic excitation forces (i.e., unbalance forces) [11].

Regarding the modal analysis, due to the nonproportional damping the standard eigenvalue problem cannot be used, since the normal modes do not decouple the damping matrix [12]. The solution of the free vibration system leads to a quadratic eigenvalue problem. To solve it, it is convenient to reformulate the second-order equation of motion into a set of $2n$ first-order differential equations:

$$\begin{bmatrix} C & M \\ M & 0 \end{bmatrix} \begin{Bmatrix} \dot{q} \\ \ddot{q} \end{Bmatrix} + \begin{bmatrix} K & 0 \\ 0 & -M \end{bmatrix} \begin{Bmatrix} q \\ \dot{q} \end{Bmatrix} = \begin{Bmatrix} 0 \\ 0 \end{Bmatrix} \quad (2)$$

Thus, writing in the state space form, the equation of motion becomes:

$$Ax + \dot{x}x = 0 \quad (3)$$

where the state vector with $2n$ elements is:

$$x = \begin{Bmatrix} q \\ \dot{q} \end{Bmatrix} \quad (4)$$

Solutions are sought of the form:

$$x(t) = ve^{st} \quad (5)$$

Thus, the eigenvalue problem is defined as:

$$[sA + B]v = 0 \quad \text{or} \quad [-A^{-1}B - sI]v = 0 \quad (6)$$

where the dynamic matrix is $-A^{-1}B$, v are the eigenvectors and the eigenvalues are:

$$s_i, s_{n+i} = \omega_i \left(-\zeta_i \pm j\sqrt{1 - \zeta_i^2} \right) = -\zeta_i\omega_i \pm j\omega_{d_i} \quad (7)$$

The response of the system to a generic force varying harmonically in time such as synchronous mass unbalance can be determined by assuming a harmonic solution for the equation of motion and obtaining a solution in the frequency domain:

$$Y(\omega) = [-\omega^2 M + j\omega C + K]^{-1} F(\omega) \quad (8)$$

2.2 Overview of Kriging Method

The interpolation method known as Kriging is popular in approximating computation-intensive generated data which are deterministic in nature [13]. It was conceived by the mining engineer Krige [14] in geostatistics and later developed by Matheron [15]. Kriging was definitely introduced into engineering design following the work of Sacks *et al.* [16], who applied the method to construct an approximation model based on data from computer experiments [17].

The Kriging approach treats the function of interest as a realization of a stochastic process [18, 19]. It is a statistical-based approximation method for design and analysis of computer experiments [20]. Prediction with a Kriging model requires the inversion and multiplication of several matrices, thus the Kriging model does not exist as a “closed-form” polynomial equation.

In order to train the Kriging model it is necessary to start with a set of sample data and observed responses. After a first identification of k input variables that have a significant impact on system output, the design variable vector $x = \{x_1, x_2, \dots, x_k\}^T$ is determined as well as the ranges of each variable. The next step is the definition of n of

these k -vectors, $X = \{x^{(1)}, x^{(2)}, \dots, x^{(n)}\}^T$, that will represent the design space. The notion of design space covers the set of all possible experiments or simulations that may interest the analyst. In this regard, the design of experiments is used to intelligently determine a few points out of the full factorial set that provide sufficient information about the full response space instead of covering the whole design space. The Latin hypercube sampling (LHS) is a commonly used technique to select the values of input variables [21]. The observed responses are stored in a vector $y = \{y^{(1)}, y^{(2)}, \dots, y^{(n)}\}^T$.

As stated before, the observed responses are considered as if they were from the realization of a random process. The vector $Y = \{Y(x^{(1)}), Y(x^{(2)}), \dots, Y(x^{(n)})\}^T$ denotes the random field and the random variables are correlated using the Kriging basis function with Gaussian form:

$$cor[Y(x^{(i)}), Y(x^{(l)})] = exp\left(-\sum_{j=1}^k \theta_j |x_j^{(i)} - x_j^{(l)}|^{p_j}\right) \tag{9}$$

This correlation function shows that if $x_j^{(i)} = x_j^{(l)}$ the correlation is one. Likewise, if the distance between the two points grows, the correlation tends to zero. The parameter θ_j allows the width of the basis function to change from variable to variable. By looking at the elements of the vector θ , the most important variables can be determined. The smoothness parameter p_j is typically fixed at two (Gaussian basis exponent) for smooth correlations. From this expression, we obtain the correlation matrix:

$$\Psi = \begin{bmatrix} cor[Y(x^{(1)}), Y(x^{(1)})] & \dots & cor[Y(x^{(1)}), Y(x^{(n)})] \\ \vdots & \ddots & \vdots \\ cor[Y(x^{(n)}), Y(x^{(1)})] & \dots & cor[Y(x^{(n)}), Y(x^{(n)})] \end{bmatrix} \tag{10}$$

One advantage of using a basis function with Gaussian form is that it always lead to a symmetric positive definite correlation matrix, thereby guaranteeing the computation of its inverse via Cholesky factorization [17].

Once we have a set of correlated random variables Y , where the correlations depend on the absolute distance between the sample data and the parameters θ and p , the next step is to tune the Kriging model by choosing θ and p to maximize the likelihood of the observed data y . For this, we use a metaheuristic global search method such as a genetic algorithm or simulated annealing, which has proved to produce the best results.

After the search, we can finally use the maximum likelihood estimation (MLE) values for the model parameters θ and p to calculate the correlation matrix and make predictions of the response at new points using the Kriging model.

According to Jones [22], the standard formula for the Kriging prediction at a new point x^* , can be written as:

$$\hat{y}(x^*) = \hat{\mu} + \psi^T \Psi^{-1} (y - 1\hat{\mu}) \tag{11}$$

where $\hat{\mu}$ is the MLE for the mean μ :

$$\hat{\mu} = (1^T \Psi^{-1} y) / (1^T \Psi^{-1} 1) \tag{12}$$

and ψ is the vector of correlations between the observed data and our new prediction:

$$\psi = \left\{ \begin{matrix} cor[Y(x^{(1)}), Y(x^*)] \\ \vdots \\ cor[Y(x^{(n)}), Y(x^*)] \end{matrix} \right\} = \left\{ \begin{matrix} \psi^{(1)} \\ \vdots \\ \psi^{(n)} \end{matrix} \right\} \tag{13}$$

3 Numerical Results and Discussion

In order to demonstrate the applicability and accuracy of the Kriging-based surrogate in rotordynamics prediction, a numerical study of a rotor-bearing system was carried out using the MATLAB[®] software package. Figure 1 illustrates the FE model to be evaluated [5].

The rotor-bearing system is composed of a steel shaft ($E = 211 \text{ GPa}$, $\nu = 0.3$ and $\rho = 7,810 \text{ kg/m}^3$) with 6 beam elements, two rigid steel disk elements, and it is supported by oil-film journal bearings located in both ends. The nominal bore diameter of the journal bearing is the same as the shaft.

A synchronous excitation is also added by an unbalance moment of $5 \times 10^{-4} \text{ kg-m}$ positioned at the right disk element. Details of the rotor-bearing baseline parameters are presented in Table 1.

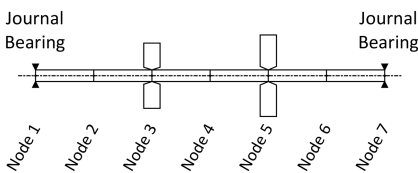


Fig. 1. Rotor-bearing FE model.

Table 1. Rotor-bearing model baseline

Shaft length, m	1.500
Shaft diameter, m	0.050
Left disk diameter, m	0.280
Right disk diameter, m	0.350
Disk thickness, m	0.070
Bearing diameter, m	0.050
Bearing length, m	0.030
Bearing radial clearance, μm	100
Bearing oil film viscosity, Pa-s	0.1
Bearing static load, N	525

The rotor-bearing system dynamic behavior was assessed with the shaft spinning at 4,000 rev/min. The modal analysis for this condition indicates a first undamped natural frequency of 17.08 Hz and the first six modes shapes are illustrated in Fig. 2. Observe

that when the displacement at the bearings location is small, fluid-film damping is expected to be less effective for the rotor-bearing system damping as a whole.

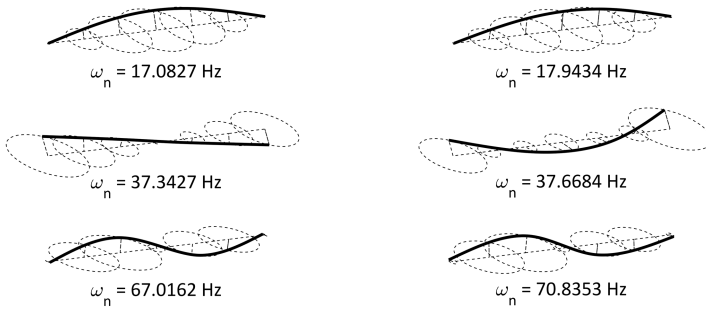


Fig. 2. Rotor-bearing mode shapes at 4,000 rev/min.

The frequency response to the mass unbalance in Fig. 3 indicates that the system passes through a first critical speed near 1,000 rev/min, which corresponds exactly to the first mode excitation. In the proximities of 4,000 rev/min, a second critical speed is experienced, however with a higher damping. There is at least an order of magnitude between the amplitudes at the right disk element (node 5) and the amplitudes at the bearings location (nodes 1 and 7).

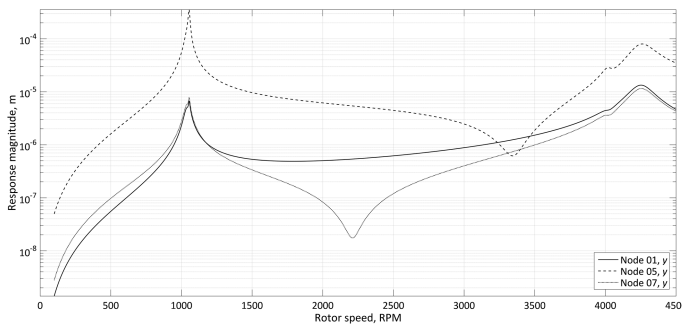


Fig. 3. Rotor-bearing unbalance response magnitude at different locations.

Since the system dynamic behavior is extremely dependent on bearing stiffness and damping, an evaluation of bearing parameters influence is desirable to rotordynamics predictions.

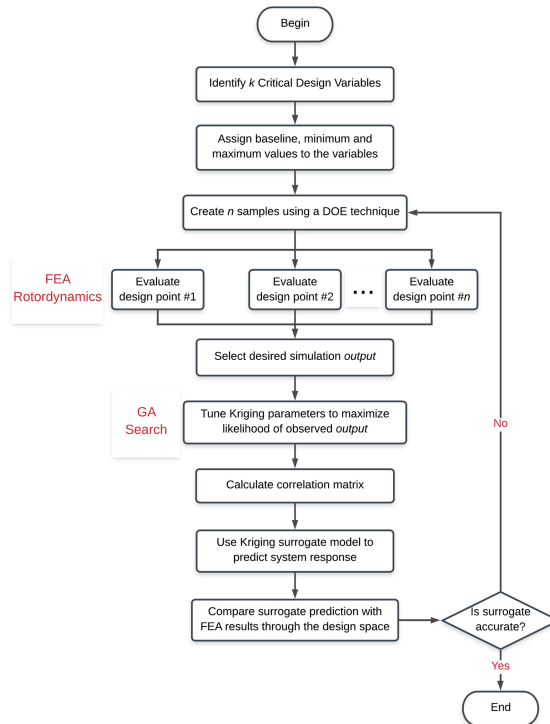
Here, both hydrodynamic journal bearings' length, radial clearance and oil film viscosity were chosen as the critical design variables, which are allowed to vary at specific ranges. Table 2 indicates the baseline, minimum, and maximum values for these parameters.

Table 2. Critical design variables baseline parameters.

Parameter	Baseline	Minimum	Maximum
Left bearing length, m	0.030	0.020	0.038
Left bearing radial clearance, μm	100	50	125
Left bearing oil film viscosity, Pa-s	0.100	0.010	0.200
Right bearing length, m	0.030	0.020	0.038
Right bearing radial clearance, μm	100	50	125
Right bearing oil film viscosity, Pa-s	0.100	0.010	0.200

Kriging methodology was then applied to construct a surrogate for the FE model based on initial samples of design points. The objective is to assess Kriging-based surrogate accuracy and efficiency in predicting system dynamic behavior.

The proposed application of Kriging interpolation to the rotor-bearing system for rotordynamics predictions is illustrated in Fig. 4 flowchart.

**Fig. 4.** Kriging method flowchart.

The LHS technique was used to generate the values of input variables, which are evaluated by the FE model. To investigate the effect of sampling size, different training

samples, containing 40, 70,100 or 200 design points, were used to construct the surrogates, as suggested by Han *et al.* [23] in his work with bearing parameter identification.

The 1st mode undamped natural frequency and the unbalance response amplitude at the right disk element, both calculated with the rotor spinning at 4,000 rev/min, were used as the observed outputs for the sample data.

3.1 Kriging-Based Surrogate for Eigenfrequency Prediction

Figure 5 shows the tile plot obtained from the Kriging-based surrogate prediction for the system 1st mode undamped natural frequency. Each tile presents a filled contour of the eigenfrequency, in hertz, versus two of the six design variables, keeping the remaining variables at the baseline value. This plot is very useful to understanding how the variables involved impact the evaluated function, in this case the natural frequency.

Clearly, the fluid-film viscosity plays a very important role in changing system natural frequency. In general, high lengths, high viscosities and low radial clearances reduce journal-bearing eccentricity, leading to higher bearing stiffness and damping. The consequence to the rotor-bearing system is increased natural frequencies.

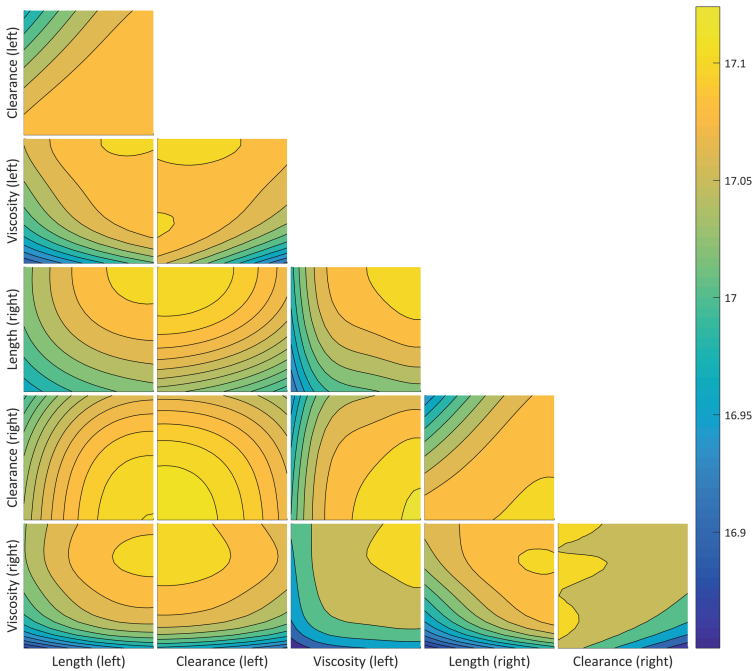


Fig. 5. 1st mode undamped natural frequency landscape, in Hz.

Figures 6 and 7 show the good agreement between Kriging-based surrogate prediction and the result from the FE model. The normalized root mean square errors

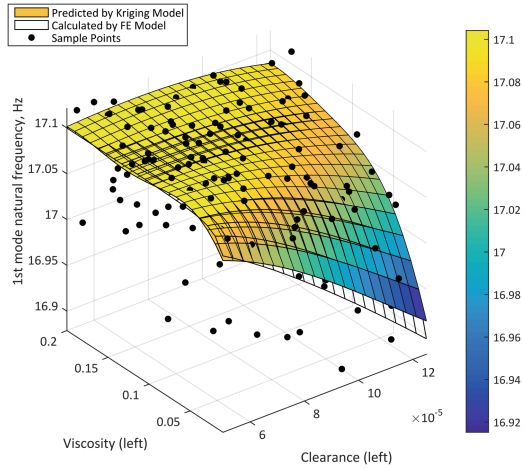


Fig. 6. Left bearing viscosity vs. clearance influence on 1st mode undamped natural frequency. NRMSE = 1.76%.

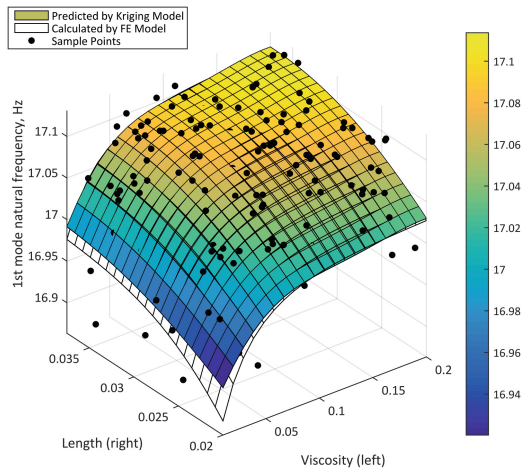


Fig. 7. Right bearing length vs. left bearing viscosity influence on 1st mode undamped natural frequency. NRMSE = 2.39%.

(NRMSE) are 1.76% and 2.39%, respectively. To give an idea of the goodness of fit, a coefficient of determination $R^2 = 0.8$ roughly corresponds to a NRMSE of 10% [17]. Notice the fine resolution of the vertical axis, also indicated in the color bar. The surrogate was trained using 200 design points, which are also displayed.

3.2 Kriging-Based Surrogate for Unbalance Response Prediction

The Kriging-based surrogate prediction for the system unbalance response amplitude at the right disk element is shown in Fig. 8 tile plot. Clearance appears to have great influence in the frequency response.

Figures 9 and 10 show that low radial clearances and high oil-film viscosities increase system response to unbalance, especially due to the stiffening effect observed at the bearings. Although journal-bearing damping is also higher in these conditions, its effectiveness in reducing system unbalance response might be low if the displacement at the bearings location is small. As observed, Kriging model predictions present good correlation with the FE results. The normalized root mean square errors (NRMSE) are 2.36% and 5.81%, respectively. Again, a fine resolution was used to enhance the visualization of the predicted surfaces.

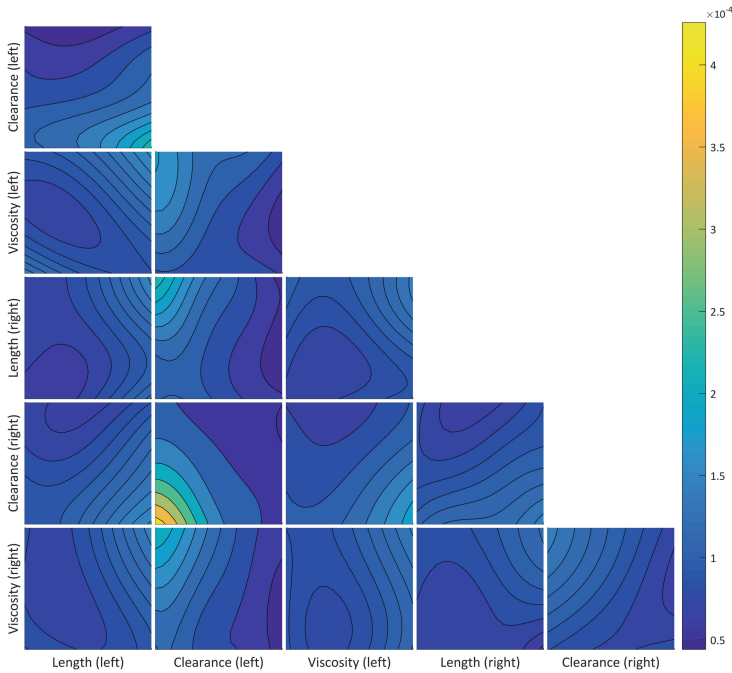


Fig. 8. Unbalance response amplitude at the right disk element landscape, in m.

3.3 Effectiveness of Kriging-Based Surrogate for Rotordynamics

The efficiency and accuracy of Kriging-based surrogate models for rotordynamics were assessed by quantifying the computational effort reduction and the normalized root mean square error (NRMSE) for Kriging predictions when compared with the full FE model predictions.

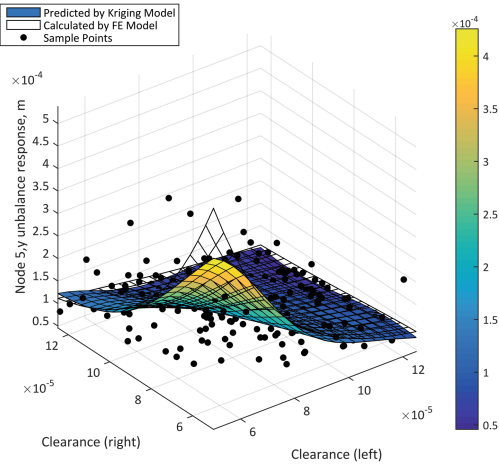


Fig. 9. Right vs. left bearing radial clearance influence on unbalance response amplitude at the right disk element. NRMSE = 2.36%.

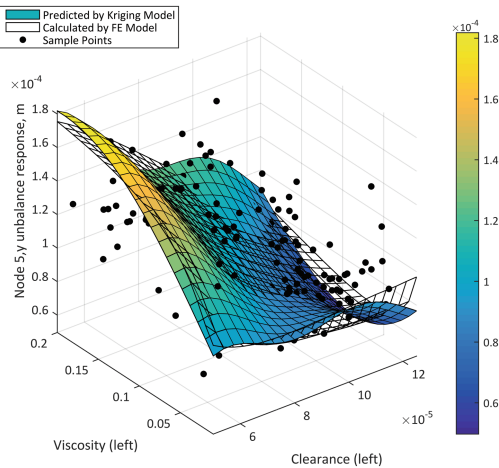


Fig. 10. Left bearing oil-film viscosity vs. left bearing radial clearance influence on unbalance response amplitude at the right disk element. NRMSE = 5.81%.

Figure 11 shows the increasing of time required in the overall training process with the number of training points. It includes sampling, full model simulations and the search for the parameters that maximize the likelihood of the observed data. We observe that time spent on intelligent sampling such as LHS grows exponentially whereas simulation time increases linearly. Thus, depending on the number of design variables and sample size, training the Kriging surrogate model might become costly.

Meanwhile, the great advantage of using a Kriging-based surrogate shows up while using the Kriging correlations to make predictions at new points. Figure 12 brings a

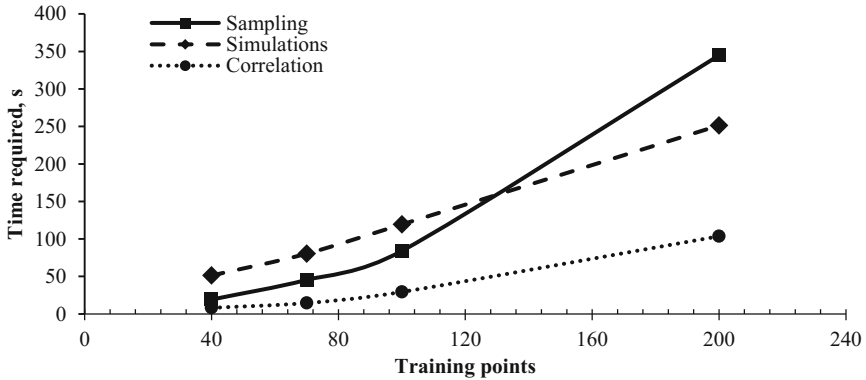


Fig. 11. Time required in the Kriging-based surrogate training.

comparison of the time required by the Kriging model and the FE model to predict the rotor-system response (i.e., eigenfrequency or unbalance response) at a single design point. The result points out that Kriging prediction is three order of magnitude faster than running the full model. Despite the reduction of this advantage with the increase of the training data size (prediction goes through all the training points, i.e., it interpolates the data), the computational effort can be reduced in more than 99% even with large training samples.

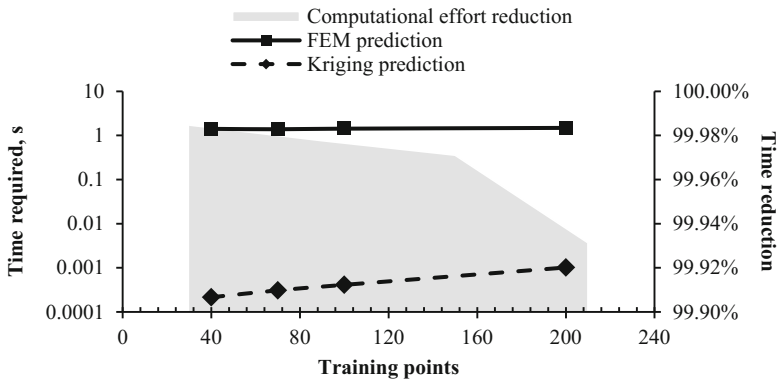


Fig. 12. Comparison of the prediction time using Kriging-based surrogate and the full model.

Regarding the surrogate model accuracy in terms of NRMSE, it is desirable this metric to be as small as possible. Figure 13 shows how Kriging predictions for the 1st undamped natural frequency approximate the FE model results when increasing the initial training data. The NRMSE for all three correlations reached values close to 2% for the training samples with 200 points.

The same is presented in Fig. 14 for the unbalance response at right disk element. The NRMSE was higher but still converged for values below 8% in this case.

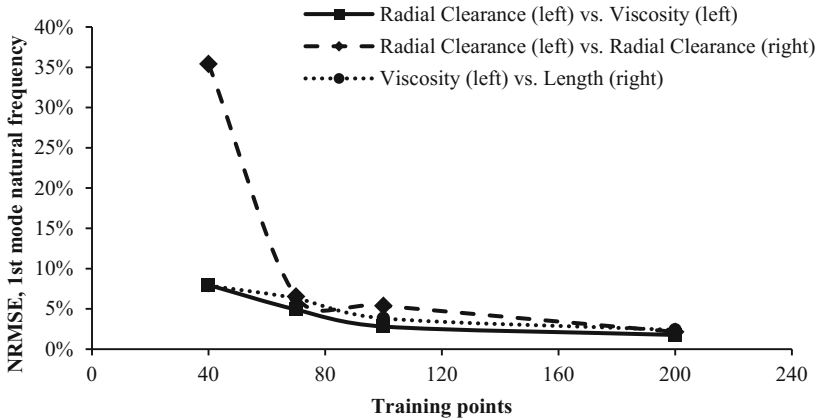


Fig. 13. Normalized root mean square error of the Kriging-based surrogate prediction for the 1st mode undamped natural frequency.

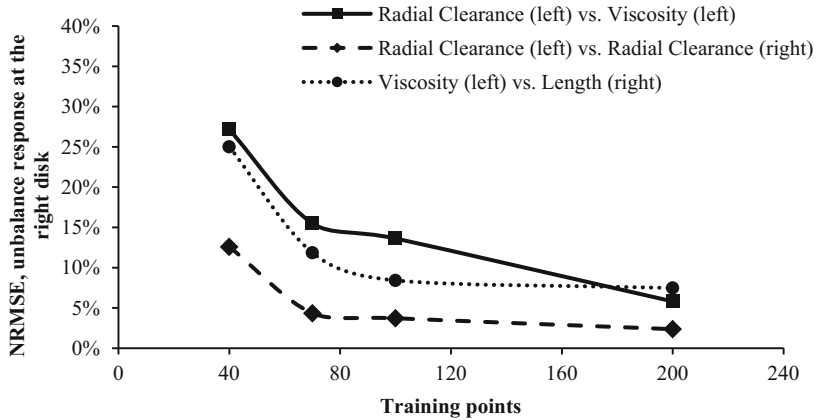


Fig. 14. Normalized root mean square error of the Kriging-based surrogate prediction for the unbalance response amplitude at the right disk element.

4 Conclusion

In this work, the applicability of Kriging-based surrogate modeling for rotordynamics prediction in rotor-bearing systems was assessed. These surrogates are used as substitutes for the rotor-bearing Finite Element model and are capable of quickly predicting responses, thus facilitating the evaluation of different points into the design space.

Kriging surrogate predictions for eigenfrequencies and unbalance response were compared with the FE model using the root mean square error metric for different training samples and the results indicate that the models can accurately predict rotor-bearing system outputs with considerably low computational effort. Ultimately, given Kriging model efficiency in rotordynamics prediction, the results demonstrate the feasibility and effectiveness of the proposed application for purposes such as multi-disciplinary design optimization and uncertainty propagation in rotor-bearing systems.

References

1. Wu, X., Wang, C., Kozłowski, T.: Kriging-based surrogate models for uncertainty quantification and sensitivity analysis. Presented at the International Conference on Mathematics and Computational Methods Applied to Nuclear Science & Engineering, Korea (2017)
2. Viana, F.A.C., Simpson, T.W., Balabanov, V., Toropov, V.: Metamodeling in multidisciplinary design optimization: how far have we really come? *AIAA J.* **52**(4), 670–690 (2014)
3. Yu, J.J.: Dynamic analysis of rotor-bearing systems using three-dimensional solid finite elements. Dissertation, University of Alberta (1997)
4. Lalanne, M., Ferraris, G.: *Rotordynamics Prediction in Engineering*, 2nd edn. Wiley, New York (1999)
5. Friswell, M.I., Penny, J.E.T., Garvey, S.D., Lees, A.W.: *Dynamics of Rotating Machines*. Cambridge University Press, New York (2010)
6. Chen, W.J.: *Practical Rotordynamics and Fluid Film Bearing Design*. CreateSpace (2015)
7. Paulo, P.V.D.L.: A time-domain methodology for rotor dynamics: analysis and force identification. Dissertation, Universidade Tecnica de Lisboa (2011)
8. Ocvirk, F.W.: *Short-Bearing Approximation For Full Journal Bearings*. National Advisory Committee for Aeronautics, Washington, USA (1952)
9. van Beek, A.: *Advanced Engineering Design: Lifetime Performance and Reliability*, 6th edn. TU Delft (2015)
10. San Andres, L.: Hydrodynamic fluid film bearings and their effect on the stability of rotating machinery. *Design and Analysis of High Speed Pumps*, Educational Notes RTO-EN-AVT-143, pp. 10-1–10-36, Neuilly-sur-Seine, France (2006)
11. Vance, J., Zeidan, F., Murphy, B.: *Machinery Vibration and Rotordynamics*. Wiley, New Jersey (2010)
12. Brandt, A.: *Noise and Vibration Analysis: Signal Analysis and Experimental Procedures*. Wiley, West Sussex (2011)
13. Ulaganathan, S., Couckuyt, I., Deschrijver, D., Laermans, E., Dhaene, T.: A Matlab toolbox for Kriging metamodeling. *Procedia Comput. Sci.* **51**, 2708–2713 (2015)
14. Krige, D.: A statistical approach to some basic mine valuation problems on the Witwatersrand. *J. Chem. Metall. Min. Eng. Soc. South Africa* **52**(6), 119–139 (1951)
15. Matheron, G.: Principles of Geostatistics. *Econ. Geol.* **58**, 1246–1266 (1963)
16. Sacks, J., Welch, W.J., Mitchell, T.J., Wynn, H.P.: Design and analysis of computer experiments. *Stat. Sci.* **4**(4), 409–423 (1989)
17. Forrester, A.I.J., Sobester, A., Keane, A.J.: *Engineering Design via Surrogate Modelling: A Practical Guide*. Wiley, West Sussex (2008)
18. Hussein, R., Deb, K.: A generative Kriging surrogate model for constrained and unconstrained multi-objective optimization. In: *Proceedings of the Genetic and Evolutionary Computation Conference*, Colorado, USA, pp. 573–580 (2016)

19. Gaspar, B., Teixeira, A.P., Soares, C.G.: Assessment of the efficiency of Kriging surrogate models for structural reliability analysis. *Probab. Eng. Mechan.* **37**, 24–34 (2014)
20. Simpson, T.W.: Comparison of response surface and Kriging models in the multidisciplinary design of an Aerospoke Nozzle. Institute for Computer Applications in Science and Engineering, Report No. 98-16, Virginia, USA (1998)
21. McKay, M.D., Beckman, R.J., Conover, W.J.: A comparison of three methods for selecting values of input variables in the analysis of output from a computer code. *Technometrics* **21** (2), 239–245 (1979)
22. Jones, D.R.: A taxonomy of global optimization methods based on response surfaces. *J. Glob. Optim.* **21**, 345–383 (2001)
23. Han, F., Guo, X., Gao, H.: Bearing parameter identification of rotor-bearing system based on Kriging surrogate model and evolutionary algorithm. *J. Sound Vib.* **332**, 2659–2671 (2013)

Nonlinear Phenomena in Rotordynamics



A Rotordynamics Model for Rotary Drillstring with Nonlinear Interactions in a 3D Well

Khac-Long Nguyen¹(✉), Quang-Thinh Tran¹, Marie-Ange Andrianoely¹,
Lionel Manin¹, Stéphane Menand², and Régis Dufour¹

¹ LaMCoS, CNRS UMR5259, Insa de Lyon, 69621 Lyon, France
khac-long.nguyen@insa-lyon.fr

² DrillScan, 69100 Villeurbanne, France

Abstract. Rotating drilling for oil or geothermic applications uses a very slenderness structure hanging from to a derrick and made of a drill-string inside the drill well and linked to the bottom hole assembly (BHA). Vibrations provided by the nonlinear dynamics is due to the distributed unbalance masses, to well-assembly interactions, pulsating mud flow, bit-bouncing, stick-slip phenomena, etc. Understanding and controlling the vibration level of the rotating assembly in the well becomes an important key to avoid the fatigue failures and improve the reliability of the drilling operations. The paper focuses on the finite element modelling of the drilling assembly non-linear dynamics. The drill string-well bore contacts are modeled by a set of elastic stops. First, the static position of drilling assembly in the 3D-geometry well is calculated. Therefore, contact points and pre-stresses are predicted. The effect of the speed of rotation on the eigenvalues is then studied by plotting the Campbell diagram.

Keywords: Rotating drillstring · Nonlinear dynamics
Numerical simulation · Well bore-drillstring interactions

1 Introduction

Rotating drilling for oil or geothermic applications uses a very slenderness structure hanging from to a derrick and made of a drill-string inside the drill well and linked to the bottom hole assembly (BHA). The drill-string is composed with a great amount of screwed steel nine-meter pipes. The BHA is equipped with drill-collars, stabilizers and with a drill-bit. The BHA made of extra-heavy pipes insures the Weight-On-Bit (WOB). The stabilizers act as bearings to make easier the drilling direction and faster the penetration speed. The drilling assembly rotates in a well bore which is several hundred meters long and whose top part is equipped of steel tube casings. The downward mud flow is pumped in the interior of drill-pipes and the mud flow rides up in the well-pipe annular space to clear out the cut rock debris, the calories and to insure a lubrication.

Vibrations [1] provided by the nonlinear dynamics is due to the distributed unbalance masses, to the well-assembly interactions, pulsating mud flow, bit-bouncing, stick-slip phenomena [2–4], etc. Multiple vibrations induce premature wear and damage of equipment, mainly due to fatigue failures [5]. Understanding and controlling the vibration level of the rotating assembly in the 3D well becomes an important key to improve the reliability of the drilling operations.

One of the existing controlling techniques is the determination of the natural frequencies of the axial, the torsional and lateral vibrations. The analytical investigation of axial vibrations has been conducted since the 1960s [6]. The torsional behavior was modeled by using the wave equation [7], a single degree of freedom approach [8] or the continuous system approach [9]. Lateral vibrations have been the focus of several publications by two modeling techniques involving the finite-element discretization [10–12]. However, the dependence of natural frequencies of drilling assembly on the rotating velocity has not been thoroughly investigated. This analysis is well known in rotordynamics [19] as the Campbell diagrams to identify the speeds of rotation which may induce the system instabilities and the critical speeds which may yield the response resonances. The drilling assembly can be considered as a long rotor which has a more complicated dynamics due to the fluids effects and the multiple contacts with the well. The Campbell diagrams of simple rotors in fluid have been studied in a few works [14–17] involving both theoretical and experimental approaches.

This paper focuses on the finite element modelling of the drilling assembly to plot the Campbell diagram by using Timoshenko beams. Section 2 represents the beam element formulation and summarizes the modelling of well-bore-assembly contacts and the fluid forces and interactions with the drill strings. Section 3 shows the algorithm of the Campbell computation. First, the static position of the drilling assembly in the 3D-geometry well is calculated. Contact points and pre-stresses are then predicted. The following step consists in analyzing the effect of the speed of rotation on the eigenvalues by plotting the Campbell diagram. Finally in Sect. 4, the results are discussed to identify the instability ranges of speeds of rotation and the critical speeds of rotation. The modal coupling is also illustrated by some mode shapes.

2 Modeling of the System Dynamics by Beam Elements

2.1 Drilling Assembly

All components of the drilling assembly are modeled by using beam elements. Each element contains two nodes and six degrees of freedom (dofs) per node. The energy of one beam element is characterized by its kinetic and strain energies.

The kinetic energy of a rotating element is given by

$$\begin{aligned}
 E_{ca}^e = & \int_0^l \frac{\rho S}{2} \dot{w}^e{}^2 dz + \int_0^l \frac{\rho I_p}{2} \dot{\theta}_z^e{}^2 dz + \int_0^l \left[\frac{\rho S}{2} (\dot{u}^e{}^2 + \dot{v}^e{}^2) + \frac{\rho I_p}{2} (\dot{\theta}_x^e{}^2 + \dot{\theta}_y^e{}^2) \right] dz \\
 & + \int_0^l \rho I \Omega \dot{\theta}_x^e \dot{\theta}_y^e dz
 \end{aligned} \tag{1}$$

where $u^e(z)$, $v^e(z)$, $w^e(z)$, $\theta_x^e(z)$, $\theta_y^e(z)$, $\theta_z^e(z)$ are the displacements and rotations in the element frame of reference (see Fig. 1a), ρ is the mass density, l is the element length. The beam elements considered in this work have circular cross-sections with the inner and outer radii R_e and R_i , the cross-sectional area S is $\pi(R_e^2 - R_i^2)$. The cross-sectional moment of inertia I is $\pi(R_e^4 - R_i^4)/4$ and the polar moment of inertia around the z -axis $I_p = 2I$. The first two terms represents the kinetic energies due to the axial and torsional movements respectively. The next two terms correspond to the lateral displacements. The last term shows the Coriolis effect due to the rotating velocity Ω .

The strain energy is defined by

$$E_{da}^e = \frac{1}{2} \int_0^l ES \left(\frac{dw^e}{dz} \right)^2 dz + \frac{1}{2} \int_0^l G(2I) \left(\frac{d\theta_z^e}{dz} \right)^2 dz + \frac{1}{2} \int_0^l EI \left[\left(\frac{d^2u^e}{dz^2} \right)^2 + \left(\frac{d^2v^e}{dz^2} \right)^2 \right] dz \quad (2)$$

where E and G are the Young and shear modulus.

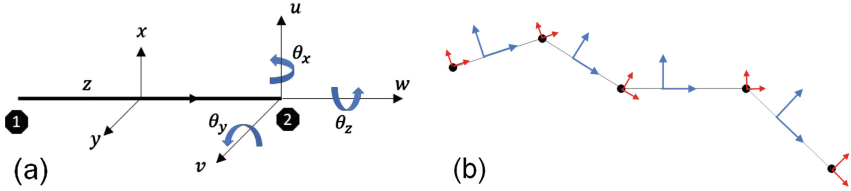


Fig. 1. (a) Element frame, (b) element (blue) and nodal (red) frames of reference.

For each node of an element, six displacements can be interpolated by the nodal displacements as

$$\begin{aligned} u^e &= N_1 u_1^e + N_2 \theta_{y1}^e + N_3 u_2^e + N_4 \theta_{y2}^e, & v^e &= N_1 v_1^e - N_2 \theta_{x1}^e + N_3 v_2^e - N_4 \theta_{x2}^e, \\ \theta_x^e &= -\frac{dN_1}{dz} v_1^e + \frac{dN_2}{dz} \theta_{x1}^e - \frac{dN_3}{dz} v_2^e + \frac{dN_4}{dz} \theta_{x2}^e, & \theta_y^e &= \frac{dN_1}{dz} u_1^e + \frac{dN_2}{dz} \theta_{y1}^e \\ &+ \frac{dN_3}{dz} u_2^e + \frac{dN_4}{dz} \theta_{y2}^e, \\ w^e &= N_5 w_1^e + N_6 w_2^e, & \theta_z^e &= N_5 \theta_{z1}^e + N_6 \theta_{z2}^e \end{aligned} \quad (3)$$

where the interpolating functions are defined by :

$$\begin{aligned} N_1 &= 1 - \frac{3z^2}{l^2} + \frac{2z^3}{l^3}, & N_2 &= z - \frac{2z^2}{l} + \frac{z^3}{l^2}, & N_3 &= \frac{3z^2}{l^2} - \frac{2z^3}{l^3}, \\ N_4 &= -\frac{z^2}{l} + \frac{z^3}{l^2}, & N_5 &= 1 - \frac{z}{l}, & N_6 &= \frac{z}{l}. \end{aligned} \quad (4)$$

Considering the nodal displacement vector $\boldsymbol{\delta}^e = [u_i^e, v_i^e, w_i^e, \theta_{xi}^e, \theta_{yi}^e, \theta_{zi}^e]_{i=1,2}^T$, the elementary kinetic and strain energies are then rewritten as

$$E_{ca}^e = \frac{1}{2} \dot{\boldsymbol{\delta}}^{eT} \mathbf{M}_a^e \dot{\boldsymbol{\delta}}^e + \boldsymbol{\delta}^{eT} (\Omega \mathbf{C}_{ac}^e) \boldsymbol{\delta}^e \tag{5}$$

and

$$E_{da}^e = \frac{1}{2} \boldsymbol{\delta}^{eT} \mathbf{K}_a^e \boldsymbol{\delta}^e. \tag{6}$$

Assembling all element gives the total kinetic and strain energies of the structure $E_{ca} = \frac{1}{2} \dot{\boldsymbol{\delta}}^T \mathbf{M}_a \dot{\boldsymbol{\delta}} + \boldsymbol{\delta}^T (\Omega \mathbf{C}_{ac}) \boldsymbol{\delta}$ and $E_{da} = \frac{1}{2} \boldsymbol{\delta}^T \mathbf{K}_a \boldsymbol{\delta}$ where $\boldsymbol{\delta}$ contains dofs of all nodes defined in the nodal frame. As shown in Fig. 1b, the frame of one node is the frame of its left element. The shear effect is introduced by a coefficient $12EI/(GS\beta^2)$ which slightly modifies the terms of stiffness matrix. $S\beta$ is the reduced cross-sectional with $\beta = 0.9$.

The axial force F_0^e and torque T_0^e modify also the structure stiffness. The axial force gives a supplementary strain energy while the non conservative axial torque is modelled by using the virtual work:

$$E_{GF}^e = \frac{F_0^e}{2} \int_0^l \left[\frac{du^e}{dz} + \frac{dv^e}{dz} \right] dz, \delta T_{GT}^e = T_0^e \int_0^l \left[\frac{dv^e}{dz} \delta \left(\frac{d^2 u^e}{dz^2} \right) - \frac{du^e}{dz} \delta \left(\frac{d^2 v^e}{dz^2} \right) \right] dz \tag{7}$$

These energies yields the geometric stiffness matrices $\mathbf{K}_{GF}^e, \mathbf{K}_{GT}^e$ of each element and the total matrices $\mathbf{K}_{GF}, \mathbf{K}_{GT}$.

2.2 Well-Assembly Interactions

When the structure deforms laterally, the contact between the rotating drillstring and the well may occur and gives rise to friction and shock effects. The contact between one node of structure and the well is modeled by a radial elastic stop of nominal stiffness k_c and damping c_c . As shown in Fig. 2, the normal contact force is defined in the frame of reference of the contact node as:

$$\vec{F}_{cn} = - \left(K_c(G)G + C_c(G)\dot{G} \right) [u/r, v/r, 0]^T \tag{8}$$

with $G = \sqrt{u^2 + v^2} - j_0$ the contact gap, j_0 the radial clearance and $\dot{G} = (\dot{u}u + \dot{v}v)/r$ the penetration velocity. The contact law is regularized by using the arctan function for the stiffness and damping, see [13]:

$$K_c(G) = \frac{k_c}{2} \left[\frac{2}{\pi} \arctan(\pi \lambda G) + 1 \right], C_c(G) = \frac{c_c}{2} \left[\frac{2}{\pi} \arctan(\pi \lambda G) + 1 \right] \tag{9}$$

where λ is the regularization parameter.

The tangent friction force is related to the sliding velocity v_g [13]. Both the tangential force and torque are modeled by the smoothed Coulomb law, so that the force is given by

$$\vec{F}_{ct} = -\mu(v_g) \left(K_c(G)G + C_c(G)\dot{G} \right) [-v/r, u/r, 0]^T \tag{10}$$

and the friction torque is described by

$$\vec{T}_{ct} = -\mu(v_g) \left(K_c(G)G + C_c(G)\dot{G} \right) R_e \vec{z}. \tag{11}$$

The friction function $\mu(v_g)$ is defined by the dynamic and static friction coefficients and is regularized as in [13].

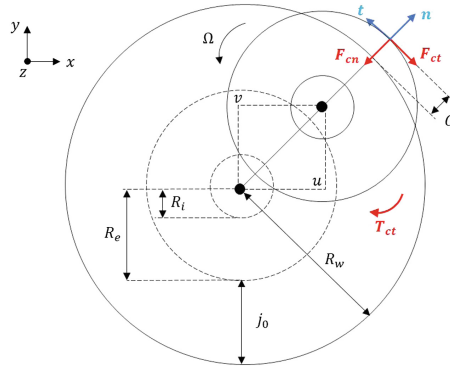


Fig. 2. Contact between one node of drillstring and the well casing represented in the local frame of this node.

2.3 Fluid Effects

The fluid inside the drill-pipes and in the well-pipe annular space induces the elastic forces on the structure. In this work, the effects of inner fluid are characterized by the inertial force while the effects of the outer fluid are based on the model developed in [14–17]. The authors considered the influence of fluid elastic forces induced by co-rotating flow surrounding the shaft with a relatively slow speeds of rotation. This model does not take into account the axial fluid flow can be applied for fluids with the small compressibility and the cylindrical beams of a large length-radius ratio.

The viscosity effects are defined in the modal basis [15, 16] and are detailed in Sect. 3.2. The inertial force of outer fluid in the $x - y$ plane of the element frame is taken from [16] and reads as:

$$- \begin{bmatrix} m_a \left(\ddot{u}^e + \Omega \dot{v}^e - \frac{\Omega^2}{4} u^e \right) \\ m_a \left(\ddot{v}^e - \Omega \dot{u}^e - \frac{\Omega^2}{4} v^e \right) \end{bmatrix} \tag{12}$$

with $m_a = \rho_f \pi R_{fi}^2 (R_{fi}^2 + R_{fe}^2) / (R_{fe}^2 - R_{fi}^2)$ the added mass, R_{fe} and R_{fi} the outer and inner radii of the annular space, ρ_f the mass density of fluid.

Dissipation in the steady state rotating outer fluid is taken into account by the friction force [16]:

$$- m_a \gamma \Omega \begin{bmatrix} \dot{u}^e + \frac{\Omega}{2} v^e \\ \dot{v}^e - \frac{\Omega}{2} u^e \end{bmatrix}, \quad \gamma = f_f \frac{R_{fe} + R_{fi}}{2h}, \quad h = R_{fe} - R_{fi} \tag{13}$$

where f_f is the friction coefficient.

By using Eq. (3), the inertial and friction forces from the outer fluid are rewritten as $\mathbf{M}_{fe}^e \delta^e + \Omega \mathbf{C}_{fe}^e \delta^e + \Omega^2 \mathbf{K}_{fe}^e \delta^e$ and the element inertial force of the inner fluid corresponds to $\mathbf{M}_{fi}^e \delta^e$. The assembly of all elements yields the total matrices \mathbf{M}_{fe} , \mathbf{C}_{fe} , \mathbf{K}_{fe} and \mathbf{M}_{fi} .

3 Computation of the Campbell Diagram

In this section, the algorithm for the Campbell diagram computation is presented (see Fig. 3). First, the static position of the drilling assembly in the well is calculated by taking into account the well-pipe contacts and all static external forces. The internal axial force and torque of each beam element are then computed and give the geometric stiffness matrices \mathbf{K}_{GF} and \mathbf{K}_{GT} by using Eq. (7). The prestressed state of the drilling assembly is applied by adding these matrices to the structure stiffness. The contact nodes from the static position are identified and presumed to be in the permanent contact with the well for the modal analysis. Their lateral displacements are limited by adding the contact stiffness matrix \mathbf{K}_b . Finally, the Campbell diagram is computed by implementing the modal reduction technique. These two steps are shown in details in the following subsections.

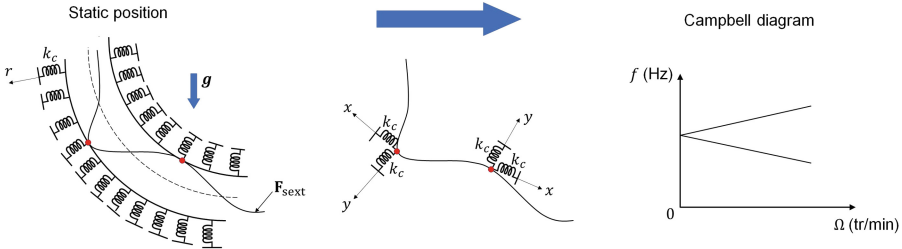


Fig. 3. Principle for computing the Campbell diagram.

3.1 Static Computation

The static equilibrium equation is given by

$$\mathbf{K}_a \delta = \mathbf{F}_s + \mathbf{F}_c(\delta) \tag{14}$$

where \mathbf{F}_s is the static force vector due to the gravity, to the Archimède force, to the external static forces and torques. \mathbf{F}_c denotes the contact forces and torques. \mathbf{F}_c contains the normal contact force \mathbf{F}_{cn} . In the case where the drill-pipe is rotated and stuck on the well casing, \mathbf{F}_c includes also the static tangential friction forces and torques \mathbf{F}_{cts} . The static friction force and torque applied at each contact node can be obtained from Sect. 2.2:

$$\vec{F}_{cts} = -\mu_s K_c(G)G[-v/r, u/r, 0]^T, \quad \vec{T}_{cts} = -\mu_s K_c(G)GR_e \mathbf{z} \tag{15}$$

In this case, Eq. (14) describes the “quasi”-static equilibrium. Otherwise, no friction terms are considered and Eq. (14) shows the real static equilibrium. This equation is solved by applying the Newton-Raphson method with four steps:

1. Initial guess δ_0 is chosen as $\mathbf{K}_a^{-1}\mathbf{F}_s$.
2. Assuming that δ_i is known at the i -th iteration, the correction term is defined by :

$$d\delta_i = - \left(\mathbf{K}_a - \frac{\partial \mathbf{F}_c}{\partial \delta}(\delta_i) \right)^{-1} (\mathbf{K}_a \delta_i - \mathbf{F}_s - \mathbf{F}_c(\delta_i)) \quad (16)$$

where $\frac{\partial \mathbf{F}_c}{\partial \delta}$ denotes the total Jacobian matrix \mathbf{F}_c with respect to δ .

3. Applying the correction : $\delta_{i+1} = \delta_i + d\delta_i$.
4. If $\frac{\|d\delta_i\|_2}{\|\delta_{i+1}\|_2} < \varepsilon_0$, ε_0 being the criterion error, the convergence is obtained. Otherwise, the process returns to step 2.

3.2 Reduction in the Modal Basis

Since the drilling assembly is a large system with a potential length of several kilometers, the pseudo-modal method is applied to reduce the dof number. This method is based on the modal basis which is the solution of the following eigenproblem:

$$\tilde{\mathbf{K}}_1 \phi_m = \omega_m^2 \mathbf{M} \phi_m \quad (17)$$

where (ω_m, ϕ_m) denotes the set of eigenvalue and eigenvector of each mode, $\tilde{\mathbf{K}}_1 = (\mathbf{K}_1 + \mathbf{K}_1^T)/2$ with $\mathbf{M} = \mathbf{M}_a + \mathbf{M}_{fi} + \mathbf{M}_{fe}$ and $\mathbf{K}_1 = \mathbf{K}_a + \mathbf{K}_{GF} + \mathbf{K}_{GT} + \mathbf{K}_b$.

The eigenmodes of a rotating system, $\delta_k = \mathbf{X}_k e^{r_k t}$, is the solution of quadratic eigenproblem:

$$(r_k^2 \mathbf{M} + r_k \mathbf{C} + \mathbf{K}) \mathbf{X}_k = \mathbf{0} \quad (18)$$

where $\mathbf{C} = \mathbf{C}_{ad} + (\mathbf{C}_{ac} + \mathbf{C}_{fe})\Omega$ and $\mathbf{K} = \mathbf{K}_1 + \mathbf{K}_{fe}\Omega^2$. \mathbf{C}_{ad} denotes the structural damping matrix defined by $c_M \mathbf{M}_a + c_K (\mathbf{K}_a + \mathbf{K}_{GF} + \mathbf{K}_{GT})$ with c_M, c_K the two Rayleigh coefficients.

By using the modal reduction matrix Φ whose each column corresponds to the eigenvector ϕ_m of the modal basis, Eq. (18) is transformed as :

$$(r_k^2 \mathbf{m} + r_k \mathbf{c} + \mathbf{k}) \mathbf{q}_k = \mathbf{0} \quad (19)$$

with $\mathbf{X} = \Phi \mathbf{q}$, $\mathbf{m} = \Phi^T \mathbf{M} \Phi$, $\mathbf{k} = \Phi^T \mathbf{K} \Phi$, $\mathbf{c} = \Phi^T \mathbf{C} \Phi + \mathbf{c}_\eta$. \mathbf{c}_η is a diagonal matrix representing the viscous damping [15, 16] in which η is the kinematic viscosity coefficient.

Since \mathbf{k} and \mathbf{c} are not symmetric, the eigenvalue r_k is a complex with the form $2\pi(\alpha \pm jf)$ where f is the eigen-frequency. The system is stable if $\alpha \leq 0$ and becomes unstable if $\alpha > 0$. The dependence of f on the speed of rotation gives the Campbell diagram. The rotating modes are classified by three categories: (F) like-flexural modes, (T) like-torsional modes and (L) like-longitudinal modes.

The classification criterion is based on three coefficients defined by the ratios of energies:

$$N_i = \frac{\sum E_{ci}^e}{E_{ca}} + \frac{\sum E_{di}^e}{E_{da}}, \quad i = \{F, T, L\} \tag{20}$$

where $E_{ci}^e = \frac{1}{2} |(r\mathbf{X}_i)^* \mathbf{M}_a (r\mathbf{X}_i)|$, $E_{di}^e = \frac{1}{2} |\mathbf{X}_i^* \mathbf{K}_a \mathbf{X}_i|$. * denotes the transposed conjugately operator. One mode is qualified (F) if $N_F > N_T, N_L$; (T) if $N_T > N_F, N_L$; (L) if $N_L > N_F, N_T$.

4 Results

4.1 Test Cases

Let a 2000 m drilling assembly be presented in Fig. 4. It consists of a polycrystalline diamond compact (PDC) drill-bit, drill-collars, stabilizers-gauges and a chain of drill-pipes. The drilling assembly are made of steel and characterized by $\rho = 7860 \text{ kg.m}^{-3}$, $E = 2.1 \cdot 10^{11} \text{ Pa}$, $\nu = 0.3$. The two Rayleigh damping coefficients are: $c_M = 0.03 \text{ s}^{-1}$ and $c_K = 0 \text{ s}$. The geometric properties of each component are shown in Table 1. A drill-pipe consists of two tooljoints of 0.3 m length and a body of 8.9 m length (see Fig. 4). The outer and inner diameters of the tooljoint are 0.162 m and 0.095 m. Two geometries of the well neutral lines are plotted by Fig. 5. As shown in Table 2, the well consists of three parts (casing 1, casing 2, openhole) of decreasing diameter from the surface. The static friction coefficients of the contact between the structure and the casings, openhole are respectively 0.2 and 0.3. The inner and outer fluids have the rheological properties: $\rho_f = 1200 \text{ kg.m}^{-3}$, $f_f = 0.013$, $\eta = 10^{-6} \text{ m}^2.\text{s}^{-1}$.

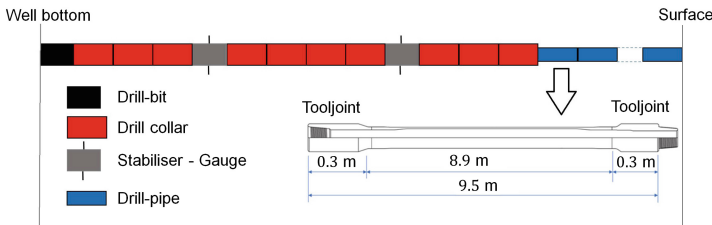
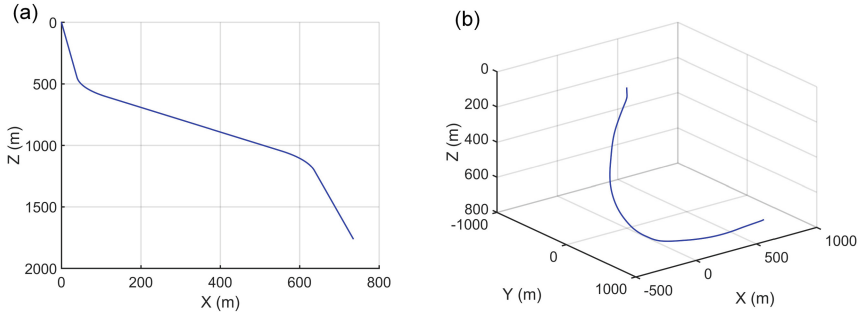


Fig. 4. Components of drilling assembly and geometry of drill-pipe.

The mesh contains 1811 beam elements and 1812 nodes. The drill-bit and a tooljoint are modeled by one element. The pipe body contains 5 elements. Each drill collar and stabilizer are discretized by 20 and 5 elements respectively. The lateral displacements of gauge nodes, of last bit node and six dofs of the surface node are blocked. An axial torque of -4905 N.m and a axial force of -49050 N are applied at the bit to model the Torque on Bit (TOB) and the Weight on Bit (WOB).

Table 1. Geometric properties of the components of drilling assembly

Type	Length (m)	Outer diameter (m)	Inner diameter (m)
Drill-bit	0.5	–	–
Drill-collar	10	0.159	0.071
Stabilizer	5	0.159	0.071
Drill-pipe	9.5	0.127	0.108

**Fig. 5.** (a) 2D-S well, (b) 3D well represented in the Cartesian coordinates.

The elastic stops modelling the contacts have the nominal stiffness $k_c = 10^7$ N/m with the regularized parameter $\lambda = 7 \cdot 10^7$ m⁻¹. Different clearances j_0 between the undeformed drilling components and the well are: 0.163 m (pipe-body - casing 1), 0.048 m (pipe-body - casing 2), 0.045 m (pipe-body - openhole), 0.029 m (stabilizer - openhole and drill-collar - openhole), 0.145 m (tooljoint - casing 1), 0.030 m (tooljoint - casing 2), 0.0270 m (tooljoint - openhole). Supplementary clearances are considered to take into account the change of the structure and well cross-section: 0.031 m, 0.145 m.

4.2 Static Computation

The quasi-static equilibrium position of the structure is computed for the two wells of Fig. 5 by taking into account the friction contacts. The difference between the quasi-static and static positions are then highlighted.

Table 2. Geometric properties of the well

Type	Outer diameter (m)	Inner diameter (m)
Casing 1	0.473	0.451
Casing 2	0.244	0.222
Openhole	0.216	0.216

Figure 6 shows three displacements of the quasi-static positions of the structure as a function of the curvilinear position. One can observe that the lateral displacements u and v are limited by the structure-well contacts. Since the geometry of the S well is steeper than the 3D well (see Fig. 5), the structure weight induces a larger axial displacement w of the structure in the S well than in the 3D well. Figure 7 represents the normal and tangential friction forces, the tangential friction torque applied to the structure. For the S well, the contact forces are the largest for a depth Z from 400 m to 1200 m, especially for the curved zones of the well. For the 3D well, the most important contact forces are observed at $Z \simeq 50$ m close to the surface and $Z \simeq 800$ m close to the bit.

Figure 8 compares the quasi-static/static positions of one cross section at the curvilinear position 113 m from the surface, computed with/without friction. The friction effects modify slightly the contact direction. Figure 9 represents the axial force and torque for each finite element. The continuous and dash lines denote the results computed with/without friction. The axial force and torque of one element are proportional to the difference between two nodal axial displacements and two nodal torsion angles respectively. The axial force and torque of the last element are equal to the ones imposed at the bit. The friction effects have no influence on the element axial forces. However, the element axial torque is strongly modified by the tangential friction torque. Moreover, the element axial torque curve shows more oscillations with the friction effect. Indeed, the friction torque applied to one contact node yields the jump of the axial torque curve between two adjacent beam elements associated with this node.

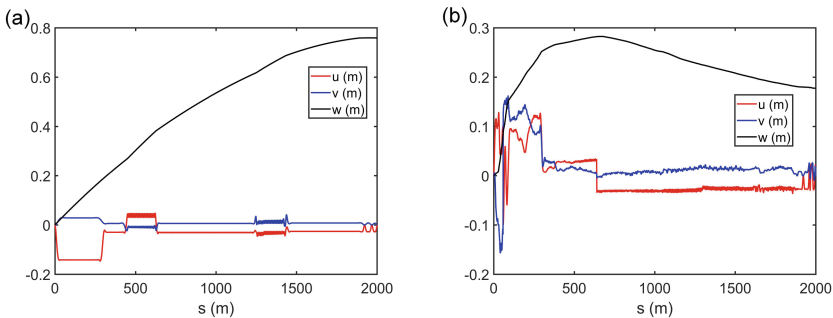


Fig. 6. Node displacements for the static equilibrium position of the drilling assembly in the cases: (a) 2D-S well, (b) 3D well as a function of the curvilinear position by taking into account the friction forces.

The results computed with the friction effects are used for plotting the Campbell diagrams in the next section. The geometric stiffness obtained from the static equilibrium computation represents the pre-loaded state of the structure due to the curve well geometry, the structure-well contacts, the fluid effects and the static forces such as the gravity, the constant TOB and WOB. The system stiffness is modified by adding this geometric stiffness to compute the Campbell

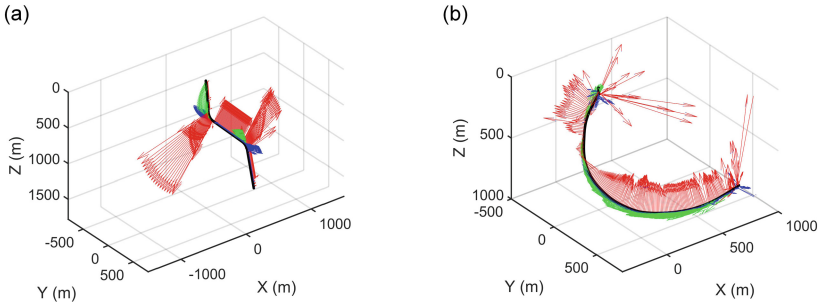


Fig. 7. Normal contact force (red), tangential friction force (blue) and torque (green) applied to the drilling assembly for the (a) 2D-S well and for the (b) 3D well.

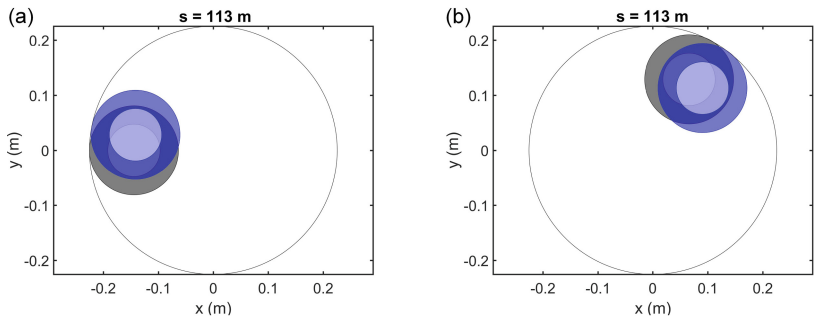


Fig. 8. Cross-section of the drilling structure at the curvilinear abscissa $s = 113$ m for the (a) 2D-S well and in the (b) 3D well. Black: no friction, blue: with friction

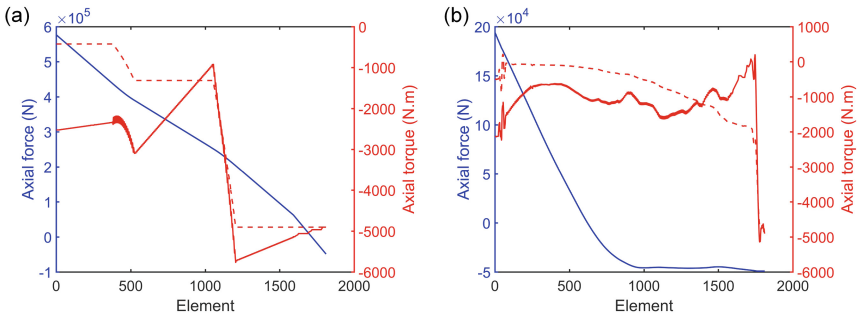


Fig. 9. Element axial force and torque obtained from the equilibrium positions. Continuous lines: with friction, dash lines: no friction.

diagram. Analyzing the Campbell diagram with constant TOB and WOB is a first approach which permits understanding roughly the modal contribution of the drilling structure.

4.3 Campbell Diagram

In this section, the natural frequencies are computed as a function of the speed of rotation to determine the Campbell diagram. The speed range which may induce the system instability is then identified. Some mode shapes are studied to show the phenomenon of the modal coupling.

The pseudo-modal method with the first 10 modes is applied to reduce the computational system size. Figure 10 represents the Campbell diagrams of the drilling structure from 0 rpm to 600 rpm. The drilling assembly has low-frequency modes due to its long structure. The dotted lines denote the (L), (T), (F) modes. The cyan color shows the (F) modes which make the system unstable. The system becomes unstable from the rotating speed of 250 rpm for the S well and 200 rpm for the 3D well. The gray continuous curves linking the points represents the mode shape tracking, based on the NC²O criterion [18]. The intersection between the mode curves and the dashed line gives the frequencies equal to the speeds of rotation. They are considered as the critical speeds which may yield to the dangerous resonances when the system is excited by the external forces (the mass-unbalanced and asynchronous forces) [19].

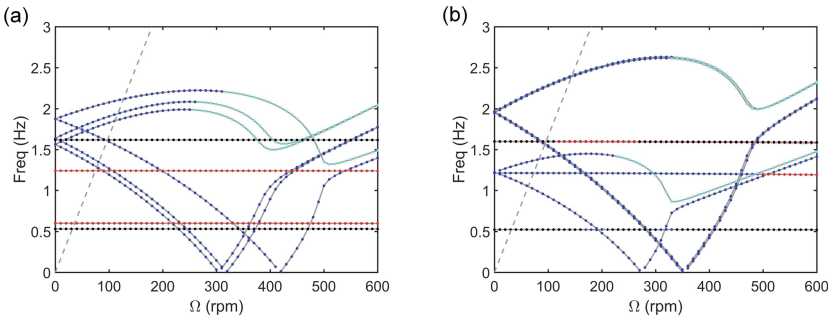


Fig. 10. Campbell diagram of the drilling structure for (a) 2D-S well and for (b) 3D well. Blue : (F) modes, red : (T) modes, black: (L) modes, cyan : instable (F) modes, dashed line : critical line, gray continuous curves : the mode shape tracking.

For the case of S well, the Campbell diagram represented by Fig. 10a shows that two curves of each (F) mode are strongly deviated at the low speeds of rotation due to the outer fluid effects and then converge at the high speeds of rotation. The gap between these curves at high speeds of rotation is due to the damping effects such as the structural damping, the fluid viscosity and friction. As shown in [16], the outer fluid friction has more important effects than the viscous and structural damping. The horizontal curves of (L) and (T) modes show the negligible dependence on the rotating speed. On the contrary to the S well, the Campbell diagram for 3D well in Fig. 10b shows two horizontal curves which do not have a pure flexural, torsional or longitudinal nature. Since the

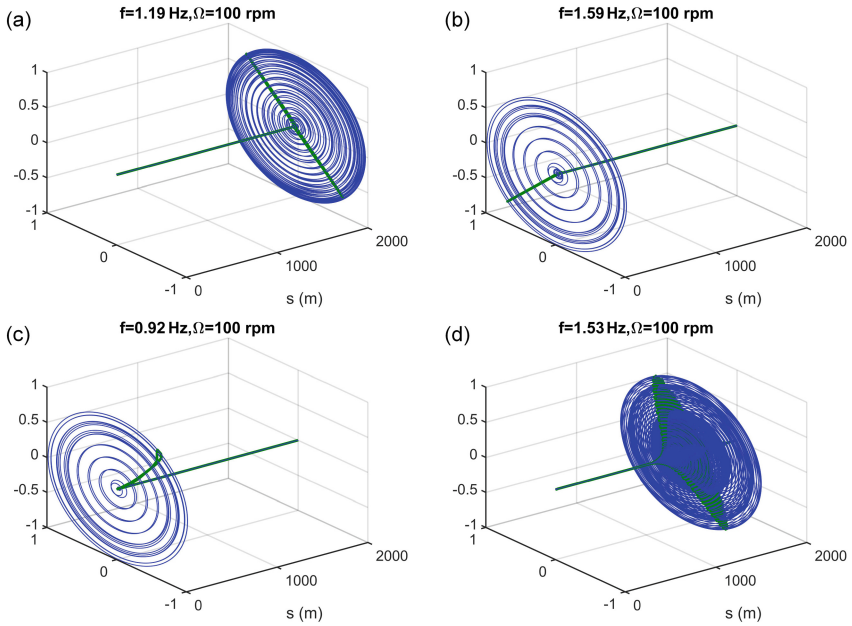


Fig. 11. Normalized lateral displacement of some (F) modes of the drilling structure in the (a, b) 2D-S well and in the (c, d) 3D well. Blue : orbit, green : the mode shape at $t = 0$.

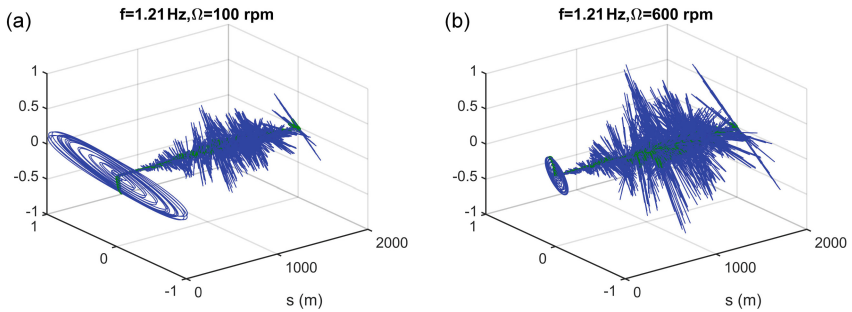


Fig. 12. Normalized lateral displacement orbits of one (F) modes and one (T) modes of the drilling structure in the 3D well.

geometry of this well is more complicated than the 2D well, the modal coupling mechanism occurs stronger and will be illustrated by Fig. 12.

Figure 11 shows the orbits of some (F) modes as a function of the curvilinear position. Their most important displacements can be observed in the vicinity of the surface ($s = 0$ m) and of the drill-bit ($s \simeq 1800$ m).

Figure 12 shows two modes representing the coupling between the flexural and torsional motions for the case of 3D well. These modes are on the horizontal

curve of Fig. 10b with the blue and red colors. The orbits of flexural motions can be observed only in the vicinity of the surface. The lower part of the structure have both torsional and flexural motions. The mode in Fig. 12a shows more energy related to flexural motions than to torsional ones. Hence, the classification criterion given by Eq. (20) consider it as a (F) mode. On the contrary, this mode in Fig. 12b shows that the torsional motions has more important energy than the flexural ones, which suggest to consider it as a (T) mode.

5 Conclusion

In this work, the static position is computed by taking into account the structure-well contact. The influence of the static friction effects on the equilibrium position is studied. The Campbell diagram is then computed over an operating range of the drilling speeds of rotation by considering the prestressed structure with a constant TOB and WOB and by assuming that the contact nodes remains in the permanent contact with the well. The unstable speeds of rotation and the critical speeds are observed. The rotating fluids show a strong influence on the (F) modes, contrary to the (L) and (T) modes. The modal coupling mechanisms are more remarkable for the structure in a 3D well than in a 2D well. In the future works, the model can be extended to take into account the speed dependent TOB and WOB for the Campbell diagram computation.

Acknowledgment. This research investigation is a product of DrillLab, a laboratory common to DrillScan and INSA Lyon LaMCoS in the framework of the LaBCoM-SME program of the Agence Nationale de la Recherche (ANR 15-LCV4-0010-01). The authors are indebted to ANR for its support.

References

- Spanos, P.D., Chevallier, A.M., Politis, N.P., Payne, M.L.: Oil well drilling: a vibrations perspective. *Shock Vib. Dig.* **35**, 81–99 (2003)
- Melakhessou, H., Berlioz, A., Ferraris, G.: A nonlinear well-drillstring interaction model. *J. vibr. acoust. Trans. ASME* **125**, 46–52 (2003)
- Dunayevsky, V., Abbassian, F., Judzis, A.: Dynamic stability of drillstrings under fluctuating weight on bit. *SPE Drilling Completion* **8**, 84–92 (1993)
- Dufeyte, M.P., Henneuse, H.: Detection and monitoring of the slip-stick motion: field experiments. *SPE/IADC Drilling Conf. Amsterdam* **21945**, 429–437 (1991)
- Macdonald, K.: Failure analysis of drillstring and bottom hole assembly components. *Eng. Fail. Anal.* **1**(2), 91–117 (1994)
- Dareing, D., Livesay, B.: Longitudinal and angular drill-string vibrations with damping. *J. Eng. Ind. Trans. ASME* **90**, 671–679 (1968)
- Bailey, J., Finnie, I.: An analytical study of drillstring vibration. *J. Eng. Ind. Trans. ASME* **82**, 122–128 (1960)
- Dawson, R., Lin, Y.Q., Spanos, P.D.: Drill string stickslip oscillations. In: *Proceedings of the 1987 Conference of the Society of Experimental Mechanics, Houston, TX*, pp. 590–595 (1987)

9. Brett, J.: The genesis of torsional drillstring vibrations. *SPE Drill. Eng.* **7**, 168–174 (1992)
10. Vaz, M., Patel, M.: Analysis of drill strings in vertical and deviated holes using the Galerkin method. *Eng. Struct.* **17**, 437–442 (1995)
11. Dufour, R., Berlioz, A.: Parametric instability of a beam due to axial excitations and to boundary conditions. *J. Vibr. Acoust. Trans. ASME* **120**, 461–467 (1998)
12. Berlioz, A., Der Hagopian, J., Dufour, R., Draoui, E.: Dynamic behavior of a drill-string: experimental investigation of lateral instabilities. *J. vibr. Acoust. Trans. ASME* **118**, 292–298 (1996)
13. Duran, C., Manin, L., Andrianoely, M.-A., Bordegaray, C., Battle, F., Régis, D.: Effect of rotor-stator contact on the mass unbalance response. In: *Proceedings of the 9th IFToMM International Conference on Rotor Dynamics*, pp. 1965–1975 (2015)
14. Fritz, R.J.: The effects of an annular fluid on the vibration of a long rotor, part 1 - theory. *J. Basic Eng. ASME* **92**(4), 923–929 (1970)
15. Chen, S.S.: Fluid damping for circular cylindrical structures. *Nucl. Eng. Des.* **63**, 81–100 (1981)
16. Axisa, F., Antunes, J.: Flexural vibrations of rotors immersed in dense fluids part I : theory. *J. Fluids Struct.* **6**, 3–21 (1992)
17. Antunes, J., Axisa, F., Hareux, F.: Flexural vibrations of rotors immersed in dense fluids part II : experiments. *J. Fluids Struct.* **6**, 23–38 (1992)
18. Mogenier, G., Baranger, T., Ferraris, G., Dufour, R., Durantay, L.: A criterion for mode shape tracking: application to campbell diagrams. *J. Vibr. Control* **20**, 179–190 (2012)
19. Lalanne, M., Ferraris, G.: *Rotordynamics Prediction in Engineering*, 2nd edn. Wiley, Hoboken (1998)



Dynamic Behavior of a Rotor-AMB System Due to Strong Base Motions

C. Jarroux¹, J. Mahfoud¹(✉), R. Dufour¹, F. Legrand¹, B. Defoy²,
and T. Alban²

¹ Univ Lyon, INSA Lyon, CNRS UMR5259, LaMCoS, 69621 Lyon, France
jarir.mahfoud@insa-lyon.fr

² GE Oil and Gas, 480 Avenue Gustave Eiffel, 71200 Le Creusot, France

Abstract. The paper investigates experimentally and numerically the nonlinear dynamics of a rotor supported by Active Magnetic Bearings (AMBs) and subjected to more or less severe motions from its support. In case of strong base excitations, the rotor can contact its touchdown bearings (TDBs) which are emergency bearings. The objective is to analyze the effect of the combination of mass unbalance forces, base motion excitations and contact nonlinearities on a rotor-AMB system response. The Finite Element method was used to model the on-board rotor. External force vectors and matrices with parametric coefficients related to the base motions appear in the equations of motion. The contact was modelled with a bilinear normal contact law and the tangential sliding friction effects are considered. Experiments were carried out on a lab-scale test rig that was mounted on a 6-axis shaker. At this stage, only harmonic base motions were considered. The numerical model was able to describe accurately the observed phenomena. AMBs were able to maintain the system under control, and the system remains stable even during the contact phase.

Keywords: Active Magnetic Bearings · Rotordynamics · Base motion
Rotor-stator contact · Touchdown bearings

1 Introduction

Turbomachinery play a key role in the transformation, extraction or transport of the different types of available energies. Depending on the targeted applications, these machines may have to face more or less severe environmental conditions, such as turbomachinery used in nuclear plant when subjected to earthquake, as recently in Fukushima where the station was deeply damaged. The same behavior could be observed for Floating Production Storage and Offloading (FPSO) units used for the offshore production and storage of oil due to large waves or stormy events. Turbo-machines have to be able to withstand severe environmental conditions.

The base motion generates complex rotordynamics in particular in the case of deformable foundations or base rotations yielding parametric instabilities. At certain angular speed of the support, combined with the natural frequencies of the rotor, instability zones emerge and depend on the amplitude of the rotation angle [1–3]. When on-board rotors are supported by nonlinear bearings, complex dynamics are expected

[4, 5]. Depending on the amplitude of the applied sinusoidal base motion (translation or rotation), the rotor-bearing system exhibits periodic, quasi-periodic or even chaotic motions. Therefore, the dynamic behavior of on-board rotating machines should be carefully analyzed to improve the reliability and to maintain a maximal operability of the machines.

Active magnetic bearings (AMBs) are increasingly utilized in industrial applications for their many advantages such as frictionless support, no lubrication system, and a reduced footprint. They are inherently unstable, therefore a feedback control is needed and the PID is the most implemented controller in industrial applications [6]. Rotor-AMB systems are systematically equipped with touchdown bearings (TDBs) supporting the shaft when magnetic levitation is no more provided. In case of large displacements, contact between the rotor and the TDBs could occur leading to potential instabilities.

The use of magnetic forces can limit the effects of base motions. Several studies showed the effectiveness of AMBs to maintain the system stable [7–9]. However, in most cases, the amplitude of the rotor response due to the base motions was limited and interaction with TDBs was not generated. Few studies have considered this nonlinearity triggered by base motions while AMBs still operate. This could lead to dangerous rotordynamics such as backward whirl followed by dry whip instabilities [10].

This research project contributes to the improvement of knowledge concerning the dynamic behavior of turbomachinery supported by AMBs when subjected to external events. In particular, to investigate, numerically and experimentally, the dynamic behavior of a rotor-AMB system subjected to strong base motion leading the rotor to contact TDB while AMB still operate. The effects of flexible support was considered by other researchers [11], in this study the support is considered rigid.

First, the modelling approach is developed with the implementation of the rigid base motion inputs in the equations of motion. Then the experimental dispositive is described. The results obtained are shown and discussed at the end.

2 Numerical Model

The different models needed to perform transient simulations considering a rotor-AMB system subjected to external disturbances and potential TDB contacts are presented. The on-board rotor and the touchdown bearing models are described separately; the modelling approach is modular and each model can be either employed or not in the simulations.

2.1 On-Board Rotor

Usually, the rotor is composed of shaft, bearings, discs, and unbalance distribution, and here, the support is considered (Fig. 1). It is assumed that: the shaft is flexible and modelled by beam elements for lateral analysis; the discs are rigid and symmetric; the unbalance distribution is modelled by discrete masses and the support is rigid but mobile.

Lagrangian method is used. It consists in describing the motion of the rotor with respect to the rigid support R , as usually done in conventional rotordynamics studies [12], and the support motion with respect to the ground R_g , which is a Galilean frame. An intermediate frame is set-up to take into account the energy formulation of base motion inputs and to investigate the deflection of the rotor neutral line in the frame attached to the rigid support [13].

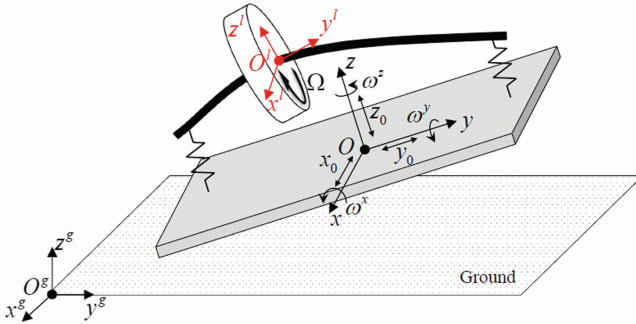


Fig. 1. On-board rotor frame

The Galilean frame R_g of center O_g is fixed and attached to the ground. The non-inertial frame R of center O is attached to the rigid base. And the local non-inertial frame R_1 of center O_1 is attached to the deflection line of the rotor. The frames of reference are first established and then vectors describing the different motions between each others are calculated. To derive the different energies of each components of the rotor, the instantaneous angular velocity vector and the position vector are needed. These vectors are expressed with respect to the Galilean frame R_g in the rigid support frame R . The energetic contribution and the virtual work of each components should be calculated: the flexible shaft contributes with the kinetic and strain energies; the discs with the kinetic energy; the discrete mass unbalances with the kinetic energy, and the bearing restoring forces with the virtual work.

The different contributions of the base are expressed in the frame associated with the rigid base in motion with respect to the Galilean frame. The base motions modify only the kinetic energies. Once the energies are set-up, they are derived by using the Lagrange's equations leading to the equations of motion as:

$$M\ddot{\delta} + \left(\Omega C^g + \omega^y C_{bm}^{\omega^y}\right)\dot{\delta} + \left(K^e + \dot{\omega}^y K_{bm}^{\omega^y} + \Omega \omega^y K_{bm}^{\Omega\omega^y} + \omega^{x2} K_{bm}^{\omega^{x2}} + \omega^{y2} K_{bm}^{\omega^{y2}} + \omega^{z2} K_{bm}^{\omega^{z2}} + \omega^x \omega^z K_{bm}^{\omega^x\omega^z}\right)\delta = F_{mu} + F_{bm} + F_g + F_{amb} + F_c \tag{1}$$

with M, K^e and C^g are respectively the mass, the structural stiffness and the gyroscopic matrices. Ω is the rotor rotational speed, $\delta, \dot{\delta}, \ddot{\delta}$ are the rotor displacement, velocity and acceleration. F_{mu} is the mass unbalance force vector taking into account the normal centrifugal and tangential centripetal forces. The subscript bm stands for the base

motion effects. The external force vector F_{bm} contains all the contribution of the translations of the support combined with its rotations, F_g the effect of gravity, F_{amb} the forces delivered by the AMBs, which is the output of an augmented PID that takes into account the characteristics of the utilized AMBs. The model used is not developed in this paper. F_c represents the TDBs contact force vectors that will be developed in the next section. $\omega^x; y; z$ is the rotational speed of the support along the direction x, y or z. C_{bm}^ω , K_{bm}^ω are the additional (gyroscopic or stiffness) matrices due to the support rotations. Obviously, the support rotations introduce time-varying parametric excitations that could generate lateral instabilities.

2.2 TouchDown Bearing Model

TDBs have two main functions. The first one is to protect the AMBs from large unexpected transient loads that exceed the design capacity of AMBs. The second is to ensure a back-up support when AMBs are no longer available.

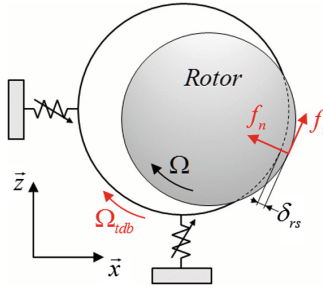


Fig. 2. TDB model

Usually, a ribbon damper is fitted between the outer race and the housing; it brings softness and damping when rotor-TDB interactions occur. TDBs generate contact forces in normal f_n and tangential f_t directions, as shown in Fig. 2. The normal component f_n is described by a contact law. Its mechanical expression is given by Eq. (2), where δ_{rs} is the rotor-TDB relative clearance and δ_{rd} is the ribbon crushing capacity.

$$f_n = \begin{cases} k_{brg}(\delta_{rs} - \delta_{rd}) + c_{brg}\dot{\delta} + k_{eq}\delta_{rd} & ; \delta_{rs} \geq \delta_{rd} \\ k_{eq}\delta_{rs} + c_{eq}\dot{\delta}_{rs} & ; \delta_{rd} > \delta_{rs} \geq 0 \\ 0 & ; \delta_{rs} > 0 \end{cases} \quad (2)$$

with k_{brg} , c_{brg} the dynamic parameters of the ball bearing. When the rotor interacts with the TDB, it first contacts the coupled ball bearing ribbon damper system, considered in series mode. The related contact force is composed of the equivalent stiffness k_{eq} and damping c_{eq} . When the ribbon is fully crushed, meaning that $\delta_{rs} \geq \delta_{rd}$ it only has a static contribution and the rotor faces the ball bearing stiffness. This model is characterized by softness and large damping when the ribbon is not crushed, then by a high stiffness and a low damping.

The tangential component f_t considers the sliding friction generated at the rotor-TDB interface due to different rotational speeds and considers the tangential damping provided by the ribbon damper counteracting the rotor whirl. The sliding friction is generated by using the regularized Stribeck model. The latter drives the TDB in rotation and Ω_{tdb} represents its speed of rotation. An equivalent rotational inertia (balls and inner race) as well as a resistive torque are considered to compute this component.

The modelling approach that takes into account base motions, AMBs, mass unbalance, gyroscopic effects, gravity and contact with TDBs is schemed in Fig. 3.

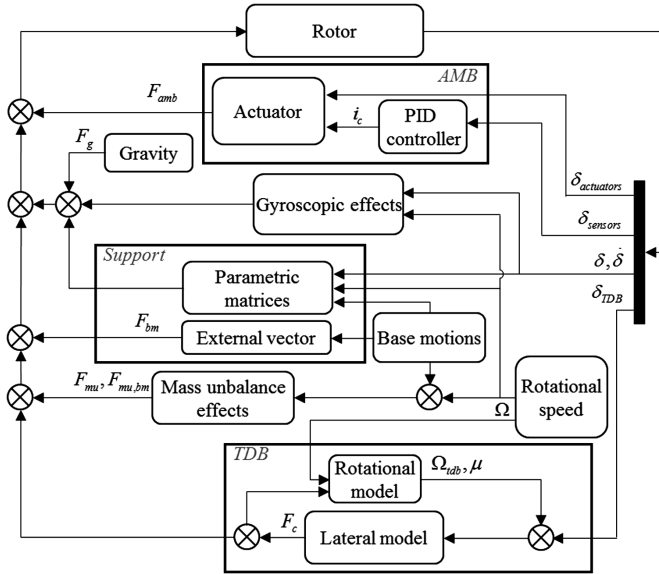


Fig. 3. Numerical model schema

The nonlinear contributions such as the additional forces due to the base motion (support block) or the efforts due to the contact of the rotor with the TDB (TDB block) are considered as restoring forces. It was the same concerning the forces delivered by the AMB (AMB block). The gravity as well as the gyroscopic effects were also considered in the second member of the equation of motion. This modelling approach is able to have a linear part concerning the rotor, consequently, the modal reduction can be applied easily [14].

The model developed enables system simulation in different configurations. For this work, only harmonic base motions were considered.

3 Experimental Model

The experiments were performed using an academic test rig, which is a commercial product manufactured by SKF® and was delivered with a dedicated PID controller. The test rig is equipped with two identical AMB called NDE (Non Drive End) and DE

(Drive End) bearings. Each bearing has a maximum static capability of 280 N with air gaps of 0.432 mm. The action lines are positioned in the configuration load between axes. They are powered in differential driving mode with a bias current of 1 A. Currents are provided in the range of 0–3A using PWM amplifiers. Two displacement sensors (variable reluctance probes) are integrated in the housing of each bearing and are non-colocalised with actuators.

The rotor is designed to obtain the dynamic behavior of high speed turbomachinery with a rigid shaft in the operating speed range and low gyroscopic effects. The rotor is made of standard steel, its mass is 6.5 kg and its length is 645 mm with a disc, 120 mm in diameter and 25 mm in thickness, placed at two-thirds of the bearing span from the DE side. The rotor is driven by a 500 W electric motor with a maximum speed of 12 600 rpm. The torque transmission is provided through a flexible coupling. The operating speed range is from 0 to 9 500 rpm (160 Hz), which includes the first two rigid modes. The rotational speed is measured by using a tachometer placed close to the motor. TDBs are cageless single row deep groove ball bearings with 0.1 mm clearance that was provided by the manufacturer.

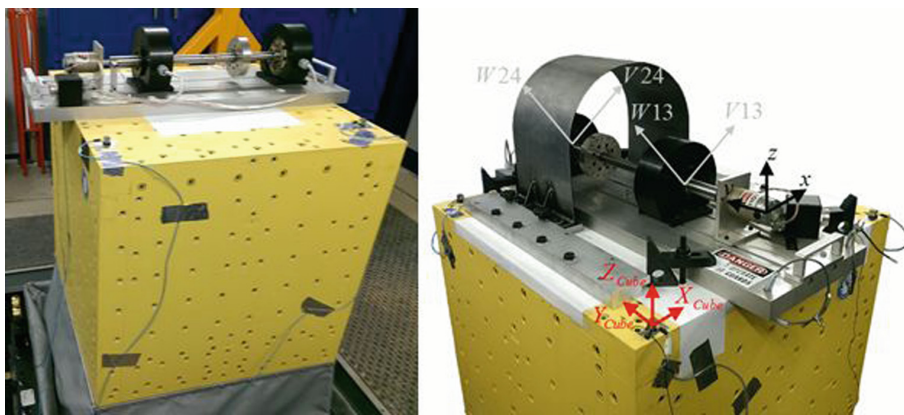


Fig. 4. Experimental test rig

To perform base motion tests, the academic test rig was mounted on a 6-axis hydraulic shaker as shown in Fig. 4 (the yellow cube). The shaker, provided by TEAM Corporation, is a fully integrated system. It has 6 real-time pilots able to apply various combinations of solicitations along and around the 3 axes (translations and rotations) to a maximum mass of 450 kg in a range [0–250] Hz. A maximum acceleration of 10 G, ± 50 mm in translation and $\pm 4^\circ$ in rotation can be generated.

The data acquisition system of the shaker was used. Base accelerations were recorded in the three directions (Xcube, Ycube, Zcube) using four tri-axial accelerometers fixed on the shaker. The displacement and current sensors for each action line (V13, W13, V24, W24), and the rotational speed were also recorded. The sampling frequency was set to 24 756 Hz.

The tests were carried out in vertical translation, by using harmonic excitations. For all the configurations tested, the same level of mass unbalance was applied; 32 g.mm at 0 degree that corresponds to four times the recommended unbalance by the API standards. The support motion was a 20 Hz sine translation ranging from 0.1 to 1.1 G. The chosen frequency and amplitude represent the best frequency range to exhibit TDB contact phenomena. The rotor rotational speed was set to 6 000 rpm. To smoothly trigger the rotor-TDB contact, the acceleration level targeted by the shaker is set-up progressively enabling reduced overshoot. This phase of operation lasted almost 30 s. Once reached, the shaker motion was maintained for approximately 40 s to catch potential onset of nonlinear dynamic regimes. The excitation signals were not purely sinusoidal, the contribution of the shaker operating frequencies were present. During the different test configurations, AMBs were kept operational. The shaker stop was also recorded to check and analyze the capacity of the controller and the AMBs to center and to control the rotor after severe contact situations.

4 Results

Measured and predicted rotor vertical displacements were compared. The accelerations recorded on the shaker were implemented in the numerical model.

First, the results obtained are analyzed for the whole test duration then, a zoom on ten periods using orbit plots provides better insights into the involved phenomena. Figure 5 shows the predicted and measured rotor displacements in vertical direction for a rotating speed of 6 000 rpm and subjected to a progressively increased acceleration of the shaker up to 1.1 G. The dotted lines represent the TDBs at both DE and NDE.

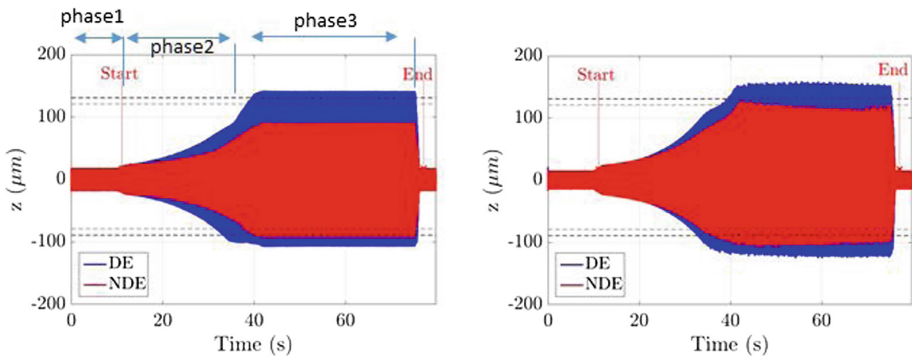


Fig. 5. Predicted (a) and measured (b) vertical displacements, 6 000 rpm, 0–1.1 G, 20 Hz

The base motion starts close to 10 s and contact occurred close to 35 s. The measured vertical responses seem to be described qualitatively well by the numerical model. The controller manages the unbalance forces combined with base motions and TDB contacts. Once the shaker stops, the rotor quickly recovers its centered position in both predictions and measures.

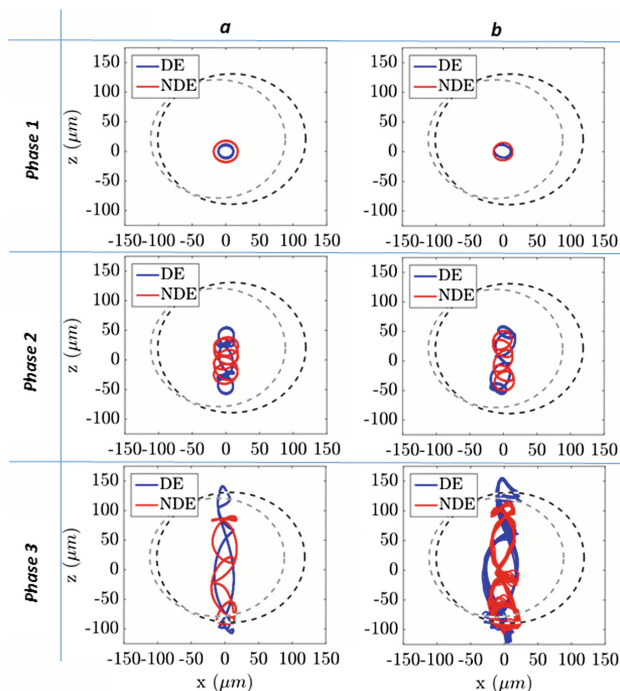


Fig. 6. Predicted (a) and measured (b) orbits, 6 000 rpm, 0–1.1 G, 20 Hz

As the acceleration level was set-up progressively, orbit plots permit analyzing the combined effects of mass unbalance and base motion loads for cases without or with TDB interactions. In Fig. 6, the orbits during the different phases were analyzed. For each phase, the last ten periods according to the base motion frequency were presented. At phase 1 (recorded results at 5 s), the shaker was shut down and only the mass unbalance forces were present. The orbits obtained were relatively circular (symmetric system), and the amplitude is largely smaller than the TDB clearance. Then during phase 2, the excitation level was increased progressively from 0 to 1.1 G (recorded results at 28.6 s, when the acceleration level equals 0.3 G). It could be noticed that the model describes closely the phenomena observed. Here, no contact between the rotor and the TDBs, and typical combinations of vertical base motion, unbalance forces were exhibited. Orbits were periodic due to integer ratio between the rotor speed and the excitation frequency. During phase 3, the highest level was maintained (recorded results at 60.7 s and 1.1 G acceleration level). The predicted and measured orbits were close. Rotor-TDBs interactions were generated and the periodicity of orbits was conserved with respect to the non-contacting case. Orbit shapes were flattened and the rotor had mainly forward whirl, indicating weak sliding friction effects. This could be due to the fact that the TDBs were driven in rotation and therefore, the sliding friction coefficient was small at the rotor-TDB interface.

Finally, the AMBs remained stable in both numerical and experimental analysis. The model is able to correctly describe the combination of base motion, mass unbalance, AMBs and TDBs contacts generating complex dynamics.

Measured orbits are slightly tilted and this may be related to small discrepancies in the proximity sensor sensitivity. The global measured energetic level of vibrations is higher than the predicted one since the acceleration signals were filtered before being implemented in the model. Moreover, the vibrations coming from the foundation were not considered in the numerical model since the support is assumed infinitely rigid. However, the model describes closely the main observed phenomena.

5 Conclusions

The aim was to investigate experimentally and numerically the nonlinear dynamics of a rotor supported by Active Magnetic Bearings and subjected to severe motions from its support. The test configurations were chosen to be representative of real turbomachines operating conditions. The PID controller was tuned for conventional operating conditions, and no specific work on the control loop was done. The aim was to check if the control could be able to withstand the nonlinearities due to the contact.

The model was able to reproduce the overall dynamics and the main observed phenomena considering an academic on-board rotor-AMB system.

Even if the PID controller was tuned without considering this particular excitation, the controller remains globally stable in both numerical and experimental tests. No dry whip instabilities were noticed in both experimental and numerical investigations. Orbit shapes were flattened and the rotor has mainly forward whirl, indicating weak sliding friction effects. The behavior observed may indicate that the TDBs were driven in rotation reaching the rotor rotational speed during harmonic tests; therefore, tangential friction effects were limited.

Even if the model of the AMB and the controller were not presented, we observed that the restoring magnetic forces generated by actuators remained in an acceptable linear range. Neither AMB nonlinearities nor amplifier saturation were exhibited in both predictions and measures. The dynamic capacity of the AMBs are oversized considering the test rig. We are now investigating the same behavior by using adapted dynamic capacity.

This numerical validation provides confidence considering the prediction of the dynamic behavior of on-board industrial turbomachinery.

Acknowledgements. This work was supported by the French National Agency of Research and Technology (ANRT) [CIFRE grant number: 2013/1376] and by French National Research Agency (ANR) Equipex PHARE 10-EQPX-0043.


References

1. Driot, N., Lamarque, C.H., Berlioz, A.: Theoretical and experimental analysis of a base-excited rotor. *J. Comput. Nonlinear Dyn.* **1**, 257–263 (2006)
2. Duchemin, M., Berlioz, A., Ferraris, G.: Dynamic behavior and stability of a rotor under base excitation. *J. Vib. Acoust.* **128**, 576–585 (2006)

3. Han, Q., Chu, F.: Parametric instability of flexible rotor-bearing system under time-periodic base angular motions. *Appl. Math. Model.* **39**, 4511–4522 (2015)
4. Dakel, M., Baguet, S., Dufour, R.: Nonlinear dynamics of a support-excited flexible rotor with hydrodynamic journal bearings. *J. Sound Vibr.* **333**(10), 2774–2799 (2014)
5. El-Saeidy, F.M.A., Sticher, F.: Dynamics of a rigid rotor linear/nonlinear bearings system subject to rotating unbalance and base excitations. *J. Vibr. Control* **16**, 403–438 (2010)
6. Schweitzer, G., Maslen, E.H.: *Magnetic Bearings, Theory, Design, and Application to Rotating Machinery*. Springer, Heidelberg (2009)
7. Das, A.S., Dutt, J.K., Ray, K.: Active vibration control of unbalanced flexible rotor-shaft systems parametrically excited due to base motion. *Appl. Math. Model.* **34**(9), 2353–2369 (2010)
8. Cole, M.O.T., Keogh, P.S., Burrows, C.R.: Vibration control of a flexible rotor/magnetic bearing system subject to direct forcing and base motion disturbances. *Proc. Inst. Mech. Eng. Part C: J. Mech. Eng. Sci.* **212**(7), 535–546 (1998)
9. Hawkins, L.A., Murphy, B., Zierer, J., Hayes, R.: Shock and vibration testing of an AMB supported energy storage flywheel. *JSME Int. J. Ser. C Mech. Syst. Mach. Elements Manuf.* **46**(2), 429–435 (2003)
10. Bartha, A.R.: Dry friction backward whirl of rotors. Ph.d. dissertation, ETH, Zurich (2000)
11. Cavalca, K.L., Cavalcante, P.F., Okabe, E.P.: An investigation on the influence of the supporting structure on the dynamics of the rotor system. *Mech. Syst. Sig. Process.* **19**(1), 157–174 (2005)
12. Lalanne, M., Ferraris, G.: *Rotordynamics Prediction in Engineering*. Wiley, Hoboken (1998)
13. Jarroux, C.: Nonlinear transient dynamics of on-board rotors supported by active magnetic bearings. Ph.D. dissertation, INSA Lyon, Lyon (2017)
14. Defoy, B., Alban, T., Mahfoud, J.: Assessment of the effectiveness of a polar fuzzy approach for the control of centrifugal compressors. *ASME J. Dyn. Syst. Measur. Control* **136**, 041004-1–041004-8 (2014)



Computational Analysis of Nonlinear Dynamics of a Multi-disk Rotor-Bearing-Brush Seal System

Yuan Wei^{1,2} , Zhaobo Chen², Yinghou Jiao², and Shulin Liu¹

¹ School of Mechatronics Engineering and Automation, Shanghai University, Shanghai 200072, China

weiyuan0315@sina.com

² School of Mechatronics Engineering, Harbin Institute of Technology, Harbin 150001, China

Abstract. The seal force and oil-film force are two of the main factors which would cause the instability of rotor system, so it is important to further study the nonlinear dynamic characteristics of the multi-disk rotor-bearing-seal system. In order to establish the multi-disk rotor-bearing-brush seal system model of a gas turbine, the seal force model of brush seal and the nonlinear oil-film force model based on short bearing theory were adopted considering the lateral deflection of the disks. The equation of motion was solved by time simulation using the fourth order Runge-Kutta method. The influences of key parameters including rotor speed and eccentricity phase-difference on the vibration response and dynamic behavior of multi-disk rotor-bearing-brush seal system were discussed. The result showed that the system became more stable when the eccentricity phase-difference decreased.

Keywords: Nonlinear dynamics · Brush seal
Multi-disk rotor-bearing-seal system · Numerical analysis

1 Introduction

Brush seals have superior sealing performance, which could enhance the thrust force and working efficiency of gas turbine [1, 2]. When the gas turbine is working under high temperature, high pressure, and high velocity condition, there would be some complex dynamic behavior fault arising, which could seriously affect the security and reliability of the system [3–5].

Currently the dynamic behaviors of multi-disk rotor-brush seal system are mostly studied by numerical simulation or test results for a specific structure. Chu and Lu [6] proposed a dynamic stiffness-based method to detect the rubbing position effectively in a multi-disk rotor system. The authors found that the dynamic stiffness at the position with rotor-to-stator rub increased as the rubbing developed, but the variation of stiffness at other positions was not obvious. Wan et al. [7] theoretically and experimentally studied the dynamic response of an unbalanced multi-disk rotor system with flexible coupling misalignment, and the governing equations of the system was deduced by the lumped mass model considering the nonlinear oil film force. But these researches are still not

perfect, so the effects of coupling of the contact of bristle pack and rotor surface, and the fluid flow in the bristle pack to the dynamic behavior of the system need further study.

In this paper, the authors adopted the seal force model of brush seal and the nonlinear oil-film force model based on short bearing theory considering the lateral deflection of the disks, in order to build the nonlinear dynamic model of a multi-disk rotor-bearing-brush seal system. The effects of the rotor speed and eccentricity phase difference on the vibration response and dynamic behavior of a multi-disk rotor-bearing-seal system were discussed under different operating conditions by axis orbit, Poincaré map, and spectrum cascade.

2 Nonlinear Dynamic Model of a Multi-disk Rotor-Bearing-Brush Seal System

2.1 Nonlinear Dynamic Model of the Multi-disk Rotor-Bearing-Seal System

Figure 1 shows the rotor-bearing-seal system of a gas turbine. The finite element model is obtained by discretization based on the structural features of the system, as shown in Fig. 1a. In this paper, the compressor and turbine are simplified as disk m_8 and disk m_9 , which located at joint 8 and joint 9, respectively. Similarly, the supporting bearings are simplified as disk m_4 and disk m_{12} , which located at joint 4 and joint 12, respectively.

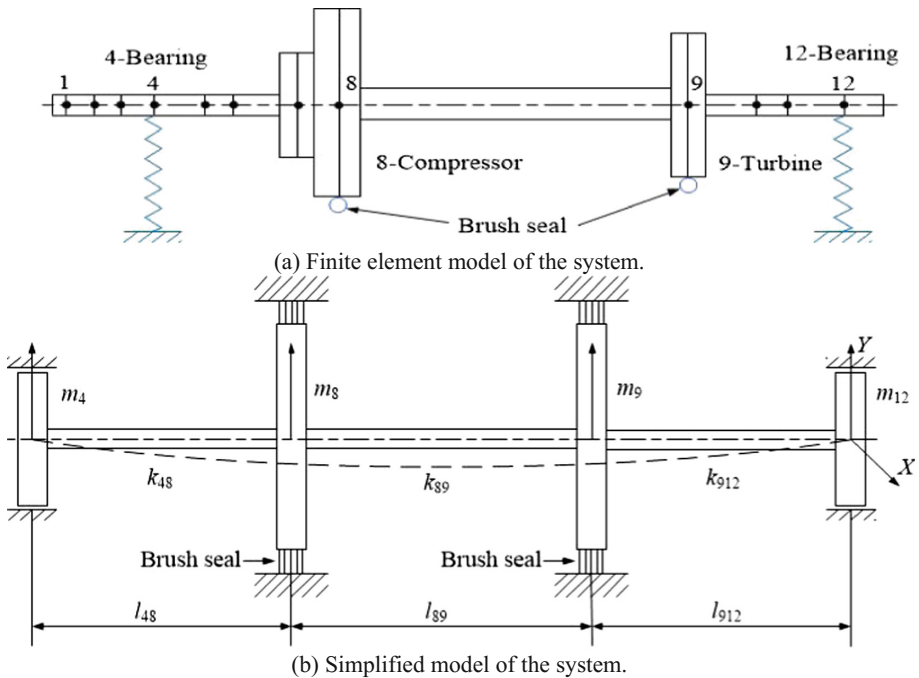


Fig. 1. Rotor-bearing-seal system of a gas turbine.

Considering the lateral deflection of the disks, the nonlinear dynamic equation of the system can be obtained by the simplified model as below:

$$M\ddot{q} + C\dot{q} + Kq = -F_g + F_b + F_s + F_e \quad (1)$$

With

$$\Gamma = Kq = \begin{bmatrix} -6EI \left[\frac{1}{l_{48}^3} (-2x_8 + 2x_4 + \theta_{y8}l_{48} + \theta_{y4}l_{48}) \right] \\ -6EI \left[\frac{1}{l_{48}^3} (-2y_8 + 2y_4 + \theta_{x8}l_{48} + \theta_{x4}l_{48}) \right] \\ 6EI \left[\frac{1}{l_{48}^3} (-2x_8 + 2x_4 + \theta_{y8}l_{48} + \theta_{y4}l_{48}) \right] + \frac{1}{l_{89}^3} (-2x_9 + 2x_8 + \theta_{y9}l_{89} + \theta_{y8}l_{89}) \\ 6EI \left[\frac{1}{l_{48}^3} (-2y_8 + 2y_4 + \theta_{x8}l_{48} + \theta_{x4}l_{48}) \right] + \frac{1}{l_{89}^3} (-2y_9 + 2y_8 + \theta_{x9}l_{89} + \theta_{x8}l_{89}) \\ -2EI \left[\frac{1}{l_{89}^3} (3y_9 - 3y_8 - \theta_{x9}l_{89} - 2\theta_{y8}l_{89}) - \frac{1}{l_{48}^3} (3y_8 - 3y_4 - \theta_{x8}l_{48} - 2\theta_{y4}l_{48}) \right] \\ -2EI \left[\frac{1}{l_{89}^3} (3x_9 - 3x_8 - \theta_{y9}l_{89} - 2\theta_{y8}l_{89}) - \frac{1}{l_{48}^3} (3x_8 - 3x_4 - \theta_{y8}l_{48} - 2\theta_{y4}l_{48}) \right] \\ 6EI \left[\frac{1}{l_{89}^3} (-2x_9 + 2x_8 + \theta_{y9}l_{89} + \theta_{y8}l_{89}) \right] + \frac{1}{l_{912}^3} (-2x_{12} + 2x_9 + \theta_{y12}l_{912} + \theta_{y9}l_{912}) \\ 6EI \left[\frac{1}{l_{89}^3} (-2y_9 + 2y_8 + \theta_{x9}l_{89} + \theta_{x8}l_{89}) \right] + \frac{1}{l_{912}^3} (-2y_{12} + 2y_9 + \theta_{x12}l_{912} + \theta_{x9}l_{912}) \\ -2EI \left[\frac{1}{l_{912}^3} (3y_{12} - 3y_9 - \theta_{x12}l_{912} - 2\theta_{x9}l_{912}) - \frac{1}{l_{89}^3} (3y_9 - 3y_8 - \theta_{x9}l_{89} - 2\theta_{x8}l_{89}) \right] \\ -2EI \left[\frac{1}{l_{912}^3} (3x_{12} - 3x_9 - \theta_{y12}l_{912} - 2\theta_{y9}l_{912}) - \frac{1}{l_{89}^3} (3x_9 - 3x_8 - \theta_{y9}l_{89} - 2\theta_{y8}l_{89}) \right] \\ 6EI \left[\frac{1}{l_{912}^3} (-2x_{12} + 2x_9 + \theta_{y12}l_{912} + \theta_{y9}l_{912}) \right] \\ 6EI \left[\frac{1}{l_{912}^3} (-2y_{12} + 2y_9 + \theta_{x12}l_{912} + \theta_{x9}l_{912}) \right] \end{bmatrix}$$

where M is the mass matrix of the system, $M = \begin{pmatrix} M_x & 0 \\ 0 & M_y \end{pmatrix}$, $M_x = M_y = \text{diag}$

$[m_4, m_8, J_{d8}, m_9, J_{d9}, m_{12}]$, C is the damping matrix of the system, $C = \begin{pmatrix} C_x & 0 \\ 0 & C_y \end{pmatrix}$,

$C_x = C_y = \text{diag}[c_4, c_8, c_{\theta 8}, c_9, c_{\theta 9}, c_{12}]$, K is the stiffness matrix of the system, q is the displacement of geometry center O_i in the X and Y direction, respectively,

$q = [x_4, y_4, x_8, y_8, \theta_{x8}, \theta_{y8}, x_9, y_9, \theta_{x9}, \theta_{y9}, x_{12}, y_{12}]^T$, F_g is the gravity vector of the system, $F_g = [0, m_4g, 0, m_8g, 0, 0, 0, m_9g, 0, 0, 0, m_{12}g]^T$, F_b is the nonlinear oil-film force

vector [8, 9], $F_b = [F_{bx4}, F_{by4}, 0, 0, 0, 0, 0, 0, 0, 0, F_{bx12}, F_{by12}]^T$, $\begin{bmatrix} F_{bxi} \\ F_{byi} \end{bmatrix} = S_0 \begin{bmatrix} f_{bxi} \\ f_{byi} \end{bmatrix}$,

$i = 4, 12$, F_s is the seal force vector [10], $F_s = [0, 0, F_{sx8}, F_{sy8}, 0, 0,$

$F_{sx9}, F_{sy9}, 0, 0, 0, 0]^T$, $\begin{bmatrix} F_{sxi} \\ F_{syi} \end{bmatrix} = \begin{bmatrix} F_{bi} \cos(\alpha + \theta - \mu - \phi) \\ F_{bi} \sin(\alpha + \theta - \mu - \phi) \end{bmatrix}$, $i = 8, 9$, F_e is the unbalanced force vector,

$$F_e = [0, 0, m_8 e_{u8} \omega^2 \cos(\omega t), m_8 e_{u8} \omega^2 \sin(\omega t), 0, 0, m_9 e_{u9} \omega^2 \cos(\omega t + \sigma), m_8 e_{u8} \omega^2 \sin(\omega t + \sigma), 0, 0, 0, 0]^T.$$

For the facility of calculation, dimensionless transformations are introduced into the Eq. (1):

$$\omega t = \tau, X_i = \frac{x_i}{\delta}, Y_i = \frac{y_i}{\delta}, \frac{d}{d\tau} = \frac{d}{\omega dt}, \frac{d^2}{d\tau^2} = \frac{d^2}{\omega^2 dt^2}$$

where $\dot{X}_i = \frac{\dot{x}_i}{\omega\delta}$, $\dot{Y}_i = \frac{\dot{y}_i}{\omega\delta}$, $\ddot{X}_i = \frac{\ddot{x}_i}{\omega^2\delta}$, $\ddot{Y}_i = \frac{\ddot{y}_i}{\omega^2\delta}$, $\dot{\Theta}_i = \frac{\dot{\theta}_i}{\omega}$, $\ddot{\Theta}_i = \frac{\ddot{\theta}_i}{\omega^2}$, $E_{ui} = \frac{e_{ui}}{\delta}$, $G = \frac{g}{\omega^2\delta}$, $M_i = \frac{m_i\omega\psi^3}{\mu_{412}}$, $k_i = \frac{6EI_i}{l_i^3}$, $K_i = k_i \cdot \frac{\psi^3}{\omega\mu_{412}}$, $C_i = c_i \cdot \frac{\psi^3}{\omega\mu_{412}}$, $C_{\theta i} = c_{\theta i} \cdot \frac{\omega\psi^3}{\mu_{412}c^2}$, $L_i = \frac{l_i}{l_{412}}$, $J_{di}^* = \frac{J_{di}\omega\psi^3}{\mu_{412}\delta^2}$, $J_{pi}^* = \frac{J_{pi}\omega\psi^3}{\mu_{412}\delta^2}$, $f_{si} = \frac{F_{si}\psi^3}{\mu_{412}\omega\delta}$, $f_{bi} = \frac{S_0 F_{bi}\psi^2}{\mu_{412}\omega r}$, $S_0 = \mu_0 \omega r l \left(\frac{r}{\delta}\right)^2 \left(\frac{l}{2r}\right)^2$, μ_0 is the absolute viscosity of lubricate, δ is the clearance of radius, ω is the rotor speed.

Then Γ can be rewritten as below:

$$\Gamma' = \begin{bmatrix} \frac{K_{48}}{M_4} (-2X_8 + 2X_4 + \Theta_{y8}L_{48} + \Theta_{y4}L_{48}) \\ \frac{K_{48}}{M_4} (-2Y_8 + 2Y_4 + \Theta_{x8}L_{48} + \Theta_{x4}L_{48}) \\ -\frac{K_{48}}{M_8} (-2X_8 + 2X_4 + \Theta_{y8}L_{48} + \Theta_{y4}L_{48}) + \frac{K_{89}}{M_8} (-2X_9 + 2X_8 + \Theta_{y9}L_{89} + \Theta_{y8}L_{89}) \\ -\frac{K_{48}}{M_8} (-2Y_8 + 2Y_4 + \Theta_{x8}L_{48} + \Theta_{x4}L_{48}) + \frac{K_{89}}{M_8} (-2Y_9 + 2Y_8 + \Theta_{x9}L_{89} + \Theta_{x8}L_{89}) \\ \frac{K_{89}L_{89}}{3J_{d8}^*} (3Y_9 - 3Y_8 - \Theta_{x9}L_{89} - 2\Theta_{x8}L_{89}) - \frac{K_{48}L_{48}}{3J_{d4}^*} (3Y_8 - 3Y_4 - \Theta_{x8}L_{48} - 2\Theta_{x4}L_{48}) \\ \frac{K_{89}L_{89}}{3J_{d8}^*} (3X_9 - 3X_8 - \Theta_{y9}L_{89} - 2\Theta_{y8}L_{89}) - \frac{K_{48}L_{48}}{3J_{d4}^*} (3X_8 - 3X_4 - \Theta_{y8}L_{48} - 2\Theta_{y4}L_{48}) \\ -\frac{K_{89}}{M_9} (-2X_9 + 2X_8 + \Theta_{y9}L_{89} + \Theta_{y8}L_{89}) + \frac{K_{912}}{M_9} (-2X_{12} + 2X_9 + \Theta_{y12}L_{912} + \Theta_{y9}L_{912}) \\ -\frac{K_{89}}{M_9} (-2Y_9 + 2Y_8 + \Theta_{x9}L_{89} + \Theta_{x8}L_{89}) + \frac{K_{912}}{M_9} (-2Y_{12} + 2Y_9 + \Theta_{x12}L_{912} + \Theta_{x9}L_{912}) \\ \frac{K_{912}L_{912}}{3J_{d12}^*} (3Y_{12} - 3Y_9 - \Theta_{x12}L_{912} - 2\Theta_{x12}L_{912}) - \frac{K_{89}L_{89}}{3J_{d8}^*} (3Y_9 - 3Y_8 - \Theta_{x9}L_{89} - 2\Theta_{x8}L_{89}) \\ \frac{K_{912}L_{912}}{3J_{d12}^*} (3X_{12} - 3X_9 - \Theta_{y12}L_{912} - 2\Theta_{y12}L_{912}) - \frac{K_{89}L_{89}}{3J_{d8}^*} (3X_9 - 3X_8 - \Theta_{y9}L_{89} - 2\Theta_{y8}L_{89}) \\ -\frac{K_{912}}{M_{12}} (-2X_{12} + 2X_9 + \Theta_{y12}L_{912} + \Theta_{y9}L_{912}) \\ -\frac{K_{912}}{M_{12}} (-2Y_{12} + 2Y_9 + \Theta_{x12}L_{912} + \Theta_{x9}L_{912}) \end{bmatrix}$$

where m_i and M_i are the mass of disk and dimensionless mass of disk, respectively, k_i and K_i are the stiffness of shaft and dimensionless stiffness of shaft, respectively, c_i and C_i are the damping of disk and dimensionless damping of disk, respectively, $c_{\theta i}$ and $C_{\theta i}$ are the deflection damping of disk and dimensionless deflection damping of disk, respectively, J_{di} and J_{di}^* are the moment of inertia of disc diameter and dimensionless moment of inertia of disc diameter, respectively, J_{pi} and J_{pi}^* are polar moment of inertia of disc and dimensionless polar moment of inertia of disc, respectively, e_{ui} and E_{ui} are the eccentricity of disk mass and dimensionless eccentricity of disk mass, respectively, f_{si} and F_{si} are the dimensionless seal force and seal force, respectively, f_{bi} and F_{bi} are the dimensionless oil-film force and oil-film force, respectively, σ is the phase-difference of disk 8 and disk 9, r is the radius of bearing, ψ is the clearance ratio, $\psi = c/r$, l_i and L_i are

the span between disk and dimensionless span between disk, respectively, g and G are the acceleration of gravity and dimensionless acceleration of gravity, respectively, E is the elastic modulus, and I_i is the moment of inertia of cross-section of shaft.

As the moment of inertia of discs M_4 and M_{12} can be negligible, the rotation angle of disc 4 and disc 12 $\theta_{x4}, \theta_{y4}, \theta_{x12}, \theta_{y12}$ can be obtained through the bending moment equation and shear equation in the bending deformation formula of the beam. Assuming the left side and right side bending moment of disk 4 and disk 12 are equal, that is $M_4^R = M_{48}(0)$ and $M_{12}^L = M_{912}(l)$, then the expression of the rotation angle can be derived as follows:

$$\begin{cases} \theta_{x4} = (3y_8 - 3y_4 - \theta_{x8}l_{48})/(2l_{48}) \\ \theta_{y4} = (3x_8 - 3x_4 - \theta_{y8}l_{48})/(2l_{48}) \end{cases} \quad (2)$$

$$\begin{cases} \theta_{x12} = (3y_{12} - 3y_9 - 2\theta_{x9}l_{912})/l_{912} \\ \theta_{y12} = (3x_{12} - 3x_9 - 2\theta_{y9}l_{912})/l_{912} \end{cases} \quad (3)$$

Suppose

$$\begin{aligned} \lambda &= [\lambda_1, \lambda_2, \dots, \lambda_i, \dots, \lambda_{24}]^T \\ &= [x_4, \dot{x}_4, y_4, \dot{y}_4, x_8, \dot{x}_8, y_8, \dot{y}_8, \theta_{x8}, \dot{\theta}_{x8}, \theta_{y8}, \dot{\theta}_{y8}, x_9, \dot{x}_9, y_9, \dot{y}_9, \theta_{x9}, \dot{\theta}_{x9}, \theta_{y9}, \dot{\theta}_{y9}, x_{12}, \dot{x}_{12}, y_{12}, \dot{y}_{12}]^T \end{aligned}$$

then

$$\begin{aligned} \dot{\lambda} &= [\dot{\lambda}_1, \dot{\lambda}_2, \dots, \dot{\lambda}_i, \dots, \dot{\lambda}_{24}]^T \\ &= [\dot{x}_4, \ddot{x}_4, \dot{y}_4, \ddot{y}_4, \dot{x}_8, \ddot{x}_8, \dot{y}_8, \ddot{y}_8, \dot{\theta}_{x8}, \ddot{\theta}_{x8}, \dot{\theta}_{y8}, \ddot{\theta}_{y8}, \dot{x}_9, \ddot{x}_9, \dot{y}_9, \ddot{y}_9, \dot{\theta}_{x9}, \ddot{\theta}_{x9}, \dot{\theta}_{y9}, \ddot{\theta}_{y9}, \dot{x}_{12}, \ddot{x}_{12}, \dot{y}_{12}, \ddot{y}_{12}]^T \end{aligned}$$

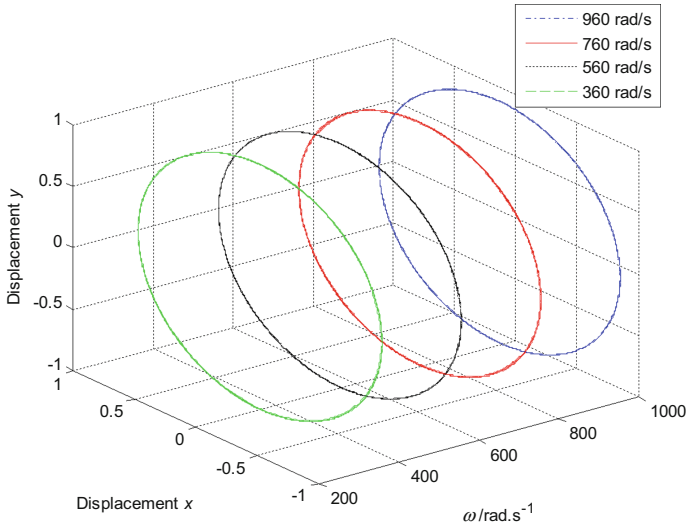
Thus, the Eq. (1) can be converted to a first-order equation.

2.2 Numerical Results and Discussion

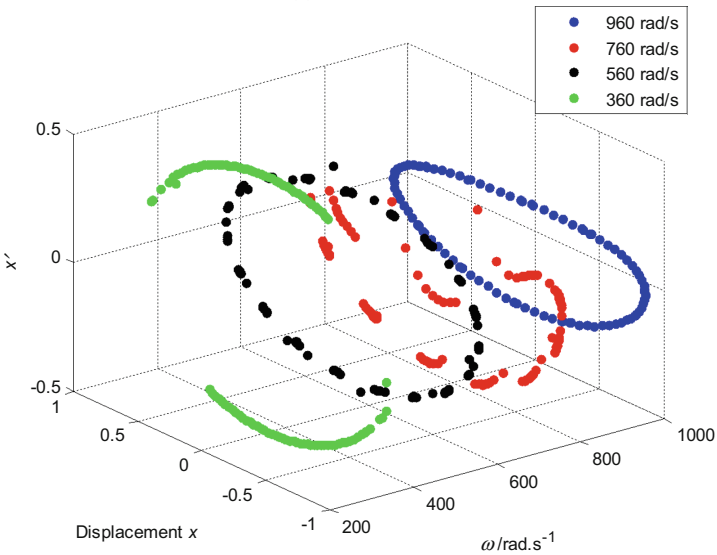
The fourth order Runge-Kutta method is adopted to solve the dimensionless equation of Eq. (1). And then the vibration response of the system under a certain parameter condition can be obtained and the response results can be analyzed. In order to make the selected parameters close to the actual structure of the gas turbine, the geometry parameters of the rotor-bearing-brush seal system are given as follows: $m_8 = 10000$ kg, $m_9 = 3200$ kg, $m_4 = m_{12} = 400$ kg, $k_{48} = 3.19 \times 10^8$ N/m, $k_{89} = 3.02 \times 10^8$ N/m, $k_{912} = 3.13 \times 10^8$ N/m, $l_{48} = 1.5$ m, $l_{89} = 2$ m, $l_{912} = 1.5$ m, $\mu = 0.02$.

The influence of the rotor speed on the response of the rotor-bearing-brush seal system usually is more obvious. Figures 2, 3, 4 and 5 show the axis orbit and Poincaré map of joint 4, joint 8, joint 9, and joint 12 with different rotor rotational speed, respectively. As observed in Figs. 2 and 5, the variation of amplitude versus rotor speed at the position of bearing is not obvious, and all of the axis orbits are regular ellipse. When the rotor speed is 960 rad/s, the Poincaré map of joint 4 and joint 12

presents a closed circle, which shows the system are in quasi-periodic motion. But when the rotor speed is 760 rad/s, the Poincaré map of joint 4 and joint 12 are discrete scattered points, which shows the system are in chaos motion and the system is unstable.

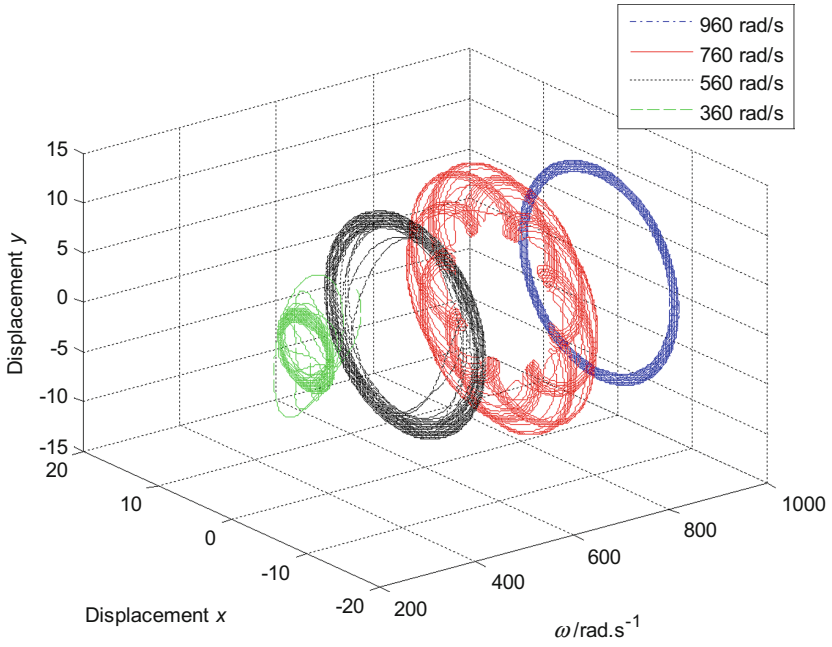


(a) Axis orbit.

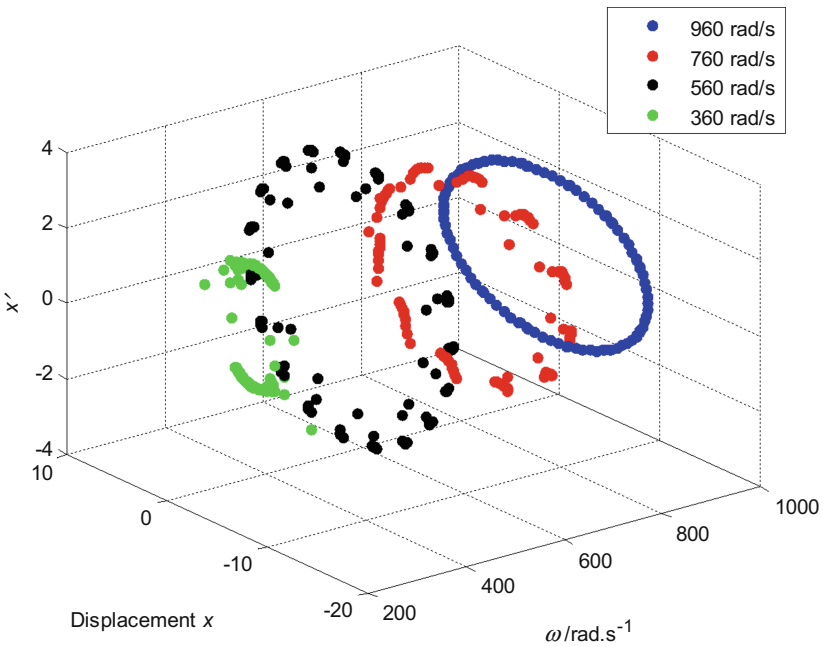


(b) Poincaré map.

Fig. 2. Axis orbit and Poincaré map of joint 4 with different rotor rotational speed.

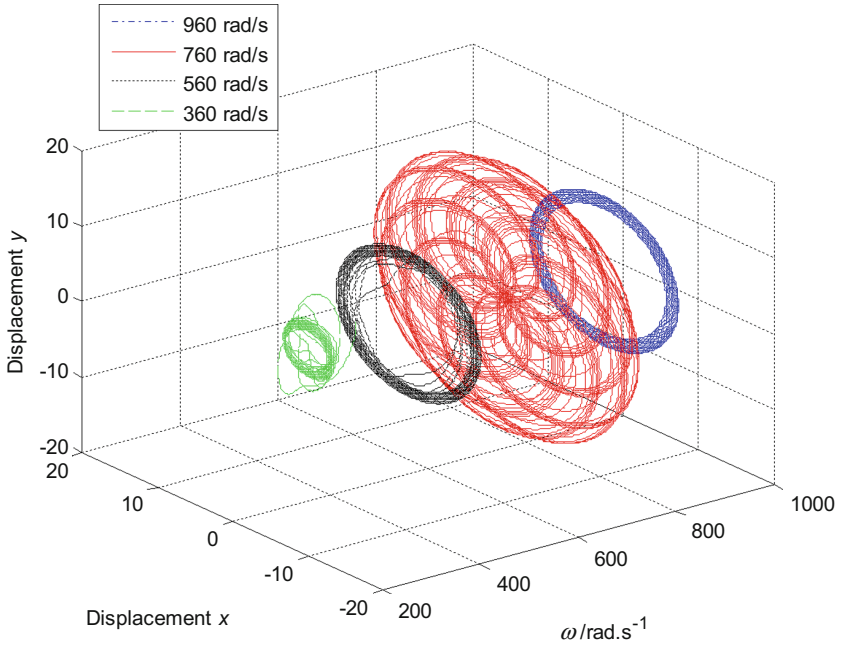


(a) Axis orbit.

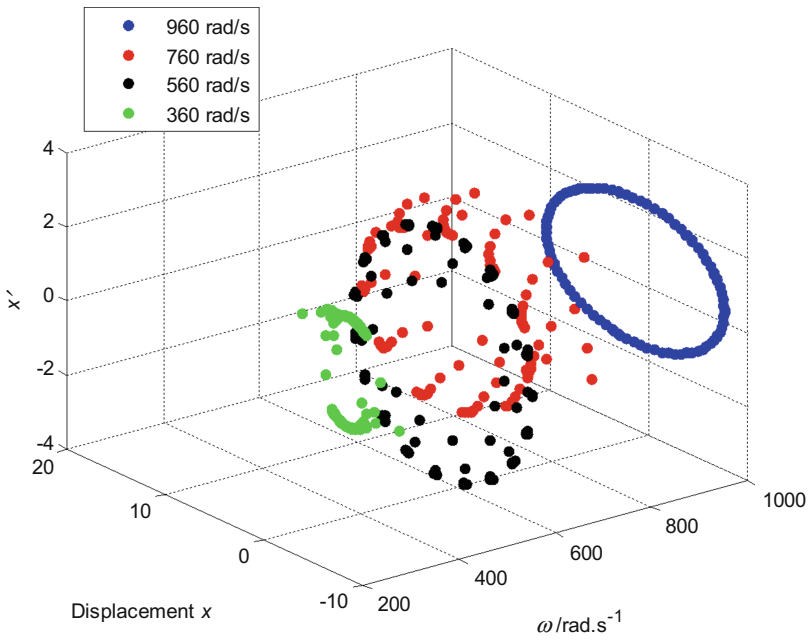


(b) Poincaré map.

Fig. 3. Axis orbit and Poincaré map of joint 8 with different rotor rotational speed.

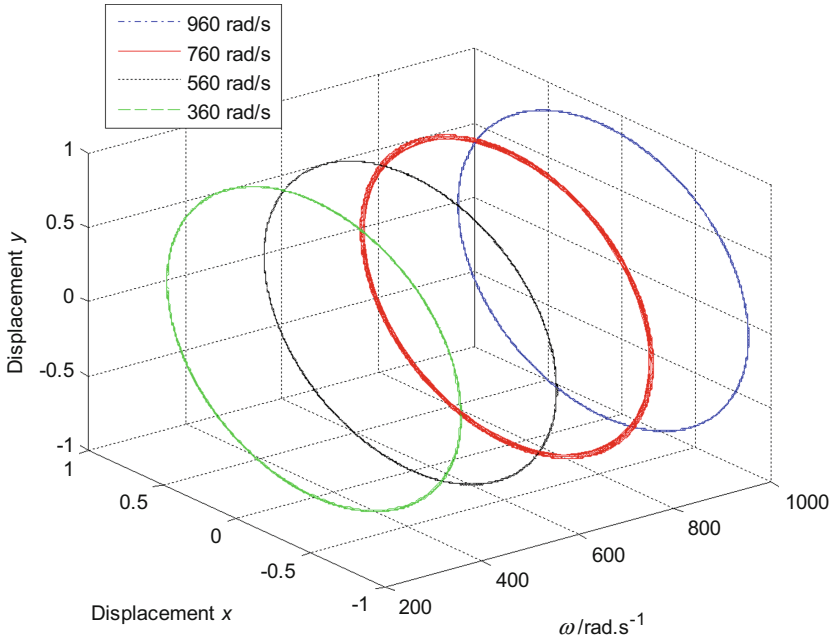


(a) Axis orbit.

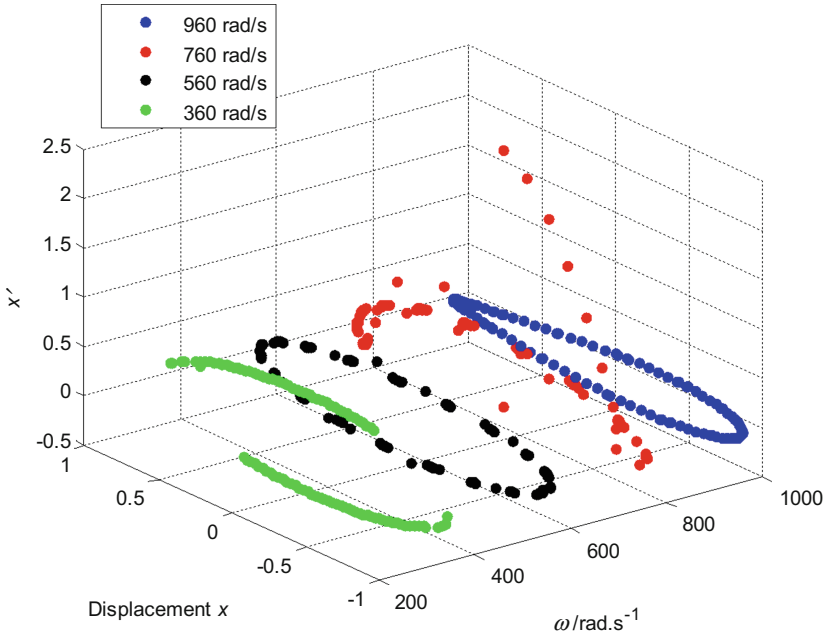


(b) Poincaré map.

Fig. 4. Axis orbit and Poincaré map of joint 9 with different rotor rotational speed.

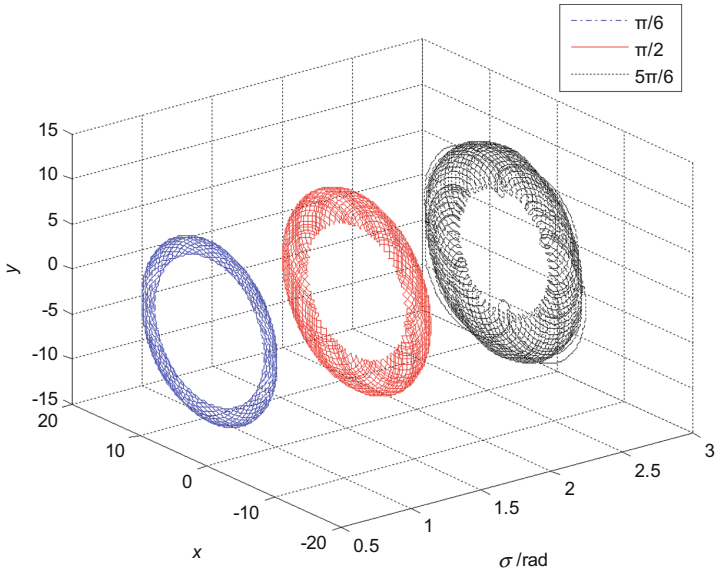


(a) Axis orbit.

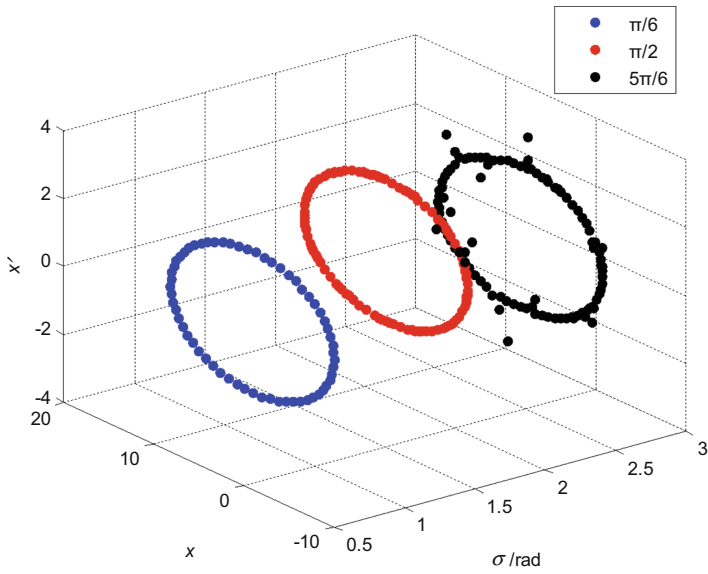


(b) Poincaré map.

Fig. 5. Axis orbit and Poincaré map of joint 12 with different rotor rotational speed.

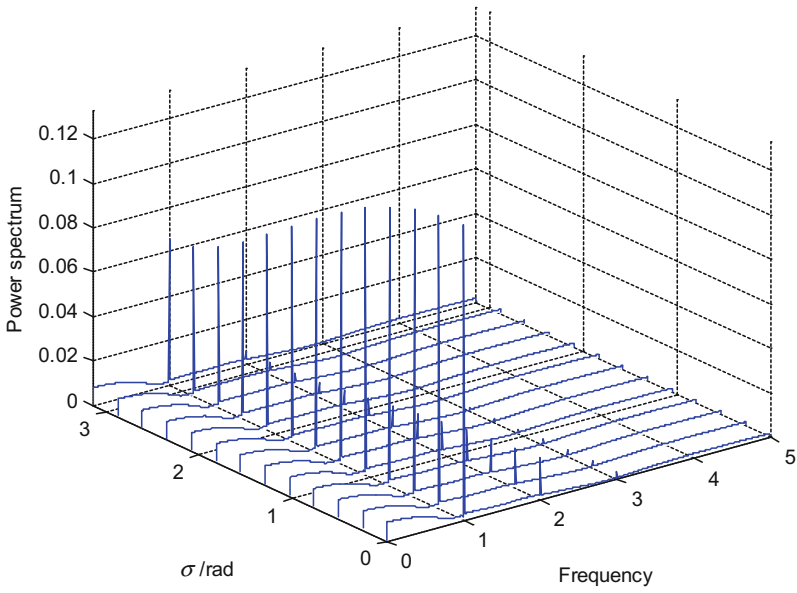


(a) Axis orbit.

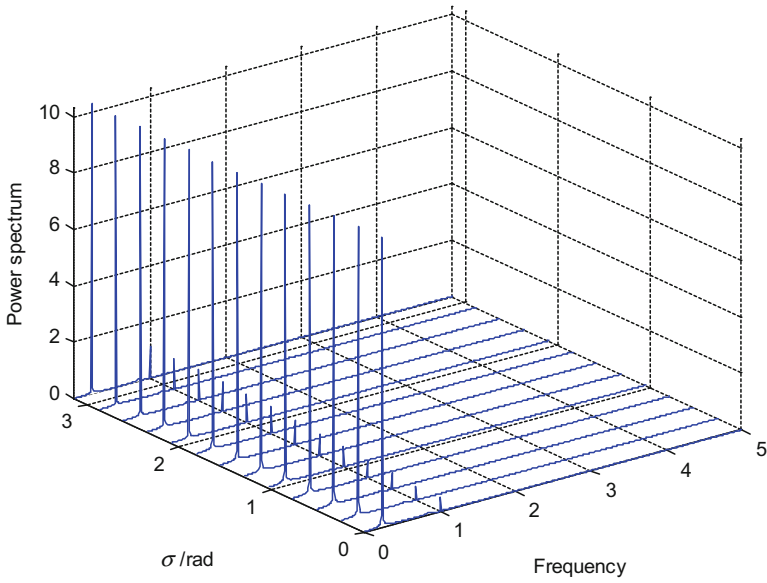


(b) Poincaré map.

Fig. 6. Axis orbit and Poincaré map with different eccentricity phase-difference when rotor rotational speed $\omega = 900 \text{ rad/s}$.



(a) Rotational speed $\omega=30$ rad/s.



(b) Rotational speed $\omega=900$ rad/s.

Fig. 7. Spectrum cascade with different eccentricity phase-difference.

As observed in Figs. 3 and 4, the amplitude at the position of disk increase with the rotor speed at first, and then decrease with the increase of rotor speed. The axis orbit of joint 8 and joint 9 is a circular ring, when the rotor speed is 360, 560, and 960 rad/s. And the Poincaré map of joint 8 and joint 9 is a closed ring when the rotor speed is 960 rad/s, which indicates the system are in quasi-periodic motion. But when the rotor speed is 760 rad/s, the axis orbit of joint 9 is irregular, which shows the system is in chaos motion.

The eccentricity phase-difference between the discs of joint 8 and joint 9 would affect the unbalanced force and the dynamic characteristics of the rotor system. Figure 6 shows the axis orbit and Poincaré map with different eccentricity phase-difference when rotor rotational speed is 900 rad/s. As observed in Fig. 6a, with different phase-difference, the axis orbits are circular ring, and the amplitude increases with the increase of the phase difference. As observed in Fig. 6b, when the phase-difference is $\pi/6$ and $\pi/2$, the Poincaré map is a closed ring, which indicates the system is in quasi-periodic motion. But when the phase-difference is $5\pi/6$, some scattered points are appeared around the closed circle in the Poincaré map, and the axis orbit tends to be unstable. Therefore, decrease the eccentricity phase-difference between two disks during installation is beneficial to the stability of the system.

Figure 7 shows the spectrum cascade as a function of the eccentricity phase-difference. As observed in Fig. 7a, when the rotor speed is 30 rad/s, the power spectrum at the position of fundamental frequency is much greater than other position. The frequency division gradually decreases from the initial position to the 1 times fundamental frequency, and some small frequency division appear at the position of 2 times and 3 times fundamental frequency. As observed in Fig. 7b, when the rotor speed is 900 rad/s, there is a larger frequency division at the position of 1/3 times fundamental frequency, but power spectrum is very small at the position of 1 times fundamental frequency.

3 Conclusions

In order to build the nonlinear dynamic model of a multi-disk rotor-bearing-brush seal system, the seal force model of brush seal and the nonlinear oil-film force model based on short bearing theory were adopted considering the lateral deflection of the disks. The influences of the rotor speed and eccentricity phase-difference on the dynamic response of a multi-disk rotor-bearing-brush seal system were discussed. The conclusions were drawn below:

1. The variation of amplitude versus rotor speed at the position of bearing is not obvious.
2. The amplitude at the position of disk increase with the rotor speed at first, and then decrease with the increase of rotor speed.
3. Decrease the eccentricity phase-difference of the rotor system between two disks during the installation is beneficial to the stability of the system.

Acknowledgments. The research is financially supported by National Natural Science Foundation of China (Grant Nos. 11272100, 11672083, 51575331).

References

1. Chupp, R.E., Raymond, E., Nelson, P.: Evaluation of brush seals for limited-life engines. *J. Propul. Power* **9**, 113–119 (1993)
2. Chupp, R.E., Loewenthal, R.G.: Brush seals can improve power plant efficiency by one-fourth of a percentage point yielding huge annual savings. *Lubr. Eng.* **53**(6), 10–14 (1997)
3. Muszynska, A.: *Rotordynamics*. CRC Taylor & Francis Group, New York (2005)
4. Vance, J.: *Machinery Vibration and Rotordynamics*. Wiley, Hoboken (2005)
5. Chupp, R.E., Hendricks, R.C., Lattime, S.B., Steinetz, B.M.: Sealing in turbomachinery. *J. Propul. Power* **22**(2), 313–349 (2006)
6. Chu, F., Lu, W.: Determination of the rubbing location in a multi-disk rotor system by means of dynamic stiffness identification. *J. Sound Vib.* **248**(2), 235–246 (2001)
7. Wan, Z., Jing, J., Meng, G., Yang, Y., Bai, H.: Theoretical and experimental study on the dynamic response of multi-disk rotor system with flexible coupling misalignment. *Proc IMechE Part C J. Mech. Eng. Sci.* **226**(12), 2874–2886 (2012)
8. Capone, G.: Orbital motions of rigid symmetric rotor supported on journal bearings. *La Mecc. Ital.* **199**, 37–46 (1986)
9. Capone, G.: Analytical description of fluid-dynamic force field in cylindrical journal bearing. *L'Energ. Elettr.* **3**, 105–110 (1991)
10. Wei, Y., Chen, Z., Dowell, E.H.: Nonlinear characteristics analysis of a rotor-bearing-brush seal system. *Int. J. Struct. Stab. Dyn.* **18**(5), 1850063-1–1850063-23 (2018)



Numerical Analysis of the Dead-Band Clearance Effect on the Vibrations of a Vertical Rotor

Lassad Amami, Mihai Arghir^(✉), and Pascal Jolly

Institut PPRIME, UPR CNRS 3346, Université de Poitiers, ISAE ENSMA,
11 bd. Pierre et Marie Curie, BP 30179,
86962 Futuroscope Chasseneuil Cedex, France
mihai.arghir@univ-poitiers.fr

Abstract. The present work tackles the dead band clearance problem of rotors guided by ball or roller bearings. There are situations when the rotor can be only temporary in contact with the casing. The closed-loose nature of the rotor-stator contact leads to a non-linear rotordynamic response. A test rig dedicated to the experimental analysis of this problem was presented in a previous paper [8]. The test rig is based on a vertical rotor guided by ball bearings and lifted by an aerostatic thrust bearing. The ball bearings are mounted with three different radial clearances: “small”, “medium” and “large”. The results for the low and mild radial clearances showed a linear behavior of the rotor characterized by synchronous responses with forward or backward whirls. A non-linear signature of the rotor was obtained for the large radial clearance with sub-synchronous bifurcations and internal resonances. The present paper presents the numerical analysis of the same rotor and is intended to reproduce the experimental results. The rotor was modeled with Timoshenko beam elements. Full non-linear calculations were performed by simulating a constant acceleration of the rotor from zero to 400 Hz in 50 s. Calculations showed that the value of the dead-band clearance is a capital parameter for triggering non-linear responses of the rotor.

Keywords: Rotordynamics · Dead-band clearance problem

1 Introduction

Ball and roller bearings guiding rotors are generally mounted with no radial clearance between the outer ring and the casing of the machine. However, there are situations when a small radial clearance is present. Therefore, when operating, the rotor may be only temporary in contact with the casing. The gap between the rotor and the casing might be closed or loose. This closed-loose nature of the rotor-stator contact leads to a non-linear rotordynamic response known as the dead-band clearance (DBC) problem. The literature shows that when present in a rotating machinery, a dead-band clearance triggers a typical non-linear response of the rotor.

A non-linear analytic model for investigating the influence of the radial clearance was developed by Yamamoto early in 1959 [1]. It was shown that an increase of the ratio between the radial clearance and the unbalance eccentricity lead to a decrease of

the rotor critical speed. Following this results, the DBC is associated with a modification of the critical speed. Childs performed a similar theoretical analysis [2]. His results confirmed Yamamoto's findings but also showed that the radial clearance between the outer ring of the ball bearings and the casing is the source of sub-synchronous vibrations. Moreover, Childs underlines that the amplitudes of sub-synchronous vibrations increase with increasing unbalance while the amplitudes of synchronous components decrease. Other theoretical analyses [3, 4] confirmed the previous findings, namely that the increase of the DBC decreases the critical speeds and the vibration amplitudes at critical speeds.

In 1993 Lin [5] presents a simple experimental test rig based on a slender rotor with a disk at its mid-length and guided by two ball bearings at its ends. The ball bearing situated at the non-drive end had an adjustable DBC. Sub-synchronous vibrations due to the DBC were measured when the rotation speed was close to twice the first critical frequency. The frequency of the sub-synchronous vibrations was constant and equal to the first critical frequency. The sub-synchronous vibrations were present only near the rotation speed equal to twice the first critical and disappeared once the rotation speed increases. Lin [5] considers that the sub-synchronous component is not a self-sustained vibration but a benign regime triggered by the DBC. This observation was also underlined in a slightly different context [6, 7].

A paper recently presented by Amami et al. [8] was focused on the experimental analysis of the DBC problem in a vertically mounted, complex rotor. The test rig components were designed for three values of the DBC (small, medium and large) but, due to manufacturing errors, the experiments enlightened a somewhat different situation. The results for the small and medium radial clearances showed a linear behavior of the rotor characterized by synchronous responses with forward or backward whirls. A non-linear signature of the rotor was obtained for the large radial clearance with sub-synchronous bifurcations and internal resonances.

The present paper presents the numerical analysis of the rotor tested in [8] and is intended to reproduce the experimental results. The rotor was modeled with Timoshenko beam elements and contacts between the rotor and the casing were modeled with a contact stiffness. Full non-linear calculations were performed by simulating a constant acceleration of the rotor from zero to 400 Hz in 50 s.

Calculations showed that the value of the dead-band clearance is a capital parameter for triggering non-linear responses of the rotor. The numerical results for zero clearance and anisotropic support stiffness reproduced qualitatively the linear responses evidenced by experimental findings for small and medium DBC. High amplitude, sub synchronous vibrations were obtained for non-zero values of the clearance.

2 Summary of the Experimental Results

2.1 Description of the Test Rig

Figure 1 depicts the rotor and its vertical installation in the test rig. The rotor has three disks. It is guided by two pair of ball bearings, by two aerostatic bearings, is supported

at its bottom end by an aerostatic thrust bearing and is entrained at its upper end by an impulse (Pelton) turbine. The aerostatic bearings replace the annular straight seals normally present in the rotating machine. They are strongly pressurized and they represent the only source of radial damping of the rotor. The thrust bearing lifts the rotor and enables its rotation with a minimal torque. It is mounted on a wire mesh damper for minimizing the amplitudes of any axial vibration that could interfere.

The ball bearings are mounted by pairs and are axially preloaded by a wave spring. They are mounted with a radial clearance between the outer rings and the casing of the test rig. The variation of this clearance is obtained by manufacturing the casing parts of the test rig with different inner diameters. Each disk of the rotor is provided with two inductive, orthogonally mounted displacements probes. An optical probe and a mark on the top disk measure the rotation speed and the reference phase.

2.2 Experimental Results

Experimental results were obtained in [8] with three different radial clearances between the outer rings and the casing of the test rig. These clearances are designated as “small”, “medium” and “large”. Tests were performed by entraining the rotor up to 400 Hz followed by a free coast down.

Figure 2 depicts the full spectrum plots recorded on the upper (# 1) and on the lower disk (# 3) for the “small” DBC during acceleration from 0 to 400 Hz. The vibration amplitudes of the middle disk (# 2) are much lower because it is mounted very close to the node of the rigid conical mode. Therefore, for brevity, the results obtained for this disk are not presented.

The presence of only the synchronous component on Fig. 2 indicates a linear response of the rotor. This means that the outer ring of the ball bearings is continuously in contact with the casing. The explanation of this result is the fact that the “small” DBC was eliminated by the manufacturing errors.

The full spectrum diagrams show distinct zones of forward and backward whirls. The switch from forward to backward whirl and again to forward whirl occurs when the direct stiffness of the support is anisotropic. This means that the contact conditions of the outer rings of the ball bearings with the casing are anisotropic.

The results obtained with the “medium” DBC, twice larger than the previous one are depicted in Fig. 3 and show the same linear response. However, the backward precession is present on a shorter interval and for lower values of the rotation frequency. This means the contact stiffness decreased following the increase of the DBC from “small” to “medium”.

The results obtained with the “large” DBC, three times larger than the “small” DBC are depicted in Fig. 4. A net clearance between the outer rings of all ball bearings and the casing is now obtained. The diagrams show a clear non-linear response. A first critical frequency close to 140 Hz following X and Y is detected. This critical frequency was close to 230 Hz for the “small” DBC, decreased to 160 Hz for the “medium” DBC and was identified only following the X direction. A second critical speed following the Y direction is visible at 220 Hz. This critical speed was identified close to 320 Hz for the “small” DBC and decreases to 225 Hz for the “medium” DBC.

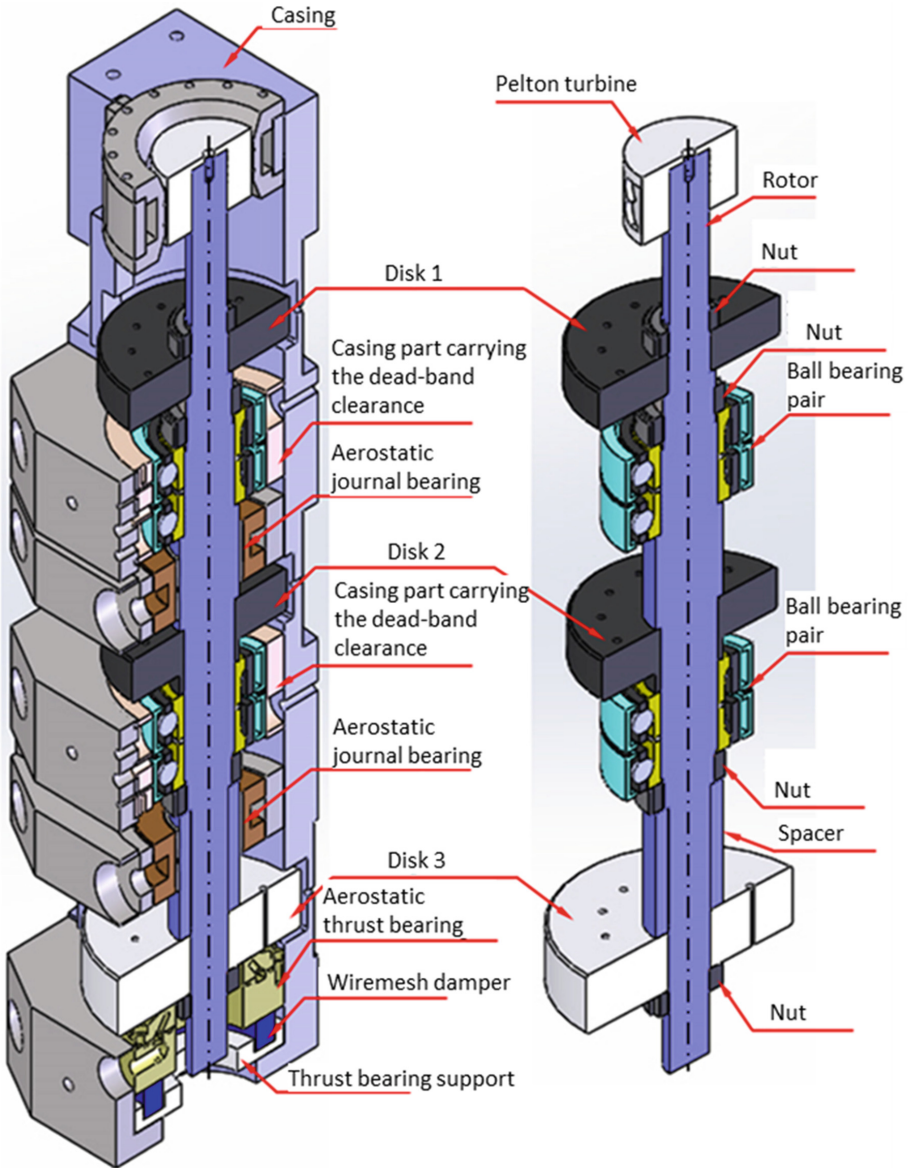


Fig. 1. The rotor and its installation in the test rig [8]

The critical speeds identified for the “large” DBC are systematically lower than those identified for the “small” and “medium” DBC. For rotation frequencies higher than 220 Hz, the response is clearly non-linear, the results showing a bifurcation followed by sub-synchronous vibrations. A clear sub-synchronous component detaches at a rotation frequency close to 220 Hz. This component becomes rapidly vertical and of large amplitude, its frequency being fixed at a constant value comprised between 130 and 140 Hz and corresponding to the first critical speed.

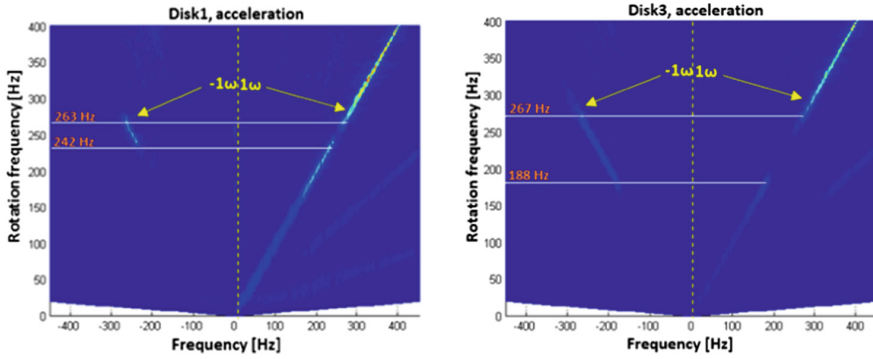


Fig. 2. Full-spectrum plot for the «small» DBC [8]

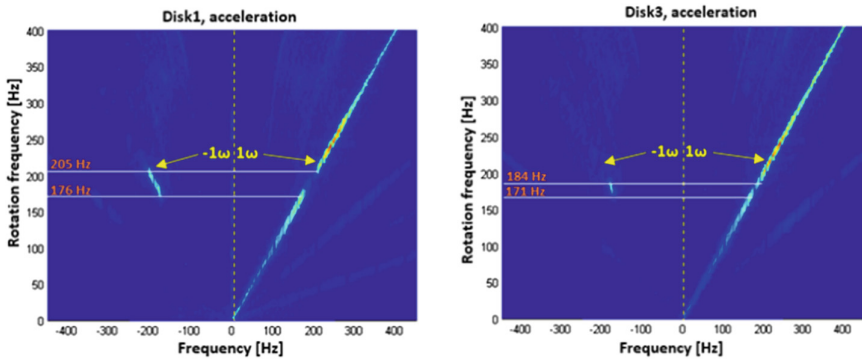


Fig. 3. Full-spectrum plot for the «medium» DBC [8]

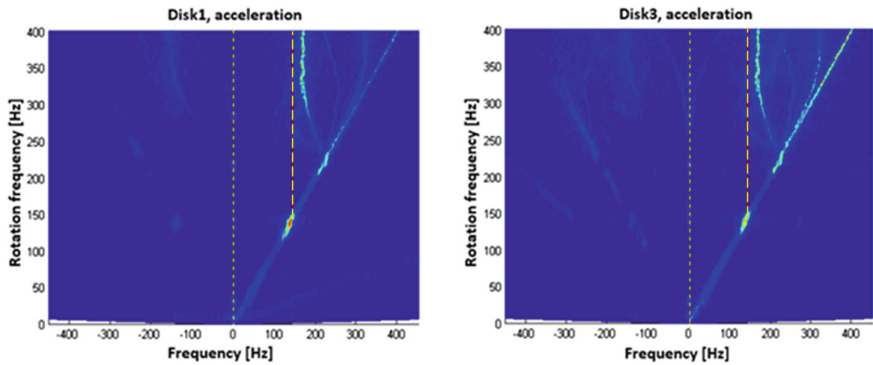


Fig. 4. Full-spectrum plot for the «large» DBC [8]

3 Rotor Model

The rotor was modeled with Timoshenko beam elements. The ball bearings and the contacts were modeled with a contact stiffness as further indicated in Sects. 4.1 and 4.2.

Rayleigh damping was added to the rotor model after experimental tests. As indicated in Fig. 5a, impacts were applied at one end of the suspended rotor and acceleration responses were measured on the second disk. The frequency response is depicted in Fig. 5b. Modal damping was identified by using the half power method and the approximation of Rayleigh damping is depicted in Fig. 6.

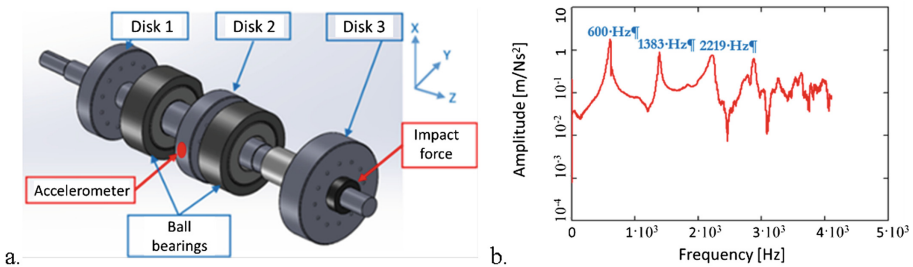


Fig. 5. Frequency response of the suspended (free-free) rotor

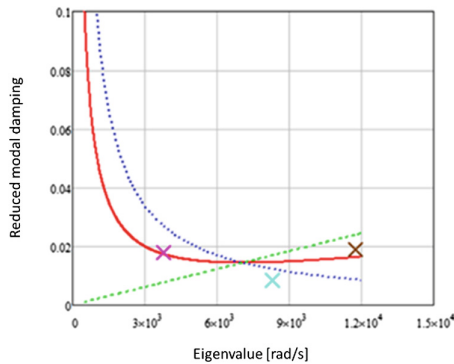


Fig. 6. Approximation of the Rayleigh damping

4 Numerical Analysis

The numerical simulation of this DBC problem is a quite difficult task due to the large number of unknown parameters that must be selected and triggered. The simulation is performed in two steps: first for the “small” and “medium” DBC where, due to manufacturing errors, the non-linear response was not present and then for the “large” DBC.

4.1 Results for the “Small” and “Medium” DBC

As mentioned, for the “small” and “medium” DBC configurations, the experimental results showed a linear response of the rotor. This was a clear indication that the outer rings of the ball bearings were constantly in contact with the casing and no DBC was present. However, the contact stiffness proved to be anisotropic because the results enlightened two conical modes, following X and Y and a shift from forward to backward and again to forward whirl. After trials, a value of $2.5 \cdot 10^6$ N/m was adopted for the X stiffness of each ball bearing and 10^7 N/m for the Y stiffness. These parameters were further refined by adopting a $3.5 \cdot 10^6$ N/m value for the X stiffness of the lower pair of ball bearings depicted in Fig. 1. The two aerostatic bearings were considered to have a direct stiffness of $2.6 \cdot 10^6$ N/m; their cross coupling stiffness and direct damping was discarded. Full non-linear calculations were performed by simulating a constant acceleration of the rotor from zero to 400 Hz in 50 s. Estimating the unbalance amount is also difficult. After trials and comparisons with the experimental results, two 1.5 g mm unbalances were added at the ends of the rotor with a 120° phase difference.

The results are depicted in Figs. 7 and 8 for disks 1 and 3.

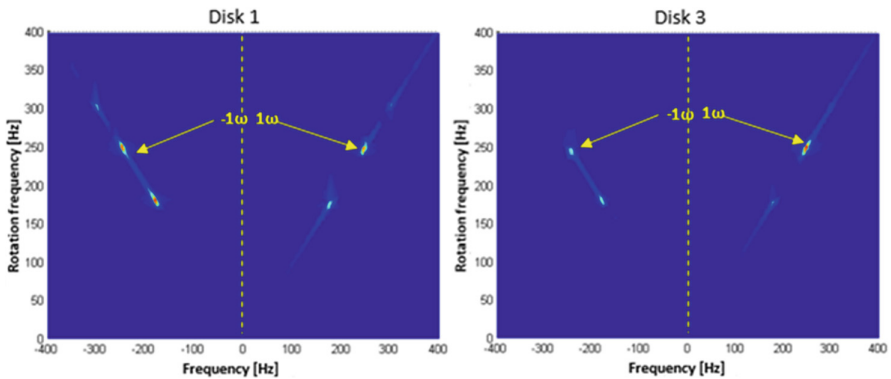


Fig. 7. Numerical full-spectrum plots obtained for the rotor model without DBC

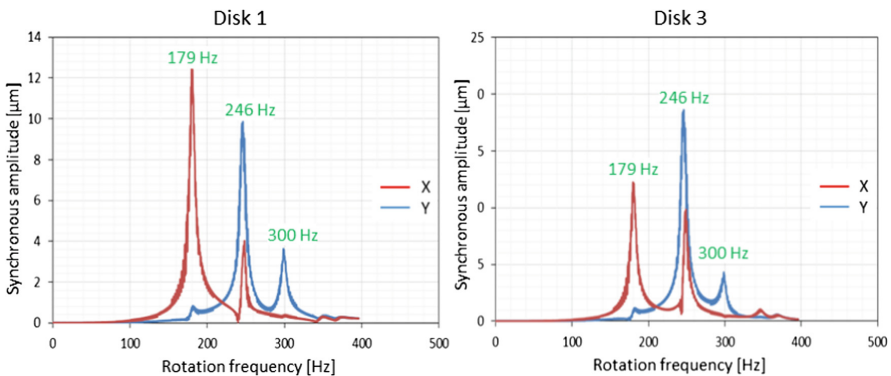


Fig. 8. Synchronous amplitudes obtained for the rotor model without DBC

The full-spectrum diagrams depicted in Fig. 7 clearly show the backward whirl. The disks 1 and 3 show a forward whirl from 0 to 179 Hz, a backward whirl between 179 and 246 Hz and again a forward whirl up to 400 Hz. The synchronous amplitudes of the disks depicted in Fig. 8 enable also to identify the X and Y modes. These plots are close to the experimental results obtained for the “small” DBC depicted in Fig. 2.

4.2 Results for the “Large” DBC

The experimental results obtained for the “large” DBC showed a different, non-linear signature. The loose contact between the outer rings of the ball bearings and the casing was modeled by imposing a radial clearance and a contact stiffness of 10^{12} N/m. If the radial displacement of the corresponding discretization node is lower than the radial clearance, then no force is imposed, otherwise the contact stiffness becomes active. No friction arising from contact was considered. This is a realistic assumption because the outer rings of the ball bearings can freely rotate. The value of the radial clearance was the same in X and Y directions and for all ball bearings. The values of the other parameters were the same as for the “small” and “medium” DBC and calculations were again performed by simulating a constant acceleration from zero to 400 Hz in 50 s.

Figure 9 depicts the results obtained with values of the DBC from 5 to 20 μm . Results obtained with a DBC of 5 μm show two synchronous amplitude peaks at 125 and 170 Hz and two corresponding sub-synchronous components starting with 300 Hz. A backward whirl regime is also present in the response of disk 3. The results are similar for a DBC of 10 μm but a chaotic regime is present for rotation frequencies comprised between 170 and 280 Hz. Moreover, the backward whirl regime vanishes. Following the increase of the DBC at 15 μm , the 170 Hz synchronous amplitude peak of disk 1 disappears with but remains present on disk 3. The chaotic regime is still present but on a lesser extent. The chaotic regime disappears with the further increase of the DBC at 20 μm . Two amplitude peaks are identified on disk 3 at 125 and 190 Hz and a single peak on disk 1 at 125 Hz. The chaotic regime is absent and sub-synchronous vibrations of constant frequency are triggered at 125 and 190 Hz. In all cases, the amplitudes of the sub-synchronous vibrations are very large if not dominant.

A 12 μm value of the DBC gave the closest agreement with the experimental results depicted in Fig. 4. The theoretical full spectrum diagrams of the amplitudes are depicted in Fig. 10. The diagrams show no backward whirl. A first amplitude peak is identified at 120 Hz for both disks; a second peak appears at 170 Hz but only for the disk 3. These values are lower than the frequencies of the corresponding modes underlined for the “small” and “medium” DBC. A sub synchronous component is visible on disk 1 for rotation frequencies larger than 120 Hz followed by a quasi-periodic regime after 170 Hz. Two sub synchronous components appear for disk 3, triggered at rotation frequencies of 120 and 170 Hz. Figure 11 depicts the synchronously filtered amplitudes. It should be underlined that for rotation frequencies larger than 120 and 170 Hz, when the regime is highly non-linear, a large percentage of energy is carried by the sub synchronous components (i.e. their amplitudes are larger than the synchronous ones).

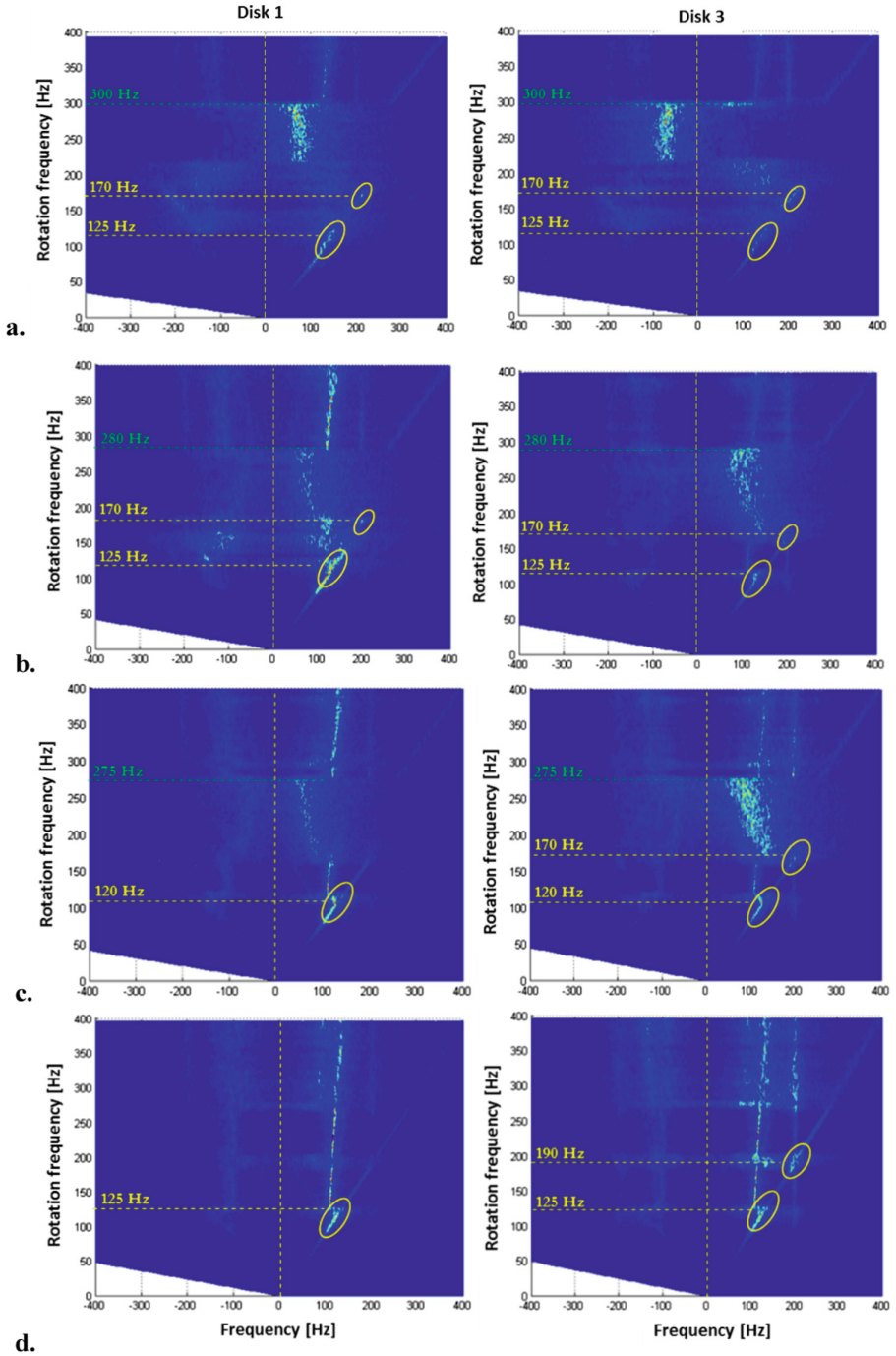


Fig. 9. Parametric analysis of the impact of the DBC (a. 5 μm , b. 10 μm , c. 15 μm , d. 20 μm)

The comparison between Figs. 4 and 10 shows only a limited agreement. This is due to the large number of parameters that must be selected and carefully triggered. A systematic parametric analysis including also the contact stiffness can be found in [9].

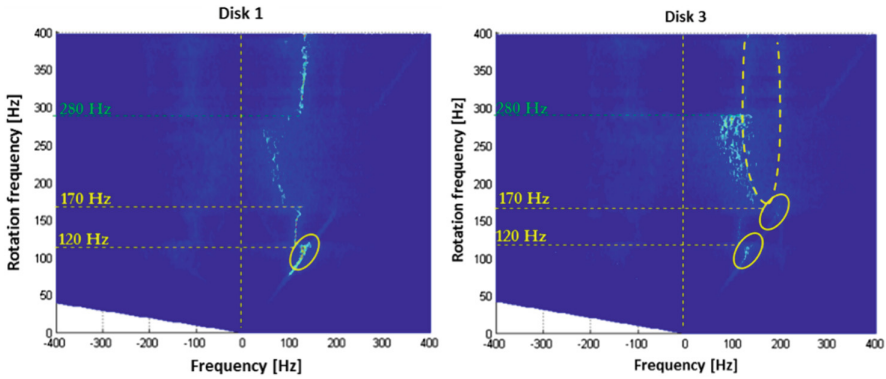


Fig. 10. Numerical full-spectrum plots obtained for the rotor model with a 12 μm DBC

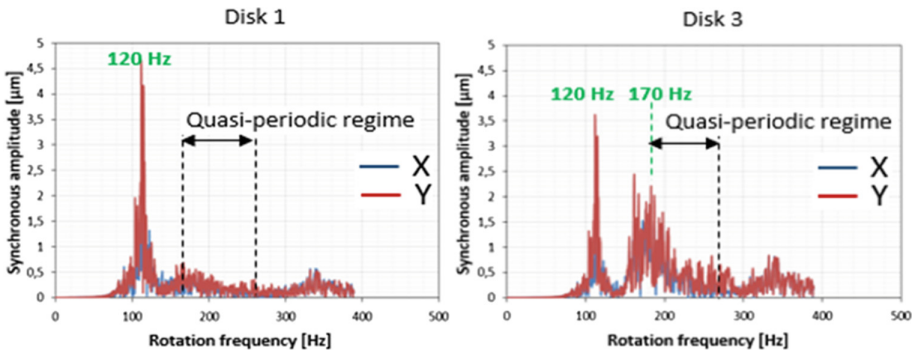


Fig. 11. Synchronous amplitudes obtained for the rotor model with a 12 μm DBC

5 Summary and Conclusions

The paper presents the impact of the DBC on the dynamic response of a complex rotor. Two pairs of ball bearings guided the vertically mounted rotor. Numerical results were obtained by performing a full non-linear analysis with a traditional rotordynamic model. The analysis was performed for a case with no DBC but with anisotropic stiffness and for cases with DBC comprised between 5 and 20 μm . The results show that the value of the DBC is a capital parameter: high amplitude, sub synchronous vibrations or chaotic regimes can be triggered depending on the value of this clearance.

It was found that the results obtained with a DBC of 12 μm agree qualitatively with the test rig measurements for the “large” radial clearance. They also confirm the

theoretical predictions from the references discussed in the introduction part of the paper, namely, the presence of the DBC lowers the critical frequencies and triggers a non-linear response with high amplitude sub-synchronous components. The numerical simulations also underline the multitude of parameters that must be introduced into a rotordynamic model for correctly simulating non-linear responses, the value of the dead-band clearance being of capital importance.

Acknowledgements. The authors are grateful to Centre National d'Etudes Spatiales and to Airbus Safran Launchers for supporting this work.

References

1. Yamamoto, T.: On Critical Speeds of a Shaft. *Memoirs of the Faculty of Engineering, Nagogo University*, vol. 6, no. 12 (1959)
2. Childs, D.W.: Fractional frequency rotor motion due to non-symmetric clearance effects. *J. Eng. Power* **104**, 533–541 (1982)
3. Gogging, D.G., Darden, J.M.: Limiting critical speed response on the SSME alternate high pressure fuel turbopump (ATD HPFTP^o with bearing deadband clearance). 28th Joint Propulsion Conference and Exhibit, Nashville (1992)
4. Butner, M.F., Murphy, B.T., Akian, R.A.: The influence of mounting compliance and operating conditions on the radial stiffness of ball bearing: analytic and test results. *ASME, DE-Vol. 35, Rotating Machinery and Vehicle Dynamics*, pp. 155–162 (1991)
5. Lin, Y.-Q.: Rotor instability induced by deadband clearance in bearing supports. Ph.D. thesis, Texas A&M University, USA (1993)
6. Rahul, K.: Diagnostics of subsynchronous vibrations in rotating machinery - methodology to identify potential instability. MS thesis, Texas A&M University, USA (2005)
7. Rajagopalan, V.N.: Diagnostic subsynchronous vibration turbomachinery - stable or unstable. MS Thesis, Texas A&M University, USA (2007)
8. Amami, L., Arghir, M., Jolly, P.: Experimental analyses of the dead-band clearance effect on the vibrations of a vertical rotor, *IMEchE VIRM 4*, Manchester, UK (2016)
9. Amami, L.: Analyse expérimentale de la réponse dynamique d'un rotor vertical guide par des roulements avec jeu. Thèse de doctorat, Université de Poitiers, France (2016)



A Case Study of the Contact Force and Stress in the Backup Bearing of a Generator: Experimental Study and Numerical Simulation of Dropdown

Neda Neisi¹  , Behnam Ghalamchi^{1,2}, Janne E. Heikkinen¹, Teemu Sillanpää¹, Toni Hartikainen³, and Jussi Sopanen¹

¹ Lappeenranta University of Technology,
Skinnarilankatu 34, 53850 Lappeenranta, Finland
neda.neisi@lut.fi

² Department of Mechanical Engineering,
Laboratory of Unmanned Aerial Robotics, University of California, Berkeley,
2000 Carleton Street, Berkeley, CA 94720-2284, USA

³ Aurelia Turbines, Höyläkatu, 1, 53500 Lappeenranta, Finland

Abstract. This paper presents both experimental and numerical study on the dropdown of a generator rotor in a two-stage radial gas turbine utilizing AMB system. The simulation unifies the FE-model of the flexible rotor and the dynamic model of backup bearings. The system under investigation includes a flexible rotor, an axial and two radial AMBs and two backup bearings, double row angular contact ball bearings. The recorded behavior of the studied rotor in the sudden failure of the electromagnetic field is demonstrated. Furthermore, the fine-tuned rotor-system model is used for studying the contact force and the contact stress in the backup bearing. The comparison between the measured results and the simulated results confirms that the used simulation tool can be applied for the design consideration of rotor-backup bearing system and enables to investigate the effect of various design parameters on the dynamic behavior of rotor in the dropdown.

Keywords: Backup bearing · Rotor · Dropdown

1 Introduction

Applying active magnetic bearing (AMB) system in high-speed turbomachinery has numerous advantages in preference to utilizing the conventional mechanical bearing. In order to avoid fatal failure in loss of electromagnetic field principally because of the electric short circuit and the fault in the control system, these machineries are equipped with the backup bearings to secure the rotor and AMB components, mainly the radial actuators and position sensors, from the damages in the dropdown. The backup bearings bear the high contact load and a friction rub. The backup bearing can be also known as either auxiliary bearing or touchdown bearing. During the last years, several researches have been conducted on the simulation of the dropdown. In the study of

Kärkkäinen et al. [1] the contact forces and friction force during the dropdown has been demonstrated. The contact of the rotor and backup bearing, open-loop, and closed-loop control system for AMB as well as transient analysis of the temperature in the rotor drop have been also discussed in the papers presented by Keogh [2, 3]. Recently, Liu et al. [4] developed a numerical model based on signal processing to recognize the complete rub of the rotor, bounce of the rotor after the contact with backup bearing and the pendulum movement of the rotor.

In the design aspect of the backup bearing, it is essential to decrease the deformation of the backup bearing and maintain the maximum stress in bearing below the endurance limit for the stress in the bearing. There are a limited number of studies about the contact stress in the backup bearing [5, 6]. Sun [5] applied the Lundberg-Palmgren theory to evaluate the fatigue life of the backup bearing. This theory specifically can be used for the steady state condition of the bearing. Lee and Palazzolo [6] considered the stress counting method, rainflow method, for calculation of the fatigue life of the backup bearing. Besides that, the effect of the off-sized ball in the contact stress of the backup bearing has been studied by Neisi et al. [7]. Above study indicated that the dimension and location of the off-sized ball/balls can influence the contact stress in the backup bearing. Apart from this several researches have been conducted on the thermal analysis of backup bearings [8–10].

Most of the available studies on the AMB supported rotors are devoted to the numerical simulation of dropdown and few publications can be found studied the rotor dropdown both experimentally and numerically. An experimental study on the dropdown test by Schmied and Pradetto [11] showed that because of the time lag in the control system, the electromagnetic force might exist in the machine. Therefore, the results of the simulation can be different compared to the recorded behavior of the rotor in the test bench. The comparison between the measured and the simulated results can be used for the design consideration of rotor-backup bearing system and enables to evaluate the influence of various design parameters on the dynamic behavior of rotor in the dropdown and still needs to be studied. For this reason, this work presents both experimental and numerical study on the dropdown of a generator rotor in a two-stage radial gas turbine employing AMB system. The unit composed of LP and HP rotors operating at supercritical speed. This work concentrates on the study the dropdown of LP rotor. The normal operation speed of both rotors is 550 Hz and the unit generates up to 400 kW electric power. The FE-model of the rotor is validated with the experimental modal analysis. The system under investigation includes a flexible rotor, an axial and two radial AMBs and two backup bearings, double row angular contact ball bearings. In this study, the recorded behavior of the studied rotor in sudden failure of the electromagnetic field is demonstrated. The description of the support stiffness and friction coefficients in the bearings are fine-tuned in the rotor model to meet the measured results during the dropdown. In addition, the fine-tuned rotor-system model is used for studying the contact force and contact stress in the backup bearing. Furthermore, the rotor orbit and the displacement of the rotor during the dropdown are featured.

2 Model of Rotor and Backup Bearing

Figure 1 shows the rotor under investigation. The rotor is modeled using shear deformable beam elements. In a rotor dropdown, the backup bearing supports the rotor by nonlinear contact load. The equation of motion is as follows [12]:

$$\mathbf{M}\ddot{\mathbf{X}} + (\mathbf{C} + \omega\mathbf{G})\dot{\mathbf{X}} + \mathbf{K}\mathbf{X} = \omega^2\mathbf{F}_1 + \mathbf{F}_2 \tag{1}$$

where \mathbf{M} , \mathbf{C} , \mathbf{K} , and \mathbf{G} are mass, damping, stiffness and gyroscopic matrix, respectively. \mathbf{X} is the vector of the generalized coordinate. The vector \mathbf{F}_1 is the vector of nodal unbalance and \mathbf{F}_2 represents the vector externally applied forces. The angular velocity of the rotor is ω .

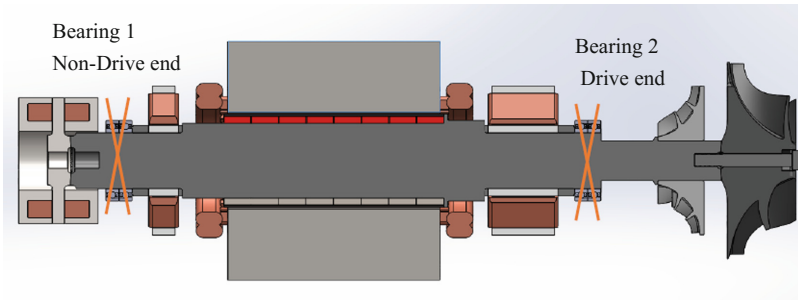


Fig. 1. Rotor under investigation

Applying a pair of angular contact ball bearings as backup bearings enable to take the advantage of the ability of backup bearing to withstand both the axial and radial loads, low friction, lubricant free and compact size. The backup bearings are considered as consumable parts. After several dropdowns, because of the high contact forces and mechanical rub, it is required to replace them. The model for the backup bearing, duplex pair of angular contact ball bearing, is developed on the basis of the ball bearing model introduced by Sopianen and Mikkola [13]. The bearing forces are calculated based on the bearing geometry, material property and the deformation of the bearing in the dropdown. In the model, the relative displacement between races is given by:

$$\begin{aligned} e_j^r &= e_x \cos \beta_j + e_y \sin \beta_j \\ e_j^t &= e_z - (\psi_x \sin \beta_j + \psi_y \cos \beta_j)(R_{in} + r_{in}) \end{aligned} \tag{2}$$

where $e_{x,y,z}$ represent the relative displacements of the bearing races (Fig. 2), and ψ_x and ψ_y show the tilting of the inner race in x , y -axis. β_j is the attitude angle of j^{th} ball. Thus, the distance between the races can be calculated as follows:

$$D_j = r_{out} + r_{in} - \frac{R_{in} + r_{in} + e_j^r - R_{out} + r_{out}}{\cos \varphi_j} \tag{3}$$

where φ_j is the contact angle.

$$\varphi_j = \tan^{-1} \left(\frac{e_j^t}{R_{in} + r_{in} + e_j^r - R_{out} + r_{out}} \right) \quad (4)$$

where R_{in} and r_{in} represent the inner race radius and inner race groove radius, correspondingly.

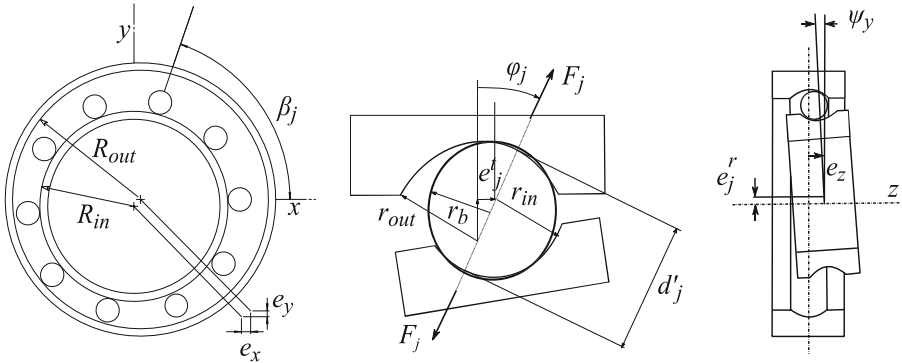


Fig. 2. Ball bearing model

The following equation expresses the total elastic deformation of the inner ring.

$$\delta_j^{tot} = d_j - D_j \quad (5)$$

The Hertzian contact theory has been used for the calculation of the contact force in the dropdown. Where the contact force between ball j^{th} and the inner race is as follows [12]:

$$F_j = K_c^{tot} \left(\delta_j^{tot} \right)^{3/2} \quad (6)$$

where the total contact stiffness is denoted as K_c^{tot} [13].

2.1 Model of the Contact Between Rotor and Backup Bearing

The contact between the rotor and backup bearing is modeled based upon the modified Hertzian contact model [1]:

$$F_r = \begin{cases} K \delta^{10/9} \left(1 + (3/2) \lambda \dot{\delta} \right); & e_r > c_r \text{ and } F_r > 0 \\ 0; & e_r \leq c_r \text{ and } F_r \leq 0 \end{cases} \quad (7)$$

where K represents the contact stiffness between the rotor and inner race and λ , is a contact parameter. In above equation, the penetration of the rotor in the backup bearing can be calculated as follows:

$$\delta = e_r - c_r \tag{8}$$

where c_r is the radius of the air gap between the rotor and backup bearing, and the radial displacement of the rotor is denoted as e_r [1].

The friction force between the rotor and backup bearing can be obtained by:

$$F_\mu = \mu F_r \tag{9}$$

where μ is the friction coefficient and the detailed calculation of the friction coefficient is described in the study of Kärkkäinen et al. [1]. In the model, the coordinate system in the FE-model of rotor and bearing model are mapped together.

2.2 Model of Contact Stress in Backup Bearing

The design of the backup bearing requires to evaluate the contact load, deformation of the bearing and make sure that the stress carried by backup bearings does not exceed the maximum allowable stress for bearings. The Hertzian contact model can be implemented for the calculation of the contact stress in the backup bearing. In this method, the stress can be calculated from the projection of elliptic contact area between the ball and bearing race. The highest stress can be found at the at the geometrical contact area [14]:

$$\sigma_{\max} = \frac{3Q_j}{2\pi ab} \tag{10}$$

where the semi-major and minor axes of the elliptic contact are denoted as a and b , correspondingly.

3 Case Studies and Results

The parameters required to analyze the case study of the rotor are shown in Table 1. The FE-model of the rotor is depicted in Fig. 3. The backup bearings are a pair of angular contact ball bearings type XCB71914-E-2RSD-T-P4S-U (Schaeffler) mounted in X-arrangement. The parameter used for the supports is shown in Table 2.

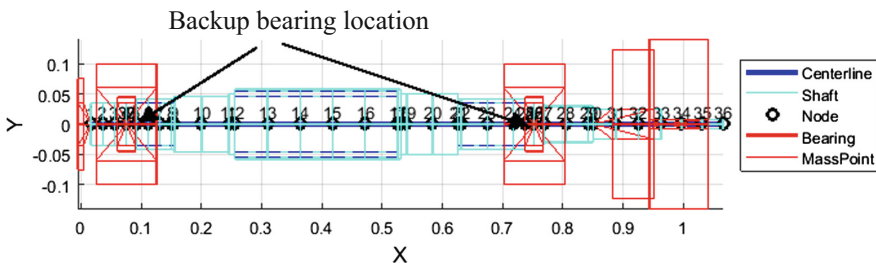


Fig. 3. The main dimensions and finite element model of the rotor.

Table 1. The main data for the simulation of the rotor dropdown

Initial rotation speed of the rotor	60 Hz
Modulus of elasticity	$2.0 \cdot 10^{11}$ Pa
Mass of rotor	59.5 kg
Poisson's ratio	0.3
Contact stiffness between rotor and backup bearings	$2.4 \cdot 10^9$ N/mm ^{1.11}
Air gap	250 μ m
Unbalance mass at Non drive end of generator active part	$4.4 \cdot 10^{-6}$ kg m @ 0°
Unbalance mass at drive end of generator active part	$4.4 \cdot 10^{-6}$ kg m @ 0°
Unbalance mass at compressor impeller	$0.6 \cdot 10^{-6}$ kg m @ 0°
Unbalance mass at turbine impeller	$3.1 \cdot 10^{-6}$ kg m @ 0°
Static contact friction coefficient between rotor and inner race	0.15
Dynamic contact friction coefficient between rotor and inner race	0.1

Table 2. The parameters used for rigid and soft supports

Mass	5 kg
Stiffness	$2.4 \cdot 10^9$ N/m
Damping	$2.8 \cdot 10^3$ Ns/m

The mass properties of the compressor and turbine impellers are shown in Table 3. In the FE-model of the rotor, the impellers are modeled as mass points and they are connected to the rotor by spring model.

Table 3. Mass properties of the impellers

	Compressor	Turbine
Material	Aluminum alloy 7075-T6	Heat resistant alloy steel
Mass (kg)	2.7	9.9
Center of mass x, y, z (m)	0, 0, 0.0648	0, 0, 0.03749
Moment of inertia Id, Ip (kg m ²)	0.0197, 0.0126	0.0436, 0.0449

3.1 Orbital Motion of Rotor

Figure 4 features the rotor orbit at the location of backup bearings. In the dropdown, the rotor falls down and contacts the backup bearing. After the initial hit, the rotor bounces back and again hits the bearing. This can repeat until the rotor steady set in the bearing.

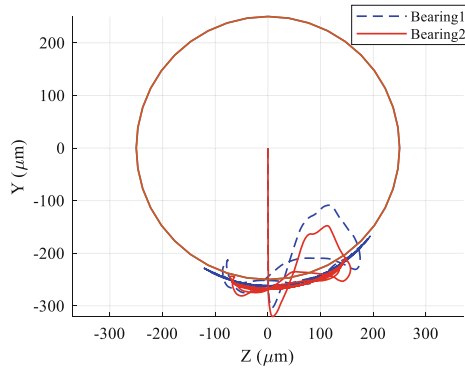


Fig. 4. Rotor orbit, dropdown simulation at 60 Hz

3.2 Contact Forces and Stress

The contact force in the backup bearing is modeled on the basis of the bearing model presented in the paper by Kurvinen et al. [15]. As can be seen in Fig. 5, in the first hit of the rotor with backup bearing, the bearing bears high contact force, about 2346 N at the drive end (Bearing 2). In the subsequent contacts, the magnitude of the contact force is decreased and after continues rub in the backup bearing reaches to the stable value. The figure shows that in the initial contacts of the rotor and bearing, the contact force in the drive end (Bearing 2) is approximately 1.36 times of the force in the Non-drive end (Bearing 1) and in the following contacts, the difference between the contact forces in the bearings is reduced. In the beginning of the dropdown, the rotor has a considerable kinematic energy. Therefore, when the rotor hits the bearing for the first time, the highest contact force is observed. As a result of the friction between the rotor and backup bearing, part of the kinetic energy of rotor is dissipated as friction heat generation. For this reason, in the subsequent contacts, the magnitude of contact force is reduced. It should be noted that due to the movement of the ball inside the bearing, the location where the highest contact force exists is changing. Furthermore, the center

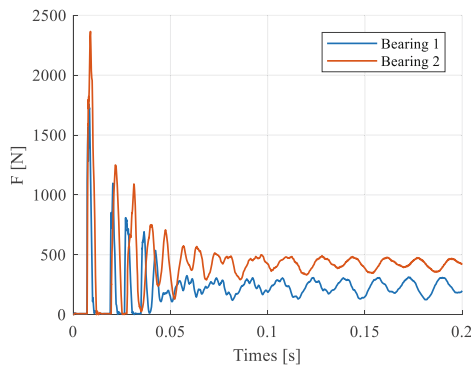


Fig. 5. Contact force in the bearing

of mass of the rotor is close to the drive end or rotor (Bearing 2). Therefore, the force in the Bearing 2 is higher than the Bearing 1. After obtaining the contact force between the balls and inner race, the maximum Hertzian contact stress between balls and bearing ring is obtained (Eq. 10). The highest contact stress in the contact of the rotor and Bearing 1 and Bearing 2 found to be 3451 and 3549 MPa, respectively.

3.3 Experimental Result

The prototype of two-stage radial gas turbine shown in Fig. 6 produces 400 kW electricity. The nominal operation speed of both rotors is 550 Hz. The dropdown test of the rotor was carried out at two different speeds: 60 and 100 Hz. Before the dropdown, the rotor was supported by active magnetic bearings. Then, the magnetic bearing source was switched off and the unit is shut down. The measurement setup is equipped with two non-contact displacement sensors at the location of each backup bearings and the relative displacement of the rotor is recorded. These sensors are mounted at 45° with respect to the vertical axis of the rotor. For this reason, it is required to map the recorded data to the coordinate system used in the FE-model of the rotor. By means of a third noncontact probe, the displacement of the rotor in the axial direction is measured. The dropdown speed has been also recorded.

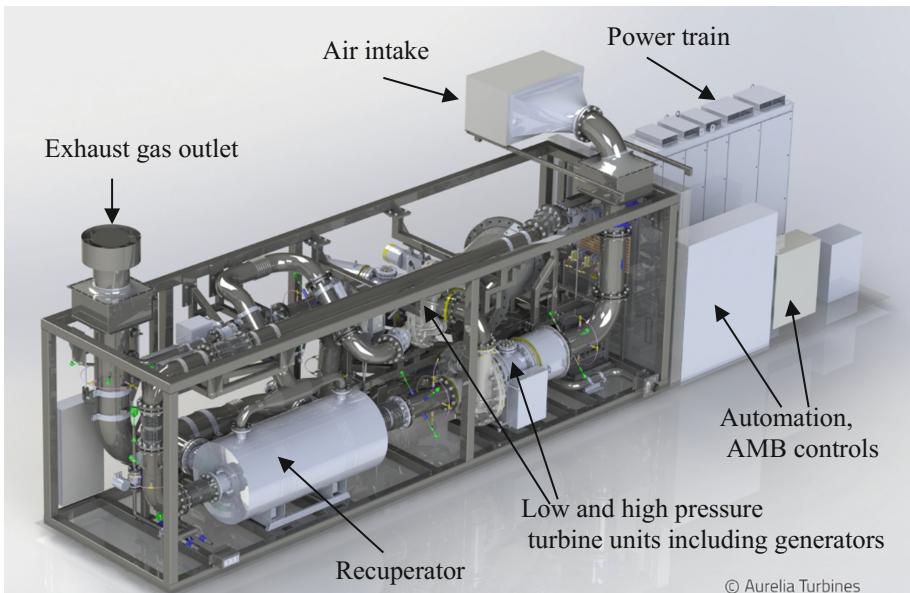


Fig. 6. The figure of the prototype for two-stage radial gas turbine under investigation.

Figure 7 depicts the recorded orbital movement of the rotor for the dropdown test at 60 and 100 Hz. As can be seen in Fig. 7(a and b), when the rotor drops, the rotor moves downward, then bounces back and it hits the backup bearing over and over until

thoroughly settles on the bottom of the bearing inner ring. When the rotor is dropped at higher initial rotational speed, the first bounce is higher.

The comparison of the orbital movement of the rotor shown in Fig. 4 (simulation tool) and the rotor orbit measured in the test (Fig. 7a and b) reveals that the simulation model is able to feature the orbital movement of the rotor. However, the amplitude of the rotor orbit in the measurement found to be different from the simulation. The test results show that the radial displacement of the rotor exceeds $280\ \mu\text{m}$, while the simulation results indicated that in the first contact, the displacement of the rotor exceeds $250\ \mu\text{m}$. Then, the radial displacement is reduced around the air gap and the rotor starts to have a wobbling movement on the bottom of the bearing and the radial displacement is reduced around the air gap. There are several possible explanations can be found for this difference between the amplitude of orbit in the simulation and test result. In the numerical simulation, the air gap clearance is in accordance to the air gap clearance in the design phase of machine. One of the primary reasons for this discrepancy can be due to the problem in the sensitivity of sensor and the electrical runout particularly because of the dent, scratch in the probe area of the rotor and rotor runout. Furthermore, the structure of the support of the machine is complicated and the simulation of dropdown generally requires simplifications in supports definition. The rotor orbit is obtained from the displacement of the rotor in horizontal and vertical direction and the effect of the support stiffness in the amplitude of the rotor displacement cannot be neglected.

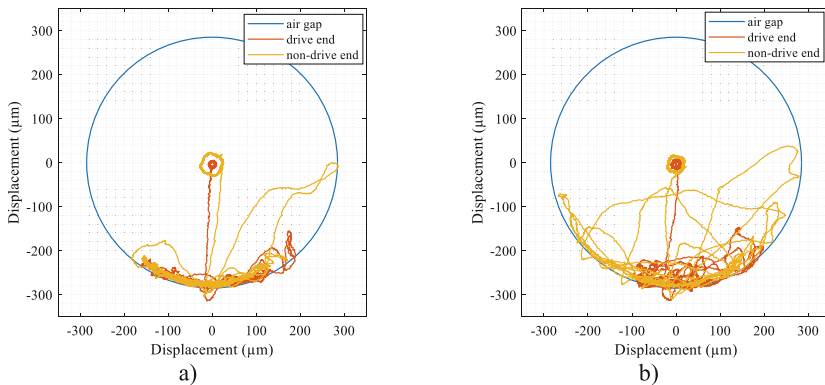


Fig. 7. Orbit movement of rotor at different dropdown speeds (a) 60 Hz (b) 100 Hz

Figure 8 depicts the displacement of the rotor for the dropdown at 60 Hz at the drive end backup bearing. It is clear from Fig. 8 that when the electromagnetic field switched off, the rotor has high displacement in the vertical direction, while the horizontal displacement of the rotor is considerably lower. Figure 8a shows that the rotor starts to have the highest oscillation in the horizontal direction about $200\ \mu\text{m}$ which is less than the air gap and gradually the horizontal displacement of the rotor is reduced and the rotor stabilized around the vertical centerline of the bearings. Figure 8b features

that the rotor descends and the vertical displacement of the rotor is over $320\ \mu\text{m}$. Afterwards, the rotor moves up. In the following contacts, the displacement of the rotor decreases. In the first interaction of rotor and backup bearing, the contact force is so high that the vertical displacement of the rotor exceeding the air gap, then the rotor is reflected from the inner ring. Later, the vertical displacement of the rotor is reduced and the rotor starts to stabilize within the air gap.

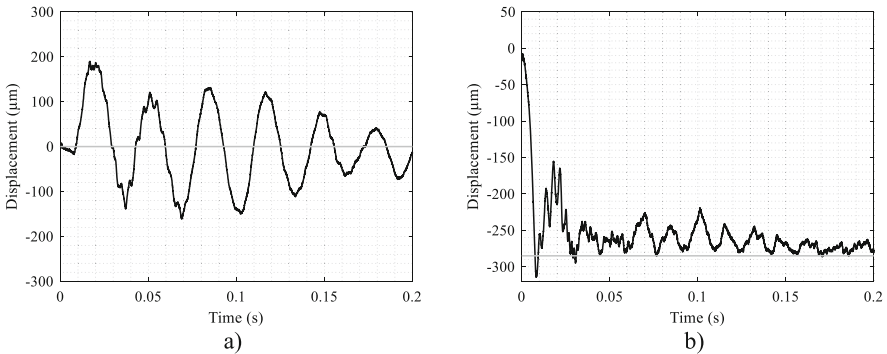


Fig. 8. Displacement of rotor at the location of backup bearing (drive end), dropdown test at 60 Hz (a) x-direction (b) y-direction

The displacement of the rotor at the location of the non-drive end backup bearing is shown in Fig. 9. The same as the drive end bearing, the highest displacement of the rotor at vertical direction was recorded at the first contact of the rotor and bearing and then the amplitude of the displacement is decreased. The results reveal a clear difference between the recorded displacement of the rotor at the backup bearing in the drive end and non-drive end. First, the recording shows that the maximum displacement of the rotor at the non-drive end is approximately $300\ \mu\text{m}$ that is less than the maximum displacement at the drive end of the rotor. Second, the comparison of Figs. 8b and 9b shows that the rotor contacts the bearings at different times. Third, it can be found from the measurement data that the rotor hits the drive end more than the non-drive end.

The mass center of the rotor is close to the drive end bearing. The static force equilibrium of the rotor shows that the force in drive end bearing is higher than non-drive end bearing. Therefore, the vertical displacement of the rotor at the drive end bearing is higher and it is confirmed by measurement results. In addition, the high number of contacts of the rotor with drive end bearing can be attributed the conical movement of the rotor that has a good agreement with the results of our previous study on the rotor dynamic analysis of the rotor (The rotor dynamic analysis indicated that at lower frequencies the rotor has a conical mode shape).

In the test setup, the axial displacement of the rotor is measured by non-contact displacement probe close to the axial disc of the rotor. The axial clearance of the axial safety bearing is $900\ \mu\text{m}$. Figure 10 shows the axial displacement of the rotor for the dropdown test at 60 Hz. The measurement shows that from the start of the dropdown until the first contact of rotor and backup bearing the rotor has an axial displacement of

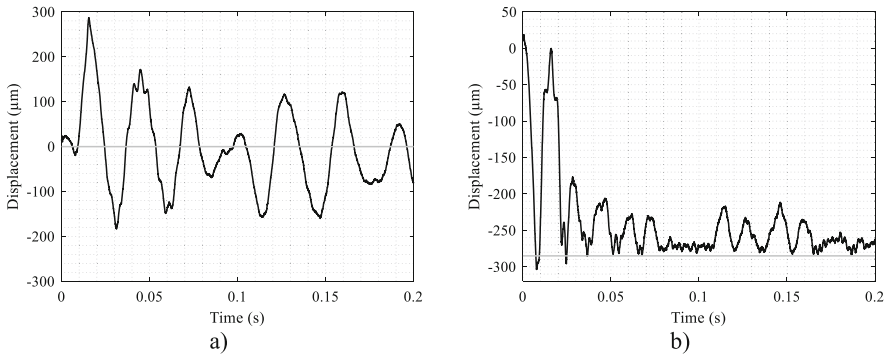


Fig. 9. Displacement of rotor at the location of backup bearing (Nondrive end), dropdown test at 60 Hz (a) x-direction (b) y-direction

80 μm. Then, very rapidly, the rotor moves axially in opposite direction. And from 40 μm at 0.02 s, the rotor experiences the higher axial displacement of 110 μm at 0.05 s. Then, the direction of the movement reversed until 0.1 s. After that, the axial displacement of the rotor is reduced and the rotor experiences several backs and forth movements.

Even though the magnitude of the axial displacement of the rotor seems to be small compared to the maximum limit for the clearance, the data provides an important information about the behavior of the rotor. In the normal operation of the machine, the pressurized air in the outlet of the compressor directed to the turbine impeller and when the switch of electromagnetic field turned off, the axial force resulted from the back pressure in the compressor impeller causes that the rotor moves reversely. The rotor undergoes several backs and forth axial movement particular because of the unstable fluid flow in the dropdown. In the numerical simulation, the axial pressure in the compressor section is not taken into account. It should be remind that this dropdown test was carried out at very low speed rather than the operation speed of rotor (550 Hz). The existence of the axial pressure from the compressor impeller can provide a physical

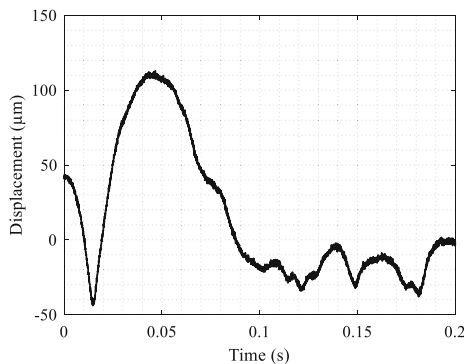


Fig. 10. Axial displacement of rotor, dropdown test at 60 Hz

explanation that the outcome of the simulation of the two-stage radial gas turbine generator rotor, mainly at operating speed, expected to be different from the real behavior of the rotor in the dropdown. In future, the effect of the force from the magnetic field and also the axial force in the compressor impeller needs to be considered.

4 Conclusion

On the circumstance that the electromagnetic field fails, the rotor drops and the backup bearing suffers from high contact load. A numerical and experimental study on the dropdown of the case study of the rotor in a two-stage radial gas turbine generator unit was carried out. The contact forces and the stress in the backup bearing were studied. For the purpose of the calculation of the contact forces in the dropdown, the Hertzian contact model was implemented. The contact force between the rotor and backup bearing and the contact force in the bearing was calculated. The results indicated that the backup bearing is exposed to time-varying load. The backup bearing bears the high contact load during the initial hit of the rotor with the bearing. In addition, the maximum Hertzian stress between the ball and the bearing race was obtained. In the test setup, the dropdown of the rotor for various dropdown speed was carried out. The displacement of the rotor in the location of backup bearing and the rotor orbits was featured. The simulation result had a agreement with the recorded behavior of the rotor in the experimental dropdown. For further improvement in the dropdown simulation, the axial pressure in the compressor impeller should be taken into account.

References

1. Kärkkäinen, A., Sapanen, J., Mikkola, A.: Dynamic simulation of a flexible rotor during drop on retainer bearings. *J. Sound Vib.* **306**, 601–617 (2007)
2. Keogh, P.S.: Contact dynamic phenomena in rotating machines: active/passive considerations. *Mech. Syst. Signal Process.* **29**, 19–33 (2012)
3. Keogh, P.S., Yong, W.Y.: Thermal assessment of dynamic rotor/auxiliary bearing contact events. *ASME J. Tribol.* **129**, 143–152 (2007)
4. Liu, T., Lyu, M., Wang, Z., Yan, S.: An identification method of orbit responses rooting in vibration analysis of rotor during touchdowns of active magnetic bearings. *J. Sound Vib.* **414**, 174–191 (2018)
5. Sun, G.: Auxiliary bearing life prediction using Hertzian contact bearing model. *ASME J. Vib. Acoust.* **128**, 203–209 (2006)
6. Lee, J.G., Palazzolo, A.: Catcher bearing life prediction using a rainflow counting approach. *ASME J. Tribol.* **134**, 031101:1–031101:15 (2012)
7. Neisi, N., Sikanen, E., Heikkinen, J.E., Sapanen, J.: Effect of off-sized balls on contact stresses in a touchdown bearing. *Tribol. Int.* **120**, 340–349 (2018)
8. Jin, C., Zhu, Y., Xu, L., Xu, Y., Zheng, Y.: The thermodynamic properties of a new type catcher bearing used in active magnetic bearings system. *Appl. Therm. Eng.* **82**, 253–263 (2015)
9. Zhao, Y., Yang, G., Shi, Z., Zhao, L.: Thermal analysis and simulation of auxiliary bearings and its application in the high temperature reactor-10. *J. Tribol.* **138**, 011102:1–011102:11 (2016)

10. Sun, G.: Rotor drop and following thermal growth simulations using detailed auxiliary bearing and damper models. *J. Sound Vib.* **289**, 334–359 (2006)
11. Schmied, J., Pradetto, J.C.: Behaviour of a one ton compressor rotor being dropped into the auxiliary bearings. In: *Proceeding of the Third International Symposium on Magnetic Bearings*, Alexandria, pp. 145–156 (1992)
12. Kärkkäinen, A.: Dynamic simulations of rotors during drop on retainer bearings. Ph.D. thesis, Lappeenranta University of Technology, Finland (2007)
13. Sapanen, J., Mikkola, A.: Dynamic model of a deep-groove ball bearing including localized and distributed defects. Part 1: Theory. *Proc. Inst. Mech. Eng. Part K J. Multi-body Dyn.* **217**, 201–211 (2003)
14. Harris, T.A., Kotzalas, M.N.: *Essential Concepts of Bearing Technology: Rolling Bearing Analysis*, 5th edn. CRC Press, Boca Raton (2007)
15. Kurvinen, E., Sapanen, J., Mikkola, A.: Ball bearing model performance on various sized rotors with and without centrifugal and gyroscopic forces. *Mech. Mach. Theory* **90**, 240–260 (2015)



Rubbing Effect Analysis in a Continuous Rotor Model

Marcus Varanis¹(✉), Arthur Mereles¹, Anderson Silva¹,
José Manoel Balthazar², and Ângelo Marcelo Tuset³

¹ Federal University of Grande Dourados, Dourados, Brazil
marcusvaranis@ufgd.edu.br

² Aeronautics Technological Institute, São Paulo, Brazil

³ Federal Technological University of Paraná, Paraná, Brazil

Abstract. One of the most important malfunction that can cause severe damage in rotating machines is the contact between fixed and rotating parts. The most common sources for rubbing is mass unbalance and instabilities due to fluid-rotor interaction. In this way, this paper presents a continuous rotor model for rubbing applications considering transverse shear, rotatory inertia, and gyroscopic moments. The contribution of it is to present a model to be applied in cases where these effects are not negligible. It is shown that for low slenderness ratio the model is equivalent to the commonly used Euler-Bernoulli continuous model. The normal and friction contact forces between the rotor and the stator are modeled using the Hertz contact theory, which is a nonlinear contact model, and the Coulomb friction model, respectively. In addition, the response of the rotor under impact was studied in the frequency domain using Wavelet Techniques for detection and characterization of rubbing phenomenon.

Keywords: Continuous model · Hertz contact model
Rotor-stator contact · Wavelet transform

1 Introduction

The occurrence of the rubbing phenomenon in a rotating machine is a serious problem that can lead to mechanical failures of the machine components. This phenomenon is seen due to many reasons such as rotor vibrations due unbalance, excessive displacements due to rotor misalignment, rotor permanent bow, or fluid related constant radial forces [1]. In turbomachines, like aircraft engines, rubbing may result from different thermal growth between the rotor and stator and from a blade loss, which induce high displacement due to the huge unbalance created. Investigations on the dynamics of rotating machinery have been made for more than a hundred years. Some primitive models, such as the Jeffcott rotor, consisting of massless shafts with rigid rotors have already been extensively studied [2,3]. Although these primitive rotor models are not suitable for modeling real

rotating machines, they provide an important insight into the physics of rotating systems. The models that are used to predict the properties of real rotating systems consist in flexible or continuous rotor models. In [4], a complete review on rotor models is provided. In order to overcome the difficulties in working with the continuous models, some discretization methods were proposed like transfer matrix method [5] and finite elements methods [6, 7]. The early models were made mainly to compute the natural frequencies of the rotating systems, and they were mostly only valid in linear systems. As nonlinear effects have been seen in many experimental procedures [8–10], the models needed to be improved to predict such effects. Some numerical works also presented the occurrence of nonlinear effects in rotating systems [11–18]. These effects were mainly due to oil bearing non-linear characteristics or rubs and impacts in journal bearing systems [19].

An initial study on rubbing was performed by Szczygielski [20], which consisted in a piecewise linear and globally nonlinear model and presented a good qualitative agreement between experimental results. A complete review on rubbing phenomena was performed by Muszynska [21]. Most of the models proposed to describe rotating systems with rub were very simplified lumped mass models, because of the computational problems related to more complex ones due to nonlinear effects. Such models are inadequate because the nonlinear effects excite a wide spectrum band and hence more detailed models need to be considered [19]. Some continuous rotor models are presented in [1, 12, 13, 19, 22]. The rubbing forces have a non-smooth behavior in stiffness, which makes the systems exhibit some complicated oscillations. Studies on the rubbing phenomenon showed that the rotating system presented a rich class of nonlinear dynamics such as sub and super-synchronous responses, quasi-periodic responses and chaotic motions [23].

A great number of the rotor models found in the literature are based on the Euler-Bernoulli beam theory. This approach does not take into account the effects of the rotatory inertia and shear deformation of the rotor, which are not significant for slender rotors. However, for rotors with high slenderness ratio, the error in the natural frequencies computed using the Euler-Bernoulli theory are high. The effect of the rotary inertia and shear deformation reduces the fundamental natural frequency by 0.3% in a uniform beam with a slenderness ratio of 1:20, and the effect is bigger for higher modes [24]. Thus, in such cases, the Timoshenko beam theory needs to be applied.

In this work, a continuous rotor model with rubbing is presented. The effects of the rotatory inertia, shear deformation and gyroscopic moments are included in the model. The contact forces are modeled using the Hertz contact theory and the Coulomb friction model. In addition, Wavelet Techniques were applied in the responses to characterize the rubbing in the frequency domain.

2 Background

2.1 Continuous Rotor Model

The model that was studied in this work consists in a continuous rotor model of a thick shaft simply supported at both ends, as depicted in Fig. 1. It is important

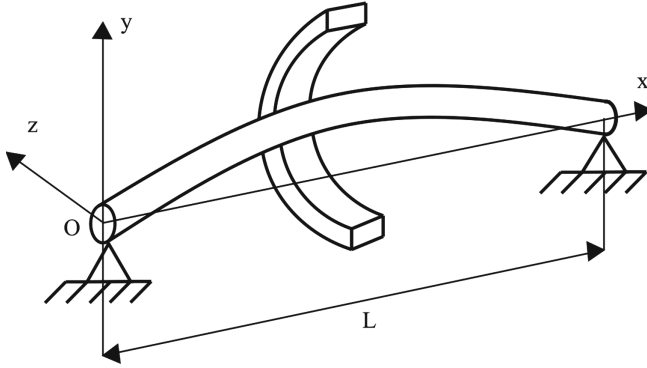


Fig. 1. Schematic representation of the rotor.

to point out that the bearing behavior was not considered in the model, as the boundaries were considered simply supported ends. Although this approach is unrealistic, it was followed to simplify the analysis of the rubbing effect in the vibration model. The equations of motion of the movement of the rotor in the vertical (v) and horizontal (w) directions are written as, respectively [25],

$$EI \frac{\partial^4 v}{\partial x^4} - \frac{EI\rho}{\kappa G} \frac{\partial^4 v}{\partial x^2 \partial t^2} + \rho A \frac{\partial^2 v}{\partial t^2} - \rho A r_0^2 \left[\left(\frac{\partial^4 v}{\partial x^2 \partial t^2} - \frac{\rho}{\kappa G} \frac{\partial^4 v}{\partial t^4} \right) + 2\Omega \left(\frac{\partial^3 w}{\partial x^2 \partial t} - \frac{\rho}{\kappa G} \frac{\partial^3 w}{\partial t^3} \right) \right] = F_{u,y}(t)\delta_d(x - a) + F_{c,y}(t)\delta_d(x - a) \tag{1}$$

$$EI \frac{\partial^4 w}{\partial x^4} - \frac{EI\rho}{\kappa G} \frac{\partial^4 w}{\partial x^2 \partial t^2} + \rho A \frac{\partial^2 w}{\partial t^2} - \rho A r_0^2 \left[\left(\frac{\partial^4 w}{\partial x^2 \partial t^2} - \frac{\rho}{\kappa G} \frac{\partial^4 w}{\partial t^4} \right) - 2\Omega \left(\frac{\partial^3 v}{\partial x^2 \partial t} - \frac{\rho}{\kappa G} \frac{\partial^3 v}{\partial t^3} \right) \right] = F_{u,z}(t)\delta_d(x - a) + F_{c,z}(t)\delta_d(x - a). \tag{2}$$

where x is the axial axis, t is time, E is the Young’s modulus, I is the area moment of inertia, ρ is the density, κ is the form factor and has the value 10/9 for circular cross-sections, G is the shear modulus, A the cross-section area, r_0 is the radius of gyration, Ω is the rotating speed, δ_d is the Dirac delta function and a is the point of application of the forces, which in the model is considered in the middle of the shaft. The forces acting on the rotor are due to unbalance F_u , considered here a point force, and the forces due to the contact F_c . Equations (1) and (2) can be written in a more convenient form by introducing the following dimensionless variables,

$$v' = \frac{v}{L}, \quad w' = \frac{w}{L}, \quad \tau = \Omega t, \quad \chi = \frac{x}{L}, \quad c^2 = \frac{A\rho L^4 \Omega^2}{EI}, \tag{3}$$

$$r = \frac{r_0}{L}, \quad \delta = \frac{9}{5}(1 + \nu), \quad a' = \frac{a}{L}.$$

where L is the length of the shaft and ν is the Poisson’s ratio. Applying the relations of Eq. (3) in Eqs. (1) and (2) and rearranging, one may have,

$$\begin{aligned} \frac{\partial^4 v'}{\partial \chi^4} - r^2 c^2 (\delta + 1) \frac{\partial^4 v'}{\partial \chi^2 \partial \tau^2} - 2r^2 c^2 \frac{\partial^3 w'}{\partial \chi^2 \partial \tau} + c^2 \frac{\partial^2 v'}{\partial \tau^2} + 2r^4 c^4 \delta \frac{\partial^4 w'}{\partial \tau^3} \\ + c^4 r^4 \delta \frac{\partial^4 v'}{\partial \tau^4} = F_{u,y}(\tau) \delta_d(\chi - a') + F_{c,y}(\tau) \delta_d(\chi - a') \end{aligned} \tag{4}$$

$$\begin{aligned} \frac{\partial^4 w'}{\partial \chi^4} - r^2 c^2 (\delta + 1) \frac{\partial^4 w'}{\partial \chi^2 \partial \tau^2} + 2r^2 c^2 \frac{\partial^3 v'}{\partial \chi^2 \partial \tau} + c^2 \frac{\partial^2 w'}{\partial \tau^2} - 2r^4 c^4 \delta \frac{\partial^4 v'}{\partial \tau^3} \\ + c^4 r^4 \delta \frac{\partial^4 w'}{\partial \tau^4} = F_{u,z}(\tau) \delta_d(\chi - a') + F_{c,z}(\tau) \delta_d(\chi - a'). \end{aligned} \tag{5}$$

The variable c denotes the dimensionless rotational speed, r is the slenderness ratio, and δ denotes the shear influence. The terms in the left side of Eqs. (4) and (5) represent, respectively, the flexural stiffness effect, the transverse shear and rotatory inertia effect, the gyroscopic effect of distributed mass, the lateral inertia effect, the interaction between the transverse shear and gyroscopic effects, and the interaction between the transverse shear and the rotatory inertia effects. The solution of the homogeneous part of Eqs. (4) and (5) are given as follows, respectively,

$$v'(\chi, \tau) = \sum_{i=1}^{\infty} \phi_i(\chi) \eta_i(\tau) = \sum_{i=1}^{\infty} A_i e^{\alpha_i \chi} e^{j a_i \tau} \tag{6}$$

$$w'(\chi, \tau) = \sum_{i=1}^{\infty} \phi_i(\chi) \zeta_i(\tau) = \sum_{i=1}^{\infty} B_i e^{\alpha_i \chi} e^{j a_i \tau} \tag{7}$$

where $a_i = \omega_i / \Omega$, being ω_i the natural frequency of the i -th mode of vibration of the system, and α_i can be found solving the characteristic equation. The values of α_i , A_i and B_i that satisfy the characteristic equation correspond to a unique value of c . Moreover, the boundary conditions should be used to obtain the system natural frequencies, which will be the values of c that make the determinant of the coefficient matrix of the algebraic system of equations zero and satisfy the characteristic equation [25]. In addition, the natural frequencies of a thick rotor are obtained in [4,26].

2.2 Rotor-Stator Rub Model

In order to model the contact of the rotor with the stator, the Hertz contact theory was used, which states that the relation between the contact force and the indentation are not linear, i.e.,[27]

$$F = k_h \varepsilon^n \tag{8}$$

where F is the contact force, k_h is the Hertz stiffness, ε is the indentation, and $n = 3/2$. Despite the good representation of the impact phenomenon given by the relation of Eq. (8), it suffers the limitation of not representing the energy

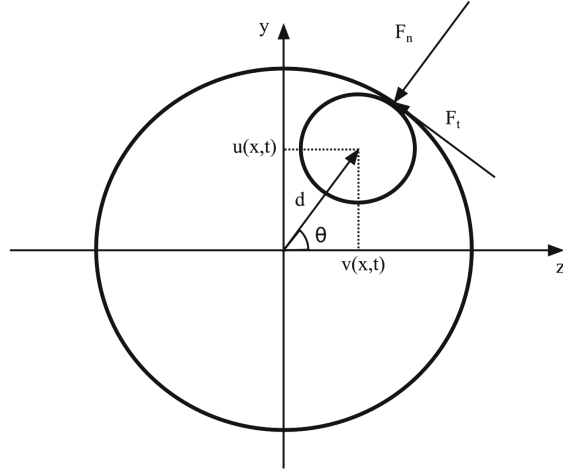


Fig. 2. Contact forces.

dissipated during the impact. To overcome this problem another model was introduced by [28], which has the following form,

$$F = k_h \varepsilon^n + b_h \dot{\varepsilon}^p \varepsilon^q \tag{9}$$

where b_h is the Hertz damping coefficient and the dot represent a time differentiation. It is generally considered that $p = n$ and $q = 1$ [29], thus one can write Eq. (9) as,

$$F = k_h \varepsilon^{3/2} (1 + b_h \dot{\varepsilon}). \tag{10}$$

Figure 2 shows the forces acting on the rotor when impacting the stator. The indentation of the rotor-stator contact will be $\varepsilon = d - g$, being $d = \sqrt{v(x, t)^2 + w(x, t)^2}$ the position of the center of the rotor and g is the gap size. Thus, the magnitude of the normal force for the rotor will be,

$$F_n = k_h (d - g)^{3/2} \left[1 + \frac{b_h}{d} \left(\frac{\partial v(a, t)}{\partial t} v(a, t) + w(a, t) \frac{\partial w(a, t)}{\partial t} \right) \right]. \tag{11}$$

It is worth noting that Eq. (11) is always positive, thus it becomes zero when $d < g$, which means that there is no contact. The horizontal and vertical components of the contact force can be obtained by, respectively,

$$F_{n,y} = -F_n \cos \theta = -F_n \frac{y}{d} \tag{12}$$

$$F_{n,z} = -F_n \sin \theta = -F_n \frac{z}{d} \tag{13}$$

being θ the angle between the rotor’s position with relation to the horizontal axis, as shown in Fig. 2. For the tangential force, the Coulomb friction model was used, thus giving,

$$F_t = \mu F_n. \tag{14}$$

where μ is the friction coefficient. Similarly to the normal force, the horizontal and vertical components are obtained by, respectively,

$$F_{t,y} = -F_t \sin \theta = -F_t \frac{z}{d}, \tag{15}$$

$$F_{t,z} = F_t \cos \theta = F_t \frac{y}{d}. \tag{16}$$

2.3 Wavelet Transform

The wavelet techniques have been used to describe the pattern of motion to verified the chaotic systems. The scale parameter is analogous to the concept of scales used in maps, so in small scales we have more compressed Wavelets with rapidly variable details. On large scales, however, there are more enlarged Wavelets, more visible features and slowly changing. In other words, small scales provide good resolution in the time domain, i.e., the temporal information is preserved. While large scales provide good resolution of the frequency domain.

It is possible to find de Continuous Wavelet Transform (CWT) of signal f at time u and scale s . Suppose that $f \in L^2(\mathbb{R})$, then the CWT is defined as,

$$Wf(u, s) := \langle f, \psi_{u,s}^* \rangle = \int_{-\infty}^{+\infty} f(t) \psi_{u,s}^* dt \tag{17}$$

where

$$\psi_{u,s}^* := \frac{1}{s} \psi \left(\frac{t-u}{s} \right), \quad u \in \mathbb{R}, \quad s > 0 \tag{18}$$

The frequency component of the signal f , as regard to the wavelet $\psi_{u,s}$ at time u and scale s , is given by $Wf(u, s)$ [30]. The scalogram of f , denoted by \wp , is defined as [30,31]:

$$\wp := \| Wf(u, s) \| = \left(\int_{-\infty}^{+\infty} | Wf(u, s) |^2 du \right)^{1/2} \tag{19}$$

Knowing this relationship, it is possible to interpret $\wp(s)$ as the energy of the CWT of f at scale s . The scalogram can be used to detect which is the most representative scales (or frequencies) of the signal f [30]. The term inner-scalogram of f at scale s was defined in [30], and is given as:

$$\wp_{inner}(s) := \| Wf(u, s) \|_{J(s)} = \left(\int_{c(s)}^{d(s)} | Wf(u, s) |^2 du \right)^{1/2} \tag{20}$$

A great number of applications of the wavelet transform in rotating machines analysis can be found in [31–33].

3 Results and Discussion

In order to solve the differential equations, the Adams-Bashforth-Moulton integration scheme was used. The most commonly used method, the Runge-kutta scheme, was not applicable, since the rotor model takes into account the rotatory inertia, which turns the problem stiff. One of the most important and challenging tasks in simulating continuous systems is the selection of the time step (Δt) and the number of modes (n). The best alternative in selecting Δt is to assuming it as one-tenth of the inverse of the bandwidth of the response [19]. The methodology followed is fixing a time step Δt and obtaining the responses. Then the time-step is then sub-divided as $\Delta t/2$, $\Delta t/4$, $\Delta t/8$, $\Delta t/16$ and the simulations are performed for each time-step. If the responses obtained do not vary much, the time-step is fixed. A similar procedure is performed for the selection of the number of modes, where the number is varied and the responses compared. The time-step and the number of modes selected were $\Delta t = 0.001$ and $n = 3$, respectively.

The parameters necessary for the simulations are listed in Table 1. The geometric parameters of the rotor were chosen so that the effects of a non-slender shaft could be significant. To first study the effect of the impact parameters in the response of the model, the values of the stiffness (k_h), damping (b_h), and the gap distance (g) were varied, obtaining three different cases. The rotating speed was maintained in 1.5 times the first critical speed of the rotor, giving a value of 2.6 kHz. Figure 3 shows the responses of the rotor for the first case, with the parameters as $k_h = 10^3 \text{ N/m}^{3/2}$, $b_h = 10^2 \text{ s/m}$ and $g = 3 \times 10^{-3} \text{ mm}$. The black lines in Fig. 3a and 4c correspond to the gap distance. These parameters of stiffness and damping correspond to a soft impact as one can note by the high indentation in the responses. In the second case, the gap distance was increased to $g = 3.5 \times 10^{-3} \text{ mm}$ and the other parameters maintained. It is seen that the responses now present a periodic characteristic, as shown in Fig. 4. This characteristic is reached in the permanent regime where the system presents periodic impacts throughout its vibrational motion, as shown in Fig. 4e. By comparing Figs. 3 and 4, one can note as well that, although the frequency of excitation in both cases were the same, the first case presented a higher frequency of

Table 1. Parameters used in the simulations.

Parameter	Variable	Value
Length of the rotor	L	0.4 m
Diameter of the rotor	d	100 mm
Slenderness ratio	r	0.0625
Young's modulus	E	71 GPa
Shear modulus	G	26.2 GPa
Poisson's ratio	ν	0.334
Density	ρ	26.6 N/m^3
Friction coefficient	μ	0.02

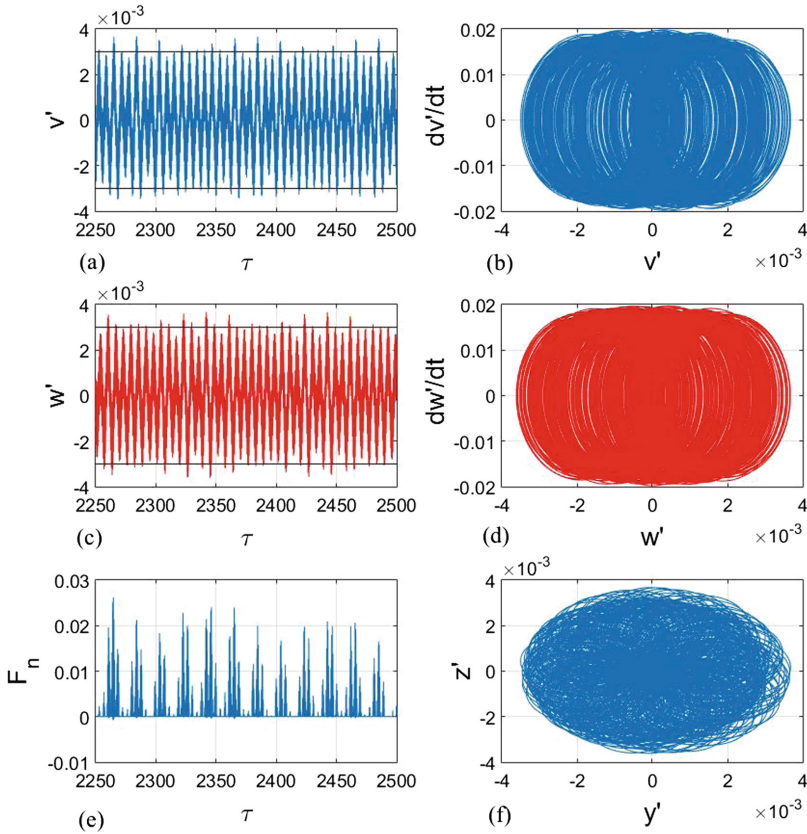


Fig. 3. Case 1, responses of the model with $k_h = 10^3 \text{ N/m}^{3/2}$, $b_h = 10^2 \text{ s/m}$ and $g = 3 \times 10^{-3} \text{ mm}$: (a) horizontal displacement, (b) horizontal state-space portrait, (c) vertical displacement, (d) vertical state-space portrait, (e) normal contact force and (f) rotor planar trajectory

oscillation. Figure 5 shows the responses obtained for the third and last case, maintaining the other parameters and altering just the Hertz damping coefficient to $b_h = 10^3$. The major difference noted in the responses is the reduction of the contact force, as seen in Fig. 5e. This reduction happens because the coefficient b_h depends inversely on the coefficient of restitution (COR), which is a parameter that represents the energy loss in the impact. Thus as b_h is increased, the impacts tend to be more elastic. Moreover, Fig. 6 presents a comparison between the vertical displacement of the model presented here with no rubbing and a classic Euler-Bernoulli model. As the Euler-Bernoulli model is a model for slender shafts, the slenderness ratio of the model presented here is reduced for a proper comparison. It is seen that the model for the thick shaft represents well a slender one, as one can note by Fig. 6.

Figure 7 presents the application of the Continuous Wavelet Transform (CWT) in the acceleration responses of the model. The CWT was also applied

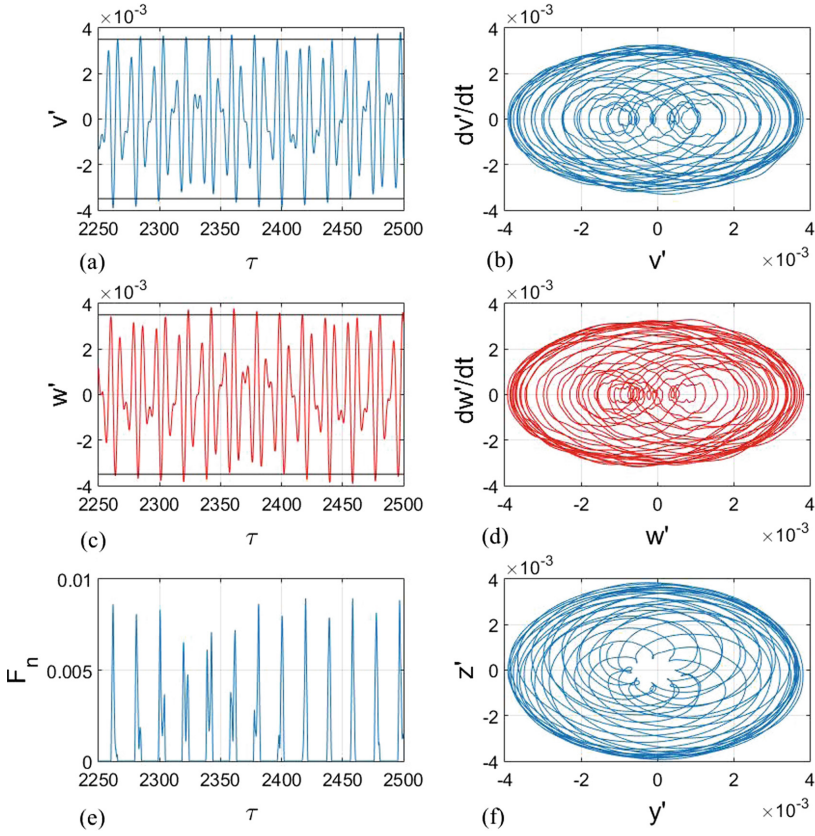


Fig. 4. Case 2, responses of the model with $k_h = 10^3 \text{ N/m}^{3/2}$, $b_h = 10^2 \text{ s/m}$ and $g = 3.5 \times 10^{-3} \text{ mm}$: (a) horizontal displacement, (b) horizontal state-space portrait, (c) vertical displacement, (d) vertical state-space portrait, (e) normal contact force and (f) rotor planar trajectory

in the case with no impact to characterize the rubbing in the responses. The figures show the three natural frequencies of the three modes considered and the frequency of excitation. By comparing the cases with impacts (Figs. 7a, b and c) with the case with no impact (Fig. 7d), it is noted that the rubbing excite a frequency of the rotor at approximately 20 kHz. The most remarkable example of this is presented in Fig. 7a, where no other frequency rather than the 20 kHz appears due to its high energy. This happens because in the Case 1 the rubbing was stronger. A same characteristic is seen in Case 2 (Fig. 7d), where the other frequencies can be seen but a high energy is concentrated in the 20 kHz frequency. In addition, despite the value of the impact force in Case 3 being smaller than the force in Case 2, as discussed before, the spectral energy due to rubbing is higher in Case 3 than in Case 2, the latter which presented little difference comparing with the case with no impact.

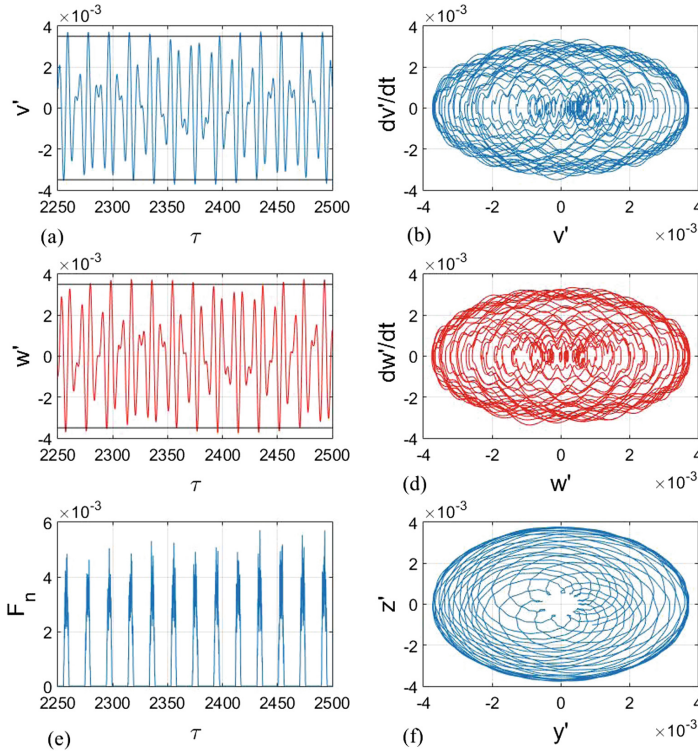


Fig. 5. Case 3, responses of the model with $k_h = 10^3 \text{ N/m}^{3/2}$, $b_h = 10^3 \text{ s/m}$ and $g = 3.5 \times 10^{-3} \text{ mm}$: (a) horizontal displacement, (b) horizontal state-space portrait, (c) vertical displacement, (d) vertical state-space portrait, (e) normal contact force and (f) rotor planar trajectory

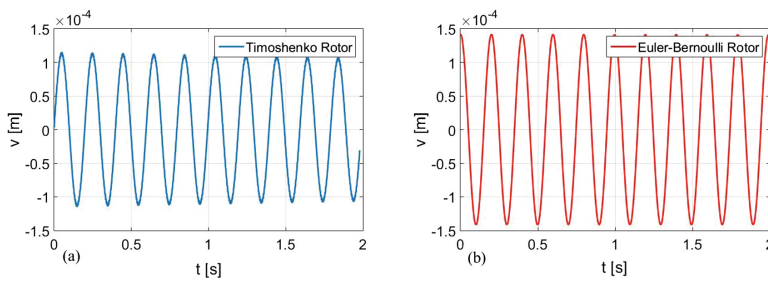


Fig. 6. Comparison between the vertical displacement given by the Timoshenko model proposed and the classic Euler-Bernoulli model for $r = 0.0013$.

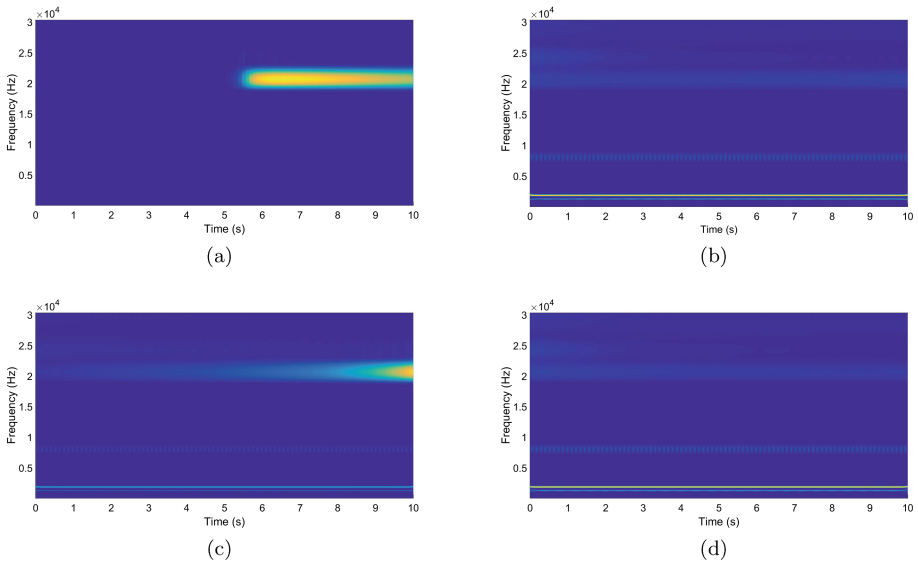


Fig. 7. Application of the CWT in the responses: (a) Case 1, (b) Case 2, (c) Case 3 and (d) Case with no impact.

4 Conclusions

This paper presented a rotor model with rubbing for a shaft with high slenderness ratio. The model considered the effects of the transverse shear, rotatory inertia and the gyroscopic moments. In order to study the rubbing, the impact parameters were studied by varying its values and analyzing the responses given by the system, which presented different characteristics. Also, to validate the model proposed, its responses with no rubbing were compared to the classical Euler-Bernoulli model. In addition, the Wavelet Transform was used to characterize the rubbing in the frequency domain, which is noted by the excitation of a certain rotor frequency.

References

1. Khanlo, H., Ghayour, M., Ziaei-Rad, S.: Chaotic vibration analysis of rotating, flexible, continuous shaft-disk system with a rub-impact between the disk and the stator. *Commun. Nonlinear Sci. Numer. Simul.* **16**(1), 566–582 (2011)
2. Tondl, A.: *Some Problems of Rotor Dynamics*. Publishing House of the Czechoslovak Academy of Sciences, Prague (1965)
3. Neilson, R.: Dynamics of electric submersible pumps. In: *Rotordynamics 1992*, pp. 302–309. Springer, Heidelberg (1992)
4. Eshleman, R., Eubanks, R.: On the critical speeds of a continuous rotor. *J. Eng. Ind.* **91**(4), 1180–1188 (1969)

5. Raffa, F., Vatta, F.: The dynamic stiffness method for linear rotor-bearing systems. *J. Vib. Acoust.* **118**(3), 332–339 (1996)
6. Nelson, H.: A finite rotating shaft element using Timoshenko beam theory. *J. Mech. Des.* **102**(4), 793–803 (1980)
7. Nelson, H., McVaugh, J.: The dynamics of rotor-bearing systems using finite elements. *J. Eng. Ind.* **98**(2), 593–600 (1976)
8. Ehrich, F.F.: High order subharmonic response of high speed rotors in bearing clearance. *J. Vibr. Acoust. Stress Reliab. Des.* **110**(1), 9–16 (1988)
9. Ehrich, F.: Observations of subcritical superharmonic and chaotic response in rotordynamics. *J. Vib. Acoust.* **114**(1), 93–100 (1992)
10. Chu, F., Lu, W.: Experimental observation of nonlinear vibrations in a rub-impact rotor system. *J. Sound Vib.* **283**(3–5), 621–643 (2005)
11. Muszynska, A., Goldman, P.: Chaotic responses of unbalanced rotor/bearing/stator systems with looseness or rubs. *Chaos, Solitons Fractals* **5**(9), 1683–1704 (1995)
12. Shaw, J., Shaw, S.: Instabilities and bifurcations in a rotating shaft. *J. Sound Vib.* **132**(2), 227–244 (1989)
13. Shaw, J., Shaw, S.: Non-linear resonance of an unbalanced rotating shaft with internal damping. *J. Sound Vib.* **147**(3), 435–451 (1991)
14. Flowers, G.T., Wu, F.: Disk/shaft vibration induced by bearing clearance effects: analysis and experiment. *J. Vib. Acoust.* **118**(2), 204–208 (1996)
15. Abu-Mahfouz, I.A.: Routes to chaos in rotor dynamics. Ph.D. thesis. Case Western Reserve University (1993)
16. Ishida, Y.: Nonlinear vibrations and chaos in rotordynamics. *JSME Int. J. Ser. C Dyn. Control Robot. Des. Manuf.* **37**(2), 237–245 (1994)
17. Adiletta, G., Guido, A., Rossi, C.: Chaotic motions of a rigid rotor in short journal bearings. *Nonlinear Dyn.* **10**(3), 251–269 (1996)
18. Zhao, J., Linnett, I., Mclean, L.: Subharmonic and quasi-periodic motions of an eccentric squeeze film damper-mounted rigid rotor. *J. Vib. Acoust.* **116**(3), 357–363 (1994)
19. Azeez, M.F.A., Vakakis, A.F.: Numerical and experimental analysis of a continuous overhung rotor undergoing vibro-impacts. *Int. J. Non-Linear Mech.* **34**(3), 415–435 (1999)
20. Szczygielski, W.M.: Dynamisches Verhalten eines schnell drehenden Rotors bei Anstreifvorgängen. Ph.D. thesis. ETH Zurich (1986)
21. Muszynska, A.: Rotor-to-stationary element rub-related vibration phenomena in rotating machinery. *Shock Vib. Dig.* **21**, 3–11 (1989)
22. Cveticanin, L.: Resonant vibrations of nonlinear rotors. *Mech. Mach. Theory* **30**(4), 581–588 (1995)
23. Lahrii, S., Weber, H.I., Santos, I.F., Hartmann, H.: Rotor-stator contact dynamics using a non-ideal drive-theoretical and experimental aspects. *J. Sound Vib.* **331**(20), 4518–4536 (2012)
24. Inman, D.J.: *Engineering Vibration*, vol. 3. Prentice Hall, Upper Saddle River (2008)
25. Lee, C.W.: *Vibration Analysis of Rotors*, vol. 21. Springer, Heidelberg (1993)
26. Jun, O., Kim, J.: Free bending vibration of a multi-step rotor. *J. Sound Vib.* **224**(4), 625–642 (1999)
27. Püst, L., Peterka, F.: Impact oscillator with Hertz's model of contact. *Meccanica* **38**(1), 99–116 (2003)
28. Hunt, K., Crossley, F.: Coefficient of restitution interpreted as damping in vibroimpact. *J. Appl. Mech.* **42**(2), 440–445 (1975)

29. Gilardi, G., Sharf, I.: Literature survey of contact dynamics modelling. *Mech. Mach. Theory* **37**(10), 1213–1239 (2002)
30. Addison, P.S.: *The Illustrated Wavelet Transform Handbook: Introductory Theory and Applications in Science, Engineering, Medicine and Finance*. CRC Press, Boca Raton (2017)
31. Yan, R., Gao, R.X., Chen, X.: Wavelets for fault diagnosis of rotary machines: a review with applications. *Sig. Process.* **96**, 1–15 (2014)
32. Peng, Z., Chu, F.: Application of the wavelet transform in machine condition monitoring and fault diagnostics: a review with bibliography. *Mech. Syst. Sig. Process.* **18**(2), 199–221 (2004)
33. Chandra, N.H., Sekhar, A.: Fault detection in rotor bearing systems using time frequency techniques. *Mech. Syst. Sig. Process.* **72**, 105–133 (2016)



A Modified Model Reduction Technique for the Dynamic Analysis of Rotor-Stator Rub

K. Prabith and I. R. Praveen Krishna^(✉)

Department of Aerospace Engineering, Indian Institute of Space Science and Technology, Valiamala, Thiruvananthapuram 695547, India
praveenkrishna@iist.ac.in

Abstract. This paper discusses a modified model reduction technique for the nonlinear rubbing analysis of a rotor disk with its stator. The rotor system consisting of a rigid disk, shaft and bearings is modeled using finite elements, incorporating the effects of rotary inertia and gyroscopic moments of both shaft and disk. The stator is modeled as an added stiffness to the rotor system without considering the stator dynamics and dry friction effect at the contact. The nonlinearities are localized at the rub location which permits the use of model reduction techniques, making the finite element model more compact. Component Mode Synthesis with a Craig-Bampton type sub-structuring is an efficient technique for model reduction. But, this method has some limitations due to the presence of nonlinearities in the system. In this paper, a modified Component Mode Synthesis method with dynamic sub-structuring is developed for the reduction of complete finite element model into a smaller model containing nonlinear degrees of freedom (DOF) only. This method has an advantage over existing methods is that it can be used for systems with non-symmetric element matrices. The reduced model is solved using Harmonic Balance Method (HBM) coupled with a hypersphere based continuation algorithm.

Keywords: Rotor-stator rub · Component mode synthesis
Craig-Bampton type sub-structuring · Harmonic Balance Method

1 Introduction

Recent developments in the manufacturing technologies and machine design procedures enhanced the use of weightless, slender shafts in rotating machineries for achieving higher efficiency. As a consequence, the flexibility of shaft is increased, resulting in a high amplitude whirling at operating speeds. When the whirling amplitude exceeds the clearance, rotor starts to rub on the inner surface of stator. This type of rubbing alter the entire dynamics of the system which was first observed in steam turbines [1]. Later, a considerable amount of experimental, analytical and numerical research works were reported on rotor-stator rub phenomena.

In most of the earlier works, the rubbing was modeled as a Jeffcott rotor contacting the stator through springs. Even though it is a simple model, it provides lots of information regarding the rubbing phenomena. A detailed review of major physical phenomena involved in rubbing was reported in survey papers by Muszynska [2] and Ehrich [3]. As a result of rubbing, responses such as periodic synchronous full annular rubs, partial rubs in quasi-periodic whirl, chaotic motion and destructive self-excited dry friction backward whirl were observed in rotating machineries through several experimental and numerical studies. Co-existences of these responses were also noticed depending upon the physical parameters and operating conditions of the system [4]. Effect of different physical parameters such as stiffness, damping, Coulomb friction, acceleration of rotor, support structure asymmetry, thermal effects and disk flexibility on the dynamics of rubbing phenomena were summarized in the review paper by Ahmad [5].

Black [6] conducted an experimental as well as numerical study to investigate the synchronous whirling of a shaft within a radially flexible annulus having small radial clearance. Contact between shaft and annulus was observed at a speed just below the critical speed, if the mass eccentricity was sufficient in relation to the damping. After contact, the high speed behavior of the shaft was altered and a rightward leaning of critical peak was observed and was named as “Super whirling”. Later, Yu [7] noticed a similar behavior when the shaft rubs against seals made up of teflon and bronze in a two-disk rotor system. It was also reported that the behavior of rotor with decreasing speed was entirely different from that of increasing speed. The range of super whirling was small during run down compared to that during run up. In addition, a jump down and a jump up phenomena were observed during run up and run down respectively. When the mass unbalance in the system is very high enough to produce large contact force, dry whip (backward whirling) is initiated in the system [8]. Co-efficient of friction, stator stiffness and damping co-efficient are the important parameters which will control the initiation of dry whip [9]. Jiang [10] explained the physical reason for the onset of dry whip as the rotor is in resonance at a negative (natural) frequency of the coupled nonlinear rotor-stator system.

Majority of the numerical models were solved using time integration schemes like Runge-Kutta method and Newmark-beta method and some were solved using semi-analytic method like Harmonic Balance Method (HBM). Choy and Padovan [11] developed a numerical model using Jeffcott rotor and an elastically supported rigid stator to study the effects of casing stiffness, imbalance load level, friction co-efficient and system damping on rotor response behavior. Later, Choy [12] introduced a modal impact model in which the relative motion of the rotor was expressed by a linear combination of its modes. Use of this modal impact model in combination with numerical FFT reduced a significant amount of computation time in the response analysis. Goldman [13] investigated the chaotic behavior of rubbing phenomena using an impact model, incorporating the local stator stiffness and radial/tangential damping properties. The effect of anisotropy of rotor on rubbing was analyzed and an additional $1/2\times$ regime called butterfly rub was observed as a result of anisotropy. In order to represent

a loose pedestal condition, Goldman [14] included base stiffness and damping in the model and found that an increase in base damping results in a decrease of the restitution co-efficient and leads to a gradual reduction of the chaotic vibration bands on the bifurcation diagrams.

Popprath [15] developed a rub model including the contact damping and plastic deformation at the contact zone and solved the governing differential equations using an integration algorithm suitable for numerically stiff systems. The contact damping has significant effect on the type of motion generated and as damping is decreased, periodic solutions with few contacts become less likely and non-periodic behavior of the system dominated. Khanlo [16] added Coriolis and centrifugal effects in the model and found that the rub-impact occurred at lower speeds due to these effects. Karpenko [17] incorporated a visco-elastic preloaded snubber ring into the Jeffcott rotor model and observed that preloading helps in stabilizing overall dynamics of the system. von Groll [18] used a periodic harmonic balance method along with arc length continuation for obtaining the rubbing responses of a nonlinear piecewise rotor system under periodic excitations. Even though the results were not matching with the measurements from a test rig, the solution process of HBM was less expensive than time-domain methods. Peletan [19] introduced a quasi-periodic HBM coupled with a pseudo arc-length continuation algorithm to trace the partial rub branch, which was not available using periodic HBM.

Later, many researchers used finite element models for the study of rubbing phenomena in rotor-stator systems. Ma [20,21] developed a FE model of a two disk rotor-bearing system for simulating fixed point rubbing. The augmented Lagrangian method was applied to deal with contact constraint conditions and the Coulomb friction model was used to simulate rotor-stator frictional characteristics. Yang [22,23] simulated the fixed point rubbing in a dual-rotor system, representing the low and high pressure rotors of an aero-engine. Two convex points on the casing was used to simulate fixed point rubbing and the equations were solved using Runge-Kutta method. The surface of disks and casing were painted with softer coatings and the impact force between the low pressure rotor and the casing convex point was obtained [24]. Recently, Xiang [25] studied the nonlinear dynamic behavior of an asymmetric double-disk rotor-bearing system under rub-impact and oil-film forces. Rub impact was modeled with a Hertzian contact and a Coloumb friction, where as the oil-film forces were derived using Reynolds equation. The dynamic equations with coupled rub-impact and oil-film forces were numerically solved using the Runge-Kutta method.

In most of the FE models, the rubbing is localized at the bearing location or at the interface between disk and stator. Hence, it will be inadvisable to apply nonlinear solution techniques to all degrees of freedom, as it consumes more time. A complete FE model can be reduced to smaller models containing nonlinear degrees of freedom only, using some model reduction techniques such as static condensation method, dynamic reduction method, improved reduced system (IRS) and Craig-Bampton (CB) reduction method. Kim [26] used a dynamic reduction method (impedance method) along with HBM to investigate

the rubbing response in a multi-disk rotor system. This method proved to be accurate (with $\leq 5\%$ error) and efficient means for determining the rubbing responses in rotor system. Gustavsson [27] used an IRS method for reducing the complete FE model (32 DOF) of a turbine-generator rotor into a system with 8 degrees of freedom. Numerical integration techniques were used for solving the reduced set of governing equations.

Nelson [28] developed a method using component mode synthesis to perform stability analysis [29] and nonlinear analysis of a multi-shaft, rotor-bearing system. The formulation allowed the simulation of system response due to blade loss, distributed unbalance, base shock, maneuver loads, and specified fixed frame forces. The resulting equations were numerically integrated and the transient system response associated with blade loss dynamics with squeeze film dampers, and with interference rubs were also obtained. Later, Batailly [30] used a Craig-Bampton based component mode synthesis along with an in house time marching solver for studying the unilateral contact induced blade/casing vibratory interactions in impellers. Recently, Krishna and Padmanabhan [31] developed an improved reduced order solution technique [32] for the nonlinear analysis of the rotor-stator rubbing. In this technique, the whole FE model is divided into two systems, namely primary and secondary systems. The primary system consisted of all the nonlinear degrees of freedom and were retained in physical coordinates, whereas all the linear DOF were included in the secondary system and were reduced using Craig-Bampton based component mode synthesis. Gyroscopic effect and rotary inertia of the shaft were not included in this analysis. One of the major limitations of their study is that the method is not applicable to the systems having non-symmetric element matrices.

The current work mainly focuses on the development of a modified model reduction technique for the analysis of synchronous full annular rubbing in rotor system, incorporating the effects of gyroscopic moment and rotary inertia of both shaft and disk. The rotor system is modeled using a finite element formulation given by Nelson and McVaugh [33] and the stator is modeled as a single stiffness. The proposed method works efficiently for the systems with skew-symmetric and non-symmetric element matrices. Harmonic Balance method with a hypersphere based continuation technique [32] is used for solving the reduced governing equations.

2 Mathematical Model

The equations of motion of a general rotor-stator system can be written in finite element formulation as,

$$\mathbf{M}\ddot{\mathbf{x}} + \mathbf{C}\dot{\mathbf{x}} - w\mathbf{G}\dot{\mathbf{x}} + \mathbf{K}\mathbf{x} + f(\mathbf{x}, \dot{\mathbf{x}}) = \mathbf{F}_{\text{ext}}(t) \quad (1)$$

where \mathbf{M} , \mathbf{C} , \mathbf{G} and \mathbf{K} are the mass, damping, gyroscopic and stiffness matrices of size $N \times N$. $f(\mathbf{x}, \dot{\mathbf{x}})$ is the nonlinear function and $\mathbf{F}_{\text{ext}}(t)$ is the excitation vector, both having a size of $N \times 1$. \mathbf{x} , $\dot{\mathbf{x}}$ and $\ddot{\mathbf{x}}$ are the displacement, velocity and acceleration vectors of size $N \times 1$. Mass matrix \mathbf{M} is a symmetric matrix

which includes translational and rotational components of mass for both shaft and disk. Damping matrix \mathbf{C} can be symmetric or non-symmetric, depending on whether it contains the viscous damping of bearing or internal damping of shaft. Gyroscopic matrix \mathbf{G} is always skew-symmetric which includes the gyroscopic effects of shaft as well as disk. Stiffness matrix \mathbf{K} is a symmetric matrix including the stiffnesses of shaft and bearings, assuming bearing stiffnesses are symmetric (no cross coupled terms).

2.1 Formulation of Reduction Technique

As in the study of Krishna and Padmanabhan [31], the overall system is divided into primary and secondary systems in which the nonlinear DOF along with its boundary DOF constitute the primary system and the remaining linear DOF constitute the secondary system. The primary system is retained in its physical co-ordinates, whereas the secondary system is reduced using Craig-Bampton based component mode synthesis. The method used in the paper of Glasgow [29] is used for the formulation of Craig-Bampton based sub-structuring of secondary system.

The equation of motion for the secondary system is written as,

$$\mathbf{M}_s \ddot{\mathbf{x}}_s + \mathbf{C}_s \dot{\mathbf{x}}_s - w \mathbf{G}_s \dot{\mathbf{x}}_s + \mathbf{K}_s \mathbf{x}_s = \mathbf{0} \tag{2}$$

First order form of the Eq. (2) is used for the further development of reduction technique and is written as,

$$\begin{bmatrix} (\mathbf{C}_s - w \mathbf{G}_s) \mathbf{M}_s & \\ \mathbf{M}_s & \mathbf{0} \end{bmatrix} \begin{Bmatrix} \dot{\mathbf{x}}_s \\ \ddot{\mathbf{x}}_s \end{Bmatrix} + \begin{bmatrix} \mathbf{K}_s & \mathbf{0} \\ \mathbf{0} & -\mathbf{M}_s \end{bmatrix} \begin{Bmatrix} \mathbf{x}_s \\ \dot{\mathbf{x}}_s \end{Bmatrix} = \begin{Bmatrix} \mathbf{0} \\ \mathbf{0} \end{Bmatrix} \tag{3}$$

The displacement vector in the Eq. (3) is partitioned into interior and boundary co-ordinates as,

$$\mathbf{x}_s = \begin{Bmatrix} \mathbf{x}_s^i \\ \mathbf{x}_s^b \end{Bmatrix} \tag{4}$$

where \mathbf{x}_s^i is the interior co-ordinate and \mathbf{x}_s^b is the boundary co-ordinate. The associated state vector is,

$$\mathbf{h}_s = \begin{Bmatrix} \mathbf{x}_s \\ \dot{\mathbf{x}}_s \end{Bmatrix} = \begin{Bmatrix} \mathbf{x}_s^i \\ \mathbf{x}_s^b \\ \dot{\mathbf{x}}_s^i \\ \dot{\mathbf{x}}_s^b \end{Bmatrix} \tag{5}$$

For further simplicity of derivation, the state vector \mathbf{h}_s is transformed using the relation,

$$\mathbf{h}_s = \mathbf{T} \mathbf{y}_s \tag{6}$$

where

$$\mathbf{T} = \begin{bmatrix} \mathbf{I} & \mathbf{0} & \mathbf{0} & \mathbf{0} \\ \mathbf{0} & \mathbf{0} & \mathbf{I} & \mathbf{0} \\ \mathbf{0} & \mathbf{I} & \mathbf{0} & \mathbf{0} \\ \mathbf{0} & \mathbf{0} & \mathbf{0} & \mathbf{I} \end{bmatrix} \quad \mathbf{y}_s = \begin{Bmatrix} \mathbf{y}_s^i \\ \mathbf{y}_s^b \end{Bmatrix} = \begin{Bmatrix} \mathbf{x}_s^i \\ \dot{\mathbf{x}}_s^i \\ \mathbf{x}_s^b \\ \dot{\mathbf{x}}_s^b \end{Bmatrix} \tag{7}$$

The Eq. (6) is substituted in Eq. (3) and pre-multiplied with the transpose of transformation matrix, \mathbf{T} to obtain the first order component equation as,

$$\begin{bmatrix} \mathbf{A}_s^{ii} & \mathbf{A}_s^{ib} \\ \mathbf{A}_s^{bi} & \mathbf{A}_s^{bb} \end{bmatrix} \begin{Bmatrix} \mathbf{y}_s^i \\ \mathbf{y}_s^b \end{Bmatrix} + \begin{bmatrix} \mathbf{B}_s^{ii} & \mathbf{B}_s^{ib} \\ \mathbf{B}_s^{bi} & \mathbf{B}_s^{bb} \end{bmatrix} \begin{Bmatrix} \mathbf{y}_s^i \\ \mathbf{y}_s^b \end{Bmatrix} = \begin{Bmatrix} \mathbf{0} \\ \mathbf{0} \end{Bmatrix} \quad (8)$$

where

$$\mathbf{A}_s^{jj} = \begin{bmatrix} (\mathbf{C}_s^{jj} - w\mathbf{G}_s^{jj}) & \mathbf{M}_s^{jj} \\ \mathbf{M}_s^{jj} & \mathbf{0} \end{bmatrix} \quad \mathbf{B}_s^{jj} = \begin{bmatrix} \mathbf{K}_s^{jj} & \mathbf{0} \\ \mathbf{0} & -\mathbf{M}_s^{jj} \end{bmatrix} \quad \text{for } j = i, b \quad (9)$$

The state vector in Eq. (8) is transformed into a set of retained normal modes and boundary DOF using Craig-Bampton sub-structuring [34],

$$\begin{Bmatrix} \mathbf{y}_s^i \\ \mathbf{y}_s^b \end{Bmatrix} = \begin{bmatrix} \Phi_{\mathbf{R}} & \Psi \\ \mathbf{0} & \mathbf{I} \end{bmatrix} \begin{Bmatrix} \mathbf{q}_s^i \\ \mathbf{y}_s^b \end{Bmatrix} = \mathbf{V}_{\mathbf{R}} \mathbf{z}_s \quad (10)$$

The associated left transformation matrix is written as,

$$\mathbf{V}_{\mathbf{L}} = \begin{bmatrix} \Phi_{\mathbf{L}} & \Psi \\ \mathbf{0} & \mathbf{I} \end{bmatrix} \quad (11)$$

where $\Phi_{\mathbf{R}}$ and $\Phi_{\mathbf{L}}$ are respectively the matrices of m ($m \ll N$) retained right and left normal complex modes of interior DOF such that,

$$\begin{aligned} \Phi_{\mathbf{L}}^T \mathbf{A}_s^{ii} \Phi_{\mathbf{R}} &= \mathbf{D} \\ \Phi_{\mathbf{L}}^T \mathbf{B}_s^{ii} \Phi_{\mathbf{R}} &= -\Lambda \mathbf{D} \end{aligned} \quad (12)$$

where \mathbf{D} is the diagonal matrix of normalization constants of size $m \times m$, Λ is the diagonal matrix of retained eigen values of size $m \times m$, \mathbf{q}_s^i is the generalized co-ordinates of internal DOF of size $m \times 1$ and Ψ is the constraint mode matrix and is given as,

$$\Psi = \begin{bmatrix} -(\mathbf{K}_s^{ii})^{-1} \mathbf{K}_s^{ib} & 0 \\ 0 & -(\mathbf{K}_s^{ii})^{-1} \mathbf{K}_s^{ib} \end{bmatrix} \quad (13)$$

The substitution of Eq. (10) into Eq. (8) and pre-multiplying with the transpose of $\mathbf{V}_{\mathbf{L}}$ yields the reduced equation of secondary system as,

$$\mathbf{P}_s \dot{\mathbf{z}}_s + \mathbf{Q}_s \mathbf{z}_s = \mathbf{0} \quad (14)$$

The size of the Eq. (14) is equal to the sum of number of retained complex modes and twice the number of boundary co-ordinates.

In case of primary system, all the DOF are retained in physical co-ordinates due to the presence of nonlinearity. First order form of the equation of motion for primary system is written as,

$$\begin{bmatrix} (\mathbf{C}_p - w\mathbf{G}_p) & \mathbf{M}_p \\ \mathbf{M}_p & \mathbf{0} \end{bmatrix} \begin{Bmatrix} \dot{\mathbf{x}}_p \\ \dot{\mathbf{x}}_p \end{Bmatrix} + \begin{bmatrix} \mathbf{K}_p & \mathbf{0} \\ \mathbf{0} & -\mathbf{M}_p \end{bmatrix} \begin{Bmatrix} \mathbf{x}_p \\ \dot{\mathbf{x}}_p \end{Bmatrix} + \begin{Bmatrix} f(\mathbf{x}_p, \dot{\mathbf{x}}_p) \\ \mathbf{0} \end{Bmatrix} = \begin{Bmatrix} \mathbf{F}(t) \\ \mathbf{0} \end{Bmatrix} \quad (15)$$

The state vector in the Eq. (15) is transformed as in Eq. (6) and pre-multiplied with the transpose of \mathbf{T} to get the equation of motion as,

$$\begin{bmatrix} \mathbf{A}_p^{ii} & \mathbf{A}_p^{ib} \\ \mathbf{A}_p^{bi} & \mathbf{A}_p^{bb} \end{bmatrix} \begin{Bmatrix} \dot{\mathbf{y}}_p^i \\ \dot{\mathbf{y}}_p^b \end{Bmatrix} + \begin{bmatrix} \mathbf{B}_p^{ii} & \mathbf{B}_p^{ib} \\ \mathbf{B}_p^{bi} & \mathbf{B}_p^{bb} \end{bmatrix} \begin{Bmatrix} \mathbf{y}_p^i \\ \mathbf{y}_p^b \end{Bmatrix} + \begin{Bmatrix} \mathbf{f}_p^i \\ \mathbf{0} \end{Bmatrix} = \begin{Bmatrix} \mathbf{F}_p^i \\ \mathbf{0} \end{Bmatrix} \quad (16)$$

In order to keep the component mode procedure same as secondary system, an identity matrix transformation is used instead of \mathbf{V}_R as,

$$\begin{Bmatrix} \mathbf{y}_p^i \\ \mathbf{y}_p^b \end{Bmatrix} = \begin{bmatrix} \mathbf{I} & \mathbf{0} \\ \mathbf{0} & \mathbf{I} \end{bmatrix} \begin{Bmatrix} \mathbf{q}_p^i \\ \mathbf{y}_p^b \end{Bmatrix} = \mathbf{I}_p \mathbf{z}_p \quad (17)$$

The substitution of Eq. (17) into Eq. (16) and pre-multiplying with the transpose of \mathbf{I}_p yields the final equation of primary system as,

$$\mathbf{P}_p \dot{\mathbf{z}}_p + \mathbf{Q}_p \mathbf{z}_p + \mathbf{f}_p = \mathbf{F}_p \quad (18)$$

Now, the two component Eqs. (14 and 18) are assembled together using a transformation matrix \mathbf{S} such that,

$$\mathbf{P} = \mathbf{S}^T \bar{\mathbf{P}} \mathbf{S} \quad \mathbf{Q} = \mathbf{S}^T \bar{\mathbf{Q}} \mathbf{S} \quad (19)$$

where

$$\bar{\mathbf{P}} = \begin{bmatrix} \mathbf{P}_p & \mathbf{0} \\ \mathbf{0} & \mathbf{P}_s \end{bmatrix} \quad \bar{\mathbf{Q}} = \begin{bmatrix} \mathbf{Q}_p & \mathbf{0} \\ \mathbf{0} & \mathbf{Q}_s \end{bmatrix} \quad (20)$$

and transformation matrix \mathbf{S} is obtained as,

$$\begin{Bmatrix} \mathbf{q}_p^i \\ \mathbf{y}_p^b \\ \mathbf{q}_s^i \\ \mathbf{y}_s^b \end{Bmatrix} = \begin{bmatrix} \mathbf{I} & \mathbf{0} & \mathbf{0} \\ \mathbf{0} & \mathbf{I} & \mathbf{0} \\ \mathbf{0} & \mathbf{0} & \mathbf{I} \\ \mathbf{0} & \mathbf{I} & \mathbf{0} \end{bmatrix} \begin{Bmatrix} \mathbf{q}_p^i \\ \mathbf{y}_p^b \\ \mathbf{q}_s^i \end{Bmatrix} = \mathbf{S} \mathbf{z} \quad (21)$$

The final assembled equation for the complete system is written as,

$$\mathbf{P} \dot{\mathbf{z}} + \mathbf{Q} \mathbf{z} + \mathbf{f} = \mathbf{F} \quad (22)$$

In order to get an additional computational advantage, the final system Eq. (22) is further reduced using physical sub-structuring with nonlinear DOF are taken as master and remaining DOF as slave. The modified equation can be written as,

$$\begin{bmatrix} \mathbf{P}_{mm} & \mathbf{P}_{ms} \\ \mathbf{P}_{sm} & \mathbf{P}_{ss} \end{bmatrix} \begin{Bmatrix} \dot{\mathbf{z}}_m \\ \dot{\mathbf{z}}_s \end{Bmatrix} + \begin{bmatrix} \mathbf{Q}_{mm} & \mathbf{Q}_{ms} \\ \mathbf{Q}_{sm} & \mathbf{Q}_{ss} \end{bmatrix} \begin{Bmatrix} \mathbf{z}_m \\ \mathbf{z}_s \end{Bmatrix} + \begin{Bmatrix} \mathbf{f}_m \\ \mathbf{0} \end{Bmatrix} = \begin{Bmatrix} \mathbf{F}_m \\ \mathbf{0} \end{Bmatrix} \quad (23)$$

Harmonic Balance Method with hypersphere based continuation technique [32] is used to solve the Eq. (23). This method is very efficient in determining the steady state response of the system as compared to numerical integration techniques. The continuation technique helps in tracing the multiple solution branches for the given set of conditions.

2.2 Nonlinear Contact Model

In this paper, the friction effect at the contact point is not considered. The nonlinear contact force acting at the rotor-stator interface is given by,

$$f_n = \Theta k_c(r - \delta) \tag{24}$$

where k_c is the contact stiffness, r is the relative radial displacement of rotor, δ is the radial clearance and Θ is the gap function which is equal to zero when no contact occurs and is equal to 1 when contact occurs.

3 Numerical Examples

3.1 Unbalance Response of a Rotor-Bearing System

In order to demonstrate the application of proposed model reduction technique in the linear analysis of rotors, a typical rotor-bearing system reported in the paper by Nelson and McVaugh [33] is analyzed. Rotary inertia and gyroscopic effect of both shaft and disk were included in the finite element formulation of the system. In their paper, Nelson and McVaugh [33] modeled the shaft as a six element member with each element consisting of several sub-elements. A reduction technique based on static condensation was used to reduce the internal displacements into the element endpoint displacements. But, in the current work, in order to verify the proposed methodology, the rotor-bearing system is modeled with 18 elements (equal to total number of sub-elements in [33]) and are partitioned into primary and secondary systems as shown in Fig. 1. The final assembled system has a total of 20 DOF and are reduced to 2 DOF (Y&Z displacements at disk location) using dynamic sub-structuring. The details of model reduction are given in Table 1. The unbalance response of the given rotor-bearing system is obtained using the proposed methodology and is compared with the results from [33]. Figure 2 shows the comparison of results and are found to be in good agreement.

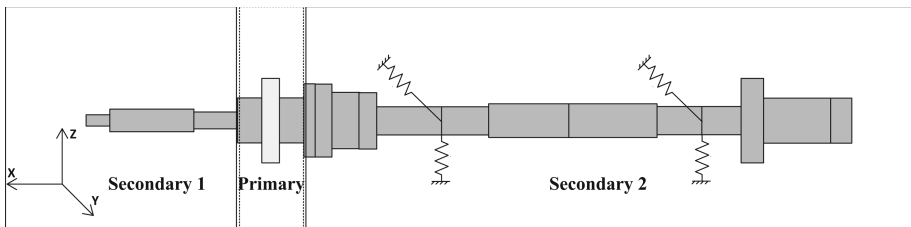


Fig. 1. Component mode partition of the rotor

Table 1. The details of model reduction applied to rotor model

System	# of nodes	Actual DOF	Retained modes	Physical DOF	Total DOF
Complete model	19	76	0	76	76
Primary	3	12	0	12	12
Secondary 1	4	16	4	4	8
Secondary 2	14	56	4	4	8
Assembled model	After component mode synthesis				20
Reduced model	After dynamic sub-structuring				2

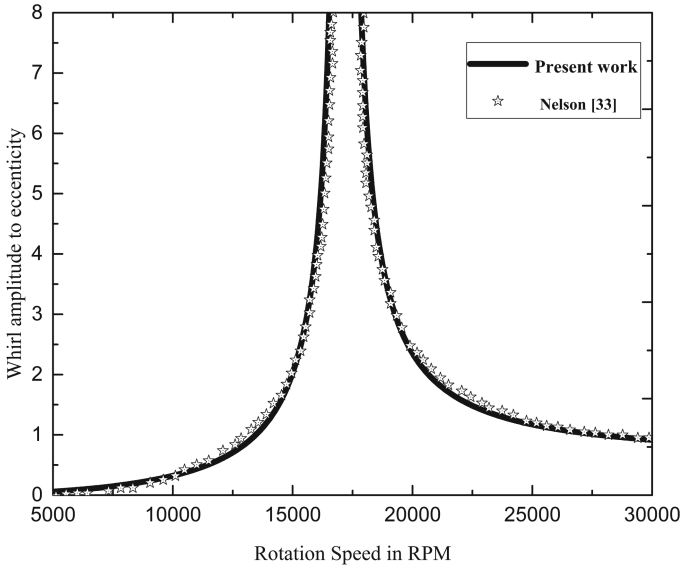


Fig. 2. Unbalance response of the rotor-bearing system

3.2 Nonlinear Analysis of Rotor-Stator Rub

A rotor-stator rub model reported in the paper by Krishna and Padmanabhan [31] is used for the nonlinear analysis of rotor using the proposed methodology. The details of geometric and material property of the model are given in [31]. The gyroscopic effect and rotary inertia of the shaft were included in the current paper which were neglected in [31]. Results of the present methodology is compared with that of [31] and is shown in Fig. 3. From the Fig. 3, it is clear that the responses of the system using present methodology and the method described in [31] are similar. This may be due to the negligible values of shaft gyroscopic effect, since the geometrical dimensions of the shaft is very small compared to that of disk.

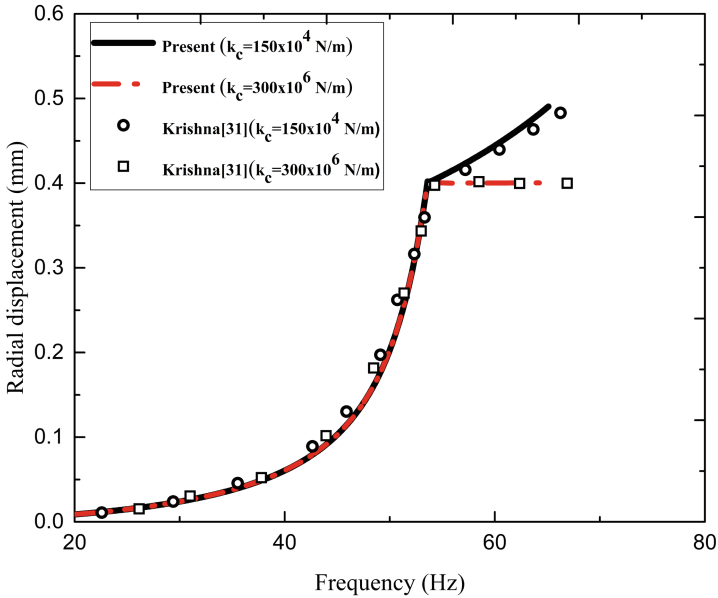


Fig. 3. Nonlinear response of the rotor system at disk location

4 Conclusions

In this paper, a modified model reduction technique is used along with Harmonic Balance Method to analyze the rubbing phenomena in rotor-stator system. The method proved to be effective in handling the FE models with skew-symmetric element matrices. The gyroscopic matrices of shaft elements that are always skew-symmetric in nature are included in the analysis. An important feature of the proposed reduction method is that it can be applied to the systems with non-symmetric element matrices. This is due to the fact that the complex eigen value decomposition is used in component mode synthesis of the system. From the current study, it was observed that for a rotor system with slender shaft and large disk, the effects of shaft gyroscopic moments and rotary inertia are negligible. This may be due to their small geometrical dimensions compared to that of disk. In future, the effects of internal viscous and hysteretic damping can be incorporated in the analysis. In addition, dry friction effect at the contact point can be included in the contact model to study the partial rubbing and dry friction backward whirl.

References

1. Dimarogonas, A., Sandor, G.: Packing rub effect in rotating machinery. I. a state of the art review. *Wear* **14**(3), 153–170 (1969)
2. Muszynska, A.: Rotor-to-stationary element rub-related vibration phenomena in rotating machinery. *Shock Vib. Dig.* **21**, 3–11 (1989)

3. Ehrich, F.F.: A state-of-the-art survey in rotor dynamics-nonlinear and self-excited vibration phenomena. In: Proceedings of the Second International Symposium on Transport Phenomena, Dynamics, and Design of Rotating Machinery, pp. 3–25 (1989)
4. Shang, Z., Jiang, J., Hong, L.: The global responses characteristics of a rotor/stator rubbing system with dry friction effects. *J. Sound Vib.* **330**(10), 2150–2160 (2011)
5. Ahmad, S.: Rotor casing contact phenomenon in rotor dynamics-literature survey. *J. Vib. Control* **16**(9), 1369–1377 (2010)
6. Black, H.: Paper 4: synchronous whirling of a shaft within a radially flexible annulus having small radial clearance. In: Proceedings of the Institution of Mechanical Engineers, Conference Proceedings, vol. 181, pp. 65–73. SAGE Publications Sage, London, England, UK (1966)
7. Yu, J., Muszynska, A., Bently, D.: Dynamic behavior of rotor with full annular rub. Bently Rotor Dynamics Research Corporation, BRDRC Report **7** (1998)
8. Bently, D.E., Yu, J.J., Goldman, P., Muszynska, A.: Full annular rub in mechanical seals, part I: experimental results. *Int. J. Rotating Mach.* **8**(5), 319–328 (2002)
9. Jiang, J.: The analytical solution and the existence condition of dry friction backward whirl in rotor-to-stator contact systems. *J. Vib. Acoust.* **129**(2), 260–264 (2007)
10. Jiang, J., Ulbrich, H.: The physical reason and the analytical condition for the onset of dry whip in rotor-to-stator contact systems. *J. Vib. Acoust.* **127**(6), 594–603 (2005)
11. Choy, F., Padovan, J.: Non-linear transient analysis of rotor-casing rub events. *J. Sound Vib.* **113**(3), 529–545 (1987)
12. Choy, F., Padovan, J., Li, W.: Seismic induced nonlinear rotor-bearing-casing interaction of rotating nuclear components. *J. Vib. Acoust. Stress Reliab. Des.* **111**(1), 11–16 (1989)
13. Goldman, P., Muszynska, A.: Chaotic behavior of rotor/stator systems with rubs. *J. Eng. Gas Turbines Power* **116**(3), 692–701 (1994)
14. Goldman, P., Muszynska, A.: Dynamic effects in mechanical structures with gaps and impacting: order and chaos. *J. Vib. Acoust.* **116**(4), 541–547 (1994)
15. Popprath, S., Ecker, H.: Nonlinear dynamics of a rotor contacting an elastically suspended stator. *J. Sound Vib.* **308**(3–5), 767–784 (2007)
16. Khanlo, H., Ghayour, M., Ziaei-Rad, S.: Chaotic vibration analysis of rotating, flexible, continuous shaft-disk system with a rub-impact between the disk and the stator. *Commun. Nonlinear Sci. Numer. Simul.* **16**(1), 566–582 (2011)
17. Karpenko, E.V., Pavlovskaja, E.E., Wiercigroch, M.: Bifurcation analysis of a preloaded Jeffcott rotor. *Chaos, Solitons Fractals* **15**(2), 407–416 (2003)
18. von Groll, G., Ewins, D.J.: The harmonic balance method with arc-length continuation in rotor/stator contact problems. *J. Sound Vib.* **241**(2), 223–233 (2001)
19. Peletan, L., Baguet, S., Torkhani, M., Jacquet-Richardet, G.: Quasi-periodic harmonic balance method for rubbing self-induced vibrations in rotor-stator dynamics. *Nonlinear Dyn.* **78**(4), 2501–2515 (2014)
20. Ma, H., Shi, C., Han, Q., Wen, B.: Fixed-point rubbing fault characteristic analysis of a rotor system based on contact theory. *Mech. Syst. Sig. Process.* **38**(1), 137–153 (2013)
21. Ma, H., Zhao, Q., Zhao, X., Han, Q., Wen, B.: Dynamic characteristics analysis of a rotor-stator system under different rubbing forms. *Appl. Math. Model.* **39**(8), 2392–2408 (2015)

22. Yang, Y., Cao, D., Wang, D., Jiang, G.: Fixed-point rubbing characteristic analysis of a dual-rotor system based on the Lankarani-Nikravesh model. *Mech. Mach. Theory* **103**, 202–221 (2016)
23. Yang, Y., Cao, D., Yu, T., Wang, D., Li, C.: Prediction of dynamic characteristics of a dual-rotor system with fixed point rubbing-theoretical analysis and experimental study. *Int. J. Mech. Sci.* **115**, 253–261 (2016)
24. Yang, Y., Cao, D., Xu, Y.: Rubbing analysis of a nonlinear rotor system with surface coatings. *Int. J. Non-Linear Mech.* **84**, 105–115 (2016)
25. Xiang, L., Hu, A., Hou, L., Xiong, Y., Xing, J.: Nonlinear coupled dynamics of an asymmetric double-disc rotor-bearing system under rub-impact and oil-film forces. *Appl. Math. Model.* **40**(7–8), 4505–4523 (2016)
26. Kim, Y., Noah, S., Choi, Y.: Periodic response of multi-disk rotors with bearing clearances. *J. Sound Vib.* **144**(3), 381–395 (1991)
27. Gustavsson, R.K., Aidanpää, J.O.: Evaluation of impact dynamics and contact forces in a hydropower rotor due to variations in damping and lateral fluid forces. *Int. J. Mech. Sci.* **51**(9–10), 653–661 (2009)
28. Nelson, H., Meacham, W., Fleming, D., Kascak, A.: Nonlinear analysis of rotor-bearing systems using component mode synthesis. *J. Eng. Power* **105**(3), 606–614 (1983)
29. Glasgow, D., Nelson, H.: Stability analysis of rotor-bearing systems using component mode synthesis. *J. Mech. Des.* **102**(2), 352–359 (1980)
30. Batailly, A., Meingast, M., Legrand, M.: Unilateral contact induced blade/casing vibratory interactions in impellers: analysis for rigid casings. *J. Sound Vib.* **337**, 244–262 (2015)
31. Praveen Krishna, I., Padmanabhan, C.: Experimental and numerical investigations on rotor–stator rub. *Proc. Inst. Mech. Eng. Part C J. Mech. Eng. Sci.* 1–13 (2017). <https://doi.org/10.1177/0954406217735348>
32. Krishna, I.P., Padmanabhan, C.: Improved reduced order solution techniques for nonlinear systems with localized nonlinearities. *Nonlinear Dyn.* **63**(4), 561–586 (2011)
33. Nelson, H., McVaugh, J.: The dynamics of rotor-bearing systems using finite elements. *J. Eng. Ind.* **98**(2), 593–600 (1976)
34. Craig, R., Bampton, M.: Coupling of substructures for dynamic analyses. *AIAA J.* **6**(7), 1313–1319 (1968)



Analysis of Variable Mass Rotordynamic Systems with Semi-analytic Time-Integration

Helmut J. Holl^(✉)

Institute of Technical Mechanics, Johannes Kepler University of Linz,
Altenbergerstraße 69, 4040 Linz, Austria
helmut.holl@jku.at
<https://www.jku.at/tmech/holl>

Abstract. The analysed rotordynamic system is modeled as a non-linear variable mass system and represents a part of a production line where an axially moving material is coiled on a rotating drum. The suitable and accurate simulation of the vibrations in a coiling process is important to predict the vibrations during standard operation and for special non-steady operation conditions. Variable parameters are present and bending vibrations of the rotor with the coiling drum and the transversal oscillations of the elastic strip are coupled. The longitudinal and transversal motion of the axially moving strip and the bending deflection of the coiling drum are considered by Rayleigh-Ritz approximations which involve the application of the extended equation of Lagrange for open systems. Simulations are performed for a non-linear rotordynamic system for different operation conditions. The results computed with a semi-analytic time-integrations algorithm are shown.

Keywords: Variable mass system · Coiling process
Variable parameters · Extended equation of Lagrange

1 Introduction

For the simulation of the vibrations in a coiling process a suitable mechanical model is necessary. In the coiling process an axially moving strip moves continuously towards a rotating drum where it is coiled. For instance between two successive coiling processes the strip passes through a Steckel mill where the thickness is reduced. In this paper the mechanical model starts at the exit of the Steckel mill and considers the axial motion of the strip with the transversal oscillations. Then the strip is coiled and when the strip is attached to the drum it contributes to the bending stiffness and increases the mass and the outer radius of the drum. As the exact description of the coiling process is very complicated, it is assumed that the coiled strip is fixed on the coiling drum when it touches the drum so that the stiffness of the drum increases with the rotation angle.

The accumulation of the mass on the coiling drum has a certain influence on the vibrations of the total system during operation. The resulting mechanical model is a non-linear dynamic model with varying mass and system parameters, which are defined by the variable outer radius of the drum, the variable bending stiffness and a variable eccentricity of the rotating drum. Due to the coiled material the mass of the coiling drum increases or decreases continuously. For the outer radius of the coiling drum an Archimedian Spiral is assumed, which gives a position dependent outer radius and bending stiffness of the rotating shaft with the drum. For the simulation of the coiling process with the long computation time a semi-analytic time integration method was implemented.

For the derivation of the equations of motion Rayleigh-Ritz approximations are used to get a minimal number of degrees of freedom in the mechanical model. The application of the extended equations of Lagrange, see [1], is necessary as the mass in the system is not constant, which is a restriction for the well-known equations of Lagrange, see [2]. In the extended equations of Lagrange the control volume concept with the surface integrals with partial derivatives as a kernel are present. The control volume concept for the non-linear dynamic system takes the flow of mass through the boundary into account. For the application of this control volume concept it is important to distinguish between the material control volume and the spatial control volume. If the relative speed between the surface of the control volume and the transported material does not depend on the applied degrees of freedom and their time derivatives, it can be seen from the equations in [1] and also [3] that the surface integral terms vanish and the classical form of the Lagrange equations results. In [4] additionally some literature on dynamic systems with variable mass is cited and in [5–9] different mechanical models with variable parameters have been analysed. In [10, 11] an alternative approach for the influence of the variable mass is considered using reactive forces, where also some examples are discussed and the effect of the reactive force is studied for the case of winding up a band. A model for an industrial application with additional strip guiding rolls was analysed in [7, 8], where the strip tension force was computed for a given entrance speed of the strip. In [12, 13] the effect of the time variable eccentricity is considered where the time derivatives of the eccentricity are involved and it is shown that very small vibration amplitudes result.

The temperature of the coiled strip is usually not constant over the long process time, so that a thermal deflection of the shaft of the coiling drum can occur due to a certain non-homogeneous temperature distribution. The thermal deflection represents a kinematic parameter in the mechanical model and has a high influence on the strip tension force. The strip tension force is a critical process parameter which should be constant and at least should be positive. The effect of the thermal deflection of the coiling drum results in high vibration amplitudes which was analysed in [9] for the uncoupled system where computed results are shown for the controlled system with thermal deflection. Predeformation or misalignment of the shaft can be caused by production tolerances, inhomogeneous temperature distribution or maintenance errors. In this paper the

coupled vibrations are analysed and numerical studies are performed in order to increase the knowledge about the complicated variable mass non-linear dynamic system of the coiling drum and the axially moving strip. For the dynamic system the initial and boundary conditions are defined and with the defined operation conditions a developed semi-analytic time-integration algorithm computes the solution. An algorithm was used which has been presented in [5,14] and has been extended in [15] to substructure analysis.

2 Mechanical Modelling of the Coiling Process

The mechanical model of the coiling process includes the coiling drum on elastic shaft in rigid bearings and the moving strip, see Fig. 1. Rayleigh-Ritz approximations and the extended equations of Lagrange have been used for the derivation of the mechanical model. The resulting mechanical model has five degrees of freedom, the horizontal and vertical deflection x, y , the rotation angle φ of the coiling drum, the transversal deflection of the moving strip q and the entrance speed of the strip \dot{s}_L . The strip tension force F_B is given as a predefined value at the entrance of the system. The torque at the coiling drum M_T is controlled to maintain a suitable process.

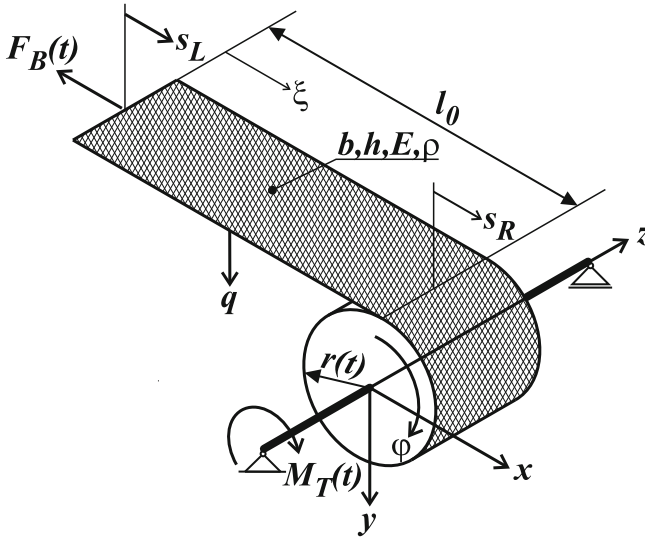


Fig. 1. Mechanical model of the rotating drum with the axially moving strip

For the derivation of the equations of motion it is important to distinguish between the material control volume and the spatial control volume, see [1]. The spatial control volume is an arbitrary moving non-material volume with a surface that has a speed \mathbf{w} which is different from the velocity of the material at

the surface \mathbf{v} . The transport of kinetic energy and mass can be determined and is related to the spatial derivative of the total kinetic energy at the boundary of the control volume so that the extended equation of Lagrange, see [1], can be written in the form

$$\frac{d}{dt} \left(\frac{\partial T}{\partial \dot{q}_i} \right) - \frac{\partial T}{\partial q_i} + \frac{1}{2} \oint_{\partial V_i} \frac{\partial \mathbf{v}^2}{\partial \dot{q}_i} \rho (\mathbf{v} - \mathbf{w}) \mathbf{n} dS - \oint_{\partial V_i} \rho \frac{\mathbf{v}^2}{2} \frac{\partial (\mathbf{v} - \mathbf{w})}{\partial \dot{q}_i} \mathbf{n} dS = Q_i, \quad (1)$$

where \mathbf{n} is the outward normal vector at the boundary of the control volume. The control volume of the mechanical system can be seen in Fig. 2. The surface integral terms vanish if the velocity at the boundary of the control volume are prescribed and independent of the degrees of freedom q_i of the system.

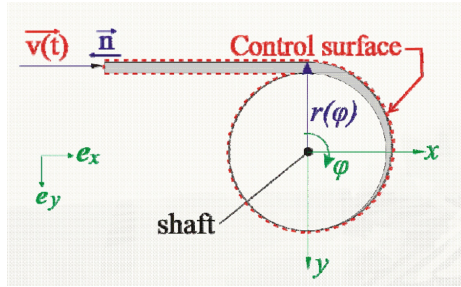


Fig. 2. Control Volume for the Mechanical model of the rotating drum with the axially moving strip

2.1 Model of the Coiling Drum

The coiling drum is modeled as a beam with varying bending stiffness. In a first step the outer radius of the drum increases in accordance to an Archimedian spiral

$$r = r_0 + \frac{h\varphi}{2\pi}, \quad (2)$$

where h is the thickness of the strip. For the actual bending stiffness of the rotating shaft it is assumed that the coiled strip is attached to the drum and contributes to the stiffness. The total mass of the coiling drum is $m_C = m_0 + \rho A s_R$ and its time derivative is $\dot{m}_C = \rho A \dot{s}_R$, where ρ is the density of the strip material, A is the cross section of the strip, s_R is the coiled length of the strip and \dot{s}_R its time derivative.

The mechanical system of the coiling drum, which is considered in this paper, is shown in Fig. 1. The equations of motion are written in the coordinates of the center of the shaft. The exact position of the center of gravity of the coiling drum including the strip changes during the coiling process and can be computed according to the results shown in [12, 13]. Because of the symmetry in the

mechanical model we consider vibrations of the coiling drum in the x - y -plane only. At the coiling drum the torsion moment M_T is applied, b is the width of the strip and h is the strip thickness. \dot{s}_L is the entrance speed of the strip and \dot{s}_R is the absolute speed of the strip when attaching the coiling drum. The coiling drum rests on rigid bearings, so that only the stiffness of the shaft is taken into account. It is assumed that the thermal deflection is caused by a non-homogeneous temperature distribution within the coiling drum and results in a total deflection a which is measured in the mid-plane of the drum. The actual coordinates of the center of gravity of the drum are denoted by x_S and y_S , whereas for the center of the shaft the coordinates denoted by x_W and y_W are used. Due to the thermal deflection the position of the center of the undeformed shaft was defined by x_{W0} and y_{W0} . In the following computations the strip tension force $F_B(t)$ is predefined and the resulting model has five degrees of freedom x_W, y_W, φ, q_i and s_L . In the special case with a prescribed speed \dot{s}_L at the left boundary, the mechanical model results in four degrees of freedom which is not considered here.

The kinetic energy of the coiling drum is computed by

$$T_C = m_C \frac{\dot{x}_S^2 + \dot{y}_S^2}{2} + J_C \frac{\dot{\varphi}^2}{2} \tag{3}$$

with the momentum of inertia defined by

$$J_C = \frac{m_C}{2} (r^2 + \bar{r}_0^2) \tag{4}$$

where \bar{r}_0 is the inner radius of the coiling drum and r is the outer radius given in Eq. (2). The potential energy is

$$V_C = \frac{c_C}{2} [(x_W - x_{W0})^2 + (y_W - y_{W0})^2] - m_C g y_S, \tag{5}$$

where c_C is the actual computed bending stiffness of the coiling drum. The controlled torque applied at the coiling drum is given by

$$M_T = M_0 + \alpha_C (\dot{s}_{L,D} - \dot{s}_L) + \beta_C (s_{L,D} - s_L) + \chi_C (\dot{x}_{WD} - \dot{x}_W) + \delta_C (x_{WD} - x_W), \tag{6}$$

where $s_{L,D}, \dot{s}_{L,D}, x_{WD}$ and \dot{x}_{WD} are the target values and $\alpha_C, \beta_C, \chi_C$ and δ_C are defined parameters of the controller.

2.2 Model of the Moving Strip

With the axial speed of the strip on the left entry position \dot{s}_L the longitudinal motion of the strip is defined by

$$u^*(\xi, t) = s_L + (s_R - s_L) \frac{\xi}{l_0}, \quad \dot{u}^*(\xi, t) = \dot{s}_L + (\dot{s}_R - \dot{s}_L) \frac{\xi}{l_0}, \tag{7}$$

where l_0 is the free length of the strip between the entry position and the drum, see Fig. 1, and ξ is the longitudinal coordinate. s_R and \dot{s}_R are the kinematic

variables for the coiled strip length and speed at the point on the coiling drum. For the transversal direction a Rayleigh-Ritz approximation

$$w_B^*(\xi, t) = \psi(\xi)q(t) \quad (8)$$

is used where the shape function

$$\psi(\xi) = \sin^2\left(\frac{\pi\xi}{l_0}\right) \quad (9)$$

is considered. The strip moves into the control volume at a fixed vertical position on the left boundary and the position where it attaches the drum is defined by the actual radius r and the vertical deflection y_W of the drum. The total transversal deflection is assumed by

$$w^*(\xi, t) = w_B^*(\xi, t) + (y_W - r)\frac{\xi}{l_0}, \quad (10)$$

where $w_B^*(\xi, t)$ is the bending deflection of the strip. The total velocity of the moving strip is

$$\dot{w}^*(\xi, t) = \dot{w}_B^*(\xi, t) + \frac{dw_B^*(\xi, t)}{d\xi}\dot{u}^*(\xi, t) + (\dot{y}_W - \dot{r})\frac{\xi}{l_0}. \quad (11)$$

The kinetic energy of the moving strip is computed by

$$T_S = \frac{1}{2} \int_0^{l_0} \rho A \dot{u}^*(\xi, t)^2 d\xi + \frac{1}{2} \int_0^{l_0} \rho A \dot{w}^*(\xi, t)^2 d\xi \quad (12)$$

resulting in

$$\begin{aligned} T_S = & \frac{m_S}{6} \left[\dot{s}_R^2 + \dot{s}_L (\dot{s}_L + \dot{s}_R) + 2(\dot{y}_W - \dot{r})^2 \right] + \frac{m_S q}{2l_0} \left[\frac{3}{8} \dot{q} (\dot{s}_L - \dot{s}_R) - \dot{s}_R (\dot{y}_W - \dot{r}) \right] \\ & + \frac{m_S \dot{q}}{4} \left(\frac{3}{4} \dot{q} + \dot{y}_W - \dot{r} \right) + \frac{\pi^2 m_S q^2}{12l_0^2} [(\dot{s}_L^2 + \dot{s}_L \dot{s}_R + \dot{s}_R^2)] - \frac{m_S q^2}{32l_0^2} (\dot{s}_L - \dot{s}_R)^2. \end{aligned} \quad (13)$$

With the strain in the strip $\varepsilon_S = \varepsilon_{xx} - zw'' + \frac{1}{2}w'^2$ the potential energy is given by

$$\begin{aligned} V_S = & \frac{1}{2} \int_0^{l_0} \left[EA \left(\frac{\partial u^*(\xi, t)}{\partial \xi} \right)^2 + EJ_S \left(\frac{\partial^2 w^*(\xi, t)}{\partial \xi^2} \right)^2 \right] d\xi \\ & + \frac{1}{2} \int_0^{l_0} F_B \left(\frac{\partial w_B^*(\xi, t)}{\partial \xi} \right)^2 d\xi \end{aligned} \quad (14)$$

with the Youngs modulus E and the bending stiffness of the strip $J_S = \frac{bh^3}{12}$. Inserting the Rayleigh-Ritz approximations from Eqs. (8) and (9) we get

$$V_S = \frac{c_C}{2} (s_R - s_L)^2 + \frac{\pi^4 E J_S}{l_0^3} q^2 + \frac{\pi^2 F_B}{4l_0} q^2 \tag{15}$$

The horizontal motion of the strip in longitudinal direction at the right position where it touches the coiling drum is defined by

$$s_R = \int_0^t r \dot{\varphi} dt + x_W - \frac{\pi^2}{l_0} \frac{q^2}{4} + a \sin(\varphi + \delta) \tag{16}$$

$$\dot{s}_R = r \dot{\varphi} + \dot{x}_W - \frac{\pi^2}{2l_0} q \dot{q} + a \dot{\varphi} \cos(\varphi + \delta) \tag{17}$$

for the Rayleigh-Ritz approximations and homogeneous initial conditions for s_R . φ is the rotation angle, a is the thermal deflection in the middle of the coiling drum and x_W is the horizontal deflection of the center of the rotating drum. For the Archimedian spiral of Eq. (2) the coiled length can be integrated to get

$$s_R = r_0 \varphi + \frac{h \varphi^2}{4\pi} + x_W - \frac{\pi^2 q^2}{4l_0} + a \sin(\varphi + \delta). \tag{18}$$

2.3 Extended Equations of Lagrange

The extended Equation of Lagrange for a non-material reference volume, which is given in Eq. (1) has to be used. In order to evaluate the surface integral terms corresponding to Fig. 2 the related velocities have to be defined. As some mass is transported into the mechanical system under consideration, we have to distinguish a material-fixed control volume (in this case a control surface) with the velocity vector

$$\mathbf{w}(t) = \begin{bmatrix} 0 \\ \dot{y}_W - \dot{r} \\ 0 \end{bmatrix} \tag{19}$$

and some material flowing through the boundary with the actual velocity vector of the mass

$$\mathbf{v}(t) = \begin{bmatrix} \dot{s}_L \\ \dot{y}_W - \dot{r} \\ 0 \end{bmatrix}. \tag{20}$$

The surface integral terms for these areas can be computed, where material flows through the surface with a constant speed within the surface. With these kinematic assumptions the integral terms can be evaluated which result from the extended Lagrange Equation (Eq. (1)) for each degree of freedom and result to

$$P_x = 0 \tag{21}$$

$$P_y = -(\dot{y}_W - \dot{r}) \rho \dot{s}_L A \quad (22)$$

$$P_\varphi = -(\dot{y}_W - \dot{r}) \frac{h}{2\pi} \rho \dot{s}_L A \quad (23)$$

$$P_{s_L} = \frac{(\dot{y}_W - \dot{r})^2 - \dot{s}_L^2}{2} \rho A \quad (24)$$

$$P_q = 0 \quad (25)$$

Finally the generalized forces which will be needed also in the extended Lagrange Equation (Eq. (1)) are given by

$$Q_x = \frac{\partial V}{\partial x_W} - d_x \dot{x}_W \quad (26)$$

$$Q_y = \frac{\partial V}{\partial y_W} - d_y \dot{y}_W \quad (27)$$

$$Q_\varphi = \frac{\partial V}{\partial \varphi} + M_D \quad (28)$$

$$Q_{s_L} = \frac{\partial V}{\partial s_L} - F_B \quad (29)$$

$$Q_q = \frac{\partial V}{\partial q} - d_q \dot{q} \quad (30)$$

It can be seen in the equations for the generalized forces, that some damping factors have been introduced with respect to the transversal motion of the coiling drum and the strip.

2.4 Equations of Motion for the Total Model

The derivation of the equations of motion based on the above equations for the kinetic and potential energy as well as the additional equations considering the flow through the boundary of the control volume the equations for the degrees of freedom of motion result. As they are lengthy equations they are not given here explicitly.

2.5 Semi-analytic Time-Integration Algorithm

The developed semi-analytic time-integration algorithm is based on the modal analysis of a modified dynamic system. For the resulting modally decoupled equations for the i -th degree of freedom

$$\ddot{q}_i + 2\zeta_i \omega_i \dot{q}_i + \omega_i^2 q_i = f_i(t) - \sum_{j=0, i \neq j}^N (\alpha_j q_j - \delta_j \dot{q}_j - \kappa_j \ddot{q}_j) \quad (31)$$

the solution is computed using the Duhamel-convolution integral with defined approximations of the evolution of the solution within a time-step. The resulting algorithm was analysed with respect to the numerical behaviour and it was found that it is superior to the conventional known time-integration methods, see [5, 14, 15]. This semi-analytic algorithm was used for the time integration and with a suitable time step converged solutions are guaranteed.

3 Computed Results

For the derived mechanical model the solution was computed for different operation conditions and parametric studies have been performed. For the computation results presented in this contribution the parameters of the coiling drum are $l_0 = 5$ m, $\bar{r}_0 = 0.45$ m, $h = 10$ mm, $b = 0.5$ m, $E = 105$ kN/mm², $c_C = 10^7$ kN/m, $\rho = 7800$ kg/m³, $m_0 = 1200$ kg. The controller parameters are given by $\alpha_C = 15$ kNs, $\beta_C = 10$ kN, $\chi_C = 10$ MNs and $\delta_C = 10$ kN. The target parameters are $s_{L,D} = \dot{s}_{L,D}t$, $\dot{s}_{L,D} = 5, 25$ m/s, $x_{WD} = 0$ m and $\dot{x}_{WD} = 0$ m/s. In all computed examples it is guaranteed that there is a converged solution based on a suitable time step.

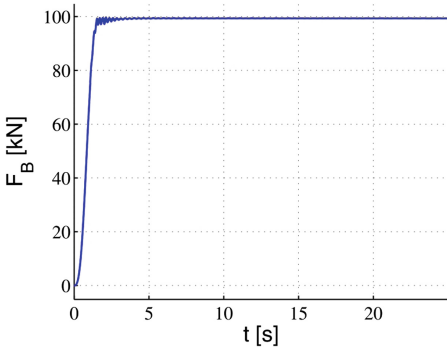


Fig. 3. First example: Strip tension force

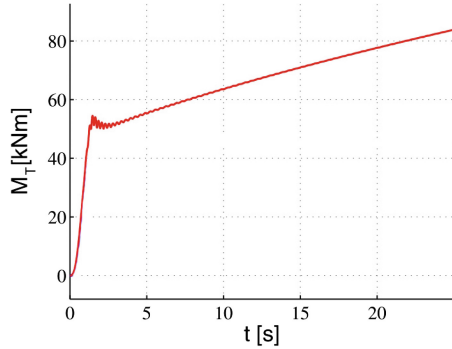


Fig. 4. First example: Computed torque at the coiling drum

For a first example a constant strip tension force of $F_B = 100$ kN is applied as shown in Fig. 3. The load is increased within 1 s and is kept constant afterwards. With the given control parameters a steady operation is performed, resulting in a torque at the drum shown in Fig. 4. The torque increases proportional with the increasing outer radius of the coiling drum. The coiled strip length and the strip speed are given in Fig. 5. The corresponding outer radius of the coiling drum is shown in Fig. 6. The results for the horizontal position of the center of the coiling drum show small vibrations, see Fig. 7 and the mean value of the deflection results from the constant strip tension force. For the vertical position small vibrations are present as the drum is rotating and the gravity of the increasing mass results in an increasing weight of the drum which causes an increasing vertical deflection y_W in Fig. 8. The small vibration amplitudes correspond to the non-homogeneous initial conditions and to the linear increase of the outer radius. It is mentioned that for the assumption of a step function of the outer radius according to $r = r_0 + h \lfloor \frac{\varphi}{2\pi} \rfloor$ high vibration amplitudes occur after every rotation. The corresponding computational results are shown in Fig. 9 for a sequence of Heaviside-functions, where the high fluctuations of the strip tension force can be seen. Some additional effort is necessary for the computation

of this case as negative strip tension forces are not permitted. Due to the coiling process and the design of the coiling drum the outer radius shows some more complicated shapes which have been analyzed.

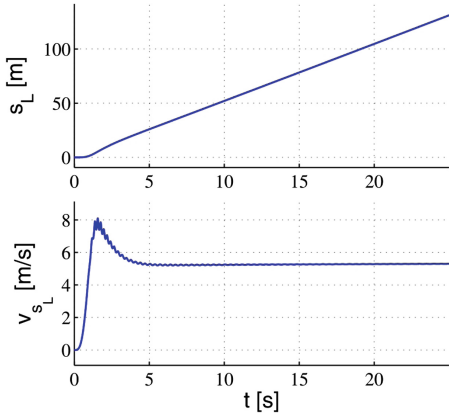


Fig. 5. First example: Coiled strip length and strip speed

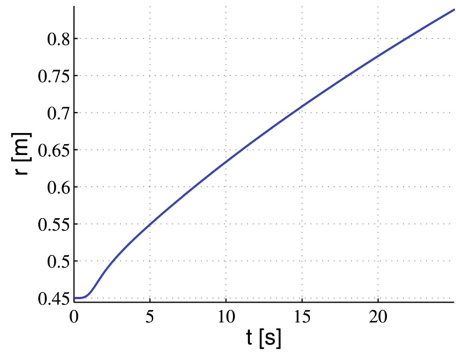


Fig. 6. First example: Outer radius of the coiling drum

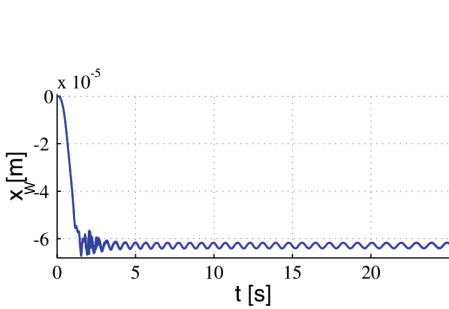


Fig. 7. First example: Horizontal position of the center of the coiling drum

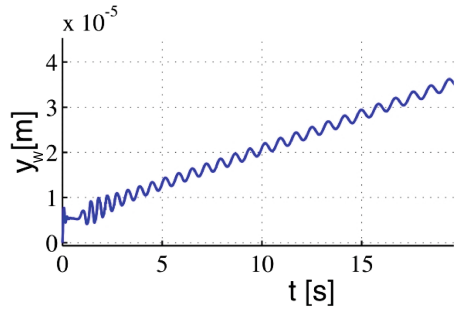


Fig. 8. First example: Vertical position of the center of the coiling drum

For a second example the strip tension force is $F_B = F_{B0} \left(1 + \frac{\sin(\pi t/2)}{2} \right)$ with $F_{B0} = 50\text{kN}$ and all the other parameters are kept unchanged. The computation is carried out and the controlled torque at the drum is shown in Fig. 10. From the results of the transversal strip vibrations in Fig. 11 the coupling effect with the varying frequency and amplitude is shown. In Figs. 12 and 13 the results for the motion of the center of gravity of the coiling drum are drawn for the horizontal and vertical direction. The horizontal motion is caused by the varying strip tension force and the vertical motion is induced by the variation of the strip

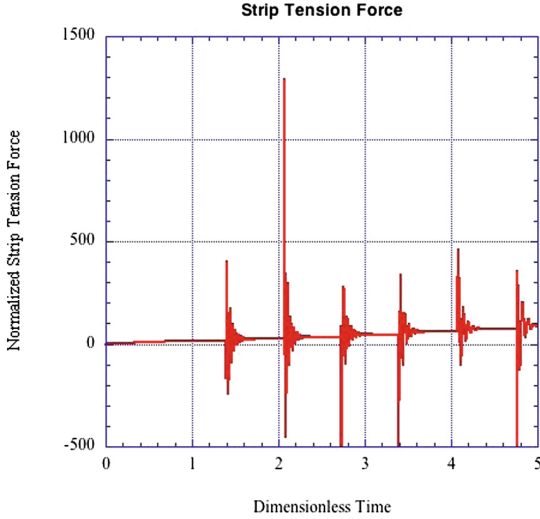


Fig. 9. First example: Normalized strip tension force for a radius function with a sequence of Heaviside-functions

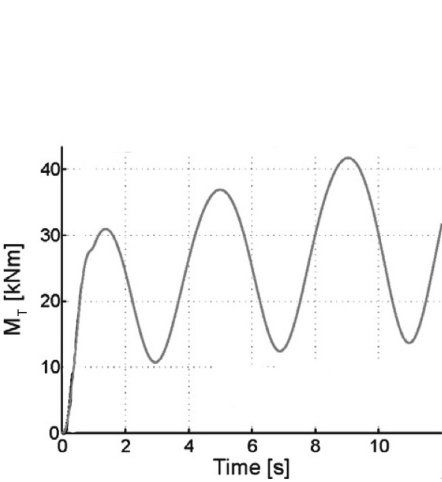


Fig. 10. Second example: Torque at the coiling drum

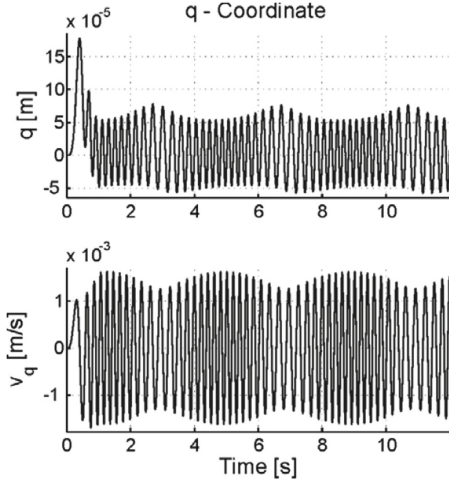


Fig. 11. Second example: Amplitude and velocity of transversal motion of the strip

tension force. In the vertical position it can be seen that the influence on the weight is not considered in this example.

For the third example the parameters for the mechanical model of Fig. 1 are the same, except for $\bar{r}_0 = 0.4$ m and $F_B = 50$ kN, which are now kept constant. The computed results are shown for two different thermal deflections of

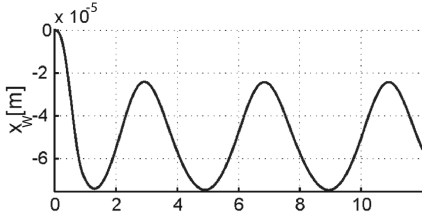


Fig. 12. Second example: Horizontal position of the center of the coiling drum

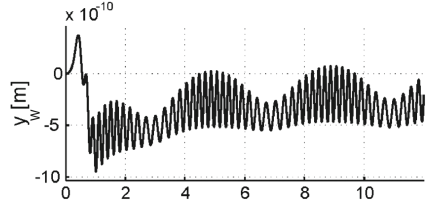


Fig. 13. Second example: Vertical position of the center of the coiling drum

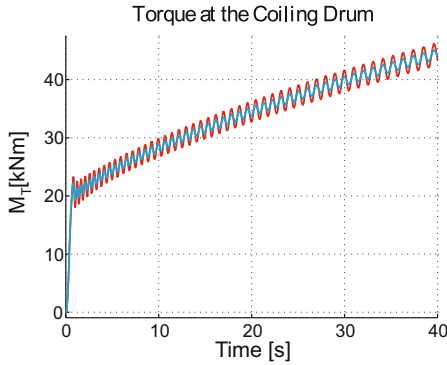


Fig. 14. Third example: Computed torque at the coiling drum for $a = 0.1$ (blue) and 0.23 mm (red)

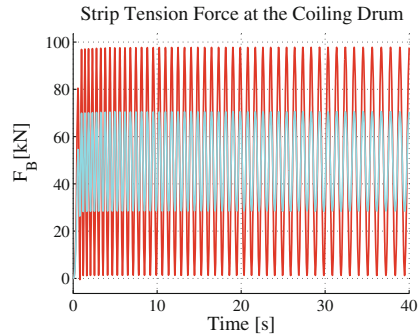


Fig. 15. Third example: Computed strip tension force for $a = 0.1$ (blue) and 0.23 mm (red)

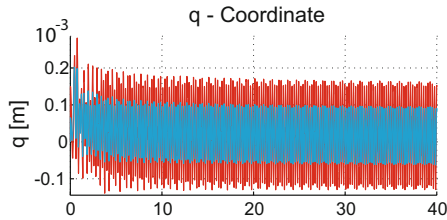


Fig. 16. Third example: Moving strip - Transversal oscillations for $a = 0.1$ (blue) and 0.23 mm (red)

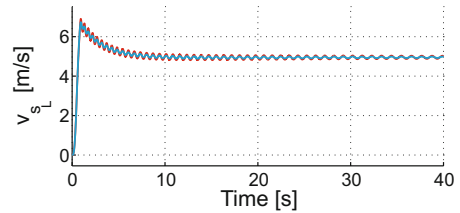


Fig. 17. Third example: Computed axial strip speed for $a = 0.1$ (blue) and 0.23 mm (red)

$a = 0.1$ mm and $a = 0.23$ mm. Figure 14 shows the computed torque and in Fig. 15 the strip tension force is shown. If $a = 0.23$ mm the minimum strip tension force is computed to be $F_B \geq 0$ N. The transversal deflection of the moving strip is given in Fig. 16 which is a results of the strip tension force F_B and the motion of the coiling drum with the thermal deflection a . For the higher excitation

amplitude of the thermal deflection the transversal oscillations of the strip are higher. The excitation frequency and the frequency of transient vibration are very different. In Fig. 17 the axial speed of the strip is shown as there is a constant F_B maintained at the left boundary. This result is similar to that for the first example, see Fig. 5, but with a much smaller strip tension force and a thermal deflection of the shaft of the coiling drum. Different fluctuations in the axial strip speed can be seen which are caused by the two different thermal deflection values.

4 Conclusion

A mechanical model with a variable mass and varying parameters of a coiling process was derived. The simulation results for three different examples show that for a steady state production process with a constant axial speed the vibration amplitudes are very small. For the non-linear dynamic system with variable mass vibrations are computed for given forces at the left entrance boundary and a controlled torque. For a defined variation of the strip tension force at the entrance the vibration amplitudes are higher than for a constant strip tension force. The frequency and amplitude for the transversal strip oscillation depend on the strip tension force. The influence of the process parameters are studied to reduce the vibrations and results are given for two different thermal deflection values.

Acknowledgments. Support of this work in the framework of the Comet-K2 Linz Center of Competence in Mechatronics (LCM), Area 2, MECON-Complete mechanical systems and automatic control, is gratefully acknowledged.

References

1. Irschik, H., Holl, H.J.: The equations of lagrange written for a non- material volume. *Acta Mech.* **153**(3–4), 231–248 (2002)
2. Ziegler, F.: *Mechanics of Solids and Fluids*, 2nd edn. Springer Verlag, New York (1998)
3. Irschik, H., Holl, H.J.: Lagrange’s equations for open systems, derived via the method of fictitious particles, and written in the Lagrange description of continuum mechanics. *Acta Mech.* **226**, 63–79 (2015)
4. Irschik, H., Holl, H.J.: Mechanics of variable-mass systems - part 1: balance of mass and linear momentum. *Appl. Mech. Rev.* **57**(2), 145–160 (2004)
5. Holl, H.J.: A time-integration algorithm for time-varying systems with non-classical damping based on modal methods. In: Wicks, A.L. (ed.) *Proceedings of the 15th International Modal Analysis Conference*, 3–6 February 1997, Orlando, pp. 1558–1564. Society for Experimental Mechanics (1997)
6. Holl, H.J., Belyaev, A.K., Irschik, H.: A time integration algorithm for nonlinear rotordynamic systems with time-varying parameters. In: Muszynska, A. (ed.) *Proceedings of the Seventh International Symposium on Transport Phenomena and Dynamics of Rotating Machinery (7th ISROMAC)*, 22–26 February 1998, Honolulu, vol. B, pp. 930-940. Bird Rock Publishing House (1998)

7. Holl, H.J., Finstermann, G., Mayrhofer, K., Irschik, H.: Vibration simulation of the Steckel mill strip coiling process. In: Mang, H.A., Rammerstorfer, F.G., Eberhardsteiner, J. (eds.) Proceedings of the Fifth World Congress on Computational Mechanics (WCCW V), 7–12 July 2002, Wien. Vienna University of Technology, Austria (2002). <http://wccm.tuwien.ac.at>
8. Holl, H.J., Finstermann, G., Mayrhofer, K., Irschik, H.: Nonlinear vibrations during the pass in a Steckel mill strip coiling process, In: Radons, G., Neugebauer, R., Wiley-VCH, (eds.) Nonlinear Dynamics of Production Systems, Weinheim, pp. 305–316 (2004)
9. Holl, H.J., Hammelmüller, F.: Simulation of a coiling process with thermal deflection of the drum. In: Ziegler, F., Heuer, R., Adam, C. (eds.) Proceedings of the Sixth International Congress on Thermal Stresses (TS2005), Vienna University of Technology, Vienna, Austria, 26–29 May 2005, vol. 1, pp. 377–380. Schriftenreihe der Technischen Universität Wien (2005)
10. Cveticanin, L.: The influence of the reactive force on the motion of the rotor on which the strip is winding up. *J. Sound Vib.* **167**, 382–384 (1993)
11. Cveticanin, L.: Dynamics of Machines with Variable Mass. Gordon and Breach Science Publishers, Philadelphia (1998)
12. Holl, H.J., Hammelmüller, F.: Zum Einfluss einer veränderlichen Exzentrizität auf die Schwingungen beim Wickelprozess 10. In: Liebich, R. (ed) Internationale Tagung Schwingungen in Rotierenden Maschinen X (SIRM X on CD-Rom), 25–27 February 2013, Berlin, paper-ID ABS-218, p. 10 (2013)
13. Hammelmüller, F., Holl, H.J.: The effect of variable eccentricity onto the oscillations in a coiling process. In: PAMM, vol. 3, no. 1, pp. 104–105 (2003)
14. Holl, H.J.: An efficient semi-analytic time-integration method with application to non-linear rotordynamic systems. *Comput. Mech.* **26**(4), 362–375 (2000)
15. Holl, H.J.: A modal-based substructure method applied to nonlinear rotordynamic systems. *Int. J. Rotating Mach.* Article ID 313526, 8 p. (2009). <https://doi.org/10.1155/2009/313526>



Nonlinear Analyses in Rotordynamic Engineering

Joachim Schmied^(✉) and Andreas Fuchs^(✉)

DELTA JS AG Technoparkstrasse 1, 8005 Zurich, Switzerland
{jschmied, afuchs}@delta-js.ch

Abstract. Linear rotor-dynamic analyses such as Campbell diagrams of damped eigenvalues and unbalance response analyses are well established for the practical design layout of rotors. They are also required according to many standards such as API. Nonlinear analyses are widely avoided because of their complexity, even if they would be necessary for relevant practical answers. Sometimes questionable substitute linear analyses are carried out in such cases. In this paper four cases requiring nonlinear analyses are described: A vertical pump with water lubricated bearings, a turbocharger with semi-floating oil lubricated bearings, an electric motor with rolling element bearings running through a resonance and a Pelton turbine on tilting pad bearings losing two buckets. The vertical pump is linearly unstable, because of the unloaded bearings. The nonlinear analyses are necessary to receive the limit cycles of the unstable system. In case of the turbocharger the outer oil film of the semi-floating ring bearing is highly nonlinear and cannot be correctly described linearly. In case of the motor running through a resonance the dynamic bearing loads are very high, because the rolling element bearings are not able to provide much damping. The behavior then becomes nonlinear. Moreover, the bearing clearance can lead to nonlinear behavior, if the bearings are not preloaded. The blade loss for the Pelton turbine leads to nonlinear behavior due to the high dynamic bearing load.

Keywords: Non-linear phenomena in rotordynamics
Dynamic analysis and stability · Fluid film bearings · Rolling element bearings

1 Introduction

Nonlinear analyses are rarely carried out in practical engineering. There are good reasons for that: In many cases linear analyses are sufficient to get correct answers for the design of a machine although real machines are always nonlinear to some extent. Nonlinear analyses take considerable more effort than well-established linear analyses such as undamped critical speed maps, damped Campbell diagrams and damped unbalance response analyses. Most of these linear analyses are required by standards such as API standards [1], whereas so far, no standard asks for nonlinear analyses. Nonlinear analyses normally take a much bigger effort for the following reasons: The nonlinear effects must be modelled, analysis times are much longer (usually the nonlinear equations are integrated in the time domain by solvers such as Runge Kutta), the

solver may be numerical unstable, and the resulting behavior can be complex requiring some effort for the interpretation of the result.

In some cases, however, nonlinear analyses cannot be avoided for correct answers. Four such cases are described in this paper:

1. A vertical pump with water lubricated bearings: Fluid film bearings are normally linearized around their static load, which yield the linear stiffness and damping coefficients. The linearized behavior can give good results in a wide range of dynamic loads, not exceeding the static load. If the static load is zero or small, then strictly speaking the behavior is always nonlinear. Moreover, in the present example the rotor is unstable, because it has unloaded cylindrical bearings. A linear analysis does not tell at which level the unstable system (limit cycle) stabilizes. To get this result, which is essential for an assessment of the rotor behavior, a nonlinear analysis is necessary.
2. A turbocharger with semi-floating ring bearings: The outer oil film of bearings functions as a squeeze film damper without centering device (e.g. a squirrel cage) for the ring. The behavior of such a damper is essentially nonlinear, because a centering force for the ring only arises by a vibration of the ring. Therefore, only a nonlinear analysis can correctly simulate such a rotor. For the investigated turbocharger, which is also described in [2], extensive measurements were made by the vendor ABB. The analyses are compared to these measurements.
3. An electric motor with rolling element bearings running through a resonance: In contrast to fluid film bearings rolling element bearings do not provide notable damping. Without additional damping device such as a squeeze film damper, rotors supported on rolling element bearings are therefore not suited to run in resonance or even above a critical, which requires crossing it. The latter may be acceptable in case of sufficient acceleration. Practically such applications exist. The example here is derived from a real motor not running above a critical. Nevertheless, we will demonstrate the effects arising when crossing the critical with this example. Since the damping is low, high vibrations and high dynamic bearing forces arise, which require a nonlinear analysis. Linearized bearing characteristics around a static equilibrium are no longer applicable.
4. A vertical Pelton turbine on tilting pad oil bearings losing three buckets: The loss of two buckets causes large dynamic forces requiring a nonlinear analysis. The results of the nonlinear simulation are compared to linear results.

All examples are practically relevant. The investigated turbocharger corresponds to a built machine, which has been measured. The other examples are derived from real applications. Crossing of resonances on ball bearings without damping device is practically done, although not for the type of motor investigated here. The speed range of the electric motor has been extended to show the corresponding effects.

All analyses were carried out with the comprehensive rotordynamic program MADYN 2000 [3].

2 Nonlinearities and Solving the Nonlinear Equations

2.1 Nonlinear Fluid Film Bearings

The nonlinear fluid film forces on the rotor are described in a 2, 3-coordinate system according to Eqs. (1) and (2) as a function of the rotor position (see Fig. 1).

$$-\begin{bmatrix} F_3 \\ F_2 \end{bmatrix} = SoFactor \left(\begin{bmatrix} So(\varepsilon, \gamma) \sin \alpha \\ So(\varepsilon, \gamma) \cos \alpha \end{bmatrix} + \begin{bmatrix} \beta_{33}(\varepsilon, \gamma) & \beta_{32}(\varepsilon, \gamma) \\ \beta_{32}(\varepsilon, \gamma) & \beta_{22}(\varepsilon, \gamma) \end{bmatrix} \frac{1}{\Delta R \Omega} \begin{bmatrix} \dot{x}_3 \\ \dot{x}_2 \end{bmatrix} \right) \quad (1)$$

$$SoFactor = \frac{F}{So} = \frac{BD\eta\Omega}{\Psi^2} \quad (2)$$

with So as the Sommerfeld number, β as dimensionless damping coefficients, ΔR as the radial minimum clearance, ε as the dimensionless eccentricity with reference ΔR , γ as the position angle, Ω as the rotor speed \dot{x} as the rotor velocities, B as the bearing width, D as the bearing diameter, η as the fluid viscosity, and Ψ as the dimensionless bearing clearance $2\Delta R/D$.

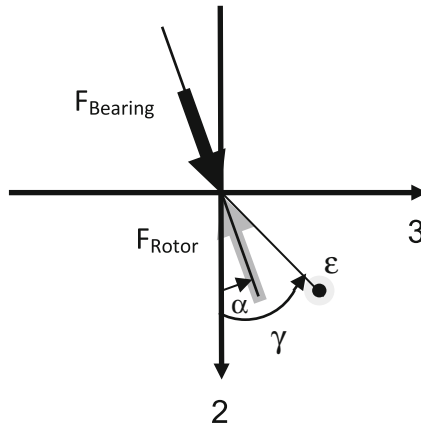


Fig. 1. Coordinate system to describe the bearing force and its direction as a function of the rotor position described by the eccentricity ε and position angle γ .

As can be seen the force is split into two parts: one part is caused by rotation of the journal (the part described by the So-number) and the other by lateral movements (the part described by the damping coefficients). Both parts are calculated by solving the Reynolds equation. The energy equation is solved simultaneously for the temperature distribution unless an analysis with constant temperature is carried out. Various effects such as turbulence and 2-phase flow in cavitation zones can be considered (see [4]). A simplified analysis neglecting turbulence and assuming iso-viscous fluid according to a mean temperature as it is described in the DIN standard [5] is also possible. The solution is done for a grid of journal positions ε, γ within the possible clearance range. Both parts of the force are highly dependent on ε, γ and thus nonlinear.

For the calculation of run-ups, the bearing analysis according to DIN is especially suited, since the Sommerfeld similarity applies for this analysis type. The speed dependence of the bearing characteristic then can be fully considered by the dimensionless damping coefficients and the Sommerfeld number, which varies with the speed. There is no additional dependency such as the Reynolds number for turbulence, which cannot be considered for this analysis type. In many applications turbulences plays a minor role.

2.2 Nonlinear Rolling Element Bearings

The rolling element bearing forces are calculated with the help of the Hertzian theory as described in ISO/TS 16281 and DIN 26281, respectively (see [6]). The forces due to Hertzian pressure can be linearized for small dynamic forces near large static forces. However, they are basically nonlinear. Moreover, dynamic loads for many bearing types such as deep groove or angular contact ball bearings can change the contact angles between the balls and the inner and outer race, which contributes to a nonlinear behavior. The bearing clearance can also cause nonlinear behavior. Additionally, a coupling between the axial and radial direction occurs for many bearing types as the above-mentioned ball bearings. The bearing forces the two radial directions 2 and 3 and moments about these axes as well as the axial force as a function of the radial and axial displacements and tilting angles about the radial axes are calculated in a routine according to the above-mentioned theory, which is provided by MESYS (see [7]).

Rolling element bearings provide almost no damping force. Nevertheless, a damping force can be considered in MADYN 2000 for harmonic response analyses by a damping matrix, which is proportional to the stiffness matrix of the statically loaded bearing. The stiffness matrix describes the linearized forces. The factor is calculated according to Eq. (3). It yields a damping according to a defined damping ratio at the exciting frequency.

$$\mathbf{D} = \frac{2D}{\omega} \mathbf{K} \quad (3)$$

with the \mathbf{D} as the damping matrix, \mathbf{K} as the stiffness matrix of the rolling element bearing, D as a damping ratio to be defined and ω as the exciting frequency. The matrices are 5×5 matrices for the two radial displacements, the two tilting angles about the radial axes and the axial displacement.

A similar damping force can be used in non-linear transient analyses. The damping matrix then is calculated with a reference frequency, which can be the speed or a specifically defined frequency.

2.3 Solving the Nonlinear Equation

For solving the system of nonlinear equations, the nonlinear bearing forces are put on the right-hand side as shown in Eq. (4).

$$\begin{bmatrix} \ddot{\mathbf{x}} \\ \dot{\mathbf{x}} \\ \dot{\mathbf{q}} \end{bmatrix} = \begin{bmatrix} -\mathbf{M}^{-1}(\mathbf{D} + \mathbf{G}) & -\mathbf{M}^{-1}\mathbf{K} & \mathbf{A}_{xq} \\ \mathbf{E} & \mathbf{0} & \mathbf{0} \\ \mathbf{A}_{qx} & \mathbf{A}_{qx} & \mathbf{A}_{qq} \end{bmatrix} \begin{bmatrix} \dot{\mathbf{x}} \\ \mathbf{x} \\ \mathbf{q} \end{bmatrix} + \begin{bmatrix} \mathbf{M}^{-1}\mathbf{F}(t) \\ \mathbf{0} \\ \mathbf{0} \end{bmatrix} + \begin{bmatrix} \mathbf{F}_{NL}(\mathbf{x}, \dot{\mathbf{x}}) \\ \mathbf{0} \\ \mathbf{B}_q \end{bmatrix} \tag{4}$$

In Eq. (4) \mathbf{M} is the mass matrix, \mathbf{D} the damping matrix, \mathbf{G} the gyroscopic matrix, \mathbf{K} the stiffness matrix and \mathbf{E} the unit matrix. The vector \mathbf{x} contains structural coordinates of the rotor and support system modelled in MADYN 2000. Supports can also be imported in the form of state space systems, which have the additional coordinates \mathbf{q} (see for example [8, 9]). The sub-matrices \mathbf{A}_{ij} describe the coupling of MADYN 2000 coordinates to the imported state space supports. These matrices are created with the help of the support system matrix, observer and control matrix. Certain bearing types such as magnetic bearings or full models of tilting pad bearings may also have additional coordinates (see for example [10]). The examples of the present paper do not have such bearings and the additional coordinates are not included in Eq. (4). \mathbf{F} is the vector of external exciting forces, which can only be applied to structural MADYN 2000 coordinates and \mathbf{F}_{NL} the vector of nonlinear forces. The stiffness matrix \mathbf{K} and damping matrix \mathbf{D} as well as the sub-matrices \mathbf{A}_{ij} may contain linear bearing coefficients, if some bearings are treated as linear. The vector \mathbf{B}_q describes the forces on the state space stator system. It is created with the help of the state space observer and control matrix.

Equation (4) can also be written in the following form:

$$\dot{\mathbf{z}} = \mathbf{A}\mathbf{z} + \mathbf{B}(t) + \mathbf{B}_{NL}(\mathbf{x}, \dot{\mathbf{x}}, \mathbf{q}) \tag{5}$$

Before solving the equation by integration with a Runge Kutta solver, it is bi-modally reduced with the help of the complex left and right eigenvectors of the system $\Phi_L \Phi_R$ as shown in Eq. (6).

$$\Phi_L' \dot{\mathbf{z}} \Phi_R = \Phi_L' \mathbf{A} \Phi_R + \Phi_L' \{ \mathbf{B}(t) + \mathbf{B}_{NL}(\mathbf{x}, \dot{\mathbf{x}}, \mathbf{q}) \} \tag{6}$$

The linear part thus is decoupled. The method is described in detail in [11] and summarized in [12]. The resulting system to solve is as follows:

$$\dot{\mathbf{w}} = \mathbf{A}\mathbf{w} + \Phi_L' \{ \mathbf{B}(t) + \mathbf{B}_{NL}(\mathbf{x}, \dot{\mathbf{x}}, \mathbf{q}) \} \tag{7}$$

with

$$\mathbf{z} = \Phi_R \mathbf{w} \tag{8}$$

The matrix \mathbf{A} hereby is the diagonal matrix of the considered eigenvalues of the linear system.

The linear system is speed dependent; hence the eigenvalues and matrices of the eigenvectors are also speed dependent. For the analyses of a run up or down, the matrices are created for a suitable number of speed steps and then interpolated during the solution of the equation for each time step.

3 Vertical Pump with Cylindrical Water Lubricated Bearings

3.1 Description of the Model

The model of the vertical pump is shown in Fig. 2. The complete length of the assembly is about 12 m. The upper part with a motor is on the left side. The pump has only one impeller at the bottom shown on the right side. The pump rotor is shaded in blue. The casing of the pump, which is a pipe, is modelled as a shaft with zero speed. It is shaded in grey (partly visible as a black line). The pipe is fixed to a foundation, which is denoted as customer support in the model. It consists of a flange of the pipe. The flange is fixed with general springs to the ground. The general springs represent the stiffness of the foundation and introduce anisotropy to the system. The motor rotor is not modelled as part of the shaft, since it is coupled to the pump shaft with a flexible coupling. The whole motor including its housing is modelled as a rigid mass fixed to the flange at the customer support stiffness (the sphere in Fig. 2). The distance of the center of gravity to the support is bridged with a rigid element.

The pump shaft is supported in the pipe with an angular contact rolling element bearing, which also carries the axial load. The upper bush and casing bearing are closed cylindrical bearings. The other bush bearings are cylindrical bearings with 3 equal pads and a deep groove between the pads. The ambient pressure of the upper bush bearing corresponds to the pump discharge pressure of 10 bar. For the other bush bearings and the casing bearing the Archimedes hydrostatic pressure adds to the discharge pressure, which is about 1 bar for the lowest bearing. The elevated ambient pressure influences the cavitation, which is considered in the bearing model with a 2-phase model (see [2, 4]). A contact stiffness to account for a surface roughness of 10 μm has been considered for all bearings according to the model in [13].

An added mass for the pipe is considered. The mass of the enclosed water is added. For the rotor an added mass according to the formula (9) published in [14] has been used to estimate the effect. It yields a mass of about 3% of the rotor mass and therefore is neglected.

$$\mu = \pi\delta \frac{OD^3}{8s} \tag{9}$$

with μ as the added mass per length, δ as the density, OD as the rotor outer diameter and s as the radial clearance, which is very large for our case (≈2 OD).

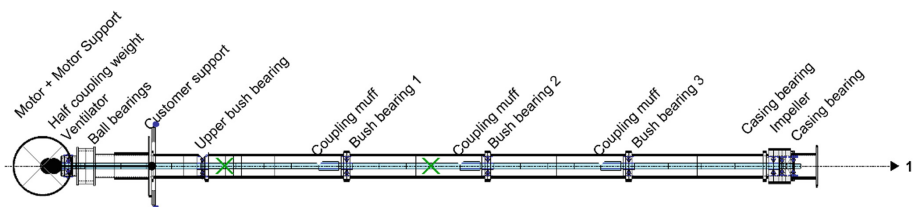


Fig. 2. Model of the vertical pump

3.2 Linear Behavior, Campbell Diagram

The Campbell diagram for a speed range up to 150% speed and a frequency range to 50 Hz, which corresponds to two times nominal speed can be seen in Fig. 3. The corresponding mode shapes can be seen in Fig. 4. Note, that the colors for corresponding modes are the same in both figures. The dashed line in the shape plot represents the pipe deformation and the solid line to the rotor deformation. The shapes are shown in two projections at the instant when the maximum deflection occurs. The two planes for the projections are indicated in the plot next to the shape plot. The first projection with the fat line is into the plane defined by the maximum deflection and the rotor axis, the second projection with the thin line into the perpendicular plane. The whirling direction and mean global orbit shape (also see [3]) are indicated as well.

Parameter Variation Analysis

Type: Campbell Diagram
 Analysis: 11-Jul-2017 14:42 - 18 rel.speeds (0.15...1.5), bearing loads from SAN

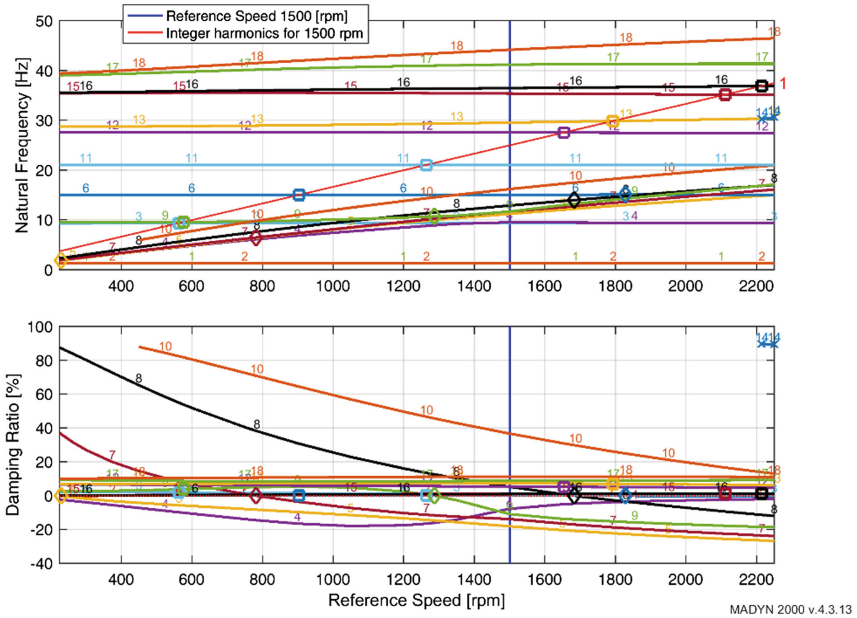


Fig. 3. Campbell diagram with eigenvalues

The first two modes are a cantilever like bending of the pipe and the rotor in two perpendicular directions. There is almost no relative displacement between rotor and pipe. The next modes are bending modes of the rotor with increasing order and increasing relative displacement. The modes appear as elliptically forward and backward whirling modes. They are elliptic due to the anisotropy of the support stiffness. The forward modes with relative displacement become unstable (mode 4, 5, 7, 9) if their frequency is below 50% speed, which is the whirling speed of the fluid in the cylindrical bearings.

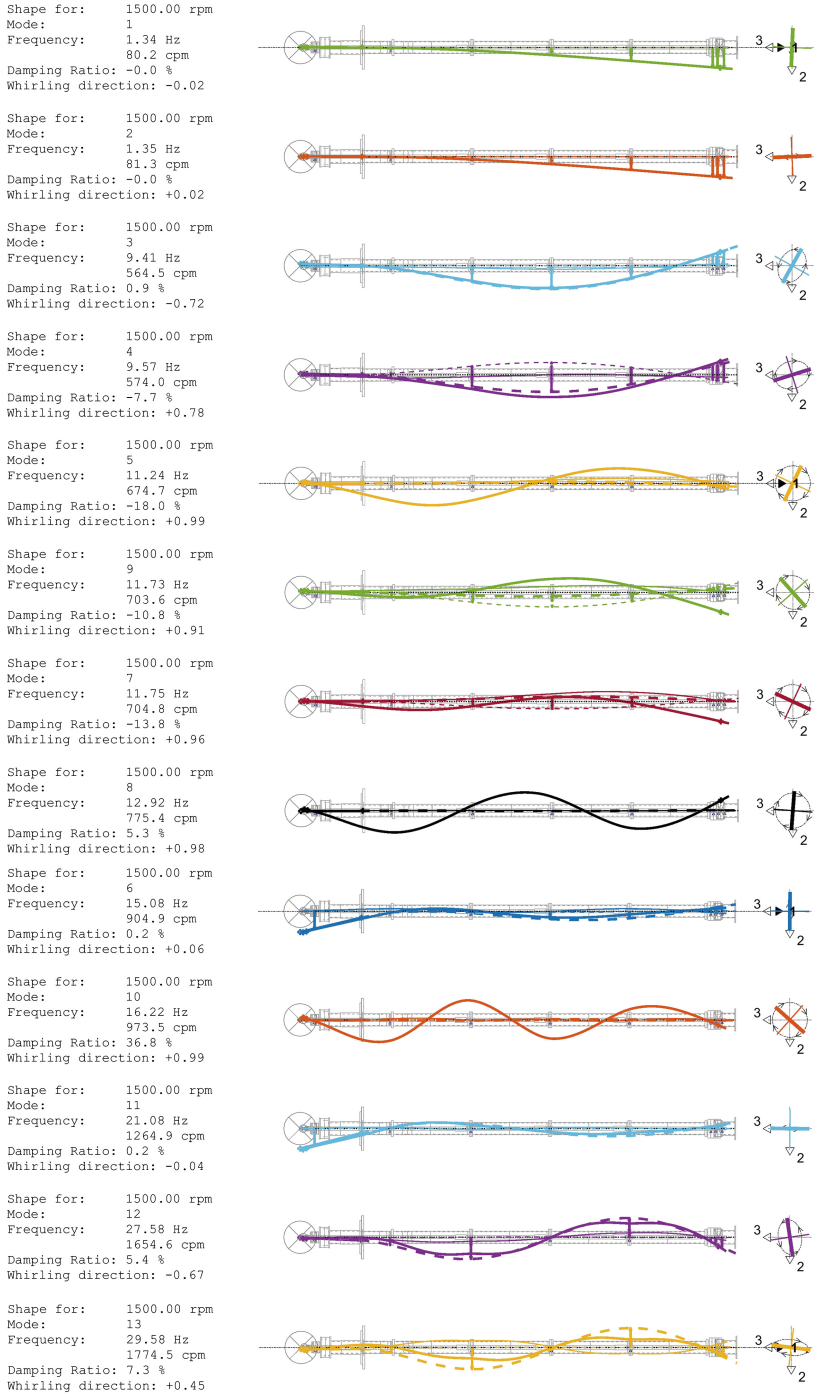


Fig. 4. Natural modes at nominal speed 1500 rpm

3.3 Results of a Nonlinear Run Up Analysis

Since the linear system is unstable, a nonlinear analysis must be carried out to determine limit cycles revealing a realistic vibration level of the rotor. A nonlinear run up analysis with an unbalance of G10 at the impeller has been carried out. The reference mass for the G value is the rotor section at the impeller. The run up has been carried out from 10% to 110% speed in 60 s, which is almost stationary for this system.

Results of this analysis can be seen in the following figures: The absolute displacements of the pipe at the bearing locations in Fig. 5, the orbits of the relative displacements in the fluid bearings in Fig. 6 and the 3D shape at 1500 rpm in Fig. 7.

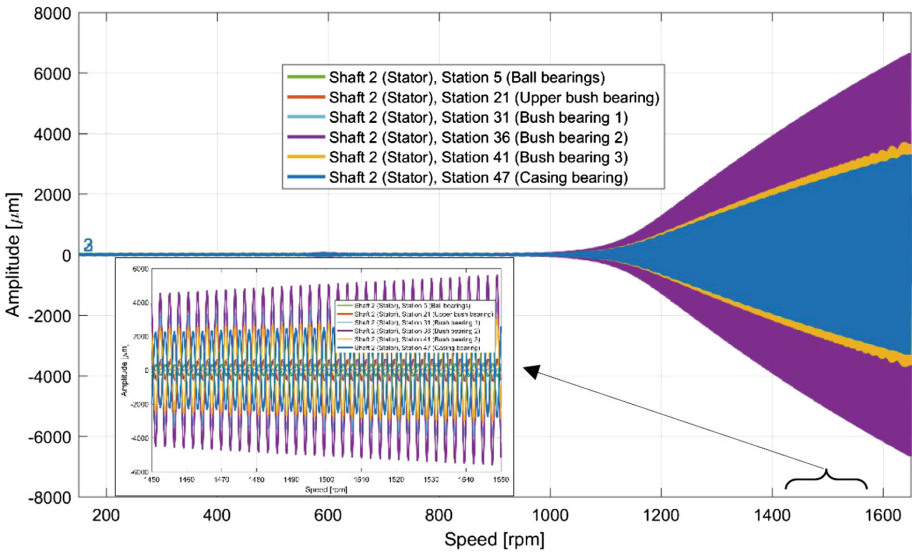


Fig. 5. Absolute vibrations of the pipe at bearing locations

The vibrations of the pipe indeed are huge. At 1500 rpm, 100% speed the level at bush bearing 2 is several mm. The shape at about 1500 rpm in Fig. 7 corresponds to the 2nd bending, mode 4 in Fig. 4. The by far dominating frequency is about 10 Hz, which approximately corresponds to the frequency of this mode. The vibration level at the ball bearing in the top is much lower. At 1500 rpm it is about 300 µm, which corresponds to a still high rms value of 33 mm/s. This is the location where vibrations of such machines are typically measured. Other locations with bearings are difficult to access.

The relative vibration level in the fluid bearings at nominal speed in Fig. 6 is about 90% of the bearing clearance for all bearings without considering the surface roughness, which means, that the contact stiffness just begins to become effective.

The force at nominal speed in bush bearing 2 is about 2400 N corresponding to a specific dynamic load of 3 bar.

The vibration behavior of the pump as presented here is not acceptable or at least at the limit. The surrounding water, which is not considered in the analysis, probably helps attenuating the vibration, especially at such levels as calculated here.

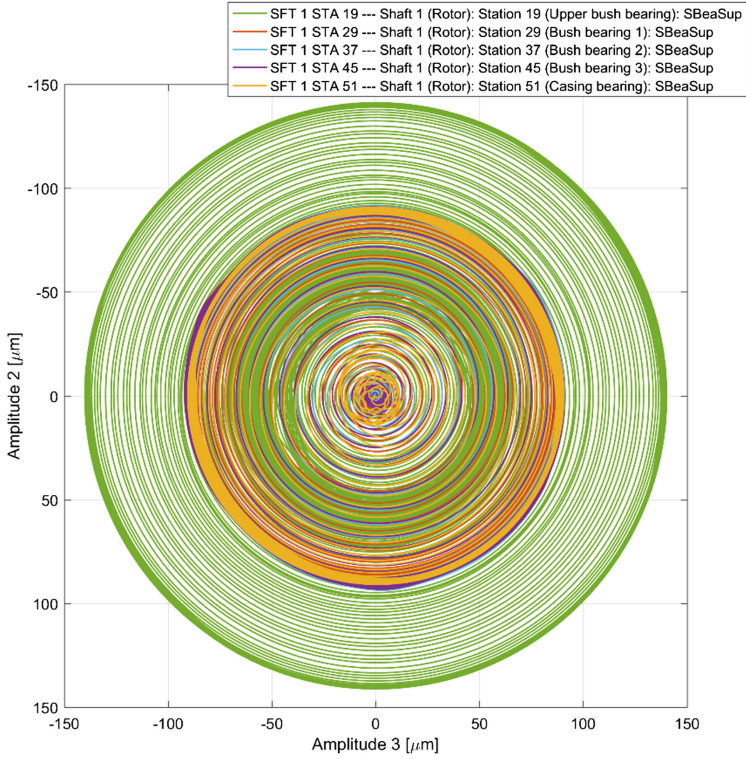


Fig. 6. Orbits of relative vibrations in the fluid bearings

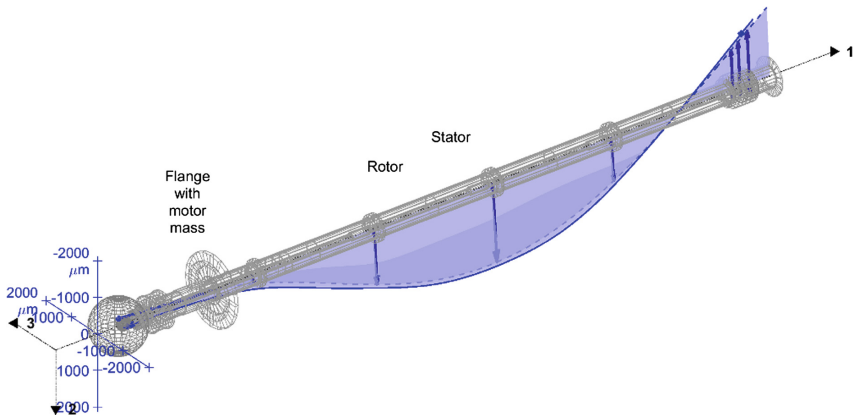


Fig. 7. Shape at nominal speed of 1500 rpm

4 Turbocharger with Semi-floating Ring Bearings

4.1 Description of the Model

The structure of the rotor model is shown in Fig. 8. The rotor is supported in two semi-floating ring bearings, which are shown in Fig. 9. The casing is considered as rigid, since it is very stiff compared to the rather soft support.

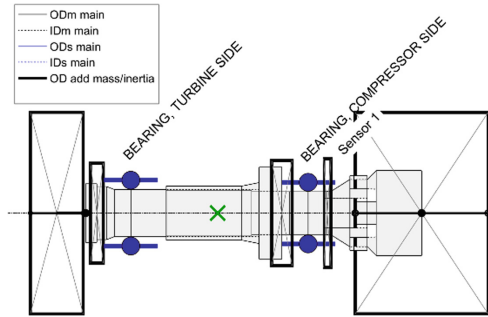


Fig. 8. Model of the turbocharger

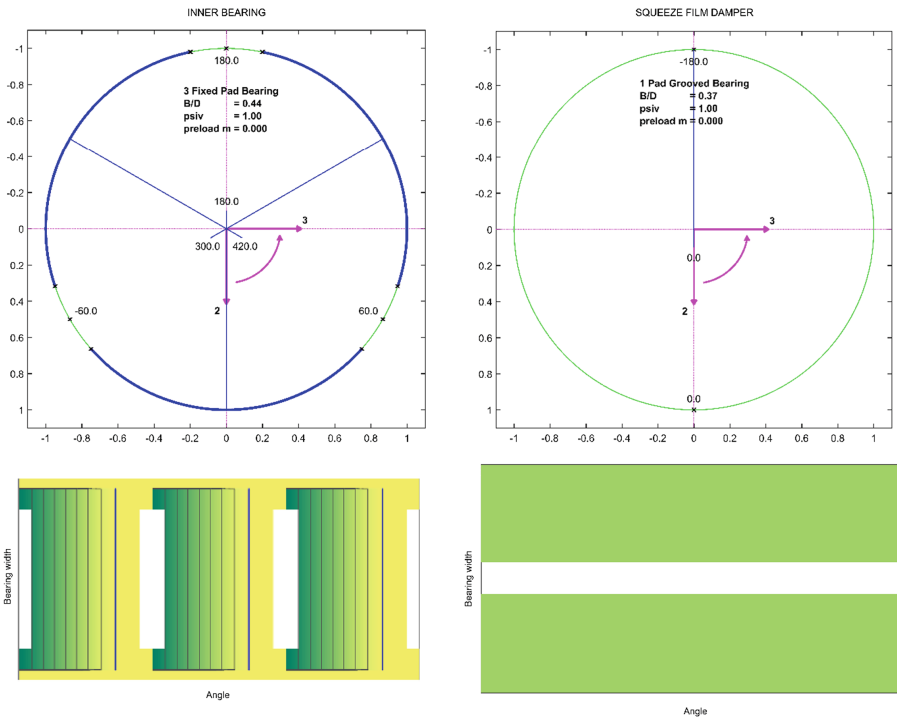


Fig. 9. Geometry and clearance of the semi-floating ring bearings, left inner film, right outer squeeze film

The inner film of the floating ring bearing has three hydrodynamic pockets, which are machined in the non-rotation ring. The outer film is plain cylindrical with a central groove distributing the oil. The outer film functions as a squeeze film.

The non-linear bearing characteristics were calculated according to DIN. Speed dependent oil temperature and thermal expansion of the ring and casing are considered. The speed dependence of the temperature and thus the viscosity as well as the clearance change influence the bearing characteristics through the Sommerfeld number.

4.2 Results of a Nonlinear Run Up Analysis with a Comparison to Measurements

The run up is calculated from 10% to 120% speed. The run up time is 10 s. The orbits of the rotor journal relative to the ring as well as the ring orbits are shown in Fig. 10. Measured and calculated vibration spectra are shown in Fig. 11.

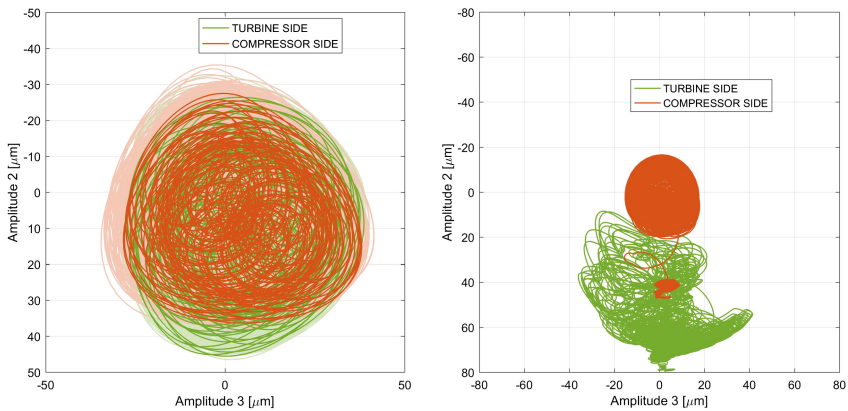


Fig. 10. Orbits of the rotor relative to the ring (left) and the ring (right)

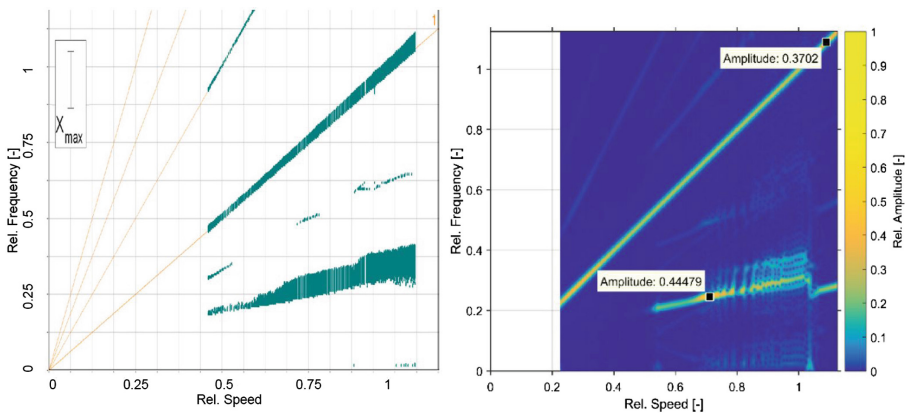


Fig. 11. Spectrogram of the run up at sensor 1 (left measurement, right simulation)

The squeeze film of the outer ring is completely free. It has no centering device such as a squirrel cage. A centering force is only created by vibrations of the ring. In the right plot of Fig. 10 the centering effect can be clearly seen. At low speed the two rings have a large eccentricity corresponding to the outer film clearances, which are different for the two bearings. With increasing speed and increasing vibration they are centered. On the compressor side the centering occurs in two stages. The 2nd stage is caused by a sudden change of pattern of the sub-synchronous vibration at about 100% speed, which can be seen in the calculated spectrum in Fig. 11.

The measured and calculated spectrograms clearly show the synchronous and sub-synchronous vibration amplitudes. A component with twice the frequency of each of the dominating frequency can also be seen. The agreement regarding frequency and amplitude between measurement and calculation is very good.

5 Motor with Deep Groove Contact Rolling Element Bearings

5.1 Description of the Model

The rotor with deep groove rolling element bearings can be seen in Fig. 12. The outer races of the deep groove ball bearings are modelled as shafts. The rolling element bearings connect the shaft and the outer races. Since for deep groove bearings the axial direction, radial direction as well as the rotation about the radial axes are coupled, all bending degrees of freedom as well as the axial degree of freedom are considered. The outer rings have only axial degrees of freedom, i.e. they are radially rigid. An axial preload is applied to the left bearing A. Bearing A is axially free, its outer ring is supported in axial direction by a weak axial spring. The outer ring of the right bearing B is rigidly supported in axial direction. It is an axially fixed bearing.

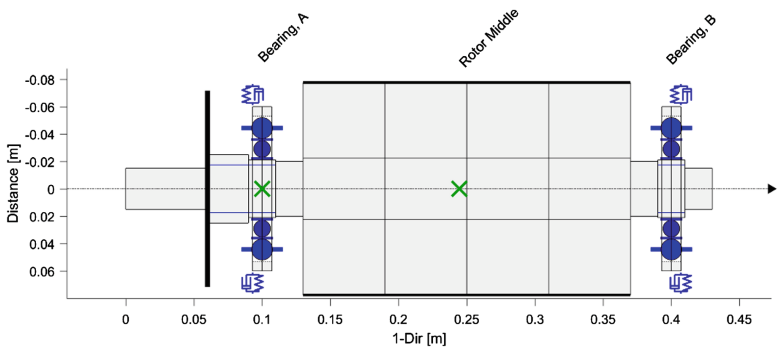


Fig. 12. Rotor with rolling element bearings

The speed dependence of the bearings due to centrifugal and gyroscopic forces of the rolling elements is considered.

5.2 Linear Behavior, Campbell Diagram

The Campbell diagram and mode shapes in the critical speeds for linearized bearing characteristics is shown in Fig. 13. The linearization is about the statically loaded bearings due to the weight and an axial preload of 700 N.

As can be seen the bending critical (mode 3 forward whirling) is above 100% speed, which is typical for rotors on rolling element bearings, since running through a critical is a problem with the poor damping, that this bearing type can provide. Beside the bending critical there is an axial mode, with a resonance close to nominal speed.

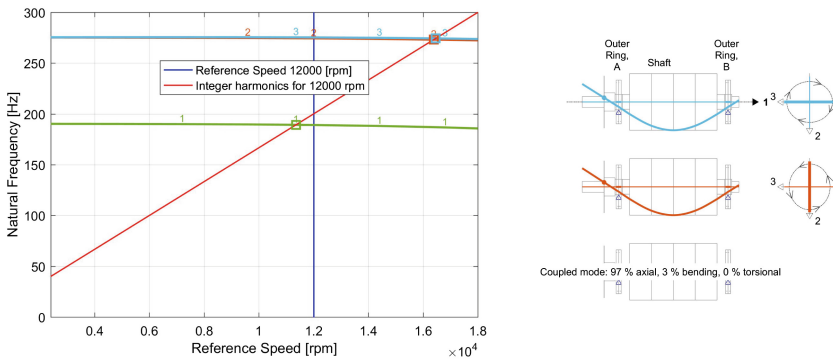


Fig. 13. Campbell diagram and shapes in the critical speeds

5.3 Results of a Nonlinear Run Up Analysis

A run up from 20% to 160% speed within 5 s for an unbalance in the middle of the rotor with a level of G2.5 has been calculated for this system with non-linear bearing properties. During the run up the critical speed is crossed, which is not foreseen for this machine, but envisaged in other cases.

The vibrations at the bearings in radial and axial direction are shown in Figs. 14 and 15. They reveal some remarkable behavior. The critical is lower than expected according to the Campbell diagram. The maximum vibration occurs at about 15500 rpm, whereas the critical in the Campbell diagram is at 16500 rpm. The axial resonance can be seen in the axial vibration at a speed where it can be expected according to the linear analysis. In the radial resonance large axial fluctuations occur combined with an axial shift, which can be explained as follows and which also explains the lower critical speed.

Due to the high radial loading of the bearing when approaching the resonance, the balls of the bearing seek a more centered position in the groove, which results in an axial shift of the shaft and a new contact angle. The new contact angle yields a lower stiffness despite the high radial load. In [15] this is explained more in detail including the change of stiffness due to the different contact angle.

Due to the axial preload the bearing does not have clearance in axial direction. In case of no preload further nonlinear effects can occur, which are described in [15].

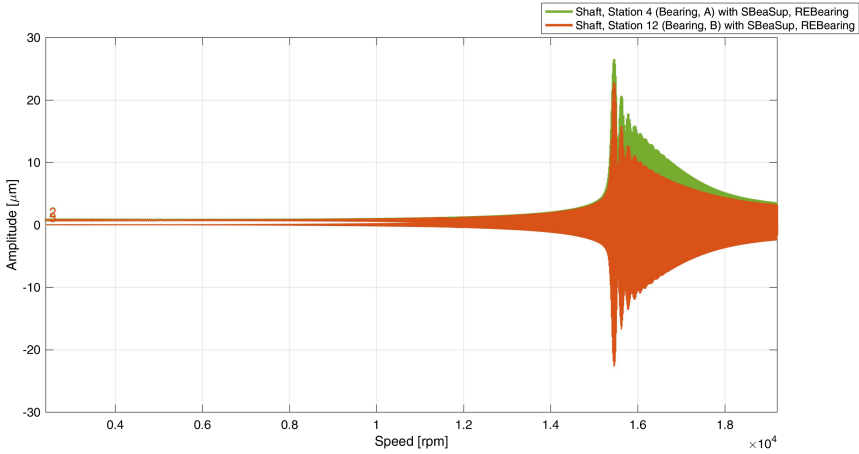


Fig. 14. Displacements in radial 2- and 3-direction at the bearings during run up

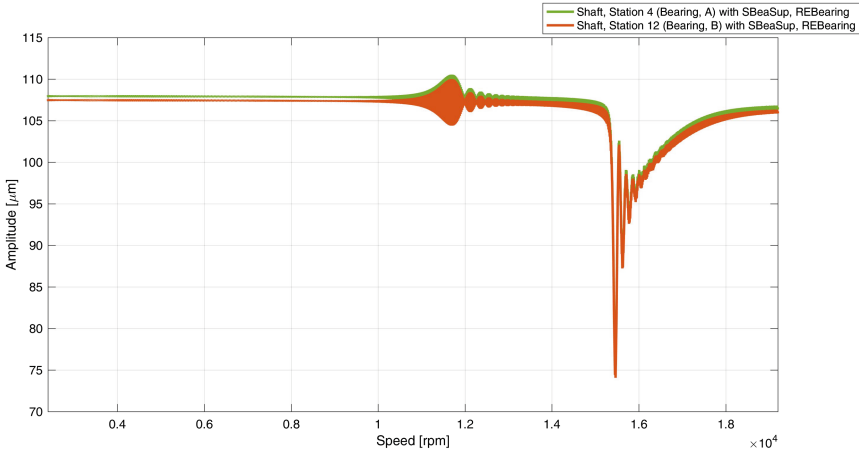


Fig. 15. Displacement in axial direction at the bearings during run up

6 Loss of Three Buckets of a Pelton Turbine

6.1 Description of the Model

The model for a vertical Pelton turbine is shown in Fig. 16. The Pelton runner is modelled as a rigid disk on the left side of the rotor. In the middle of the rotor is a generator. The rotor is supported on fluid film bearings. The bearing on the left turbine side is also shown in Fig. 16. It is a tilting pad bearing with 8 pads. In the model this bearing has a spring mass support representing the foundation. Its natural frequency is far above running speed and the rotor bending frequency. On the right side the bearing and support are modelled by a substitute spring. The turbine bearing is loaded with a static lateral force caused by the water jet.

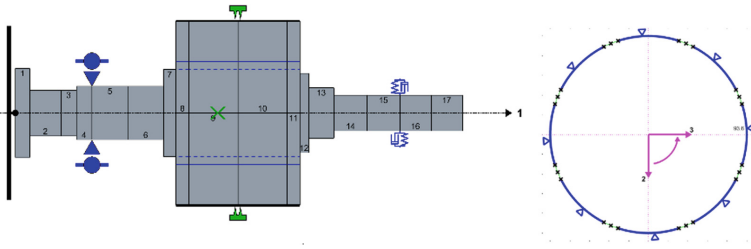


Fig. 16. Model of a vertical Pelton turbine with the geometry of the turbine bearing

6.2 Results of the Nonlinear Analysis of the Bucket Loss, Comparison to Linear Results

The bucket loss is calculated by suddenly applying a rotation force at nominal speed to the Pelton runner corresponding to the centrifugal force. In our case this force is 4.5 times the static jet force of 1000 kN. The initial condition for the analysis is the static equilibrium position due to the force from the water jet at the turbine. The turbine is running below its 1st bending mode. The separation margin is 45%.

The results of the analysis with a nonlinear turbine bearing can be seen in Fig. 17. For the orbit a comparison to a linear analysis is shown, with a linearization of the turbine bearing about its static equilibrium.

In case of the nonlinear analysis the orbit remains within the bearing clearance. It follows the bearing contour. At the pad pivot points the deflection is 85% of the minimum bearing clearance. Note, that 10 μm surface roughness is considered in the nonlinear analysis. For the linear analysis the deflections by far exceed the bearing clearance.

In the shape in Fig. 17 the arrow at the turbine bearing indicates the displacement of the support. It can be seen, that the relative displacement in the bearing is very small compared to the support displacement, which is almost 8 mm.

The maximum force on the turbine support is 13000 kN. The values are practically equal for the linear and nonlinear analysis. This applies for this model with a rather simple support structure and rather stiff rotor. It cannot be generalized.

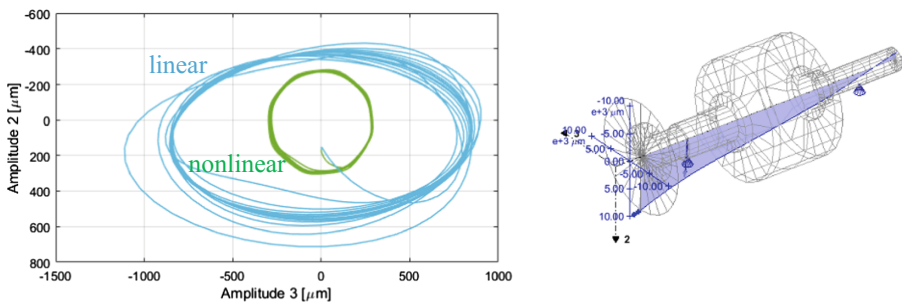


Fig. 17. Linearly and nonlinearly calculated orbit after a bucket loss, shape of nonlinear analysis at the instant of maximum deflection

7 Summary

Four examples are presented requiring unpopular nonlinear rotordynamic analyses for different reasons. In all examples the nonlinearity is in the bearings. For a vertical pump, which is linearly unstable, the nonlinear analysis is necessary for determining limit cycles. In case of a turbocharger with semi-floating ring bearings the reason for a nonlinear analysis is the essential nonlinear behavior of the outer oil film, which functions as a squeeze film damper without centering device. A motor rotor on rolling element bearings running through a resonance requires nonlinear analyses, because of the large forces, which change contact angles and do no longer allow linearizing the Hertzian pressure. For the simulation of a bucket loss of a Pelton turbine with an 8-tilting pad fluid film bearing on the turbine side, the necessity for a nonlinear analysis again arises due the large bearing forces, exceeding the static load by a factor of 4.5.

References

1. API Recommended Practice 684, 2nd edn (2005)
2. Fuchs, A., Klimpel, T., Schmied, J., Rohne, K.: Comparison of measured and calculated vibrations of a turbocharger. In: Proceedings of SIRM, 12th International Conference on Vibrations in Rotating Machines, Graz, Austria (2017)
3. MADYN 2000 program documentation (2017)
4. Fuchs, A.: Schnelllaufende Radialgleitlagerungen im instationären Betrieb. Dissertation TU Braunschweig (2002)
5. DIN 31 657. Hydrodynamische Radial-Gleitlager im stationären Betrieb. Berechnung von Mehrflächen und Kippsegmentlagern. Beuth Verlag, Berlin (1992)
6. ISO/TS 16281: Rolling bearings – Methods for calculating the modified reference rating life for universal loaded bearings (2008)
7. MESYS. http://www.mesys.ch/doc/MESYS_Rolling_Bearing_Calculation.pdf
8. Krüger, T., Liberatore, S., Knopf, E.: Complex substructures and their impact on rotordynamics. In: Proceedings of SIRM, 10th International Conference on Vibrations in Rotating Machines, Berlin, Germany (2013)
9. Schmied, J., Perucchi, M.: Coupled rotor-bearing-casing analysis. In: 22nd Swiss CADFEM ANSYS Simulation Conference (2017)
10. Schmied, J., Fedorov, A., Grigoriev, B.: Nonsynchronous tilting pad bearing characteristics. In: Proceedings of the 8th IFToMM International Conference on Rotordynamics, Seoul Korea (2010)
11. Nordmann, R.: Ein Näherungsverfahren zur Berechnung der Eigenwerte und Eigenformen von Turborotoren mit Gleitlagern, Spalterregung, äusserer und innerer Dämpfung. Dissertation TU Darmstadt (1974)
12. Krämer, E.: Dynamics of Rotors and Foundations. Springer, Heidelberg (1993)
13. Greenwood, J.A., Williamson, J.B.P.: Contact of normally flat surfaces. In: Proceedings of the Royal Society of London, Series A, Mathematical and Physical Sciences, vol. 295, no. 1442 pp. 300–319 (1966)
14. Amoser, M.: Strömungsfelder und Radialkräfte in Labyrinthdichtungen hydraulischer Strömungsmaschinen. Dissertation ETH Zurich Nr. 11150 (1995)
15. Delta JS. http://www.delta-js.ch/file/344/MADYN_2000_Release_43_Nonlinear_REB.pdf

Torsional Vibrations and Geared Systems Dynamics



Multibody Dynamics Simulation of a Mechanism for Generating Continuously Variable Motion

Krishna Prakash Bhusal¹, Behnam Ghalamchi^{1,2}(✉), Charles Nutakor¹, Jussi Sopanen¹, and Tommi Nummelin³

¹ Lappeenranta University of Technology,
Skinnarilankatu 34, 53850 Lappeenranta, Finland
behnam.ghalamchi@lut.fi

² University of California, Berkeley, Berkeley, CA, USA

³ Saimaa University of Applied Sciences,
Skinnarilankatu 36, 53850 Lappeenranta, Finland

Abstract. In this paper, the functionality of a swashplate mechanism coupled with a series of one-way overrunning clutches is studied. The novel mechanism is constructed by coupling a swashplate and one-way overrunning clutch with other mechanical components to allow producing a continuously varying gear ratio. To access the capability of the proposed mechanism, a multibody dynamic simulation of the said mechanism was carried out as follows. First, the kinematics of the components making the mechanism is studied, then followed by the dynamics of the entire system. Preliminary predictions dictate that the proposed mechanism has the potential to produce continuously variable output motion including the zero-output using a constant input. However, the results indicate that the swashplate mechanism should be studied further to allow obtaining a smooth output. Initial results indicate that the proposed mechanism has the potential of converting a constant rotational motion to a continuously variable rotational speed.

Keywords: Swash plate · One-way overrunning clutch
Continuously variable drive

1 Introduction

In recent days, the development of automotive transmission is directed towards low emission and fuel-efficient solutions. The use of internal combustion engine (ICEs) or electric motor (in hybrid and electric vehicles) is common in automotive applications. The electric motor or ICEs have their own drawbacks. The major drawback can be the tradeoff between torque and rotational speed. In general, the electrical motor maximum power can be achieved at the point where torque and rotational speed are at the half of the maximum torque and rotational speed. In case of ICEs, the maximum torque that can be achieved can be different based on the engine type but there still exists the tradeoff for achieving maximum power. For an engine or electric motor to achieve maximum power, either of the two should be running at their optimal range. In this

case, the solution which can produce continuously variable ratio with constant input can be beneficial.

The swashplate mechanism has a long history dating back to around 1930s. Different variations of the swashplate mechanism depending on the applications can be found in the literature. The main areas of application of the swashplate include the aeronautic, automotive and in hydraulic systems. The swashplate mechanism is used in the hydraulic fixed displacement and variable displacement pumps. In hydraulic systems, it can be used to convert the rotational motion to the reciprocating motion or vice-versa. In the aeronautics industry, swashplates are typically used in helicopters for controlling the blade pitch. Some studies on the development of helicopter blade pitch control system without using swashplates can be found in [1, 2]. In the automotive industries, their application is mainly in compressors for automotive air conditioners. Studies on different aspects of swashplate mechanism in regards to the application in air conditioning system can be found in [3–5]. Zeiger et al. [6] developed a mathematical model on the torque acting on the swashplate used in axial piston pump. The dynamic behavior of a swashplate with anti-rotation mechanism was studied by Ishii et al. [7]. The study on the application of swashplate mechanism in different application area but for the similar purpose is done by Zuti et al. [8].

The one-way overrunning clutches are the devices, which transmits torque and rotation in one direction and freewheels or disengages in the other. The one-way overrunning clutches are mechanically operated. The most common example of the one-way clutch can be seen on bicycles. In modern automatic transmissions, sprag type and roller type one-way clutches are used to brake members of the planetary gear set. Several different types of one-way clutches are available. The common types are ratchet and pawl, locking roller, locking needle roller, sprag clutch and wrap spring clutch. Roach et al. [9] made a comparison study on different types of one-way overrunning clutch using compliance criteria.

In this paper, the functionality of a swashplate mechanism coupled with a series of one-way overrunning clutches is studied to understand the capability of such a mechanism for producing a continuously varying gear ratio. A novel mechanism is constructed by coupling a swashplate and one-way overrunning clutches with other components like push rods and bevel gear sets. From the preliminary predictions, the proposed mechanism has the potential to produce continuously variable output motion including the zero output with constant input. This study will contribute to the development of the mechanism towards the application where there is need of converting a constant rotational motion to the continuously variable rotational speed.

To assess the capability of the proposed mechanism, a multibody dynamic simulation of the said mechanism was carried out. First, the kinematics of the components making the mechanism is studied, then followed by the dynamics of the entire system.

The main goal of this study is to develop a dynamic model of a swashplate and one-way overrunning clutch mechanism that allows the generation of a continuously varying motion. In accordance with this goal, the main objectives are:

- (1) Develop a multibody dynamic model of a swashplate and one-way overrunning clutch mechanism

- (2) Assess the operation range of the swashplate and one-way overrunning clutch mechanism using the multibody simulation approach
- (3) Devise a guideline to enhance the swashplate and one-way overrunning clutch mechanism.

2 Mechanism

The main concept of the mechanism is to convert constant rotational motion into the continuously variable rotational motion. The mechanism consists of the input shaft, a slider mechanism fixed to the shaft, tilt plate mechanism, push rods, rocker arms, a bevel gear set with three gears and a pinion. The simplified model of the mechanism is depicted in Fig. 1.

In this mechanism, the input shaft is driven by a power source with constant input. The slider mechanism can translate along the axial direction of the shaft since it is constrained to the input shaft using the translational (prismatic) joint. The major function of the slider mechanism is to change the tilt angle of the swashplate. When the input shaft is rotating, it constrains the swashplate to create wobbling motion. When the tilt angle is zero degrees, the wobbling motion is not created in the swashplate. The wobbling motion is converted to translational motion using pushrods in a similar manner as seen in hydraulic displacement pumps where reciprocating motion of the piston rods is created by connecting them to the swashplate. Pushrods are mounted along the circumference of the swashplate using the spherical joint. The other end of push rods is connected to the rocker arm that is connected to the bevel gear shaft using a one-way overrunning clutch. The translational motion of the pushrods is converted to the rotational motion using rocker arm and transferred to bevel gear shaft using one-way overrunning clutch. Three bevel gears are coupled to one bevel pinion from which output is achieved.

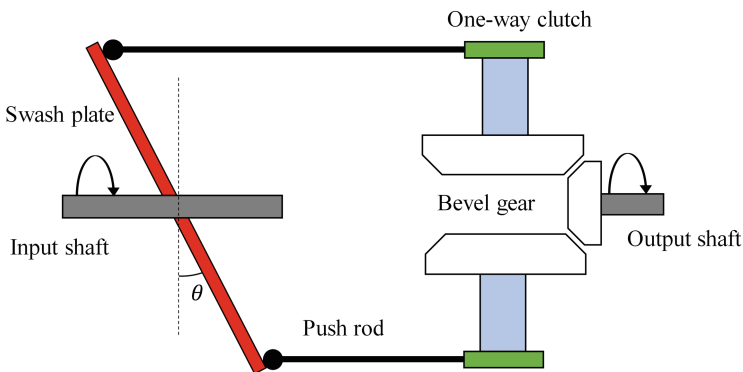


Fig. 1. Schematic of the proposed mechanism

In the proposed mechanism, with a change in tilt angle θ , the output can be continuously varied using a constant speed input. The stationary output can be achieved with tilt angle set to zero and the angle can be continuously increased resulting in the continuously increasing output. The mechanism allows the input to be constant and fixed at the optimal speed for the maximum efficiency. This feature is especially required when the input is provided using an electric motor or internal combustion engines (ICEs) since they have a certain range of rotational speed when efficiency is at peak.

2.1 Simulation Model

The simulation model is created in MSC ADAMS. The simulation model consists of several parts and joints described in ADAMS. Some of the parts are imported as cad files while some of the parts were created using inbuilt feature of ADAMS. The simulation model of the mechanism can be seen in Fig. 2. The operation of the one-way overrunning clutch is based on contacts and friction between its components. The detailed study of the one-way overrunning clutch is not the focus of this study, as such its functionality is implemented using a torque function like the torsional springs. The torque, T , transferred by the one-way overrunning clutch is defined as:

$$T = (k \cdot (\theta - \theta_{rev}) + c \cdot \dot{\theta}) \cdot STEP(\dot{\theta}, 0, 0, 0.1, 1) \tag{1}$$

where k is the torsional stiffness, c is the torsional damping, θ is the relative angle, $\dot{\theta}$ is the relative angular velocity and θ_{rev} is the angle created while overrunning. The STEP function used will return torque applied as either zero or torque depending on the direction of the rotation. Equation (1) describes the basic functionality of the one-way overrunning clutch, however, it should be noted that it is a simplified model. For example, the friction of the overrunning clutch is not described in detail. However, it is assumed that basic functionality is sufficiently captured.

The bevel gears were created using a gear geometry inbuilt feature embedded in MSC ADAMS. The details of the bevel gear used in the model are given in Table 1. The details of other machine element components like bearings, bolts, screws were not included in the simulation model.

Table 1. Details of the bevel gear

	Bevel 1	Bevel 2	Bevel 3	Bevel Pinion
No. of teeth	43	43	43	27
Pressure angle	20°			
Mean spiral angle	35°			
Face width	22 mm			
Transversal module	2.2			
Orientation (x, y, z) (°)	180, 90, 180	300, 90, 180	60, 90, 180	0, 180, 0

Most of the joints used in the simulation model are created using the standard joints like revolute joint, spherical joint, cylindrical joint, translational joint available in MSC ADAMS. In addition, some primitive joints option available were used in constraining some components. For example, a perpendicular primitive joint was used to constrain the rotation of the swashplate in the axial direction of the shaft. The perpendicular primitive joint in MSC ADAMS constraints one rotational degrees of freedom of the mechanism.

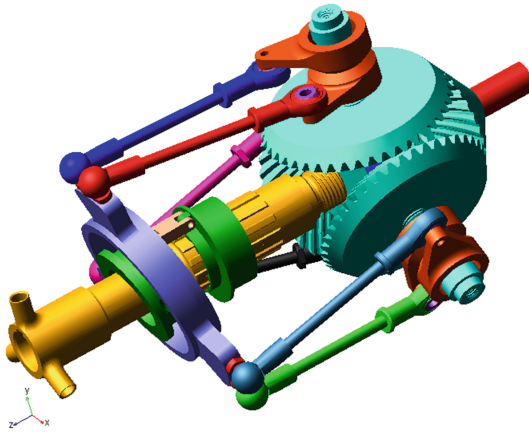


Fig. 2. Simulation model of the mechanism

3 Results and Analysis

The results reported here were achieved through several case studies. The variants of the case studies include force and torque distribution, and velocity at different load conditions. Initially, a motion study of the simulation model was carried out to understand the kinematics of the mechanism. After the motion study was carried out the simulation was performed by using a DC motor.

3.1 Case Study: Motion Study

The motion study of the mechanism was performed by using a constant input motion. Here the case studies included the following: (1) using a maximum swashplate tilt angle and (2) allowing variation of the swashplate tilt angle. The point motion feature available in ADAMS was used as the input to the simulation model.

Maximum Tilt Angle

Here a constant input motion and a maximum tilt angle of 12.5° were specified for the swashplate. The compactness of the design space (housing) dictates that the maximum tilt angle be limited to 12.5° . This limitation however, does not impose any restriction on the system design capability, as it is only for precaution to allow parts to move and wobble without crashing into other parts. The minimum and maximum

working range of tilt angle were defined to be 0° – 12.5° . Figure 3 shows the effect of tilt angle on the translational velocity of push rods.

From Fig. 3, it is evident that the velocity of each pushrod is not equal in magnitude and that there is a phase shift between the pair of rods. The placement of rods and the anti-rotation mechanism of swashplate resulted in the different velocities of the pushrods. The resulting effect of this behavior can be seen in the further results of the mechanism.

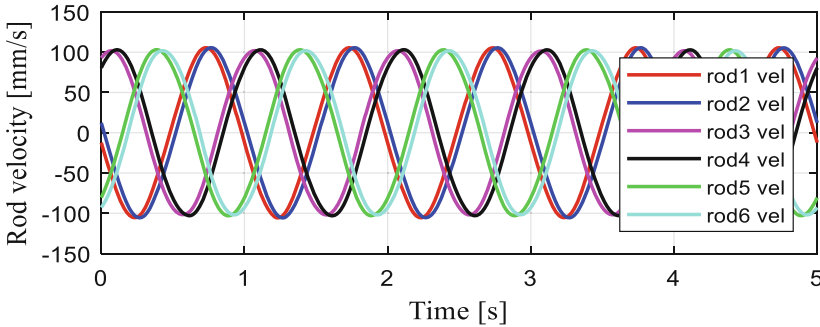


Fig. 3. Translational velocity of push rods in axial direction of input shaft with constant tilt angle

The results obtained for the output and bevel gears can be seen in Fig. 4. Here an input speed of 6.28 rad/s (60 rpm) as can be seen from Fig. 4 is implemented. Also observed from Fig. 4 is the behavior of the bevel gear speed.

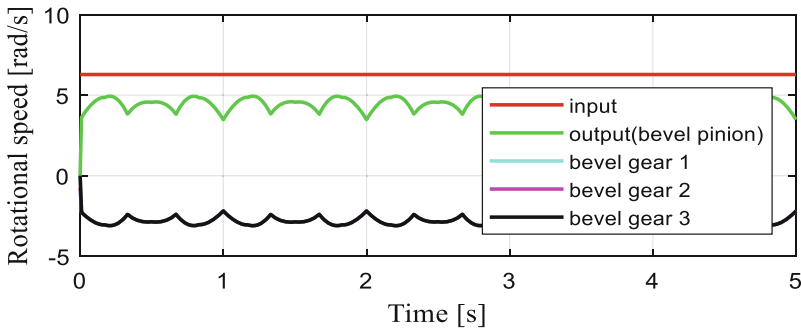


Fig. 4. Rotational speed of input, output and bevel gears

The speed of the bevel gears together with the output speed show signs of ripple effects (Fig. 4). In the mechanism three bevel gears are coupled to one bevel pinion and bevel gears are connected to the bevel shafts using one-way overrunning clutches. In such case where one bevel gear has high speed than the others, then it will become the

only driving gear and bevel pinion including other two bevel gears will be the driven ones. This phenomenon is caused by the characteristic (overrunning) of the one way overrunning clutch. Equal speed of bevel gears can be observed from Fig. 4 which suggests that the simplified model of one-way overrunning clutch is functional.

The different translational velocity of the push rods causes the ripple seen in the output rotational speed. The anti-rotation constraint used in the tilt plate results in the complicated behavior of the pushrods. However, the ripple can be optimized by optimizing the placement of push rods.

Changing Tilt Angle

This study was performed to understand the influence of continuously changing the tilt angle of the swashplate on the entire mechanism. The input and output motion were studied as well. The results of the simulation can be seen in Fig. 5. The figure shows the constant input motion of 6.28 rad/s (60 rpm) and achieved continuously variable output motion with changing tilt angle. The tilt angle is changed using a step function. The step function changes the tilt angle of the swashplate continuously from 12.5° to 0° within a specified duration of 5 s. It can be seen from Fig. 5b that the output rotational speed is varying continuously with the changing tilt angle of the swashplate. Also seen in Fig. 5 is how output rotational speed is varying continuously with the changing tilt angle of the swashplate.

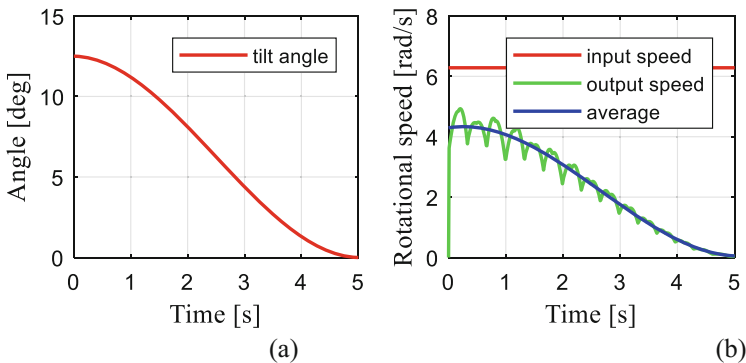


Fig. 5. (a) Changing tilt angle, (b) Input and output with changing tilt angle

The minimum and maximum output rotational speeds of the mechanism can be observed when the tilt angle is 0° and 12.5° respectively. The output rotational speed of the bevel pinion showed some ripple, so an average of rotational speed is plotted using a cubic polynomial function. The trend line of cubic polynomial was used to plot the trend line to represent the smooth behavior of the output without a ripple. See Fig. 5b.

3.2 Case Study: Study with Load at Output

Here a resistance load is applied to the output of the mechanism. The input was provided by using Eq. (2) which describes the torque provided by the DC motor as

$$T_{motor} = T_s - \omega T_s / \omega_n \tag{2}$$

where, T_{motor} represents the torque provided by the motor, T_s represents the stall torque of the DC motor, ω_n represents the no-load speed of the motor and ω represents the rotational velocity. The stall torque and no-load speed were defined as the design variable and rotational velocity was created as the function measure. The simulation was conducted by setting stall torque to 3000 Nmm and no-load speed to 60 rpm (6.28 rad/s). The resistance load was defined as the single component torque input of -1500 Nmm to the bevel pinion, which is the output of the mechanism. The direction of the resistance torque was opposite to the rotation direction of the output. Here the resistance torque is applied to the 50% of the maximum input torque that DC motor can produce.

The proposed mechanism has the limit of 0°...12.5° tilt angle, and in this part, it is assumed that swashplate is operating with maximum tilt angle. The results were obtained for the input and output torques, forces on components like pushrods and other mechanisms. The simulation was studied with the constant tilt angle of the swashplate. Figure 6 shows the input and output rotational speeds while the torque in different components can be seen from Fig. 7. The ripple which was observed earlier can also be seen from the results obtained here as well. Similar kind of behavior of the ripple can be observed from both the rotational speed and torque results.

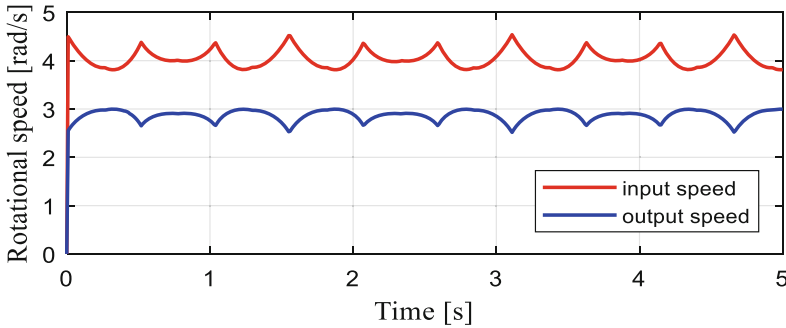


Fig. 6. Input motor speed and output speed

The DC motor specification were used for the input torque and speed while constant resistance load was applied to the output. The ripple in the input can be observed from Figs. 6 and 7. The input from the DC motor depends on the resistance load and in this case, constant resistance load was applied to the output. As seen from earlier results, the ripple was observed in the output when constant input was provided. In this case, since constant resistance load was applied to the output and DC motor was used as the input, the ripple is observed in the input.

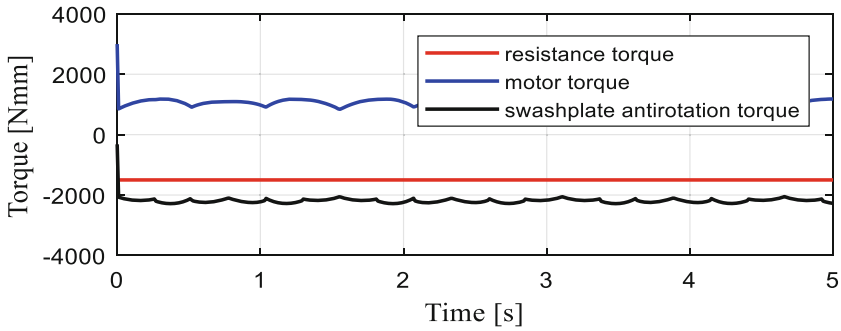


Fig. 7. Torque in different components

The different components of the forces in the rods were studied. The study showed that the z -component force (shaft axial direction) present in the rod is dominant over other components and is the most contributing. The study was focused on the z -component of the forces present in the rods.

It can be seen from Fig. 8 that the forces in all the rods are not equal. This will result in the torque ripple in the output. If the magnitude of the forces in the push rods are observed, the trend of the torque ripple observed in the output can be related to the magnitude of the forces in the rods. It can be also noticed that only one pushrod seems to be functional at a time. It is mainly due to use of one-way overrunning clutches. The overrunning feature of the one-way overrunning clutch caused this phenomenon. The magnitude of the force in the push rods is not constant and each rod is functional when the maximum force is present in the rod. The rod with maximum force dominates the functionality of other rods due to the overrunning feature of the one-way clutch. Similar trend was also observed in the motion study of the bevel gear set where one high speed bevel gear was dominating the speed of the whole bevel gear set. It can be concluded that the force is not distributed equally among the push rods.

The magnitude of the forces present in different pushrods can be seen from Fig. 8. The trend of the magnitude of the push rods can be compared to the trend seen in the behavior of the torque and rotational speed. The trend of the magnitude of push rods correlates the behavior seen earlier in torque and rotational speed case.

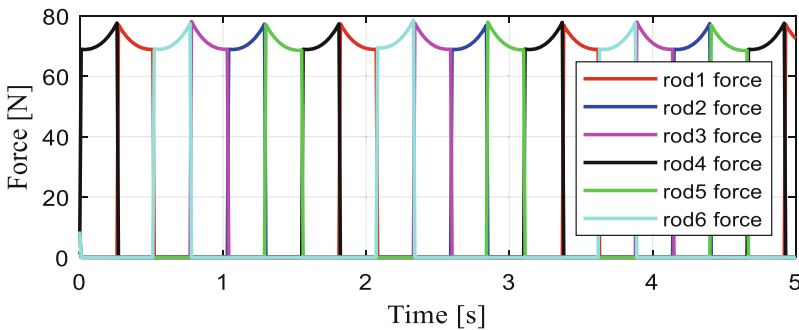


Fig. 8. Magnitude of force in pushrod

4 Conclusion

A mechanism for generating continuously variable motion has been proposed. A simulation model using multibody dynamics approach has been developed. A variety of case studies have been conducted to understand the intrinsic characteristics of the proposed mechanism. The results obtained from the simulation suggests that the mechanism can produce continuously variable output, using constant input, however in this design the output speed is not smooth dictating the need for future improvement to the model. Nonetheless, the mechanism presented in this paper can be used in place of push belt pulley mechanisms commonly found in CVTs. In terms of performance, push belts can be considered as the weakest part of a CVT. The proposed mechanism is fully mechanical and can be assumed to be efficient to serve a purpose of producing continuously varying motion. As seen from the simulation results the proposed mechanism can produce continuously varying speed and can produce a neutral output when the input is running at constant speed. Additional components like those used in several CVTs can be added together to form the Infinitely Variable Transmission which can produce continuously variable forward ratio, neutral and continuously variable reverse. Several issues with one-way overrunning clutches and swashplate mechanism were identified during the study of the mechanism. The issue of ripple was observed during the study and it is claimed to be a consequence of the swashplate. Some further studies on swashplate mechanism are required to achieve smooth output (without ripple). Addition of a flywheel in the proposed mechanism can be considered for the further studies in order to reduce the ripple observed in this study. Studies on push rods and their placement should be considered as the further studies to make the mechanism more smooth and efficient. Also, flexibility of the push rods and their impacts on the dynamic behavior of the system should be considered for the further studies.

References

1. Shen, J., Chopra, I.: Swashplateless helicopter rotor with trailing-edge flaps. *J. Aircr.* **41**(2), 208–214 (2004)
2. Wang, J., Wang, H., Wu, C.: Development of swashplateless helicopter blade pitch control system using the limited angle direct-drive motor (LADDM). *Chin J Aeronaut* **28**(5), 1416–1425 (2015)
3. Tian, C., Liao, Y., Li, X.: A mathematical model of variable displacement swashplate compressor for automotive air conditioning system. *Int J Refrig* **29**(2), 270–280 (2006)
4. Zhang, Y., Wang, W.: Using overflow in a swash plate compressor for automotive air conditioning system. *Proc. Inst. Mech. Eng. A: J. Power Energy* **226**(4), 564–579 (2012)
5. Lee, G.H., Lee, T.J.: A study on the variable displacement mechanism of swash-plate type compressor for automotive air conditioning system. In: *Proceedings of International Compressor Engineering Conference*, p C079 (2004)
6. Zeiger, G., Akers, A.: Torque on the swashplate of an axial piston pump. *J Dyn Syst Meas Contr* **107**(3), 220–226 (1985)

7. Ishii, N., Abe, Y., Taguchi, T., Kitamura, T.: Dynamic behavior of a variable displacement wobble plate compressor for automotive air conditioners. In: Proceedings of International Compressor Engineering Conference, p C723 (1990)
8. Zuti, Z., Shuping, C., Xiaohui, L., Yuquan, Z., Weijie, S.: Design and research on the new type water hydraulic Axis piston pump. *J. Press. Vessel Technol.* **138**(3), 031203 (2016)
9. Roach, G.M., Howell, L.L.: Evaluation and comparison of alternative compliant overrunning clutch designs. *Trans. Am. Soc. Mech. Eng. J. Mech. Design* **124**(3), 485–491 (2002)



Analysis of a Drill-String Experimental Set-Up with Dry Friction-Induced Torsional Vibration

Bruno C. Cayres^{1,2(✉)}, Cesar A. Fonseca¹, Guilherme Sampaio¹,
and Hans I. Weber¹

¹ Pontifícia Universidade Católica do Rio de Janeiro,
225 Marquês de São Vicente Street, Gávea, Rio de Janeiro, RJ, Brazil
cayres.bruno@gmail.com

² Centro Federal de Educação Tecnológica Celso Suckow da Fonseca,
Mario Covas Avenue, Itaguaí Industrial District, Itaguaí, RJ, Brazil

Abstract. The drilling process consists basically of a drive motor at the top end (surface) that provides torque to rotate a cut tool (drill-bit) at the bottom end. To connect these extremities there is a torque transmitting slender element so-called drill-string. Due to the slenderness, the borehole wall/drill-string, and, mainly, the drill-bit/rock interactions, the system undergoes axial, lateral and torsional vibrations. Among these modes, torsional vibration is present in most drilling processes and may reach an undesired severe phenomenon: stick-slip. In this work, we perform experiments on a torsional test rig, which executes dry friction-induced vibrations. The test bench consists in a DC-motor, a low-stiffness shaft and two discs. The motor provides rotation to the whole set-up: one disc (R_1) is placed on the opposite extremity of the motor, and the second one is intermediately placed (R_2). Resistive torques may be applied in both discs and the behaviour of the system is analysed. It is possible to observe torsional vibrations and the stick-slip when a friction torque is applied on R_1 and during this phenomenon, another friction torque is applied on R_2 . The presence of the second frictional torque as strategy of mitigation has a major influence on the dynamics as it may change from a stable limit cycle to a stable equilibrium and then preventing stick-slip phenomenon.

Keywords: Torsional vibration · Nonlinear dynamics
Drilling system · Stick-slip mitigation

1 Introduction

A drilling system consists in a set of equipment (surface and downhole) capable to create holes in the earth sub-surface for oil and/or natural gas extractions [26]. The equipment may be located onshore or offshore. Most of oil wells are vertically placed, but there are also inclined and/or even horizontal configurations [7].

It happens in order to overcome some constraints that a vertical well could not attend, such as, *blowout* well control via relief wells, hit reservoir targets which are located under inaccessible locations (ex: rivers, cities, etc.), to contour geological accidents (ex: salt and rock failures), among other [23]. Also, the directional drilling technique provides a larger contact area between well and oil reservoir which may enhance oil extraction, since the these reservoirs often present a larger horizontal dimension than its vertical dimension [1].

Basically, the drilling system comprises a motor (electric or hydraulic) located at the top end position and the bottom end part, named the Bottom-Hole Assembly (BHA). The former imposes the rotational motion in the drilling system (surface RPM - SRPM), while the latter comprises the *heavyweight drill-pipes* and the *drill-collars* that are responsible to transmit the necessary weight to drill without buckling. Also, in the bottom there is a cut tool named *drill-bit* responsible to gouge the rock. Between these extremities, there is torque-transmitting element called *drill-string* (connection of a series of pipes). At the top end, the top-drive imposes an angular velocity (surface RPM - SRPM). Thereafter, an axial force called weight-on-bit (WOB) is imposed, and this combination of WOB and SRPM provides the needed torque on bit (TOB) to induce rock failures (crushing, shearing or grinding) [2].

Because of slenderness diameter-to-length ratio of the drilling system, torsional vibration mode is present in most drilling processes and may reach an undesired severe stage: stick-slip. This stage causes a complete arrest of the drill-bit (stick phase), while the top continues to rotate and to store elastic torsional energy in the drill-string. Suddenly, the stored energy overcomes the friction torque and the drill-bit is released to rotate (slip phase) - converting potential energy into kinetic energy. During slip phase, the angular velocity of the drill-bit may increase till three times the imposed nominal angular velocity [4,5,18].

The stick-slip phenomenon occurs approximately 50% of the total drilling time [8] (*apud* [17]) and it is the main source of component failures during the drilling process, and also, it may excite axial vibration in its severe way: bit-bounce [21]. Patil *et al.* [17] also states that torsional vibrations while drilling is one of the severe types of drill-string vibration which deteriorates the overall drilling performance, causing damaged bit, failure of bottom-hole assembly, torsional fatigue of drill-string, and excites other vibration modes. Also, during the stick phase, the system does not drill which also increases costs and time of operation [10,11].

In order to propose a mitigation strategy of the torsional vibration in slender structures, this paper analyses the nonlinear dynamics of an experimental set-up isolating torsional vibrations from other effects. First, the dynamic characteristics of the test rig are obtained and should be coherent with a drill-string model. Then, the occurrence of stick-slip of the bottom disc and its dependence on force and rotation is observed. The scope of this analysis is the investigation of a mitigation strategy to prevent torsional vibration via a resistive torque on the middle disc, which can be imagined as a bottom hole driver.

This paper is presented as follows: Sect. 2 describes the drill-string experimental set-up and contains physical parameter values of the test rig. Section 3 presents the modelling of the system described in Sect. 2. Also, a model validation and stability analysis are performed. Following in the Sect. 4, the mitigation strategy and results are presented. Finally, Sect. 5 contains the conclusions of this work.

2 Drill-String Experimental Set-Up

2.1 Description of the Test Rig

The test rig consists of three degrees of freedom: disc 1 (R_1), disc 2 (R_2) and the DC-motor inertia (R_3): one disc (R_1) is placed on the opposite extremity of the motor, and the second one (R_2) is intermediary placed. Resistive torques may be independently applied on both discs and the behaviour of the system is analysed. It is fully instrumented so it is possible to observe torsional vibrations and the stick-slip when a friction torque is applied on R_1 and during this phenomenon, another friction torque is applied on R_2 . A low-stiffness shaft (2.40 m length and 3 mm diameter) is responsible to transmit rotation from DC-motor to the discs (see Fig. 1).

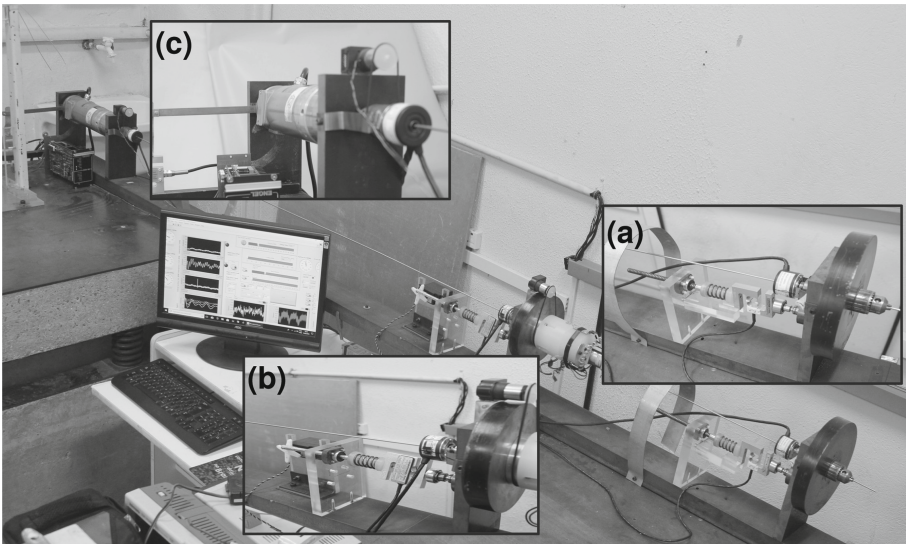


Fig. 1. Drill-string experimental set-up. (a) R_1 and brake device 1, (b) R_2 and brake device 2 and (c) DC-motor.

The brake devices consist of pins in contact with the discs R_1 and R_2 . This dry contact generates a friction torque leading to torsional vibration (or even

stick-slip). The normal forces (N_1 and N_2) created by contact of the pins with the discs are acquired by force sensors. For the friction torque on R_2 , there is a servo motor responsible for moving the pin (active torque). The mitigation strategy is based on this mechanical component. Figure 2 illustrates the components located on R_1 and R_2 , while Fig. 3 shows a scheme of the experimental set-up.

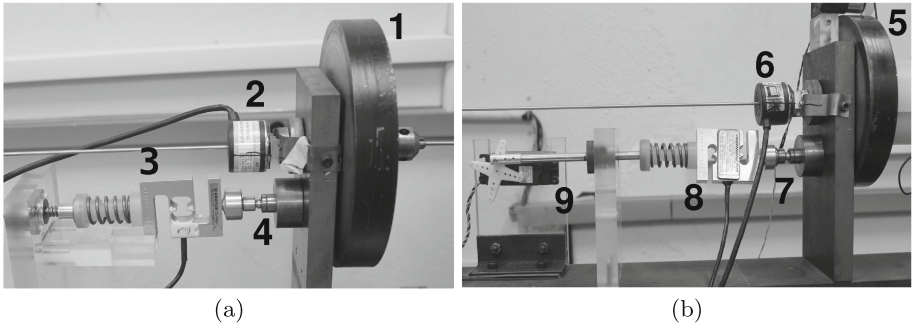


Fig. 2. Discs, brake devices and measure components: 1, 5 - the discs R_1 and R_2 ; 2, 6 - incremental encoders; 3, 8 - force sensors; 4, 7 - contact pins; 9 - servo motor.

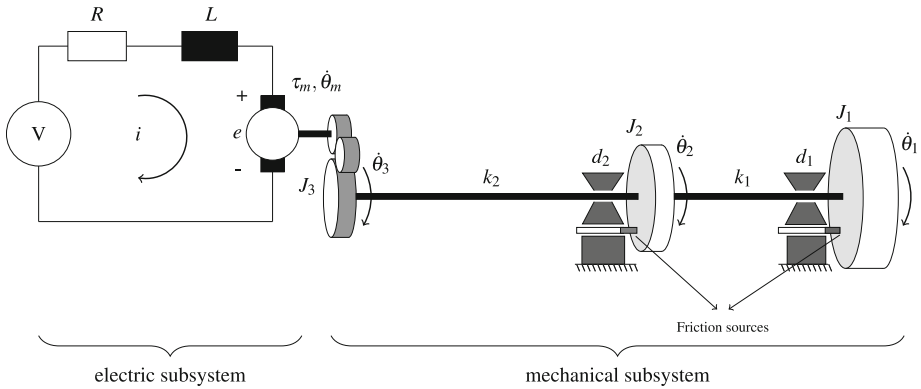


Fig. 3. Electric-mechanical test rig system [19].

3 Modelling of the Test Rig

3.1 Equations of Motion

The electric subsystem is modelled as a voltage source connected in series with a resistor and an inductor, providing torque τ_m . The angular velocity $\dot{\theta}_m$ imposed by τ_m is eight times greater than the angular velocity $\dot{\theta}_3$ transmitted to the mechanical subsystem due to the transmission factor $\eta = 8 : 1$.

Mathematically, the electric subsystem may be expressed as

$$L \frac{di}{dt} = u - Ri - K_E \dot{\theta}_m$$

$$\tau_m = K_T i - C_m \dot{\theta}_m - T_f - J_m \ddot{\theta}_m, \tag{1}$$

where i denotes electric current of the DC-motor. L and R are the armature inductance and resistance, respectively. The angular velocity $\dot{\theta}_m$ is the velocity of the inertia of the DC-motor J_m . C_m and K_T are the speed regulation and constant torque of the motor, respectively. Further, K_E consists in the voltage constant and T_f is the internal friction torque. The input voltage is denoted by u .

The mechanical subsystem illustrated above corresponds mathematically to

$$J_1 \ddot{\theta}_1 + d_1 (\dot{\theta}_1 - \dot{\theta}_2) + k_1 (\theta_1 - \theta_2) = -T_{r_1}$$

$$J_2 \ddot{\theta}_1 + d_1 (\dot{\theta}_2 - \dot{\theta}_1) + d_2 (\dot{\theta}_2 - \dot{\theta}_3) + k_2 (\theta_2 - \theta_3) + k_1 (\theta_2 - \theta_1) = -T_{r_2} \tag{2}$$

$$d_2 (\dot{\theta}_3 - \dot{\theta}_2) + k_2 (\theta_3 - \theta_2) = \tau_s,$$

where J_i for $i = 1, 2$ represents the moment of inertia of each degree of freedom. The angular displacements, velocities and accelerations are denoted by θ_i , $\dot{\theta}_i$ and $\ddot{\theta}_i$ for $i = 1, 2, 3$, respectively. The relations between the subsystems are $\tau_s = \eta \tau_m$ and $\dot{\theta}_m = \eta \dot{\theta}_3$. The third equation of 2 will be changed to

$$d_2 (\dot{\theta}_3 - \dot{\theta}_2) + k_2 (\theta_3 - \theta_2) = \eta (K_T i - C_m \eta \dot{\theta}_3 - T_f - J_m \eta \ddot{\theta}_3)$$

$$L \frac{di}{dt} + Ri + K_E \eta \dot{\theta}_3 = u. \tag{3}$$

The stiffnesses are denoted by k_1 and k_2 , as well as d_1 and d_2 denote the damping. The parameters k_1 and d_1 correspond the stiffness and the damping between R_1 and R_2 , respectively, while k_2 and d_2 represent the stiffness and damping between R_2 and R_3 (see Fig. 3). From Eq. 3, the system may be rewritten as state space formulation in order to be integrated. The following equations (Eqs. 4 and 5) show the state variables and state equations, respectively.

$$\mathbf{x} = \begin{bmatrix} \theta_1 - \theta_2 \\ \theta_2 - \theta_3 \\ \dot{\theta}_1 \\ \dot{\theta}_2 \\ \dot{\theta}_3 \\ i \end{bmatrix} = \begin{bmatrix} x_1 \\ x_2 \\ x_3 \\ x_4 \\ x_5 \\ x_6 \end{bmatrix}, \tag{4}$$

$$\dot{x}_1 = x_3 - x_4$$

$$\dot{x}_2 = x_4 - x_5$$

$$\dot{x}_3 = [-d_1 x_3 + d_1 x_4 - k_1 x_1 - T_{r_1}] / J_1$$

$$\dot{x}_4 = [d_1 x_3 - (d_1 + d_2) x_4 - d_2 x_5 + k_1 x_1 - k_2 x_2 - T_{r_2}] / J_2 \tag{5}$$

$$\dot{x}_5 = [k_2 x_2 - (\eta^2 C_m + d_2) x_5 + d_2 x_4 + \eta K_T x_6 - \eta T_f] / J_3$$

$$\dot{x}_6 = [-R x_6 - \eta K_E x_5 + u] / L,$$

where $J_3 = \eta^2 J_m$. The DC-motor internally contains a PI controller to maintain the desired velocity $\dot{\theta}_3$. The input voltage was modelled as

$$u = k_p(\omega_{ref} - x_5) + k_i \int_0^t (\omega_{ref} - x_5) dt. \quad (6)$$

Next, the friction torque model [12, 22, 25] is expressed as

$$T_{r_1}(\dot{\theta}_1) = N_1 r_1 \left[\mu_k + (\mu_s - \mu_k) \cdot e^{-v_b |\dot{\theta}_1|} \right] \cdot \text{sign}(\dot{\theta}_1), \quad (7)$$

N_1 and r_1 are the normal force and distance between the contact point and the rotation centre of the disc 1. The static and kinetic friction coefficients are represented by μ_s and μ_k , respectively. The parameter v_b represents the decay factor. Herein, the $\text{sign}(\dot{\theta}_1)$ is defined as

$$\text{sign}(\dot{\theta}_1) = \begin{cases} 1 & \text{for } \dot{\theta}_1 \geq 0 \\ -1 & \text{for } \dot{\theta}_1 < 0 \end{cases}. \quad (8)$$

To solve Eq. 5 numerically while avoiding the discontinuity of equation 7 one needs to rewrite the last one as follows [24]

$$T_{r_1}(\dot{\theta}_1) = N_1 r_1 \begin{cases} \mu_s \dot{\theta}_1 / \omega_s & \text{for } |\dot{\theta}_1| < \omega_s \\ \left[\mu_k + (\mu_s - \mu_k) \cdot e^{-v_b |\dot{\theta}_1|} \right] \cdot \text{sign}(\dot{\theta}_1) & \text{for } |\dot{\theta}_1| \geq \omega_s \end{cases}, \quad (9)$$

where $\omega_s = 10^{-3}$.

3.2 Model Validation

In order to verify the correct correlation between numerical and experimental results, a qualitative and quantitative validation is addressed. This procedure aims to illustrate that the numerical modelling corresponds to the experimental set-up. The identification of the mechanical parameters were performed and the values are described in Table 1, while Table 2 contains the electrical constants of DC-motor (via DC-motor manual).

Qualitative Comparison. For this analysis, the voltage relating to 3.14 rad/s (30 rpm) was imposed on the DC-motor, thus the angular velocities of the model were compared with experimental data. The friction torques on R_1 and R_2 were unconsidered ($T_{r_1} = T_{r_2} = 0$). Figure 4 depicts the numerical and experimental data, where the numerical one presents a similar behaviour of the acquired data.

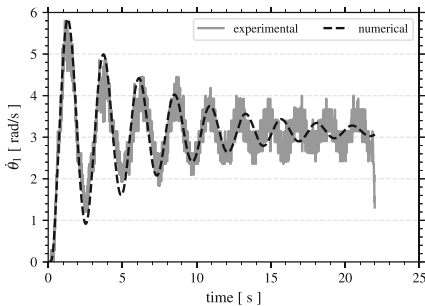
Quantitative Comparison. Quantitatively, the numerical model also presented very matched results. According to [6], the *Correlation Method* is widely used for its easy implementation. This method (Pearson correlation coefficient) consists in

Table 1. Mechanical parameters of test rig.

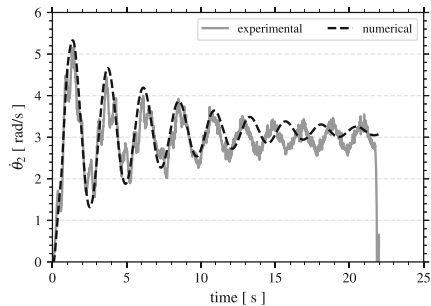
Mechanical constants			
Parameter	Description	Value	unit
J_1	R_1 moment of inertia	0.0288	kgm ²
J_2	R_2 moment of inertia	0.0149	kgm ²
J_3	DC-motor moment of inertia	0.0237	kgm ²
k_1	Stiffness between R_1 - R_2	1.1175	Nm/rad
k_2	Stiffness between R_2 -Motor	0.3659	Nm/rad
d_1	Damping between R_1 - R_2	0.0202	Nms/rad
d_2	Damping between R_2 -Motor	0.0167	Nms/rad
μ_s	Static friction coefficient	0.47	—
μ_k	Kinetic friction coefficient	0.30	—
v_b	Decay factor	0.978	s/rad

Table 2. Electrical parameters of DC-motor.

Parameter	Description	Value	Unit
L	Armature inductance	$8.437 * 10^{-4}$	H
R	Armature resistance	0.33	Ω
K_T	Torque constant	0.126	Nm/A
K_E	Voltage constant	0.0602	V/(rad/s)
T_f	Friction torque	0.1196	Nm
C_m	Speed regulation constant	$1.784 * 10^{-4}$	Nm/(rad/s)
k_p	Proportional constant	2.800	—
k_i	Integral constant	3.500	—



(a)



(b)

Fig. 4. Numerical and experimental angular velocity (a) $\dot{\theta}_1$ and (b) $\dot{\theta}_2$ for 3.14 rad/s.

$$P_C = \frac{\sum_{i=0}^n X_{1_i} \cdot X_{2_i} - \frac{\sum_{i=0}^n X_{1_i} \cdot \sum_{i=0}^n X_{2_i}}{n}}{\sqrt{\left(\sum_{i=0}^n X_{1_i}^2 - \frac{(\sum_{i=0}^n X_{1_i})^2}{n}\right) \cdot \left(\sum_{i=0}^n X_{2_i}^2 - \frac{(\sum_{i=0}^n X_{2_i})^2}{n}\right)}}, \quad (10)$$

where X_{1_i} and X_{2_i} are data of the experimental and numerical model, and n is the number of points. If P_C is equal to 1 it means a perfect match between experimental and numerical data. Otherwise, $P_C = 0$ means a total mismatch between data.

Another indicator is the *Amplitude Pulse Level (APL)* which measures the difference between the data maximum amplitudes [6]. This is quantified as

$$APL = \frac{|\max(X_1) - \max(X_2)|}{|\max(X_1)|}. \quad (11)$$

In this indicator, $APL = 0$ means a perfect match whereas $APL = 1$ means a total mismatch. In the Table 3 is shown the validation method indicators expressed by Eqs. 10 and 11 for the angular velocity $\dot{\theta}_1$ of the experimental and numerical results.

Table 3. Quantitative comparison between experimental and numerical of the $\dot{\theta}_1$.

ω_{ref} [rpm]	P_C [-]	APL [-]
30	0.898	0.010
40	0.893	0.172
50	0.941	0.114
70	0.955	0.119

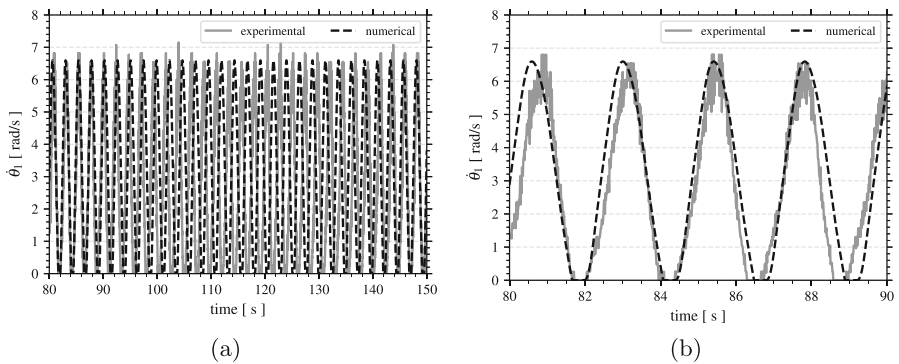


Fig. 5. Test rig response for 3.14 rad/s (30 rpm) with (a) stick-slip and (b) stick-slip zoomed. $N_1 = 25.0$ N and $T_{r_2} = 0.0$ Nm. Continuous gray and dashed black lines contain experimental and numerical results respectively.

Stick-Slip Behaviour Comparison. Moreover, the behaviour during stick-slip of the system is compared (see Fig. 5). The stick time (which means the time during the stick phase [11]) and the amplitude of oscillations are similar. However, in the Fig. 5(a), one may observe the increasing phase loss between the amplitude oscillations of the numerical and experimental models.

3.3 Local Stability and Bifurcation Diagrams

Herein from this section the angular phases are denote as

$$\delta_{12} = \theta_1 - \theta_2, \quad \delta_{23} = \theta_2 - \theta_3. \quad (12)$$

Firstly, a local stability analysis in other to identify periodic and equilibria solution zones is performed. The torsional vibration map (TVM) is obtained via Hurwitz criterion [5, 9, 14]. Figure 6(a) illustrates two zones: one with stable periodic solutions and the other with equilibrium solutions [15]. This means that in the left side of the curve, the system undergoes torsional vibrations (upper Fig. 6(b)) and, in right side, it presents no vibration (lower Fig. 6(b)).

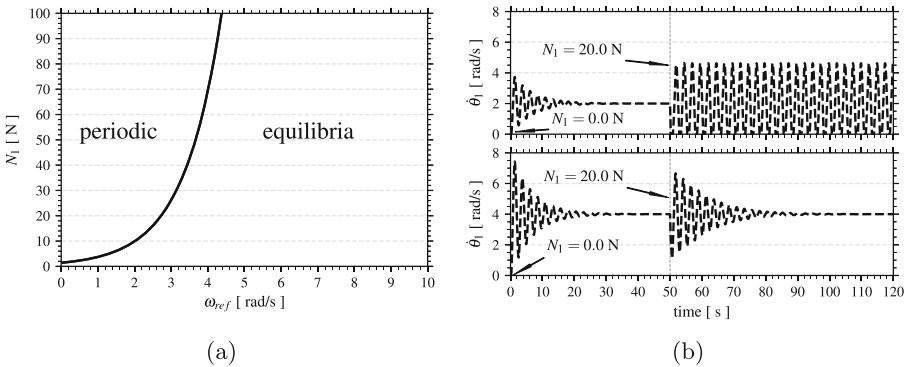


Fig. 6. (a) Torsional vibration map and (b) time response of the R_1 for 2 rad/s and 4 rad/s. $N_1 = 0.0\text{ N}$ at $0 < t < 50$ and $N_1 = 20.0\text{ N}$ at $t > 50$.

Furthermore, in order to identify stable solutions with ω_{ref} as bifurcation parameter, path-following technique and shooting method via PyDSTool package [3] are used to obtain limit cycles numerically [13, 16] for the experimental set-up model as illustrated in Fig. 7. In this figure, the applied normal N_1 is kept constant and equal to 10 N.

One may note that the set-up system presents two Hopf bifurcations denoted by H_1 and H_2 . A periodic branch p_1 rises at H_1 and stable limit cycles are present in the response of the system for $\omega_{ref} = 0.04\text{ rad/s}$, while e_1 denotes an unstable equilibrium branch. The points 1, 2 and 3 on the periodic branch p_1 were depicted in order to illustrate the the orbit in the phase plane. At $\omega_{ref} = 2.9\text{ rad/s}$, an unstable periodic branch p_2 appears and e_2 rises as an equilibrium branch at $\omega_{ref} = 2.02\text{ rad/s}$ (H_2).

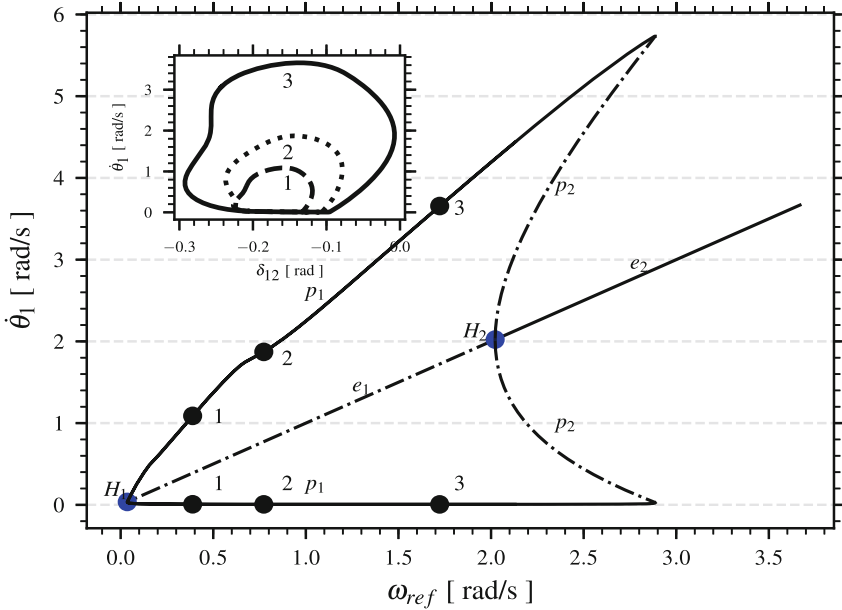


Fig. 7. Bifurcation diagram of the experimental set-up with ω_{ref} as control parameter for $N_1 = 10.0$ N and $T_{r2} = 0.0$ Nm.

4 Mitigation Strategy and Results

Analysing Fig. 7, one may observe the possibility of periodic and equilibrium solutions for $2.0 \leq \omega_{ref} \leq 2.9$ rad/s. To check the possibility of solution in this velocity range, the torsional vibration factor¹ was used [2, 19, 20] as expressed below:

$$f_{TV} = \frac{\max(\dot{\theta}_1) - \min(\dot{\theta}_1)}{2\omega_{ref}}, \quad (13)$$

where $f_{TV} = 0$ means no torsional vibration prevails, $\dot{\theta}_1 = \omega_{ref}$ and the solution is an equilibrium point, otherwise $f_{TV} > 0$ means torsional oscillations and the system presents stable limit cycles. Basins of attraction are depicted in Fig. 8. The initial conditions were

$$x_0 = [\delta_{12}, \delta_{23}, \dot{\theta}_1, \dot{\theta}_2, \dot{\theta}_3, i]^T = [\delta_{12}, 0.0, \dot{\theta}_1, \omega_{ref}, \omega_{ref}, 1.022]^T. \quad (14)$$

Herein, the current $i = 1.022$ A is the necessary value for steady-state with no perturbation obtained via simulation (acquired numerically). Therewith, the solution depends on the perturbation to which the system is subjected in this angular velocity range. Thereby, the mitigation strategy consists in applying a

¹ Some authors denote this factor as “stick-slip severity”, but the system may oscillate without stick-slip phenomenon.

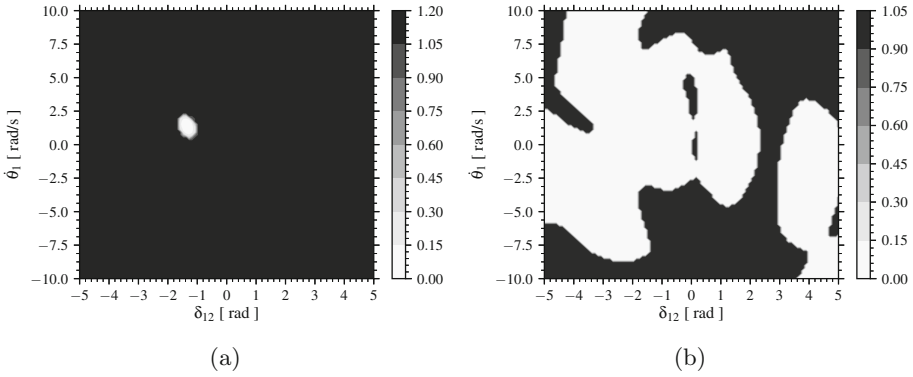


Fig. 8. Basins of attraction for (a) $\omega_{ref} = 2.0$ rad/s and (b) $\omega_{ref} = 2.9$ rad/s. The applied forces $N_1 = 10.0$ N and $T_{r_2} = 0.0$ Nm. The white and black regions mean equilibria and periodic solutions, respectively.

resistive torque in R_2 in order to create an *acceptable* and *sufficient* perturbation to change the solution from the periodic branch to the equilibrium branch, *i.e.*, the system may pass from torsional vibration to no torsional vibration.

The resistive torque T_{r_2} may be written as follows

$$T_{r_2} = N_2 r_2 \mu_s \begin{cases} \sin(\pi\delta_{12}) & \text{for } \dot{\delta}_{12} > 0 \\ \sin(-\pi\delta_{12}) & \text{for } \dot{\delta}_{12} < 0. \end{cases} \quad (15)$$

Equation 15 is equivalent to applying impulsive torques depending on the magnitude of the phase, δ_{12} , and direction of the phase variation, $\dot{\delta}_{12}$. Equation 16 provides the main energies involved. The damping energy is very small compared to the others.

$$\begin{aligned} E_{k_1} &= \frac{1}{2} J_1 (\omega_{ref} - \dot{\theta}_1)^2, & E_{k_2} &= \frac{1}{2} J_2 (\omega_{ref} - \dot{\theta}_2)^2, \\ E_{p_1} &= \frac{1}{2} k_1 \delta_{12}^2, & E_{p_2} &= \frac{1}{2} k_2 \delta_{23}^2, \\ W_{r_2} &= T_{r_2} \int_{t_1}^{t_2} (\omega_{ref} - \dot{\theta}_2) dt. \end{aligned} \quad (16)$$

This resistive torque T_{r_2} prevents the kinetic energy E_{k_1} increasing by the extraction of potential energies E_{p_1} and E_{p_2} . Therewith, it acts as an energy transfer control from potential energy to kinetic energy. In other words, the resistive torque represented by Eq. 15 avoid large values of δ_{12} .

It worth to remark that the energy and work of the unperturbed system were subtracted in order to observe only the variation of these magnitudes. The potential and kinetic energies of the system are depicted before and after the application of the resistive torque T_{r_2} (Eq. 15) in Fig. 9 for $\omega_{ref} = 2.5$ rad/s. The strategy mitigation is applied during 50 s - from 100 to 150 s.

Moreover, in Fig. 10(a)–(b) it is depicted the influence of the W_{r_2} on the kinetic and potential energies, respectively, over time. Following, Fig. 10(c)–(d) illustrates the mitigation of the $\dot{\theta}_1$ and $\dot{\theta}_2$, respectively, over time.

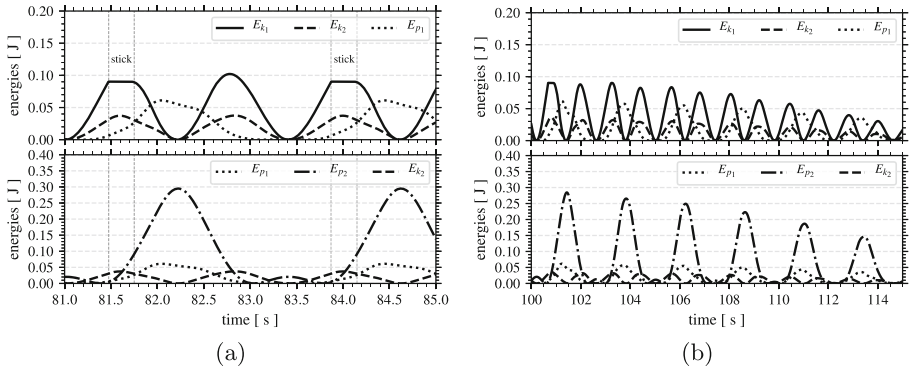


Fig. 9. Kinetic and potential energies as function of time (a) before and (b) after the application T_{r2} . $N_1 = 10.0$ N, $N_2 = 1.0$ N and $\omega_{ref} = 2.5$ rad/s.

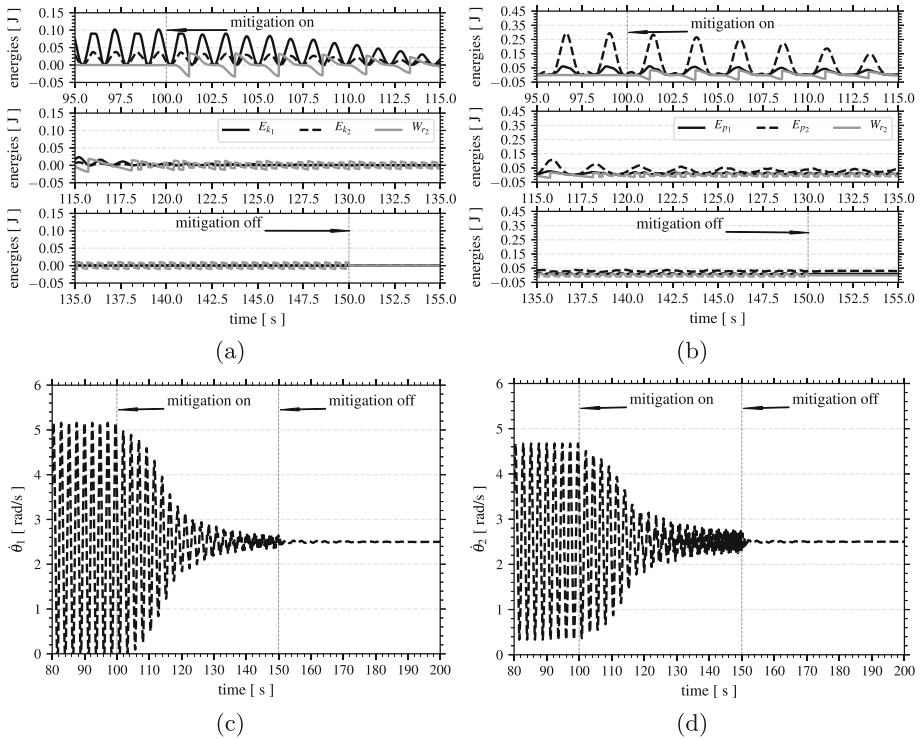


Fig. 10. Influence of the mitigation strategy (a) on the kinetic energies over time, (b) on the potential energies over time, (c) on $\dot{\theta}_1$ and (d) on $\dot{\theta}_2$. $N_1 = 10.0$ N, $N_2 = 1.0$ N and $\omega_{ref} = 2.5$ rad/s.

5 Conclusions

This work proposed a mitigation of the torsional vibration of a slender mechanical system. The experimental set-up may represent a drilling system under torsional vibration in its severe stage: stick-slip.

The validation of the numerical model was performed and presented a good match, qualitatively and quantitatively. This validation is important in order to investigate severe circumstances that may be not possible to verify experimentally. Some non-modelled phenomena may influence the response of the system such as temperature between the disc and pin. For example, it may increase the friction coefficients which herein were considered constants. Furthermore, manufacturing limitations imposed a slight rotation out of plane of the disc R_1 and therewith variation in the normal force N_1 is observed. An improvement of the experimental set-up and the friction model, as one may see in Fig. 5, may provide an even better match between numerical and experimental models.

The numerical results proved that a friction torque acting on R_2 may provide the *sufficient* perturbation to change the solution of the system. Thereby, in the ω_{ref} range, the system must present bi-stable behaviour. In Fig. 8, one may observe the mentioned bi-stable solutions: Fig. 8(a) presents a small equilibrium region which may difficult the change between stable solutions and the amplitudes are 2.4 times the ω_{ref} , whereas Fig. 8(b) presents a significant equilibrium region which may lead to an effortless change of solutions with maximum amplitude of 2.10 times the ω_{ref} . Comparing the energy magnitudes in Figs. 9 and 10, the W_{r_2} provides *acceptable* values of energy extraction via friction with $N_2 = N_1/10$. In fact, it must also be investigate in order to assume the minimum value possible. It should be remarked that the combination of N_1 and ω_{ref} (representing weight-on-bit and Surface RPM, respectively, in field operation) was not modified to mitigation purpose.

At the moment in field operations, there is no tool capable to induce torsional oscillations as studied here. However, this work aims to provide theoretical basis for improvement of future operations and better understanding about stick-slip phenomenon.

References

1. Alamo, F.J.C.: Dynamics of slender one-dimensional structures using cosserat continuum. D.Sc. thesis, Pontificia Universidade Católica do Rio de Janeiro, Rio de Janeiro, Brazil (2006)
2. Cayres, B.C.: Numerical and experimental analysis of nonlinear torsional dynamics of a drilling system. M.Sc. thesis, Pontificia Universidade Católica do Rio de Janeiro, Rio de Janeiro, Brazil (2013)
3. Clewley, R., Sherwood, E., LaMar, D., Guckenheimer, J.: Pydstool: a software environment for dynamical systems modeling (2008). <http://sourceforge.net/projects/pydstool>
4. Cunha Jr., A.: Modeling and uncertainty quantification in nonlinear stochastic dynamics of horizontal drillstring with friction and shocks effects. D.Sc. thesis, Pontificia Universidade Católica do Rio de Janeiro, Rio de Janeiro, Brazil (2015)

5. Franca, L.F.P.: Self-excited percussive-rotary drilling in hard rocks. D.Sc. thesis, Pontifícia Universidade Católica do Rio de Janeiro, Rio de Janeiro, Brazil (2004)
6. Jauregui, R., Silva, F.: Numerical validation methods. In: Numerical Analysis-Theory and Application. InTech (2011)
7. King, H.M.: Directional and horizontal drilling in oil and gas wells (2012). <http://geology.com/articles/horizontal-drilling>. Accessed 13 Nov 2014
8. Kriesels, P., Keultjes, W., Dumont, P., Huneidi, I., Owoeye, O., Hartmann, R., et al.: Cost savings through an integrated approach to drillstring vibration control. In: SPE/IADC Middle East Drilling Technology Conference. Society of Petroleum Engineers (1999)
9. Leipholz, H.: Stability Theory: An Introduction to the Stability of Dynamic Systems and Rigid Bodies. Academic Press, Cambridge (1970)
10. Lima, R., Sampaio, R.: Construction of a statistical model for the dynamics of a base-driven stick-slip oscillator. *Mech. Syst. Sign. Process.* **91**, 157–166 (2017)
11. Lima, R., Sampaio, R.: Parametric analysis of the statistical model of the stick-slip process. *J. Sound Vib.* **397**, 141–151 (2017)
12. Mihajlović, N.: Torsional and lateral vibrations in flexible rotor systems with friction. D.Sc. thesis, Eindhoven University of Technology, Eindhoven, Netherlands (2005)
13. Mihajlović, N., van de Wouw, N., Hendriks, M.P.M., Nijmeijer, H.: Friction-induced limit cycling in flexible rotor systems: an experimental drill-string set-up. *Nonlinear Dyn.* **46**, 273–291 (2005)
14. Navarro-López, E.M., Suárez, R.: Modelling and analysis of stick-slip behaviour in a drillstring under dry friction. In: Congress of the Mexican Association of Automatic Control, pp. 330–335 (2004)
15. Nayfeh, A.H., Balachandran, B.: Applied Nonlinear Dynamics: Analytical Computational and Experimental Methods. Wiley, Hoboken (2008)
16. Parker, T.S., Chua, L.: Practical Numerical Algorithms for Chaotic Systems. Springer, Heidelberg (2012)
17. Patil, P.A., Teodoriu, C.: Model development of torsional drillstring and investigating parametrically the stick-slips influencing factors. *J. Energy Resour. Technol.* **135**(1), 013–103 (2013)
18. Pereira, L.D.: Minimizing drill string torsional vibration using surface active control. M.Sc. thesis, Pontifícia Universidade Católica do Rio de Janeiro, Rio de Janeiro, Brazil (2017)
19. Pereira, L.D., Cayres, B.C., Weber, H.I.: Numerical application of a stick-slip control and experimental analysis using a test rig. In: MATEC Web of Conferences, vol. 148, p. 16009. EDP Sciences (2018)
20. Ritto, T.G., Aguiar, R.R., Hbaieb, S.: Validation of a drill string dynamical model and torsional stability. *Meccanica* **52**(11), 2959–2967 (2017). <https://doi.org/10.1007/s11012-017-0628-y>
21. Saldivar, B., Mondie, S., Loiseau, J.J., Rasvan, V.: Suppressing axial-torsional coupled vibrations in drillstrings. *J. Control Eng. Appl. Inf.* **15**(1), 3–10 (2013)
22. Sampaio, G.: Dynamics and control of stick-slip and torsional vibrations of flexible shaft driven systems applied to drillstrings. D.Sc. thesis, Pontifícia Universidade Católica do Rio de Janeiro, Rio de Janeiro, Brazil (2017)
23. Thomas, J.E.: Fundamentos de engenharia de petróleo. Interciência (2001)
24. Thomsen, J.J.: Using fast vibrations to quench friction-induced oscillations. *J. Sound Vib.* **228**(5), 1079–1102 (1999)
25. Vromen, T.G.M.: Control of stick-slip vibrations in drilling systems. D.Sc. thesis, Eindhoven University of Technology, Eindhoven, Netherlands (2015)
26. Wikipedia: Drilling rig (2017). https://en.wikipedia.org/wiki/Drilling_rig



Modeling and Simulation of the Drivetrain of a Metal Lathe

Eduardo Paiva Okabe^(✉) and Daniel Iwao Suyama

School of Applied Sciences, University of Campinas - UNICAMP,
PO Box 1068, Limeira, Brazil
{[eduardo.okabe](mailto:eduardo.okabe@fca.unicamp.br),[daniel.suyama](mailto:daniel.suyama@fca.unicamp.br)}@fca.unicamp.br

Abstract. Vibrations in turning machining are one of the most common sources of problems. Bad quality finishing, decrease of the tool life, dimensional errors, and noise are some of the issues generated by these vibrations. To understand the role of each component, this work presents a model of a metal lathe including its drivetrain, and simulates it during the internal turning operation. The drivetrain is composed by an electric motor connected to the spindle through a pulley and belt transmission. The spindle was modeled as a rotor supported by rolling bearings, while the chuck with jaws and the workpiece were considered to be rigidly attached to the spindle. The interface between the workpiece and the tool was modeled considering their relative displacement and the machining condition, thus generating a set of cutting and drag forces that varies during the operation. The tool holder was modeled by three-node finite volume beam elements that are attached to the turret. The turret was connected to the machine frame through a total joint (configured as prismatic). This model was implemented in the dynamic simulation software MBDyn and a module was developed in C++ to mimic the interaction between workpiece and tool. Different configurations of the machine were tested, such as the diameter of the tool holder and the rotation speed of the spindle, and their influence on the drivetrain is reported.

Keywords: Metal lathe · Drivetrain vibrations · Multibody dynamics

1 Introduction

Machining is one of the most important manufacturing process in the metal-work industry. Operations like turning, milling, drilling, and grinding lead to the achievement of pre-established form, dimension, and surface finish of a part. Turning is a relatively fast, precise and cheap operation, which renders it the one of the most effective ways to produce mechanical cylindrical components. However, machining processes usually relies on rotating parts that are subjected to a large variety of vibration phenomena. These vibrations are one of the most common sources of problems, causing bad quality finishing, decrease of the tool life, dimensional errors and noise [15].

The drivetrain of a machining equipment is one of its main components, because most of the power required to cut metal flows through it. The drivetrain is composed by an electric motor connected to the spindle through a pulley/belt transmission. To understand its behavior this work presents a model of a metal lathe and simulates it during the internal turning process, also known as boring operation.

The spindle is the main component of the drivetrain of any machining equipment. Usually being one slender rotating shaft, it brings all sorts of vibration problems, which is exactly the opposite of what its function demands. Aini et al. [1] modeled a grinding machine spindle as a rigid shaft supported by angular contact ball bearings. They studied the effect of the radial force, spindle speed, frictional damping and thrust loads. In their simulations, they discovered that the axial mode was less than half of the frequency of the radial modes and the behavior of the spindle was influenced by the preload in the bearings.

Mannan et al. [11] also studied the vibration on a grinding machine, but they focused on the torsional vibrations. They used a simple three degrees of freedom model to represent workpiece, wheel and spindle. They concluded that the width of cut can lead to the torsional instability of the system due to chatter. Altintas and Weck [2] made a review of the modeling of chatter in metal cutting and grinding processes. They highlighted that although the boring bar is the most flexible part of the hole enlargement process, other parts such as the shaft, chuck and the tool holder can lead to chatter.

Ertürk et al. [6] proposed an analytical model of the spindle-tool dynamics of a drilling machine. They modeled the spindle as a discretized beam using the Timoshenko beam model, with the spindle supported by elastic bearings. The FRF (frequency response function) of the tool generated by the proposal model was compared to the response obtained from a commercial finite element software. They presented a good agreement. Due to the geometry of the drilling machine spindle they showed that the Euler-Bernoulli beam could lead to inaccurate results at high frequencies when compared to the Timoshenko beam.

Roukema and Altintas [13] presented a time domain model of a drilling operation to study the torsional-axial chatter vibrations. The cutting force was calculated by a mechanistic model that uses the feedrate, depth of cut and drill geometry to determine the torque and thrust on the tool. The simulation also considers the generated surfaces to predict the occurrence of vibration phenomena such as chatter. The simulated results were close to the experimental ones, although the authors point out that the process damping would be required to predict the stability of the drilling operation.

Guo et al. [8] analyzed a lathe spindle system under the influence of an unbalanced workpiece. They developed a pure torsional lumped mass system to model the geared drivetrain. The authors concluded that the spindle can not operate at same speed of its natural frequencies because of the instability generated by the unbalance of the chosen workpiece, a crankshaft.

In the next section the methodology adopted to develop the computational model of the metal lathe using a multibody dynamics approach as well as the details of the cutting force calculation are presented.

2 Methodology

The metal lathe can be considered a mechanical constrained system, which can be formulated as a system of Differential-Algebraic Equations (DAE) [12]:

$$\begin{aligned}
 \mathbf{M}\dot{\mathbf{q}} - \boldsymbol{\beta} &= \mathbf{0} \\
 \dot{\boldsymbol{\beta}} + \left(\frac{\partial\boldsymbol{\phi}}{\partial\mathbf{q}}\right)^T \boldsymbol{\lambda}_\phi + \left(\frac{\partial\boldsymbol{\psi}}{\partial\dot{\mathbf{q}}}\right)^T \boldsymbol{\lambda}_\psi &= \sum \mathbf{f}(\mathbf{q}, \dot{\mathbf{q}}, t) \\
 \boldsymbol{\phi}(\mathbf{q}, t) &= \mathbf{0} \\
 \boldsymbol{\psi}(\mathbf{q}, \dot{\mathbf{q}}, t) &= \mathbf{0}
 \end{aligned} \tag{1}$$

where \mathbf{M} is the inertia matrix, $\boldsymbol{\beta}$ is the momentum vector, \mathbf{q} is the position vector, $\boldsymbol{\phi}$ is the system of holonomic constraint equations, $\boldsymbol{\psi}$ is the system of non-holonomic constraint equations, $\boldsymbol{\lambda}_\phi$ is the Lagrange multiplier associated with the holonomic constraints, $\boldsymbol{\lambda}_\psi$ is the Lagrange multiplier associated with the non-holonomic constraints, \mathbf{f} is the vector of external loads, and (\clubsuit) represents the time derivative of (\clubsuit) .

This formulation is implemented in the open source software MBDyn, which is a multiphysics platform that can simulate complex systems. The models on MBDyn are based on nodes, like the ones used on finite element softwares. Nodes provide degrees of freedom, and they can be associated to different physical domains, such as mechanical, thermal and electrical. This structure makes easier to integrate different components of the same machine in one simulation.

Constraints and forces have to be applied on nodes, thus they become part of the modeled system. This is performed by adding two sets of equations to variables associated with each node. The first set is used in the assembly of the system of Eq. (1), and the second set is used during the nonlinear solution phase, if it is necessary.

New elements can be created to compose the model by adding new modules to MBDyn. These modules are written in C++, and they basically contain the system of equations that model the dynamic behavior of the element and its Jacobian matrix. These modules are compiled with MBDyn, and they become part of the software which enable the use of this new element in any model.

The next section presents the set of equations that model the cutting forces in the turning process, which were implemented in a module of MBDyn to compose the complete model of the lathe drivetrain.

2.1 Cutting Model

Using the geometry represented in Fig. 1 it is possible to reproduce the behavior of the cutting process using a semi-analytical model that relates one node fixed to the tool holder (Node 1) and one node attached to the workpiece (Node 2). The

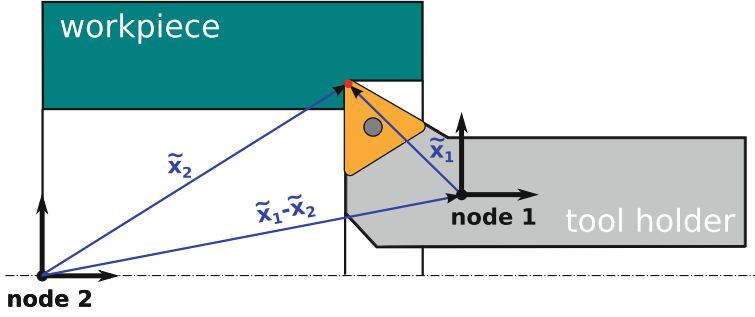


Fig. 1. Geometry of the cutting model.

tool (insert) is considered to be rigidly attached to the tool holder. The kinematic relationship between nodes 1 and 2 is used to calculate the forces through the cutting model, then these forces are transformed to the absolute coordinates and applied to each one of the nodes. The calculation of the moments generated by these forces should consider the point of application of the cutting force, which moves during the machining process. The forces and moments applied to both nodes can be calculated by:

$$\begin{aligned}
 \mathbf{f}_1 &= -\mathbf{R}_{1r}\mathbf{f}_{\text{cut}} \\
 \mathbf{f}_2 &= \mathbf{R}_{1r}\mathbf{f}_{\text{cut}} \\
 \mathbf{c}_1 &= -\mathbf{R}_1\tilde{\mathbf{x}}_1 \times \mathbf{R}_{1r}\mathbf{f}_{\text{cut}} - \mathbf{R}_{1r}\mathbf{c}_{\text{cut}} \\
 \mathbf{c}_2 &= \mathbf{R}_2\tilde{\mathbf{x}}_2 \times \mathbf{R}_{1r}\mathbf{f}_{\text{cut}} + \mathbf{R}_{1r}\mathbf{c}_{\text{cut}}
 \end{aligned} \tag{2}$$

where \mathbf{f}_1 and \mathbf{f}_2 are the forces applied to nodes 1 and 2, \mathbf{c}_1 and \mathbf{c}_2 are the moments applied to nodes 1 and 2, $\mathbf{R}_{1r} = \mathbf{R}_1\tilde{\mathbf{R}}_1$ is the rotation matrix of the tool edge, \mathbf{R}_1 is the rotation matrix of the tool holder node, and $\tilde{\mathbf{R}}_1$ is the rotation matrix of tool edge in relation to the node of the tool holder (node 1), $\tilde{\mathbf{x}}_1$ is the offset between the tool holder node and the cutting edge, and $\tilde{\mathbf{x}}_2$ is the offset between the cutting edge and the node attached to the workpiece, \mathbf{f}_{cut} and \mathbf{c}_{cut} are the cutting force and moment. The calculation of cutting force \mathbf{f}_{cut} was adapted from the model proposed by Xiao et al. [17] to the multibody environment. They based their model on the analytical approach developed by Tarng et al. [16], but instead of using an analytical formulation, they obtained the cutting properties (shear and friction angles, and shear stress) from the data reported by Kashimura [10].

The cutting force is calculated using the following equation:

$$\begin{aligned}
 F_c &= R \cos(\lambda - \alpha) \\
 F_t &= R \sin(\lambda - \alpha) \\
 R &= \frac{k_{ab}t_1w}{\sin \phi \cos(\phi + \lambda - \alpha)} U(t_1) \\
 \mathbf{f}_{\text{cut}} &= \{0 \quad -F_t \quad -F_c\}^T
 \end{aligned} \tag{3}$$

where R is the cutting force magnitude, λ is the friction angle, α is the rake angle, k_{ab} is the shear stress, t_1 is the chip thickness, w is the cutting width, and $U(t_1)$ is the unit step, which is zero unless t_1 is positive. Using the experimental data reported by Kashimura [10] for the S45C carbon steel, the shear angle, the friction angle and the shear stress become:

$$\begin{aligned}\phi &= \exp(0.0587v + 1.0398t_1 + 0.6742\alpha - 1.2392) \\ \lambda &= \exp(-0.0546v - 0.8856t_1 + 0.8923\alpha - 0.2388) \\ k_{ab} &= \exp(0.0059v - 0.4246t_1 + 0.0818\alpha + 6.3211)\end{aligned}\quad (4)$$

where v is the cutting speed. The dynamic variables of the cutting model must be calculated using the relative motion between the tool edge and the workpiece:

$$\begin{aligned}\mathbf{x}_{rel} &= \mathbf{R}_1 \tilde{\mathbf{x}}_1 + \mathbf{x}_1 - \mathbf{x}_2; \\ \boldsymbol{\omega}_{rel} &= \mathbf{R}_{1r}^T (\boldsymbol{\omega}_2 - \boldsymbol{\omega}_1) \\ \dot{\mathbf{x}}_{rel} &= \dot{\mathbf{x}}_1 + \boldsymbol{\omega}_1 \times \mathbf{R}_1 \tilde{\mathbf{x}}_1 - \dot{\mathbf{x}}_2\end{aligned}\quad (5)$$

where \mathbf{x}_1 is the position of the tool holder node, \mathbf{x}_2 is the position of the workpiece node, $\boldsymbol{\omega}_{rel}$ is the relative angular velocity between the tool and the workpiece, $\boldsymbol{\omega}_1$ and $\boldsymbol{\omega}_2$ are the angular velocity of the nodes associated to the tool (node 1) and workpiece (node 2), $\dot{\mathbf{x}}_{rel}$ is the relative linear velocity, $\dot{\mathbf{x}}_1$ and $\dot{\mathbf{x}}_2$ are the linear velocities of the nodes 1 and 2.

Equation 5 provides the information to determine the dynamic variables of the cutting model:

$$\begin{aligned}w &= (x_{feed} - \mathbf{x}_{rel}[x]) \cdot 10^3 \\ t1 &= (\sqrt{\mathbf{x}_{rel}[y]^2 + \mathbf{x}_{rel}[z]^2} - r) \cdot 10^3 \\ v &= -\boldsymbol{\omega}_{rel}[x] \cdot r \\ \dot{y} &= \frac{\mathbf{x}_{rel}[y] \cdot \dot{\mathbf{x}}_{rel}[y] + \mathbf{x}_{rel}[z] \cdot \dot{\mathbf{x}}_{rel}[z]}{\sqrt{\mathbf{x}_{rel}[y]^2 + \mathbf{x}_{rel}[z]^2}} \\ \alpha &= \alpha_0 - \arctan\left(\frac{\dot{y}}{v}\right) - \arctan\left(\frac{\mathbf{x}_{rel}[y]}{\mathbf{x}_{rel}[z]}\right)\end{aligned}\quad (6)$$

where x_{feed} is a function which determines the tool feed [4], the brackets $[i]$ indicates that the i^{th} component of the vector (for instance, $\mathbf{x}_{rel}[x]$ refers to the x component of the position vector \mathbf{x}_{rel}), r is the radius of the workpiece, α_0 is the initial rake angle.

This formulation was implemented on the MBDyn as an element through a module written in C++. Once compiled this element could be included in the metal lathe model.

3 Metal Lathe Modeling

Although the cutting model is essential to model the dynamic behavior of a metal lathe, the interaction between workpiece and tool is just one of the elements of

the model. Figure 2 shows an outline of the metal lathe modeled in this work with the coordinate system adopted, which is not the usual coordinate system seen in machining research, where the X-axis would be in the place of the Y-axis of Fig. 2.

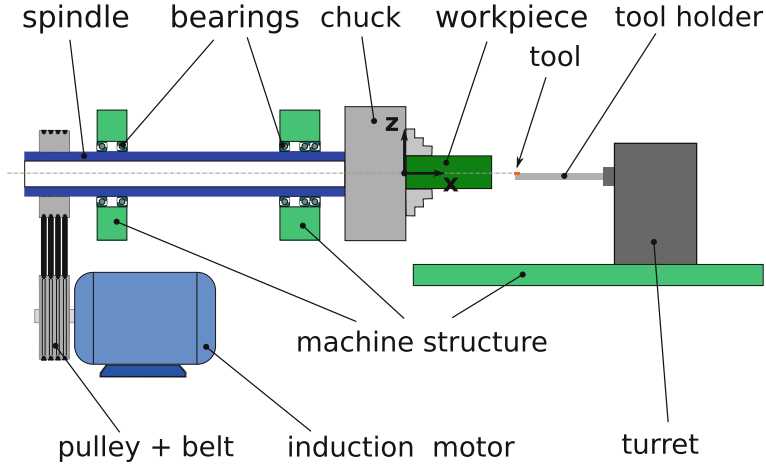


Fig. 2. Outline of the metal lathe and its coordinate system.

The spindle was modeled as discretized beam elements that uses the finite volume formulation proposed by Ghiringhelli et al. [7]. It is a large displacement slender beam that is computationally efficient and can be easily integrated in multibody models. This element is composed by three nodes that are directly related to the dynamic nodes of MBDyn.

The spindle is supported by five ball bearings that were represented by the nonlinear model proposed by Gargiulo as reported by Hambric et al. [9]. This configuration renders the support of the spindle extremely stiff, which is desirable to keep the precision of the cutting process even under heavy load machining.

One of the ends of the spindle is connected to an induction motor through a pulley-belt system. This motor was modeled using the formulation proposed by Dresig and Holzweißig [5] to represent an asynchronous motor. This element was implemented by Reinhard Resch in the MBDyn and it simplifies the electromagnetic equation expressing the dynamic behavior of the motor through only three variables: slippage, breakdown slippage and breakdown torque.

The pulley-belt system was modeled using an elastic rod element that represents the tension applied by the belts to both pulleys and a deformable axial joint (torsional spring) that transmits the rotation from the motor rotor to the spindle. The stiffness and damping properties of the belt were determined using the experimental data presented by Shangguan and Zeng [14] and Čepon et al. [3].

The chuck and the workpiece were modeled as rigid bodies that are rigidly attached to the spindle end node. The turret was also modeled as a rigid body that supports the tool holder and moves along the X-axis.

The tool holder was modeled as a discretized finite volume beams like the spindle. Internal turning is known to cause vibration problems during machining, due to the cantilever geometry of the tool holder, which is a slender beam with a tool in the tip.

Finally the holder head and tool itself (insert) were modeled as a rigid body attached to the other end of the holder.

The model has 28 structural nodes and each node has 6 d.o.f. (degrees of freedom). Thus the model has a total of 168 d.o.f. of which 116 are constrained by the algebraic equations (Eq. 1). The integration method of MBDyn is a A/L linear multistep algorithm [12] with a constant time step of 1×10^{-4} s (or a sampling frequency equals to 10 kHz).

The system is completely static in the initial time only subjected to the gravity force. The electric motor accelerates the spindle to a defined speed and then the turret moves to start the machining process.

Table 1 summarizes the parameters used in the simulation of the lathe.

4 Results

To verify the dynamic behavior of the lathe, it was simulated in six different conditions. The influence of the flexibility of the tool holder (boring bar) was verified by using two different diameters: 16 and 20 mm. They were tested under two rotation speeds: 1000 rpm (132 m/min) and 2000 rpm (264 m/min), so the cutting force could be tested under different cutting speeds. To give a realistic excitation source vibration for the system, the workpiece radius is considered to have a random variation with an amplitude of 0.1 mm.

The last two tests were used to check the effect of the chatter on the drivetrain. To mimic this behavior, a sine function with an amplitude of 0.1 mm was added to the workpiece radius. This sine function has a frequency of 650 Hz, which is close to the vibration frequency of the tool holder during the machining process. Figure 3 shows the power spectral density of the angular velocity of the chuck before the tool starts to machine the workpiece (left) and during the machining (right). Before the cutting a peak around 35 Hz can be seen on all simulated situations, which is associated to the first mode of the drivetrain system (motor, belt and spindle). That vibration comes from the fast acceleration of the spindle imposed by the motor. This peak decreases when the machining takes place, however, another peak shows up at 585 Hz related to the first flexural mode of the tool holder. Even though the frequency associated to this mode is different from the 16 mm to 20 mm tool holder, the peaks occur at the same frequency.

Another information that can be extracted from Fig. 3 is that the diameter of the tool holder had a greater influence on the angular velocity of the chuck than the increase of the rotation speed itself. In the opposite end of the spindle

Table 1. Lathe model parameters

Part	Parameter	Value
Induction motor	Slippage	0.1
	Breakdown torque	58.83 Nm
	Viscous damping	0.0015
	Rotation speed	1000 and 2000 rpm
Tool holder	Length	125 mm
	Diameter	16/20 mm
	Material	steel
Spindle	External diameter	75 mm
	Internal diameter	40 mm
	Length	567 mm
	Material	Steel
Ball bearings	Sphere diameter	11 mm
	Number of spheres	22
	Contact angle	25°
Chuck	Length	80 mm
	Mass	14.25 kg
	Moment of inertia I _{xx}	0.051 kg·m ²
	Moment of inertia I _{yy} , I _{zz}	0.033 kg·m ²
Workpiece	Mass	1 kg
	Moment of inertia I _{xx}	1·10 ⁻⁶ kg·m ²
	Moment of inertia I _{yy} , I _{zz}	8·10 ⁻⁶ kg·m ²
	Internal diameter	40 mm
	Material	steel S45C
Cutting properties	Speed	132 and 264 m/min
	Feedrate	0.1 mm/rev
	Rake angle	3°
Pulley-belt	Transmission ratio	1:1

there is the pulley set which is connected to the motor. Its angular velocity can be seen on Fig. 4 and the same behavior is observed although the second peak has a lower frequency (~ 500 Hz) and it is more damped. Figure 5 shows that the influence of the tool holder is much less pronounced in the motor than the spindle (Fig. 4), which means that the belt is filtering the vibration coming from the spindle. Another point to be observed is that the vibration power of the mode related to the drivetrain is largely reduced during the machining, which means that the cutting process effectively constrains the torsional motion of the spindle.

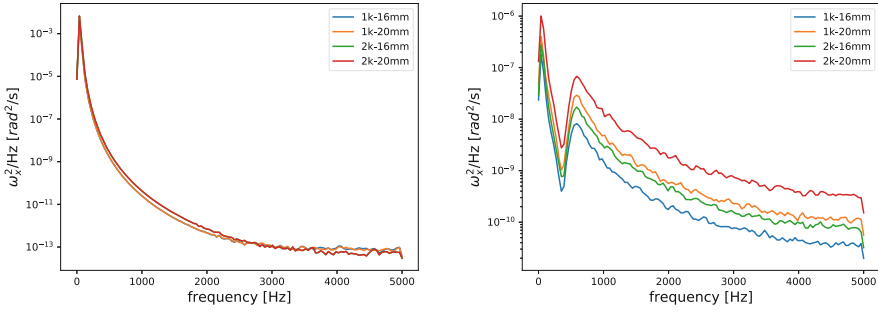


Fig. 3. Power spectral density of the angular velocity of the chuck before (left) and during machining (right).

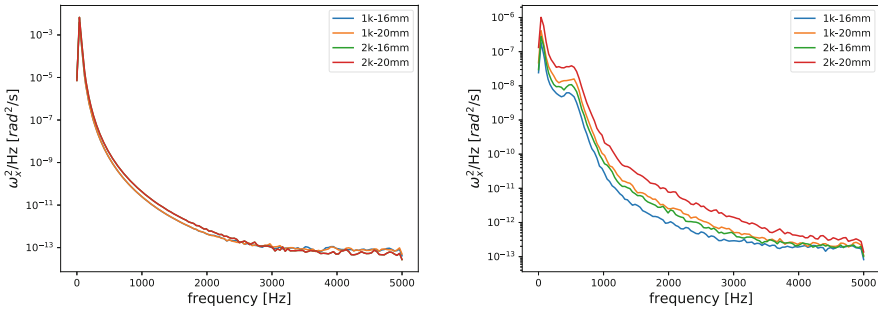


Fig. 4. Power spectral density of the angular velocity of the spindle pulley before (left) and during machining (right).

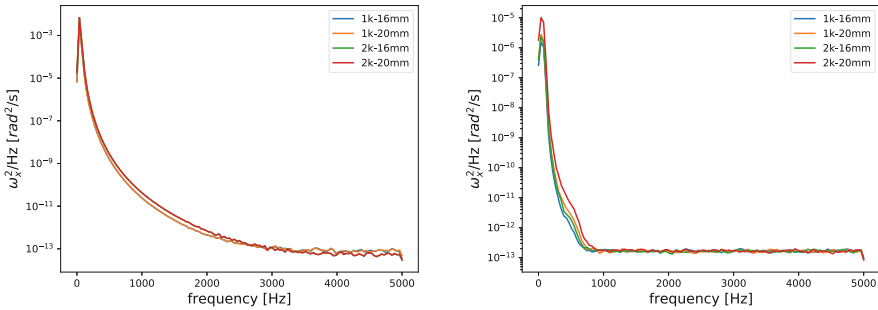


Fig. 5. Power spectral density of the angular velocity of the motor rotor before (left) and during machining (right).

To verify the effect of the drivetrain on the tool, its angular velocity is represented on Fig. 6. While there is a small influence of the tool holder on the motor (Fig. 5), the opposite is not true.

Another phenomenon very interesting to analyze is the chatter, which is more pronounced in the internal machining operation. The chatter is related

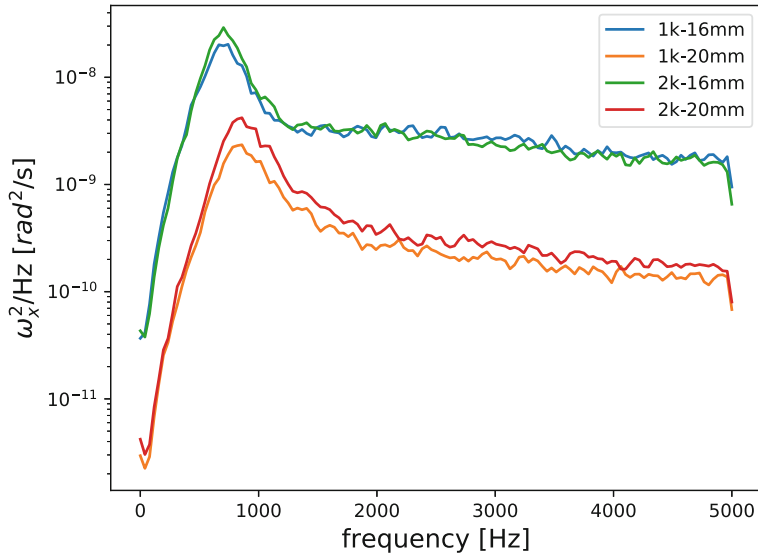


Fig. 6. Power spectral density of the angular velocity of the tool during machining.

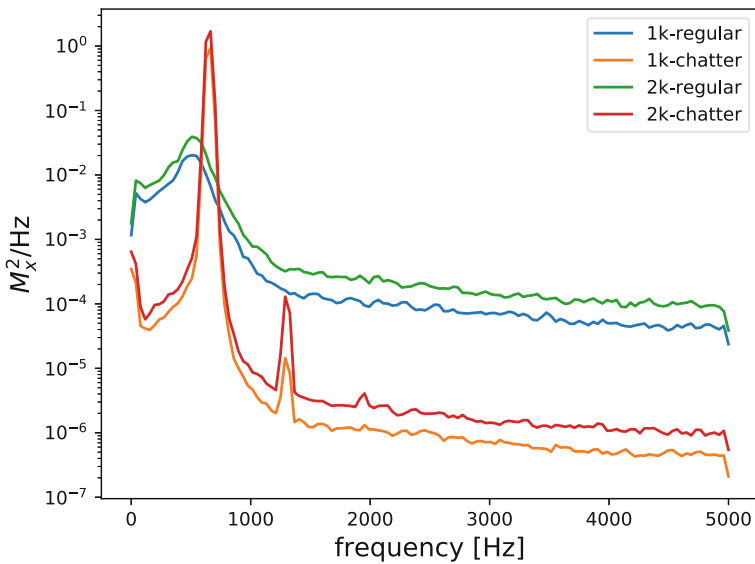


Fig. 7. Power spectral density of the moment applied to the spindle.

to the vibration of the tool holder that is imprinted in the machined surface of the workpiece. When the tool is executing other passes on this surface, the tool holder is excited by the impression left which increases the vibration and deteriorates the surface finish. The chatter phenomenon can decrease the tool

life span and it causes vibration problems on the components of the drivetrain. To simulate the chatter phenomenon, a sine wave was added to the workpiece radius profile with a frequency that matches the flexural mode of the tool holder and amplitude of 0.1 mm.

Figure 7 shows the power spectral density of the moment applied to the spindle through the chuck. The moment due to chatter is much higher than normal cutting operation (without chatter) and there is a second peak on 1285 Hz, which is approximately twice the frequency of the first peak (650 Hz).

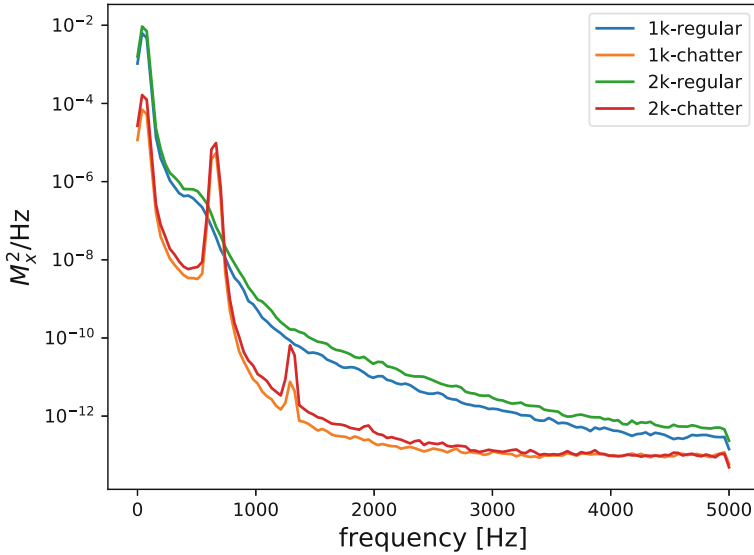


Fig. 8. Power spectral density of the moment applied to the motor.

The vibration caused by the chatter is also present in the moment applied to the motor which can be observed in Fig. 8.

5 Conclusions

A complete model of lathe drivetrain was simulated under machining conditions using a multibody dynamics software, that demonstrated the influence of the cutting process on the torsional vibration of drivetrain components. The internal turning machining was adopted in order to highlight the effect of the flexibility of the tool holder.

Results showed that there is a considerable effect of this flexibility on the spindle behavior, but this effect is filtered by the pulley-belt set to the motor. The vibration of the drivetrain does not seem to affect the tool motion, that is largely influenced by the behavior of the tool holder.

However, the influence of the chatter phenomenon is transmitted through the spindle to the electric motor, which indicates that the vibration generated by it can damage the motor.

References

1. Aini, R., Rahnejat, H., Gohar, R.: A five degrees of freedom analysis of vibrations in precision spindles. *Int. J. Mach. Tools Manuf.* **30**(1), 1–18 (1990)
2. Altintas, Y., Weck, M.: Chatter stability of metal cutting and grinding. *CIRP Ann.-Manuf. Technol.* **53**(2), 619–642 (2004)
3. Čepon, G., Manin, L., Boltežar, M.: Introduction of damping into the flexible multibody belt-drive model: a numerical and experimental investigation. *J. Sound Vib.* **324**(1–2), 283–296 (2009)
4. Diniz, A.E., Marcondes, F.C., Coppini, N.L.: *Tecnologia da usinagem dos materiais*. Artliber Editora (2006)
5. Dresig, H., Holzweiffig, F.: *Dynamics of Machinery: Theory and Applications*. Springer (2010)
6. Ertürk, A., Özgüven, H., Budak, E.: Analytical modeling of spindle-tool dynamics on machine tools using timoshenko beam model and receptance coupling for the prediction of tool point frf. *Int. J. Mach. Tools Manuf.* **46**(15), 1901–1912 (2006)
7. Ghiringhelli, G.L., Masarati, P., Mantegazza, P.: A multibody implementation of finite volume beams. *AIAA J.* **38**(1), 131–138 (2000)
8. Guo, R., Jang, S.H., Choi, Y.H.: Torsional vibration analysis of lathe spindle system with unbalanced workpiece. *J. Central South Univ. Technol.* **18**(1), 171–176 (2011)
9. Hambric, S.A., Shepherd, M.R., Campbell, R.L., Hanford, A.D.: Simulations and measurements of the vibroacoustic effects of replacing rolling element bearings with journal bearings in a simple gearbox. *J. Vib. Acoust.-Trans. ASME* **135**(3) (2013)
10. Kashimura, Y.: Study on prediction of tool flank wear by means of cutting force ratios (1st report). *J. Jpn. Soc. Prec. Eng.* **51**(11), 2115–2121 (1985). (in Japanese)
11. Mannan, M., Fan, W., Stone, B.: The effects of torsional vibration on chatter in grinding. *J. Mater. Process. Technol.* **89**, 303–309 (1999)
12. Masarati, P., Morandini, M., Mantegazza, P.: An efficient formulation for general-purpose multibody/multiphysics analysis. *J. Comput. Nonlinear Dyn.* **9**(4), 041001 (2014)
13. Roukema, J.C., Altintas, Y.: Time domain simulation of torsional-axial vibrations in drilling. *Int. J. Mach. Tools Manuf.* **46**(15), 2073–2085 (2006)
14. Shangquan, W.B., Zeng, X.K.: Modeling and validation of rotational vibration responses for accessory drive systems part i: experiments and belt modeling. *J. Vib. Acoust.* **135**(3), 031002 (2013)
15. Suyama, D., Diniz, A., Pederiva, R.: Tool vibration in internal turning of hardened steel using cBN tool. *Int. J. Adv. Manuf. Technol.* **88**(9–12), 2485–2495 (2017)
16. Tarng, Y., Young, H.T., Lee, B.: An analytical model of chatter vibration in metal cutting. *Int. J. Mach. Tools Manuf.* **34**(2), 183–197 (1994)
17. Xiao, M., Karube, S., Soutome, T., Sato, K.: Analysis of chatter suppression in vibration cutting. *Int. J. Mach. Tools Manuf.* **42**(15), 1677–1685 (2002)



Comparison of Lubricant Force Models for Rattle Analysis on Gear Transmissions

A. Fernandez-del-Rincon^(✉), A. Diez-Ibarbia, M. Iglesias, P. Garcia, A. De-Juan, and F. Viadero

University of Cantabria, 39007 Santander, Spain
fernandra@unican.com

Abstract. In conventional automotive gearboxes, all gears are engaged, but not all of them are involved in transmitting power to the wheels. These unloaded gear pairs are, nevertheless, subjected to light forces due to slight torque and speed variations and also to the interaction between the tooth surfaces and the lubricant. Under certain circumstances, these conditions can lead to repeated impacts among teeth flanks and counter flanks. As a consequence, undesirable vibrations and noises are produced, which are commonly denominated as rattle phenomena, that result in premature fails and damage of other elements coupled to the transmission, as well as in a lack of passengers comfort. Within this framework, in this study, a survey of the available formulations, which simulate the forces behavior in lubricant environment under rattle conditions, has been performed. In a previous work, the authors assessed different formulations for this purpose, observing significant differences among them and also concluding that two effects should be considered in order to properly model rattle conditions. One is linked with the pressure variation due to the fluid entrance in the tooth conjunction, whilst the other is related to the lubricant squeeze when teeth profiles are approaching. Having this in mind, in this paper, the dynamic behavior of gear transmissions under low-torque conditions were assessed with different hydrodynamic formulations, which consider both squeeze and fluid entrance effects. With this purpose, these nonlinear forces derived from each formulation were obtained and compared for a sample transmission, simulating several working conditions of torque, speed and lubricant viscosity. The results are shown by means of the dynamic transmission error as well as the forces present in the conjunction.

Keywords: Rattle · Lubricant · Low-torque conditions and squeeze

1 Introduction

Gear rattle is a phenomenon that occurs in multistage gearboxes, which gear pairs are constantly in mesh. During their operation, there are stages which actually transmit the power from the input to the output shaft, whilst there are others which are engaged but their goal is not to transmit the torque in that specific moment. The former are usually called as active gear pairs and the latter as inactive stages. This rattle phenomenon is located in the inactive gear pair and consists of repeated contacts between their flanks and counter-flanks. These contacts are mainly produced by the engine dynamics effect

on inactive stages and results into a lack of passenger comfort and harmful vibrations to the elements connected to the gearbox [1–3].

In order to understand this phenomenon, this study is focused on the simulation of inactive stage dynamics, thus, the studied gear pair is subjected to low levels of torque. In these operating conditions, the lubricant between teeth does not behave as in the active stages. This is the reason why comprehending the lubricant role is the major challenge to solve this issue.

This work goal is to analyze the role of the lubricant under rattle conditions and, for this reason, a survey of the available formulations, which simulate the forces in the conjunction under these operating conditions, has been performed. Specifically, as the regime of lubrication is hydrodynamic, several approximations can be made in the Reynolds equation, leading to an expression which superposes two fluid effects. The first is produced by the lubricant squeeze when the tooth profiles are approaching and the second is due to the lubricant entrance to the conjunction.

In literature, there are some studies which simulate transmissions under these conditions [2, 4–11], but surprisingly they propose formulations which take into account only one of these effects or consider both effects but with different constraints. From this state of the art, the conclusion was that there is not a unique solution to model the lubricant forces. Nevertheless, in previous authors' works [12], some of these formulations were assessed, leading to establish that both effects were necessary to accurately simulate rattle conditions.

This is the reason why, continuing this previous preliminary study [12], this study assesses a gear pair dynamics under rattle conditions for different fluid viscosities, implementing formulations which consider both squeeze and entraining fluid effects. To do so, the use of an enhanced model previously developed by the authors [13–15], which is characterized by considering simultaneously meshing efforts on both tooth sides, was required, in which six hydrodynamic formulations were implemented.

2 Hydrodynamic Force Formulations

The role played by the lubricant in rattle conditions is of crucial importance in order to accurately simulate the gear pair dynamics. In this framework, the first step to obtain the forces present in the contact between teeth is to determine the lubrication regime. In this regard, Greenwood and Stribeck non-dimensional parameters were calculated [16]. Once was assured that the lubrication regime was hydrodynamic, the lubricant force was defined by calculating the lineal viscous damping following Kelvin-Voigt's model:

$$F_C = C_{eq} \dot{\delta} \quad (1)$$

In this respect, in order to obtain the equivalent viscous damping, the Reynolds equation was solved considering the hydrodynamic regime constraints. These constraints are related to the local deflections of the teeth and the rheological properties of the fluid. Specifically, no local tooth deflections are produced under hydrodynamic

lubrication since low-torque levels are applied as well as the fluid properties, such as density and viscosity, could be approximated to be constant in the conjunction vicinity. Taking these considerations into account, the Reynolds equation can be simplified to:

$$\underbrace{\frac{\rho}{12\eta} \frac{\partial}{\partial x} \left(h^3 \frac{\partial p}{\partial x} \right)}_{\text{Poiseuille}} = \underbrace{\rho V_e \frac{\partial h}{\partial x}}_{\text{Wedge}} + \underbrace{\rho \dot{h}}_{\text{Squeeze}} \tag{2}$$

Where ρ and η are the density and dynamic viscosity of the fluid, h is the fluid film thickness, p the fluid pressure distribution and u_i are the profile velocities in the x direction (tangential to the teeth profile).

Solving this expression 2, the pressure distribution is obtained, which is the previous step to calculate the hydrodynamic force. In order to do this, the film thickness is considered to be the gear profile cross-section, which in turn can be represented by its Taylor series expansion:

$$h = h_C + \frac{x^2}{2\rho_{eq}} \tag{3}$$

As can be observed, only two terms of the Taylor expansion are enough to reproduce the profile curve since the contact only affects a small area (microns order). This equations depends on the central film thickness h_C and the equivalent radius of curvature ρ_{eq} .

Moreover, in order to integrate Reynolds equation, the limits of the affected area have to be defined ($x_1 < x < x_2$):

$$\begin{aligned} p(x) &= 12\eta \int \left[\frac{1}{h^3} \int \left(V_e \frac{\partial h}{\partial x} + \dot{h} \right) \partial x \right] \partial x \rightarrow F_{HDL} = b \int_{x_1}^{x_2} p(x) \partial x \\ &= C_{eq}^{Wedge} V_e - C_{eq}^{Squeeze} \dot{\delta} \end{aligned} \tag{4}$$

In this respect, most of the authors which have dealt with gear rattle phenomena consider different x domains and different approaches to obtain the pressure distribution [2–11]. For the sake of simplicity, a summary of the six formulations implemented in the model is presented in the next section and the reader interested in this matter is referred to [2–12], where each formulation is described.

3 Model Description

Although the gear transmission dynamic model previously developed by the authors is of 19 degrees of freedom (d.o.f.), in this application, an isolated gear pair was assessed, and therefore a 2 d.o.f. model, which is represented in Fig. 1, was used.

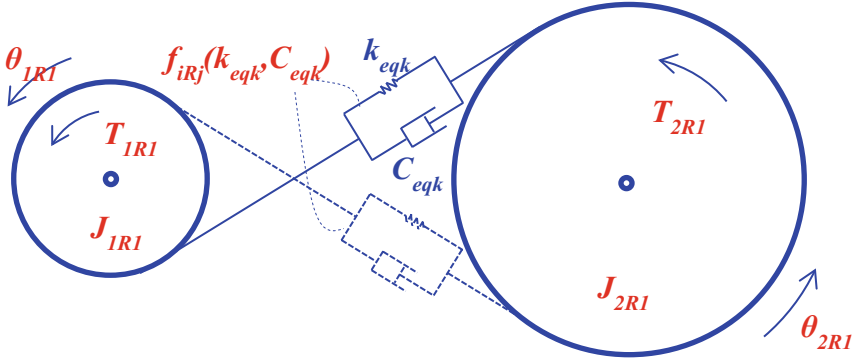


Fig. 1. 2 d.o.f. gear dynamic model scheme.

Its dynamic equations are detailed next:

$$\begin{cases} J_{1R1} \ddot{\theta}_{1R1} + f_{1R1}(\theta_{1R1}, \theta_{2R1}, \dot{\theta}_{1R1}, \dot{\theta}_{2R1}) = T_{1R1}; \\ J_{2R1} \ddot{\theta}_{2R1} + f_{2R1}(\theta_{1R1}, \theta_{2R1}, \dot{\theta}_{1R1}, \dot{\theta}_{2R1}) = T_{2R1}; \end{cases} \quad (5)$$

θ_{iRj} is the rotational degree of freedom linked to J_{iRj} inertia, where i is referred to the shaft number and j to the gear number. In this application, there are 2 shafts with one gear each. Moreover, T_{iRj} represents the external torque and f_{iRj} the torque due to the forces in the conjunctions (F_k), which in turn depends on the equivalent stiffness and viscous damping of the contact K_{eqk} and C_{eqk} , as presented in Eq. 6.

$$F_k = \begin{cases} 0 \\ F_{HDL_k} = C_{eqk}^{Wedge} V_{ek} - C_{eqk}^{Squeeze} \dot{\delta}_k \\ F_{EHL_k} = K_{eqk} \delta_k \end{cases} \begin{cases} h_C = \delta_k & \delta_k > h_{max} \\ h_C = h_{min} & h_{max} > \delta_k > h_{min} \\ & h_{min} > \delta_k > 0 \\ & \delta_k < 0 \end{cases} \quad (6)$$

The force formulation choice is dependent of the distances δ_k (being k the number referred to each contact) between pairs of teeth potentially in contact. If this distance is higher than a fixed value h_{max} , the fluid effect is considered to be negligible. Furthermore, in order to avoid infinite values of viscous damping, a saturation film thickness value equal to ten times the mean profile roughness was adopted ($h_{min} = 10R_a$). It can be observed that there is not a transition from hydrodynamic to elasto-hydrodynamic regime, since only rattle conditions are analyzed. When geometric overlap exists, the force is calculated by a no-linear spring which simulates the meshing stiffness. This stiffness is obtained by the superposition of a finite element model (FEM) of the gears and a hertzian formulation, which provides the local deformations of the teeth in contact. Then, the dynamic equilibrium among inertial, external and meshing forces is reached by an iterative process, checking the existence of new contacts in both flanks. For the sake of brevity, the stiffness calculation methodology is not further presented in this work, referring to the interested reader to [13–15].

Regarding the hydrodynamic forces, the negative value of the squeeze term is due to the fact that the force is positive when the profiles are approaching. Conversely, when the profiles are moving away, this term is null, since the actual effect is not represented by this formula, as shown in Eq. 7:

$$F_{HDL_k} = \begin{cases} C_{eq}^{Wedge} V_{ek} - C_{eq}^{Squeeze} \dot{\delta}_k & \dot{\delta}_k < 0 \\ C_{eq}^{Wedge} V_{ek} & \dot{\delta}_k > 0 \end{cases} \quad (7)$$

The equivalent viscous damping C_{eq}^{Wedge} and $C_{eq}^{Squeeze}$ of the six formulations implemented are listed in Table 1.

Table 1. Equivalent viscous damping expressions of the implemented hydrodynamic forces.

Formulation	C_{eq}^{Wedge}	$C_{eq}^{Squeeze}$
Rahnejat	$2b\eta \frac{\rho_{eq}}{h_c}$	$\frac{3\sqrt{2}\pi b\eta}{2} \left(\frac{\rho_{eq}}{h_c}\right)^{3/2}$
Rahnejat/Martins	$\sqrt{6}b\eta \frac{\rho_{eq}}{h_c}$	$\frac{3\sqrt{2}\pi b\eta}{2} \left(\frac{\rho_{eq}}{h_c}\right)^{3/2}$
Sasaki	$2b\eta \frac{\rho_{eq}}{h_c}$	$\frac{3\sqrt{2}\pi b\eta}{2} \left(\frac{\rho_{eq}}{h_c}\right)^{3/2} \left[1 - \frac{2}{\pi} \arctan\left(\frac{3\sqrt{2}}{2} \sqrt{\frac{\rho_{eq}}{h_c}} \frac{h}{V_e}\right)\right]$
Sasaki/Martins	$\sqrt{6}b\eta \frac{\rho_{eq}}{h_c}$	$\frac{3\sqrt{2}\pi b\eta}{2} \left(\frac{\rho_{eq}}{h_c}\right)^{3/2} \left[1 - \frac{2}{\pi} \arctan\left(\frac{3\sqrt{2}}{2} \sqrt{\frac{\rho_{eq}}{h_c}} \frac{h}{V_e}\right)\right]$
Wiegert _{0.02}	$\sqrt{6}b\eta \frac{\rho_{eq}}{h_c}$	$\frac{3\sqrt{2}\pi b\eta}{2} \left(\frac{\rho_{eq}}{h_c}\right)^{3/2} \left[1 - \frac{2}{\pi} \arctan\left(\sqrt{3} \sqrt{\frac{\rho_{eq}}{h_c}} \frac{h}{V_e}\right)\right]$
Wiegert _{0.2}	$\sqrt{6}b\eta \frac{\rho_{eq}}{h_c}$	$\frac{3\sqrt{2}\pi b\eta}{2} \left(\frac{\rho_{eq}}{h_c}\right)^{3/2} \left[1 - \frac{\sqrt{3}\pi h}{2V_e \sqrt{\frac{h_c}{\rho_{eq}} + \sqrt{3}\pi h }}\right]$

4 Case of Study

The parameters of the assessed gear transmission are presented in Table 2.

Table 2. Gear transmission parameters.

Parameter	Value	Parameter	Value
Pinion teeth	18	Rack addendum	1.25 m
Wheel teeth	36	Rack dedendum	1 m
Pinion Inertia [Kgm ²]	1.7519 e-04	Rack tip radius	0.25 m
Inercia Rueda [Kgm ²]	0.0028	Face width [mm]	26.7
Module [mm]	3	Oil viscosity [Pas]	0.08/0.008
Young Modulus [GPa]	210	Center distance [mm]	81.1
Poisson Coef.	0.3	h _{min} [mm]	8 e-3
Pressure angle [degree]	20	h _{max} [mm]	1
Half-width contact (a) [mm]	1	Mean roughness (R _a) [mm]	8 e-4

The tests performed to this gear transmission consist of introducing speed perturbations to two specific mean pinion velocities (Ω), as well as applying a viscous resistive torque to the driven wheel which simulates a journal bearing behavior, since the automotive gears are generally supported by them, and therefore, they are the typical resistance which gears under rattle conditions have to overcome.

$$\dot{\theta}_{1R1} = \Omega + \vartheta \sin \Delta\omega t \quad \text{and} \quad T_{2R1} = \frac{\pi \eta_b l_b r_b^3}{2C} \dot{\theta}_{2R1} \quad (8)$$

Where Ω is the mean velocity which takes values of 500 and 1000 rpm, ϑ and $\Delta\omega$ are the amplitude and frequency of the speed perturbation, which values are shown in Table 3.

Table 3. Perturbation parameters.

$\Delta\omega$ [Hz]	ϑ [rad/s]
4	10.472
8	5.236
16	2.618

These values of perturbation amplitude were chosen in order to obtain the same displacement in the three tests. Moreover, the external torque T_{2R1} is defined by the lubricant, length, radius and clearance of the journal bearing (η_b , l_b , r_b and C), which values are listed in Table 4.

Table 4. Bearing parameters.

Parameter	Value	Parameter	Value
Bearing radius (r_b) [mm]	10	Bearing length (l_b) [mm]	15
Radial clearance (C) [mm]	0.025	Bearing viscosity (η_b) [Pas]	0.08/0.008

5 Results

As the pinion velocity is predefined in the tests performed, there is only one d.o.f., which is represented by the Dynamic Transmission Error (DTE). In Fig. 2, the DTE is shown when the pinion mean velocity is 500 rpm for the three considered perturbations. Furthermore, each column correspond to a different value of lubricant dynamic viscosity, 0.08 Pas on the left graphics and 0.008 Pas on the right. The horizontal black lines represent the backlash, therefore when the DTE is outside this range, physical interference between profiles occurred. The pitch point is considered as the reference of angular position, being this the reason why the backlash lower value is zero.

On the left side, it can be observed that the six implemented formulations follow a similar trend, observing that Martin’s consideration in the fluid entraining effect makes

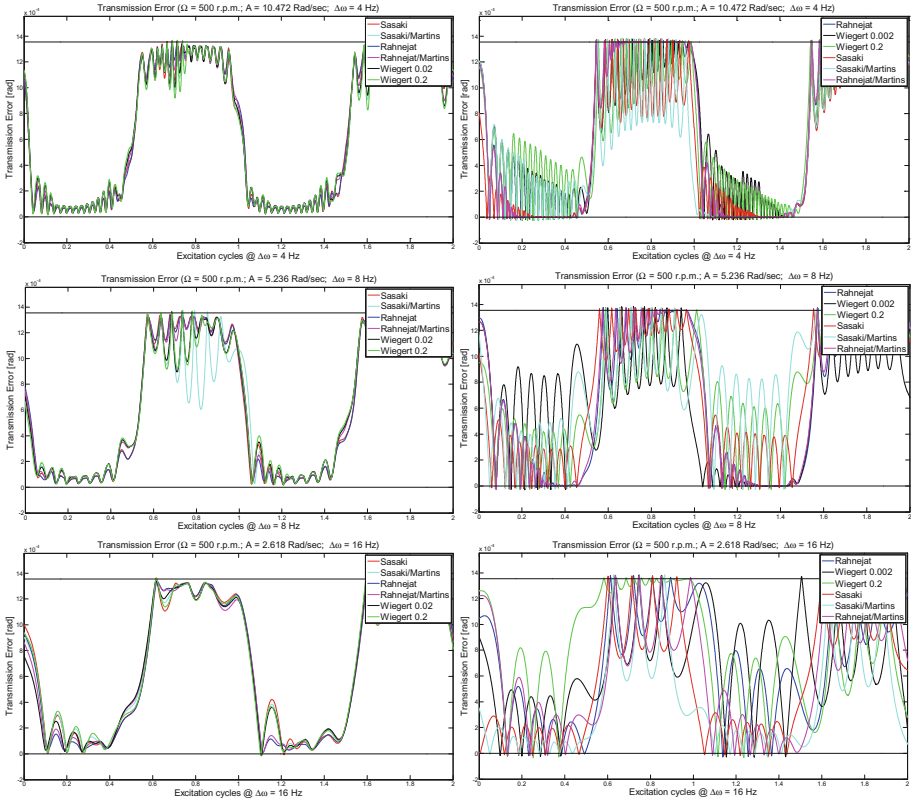


Fig. 2. DTE when six hydrodynamic force formulations were implemented ($\Omega = 500$ rpm). On the left column, the dynamic viscosity was 0.08 Pas whilst on the right one, it was 0.008 Pas.

the difference between Rahnejat’s and Sasaki’s formulations and the other four. Specifically, in these four formulations, some impacts occurred, provoking some dispersion among results.

Nevertheless, on the right side, the opposite occurs with low viscosities, observing that squeeze effect is more important in this case, and therefore, some discrepancies among formulations are perceived.

In Fig. 3, the results are presented when the pinion mean velocity is 1000 rpm, following the same structure as in the previous figure.

Regarding the results, similar conclusions as in 500-rpm case were perceived. The Martin’s consideration makes the difference in high-viscosity case, although no impacts existed with this mean velocity, whilst in low-viscosity case, as impacts occurred, squeeze effect outweighs the entraining velocity one.

Thus, in both pinion-speed cases, the fluid entraining effect is dominant for higher values of dynamic viscosity because it tends to separate teeth and locate them in the half of the backlash. However, as viscosity decreases, this effect is palliated, and therefore, fluctuations and impacts are provoked, being the squeeze effect predominant in this scenario.

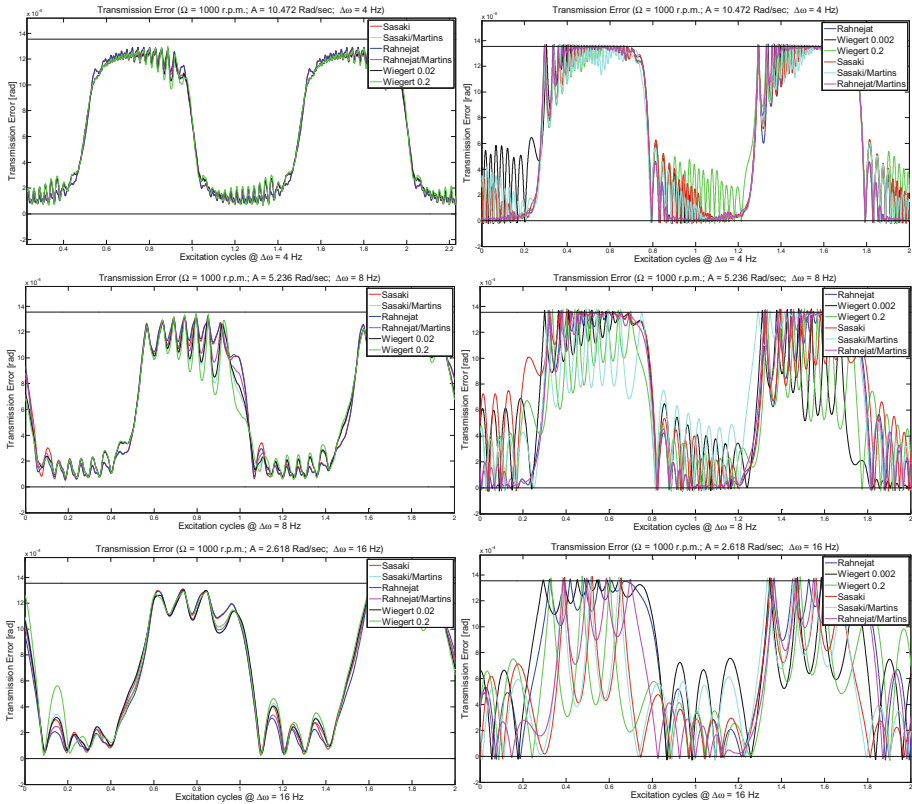


Fig. 3. DTE for the six hydrodynamic force formulations ($\Omega = 1000$ rpm). The dynamic viscosity was 0.08 Pas on the left column, whilst on the right, it was 0.008 Pas.

6 Conclusions

A gear rattle assessment was performed in this study, where six hydrodynamic force formulations were implemented to the gear transmission model previously developed by the authors.

The six implemented formulations follow a similar trend, observing that Martin’s consideration in the fluid entraining effect makes the difference between Rahnejat’s and Sasaki’s formulations and the other four. This is specially discerned in the high value of dynamic viscosity case, in which the entraining effect outweighs the fluid squeeze. Nevertheless, the opposite occurs with low viscosities, observing that squeeze effect is more important in this case, and therefore, some discrepancies among formulations are perceived. This is produced because the entraining effect tends to separate teeth and locate them in the half of the backlash, occurring when the viscosity is significant. Thus, the viscosity parameter clearly influences the role of the effects present in the conjunction, specifically, with the increment of the viscosity, the entraining velocity effect becomes more important than the squeeze one, being the contrary case when the viscosity decreases.

Acknowledgments. This work has been supported by project DPI2017-85390-P funded by the Spanish Ministry of Science and Technology, EUIN2017-88667 funded by the Spanish Ministry of Economy, Industry and Competitiveness and PRX14/00451 project funded by the Spanish Ministry of Education, Culture and Sports.

References

1. Ankouni, M., Lubrecht, A.A., Velex, P.: Modelling of damping in lubricated line contacts – applications to spur gear dynamic simulations. *Proc. Inst. Mech. Eng. Part C: J. Mech. Eng. Sci.* **230**(7–8), 1222–1232 (2015)
2. Brancati, R., Rocca, E., Russo, R.: An analysis of the automotive driveline dynamic behaviour focusing on the influence of the oil squeeze effect on the idle rattle phenomenon. *J. Sound Vib.* **303**(3–5), 858–872 (2007)
3. De la Cruz, M., Theodossiades, S., Rahnejat, H., Kelly, P.: Analysis of non-linear impact dynamics in automotive transmissions: gear rattle. In: *Proceedings of the 7th International Conference on Engineering Computational Technology* (2010)
4. Gill-Jeong, C.: Analysis of the nonlinear behavior of gear pairs considering hydrodynamic lubrication and sliding friction. *J. Mech. Sci. Technol.* **23**(8), 2125–2137 (2009)
5. Guilbault, R., Lalonde, S., Thomas, M.: Nonlinear damping calculation in cylindrical gear dynamic modeling. *J. Sound Vib.* **331**(9), 2110–2128 (2012)
6. Liu, F.H., Theodossiades, S., Bergman, L.A., Vakakis, A.F., McFarland, D.M.: Analytical characterization of damping in gear teeth dynamics under hydrodynamic conditions. *Mech. Mach. Theory* **94**, 141–147 (2015)
7. Russo, R., Brancati, R., Rocca, E.: Experimental investigations about the influence of oil lubricant between teeth on the gear rattle phenomenon. *J. Sound Vib.* **321**(3–5), 647–661 (2009)
8. Rahnejat, H., Gohar, R.: The vibrations of radial ball bearings. *Proc. Inst. Mech. Eng. Part C: J. Mech. Eng. Sci.* **199**(3), 181–193 (1985)
9. Wiegert, B., Hetzler, H., Seemann, W.: A comparison between elastohydrodynamic and dry hertzian line contacts with regard to their nonlinear vibration behaviour. *Proc. Appl. Math. Mech.* **11**, 335–336 (2011)
10. Wiegert, B., Hetzler, H., Seemann, W.: An analytical expression of the normal force of hydrodynamic line contacts under transient conditions. *Tribol. Int.* **61**, 32–39 (2013)
11. Ottewill, J.R., Neild, S.A., Wilson, R.E.: An investigation into the effect of tooth profile errors on gear rattle. *J. Sound Vib.* **329**(17), 3495–3506 (2010)
12. Fernandez-Del-Rincon, A., Diez-Ibarbia, A., Theodossiades, S.: Gear transmission rattle: assessment of meshing forces under hydrodynamic lubrication. *Appl. Acoust.* (2017). In press
13. Diez-Ibarbia, A., del Rincon, A.F., Iglesias, M., de Juan, A., Garcia, P., Viadero, F.: Efficiency analysis of spur gears with a shifting profile. *Meccanica* **51**(3), 707–723 (2016)
14. Fernández-del Rincón, A., Iglesias, M., de Juan, A., Diez-Ibarbia, A., García, P., Viadero, F.: Gear transmission dynamics: effects of index and run out errors. *Appl. Acoust.* **108**, 63–83 (2016)
15. Fernández Del Rincón, A., Viadero, F., Iglesias, M., García, P., De-Juan, A., Sancibrian, R.: A model for the study of meshing stiffness in spur gear transmissions. *Mech. Mach. Theory* **61**, 30–58 (2013)
16. Evans, C.R.: *Measurement and Mapping of the Rheological Properties of Elastohydrodynamic Lubricants*. University of Cambridge, Cambridge (1983)



Hysteretic (Non-reversible) Bit-Rock Interaction Model for Torsional Vibration Analysis of a Drillstring

F. F. Real¹(✉), A. Batou², T. G. Ritto³, C. Desceliers⁴, and R. R. Aguiar⁵

¹ National Institute of Metrology, Quality and Technology-INMETRO,
Rua Santa Alexandrina, 416, Rio de Janeiro, RJ 20261-232, Brazil
ffreal@inmetro.gov.br

² Department of Mechanical, Materials and Aerospace Engineering,
School of Engineering, University of Liverpool, Liverpool L69 7ZF, UK
anas.batou@liverpool.ac.uk

³ Department of Mechanical Engineering, Federal University of Rio de Janeiro,
Ilha do Fundão, Rio de Janeiro, RJ 21945-970, Brazil
tritto@mecanica.ufrj.br

⁴ Université Paris-Est, Laboratoire Modélisation et Simulation Multi Echelle,
MSME, UMR 8208 CNRS, 5 bd Descartes, 77454 Marne-la-Vallée, France
christophe.desceliers@univ-paris-est.fr

⁵ Brazil Research and Geoenengineering Center,
Schlumberger Oilfield Services, Rio de Janeiro, Brazil
raguiar@slb.com

Abstract. This paper aims at constructing a novel hysteretic (non-reversible) bit-rock interaction model for the torsional dynamics of a drillstring. Non-reversible means that the torque on bit is not represented only in terms of the bit speed, but also of the bit acceleration, producing a hysteretic behavior. Here, the drillstring is considered as a continuous system which is discretized by means of the finite element method, where a reduced-order model is applied using the normal modes of the associated conservative system. The nonlinear torsional vibrations of the drillstring system are analyzed comparing the proposed bit-rock interaction model to a commonly used reversible model (without hysteresis). The parameters of the proposed hysteretic bit-rock interaction and of the commonly used reversible model are fitted to field data. Results show the system including a bit-rock interaction model with hysteresis effects reproduces a good approach of stick-slip cycle, and the simulated drill-string dynamics using the bit-rock interaction presents a similar behavior comparing to the field data.

Keywords: Drill string nonlinear dynamics
Bit/rock interaction model · Torsional vibrations
Stick-slip oscillations · Stability map · Hysteresis

1 Introduction

Drillstring is a slender structure used for exploitation of oil reserves. It is composed mainly of two parts: drillpipes and bottomhole-assembly. A top drive rotates the system at the top, which transmits the torque to the bit that drills the rock. One of the concerns with the drillstring dynamics is its torsional vibrations that might lead to stick-slip oscillations [5, 8–10, 28]. In this severe conditions, the bit sticks (zero speed) then slips (high speed), and that might cause, for instance, measurement equipment failure, low rate of penetration, bit damage, and fatigue [31].

Spanos et al. [27] has published an overview of drilling vibrations. Specially for bit-rock interaction during the drilling process, [18, 24] have shown that the torque on bit varies nonlinearly with the bit speed, presenting large fluctuations. Concerning drillstring torsional dynamics and stick-slip oscillations, several papers discuss about them [8, 9, 15, 16, 23, 24, 29], and normally a pure torsional model is enough to represent this kind of system: to represent test rigs, [15] applied a torsional model successfully to analyze the friction-induced limit cycling, and in [9] a torsional model is used to implement a control strategy. Field data of a five kilometer drill string is analyzed in [24], where again a pure torsional model presented satisfactory results reproducing field data, where torsional vibration was the dominant phenomenon observed. More generally, a coupled axial-lateral-torsional model should be applied [23, 28].

There are many phenomena involved during the drilling process: fluid-rock interaction, proper well profile (inclination and azimuth), pipe-rock interaction, among others. Therefore, a full description model of bit-rock interaction including all dynamics is really hard to obtain due to lack of downhole data. Experimentally, hysteretic cycles for the bit-rock interaction were observed in [11, 18–20], which can be caused by tangential stiffness during the bit-rock interaction, and by the frictional memory due a delay in the friction force, being evident during the stick phase and the switch between stick and slip phases [30]. Although of these observations, up to the authors knowledge the only hysteretic bit-rock interaction model found in the literature was proposed in [5]. The authors in [5] used the experimental results presented in [11], and applied their hysteretic model, which employs a switching mechanism, in the analysis of Proportional-Integral (PI) control strategy, aiming at mitigating stick-slip oscillations.

This paper aims at constructing a novel hysteretic (non-reversible) bit-rock interaction model for the torsional dynamics of a drillstring [19] based on the field data presented in [24]. Non-reversible means that the torque on bit is not represented only in terms of the bit speed, but also of the bit acceleration, producing a hysteretic behavior. The drillstring is considered as a continuous system which is discretized by means of the finite element method [6, 7, 25], where a reduced-order model is applied using the normal modes of the associated conservative system. The nonlinear torsional vibrations of the drillstring system are analyzed comparing the proposed bit-rock interaction model to a commonly used reversible model (without hysteresis). Least-Square method is used for param-

ter identification is applied to obtain the parameters of the models according to field data [24].

The main contribution of this paper is to propose an original model for the bit-rock interaction taking into account the hysteretic effects. Here, (1) a new nonlinear hysteretic model is constructed to describe the bit-rock interaction (nonlinear torque function) as a function of the bit speed and bit acceleration, (2) experimental identification using Least-Square method is applied to obtain the parameters of the mean nonlinear part, and (3) a hysteretic function is proposed for the envelope of this process, which is also a function of the acceleration and bit speed.

This article is organized as follows. The drillstring torsional dynamical model is presented in Sect. 2.1. The continuous system is discretized by means of the finite element method and a reduced-order model is constructed using the normal modes of the associated conservative system. In Sect. 2.1, the proposed bit-rock interaction model including hysteresis is also presented, as well as the reversible model (without hysteresis). This proposed model is compared with field data in Sect. 5. The numerical analysis is presented in Sect. 6 and, finally, the concluding remarks are made in Sect. 8.

2 Dynamical Model

2.1 Torsional Model

As mentioned before, the drillstring is basically composed by (1) the drillpipes (DP) and (2) the bottomhole-assembly (BHA), as it is schematically represented in Fig. 1. DP are slender tubes that can reach kilometers, while BHA is composed by thicker tubes (drill collars) together with the measurement equipment and a drill bit on its bottom, and its length can reach hundreds of meters.

A vertical wellbore is considered, and only torsional vibrations are taken into account in the modeling. That is, it is assumed that there are no contact between the column and the wellbore, as well as the lateral and axial vibrations are small. A constant speed Ω is imposed at the top and a reaction torque appears due to the bit-rock interaction. Therefore, $\theta(x, t)$ is the solution of the following boundary value problem:

$$\rho I_p \frac{\partial^2 \theta(x, t)}{\partial t^2} - G I_p \frac{\partial^2 \theta(x, t)}{\partial x^2} = \mathbf{T}(x, t), \tag{1}$$

in which the boundary conditions are

$$\begin{cases} \theta(0, t) = \Omega t \\ \dot{\theta}(0, t) = \Omega \end{cases}, \tag{2}$$

and the initial conditions are

$$\theta(x, 0) = 0, \quad \dot{\theta}(x, 0) = \Omega, \tag{3}$$

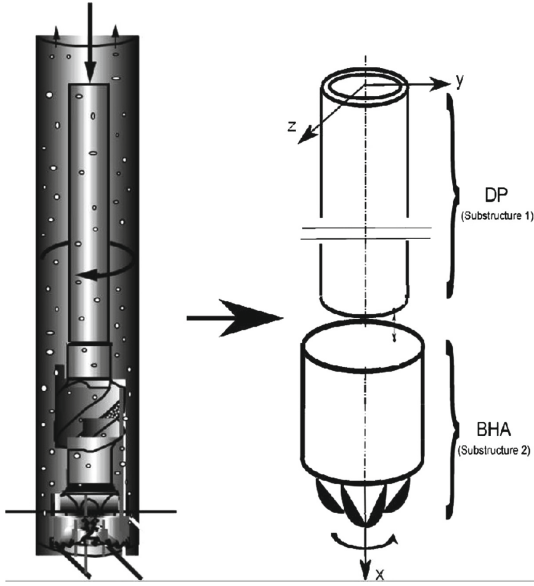


Fig. 1. General scheme of a drillstring.

where $\theta(x, t)$ is the angular rotation about the x -axis, $\mathbf{T}(x, t)$ is the torque vector, I_p is the cross sectional polar moment of inertia, and ρ and G are the density and shear modulus of the material of the column.

Different from [21, 22], the present paper will solve the system considering its rotational displacements about a rotating frame. Let $\theta^{rel}(x, t)$ be the relative torsional degree of freedom in the rotating frame associated to the top sectional area (at $x = 0$). We introduce the absolute rotational displacement as

$$\theta(x, t) = \Omega t + \theta^{rel}(x, t). \tag{4}$$

Let $\mathbf{u}(t)$ be the vector of $\theta^{rel}(x, t)$ nodal values of a mesh of the drillstring. A computational model is constructed by the finite element method considering the drillstring top clamped (there is not relative displacement between the top drive and the first element on the top of the drillstring). Adding a proportional damping to the system, the vector $\mathbf{u}(t)$ is solution of the non-linear differential equation

$$[M]\ddot{\mathbf{u}}(t) + [D]\dot{\mathbf{u}}(t) + [K]\mathbf{u}(t) = \mathbf{T}(\dot{\mathbf{u}}(t)), \tag{5}$$

with the initial conditions

$$\mathbf{u}(0) = \mathbf{0}, \quad \dot{\mathbf{u}}(0) = \mathbf{0}. \tag{6}$$

where $[M]$ is the mass matrix, $[D]$ is the damping matrix, $[K]$ is the stiffness matrix, and $\mathbf{T}(\dot{\mathbf{u}}(t))$ is the generalized torque vector. All the components of generalized torque vector are zero except the one corresponding to the drill bit.

The nonlinear torque applied to the bit (corresponding to the drillstring’s length equal to L) is denoted by $\bar{T}_{bit}(\dot{\theta}_{bit}(t))$ and will be described further in this text.

The normal modes of the conservative homogeneous system are used to construct a reduced-order model. The m first eigenvalues $0 < \lambda_1 \leq \lambda_2 \leq \dots \leq \lambda_m$ associated with elastic modes $\{\phi_1, \varphi_2, \dots, \varphi_m\}$ are solutions of the generalized eigenvalue problem

$$[K] \varphi = \lambda [M] \varphi. \tag{7}$$

The reduced-order model is obtained by projecting the full computational model on the subspace spanned by the m first elastic modes calculated using Eq. (7). Let $[\Phi]$ be $n \times m$ matrix whose columns are the m first elastic modes. We can then introduce the following approximation

$$\mathbf{u}(t) = [\Phi] \mathbf{q}, \tag{8}$$

in which \mathbf{q} is the vector of the m generalized coordinates which are solution of the reduced matrix equation

$$[\widetilde{M}]\ddot{\mathbf{q}}(t) + [\widetilde{D}]\dot{\mathbf{q}}(t) + [\widetilde{K}]\mathbf{q}(t) = \widetilde{\mathbf{T}}(\dot{\mathbf{q}}(t)), \tag{9}$$

with the initial conditions

$$\mathbf{q}(0) = \mathbf{0}, \quad \dot{\mathbf{q}}(0) = 0. \tag{10}$$

In these equations, $[\widetilde{M}] = [\Phi]^T [M] [\Phi]$, $[\widetilde{D}] = [\Phi]^T [D] [\Phi]$ and $[\widetilde{K}] = [\Phi]^T [K] [\Phi]$ are $m \times m$ mass, damping and stiffness reduced-order matrices, and where $\mathbf{T}(\dot{\mathbf{q}}(t)) = [\Phi]^T \mathbf{f}([\Phi]\dot{\mathbf{q}}(t))$ is the vector of the reduced-order generalized torque. The set of Eqs. (8), (9) and (10) can be solved using commonly used integration schemes, such as the Euler scheme or the Runge-Kutta, for instance.

3 Deterministic Model - A Reversible Model

Now, let us introduce the deterministic bit-rock interaction model. This model introduced by Eq. 11 represents an average approximation of stick-slip behavior, that means a reversible model. The following nominal bit-rock interaction model is presented in [8, 25, 28] which combines Coulomb friction (hyperbolic tangent behavior), Stribeck friction (negatively sloped behavior), and viscous friction (directly proportional to the bit speed):

$$\bar{T}_{bit}(\dot{\theta}_{bit}(t)) = \alpha_0 \left[\tanh(\alpha_1 \dot{\theta}_{bit}(t)) + \frac{\alpha_2 \dot{\theta}_{bit}(t)}{1 + \alpha_3 \dot{\theta}_{bit}^2(t)} \right], \tag{11}$$

where α_0 , α_1 , α_2 , and α_3 , are calibration parameters of this model with appropriate units. All these parameters must be identified experimentally, and α_0 is a remarkable parameter because of its dependence of weight on bit and friction coefficient.

4 Hysteretic Model

Stick-slip is a self-excited drilling torsional oscillation due the friction between the bit and the rock, because of the cumulative of energy throughout the drill-string (top drive does not stop during the stick phase). This energy induces the slip phase behavior, which is released promoting the acceleration of bit above the top drive acceleration. This oscillation reaches a maximum value of the bit speed during this cycle, decelerating after that.

Therefore, these stick-slip oscillations can present a hysteretic behavior, which is formed by two motion phenomenons: one of microscopic magnitude (being evident during the stick phase), and another one of macroscopic magnitude (being evident during the switch between stick and slip phases). This microscopic motion phenomenon is caused by tangential stiffness during the interaction between the bodies [1, 3, 12–14]. The macroscopic motion phenomenon is related to the frictional memory due a delay in the friction force, where the size of the loops increase according to the angular velocity variations become faster [4, 17], that means according to the acceleration.

Let $\dot{\theta}_{bit}(t)$ be the absolute angular speed at the bit. As a first attempt, we propose the following model for bit-rock interaction considering hysteretic effects:

$$T_{bit}(\dot{\theta}_{bit}(t), t) = \left[\bar{T}_{bit}(\dot{\theta}_{bit}(t)) \right] (H\eta(\dot{\theta}_{bit}(t), \ddot{\theta}_{bit}(t))), \quad (12)$$

in which

- (1) $\bar{T}_{bit}(\dot{\theta}_{bit}(t))$ is the deterministic bit-rock interaction model considering hysteretic effects;
- (2) $H\eta(\dot{\theta}_{bit}(t), \ddot{\theta}_{bit}(t))$ is the hysteresis function;
- (3) $\ddot{\theta}_{bit}(t)$ is the instantaneous bit acceleration in hysteresis function. The hysteretic effect can be described by a simple function ($H\eta(\dot{\theta}_{bit}(t), \ddot{\theta}_{bit}(t))$) that depends on the instantaneous bit acceleration $\ddot{\theta}_{bit}(t)$ (see 13), as follows [19],

$$H\eta(\dot{\theta}_{bit}(t), \ddot{\theta}_{bit}(t)) = 1 + \text{sign}(\dot{\theta}_{bit}(t))\gamma_1 \tanh(\gamma_2\ddot{\theta}_{bit}(t)) \quad (13)$$

where γ_1 and γ_2 are calibration parameters related to the hysteresis effects with appropriate units.

This simple function is dependent of the instantaneous bit acceleration $\ddot{\theta}_{bit}(t)$, which can be obtained by the differential of $\dot{\theta}_{bit}(t)$ related to time. It is noticed that the hysteresis function has a hyperbolic tangent term instead of $\text{sign}\dot{\theta}_{bit}(t)$, because of function's smoothness, and due its simplicity can be applied in another deterministic models of bit-rock interaction [19].

5 Bit-Rock Interaction: Proposed Model vs. Field Data

Field data (downhole information) presented in [24] are considered in this paper, which were acquired using a downhole mechanics measurement unit capable of

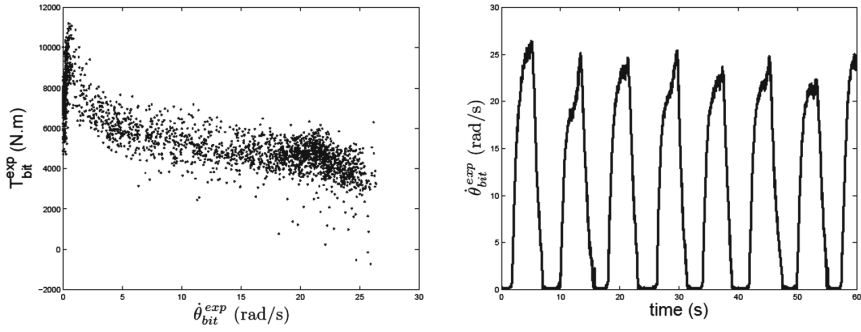


Fig. 2. Experimental torque on bit versus bit speed filtered prior to recording at 50 Hz, and bit speed related to time of sampling, both were reproduced from [24] graphs.

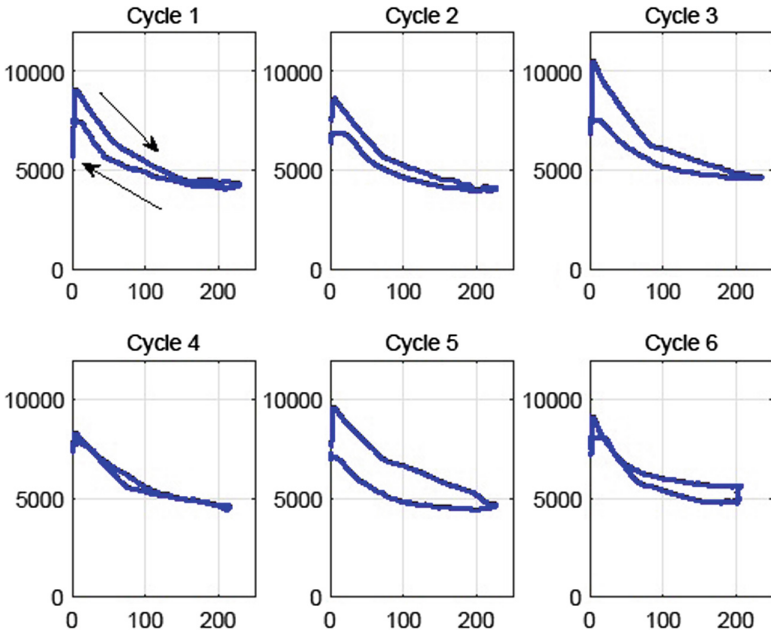


Fig. 3. Experimental torque on bit, bit speed, torque on bit versus bit speed and bit acceleration in 6 stick-slip cycles over a regular grid (395 records), and its sliding-window average, using a length equal to 0.01 rad/s (395 records).

providing both real-time measurement through mud telemetry and continuously recorded high-frequency data throughout the run. This unit was installed at the BHA above the bit with a suite of 19 sensors, which are able to sample triaxial accelerations, gyro rpm, magnetometer rpm, axial loading, torque, bending moment [26] at 10,000 Hz. These data are filtered prior to recording at 50 Hz.

Figure 2 shows the field data measurements reproduced from [24], where the imposed angular rotation at the top is $\Omega = 12.57 \text{ rad/s}$ (120 RPM). Figure 2 shows how the torque increases when the bit sticks, and the bit speed alternates stick phases (almost zero speed) and slip phases (high speeds).

Field data showed here correspond to one sample, and statistic characteristics depend on the number of samples for being representative. To circumvent this limitation, let us avail each stick-slip cycle. If we consider that each slip phase depends exclusively on the previous stick phase, all the stick-slip cycles are independents. In that case, each stick-slip cycle can be considered one sample, being possible to construct statistic characteristics. Figure 3 separates the stick-slip cycles over a regular grid of 395 records in each stick-slip cycle within the range $[0, 7.9] \text{ s}$, despising the first and the last stick-slip cycle showed in Fig. 2.

Field data presented in this section show large fluctuations of the torque on bit. To have a closer look at these fluctuations and the hysteresis behavior, Fig. 3 shows the experimental measurements for one stick-slip cycle ($T_{bit}^{exp}(t)$) for each cycle, and for bit acceleration. Despite of the independence of stick-slip cycles, it can be seen that the torque fluctuations are not uncorrelated, i.e., it confirms that there is a correlation structure of the random process. The averages $T_{bit}^{SWAexp}(t)$ and $\ddot{\theta}_{bit}^{SWAexp}(t)$ are obtained by sliding-window method (SWA) [2], using a length equal to 0.01 rad/s .

6 Numerical Results

Figure 4 shows the revisited experimental records (only 6 stick-slip cycles) of the bit-rock interaction with respect to the bit speed ($T_{bit}^{exp,rev}$), together with its revisited sliding-window average over the time domain [2], and the hysteretic fitted model ($T_{bit}^{Exp\ data\ applied\ to\ Identified\ model}$). These parameters are fitted using the least square method. This interaction model is supported by measurements [18, 24]. The identified parameters for hysteresis function are given by $\gamma_1 = 1.95$, and $\gamma_2 = 3.00 \times 10^{-3}$, which are the average from identified values of the torque on bit fluctuations in each cycle. The identified values for $\alpha_{i,i=0,\dots,3}$ calibration parameters are $\alpha_0 = 4,705.80$, $\alpha_1 = 8,105.70$, $\alpha_2 = 4.02$, and $\alpha_3 = 4.00$. The averages (blue lines) are obtained by sliding-window method using a width equal to 0.01 rad/s .

Figure 5 shows the hysteretic behavior from the model over a regular grid, in order to check the mirrored offset of the curve, respecting the three models of friction considered in this work (Coulomb friction, Stribeck friction, and viscous friction models).

Figure 6 shows a reasonable agreement between the model and average experimental bit-rock interaction. Nevertheless, it can be seen that the experimental data show large fluctuations and a stochastic model for the bit-rock interaction could be used to improve the model predictions of the drillstring dynamics.

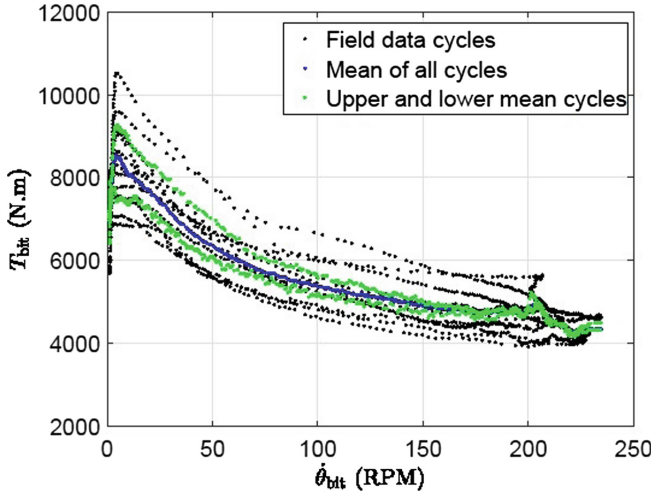


Fig. 4. Experimental bit-rock interaction and identified average model.

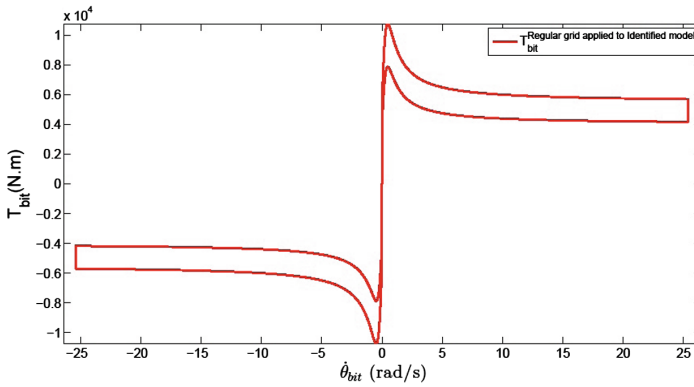


Fig. 5. Hysteretic behaviour of the bit-rock interaction from the model over a regular grid.

7 Simulation of the Torsional Dynamics

The drillstring dynamics is simulated in the condition of the experimental data. Table 1 contains the parameters of the drillstring used for the simulation.

The mass and stiffness matrices are constructed using 100 finite elements (linear shape functions). The generalized damping matrix is diagonal with damping ratios equal to 0.005 for the first mode, 0.03 for the second and third modes, and 0.005 for all the other modes. The non-linear Eq. (9) is solved using a modified Euler scheme with a time step 0.512 ms.

As it is a first attempt to construct a stochastic model for the bit-rock interaction fitting field data, one realization of the computational model is compared

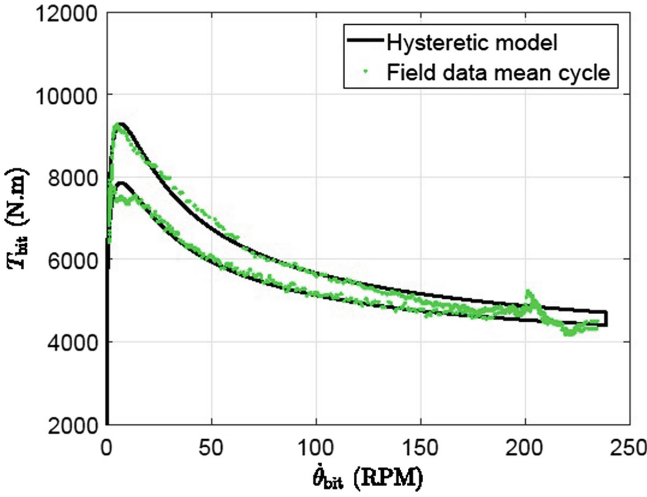


Fig. 6. Comparison between field data mean cycle and hysteresis model over a regular grid.

Table 1. Drillstring characteristics.

	DP	BHA
Elastic modulus [GPa]	220	220
Poisson’s coefficient	0.29	0.29
Volumetric mass density [kg/m ³]	7,800	7,800
Length [m]	4,733.60	466.45
Inner radius [m]	0.0595	0.0363
Outer radius [m]	0.070	0.0803

with the experimental results. The idea is to verify if the numerical results can approximate the dynamic behavior observed in the field data.

Figure 7 compares the bit speed obtained by the computational model to with the field data. It is observed that the dynamic behavior is similar. Both dynamics present stick-slip oscillations and have a similar aspect, although the amplitude of the response of the computational model is a little higher than the field data for some cycles (almost 20% higher).

Finally, Fig. 8 shows a very good agreement between the bit-rock interaction model proposed herein and the field data. The simulated levels of fluctuation are in good agreement with experiments, albeit the numerical results shows torque values for higher bit speeds. And the cycle’s trajectory has presented the same correlation tendencies as the experimental ones. The nominal bit-rock interaction model considered is a regularized Coulomb friction model with decreasing torque approaching the dynamic friction torque as the bit speed increases. Therefore,

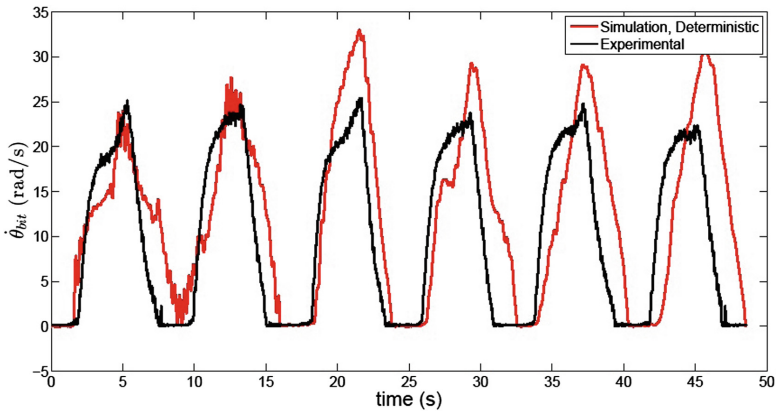


Fig. 7. Comparison between simulated and field data bit speed, where field data were reproduced from [24].

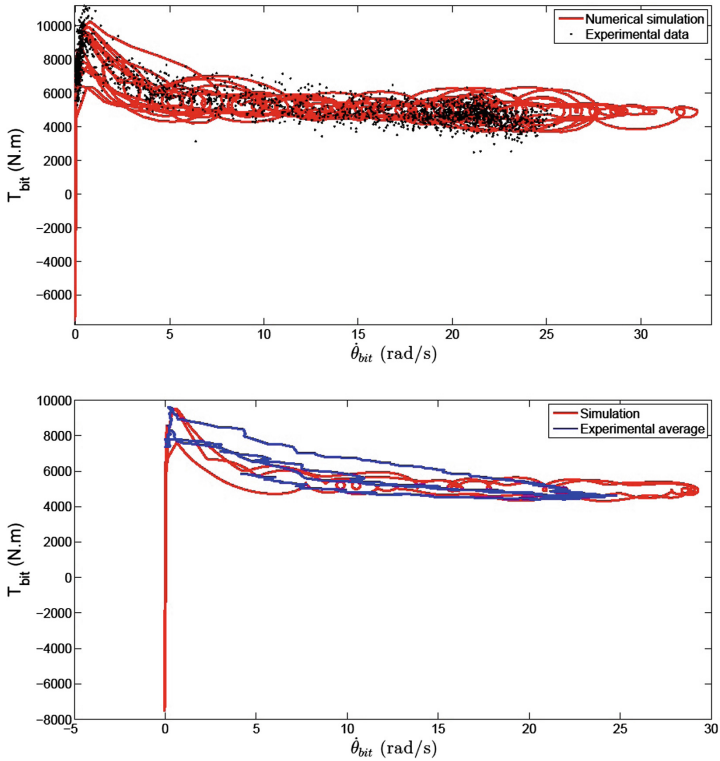


Fig. 8. Simulated bit-rock interaction and just one cycle within the range [20, 30] s.

the torque goes to zero when the bit speed approaches zero. Physically, when the bit sticks, the torque might assume any value from zero to its static friction limit. Hence, the difference in the results might be due to the deterministic model chose for the torque on bit.

8 Concluding Remarks

In this paper, a new modeling for the bit-rock interaction has been proposed considering hysteresis effects of friction. The proposed model depends on 6 parameters that can be fitted or used for a sensitivity analysis.

The torsional dynamics of the system is analyzed, which is represented as a torsion bar discretized by means of the finite element method. A reduced-order model was constructed to speed up the computations. On the bottom of this system, the proposed bit-rock interaction model with hysteresis effects is applied and this system is able to reproduce a good approach of stick-slip cycle.

The simulated drillstring dynamics using the bit-rock interaction presented a similar behavior comparing to the field data. Specially, the torque on bit as a function of the bit speed presented the same behaviour as the ones observed experimentally.

Future works concern the validation of the model through a series of laboratory experiments. It would be particularly interesting to investigate the influence of the (1) top speed Ω , (2) weight on bit, and (3) the rock characteristics. It would also be interesting to take into account uncertainties in the drillstring computational model and stochastic modeling of bit-rock interaction using hysteresis function.

Acknowledgments. The fourth author would like to acknowledgment the financial support of the Brazilian agencies CNPq, CAPES, and FAPERJ. The authors would also like to acknowledge Schlumberger Oilfield Services for publishing this article.

References

1. Courtney-Pratt, J.S., Eisner, E.: The effect of a tangential force on the contact of metallic bodies. *Philos. Trans. R. Soc. A: Math. Phys. Eng. Sci.* **238**(1215), 529–550 (1956)
2. Chou, Y.: *Statistical Analysis*. Holt International, Canada (1975)
3. Harnoy, A., Friedlanf, B., Rachoor, H.: Modeling and simulation of elastic and friction forces in lubricated bearings for precise motion control. *Wear* **172**(2), 155–165 (1994)
4. Hess, D.P., Soom, A.: Friction at lubricated line contact operating at oscillating sliding velocities. *J. Tribol.* **112**, 147–152 (1990)
5. Hong, L., Girsang, I.P., Dhupia, J.S.: Identification and control of stick-slip vibrations using Kalman estimator in oil-well drillstrings. *J. Pet. Sci. Eng.* **140**, 119–127 (2016)

6. Jansen, J.D.: Nonlinear dynamics of oil well drill strings. Ph.D. thesis, Technische Universiteit Delft (1993)
7. Khulief, Y.A., Al-Naser, H.: Finite element dynamic analysis of drillstrings. *Finite Elem. Anal. Des.* **41**, 1270–1288 (2005)
8. Khulief, Y.A., Al-Sulaiman, F.A., Bashmal, S.: Vibration analysis of drillstrings with self-excited stick-slip oscillations. *J. Sound Vib.* **299**(3), 540–558 (2007)
9. Kreuzer, E., Steidl, M.: Controlling torsional vibrations of drill strings via decomposition of traveling waves. *Arch. Appl. Mech.* **82**(4), 515–531 (2012)
10. Leine, R.I., van Campen, D.H., van den Steen, L.: Stick-slip vibrations induced by alternate friction models. *Nonlinear Dyn.* **16**, 41–54 (1998)
11. Leine, R.I., van Campen, D.H., Keultjes, W.J.G.: Stick-slip whirl interaction in drillstring dynamics. *J. Vib. Acoust.* **124**, 209–220 (2002)
12. Liang, J.-W., Feeny, B.F.: Dynamical friction behaviour in a forced oscillator with compliant contact. *J. Appl. Mech.* **65**(1), 250–257 (1998)
13. Liang, J.-W., Feeny, B.F.: Identifying Coulomb and viscous friction from free-vibration decrements. *J. Sound Vib.* **282**(35), 1208–1220 (2005)
14. Liang, J.-W., Feeny, B.F.: A comparison between direct and indirect friction measurements in a forced oscillator. *J. Appl. Mech.* **65**(3), 783–786 (1998)
15. Mihajlovic, N., van De Wouw, N., Hendriks, M.P.M., Nijmeijer, H.: Friction-induced limit cycling in flexible rotor systems: an experimental drill-string set-up. *Nonlinear Dyn.* **46**(3), 273–291 (2006)
16. Navarro-López, E.M., Licéaga-Castro, E.: Non-desired transitions and sliding-mode control of a multi-DOF mechanical system with stick-slip oscillations. *Chaos Solitons Fractals* **41**(4), 2035–2044 (2009)
17. Olsson, H., Åström, K.J., Canudas de Wit, C., Gäfvert, M., Lischinsky, P.: Friction models and friction compensation. *Eur. J. Control* **4**(3), 176–195 (1998)
18. Pavone, D.R., Desplans, J.P.: Application of high sampling rate downhole measurements for analysis and cure of stick-slip in drilling. In: *Proceedings - SPE Annual Technical Conference and Exhibition Delta*, pp. 335–345 (1994)
19. Real, F.F., Batou, A., Ritto, T.G., Desceliers, C., Aguiar, R.R.: Hysteretic bit/rock interaction model to analyze the torsional dynamics of a drill string. *Mech. Syst. Signal Process.* **111**, 222–233 (2018)
20. Richard, T., Gernay, C., Detournay, E.: A simplified model to explore the root cause of stick-slip vibrations in drilling systems with drag bits. *J. Sound Vib.* **305**(3), 432–456 (2007)
21. Ritto, T.G., Soize, C., Sampaio, R.: Non-linear dynamics of a drill-string with uncertain model of the bit-rock interaction. *Int. J. Non-Linear Mech.* **44**(8), 865–876 (2009)
22. Ritto, T.G., Sampaio, R.: Stochastic drill-string with uncertainty on the imposed speed and on the bit-rock parameters. *Int. J. Uncertain. Quantif.* **2**(2), 111–124 (2012)
23. Ritto, T.G.: Bayesian approach to identify the bit-rock interaction parameters of a drill-string dynamical model. *J. Braz. Soc. Mech. Sci. Eng.* **37**(4), 1173–1182 (2015)
24. Ritto, T.G., Aguiar, R.R., Hbaieb, S.: Validation of a drill string dynamical model and torsional stability. *Meccanica* **52**, 2959–2967 (2017)
25. Sampaio, R., Piovan, M.T., Lozano, G.V.: Coupled axial/torsional vibrations of drilling-strings by mean of nonlinear model. *Mech. Res. Comun.* **34**(5–6), 497–502 (2007)

26. Shi, J., Durairajan, B., Harmer, R., Chen, W., Verano, F., Arevalo, Y., Douglas, C., Turner, T., Trahan, D., Touchet, J., Shen, Y., Zaheer, A., Pereda, F., Robichaux, K., Cisneros, D.: Integrated efforts to understand and solve challenges in 26-in salt drilling, Gulf of Mexico. In: SPE 180349-MS, SPE Deepwater Drilling and Completions Conference, Galveston, Texas, USA (2016)
27. Spanos, P.D., Chevalier, A.M., Politis, N.P., Payne, M.L.: Oil and gas well drilling: a vibrations perspective. *Shock Vib. Dig.* **35**(2), 85–103 (2003)
28. Tucker, R.W., Wang, C.: An integrated model for drill-string dynamics. *J. Sound Vib.* **224**(1), 123–165 (1999)
29. Vigiúé, R., Kerschen, G., Golinval, J.-C., McFarland, D.M., Bergman, L.A., Vakakis, A.F., van de Wouw, N.: Using passive nonlinear targeted energy transfer to stabilize drill-string systems. *Mech. Syst. Signal Process.* **23**(1), 148–169 (2009)
30. Wojewoda, J., Stefaski, A., Wiercigroch, M., Kapitaniak, T.: Hysteretic effects of dry friction: modelling and experimental studies. *Philos. Trans. R. Soc. A: Math. Phys. Eng. Sci.* **366**(1866), 747–765 (2008)
31. Wu, X., Karuppiah, V., Nagaraj, M., Partin, U.T., Machado, M., Franco, M., Duvvuru, H.K.: Identifying the root cause of drilling vibration and stick-slip enables fit-for-purpose. In: IADC/SPE Drilling Conference and Exhibition, no. 151347 (2012)



Modeling and Simulation of Decoupler Pulley Effects on FEAD Torsional Vibration

L. F. Berto¹✉, A. C. Michelotti², P. P. Pastorelli²,
and A. L. F. Ferreira¹

¹ CNPq – RHA/E/Zen S.A., Guilherme Steffen 65, Brusque, SC, Brazil
{lucas.berto, andre.ferreira}@zensa.com.br

² Zen S.A., Guilherme Steffen 65, Brusque, SC, Brazil
{alvaro.michelotti, pedro.pastorelli}@zensa.com.br

Abstract. In current Internal Combustion Engines (ICE), efforts have been conducted in order to reduce emissions levels and improve fuel efficiency. Some alternatives consistent with this strategy are: engine downsizing and reduction of the idling speed. However, adopting such strategies incur in a trade-off between ICE efficiency and increased torsional vibration levels that could damage Front-End Accessory Drive (FEAD) systems and components. The alternator pulley is another potential source of increased torsional vibration due to being coupled to the largest inertia of the FEAD assembly. Therefore, alternator pulley technologies have evolved aiming to provide vibration attenuation capability. The objectives of this work are to demonstrate the development of an alternator pulley to reduce the torsional vibration in the FEAD, and the development of a virtual model to evaluate the FEAD performance. Development of alternator pulleys to reduce torsional vibration generated by the crankshaft fluctuation can avoid premature failure and durability issues with other components of the system. Usually, these pulleys employ two distinct types of springs: a clutch spring and a torsion spring. Through analytical and numerical models previously developed for each spring, the set of springs of the decoupling pulley under development could be properly designed. Finally, functional prototypes are evaluated in static torque tests, dynamic evaluation in test benches and in-vehicle test. Simulations based on finite element method has demonstrated excellent correlation on vibration attenuation levels of the FEAD, based on a comparison with experimental results.

Keywords: Internal combustion engines · Torsional vibration
Alternator pulley · FEAD

1 Introduction

The evolution of vehicle performance and the stringent regulations to emissions reduction together with consumer expectation of performance and low consumption, demand constant technical evolution of all automotive mechanical systems, and drives the industry towards continuous search of new solutions and new technologies.

With regard to fuel consumption improvement, several aspects have been developed, among them the downsizing of internal combustion engines (ICE) and more

precise management and control systems. The reduction of idling speed is also one of the actions driven by reaching the consumption objective, since this specific engine operational condition has great influence on the daily duty cycle, especially in large urban areas.

The idle speed reduction and increased electrical demands of modern vehicles shifts attention to the Front-End Accessory Drive (FEAD) due to the increase in torsional vibration levels, which directly influences the behavior of the FEAD belt and consequently the systems performance with impact in the comfort of the vehicle's passengers and durability of the FEAD components.

This work shows the development and optimization of an alternator pulley that contributes to the reduction of torsional vibration levels in the FEAD system and presents the construction of virtual models of the alternator pulley and complete FEAD system in order to evaluate its dynamic behavior in relation to different operational conditions during normal vehicle use.

This article is structured as follows: Sect. 2 presents details related to the alternator pulley under study, describing its operation, the procedure followed for the definition of its internal components, and briefly describing the construction of the proposed numerical models. Section 3 presents the FEAD system under analysis, its components, layout, vehicle instrumentation and the proposed virtual model. Section 4 discusses the results obtained with the virtual models, and the correlations with experimental tests. Finally, Sect. 5 summarizes the conclusions regarding the work and suggests further studies to be carried out.

2 Alternator Pulley

Alternator pulleys have the primary function of transmitting and converting the linear speed of the belt in a rotational motion of the alternator shaft, which generates electric energy for the battery and for the operation of vehicle's electric systems. This primary pulley function (torque transmission) no longer meets the current system requirements, and new technologies have been and are still being developed to evolve the functionalities of this component. Table 1 presents the terminology and main characteristics of the most usual types of alternator pulleys [1].

Table 1. Alternator pulleys models and main characteristics.

Alt pulley acronym	Acronym meaning	Functions	Standard OWC type
Solid	Solid	Torque transmission only	N/A
OAP	Overrunning alternator pulley	Torque transmission + overrunning	Roller OWC
Decoupler pulley	Overrunning alternator decoupler	Torque transmission + overrunning + damping of torsional vibrations	Spring OWC
ADP	Alternator decoupler pulley	Torque transmission + damping of torsional vibrations	N/A

As presented by [2], some of the advantages of the OAP and of the decoupler pulley concepts are: increased belt life due to reduced vibration and excessive tensioning; increased belt tensioner life, by the reduction of the angular movement; the improvements in NVH; engine kickback absorption; and reduction of fuel consumption and emissions.

The choice for the development of the decoupling model as a vibrational damping is due to the greater benefits it can provide to the FEAD system. The target alternator pulley's model is presented in a section view of Fig. 1. The large number of components that make up the assembly poses challenges during the design, in order to meet the requirements of interface with the alternator and FEAD, along with the performance and durability necessary.

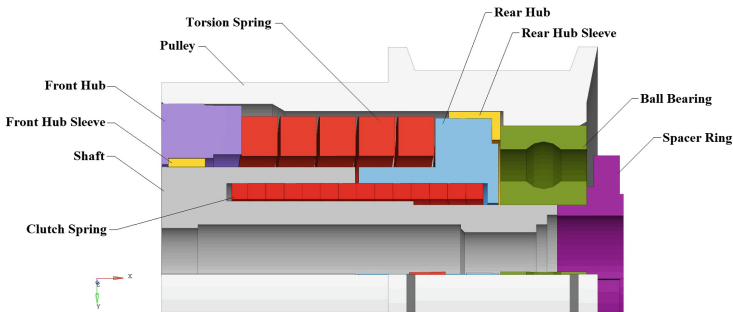


Fig. 1. Complete decoupler pulley or “One-way clutch with damper system” pulley.

With the defined geometric constraints and the requirements of the system in hands then the springs that provide the functionality of the product have been studied in detail. The following topics briefly summarize the steps necessary in order to correctly design these components.

2.1 Clutch Spring

The clutch spring has the function of providing the overrunning function for the pulley, allowing the decoupling of the alternator rotor inertia during transient changes of engine speed and, during sudden deceleration of the belt, preventing belt slip and chirp noise by allowing free-wheeling effect of alternator rotor shaft. In the direction of the alternator rotor acceleration, it must provide enough torque to meet the demand of the system.

The principle of operation of the clutch spring is the Capstan effect, as previously discussed in [3, 4, 5]. Analytical calculations were developed for the clutch spring initial parameter definition for the application; these analytical equations are described in more detail in [6].

For the numerical models presented in this article, the *Altair Radioss* commercial software was adopted. A method based on Lagrangian 3D formulation and finite

element method with explicit integration in time is applied [7]. The dynamic equilibrium equations consider inertia effects and damping forces.

In order to optimize the process of validation and evaluation of the clutch spring performance, a simplified model is proposed, as depicted in Fig. 2(a), which considers all the constraints and boundary conditions of the installation in the final geometry (diametral and axial space). In Fig. 2(b) it is possible to observe the hexagonal mesh used in the model with 0.75 mm of average size in the spring.

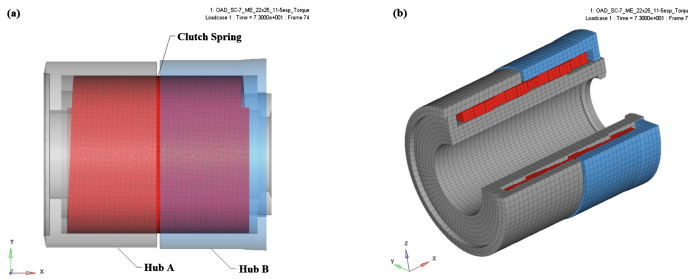


Fig. 2. (a) Simplified spring housing geometry. (b) Functional evaluation of geometry meshing.

The purpose of this model is to evaluate the level of stress on the spring, the ability to transmit torque (maximum value until the spring slips in the locking direction) and the resistive torque in the overrunning direction (clutch function). As boundary conditions applied to the model, all elements except those of the spring are rigid, hub A has all degrees of freedom (DOF) locked, hub B has the rotation imposed around the X axis of the model through an angular velocity curve over time.

All components are characterized as steel ($E = 210$ GPa, $\rho = 7800$ kg/m³, $\nu = 0.30$) and the clutch spring is treated as elastoplastic taking into account material data supplied by the manufacturer. The spring is inserted into the hubs with an interference fit. In the first stage of the simulation (before the start of the rotation imposed on hub B), the spring does not have contact with the hubs, in this initial period the diameter of the spring is adjusted through a component that varies its internal diameter, thus reducing the spring to the desired installation diameter. Upon reaching the desired diameter the contacts with the hubs are activated and the contact of the spring with the assembly component is disabled, thus enabling the spring to be installed according to the designed interference forces.

2.2 Torsion Spring

The torsion spring has the function of reducing the transmission of torsional vibrations from the engine crankshaft to the alternator and other FEAD accessories (such as water pump, air conditioning (AC) compressor and belt tensioner).

As shown by [8], this type of spring is generally used to transmit torque in the direction of wire coiling, but in the application under evaluation the torsion spring operates in the opposite direction (unwinding). This type of loading is not often

recommended, therefore studies to specify the required parameters for the correct functionality of the system had to be performed due to limited knowledge available in technical literature.

For the optimal design of the spring the design must take into consideration the requirements of the FEAD system and the geometric constraints. FEAD requirements are influenced by the number of cylinders of the target engine, idle speed and target vibration attenuation levels. Geometric constraints could limit the external diameter of the spring, its number of coils, wire cross section, axial force and maximum angular displacement of the torsion spring during operation.

The analytical calculation procedure applied can be seen in [6]. Special assumptions have been considered as the literature shows only the application of torque on torsion springs in the winding direction of the wire so a new modeling proposition has been developed for this research.

Figure 3 presents the FEA model developed for the torsion spring functional evaluation. In this model each imposed geometric constraint is considered and several variations of these parameters are evaluated until the optimal configuration for the application was achieved.

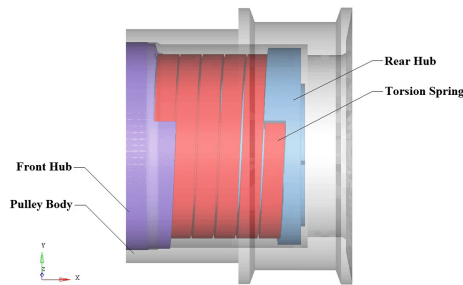


Fig. 3. Virtual model for functional evaluation of the torsion spring.

The numerical model is based on the same parameters presented for the clutch spring. The objective of the model is evaluate the torque curve by angle, the stiffness behavior during the working cycle, the maximum value provided until the spring reaches opening limiter and the resulting stresses generated. Every component except the spring are specified as rigid, steel material ($E = 210 \text{ GPa}$, $\rho = 7800 \text{ kg/m}^3$, $\nu = 0.30$) and the torsion spring is defined as a elastoplastic material, with hexahedral mesh and element average size of 1.2 mm. The torsion spring also goes through an initial stage of assembly where it has its initial axial length decreased to the installation compression defined to generate the desired axial load on the hubs.

2.3 Complete Pulley

The complete pulley considers the performance of the two springs, clutch and torsion. The analysis of this coupled system demands further evaluation of the functional behavior of the springs and components, considering that the complete pulley presents

springs in a series operation (Fig. 1). Considering the final geometry of the pulley assembly, many contact regions can be noticed, which requires studies to define parameters such as gaps and coefficients of friction (COFs). Special attention should be given to the front and rear bushings, since these regions greatly influence the dynamic response of the system.

3 FEAD

The Front-End Accessory Drive (FEAD) consists of the engine accessory system, usually comprised of a crankshaft pulley, AC pulley, alternator pulley and water pump pulley. These systems may also have power steering pump pulleys, idler pulleys and tensioners depending on the configuration. All of these accessories are connected and driven by a poly-V belt.

Some of the operating requirements for these systems are: (a) to maintain the belt tension, (b) avoid speed spikes on belt and accessories, (c) minimize slippage, decrease transmission losses, (d) low vibration in the belt span. Fulfillment of these requirements as a whole is the main goal for the FEAD operation. However, the torsional vibration generated by different types of ICE configurations, different operating conditions and different models of accessories, implies that each configuration provides a distinct response to the input parameters of the system. Depending on the engine model and configuration, the FEAD undergoes variations, as in the positioning of the accessories and the components that form the system.

In Fig. 4 two FEAD layouts are presented, in Fig. 4(a) we have one system with 6 pulleys (crankshaft, AC compressor, water pump, alternator, idler and tensioner), where it makes use of a rigid pulley in the alternator. While in Fig. 4(b), we have a configuration with only 4 pulleys (crankshaft, AC compressor, alternator and water pump), in this case the system uses a decoupler pulley as standard part of the vehicle. The FEAD of Fig. 4(b) will be adopted in the studies herein presented as a target application.

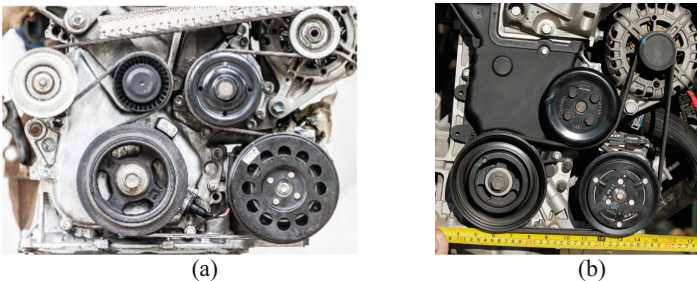


Fig. 4. Two FEAD layouts. (a) with rigid alternator pulley, (b) with decoupler pulley.

The vehicle used in the present research is a Ford Ka+, which has a naturally aspirated 1.5l, inline-4 cylinder, flex-fuel engine, equipped with a 5-speed manual transmission. Test procedures started with the vehicle having only 500 miles

accumulated. This vehicle was selected because it is equipped with a decoupler pulley as original equipment. For the system under analysis, a measurement system was set up with the following types of sensors: Hall Effect, microphone, laser tachometer, shunt and accelerometers to measure rotational speed, noise, vibration, voltage and current, respectively, as presented in detail by [1].

The numerical model constructed for the FEAD under analysis is shown in Fig. 5. As in the study of the alternator pulley, commercial code Altair Radioss was used in the analyses. In this proposed procedure, each pulley is considered as a rigid body and have the interface with the belt simplified for smooth surface; the belt is flexible and modeled with shell elements following the same methodology applied by [9].

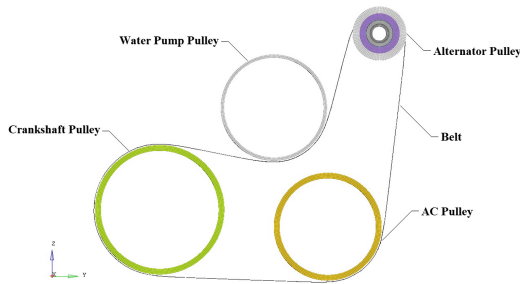


Fig. 5. FEAD virtual model.

All components are made of steel ($E = 210 \text{ GPa}$, $\rho = 7800 \text{ kg/m}^3$, $\nu = 0.30$), except the belt that is characterized as rubber with ideal elastic properties to have the equivalent behavior of the physical belt ($E = 10 \text{ GPa}$, $\rho = 2000 \text{ kg/m}^3$, $\nu = 0.49$). The thickness of the belt is 2.4 mm. Coulomb friction is considered between the belt and the pulleys and the losses occurring in the system are processed with linear viscous damping Rayleigh Damping ($\alpha = 0.02$, $\beta = 0.0$).

Considering the crankshaft pulley as the master pulley of the system, the remaining ones follow the dimensional relation: AC pulley 1:1.20; alternator pulley 1:2.64; and water pump pulley 1:1.21.

The simulation starts with a non-deformed belt configuration and then during the initial simulation period the FEAD is mounted to the installation positions, thus generating the belt tension. This simulation of belt pre-stressing is shown in Fig. 6.

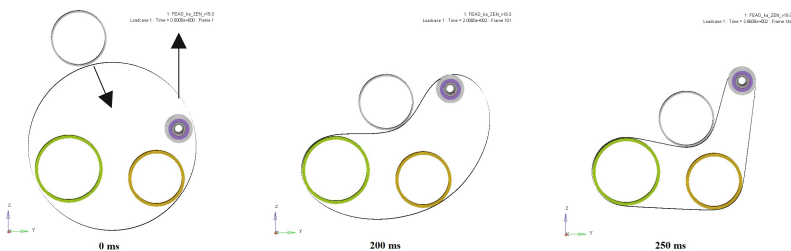


Fig. 6. FEAD pre-simulation to pre-stress belt to installation position.

Based on the modeling efforts of the research completed, the simulation results and the correlation with experimental tests are presented in the following section.

4 Simulation and Experimental Test Results

4.1 Pulley

Different pulley configurations, with different sets of clutch spring and torsion spring were evaluated during the preliminary tests, with the purpose of acquiring the knowledge about the behavior of the springs with respect to possible variations within the constraints imposed.

For the functional evaluation, bench tests based on OEM specifications were performed on an Instron MT-2 torque testing machine, as described in [6, 8]. The setup used for the bench tests in the functional evaluations used a speed of 5 rpm, with angular displacement of up to 150° and return to the zero angular position at the same speed. For the correlation with the numerical models a curve with these same parameters was adopted, however to accelerate the simulation process, a sensitivity evaluation was initially performed with respect to velocity, being assumed a speed of 30 rpm in the simulations, without influence on the results' quality.

In Fig. 7 it is shown the correlations obtained between the bench tests and the numerical models of the clutch and torsion springs. In the clutch spring (Fig. 7(a)), we see that the model was able to keep the locking torque close to the values found in the test bench, only the activation of the coils was faster in the virtual model than in the tests. This was not seen as a problem for the correct component evaluation, maintaining a correlation at 94%. The torsion spring (Fig. 7(b)) satisfactorily demonstrated all benchmarking behavior, including the maximum deflection angle. The stiffness of the virtual model was slightly above that observed in the test, but overall the correlation was evaluated as close to 90%.

By reaching good correlation between the prototypes and the models in FEA, the optimization work is carried out through virtual iterations. This process took into account the preliminary analytical calculations and the imposed geometric limitations.

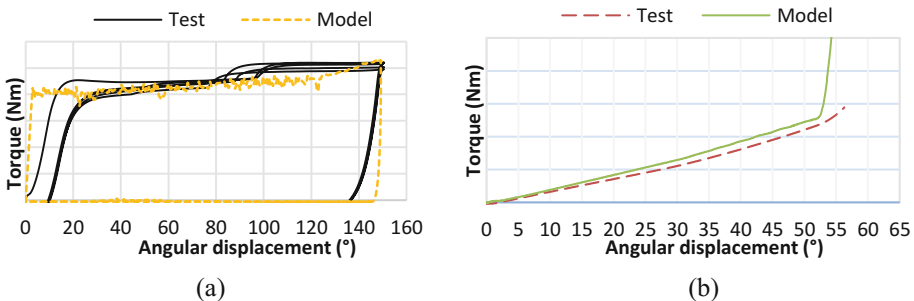


Fig. 7. (a) Experimental and simulation results of the clutch spring. (b) Experimental and simulation results comparison of the torsion spring.

Relying on the expected goals with the springs behavior individually, the next step was to build the complete pulley model. This model passes through two different stages of validation through simulation. The first is the functional validation, following the same parameters of the simulations performed in the individual springs. Figure 8 demonstrates the results obtained with one of these models, in which the initial part of the cycle up to 56° depicts the torsion spring movement until it reaches the deflection limiter. After the torsion spring reaches its maximum opening angle, the pulley operation relies upon the clutch spring only, as it transmits torque up to the slip torque limit (reached at 63°) where it allows for slippage, protecting internal components from damage.

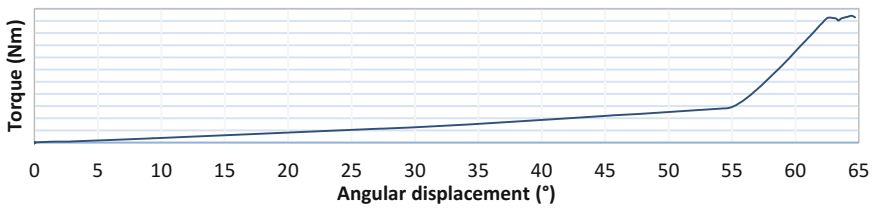


Fig. 8. Results of the functional evaluation cycle of the complete pulley.

The second step is the dynamic evaluation of the model, where the curve imposed is characterized by an average rotation of 2000 rpm and a torsional input of ±200 or ±300 rpm with a frequency of 23 Hz. These parameters come from validation tests required by OEM applications. Figure 9 presents the result obtained for the dynamic behavior with the two torsional input curves cited above, with the complete pulley model.

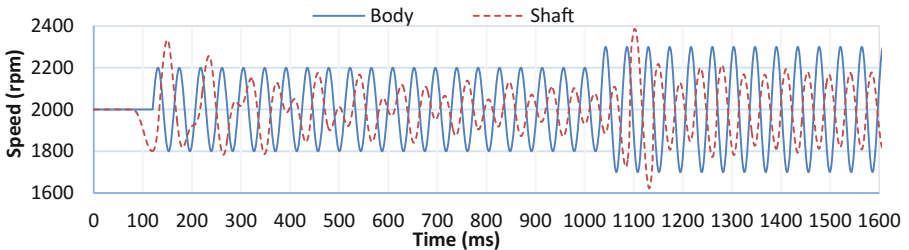


Fig. 9. Results of idling and lugging dynamic cycle.

The model is configured to start simulation with the components at the speed of 2000 rpm, thus reducing the processing time since it is not necessary to have the acceleration ramp up to the average speed of the test. An important point to note is that the speed remains constant in the initial part of the simulation because, similarly to the described in the models of the individual springs evaluated, they have installation steps that also have to be performed on the complete pulley.

After the internal components are assembled (0–75 ms), the alternator resistive load input is added (from 80–120 ms), at the end of the load input starts the torsional cycle of ± 200 rpm, 23 Hz (at 120 ms). During the initial cycles (up to 450 ms) we have a strong transient behavior, which is due to these two sources, input of the alternator load and beginning of the torsional cycle. After this period we see the attenuated behavior of the pulley shaft (450 to 1000 ms). At 1000 ms, the cycle is changed to ± 300 rpm, 23 Hz and the alternator load is increased, and we can observe a transient behavior due to change of input parameters up to 1250 ms, from which it can be observed that the system goes into a steady state regime, also showing the designed attenuation.

With these complete alternator pulley results meeting the performance requirements, the next step is to insert it into the FEAD as a whole. Therefore, studies of this system are necessary to understand the parameters to be observed. These preliminary studies are presented in the following section.

4.2 FEAD

Aiming to increase the knowledge about the system behavior, the first working stage with the FEAD analysis was carried in the vehicle, with instrumentation studies (transducer tests, evaluation of the preliminary data acquired). It has also contributed to the validation of the experimental procedure and to analyze the most relevant information to be collected to acquire comprehensive understanding about each component. Several data acquisition routines were performed, both with the vehicle stationary and in motion. Further details on instrumentation performed on the vehicle can be found in [1].

Figure 10 presents data collection of the vehicle in dynamic cycle, low speed and high load of the ICE. It is known as “lugging condition” and this test procedure is one of the toughest requirements for the validation of the FEAD and alternator pulley. These results are presented with a rigid pulley in the alternator, as baseline with no influence in changing torsional vibration behavior of the FEAD system as a whole.

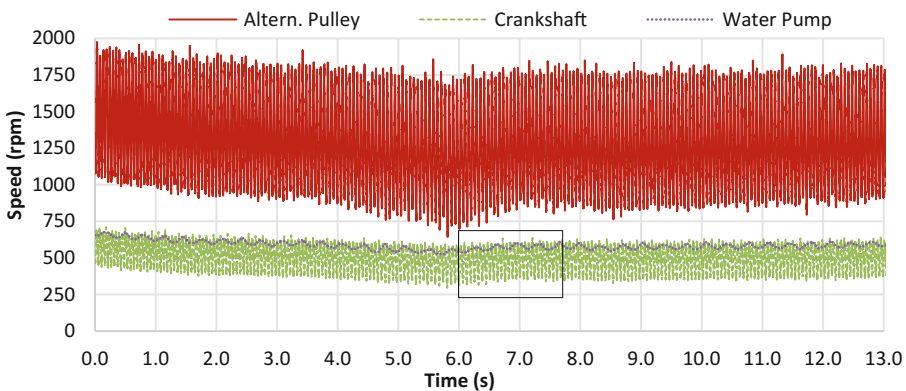


Fig. 10. Experimental data collection.

With experimental data of the vehicle available, a time interval is selected (highlighted in Fig. 10) for evaluation of the FEAD virtual model under development. The first step is to adjust the data to allow pre-simulation of the system, for belt tensioning and then acceleration of the system up to the speed provided by the engine to the crankshaft pulley. These adjustments to the curve imposed on the model can be observed in Fig. 11.

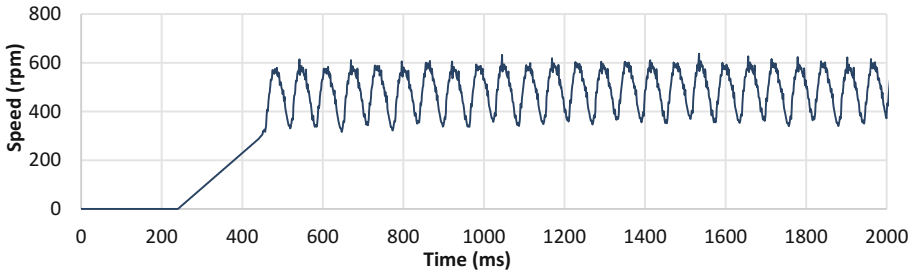


Fig. 11. Crankshaft imposed velocity.

Along with the angular velocity input data, the model also takes into account the resistive and inertial loads imposed by the ICE accessories. In the model, the inertia of the alternator rotor, water pump and AC (uncoupled pulley) are considered. After setup and acceleration of the simulation model up to the speed under analysis, the resistive torques demanded by the alternator electric load and water pump, based on their corresponding angular velocities, are applied in the model as resistive torque in opposition to the drive torque imposed by the crankshaft.

The resulting velocities in each of the pulleys are shown in Fig. 12. It can be noticed that the model has been able to accelerate all the accessories and to handle the inertia and the resistive torques imposed by the ICE accessories. The water pump pulley has a negative speed because it rotates in the opposite direction of the other pulleys.

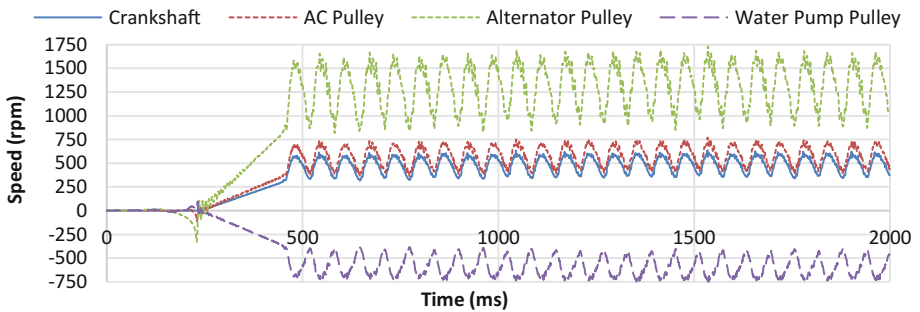


Fig. 12. Results of FEAD accessory velocities.

The friction considered in the model between the belt and the pulleys is considered a coherent value, taking into account the simplification adopted to remove the poly-v profile from the components. By bringing all the curves to the same reference with respect to crankshaft speed, it is possible to observe that the system behaves as expected, with all components having the same average rotation as depicted in Fig. 13.

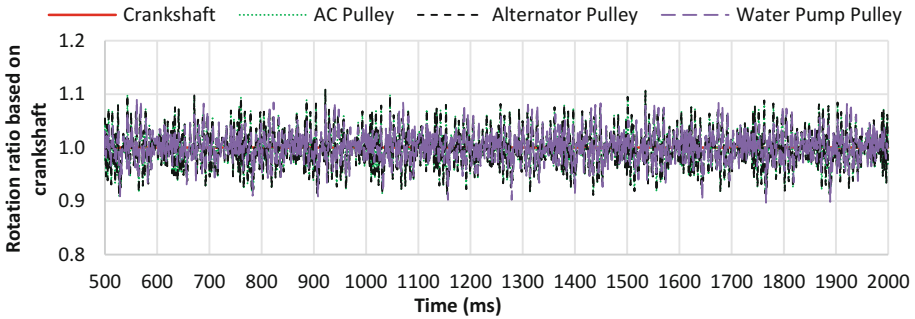


Fig. 13. Pulleys rotation ratio based on crankshaft.

The definition of the dynamic COF between the pulleys and the belt in the virtual model and the correlation was one of the main efforts to achieve virtual model validation. Since slip of the belt on the pulleys exists, the alternator pulley and their different types result in different slip rates. Figure 14 shows the comparison of angular displacement between the test data and two results of the virtual model during the calibration of the friction coefficient. A COF of 0.13 was defined as ideal for the virtual model.

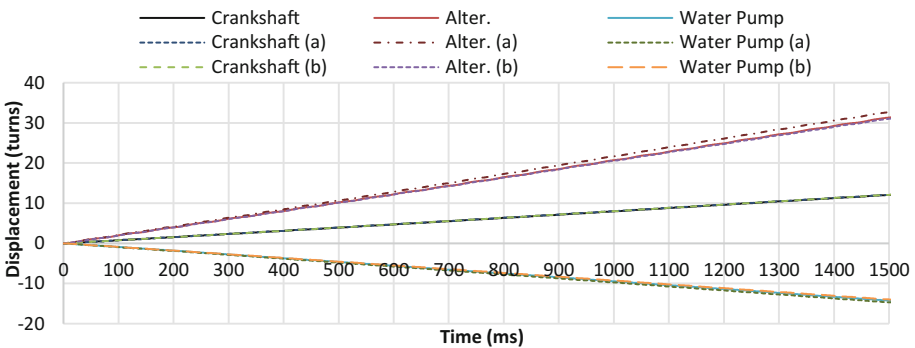


Fig. 14. Virtual model friction calibration. Curve (a): COF 0.15. Curve (b): COF 0.13

Since the alternator pulley is the main focus of the research, a comparison between the data collected through vehicle instrumentation and those obtained through the proposed virtual model is also studied. Figure 15 depicts the high correlation of the

alternator pulley model speeds in comparison with the experimental data, denoting it as a potential alternative to predict the dynamic behavior of the FEAD before an actual prototype is constructed.

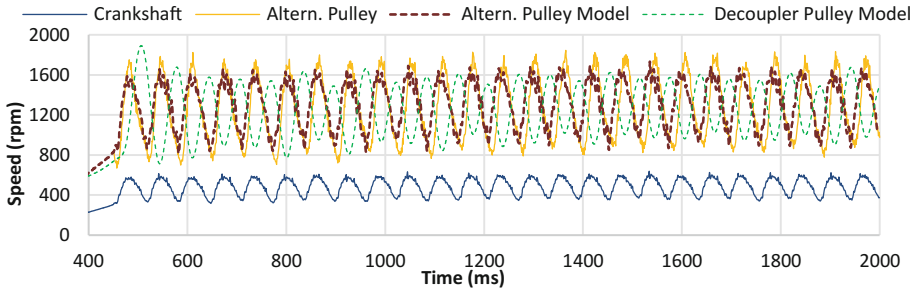


Fig. 15. Comparison between experimental and numerical model of the alternator rotational speed.

With the decoupler pulley integrated into the system, it is possible to note that the alternator shaft has a smooth response compared to the rigid pulley, as shown in Fig. 15. The main point observed in the response of the decoupler pulley is related to the attenuation of the torsional vibration represented by the smallest torsional amplitude and by the time lag of the output signal compared to the input curve.

When the results are analyzed in the frequency domain, both rigid and decoupler pulley model responses are in the same frequencies in comparison with the experimental test data as shown in Fig. 16, without the presence of other orders. In the decoupler pulley model the attenuation was around 12%, comparing the amplitude of the Rigid Pulley and the Decoupler Pulley Shaft, as shown in Fig. 16.

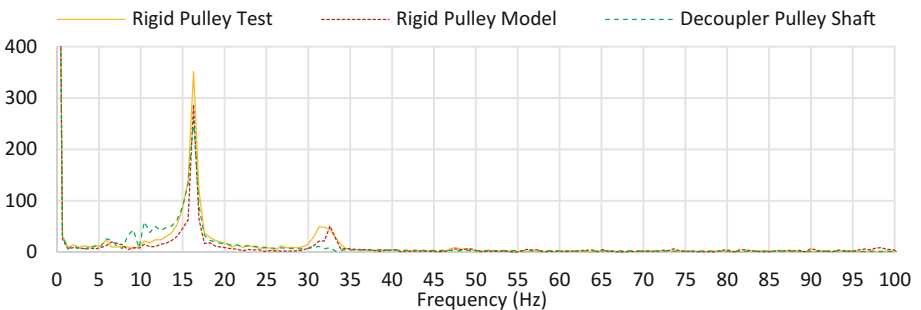


Fig. 16. Comparison between experimental and numerical models in the frequency domain.

When simulation results are observed in idling cycle in frequency domain, the attenuation of the decoupler pulley showed to be close to 60%, comparing the amplitude of the Pulley Body and Shaft, Fig. 17.

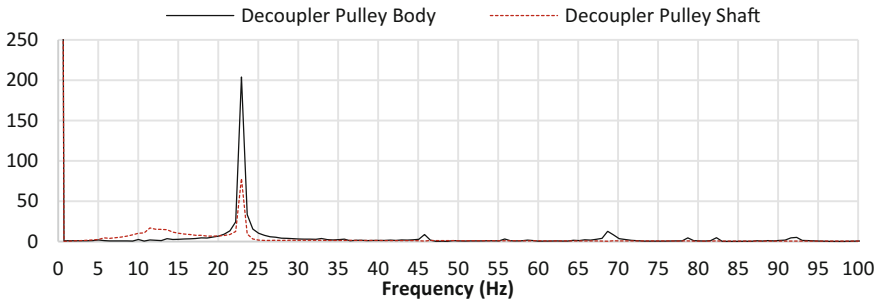


Fig. 17. Results of idling cycle in frequency domain.

Modeling and evaluation of the virtual FEAD can be considered valid to be adopted to the evaluation and analysis of the decoupler pulley influence in the response of the alternator and its interaction with remaining accessories of the FEAD system.

Some belt parameter adjustments can still be developed to improve even more the correlation shown previously, even though current results already meet the expected objective of the virtual model.

5 Conclusion

The use of virtual models presented herein have proven that FEA models can be a robust and adequate tool in the preliminary design stage of alternator pulleys. The methodology proposed in the research has shown an effective correlation in comparison with the bench tests performed.

The correlation of the virtual model with the experimental tests enables the model to be effectively used in the reduction of prototypes to be manufactured and tested. This allows for faster achievement of the desired pulley performance, thus enabling initial prototypes to efficiently reach demanding targets for performance and durability.

The FEAD model presented here includes the baseline for the development of a model to evaluate the performance of the alternator pulley presented, along with the correlations of the initial evaluations of performance. The main objective is to reduce the number of prototypes to be manufactured and tested in test benches or vehicles. The modeling methodology developed has shown satisfactory performance against the objectives of the research. The next step of the work is to evaluate the effect of the different decoupler pulley concepts in the virtual model of the FEAD and its correlation with in-vehicle experimental test data.

Acknowledgments. Authors would like to thank ZEN S.A. Industria Metalurgica (www.zensa.com.br) by project funding that allowed computational and experimental research work, to CNPq – RHAÉ scholarship funding program, and to Vibroacustica in Joinville (Brazil) by providing technical resources, expertise and support during the development work and research.

1 Definitions/Abbreviations

ICE – Internal Combustion Engine

FEAD – Front-End Accessory Drive

FEA – Finite Element Analysis

OWC – One-Way Clutch

AC pulley – Air-Conditioning Pulley

E – Young's Modulus

ρ – Density

ν – Poisson Coefficient

DOF – Degree of Freedom

ms – Millisecond

COF – Coefficient of Friction

References

1. Michelotti, A.C., et al.: In-vehicle experimental tests to evaluate the performance of alternator pulleys. SAE Technical paper 2017-36-0433. <https://doi.org/10.4271/2017-36-0433>
2. Michelotti, A., et al.: Future Trends in the conceptual design of alternator pulleys. SAE paper 2012-36-0226. SAE International (2012). <https://doi.org/10.4271/2012-36-0226>
3. King, R., Monahan, R.: Alternator pulley with integral overrunning clutch for reduction of belt noise. SAE Technical paper 1999-01-0643 (1999). <https://doi.org/10.4271/1999-01-0643>
4. Sclater, N., Chironis, N.: Mechanisms and Mechanical Devices Sourcebook, pp. 206–208. McGraw-Hill, New York (2007)
5. Yang, E.: Inventor. Pacific Scientific Company, Assignee. Capstan Spring Centrifugal Clutch. European Patent Application EP0153079, 28 August 1985
6. Pastorelli, P.P., et al.: Analytical models for spring one-way clutch and torsional vibration dampening systems with experimental correlation. SAE Technical paper 2017-36-0407. <https://doi.org/10.4271/2017-36-0407>
7. Radioss Theory Manual. 13.0 Version. Large Displacement Finite Element Analysis. Altair Engineering, Inc., January 2014
8. Berto, L.F., et al.: Finite element analysis of spring one-way clutch and torsional vibration dampening systems with experimental correlation. SAE Technical paper 2017-36-0406. <https://doi.org/10.4271/2017-36-0406>
9. Takemori, C., et al.: Analysis of the dynamic behavior of the FEAD system using numerical methodology. SAE Technical paper 2016-36-0432. <https://doi.org/10.4271/2016-36-0432>



Detection of Gear Tooth Crack in a Wind Turbine Planetary Gearbox

Rachna Joshi and Ashish K. Darpe^(✉)

Department of Mechanical Engineering, Indian Institute of Technology Delhi,
New Delhi, India

akdarpe@mech.iitd.ac.in

Abstract. A planetary gearbox of a horizontal axis wind turbine drive train is modelled as a vibratory system and vibration response is investigated for detecting a typical gear tooth flaw. A detailed dynamic model involving two translational and one rotational degree of freedom for each component of the planetary stage is formulated. The gearbox stage considered in the study is a low speed planetary gear stage (three identical planets with spur teeth, sun and fixed ring gear) as the typical arrangement commonly used in wind turbine industry. The effect of gravity is incorporated in the mathematical formulation as the mass of the drivetrain components is considerable in such application. The vibration response of the elements is influenced by the gear mesh stiffness variations. The presence of a tooth crack shifts the localized mean value of gear mesh stiffness to a lower value. The localized change in turn influences the vibration response of all the components. In order to extract fault-induced vibration features, a difference signal is generated from the synchronous time domain vibration signals for the healthy and cracked tooth. The time domain and frequency domain data of the proposed difference signal are studied. They reveal useful information for the purpose of detection of gear tooth crack. The spectral characteristics can be used for condition monitoring and early detection of gear tooth crack for a wind turbine gearbox.

Keywords: Planetary gear box · Gear mesh stiffness · Gravity excitation
Detection of crack in gears

1 Introduction

The increase in demand of electricity has triggered the search of alternative sources of power generation. Wind energy is therefore gaining more importance due to its Eco friendliness. The rise in the number of wind farms is accompanied with the challenges of its low cost operation. One of the key elements of the wind turbine power train is the gearbox. The dynamics of a typical gearbox has been investigated in detail in the past. Lin and Parker [1] investigated the natural frequencies and vibration modes of general planetary gears. This work rigorously identifies key properties of the natural frequency spectra and vibration modes. Peeters et al. [3] studied torsional vibration model of the drive train which he extended further to investigate the stresses induced. Bearing stiffness and dynamic bearing loads for rigid 6 DOF model was analyzed. Ambarisha and Parker [4] analytically derived design rules to suppress certain harmonics of planet

mode. Todorov et al. [5] proposed a dynamic multi-body model of a drive train with an electrical generator. In this model the aerodynamic torque is applied as an external load. Shi et al. [6] presented a mathematical model for a horizontal axial wind turbine drivetrain using the torsional multi-body dynamic model. Zhang et al. [7] studied the effect of gravity on the wind turbine gear box. In order to obtain accurate vibration response predictions to understand the coupled dynamic characteristics of the wind turbine gear transmission system, a comprehensive, fully coupled, dynamic model is established. In wind farms, planetary gearboxes are subject to potential damage due to tough working conditions like heavy load, wind gust and dust corrosion. The faulty planetary gearbox could lead to catastrophic failure of the entire wind turbine, and consequently heavy investment and productivity losses. Therefore, monitoring and diagnosis of planetary gearboxes is an important topic for research on wind turbines.

In this paper, influence of a fatigue crack in a gear tooth of sun on the vibration response is investigated. In order to extract fault related vibration feature, the time domain response for the two cases (with crack and without crack) are used to generate a difference signal in time domain and the spectral features of this signal are used in framing the gear tooth health diagnosis strategy.

2 Three Degree of Freedom Model for Gearbox

The gearbox investigated in this study is depicted in Fig. 1. The gearbox consists of 3 spur planet gears orbiting around the sun gear with a fixed ring. The planets, sun and ring are all treated as rigid bodies. Gear mesh stiffness is modelled as linear spring acting along the line of action. This model is valid for heavily to moderately loaded gears. The gearbox is modelled with two translational and one rotational degree of freedom. Gear mesh stiffness is time variant. The excitation consists of external aerodynamic load, gravity along with parametric excitation from the fluctuation of the gear mesh stiffness.



Fig. 1. Main components of a gear box [5]

The Lagrange's equation for the gearbox can be written by considering the total kinetic energy and the total strain energy of the system. The total potential energy of

the gearbox is contributed from the elastic deformation of the flexible components. The relevant kinetic and potential energies of the ring, carrier, sun and the three planets are listed below. The potential energy of the sun-planet and ring-planet is a function of the dynamic transmission error δ_{sp} and δ_{rp} for the sun-planet and the ring-planet gear pairs respectively. The gear mesh stiffness for various gear pairs is modelled as linear springs acting along the line of action.

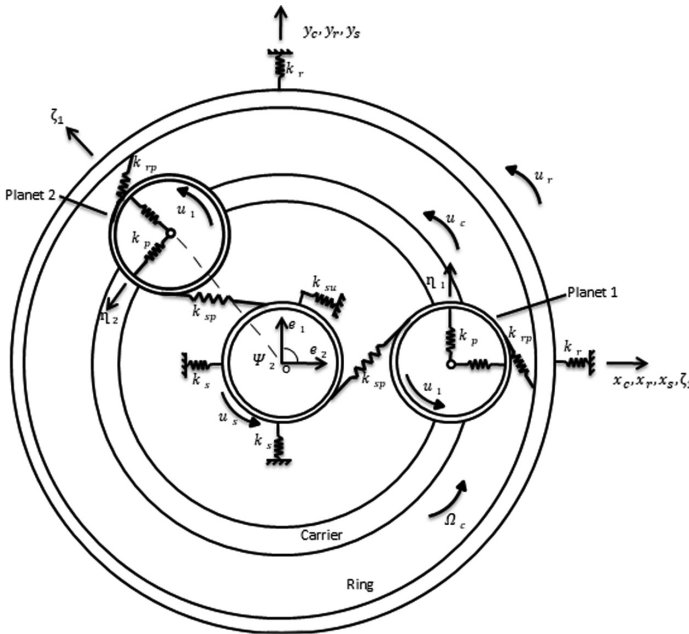


Fig. 2. Multi body representation of a planetary gear box

Extensive research has already been done in the field of planetary gears where the mathematical expressions for a lumped parameter model are widely found in literature [8]. The Lagrangian for each components of a gearbox considering three degrees of freedom are as follows:

For Ring

$$\begin{aligned}
 L_1 = & \left(\frac{1}{2} m_r (\dot{y}_r^2 + \dot{x}_r^2) + \frac{1}{2} J_r \dot{\theta}_r^2 \right) - \frac{1}{2} k_{r1} \delta_{r1}^2 - \frac{1}{2} k_{r2} \delta_{r2}^2 - \frac{1}{2} k_{r3} \delta_{r3}^2 \\
 & - \frac{1}{2} k_r y_r^2 - \frac{1}{2} k_r x_r^2 - \frac{1}{2} k_{rr} r_r^2 \theta_r^2
 \end{aligned} \tag{1}$$

For Carrier

$$\begin{aligned}
 L_2 = & \left(\frac{1}{2} m_c (\dot{y}_c^2 + \dot{x}_c^2) + \frac{1}{2} J_c \dot{\theta}_c^2 \right) - \frac{1}{2} k_p (\delta_{c1}^2 \xi^2 + \delta_{c1}^2 \eta^2) \\
 & - \frac{1}{2} k_p (\delta_{c2}^2 \xi^2 + \delta_{c2}^2 \eta^2) - \frac{1}{2} k_p (\delta_{c3}^2 \xi^2 + \delta_{c3}^2 \eta^2) \\
 & - \frac{1}{2} k_c y_c^2 - \frac{1}{2} k_c x_c^2 - \frac{1}{2} k_{cr} r_c^2 \theta_c^2
 \end{aligned} \tag{2}$$

For planet 1

$$L_3 = \frac{1}{2} \left(m_{p1} (\dot{\xi}_{p1}^2 + \dot{\eta}_{p1}^2) + J_{p1} \dot{\theta}_{cp1}^2 \right) \tag{3}$$

For planet 2

$$L_4 = \frac{1}{2} \left(m_{p2} (\dot{\xi}_{p2}^2 + \dot{\eta}_{p2}^2) + J_{p2} \dot{\theta}_{cp2}^2 \right) \tag{4}$$

For planet 3

$$L_5 = \frac{1}{2} \left(m_{p3} (\dot{\xi}_{p3}^2 + \dot{\eta}_{p3}^2) + J_{p3} \dot{\theta}_{cp3}^2 \right) \tag{5}$$

For sun

$$\begin{aligned}
 L_6 = & \frac{1}{2} (m_s (\dot{y}_s^2 + \dot{x}_s^2) + J_s \dot{\theta}_s^2) - \frac{1}{2} (k_{s1} \delta_{s1}^2) - \frac{1}{2} (k_{s2} \delta_{s2}^2) - \frac{1}{2} (k_{s3} \delta_{s3}^2) \\
 & - \frac{1}{2} k_s y_s^2 - \frac{1}{2} k_s x_s^2 - \frac{1}{2} k_s \theta_s^2
 \end{aligned} \tag{6}$$

The dynamic transmission error for the n th sun-planet and n th ring-planet gear mesh is depicted in Fig. 3.

$$\delta_{sn} = -x_s \sin(\Psi_{sn}) + y_s \cos(\Psi_{sn}) - \xi_n \sin(\alpha_s) - \eta_n \cos(\alpha_s) + u_s + u_n \tag{7}$$

$$\delta_{rn} = -x_r \sin(\Psi_{rn}) + y_r \cos(\Psi_{rn}) + \xi_n \sin(\alpha_r) + \eta_n \cos(\alpha_r) + u_r + u_n \tag{8}$$

Where, the circumferential location for n th planet (Ψ_n) is given by

$$\Psi_n = 2\pi(n - 1)/P \quad \text{and} \quad \Psi_{sn} = \Psi_n - \alpha_s \tag{9}$$

Where, P is the number of planets on the carrier

The equation of motion for the gearbox system is given by

$$M\ddot{q} + K(t)q = F(t) \tag{10}$$

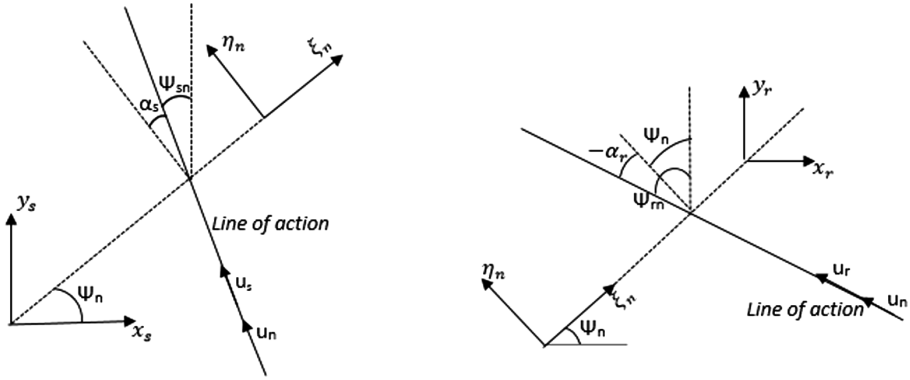


Fig. 3. Schematic of the dynamic transmission error

Where, $q(t)$ represents the response vector comprising the three degrees of freedom for each of the elements of the gear train, i.e. $\{y_i, x_i, \theta_i\}$. M and $K(t)$ are the global mass and stiffness matrices of the entire planetary stage with contribution from planets, sun and ring gear.

On solving the Lagrange’s equations, the following equation of motion are derived for each component of the gearbox.

For sun

$$m_s \ddot{y} - \sum k_{sn} \delta_{sn} \sin \psi_{sn} + k_s y_s = 0 \tag{11}$$

$$m_s \ddot{x} - \sum k_{sn} \delta_{sn} \sin \psi_{sn} + k_s x_s = 0 \tag{12}$$

$$(I_s/r_s^2) \ddot{u}_s + \sum k_{sn} \delta_{sn} = T_s/r_s \tag{13}$$

Similar equations are derived for the ring, carrier and planet.

The force vector without considering gravity effect

$$F = [0; 0; -T_c/r_c; 0; 0; 0; T_r/r_r; 0; 0; 0; T_s/r_s; 0; 0; 0; 0; 0; 0; 0; 0; 0; 0]$$

Where T_c , T_r , and T_s are the Torques and r_s , r_c , and r_s are the radii of the carrier, ring and the sun gear respectively.

The time varying gear mesh stiffness is pictorially depicted in Fig. 4.

The gear mesh stiffness is modelled as linear springs with time-varying stiffness with k_{rp} , k_{sp} as the mean components. Each mesh stiffness is expressed in the Fourier series as

$$k_{rp}(t) = k_{rp} + k_{rp}/c_{rp} \sum_{i=1}^{\infty} a_{rp} \sin \omega_m t + b_{rp} \cos \omega_m t \tag{14}$$

$$k_{sp}(t) = k_{sp} + k_{sp}/c_{sp} \sum_{i=1}^{\infty} a_{sp} \sin \omega_m t + b_{sp} \cos \omega_m t \tag{15}$$

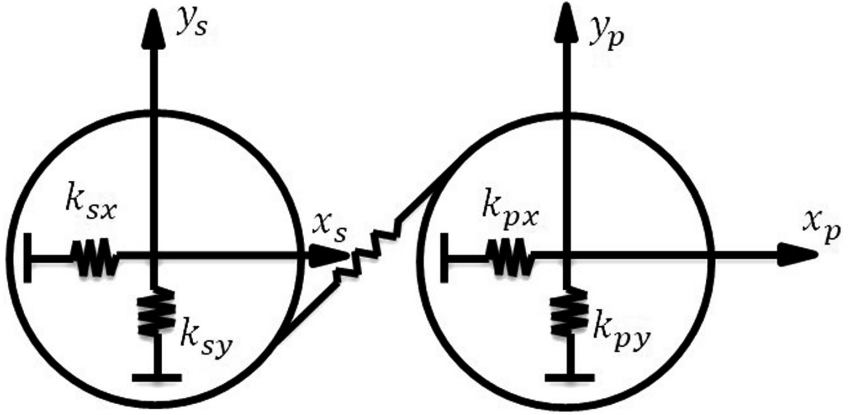


Fig. 4. Gear mesh model of two gears in contact

Where c_{rp} and c_{sp} are the contact ratios for the ring-planet and sun-planet gear pairs respectively. The Fourier coefficients in the Eqs. (14) and (15) are [2]:

$$\begin{aligned} a_{rp} &= -\frac{2}{l\pi} \sin[l\pi(c_{rp} - 2\gamma_{rp})] \sin(l\pi c_{rp}) \\ b_{rp} &= -\frac{2}{l\pi} \cos[l\pi(c_{rp} - 2\gamma_{rp})] \sin(l\pi c_{rp}) \\ a_{sp} &= -\frac{2}{l\pi} \sin[l\pi(c_{sp} - 2\gamma_{sp})] \sin(l\pi c_{sp}) \\ b_{sp} &= -\frac{2}{l\pi} \cos[l\pi(c_{sp} - 2\gamma_{sp})] \sin(l\pi c_{sp}) \end{aligned}$$

γ_{sp} and γ_{rp} are the mesh phasing angle at the sun-planet and ring-planet gear pairs.

2.1 Modelling for Gravity Effect

Gravitational force acting on the carrier, ring, sun and planets is periodic in the rotating carrier frame, resulting in fundamental external excitation source. The gravity force vector is

$$F_g(t) = [f_{cx} \ f_{cy} \ 0 \ f_{rx} \ f_{ry} \ 0 \ f_{sx} \ f_{sy} \ 0 \ f_{p1\xi} \ f_{p1\eta} \ 0 \ f_{p2\xi} \ f_{p2\eta} \ 0 \ f_{p3\xi} \ f_{p3\eta} \ 0]$$

With w representing c , r or s for carrier, ring or sun respectively, the force f_{wx} and f_{wy} are written as

$$f_{wx} = -m_w g \sin(\Omega_c t) \quad (16)$$

$$f_{wy} = -m_w g \cos(\Omega_c t) \quad (17)$$

Table 1. System design parameters

Parameter	Parameter values used in simulation
J_c inertia of carrier (kg-m ²)	57.72
m_c mass of carrier (kg)	786
J_p inertia of planet (kg-m ²)	1.12
m_{pn} mass of planet (kg)	57.799
J_s inertia of sun (kg-m ²)	0.86
m_s mass of sun (kg)	146
k_s stiffness of sun gear (N/m)	1×10^6
k_{st} torsional stiffness of sun (N-m/rad)	3×10^7
k_{rp} gear mesh stiffness between ring-planet	0.73×10^8
k_{sp} gear mesh stiffness between sun-planet	0.73×10^8
$\alpha_{r,s}$ pressure angle (deg)	24.6
k_{bp}, k_{bs} bearing stiffness at sun and planet	1×10^7
k_{g12}, k_{g34} bearing stiffness at gears	5×10^7
c_{rp} contact ratio between ring and planet	1.934
c_{sp} contact ratio between sun and planet	1.6242
r_c radius of carrier (mm)	270
r_s radius of sun (mm)	110
r_p radius of planet (mm)	160
T_c aerodynamic static torque on carrier (N-m)	15000
N_s Teeth on sun gear	16
N_p Teeth on planet gear	32
N_r Teeth on ring gear	80

and the forces on the n^{th} planet are

$$f_{pj\xi} = -m_j g \sin(\Omega_c t + \psi_n) \tag{18}$$

$$f_{pj\eta} = -m_j g \cos(\Omega_c t + \psi_n) \tag{19}$$

where, $\Omega_c = \omega_m / N_r$ (for the fixed ring)

ω_m = mesh frequency

N_r = number of teeth on the ring.

When gravity is not considered, the tooth loads at the different sun planet meshes do not vary with time and are identical on all the planets. Gravitational forces disturb the system symmetry and hence cause variation in the tooth loads causing large motion in the gears which lead to tooth wedging. The unequal load sharing between planets leads to unsymmetrical forces on the bearings and as a result bearing failure is susceptible.

3 Results and Discussion

Due to large weight of wind turbine components gravity has a significant impact on the vibration characteristics of the gearbox components. Equations of motion for all the gearbox components are derived using Lagrange method which are then solved numerically using β -Newmark method of integration with a sampling rate of 10^4 samples/sec. Time Domain data for sun gear is generated to study the effect of gravity on the vibration characteristics of the planetary gearbox of a wind turbine drivetrain. The gear mesh stiffness is assumed to be time varying as shown in Eqs. (14) and (15). As the point of contact changes, the stiffness at the gear mesh varies. This variation is directly affected by the gear contact ratio. In this study, a gear contact ratio greater than 1 is taken at all the gear pairs i.e. more than one teeth are in contact at the same time. The system parameters are given in Table 1 which are typical for a horizontal wind turbine. In order to study the dynamic behavior of the gearbox under the effect of gravity coupled with time varying mesh stiffness, time domain response of the sun is generated in the transverse directions.

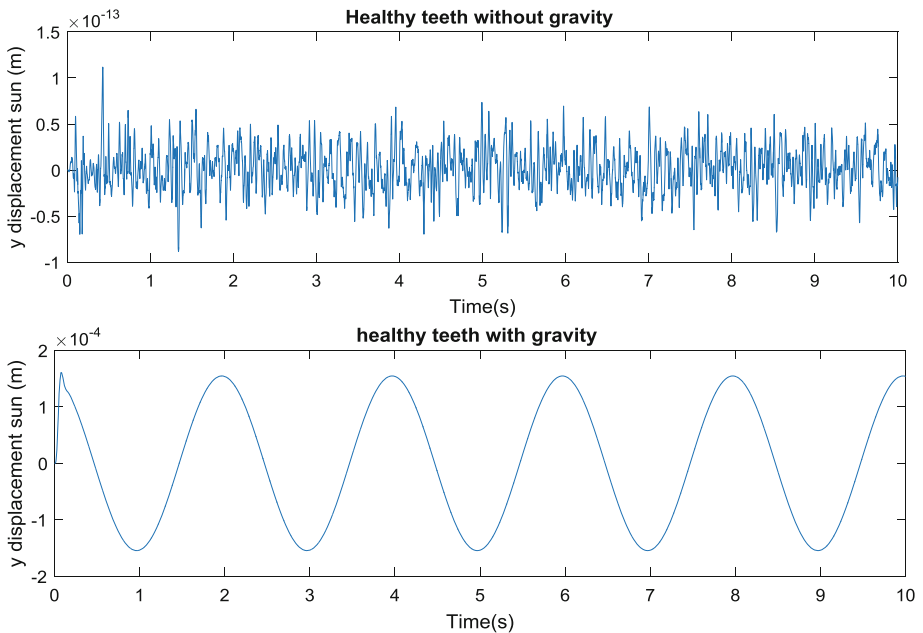


Fig. 5. Dynamic response of sun in y direction without and with gravity effect

The dynamic response of sun gear due to gear mesh stiffness variation with gravity is of higher magnitude than that without the consideration of gravity. The magnitude of response in the horizontal and vertical directions increases by several orders of magnitude (from the order of 10^{-13} to 10^{-4}) due to large mass of the drivetrain components. The response without the consideration of gravity is the result of mainly the parametric

excitation due to gear mesh stiffness variation under the influence of static torque and in absence of any dynamic external loading. It may be noted that the amplitude of the response is of the order of 10^{-13} m. When the effect of gravity is included as an external source of excitation, the vibration response in time domain is predominantly at the rotational frequency of the carrier (0.5 Hz). Similar response is noticed in the horizontal direction (not shown).

3.1 Simulation of Gear Tooth Crack

The tooth crack model is developed for a standard involute spur sun gear which is in mesh with the 3 planets. Both the planet and the sun have three degrees of freedom.

If $2\pi n\omega_s t \leq \theta_s \leq (2\pi n\omega_s t + \theta_c)$ where θ_c is the angle for which the cracked tooth remains in mesh calculated as $(2\pi/N_{ss})$, the stiffness k_{sp} is reduced by a factor of r .

The factor r depends on the depth of the crack and in this study the value of r is considered to be 0.75 for crack in the sun tooth. The gear mesh stiffness variation for the sun-planet gear pair with one cracked gear tooth in the sun gear is shown in Fig. 6. The stiffness varies during each engagement with the planet tooth and every time the cracked tooth on the sun engages with the planet tooth, the gear mesh stiffness drops during that engagement as seen in the figure. The cracked tooth is assumed to come into contact with the first planet gear at the start of the time ($t = 0$). In one cycle of the sun gear the cracked tooth comes in contact thrice but the mesh phasing phenomenon between the planets and the sun gear and the contact ratio which is greater than one (1.6242) causes the three dips to differ in shape.

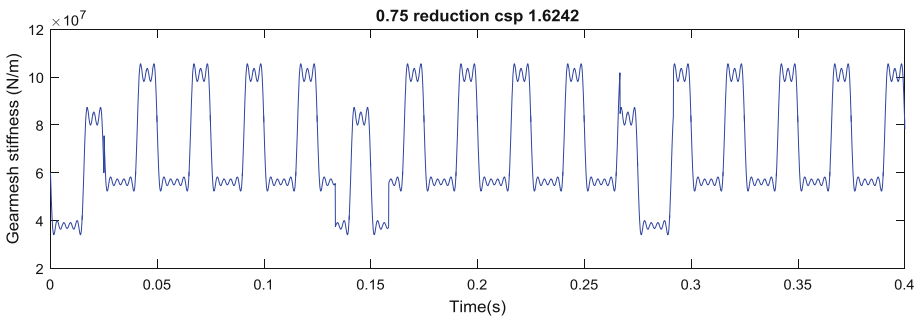


Fig. 6. Gear mesh stiffness (k_{sp}) variation for sun planet pair with crack in sun gear

3.2 Dynamic Response with Cracked Tooth

The gear mesh stiffness occurs due to elastic bending of the gear teeth in contact. This variation is directly affected by the gear contact ratio. In this study, a gear contact ratio greater than 1 is taken at all the gear pairs i.e. more than one teeth are in contact at the same time. Fault in gear tooth has a direct impact on the gear mesh stiffness at a localized region and varies in proportion to the severity of the fault.

When the cracked tooth comes in meshing the mean value of the gear mesh stiffness is shifted to a lower value due to localized reduction of effective bending stress of the tooth. In this model the crack of constant depth is assumed on the sun gear. Meshing of the sun gear with the three planet gears causes the gear mesh stiffness to dip three times in one cycle of sun rotation as shown in Fig. 6. This sudden decrease has been incorporated in the mathematical model to generate the dynamic response of the sun gear. The dynamic response of the sun gear without a cracked tooth is first simulated by solving the governing equations of motion. Once the data for several cycles are obtained, the similar vibration response for sun gear having a cracked tooth ($r = 0.75$) is obtained.

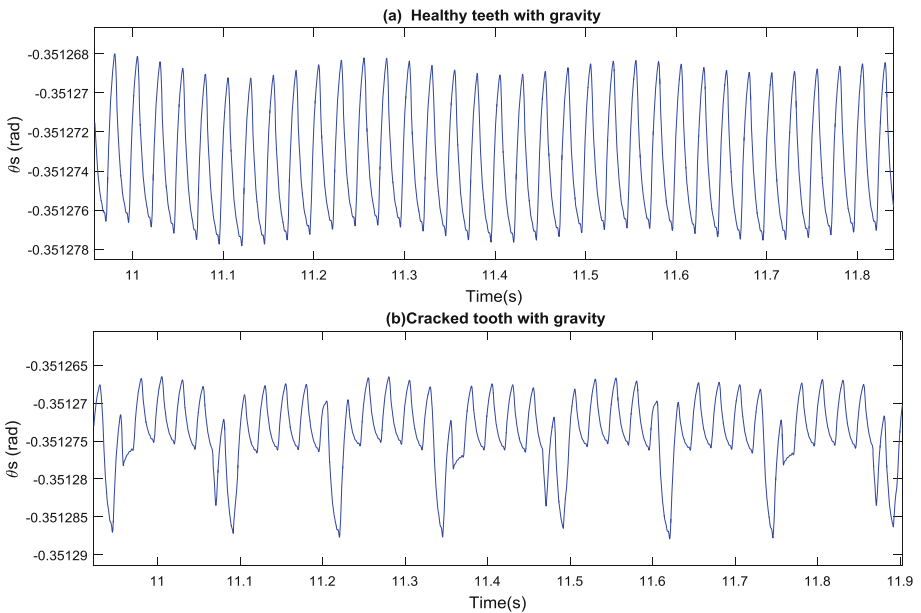


Fig. 7. Torsional vibration time domain data for sun gear (a) healthy tooth (b) cracked tooth

4 Diagnosis of Presence of Crack Using Difference Signal

Dynamic response generated for the sun gear from the healthy and defective gear tooth cases are used to generate an difference signal by subtracting the healthy gear signal from the defective one in time domain, ensuring that the initial position of the gears are identical.

Using the time domain data for sun gear torsional vibration response as shown in Fig. 7, a difference signal in time domain between healthy sun gear and sun gear with a cracked gear tooth is obtained. This Difference signal is used for further processing in exploring the possibility of gear tooth crack detection based on lateral and torsional vibration response. Similar Difference Signals are obtained for vertical and horizontal

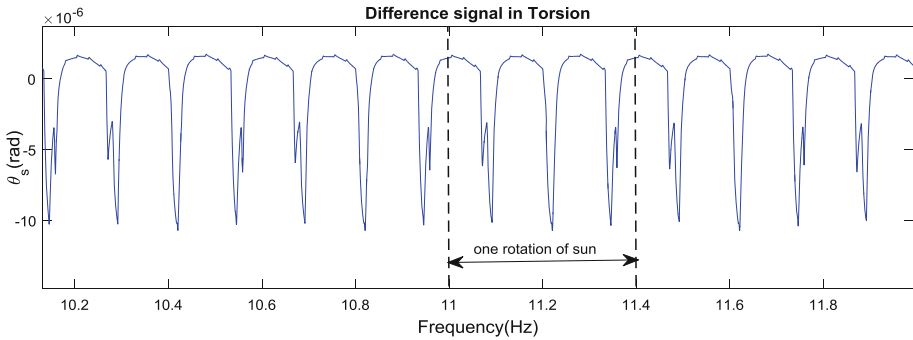


Fig. 8. Difference signal for torsional vibration response of the sun gear

directions. The Difference signal in torsional vibration is shown in Fig. 8. The simulated signal shown is a steady state difference signal after the initial transients die out within first 3–4 s. The steady state torsional vibration signal corresponding to one cycle of sun rotation exhibits sudden changes in the torsional displacement (3 times in one rotation) as can be observed in Fig. 8.

The difference Signal in time domain itself gives enough indication of presence of an anomaly in the engagement of the tooth of sun and planet. To get a better idea of the spectral nature of the Difference signal, the frequency domain decomposition of the faulty tooth time domain data is carried out and the resulting spectrum is shown in Fig. 9. The rotational speed of the sun gear is 150 rpm which is 2.5 Hz. In one cycle of rotation the cracked tooth comes into meshing three times that causes the stiffness to dip during the mesh. The amplitude of vibration suddenly increases. Thus, three peaks in the time domain data reflect the three engagements of the sun with the planet gear in one rotation of the sun. The FFT of difference signal in torsional direction (Fig. 8) shows that the frequency of 7.5 Hz is prominent, which is the frequency at which the cracked tooth of the sun meshes with the three planet gears. The harmonics of this fault frequency indicate a presence of fault in the sun gear. The harmonics of the rotational frequency of the sun (2.5 Hz) are visible in the frequency domain.

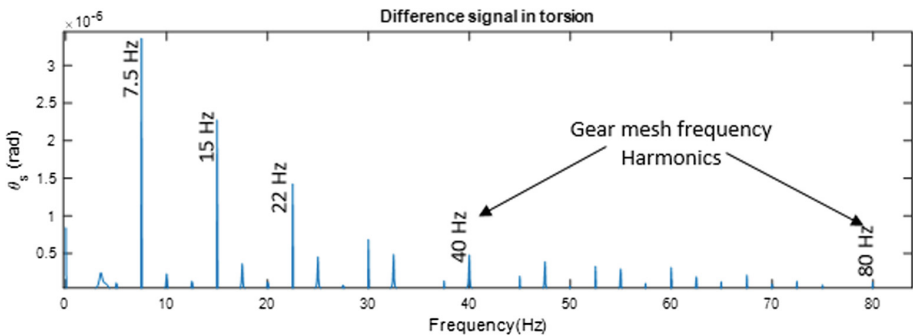


Fig. 9. Frequency spectrum of the difference signal for torsional vibration of the sun gear with a cracked tooth

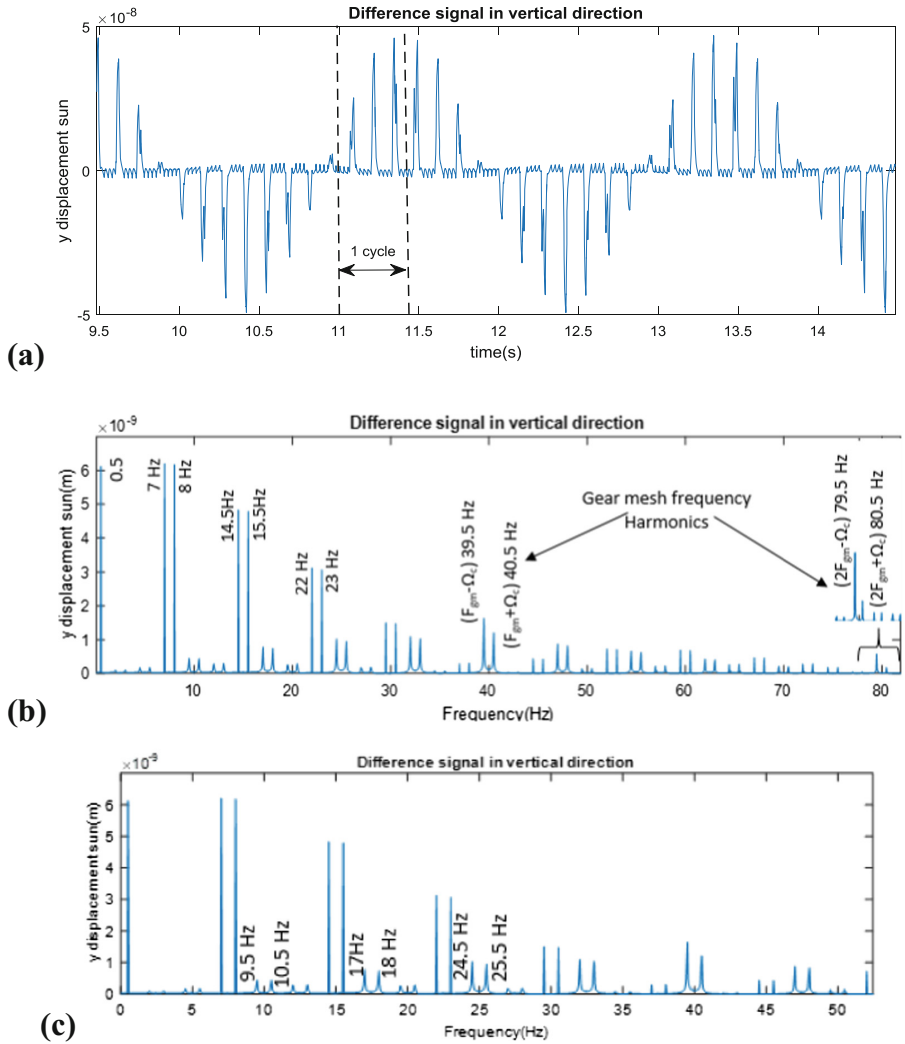


Fig. 10. Residual vibration response along x direction of the sun gear with a tooth crack (a) Time domain data (b) frequency spectrum (c) close up view of spectrum

The difference signal is also generated for vertical direction as the effect of gravity is prominent along this mode of vibration as shown in Fig. 10. One cycle of the sun gear (0.4 s) shows three peaks in the time domain. The time domain difference signal for vertical vibration of the sun gear indicates modulation of the 7.5 Hz frequency at which the sun gear tooth engages with the three planets during each orbital motion of the planet with their carrier. Due to the effect of gravity, one orbital motion of the planet causes modulation of the 3 cycles per rotation of the sun at the frequency of carrier rotation. Hence the sudden impulses in the x displacement are modulated in time with a repetition period of 2 s that corresponds to carrier rotation frequency.

The frequency spectrum of the Difference signal in vertical direction of the sun gear (shown in Fig. 10b and c) shows $(2.5 n \pm 0.5)$ Hz family of side bands. These sidebands assume significantly higher amplitudes when they are closer to the fault frequency (7.5 Hz) and its harmonics. The amplitude of these side bands for 7 Hz and 8 Hz and similarly at 14.5 Hz and 15.5 Hz are observed to have very high values.

The spectrum also distinctly exhibits the gear mesh frequency and its second harmonic. Thus, in absence of gravity, such rich spectrum would not have been noticed. The modulation is induced due to the gravity loading of the planet gear on the sun gear.

5 Conclusions

In order to explore and extract vibration response features to detect cracked gear tooth in the wind turbine gear transmission system, a dynamic mathematical model with three degrees of freedom per component is obtained using the Lagrange's method considering the effect of gravity. Using numerical integration and accounting for the gear mesh stiffness variation, the vibration response in transverse and torsional directions for the gears is evaluated. Due to the presence of a crack in the sun gear tooth, a localized stiffness reduction is simulated. To enable detection of changes in the dynamic response, the reference healthy gear vibration response is subtracted from the one for the cracked sun gear tooth in time domain to generate the difference signal. Both time-domain and frequency-domain features of the difference signals for the sun gear are studied. Presence of family of side bands around the sun rotational frequency and its harmonics separated by the carrier rotation frequency is noticed distinctly. It is noticed that these sidebands are stronger near the fault frequency (n times the rotational frequency of sun, where n is the number of planets) and its harmonics. These spectral characteristics of the difference signal can be useful in identifying the gear tooth crack in the wind turbine gearbox.

References

1. Lin, J., Parker, R.G.: Analytical characterization of the unique properties of planetary gear free vibration. *J. Vib. Acoust.* **121**, 316–321 (1999)
2. Lin, J., Parker, R.G.: Planetary gear parametric instability caused by mesh stiffness variation. *J. Sound Vib.* **249**(1), 129–145 (2002)
3. Peeters, J.L.M., Vandepitte, D., Sas, P.: Analysis of internal drive train dynamics in a wind turbine. *Wind Energy* **9**(1–2), 141–161 (2006)
4. Ambarisha, V.K., Parker, R.G.: Suppression of planet mode response in planetary gear dynamics through mesh phasing. *J. Vib. Acoust.* **128**(2), 133–142 (2006)
5. Todorov, M., Dobrev, I., Massouh, F.: Analysis of torsional oscillation of the drive train in horizontal-axis wind turbine. In: 2009 8th International Symposium on Advanced Electromechanical Motion Systems & Electric Drives Joint Symposium, Lille, pp. 1–7 (2009)

6. Shi, W., Kim, C.W., Chung, C.W., et al.: *Int. J. Precis. Eng. Manuf.* **14**, 153 (2013). <https://doi.org/10.1007/s12541-013-0021-2>
7. Zhang, A., Wei, J., Qin, D., Hou, S., Lim, T.C.: Coupled dynamic characteristics of wind turbine gearbox driven by ring gear considering gravity. In: 2017 ASME International Power Transmission and Gearing Conference, vol. 10, Cleveland, Ohio, USA, 6–9 August (2017)
8. Cooley, C.G., Parker, R.: A review of planetary and epicyclic gear dynamics and vibrations research. *Appl. Mech. Rev.* **66**, 040804 (2014). <https://doi.org/10.1115/1.4027812>



Experimental Investigations on Torsional Vibrations of a Rotor During a Rotor-Stator Rub

Md. Asjad Mokhtar, Ashish K. Darpe^(✉), and K. Gupta

Department of Mechanical Engineering, Indian Institute of Technology Delhi,
New Delhi, India
akdarpe@mech.iitd.ac.in

Abstract. Theoretical investigations on rotor-stator rub phenomenon are available on wide range of problems. However the experimental studies are limited in numbers. Further, the measurement studies on torsional vibration during rub are hardly any. The present work reports and discusses measurement of rotor's torsional vibrations during its contact with the stator and examines the possible rub diagnostic features. A simple rotor bearing system is made to interact with a stator pin mounted on a stiffer stator frame. The rotor assembly, with two discs and two support bearings, intends to model a turbopump where the central disc simulates the impeller and the overhanging disc is meant to represent turbine. A flexible coupling between the driver and the driven unit is provided to reduce the effects of any misalignment remaining in the system and to isolate the rotor from the motor. The measurement of torsional vibration is carried out using a torsional laser vibrometer. The measured signals during rub and no rub conditions are compared in time as well as in frequency domain to bring out the torsional vibrations features related to rub. Excitation of various torsional modes of the rotor system is experienced due to the frictional torque caused by the occurrence of rub. The presence of rotor's torsional mode frequencies, rotational harmonics and the bending natural frequency in the spectrum of torsional velocity signals are indicative of rub.

Keywords: Rotor-stator rub · Torsional vibration · Rotational laser vibrometer

1 Introduction

Rotating machines are essential to almost every domain of our modern world such as power generation, transportation, space application, machine tools etc. A constant pursuit of achieving higher power and efficiency makes these machines to operate under severe mechanical stresses and tighter clearances. Under these circumstances, contact between rotating and stationary part is likely to occur especially in the vicinity of critical speeds. It is one of the few causes that influence both lateral and torsional vibrations. Investigations on rotor stator rub phenomenon, discussing about the lateral vibration of the rotor, is available on wider range of problems. However the studies on torsional vibrational behaviour during rub are limited [1–3]. The unnoticed torsional vibration can lead to fatigue induced cracks and failures in any rotating machines.

The existing state of art on the rotor stator rub indicates the absence of experimental work on the torsional vibration features of the rotor during rub. However, some studies on lateral vibration measurement during rub are available. Among first few experimental work reported on rotor-stator rub, Beatty [4] correlates the proposed mathematical model with experimentally measured lateral vibration data during rub. It was observed that the amplitude of harmonic frequency component increases as the rubbing progresses to contact larger rotor circumference leading to excessive wear, instability and seizure. Muszynska and Goldman [5] have experimentally verified the presence of synchronous, sub-synchronous and chaotic vibration pattern of the rubbing rotor.

Pennacchi et al. [6] presented some results from an experimental test rig that reproduces a real machine rub condition and the effect of rotor rub on the labyrinth seal is analysed. The theoretically developed rotor model is verified and is proposed for reliable fault simulations with short-arc rub and relatively soft seal. On similar lines, Torkhani et al. [7] developed an experimental set-up for measuring rotor response during light, medium and heavy rub and have verified the theoretical model for reliable rub diagnostics. Gradually varying unbalance load is generated for different intensities of rub and the quantities such as non-linear shaft vibration, contact duration, transmitted force and the angular deceleration are measured. The theoretical and experimental findings are shown to be in good agreement except in some orbital response. In order to look for some unique rub identification characteristic, Li et al. [8] proposed a fault feature extraction method based on load identification and measured impact response. It was concluded that the impact force can characterize the rub fault and the method effectively extracts the impact force.

Theoretical and experimental works on rotor-stator rub are reviewed by Muszynska [9] and Richardet et al. [10] that help in identifying the areas exhaustively studied as well as the research gaps related to the rub problems. Features related to rub such as sub-harmonics and super-harmonics of rotational frequencies are reported by several researchers [4, 11, 12]. Prediction of instability due to cross coupling induced by frictional forces is reported [4].

Torsional vibration during rub is considered for the first time in theoretical simulations by Edwards et al. [13] that showed that the system is more stable with torsional effect included. Thereafter, few more theoretical investigation are carried out by Sun et al. [14], Al-Bedoor [15], Mohiuddin and Khuliff [16], Patel and Darpe [17] and Khanlo et al. [18]. These studies mainly discuss about incorporating the torsional degree of freedom into the system and identify rub diagnostic features.

To the best of the authors' knowledge, the first reported work on the measurement of torsional vibration during rub is by Diangui [1]. The study however is not an extensive one and only provides frequency spectrum of torsional and lateral vibration responses that exhibit natural frequencies along with the rotational harmonics. Lately, Vljajic et al. [2, 3] investigated torsional vibration response of a long flexible rotor in continuous contact with the surrounding stator for both forward synchronous whirling and backward dry-friction whirling. The torsional vibration is found to be excited by stick-slip forces during backward whirling motion. The measured torsional strain data

contain drive frequency, whirl frequency, torsional natural frequency and combination of whirl and drive frequency.

Compared to the volume of studies carried out on lateral vibrations for rub investigation, the literature on torsional vibration is very limited in theoretical work and practically insignificant in experimental studies. In view of the importance of the torsional vibration in rotating machinery, the present work reports an experimental study on the torsional vibration behaviour of a rubbing rotor for the rub diagnosis. The torsional vibration measurement is carried out using rotational laser vibrometer on a simplified two disc rotor system that undergoes through a single point contact with a stator pin. The measured vibration signals for different operating speeds identify the torsional vibration characteristics related to rub.

2 Experimental Setup of the Test Rig

The rotor system for the present test set-up is shown in Fig. 1. It consists of a bright steel rotor shaft of diameter 13 mm. There are two discs attached to the rotor shaft that is supported by two ball bearings mounted in the bearing pedestals at both the ends. Disc-1 is located at the centre of two support bearings that simulates the impeller, and the Discs-2 is placed in an overhang position close to the bearing-2 to represent the turbine. The rotor shaft is driven by a DC motor coupled through a flexible coupling at one end. The purpose of flexible coupling between the driver and the driven unit is to reduce the effects of any misalignment remaining in the system and to isolate the rotor from the motor. The stator considered for the interaction with the rotor is a slender pin mounted on a rectangular stator frame fixed to the rotor base. The full rotor-stator assembly is mounted on a platform (Fig. 1) which is fixed to a rigid base plate that is

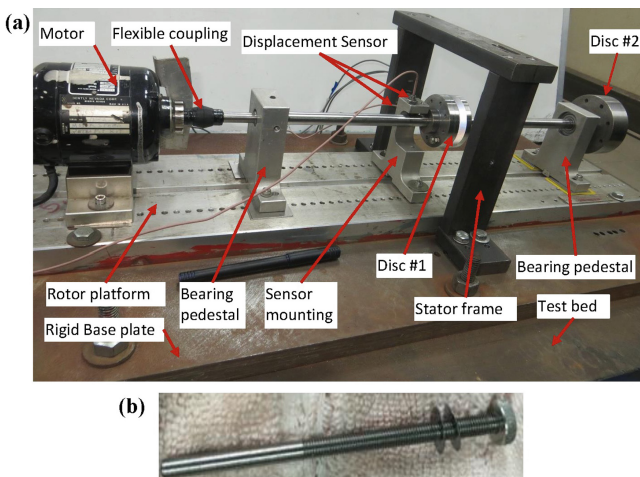


Fig. 1. (a) Experimental test rig assembly for rotor-stator rub (b) Stator pin.

further mounted on the grounded T-slot test bed. The geometric and material properties of the rotor system assembly are enlisted in Table 1.

Table 1. Material and geometrical property of the rotor-stator system

Component	Material	Parameter	Dimension
Rotor shaft	Silver steel	Length	500 mm
		Diameter	13 mm
Disc-1	EN24	Diameter	80 mm
		Thickness	35 mm
Disc-2	EN24	Diameter	78 mm
		Thickness	30 mm
Stator rod	Mild steel	Length	50 mm
		Diameter	8 mm

2.1 Test Rig Setup

The rotor shaft, discs, base plate for fixtures mounting, the stator pin and the stator frame are fabricated. Two deep groove ball bearings, one at the motor side and the second at the other end, are used to support the rotor. The schematic diagram of the full rotor-stator system with instrumentation and data acquisition process is shown in Fig. 2, and the experimental test rig with instrumentation is shown in Fig. 3.

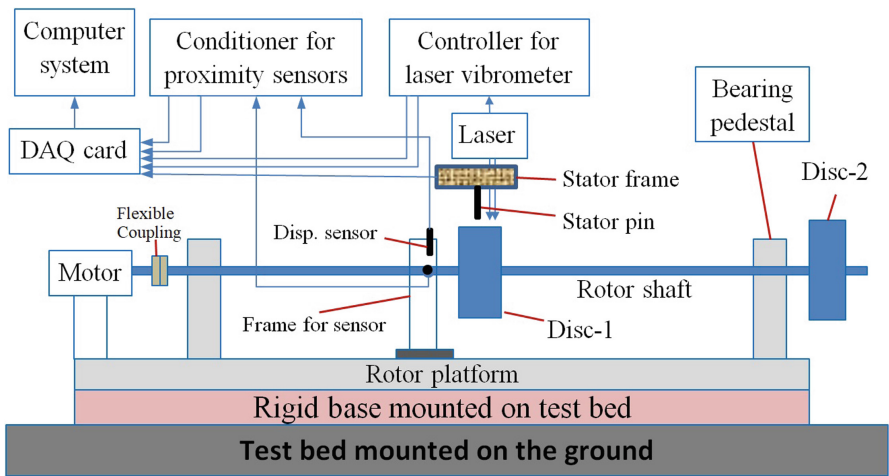


Fig. 2. Schematic diagram of the experimental set up with sensors and data acquisition system.

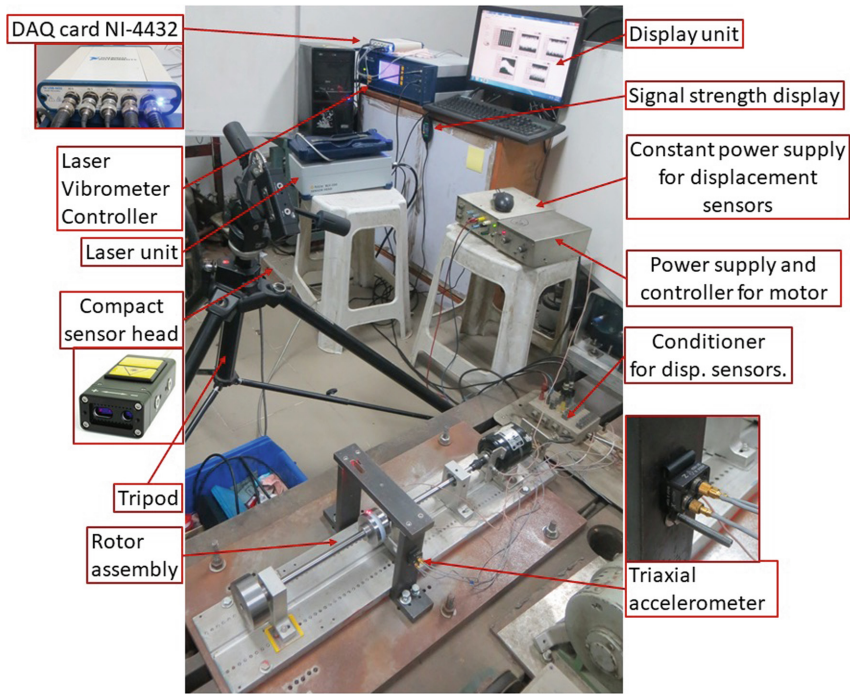


Fig. 3. Full experimental setup with instrumentation

2.2 Instrumentation and the Measurement Process

The lateral vibration of the rotor shaft in vertical and horizontal direction is acquired using proximity sensors positioned near the disc-1 as shown in Fig. 1. The torsional vibration is measured at the disc-2 location (Fig. 3) through rotational laser vibrometer (RLV5500). The data acquisition cards used for the measurement are NI-4432 in the LabView environment. A brief description of the equipment, sensors and data acquisition card is summarised below.

- DC motor with feedback controller is used to drive the rotor shaft. The feedback mechanism uses an eddy current based displacement sensor mounted on the motor shaft that provides rotational speed information to the controller which is connected to the motor for speed control.
- Two deep groove ball bearings (Bearing 1; SKF 6001-2Z and Bearing 2; SKF 6201-2Z) are used to support the rotor assembly.
- For the lateral vibration measurements, eddy current based displacement sensor of sensitivity 8 V/mm is used. The proximity sensor is from the Bentley Nevada rotor kit (Proximator model: 20885-01, Sensor sensitivity = 200 mVolt/mil = 7.87 V/mm)
- For torsional vibration measurements, Polytec make rotational laser vibrometer (RLV-5500) is used. The parallel laser beam is made to incident on the retro-reflective tape glued on the disc-1 at which the torsional vibration is being measured.

- The tachometer PLT200 of Monarch make is used for the RPM measurement and the pulse output given by the tachometer is used as the reference signal for the data processing.
- A five channel NI-4432 data acquisition card with output voltage range of ± 40 V, simultaneous sampling of 102.4 kS/s per channel and A/D converter resolution of 24 bits is used for the lateral and torsional vibration measurements in the Labview platform.

2.3 Torsional Vibration Measurement

A rotational laser vibrometer (RLV) [19, 20] is used for the torsional vibration measurement which consists of a laser sensor head (RLV-500) and a controller (RLV-5000). The sensor head has a Laser unit and a compact sensor. The laser unit includes a Helium-Neon laser and two high-precision interferometers for converting minute frequency changes of the reflected laser light into electrical signals. These signals are then decoded in Controller. The output of the decoding process is voltage signals proportional to the real-time angular velocity which can be integrated to get angular displacement. The principle of measurement in the laser vibrometer is based on the Doppler effect. The measurement of instantaneous rotational velocity is done in the first place and then it is further integrated in the controller itself to send out the angular displacement in terms of AC voltage signals.

3 Results and Discussion

This section discusses the measurement of vibration signals during rub as well as without rub. In order to understand and interpret the acquired signals properly, the system natural frequencies are first evaluated experimentally. Thereafter, the vibration response of the rotor operating at certain speed is acquired for rub and no rub conditions. The acquired signals are then analysed in time and frequency domain and the vibration characteristics of torsional oscillations and the features related to rub are explained.

3.1 Measurement of Rotor Natural Frequencies

The rap test is conducted on the rotor for the measurement of its bending and the torsional natural frequencies. During rap test, the transducer location for lateral vibration response measurement is on the shaft near disc-1 as shown in Figs. 1 and 2. The dual laser beam for the torsional vibration measurement is focused on the disc-1 during the rap test. For the evaluation of bending natural frequency, radial impact is made on the disc-1 while rotor shaft remains connected to the motor through the flexible coupling. No any constraint is imposed on the rotor system for the test. However for the measurement of torsional natural frequency motor shaft is constrained to rotate and a tangential impact is made on the disc-1. In the free-free condition, with motor coupled to the rotor, rigid rotation was dominant and it was difficult to capture the torsional natural frequency.

The observed bending mode natural frequency of the rotor is found to be 74 Hz. The acquired signals for lateral measurement during rap test are not shown here. However, the time response of the rap test in torsional measurement and the corresponding frequency spectrum are shown in Fig. 4 that depicts the torsional natural frequency of 324 Hz. In addition to that, the bending natural frequency of 74 Hz is also observed in frequency spectrum of torsional vibration response.

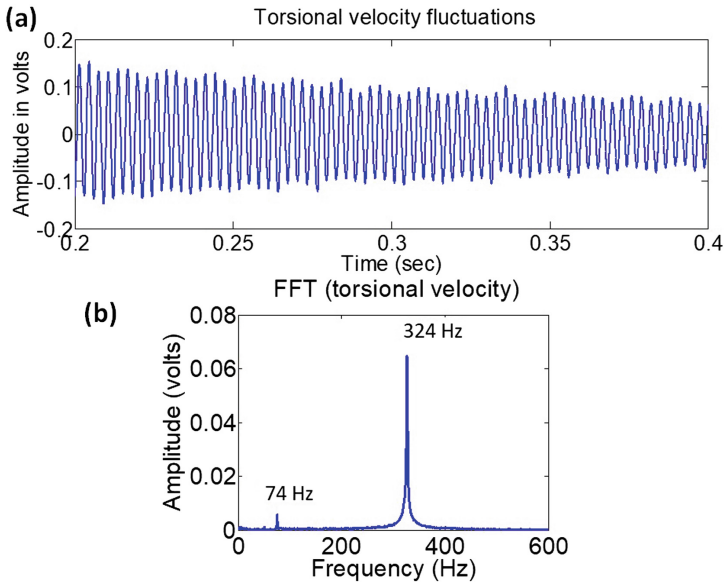


Fig. 4. Rap test for torsional natural frequency; (a) time response, (b) frequency spectrum.

3.2 Steady State Operation Without Rub

The rotor system with unbalance of 6.5 gm at an eccentricity of 1.59 cm at the central disc of the rotor system is operated at a certain speed without allowing rub to take place. The measured signal consists of horizontal and vertical vibration response acquired through the eddy current probes. The purpose of this test is to know the baseline vibration amplitudes in lateral directions under steady state operation in absence of rotor-stator contact. Based on the measured amplitudes in lateral vibration, the clearance between the rotor and stator is maintained accordingly for rub and no rub conditions. Measurements are recorded at operating speeds of 2000 rpm and 2273 rpm.

3.3 Measurement of Rotor Response with Rub at Rotational Speed of 2000 RPM (33.3 Hz)

Measurement of rotor's lateral and torsional vibration is carried out during rub for operational speed of 2000 rpm (33.34 Hz). The steady state response amplitudes in vertical and horizontal directions are observed to be 286 micron (peak-to-peak). For the

rotor stator contact, a stator pin (Fig. 1b) is mounted horizontally on a very high stiffness stator frame (Fig. 1a) which is fixed to the base plate. Depending on the observed steady state amplitude in horizontal direction, a clearance between rotor and stator is maintained at 70% of the peak amplitude. The clearance maintained in this particular case is approximately 100 micron. The spinning rotor under whirling condition comes into contact with the stator pin and the vibration measurement during rub is carried out through various sensors and data acquisition system. The measured signal consists of torsional displacement, torsional velocity and the horizontal vibration of the rotor shaft.

The time and frequency domain signals for the torsional vibration response are shown in Figs. 5 and 6. In the time response of torsional displacement (Fig. 5a), it can be observed that there is a dominant low frequency component on which a high frequency signal is riding. The corresponding spectrum (Fig. 6a) also shows that the lower frequency is 6.5 Hz and the higher frequency is 324 Hz. The higher frequency (324 Hz) is the rotor torsional natural frequency while lower one is also a torsional natural frequency of the system when the motor is coupled to the rotor through the flexible coupling (Fig. 1). As the stiffness of the flexible coupling is very low, the equivalent torsional stiffness of the parts between the two inertial components (motor and the disc-1) becomes very low. Hence, the first torsional natural frequency of the rotor system including motor becomes 6.5 Hz due to which, it is difficult to excite the rotor system in the higher torsional mode corresponding to 324 Hz during rub. However, both the frequencies are observed in the torsional vibration signal during rub

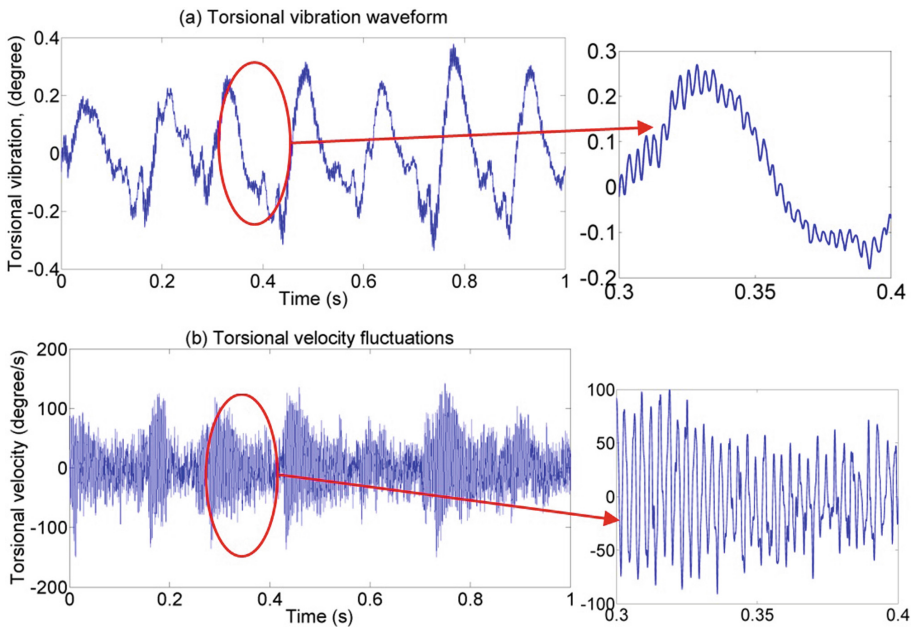


Fig. 5. Time domain response observed during rub at operating speed of 2000 rpm; (a) torsional displacement, (b) torsional velocity.

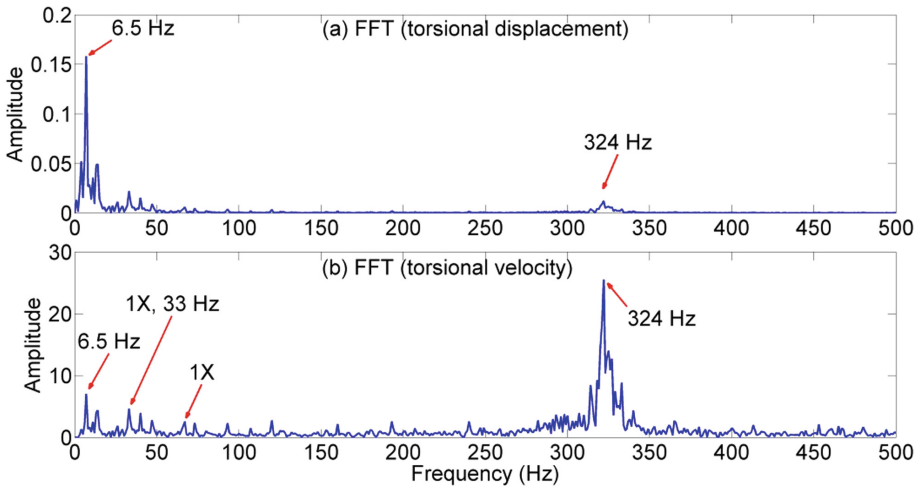


Fig. 6. Frequency spectrum of the response observed during rub at operating speed of 2000 rpm; (a) torsional displacement, (b) torsional velocity.

(Fig. 6a), although the 324 Hz frequency component is weaker as compared with the 6.5 Hz frequency component.

On the contrary, the torsional velocity response (Fig. 5b) appears to be dominated with rotor's torsional natural frequency (324 Hz) while the lower frequency (6.5 Hz) is also present in the time response signal. The corresponding frequency spectrum (Fig. 6b) reveals the same information for the presence of various frequency components. In addition to that, the frequency spectrum of torsional velocity also shows harmonics (1X, 2X) of rotational speed.

A close observation on the Fig. 5a indicates that the higher frequency (i.e. torsional natural frequency, 324 Hz) waveform is riding on the lower frequency waveform (i.e. 1st torsional natural frequency including the motor, 6.5 Hz). However, in the torsional velocity response (Fig. 5b) the higher frequency waveform is dominant and is modulated with 6.5 Hz frequency. It is important to note that the measurement of torsional vibration response is made through rotational laser vibrometer (RLV) which is based on Doppler effect principle. As explained earlier in the Sect. 2.3 that the transducer measures the rotational velocity fluctuation directly and then integrates it to convert into rotational deflection signal hence the higher frequency component weakens significantly.

3.4 Measurement of Rotor Response with Rub at Rotational Speed of 2274 RPM (37.9 Hz)

For the repeatability of the experimental findings, similar test at a speed of 2274 rpm is carried out and the frequency spectrum for torsional displacement and torsional velocity are shown in Fig. 7. At this speed the clearance between rotor and stator is maintained at 127 micron which is 70% of the peak displacement in horizontal direction under steady state operation without rubbing.

In the spectrum plot of torsional displacement, the frequency component of 6.5 Hz is observed along with the rotational harmonics and the rotor's torsional natural frequency (324 Hz). The observation is similar to the observed frequency components in the spectrum of torsional displacement for speed 2000 rpm (33 Hz) except for the dominating appearance of the rotational frequency component. The reason for such a clear rotational frequency component in the torsional response is explained in the next paragraph. Further, in the torsional velocity response spectrum, the rotor's torsional natural frequency component is clearly dominating. The rotational frequency components however are also significant.

There is a coincidence at this particular rotational speed (37.9 Hz), that it is close to the half of rotor's bending natural frequency ($37.9 \approx \frac{1}{2}(74)$). Due to the rubbing, residual misalignment and other irregularity associated with the experimental setup, the 2X frequency component gets closer to the rotor's bending natural frequency and hence a virtual resonance is experienced by the rotor that gives rise to the rotational frequency components in the spectrum plots.

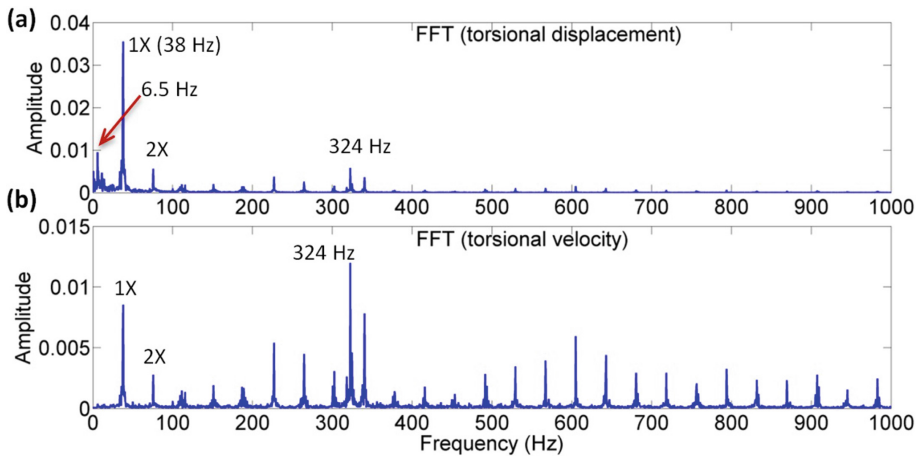


Fig. 7. Frequency spectrum of the response observed during rub at operating speed of 2274 rpm; (a) torsional displacement and (b) torsional velocity.

4 Conclusions

The primary objective of this work is to measure and study the torsional vibration characteristics for a rubbing rotor that simulates a turbopump consisting of impeller and a turbine. The experimental test rig for the present work consists of a rotor shaft with two discs and supported by two ball bearings. The experiments are performed to measure the vibration signals of rotor's torsional vibration during rotor-stator contact. During rub, the frequency content of the torsional vibration spectrum indicates a clear presence of rotor's torsional mode frequencies along with the rotational harmonics and the bending natural frequency. The torsional velocity response shows clear indications about the presence of torsional frequencies and hence the occurrence of rub.

Acknowledgment. This work is supported by Aeronautics Research and Development Board (ARDB), DRDO, Government of India (Project ref. no. DARO/08/1041661/M/I). The authors gratefully acknowledge the financial support.

References

1. Diangui, H.: Experiment on the characteristics of torsional vibration of rotor-to-stator rub in turbomachinery. *Tribol. Int.* **33**(2), 75–79 (2000)
2. Vlajic, N., Liu, X., Karki, H., Balachandran, B.: Rotor torsion vibrations in the presence of continuous stator contact. *ASME Int. Mech. Eng. Congr. Expo. Proc.* **4**, 1–10 (2012)
3. Vlajic, N., Liao, C.-M., Karki, H., Balachandran, B.: Draft: stick-slip motions of a rotor-stator system. *J. Vib. Acoust.* **136**, 21005-1–21005-8 (2014)
4. Beatty, R.F.: Differentiating rotor response due to radial rubbing. *J. Vib. Acoust. Stress Reliab. Des.* **107**, 151–160 (1985)
5. Muszynska, A., Goldman, P.: Chaotic responses of unbalanced rotor/bearing/stator systems with looseness or rubs. *Chaos, Solitons Fractals* **5**(9), 1683–1704 (1995)
6. Pennacchi, P., Bachschmid, N., Tanzi, E.: Light and short arc rubs in rotating machines: Experimental tests and modelling. *Mech. Syst. Signal Process.* **23**(7), 2205–2227 (2009)
7. Torkhani, M., May, L., Voinis, P.: Light, medium and heavy partial rubs during speed transients of rotating machines: Numerical simulation and experimental observation. *Mech. Syst. Signal Process.* **29**, 45–66 (2012)
8. Li, Y., Zhang, J., Wang, L., Chen, Y.: A fault feature extraction method for rotor rubbing based on load identification and measured impact response. *Procedia Eng.* **24**, 793–797 (2011)
9. Muszynska, A.: *Rotordynamics*. Taylor and Francis Group (2005)
10. Jacquet-Richardet, G., et al.: Rotor to stator contacts in turbomachines. *Rev. Appl. Mech. Syst. Signal Process.* **40**(2), 401–420 (2013)
11. Childs, D.W.: Rub-induced parametric excitation in rotors. *J. Mech. Des. Trans. ASME* **101**, 640–644 (1979)
12. Groll, G.V., Ewins, D.J.: A mechanism of low subharmonic response in rotor/stator contact-measurements and simulations. *J. Vib. Acoust.* **124**, 350–358 (2002)
13. Edwards, S., Lees, A.W., Friswell, M.I.: The influence of torsion on rotor/stator contact in rotating machinery. *J. Sound Vib.* **225**(4), 767–778 (1999)
14. Sun, Z., Xu, J., Zhou, T., Tan, N.: Study on the influence of bending-torsion coupling in an impacting-rub rotor system. *Appl. Math. Mech. English Ed.* **24**(11), 1316–1323 (2003)
15. AL-Bedoor, B.O.: Transient torsional and lateral vibrations of unbalanced rotors with rotor-to-stator rubbing. *J. Sound Vib.* **229**(3), 627–645 (2000)
16. Mohiuddin, M.A., Khulief, Y.A.: Coupled bending torsional vibration of rotors using finite element. *J. Sound Vib.* **223**(2), 297–316 (1999)
17. Patel, T.H., Darpe, A.K.: Coupled bending-torsional vibration analysis of rotor with rub and crack. *J. Sound Vib.* **326**, 740–752 (2009)
18. Khanlo, H.M., Ghayour, M., Ziaei-Rad, S.: The effects of lateral-torsional coupling on the nonlinear dynamic behavior of a rotating continuous flexible shaft-disk system with rub-impact. *Commun. Nonlinear Sci. Numer. Simul.* **18**(6), 1524–1538 (2013)
19. Halliwell, N.A., Pickering, C.J.D., Eastwood, P.G.: The laser torsional vibrometer: a new instrument. *J. Sound Vib.* **93**(4), 588–592 (1984)
20. Halliwell, N.A.: The laser torsional vibrometer: a step forward in rotating machinery diagnostics. *J. Sound Vib.* **190**(3), 399–418 (1996)